Brookhaven National Laboratory

Jefferson Lab

U.S. DEPARTMENT of ENERGY

Electron-Ion Collider

Preliminary Design Report 2025

Draft

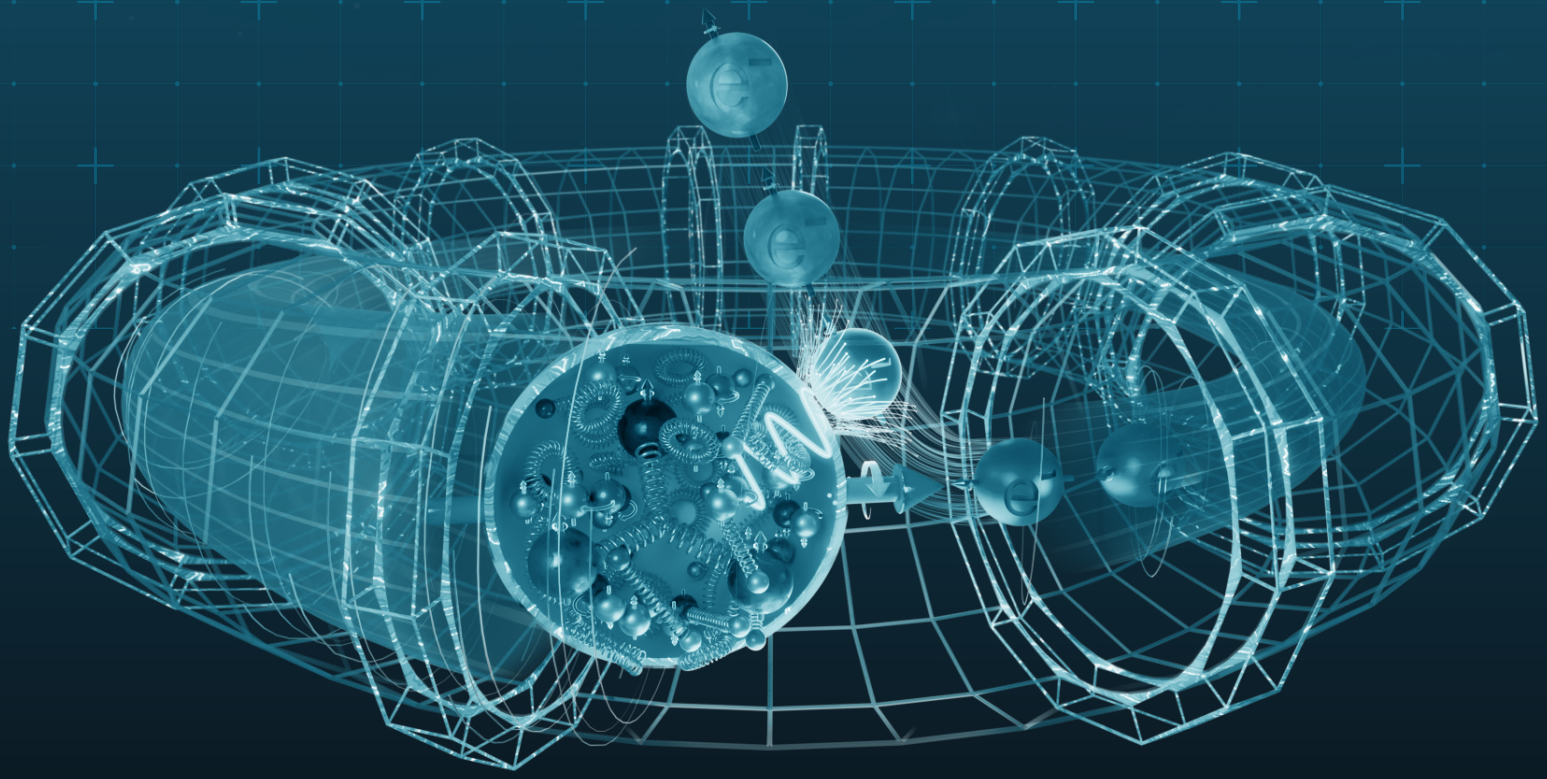

DRAFT
January 7, 2026

Electron Ion Collider
Preliminary Design Report

Executive Editors:
S. Peggs[1], T. Satogata[2].

Editors:
E-C. Aschenauer[1], M. Blaskiewicz[1], A. Blednykh[1], R. Ent[2], A. Fedotov[1], C. Folz[1], C. Montag[1], S. Nagaitsev[1], V. Ptitsyn[1], V. Ranjbar[1], C. Schaefer[1], V. Schoefer[1], K. Smith[1], J. Tuozzolo[1].

Authors:
To be completed ...

[1]Brookhaven National Laboratory, USA
[2]Thomas Jefferson National Accelerator Facility, USA

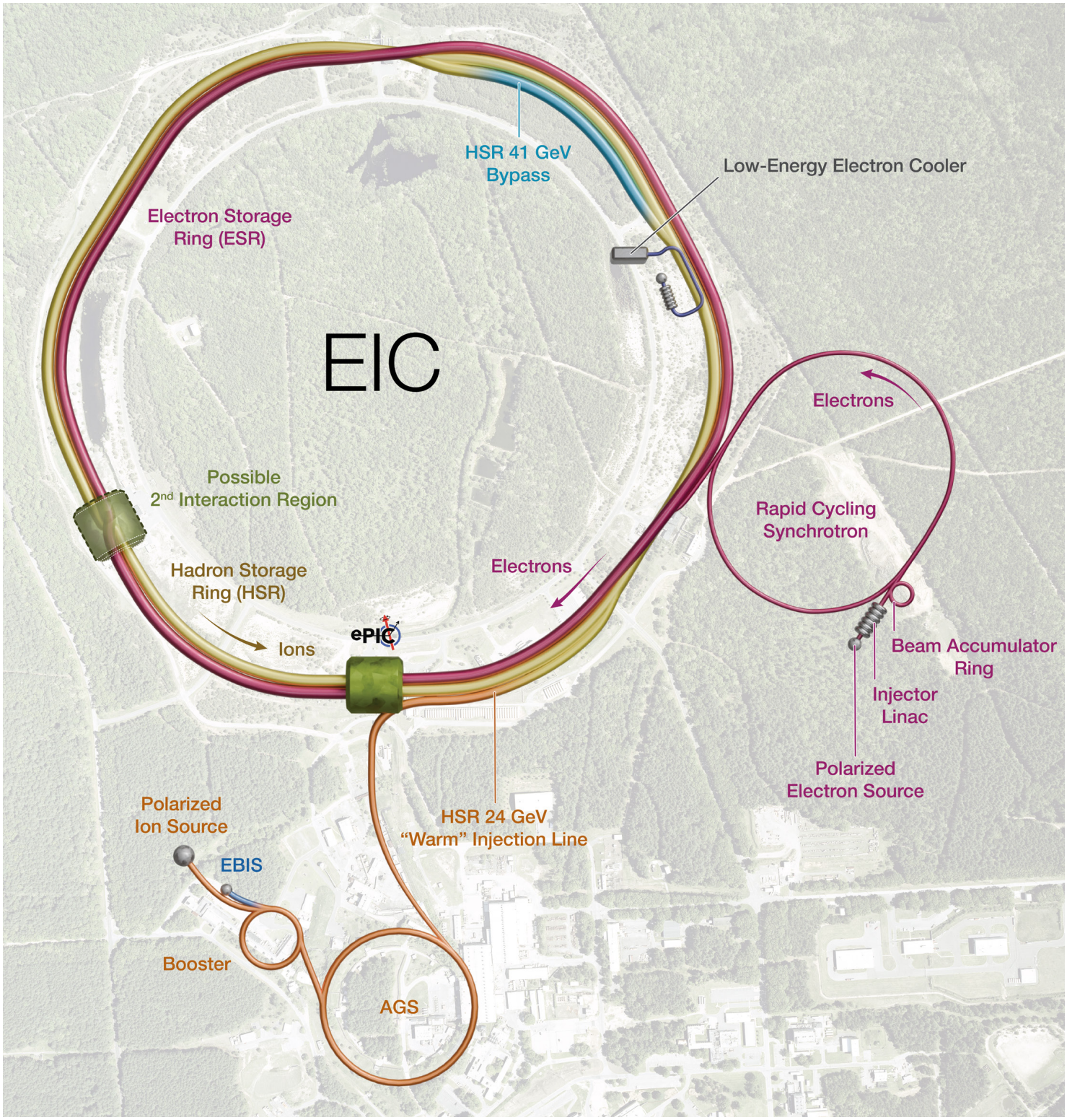
HSR 41 GeV
Bypass
Low-Energy Electron Cooler
Electron Storage
Ring (ESR)
EIC
Electrons
Possible
2nd Interaction Region
Rapid Cycling
Synchrotron
Hadron Storage
Ring (HSR)
Electrons
Ions
ePIC
Beam Accumulator
Ring
Injector
Linac
Polarized
Electron Source
Polarized
Ion Source
HSR 24 GeV
"Warm" Injection Line
EBIS
Booster
AGS

Brief Contents

Contents

List of Figures

List of Tables

Executive Summary

The Electron-Ion Collider (EIC) is being designed by Brookhaven National Laboratory (BNL), Jefferson Laboratory, and other national and international partners. It will collide polarized electrons with protons and other hadrons to produce snapshots of those particles' internal structures. The electron beam, employed as a probe, will reveal the arrangement of the quarks and gluons that make up the protons and neutrons of nuclei.

The EIC will study five pillars of a compelling science case:

- How do quarks, gluons, and orbital angular momentum contribute to proton spin?
- Does the mass of visible matter emerge from quark-gluon interactions?
- How can we understand QCD dynamics and the relation to confinement?
- How do quark-gluon interactions create nuclear binding?
- Does gluon density in nuclei saturate at high energy?

These questions lead to challenging high-level requirements:

- Peak electron-proton luminosities in a range from 10^{33} to 10^{34} $\mathrm{cm}^{-2}\mathrm{sec}^{-1}$
- Electron-proton center-of-mass energies from 29 to 100 GeV, upgradeable to 140 GeV
- Polarization levels of $\sim$70% for both electrons and light ions
- Collisions with hadron beams from protons to the heaviest stable nuclei
- Possibly more than one interaction region.

Several key accelerator physics concepts enable the EIC to meet these performance challenges:

- Large proton beam emittance ratio (11/1)
- Large crossing angle (25 mrad)
- Polarization preservation from source to collisions
- Large beam-beam tune shift parameters for both electrons (0.1) and protons (0.01)
- Very high bunch intensities.

The corresponding technology challenges include:

- Hadron beam cooling
- Spin-transparent beam optics
- Superconducting RF crab cavities
- Large-aperture superconducting magnets
- Impedance minimization
- Machine protection and collimation
- Synchrotron radiation power dissipation and heat loads.

Table 1 lists more of the key parameters of the EIC.

Parameter	**Units**	**Value**
Circumference	km	3.834
Center-of-mass energy	GeV	29 to 140
Number of bunches		1160
Proton bunch charge	nC	11
Electron bunch charge	nC	28
RMS proton bunch length	mm	60
RMS electron bunch length	mm	7.0
Proton β^* H	mm	800
V	mm	72
Electron β^* H	mm	450
V	mm	56
RMS proton emittance H	nm	11
V	nm	1
RMS electron emittance H	nm	20
V	nm	1.3
Luminosity	$10^{34}\,\mathrm{cm}^{-2}\mathrm{sec}^{-1}$	1

Table 1: Key electron-ion collision parameters.

Timeline:

2019	"Mission Need" status CD-0
2020	BNL selected as the EIC site
2021	"Alternative Selection and Cost Range" status CD-1
2024	Approval of a first round of early procurements, CD-3A
2025	Second round of early procurements awaiting approval, CD-3B
2026	"Performance Baseline" review planned, for CD-2 approval
2026	Potential approval of CD-3 "Start of Construction"
2034	Planned start of operations after CD-4 "Project Completion"

Chapter 1

Introduction and Project Overview (editor: Nagaitsev)

1.1 Physics Case of the Electron-Ion Collider

In the decades since the discovery of quarks, experiments in nuclear and particle physics have led to a fundamental theory of strong interactions — quantum chromodynamics (QCD) — that describes an extraordinary richness of nature at the subatomic level. The visible mass of matter in our universe that constitutes the galaxies, planets, and life itself, is made up of a dynamic substructure of quarks that are bound together by force-carrying gluons inside the protons and neutrons of atomic nuclei. Understanding how the properties of matter originate from the deeply fundamental constituents of QCD is the primary goal of nuclear physics, and the central motivation for polarized electron-proton and electron-ion collisions at the Electron-Ion Collider (EIC).

To date, a global program of precision measurements with high energy spin-polarized particle beams has begun to quantify how the intrinsic spins and orbital momenta of quarks, anti-quarks, and gluons each contribute to the characteristic spins of observed particles. However, the mechanism by which this complex system results in the characteristic spin $\frac{1}{2}$ of the nucleon is not yet understood. The EIC has the capability of answering this question.

Neutrons and protons bound inside atomic nuclei exhibit collective behavior that reveals the QCD substructure under extreme conditions. We now know, through laboratory experiments with high energy heavy ion collisions at RHIC [**?**] and the CERN Large Hadron Collider (LHC) [**?**], that nuclear matter is transformed into a plasma of quarks and gluons at temperatures and densities similar to those of the nascent universe, moments after the Big Bang. The observation that this quark-gluon plasma acts like a strongly coupled "perfect fluid" [**?**] came as a remarkable surprise. Together with the understanding that the formation and evolution of this extreme phase of QCD matter is dominated by the properties of gluons at high density, it brought widespread interest to the study of nuclear matter dominated by the strong force.

The most energetic nuclear collisions, including electron-proton collisions at HERA [**?**], established that gluons dominate the structure of nuclear matter when probed at high energies. This arises from the property that gluons, unlike their electromagnetic analogue (the photon), can interact directly with each other. Like quarks, gluons can interact through a "color" charge. The energy of self-interaction among the gluons accounts for a significant fraction of the nucleon mass. In collisions at

higher and higher energies the density of gluons seen in the nucleon increases rapidly and without apparent limit. While the gluon density increase must saturate at some point, this saturation has not yet been observed, and its mechanism is of fundamental interest. It is widely conjectured that such a saturated gluonic state may have universal properties for all strongly interacting particles. The EIC, through high energy collisions of electrons with heavy nuclei, is expected to enable detailed studies of this extraordinary state of matter.

Nuclear physicists have developed new phenomenological tools in the last two decades, enabling remarkable tomographic images of the quarks and gluons inside protons and neutrons. These tools are being used and will be further enhanced at the upgraded 12 GeV CEBAF [**?**] at TJNAF, and in the COMPASS [**?**] experiment at CERN. Applying these new tools to study the transition of matter from being dominated by quarks to being governed by gluons requires the higher energy and higher beam polarization of the EIC.

A worldwide community of scientists came together at many international conferences and workshops over the past several years, in the light of these advances and discoveries. They articulated the key science questions to be answered by the next-generation facility, the EIC, and broadly specified its performance requirements. A summary White Paper was published in 2014, following an intensive ten-week workshop held at the University of Washington's Institute for Nuclear Theory (INT) in 2011. Updated in 2016 [**?**], it presents the science case for an EIC, and the accelerator and detector concepts required to achieve them, including some "golden measurements".

The Department of Energy's Nuclear Science Advisory Committee addressed these studies. Its 2015 Long Range Plan for U.S. Nuclear Physics [**?**] acknowledged the "qualitative leap in technical capabilities" required for the EIC, and identified the EIC as "the highest priority new facility construction following the completion of FRIB". In 2018 this program was endorsed by the National Academies of Sciences Committee in "An Assessment of U.S.-Based Electron-Ion Collider Science" [**?**], stating:

"An EIC can uniquely address three profound questions about nucleons — neutrons and protons, and how they are assembled to form the nuclei of atoms:

- How does the mass of the nucleon arise?
- How does the spin of the nucleon arise?
- What are the emergent properties of dense systems of gluons?"

These questions call for an EIC with capabilities that far exceed any current or past collider facility:

- A range of center-of-mass energies E_{CM} from 20 to 140 GeV, enabling a kinematic reach well into the gluon-dominated regime;
- Highly polarized ($\approx$70%) electron, proton, and light nuclear ion beams (for example, deuterons, or ^{3}He), enabling a comprehensive study of the nucleon structure including their spin. The electron beam brings to bear the unmatched precision of the electromagnetic interaction as a probe, while polarized nucleon beams are needed to determine the correlations of sea quark and gluon distributions with the nucleon's spin. High values of polarization reduce the uncertainties in the determination of these correlations;
- High luminosities from 10^{33} to 10^{34} cm^{-2} s^{-1} over a broad range in E_{CM}, enabling the precise determination of the confined momentum and spatial distributions of sea quarks and gluons in nucleons and nuclei;

- Ion beams from light deuterons to the heaviest nuclei (gold or uranium), providing access to the regime of saturated gluon densities and illuminating how color propagates through nuclear matter.

This document presents the plan for realizing the EIC. Its technical design fully exploits the existing RHIC facility to produce hadron beams, including high-intensity polarized proton beams, and takes advantage of recent advances to provide a powerful, cost-effective new facility that fully meets the requirements for a compelling and lasting research program. The potential for new discovery is high, as spelled out in the EIC White Paper [**?**].

1.2 Mapping subprojects onto the Preliminary Design Report

The EIC project follows a delivery strategy with 6 subprojects:

ASR Accelerator Storage Rings: Infrastructure, ESR, HSR, installation

DET Detector: ePIC detector, solenoid magnet, auxiliary detectors, integration, installation

IR Interaction Region: Superconducting magnets, crab cavities, machine protection, installation

EIN Electron Injector: Infrastructure, Linac, BAR, RCS, installation

ELR Energy and Luminosity Ramp-up: ESR, HSR, RCS, crab cavities, 41 GeV bypass,

IPO Integrated Project Office and Beam Commissioning: Final integration, commissioning

This design report covers the technical aspects of 5 of these sub-projects in detail. The exception is the detector subproject, which is described in a separate, detailed, design report. A summary discussion of the detector is found in Chapter 7.

Chapter 2

Physics Goals and Requirements (editor: Nagaitsev)

Chapter 3

Accelerators (editor: Montag)

3.1 Overview

The polarized Electron-Ion Collider EIC provides collisions of polarized electrons and polarized protons in the center-of-mass energy region from 20 to 141 GeV, and polarized electron-heavy ion collisions up to 89 GeV/n. This is accomplished by installing an electron storage ring with up to 18 GeV beam energy in the existing RHIC tunnel, and colliding those electrons with polarized protons or heavy ions stored in the hadron storage ring (HSR) operating at energies between 41 and 275 GeV (protons), or 41 to 110 GeV/nucleon (ions). Beams will be brought into collision in up to two interaction regions, namely in IR6 and IR8. Electron-proton luminosities reach 1.0×10^{34} cm^{-2}sec^{-1}. These high luminosities require "flat" hadron beams with unequal transverse emittances with an emittance ratio of up to $\epsilon_x/\epsilon_y = 11$, generated at injection energy by an electron cooling facility

These high luminosities are achieved by increasing the number of bunches, from 110 in the present RHIC to 1160, and operating both the electron and the hadron storage rings at their respective beam-beam limits. The beam-beam limits assumed in the design are based on parameters achieved — or even slightly exceeded — at RHIC (hadrons) and the e^+e^- collider B-Factories PEP-II and KEKB (electrons). In addition, a maximum synchrotron radiation power of 10 MW is chosen to limit operational costs. It is worthwhile mentioning that this is not a technical limitation.

Parameter	Unit	Values		Comment
Center-of-mass energy E_{cm}	GeV	105	141	
Proton energy	GeV	275	275	Total particle energy
Electron energy	GeV	10	18	Total particle energy
Luminosity L	$10^{33}\mathrm{cm}^{-2}\mathrm{s}^{-1}$	10.0	1.54	Total RF power limit reduces luminosity at 18 GeV electron beam energy
Hourglass factor H		0.94	0.91	
No. of bunches M		1160	290	
RMS beam size σ_H	µm	95	119	
σ_V	µm	8.5	11.0	
$K_x \equiv \sigma_H/\sigma_V$		11.1	11.1	
Protons				
Bunch intensity	10^{10}	6.9	19.1	
Beam current	A	1.00	0.69	
Polarization	%	70	70	Longitudinal and transverse
RMS normalized emittance H	µm	3.3	5.2	Flat beams with a size ratio of 11
V	µm	0.30	0.47	
RMS emittance H	nm	11.3	18.0	
V	nm	1.0	1.6	
Collision β^* H	m	0.80	0.80	
V	m	0.072	0.071	
RMS beam divergence H	µrad	119	150	
V	µrad	119	150	
Beam-beam parameter ξ H		0.012	0.003	
V		0.012	0.003	
RMS longitudinal emittance	eV.s	0.036	0.036	
RMS bunch length	mm	60	60	
RMS $\Delta p/p$	10^{-3}	0.68	0.68	
Maximum space charge ΔQ		0.004	0.007	
Piwinski angle	rad	7.9	6.3	
IBS growth time L	h	2.9	2.0	
H	h	2.0	2.0	
V	h	67	82	
Electrons				
Bunch intensity	10^{10}	17.2	6.2	
Beam current	A	2.5	0.227	
Polarization	%	70	70	Longitudinal only
RMS normalized emittance H	µm	391	845	
V	µm	26	71	
RMS emittance H	nm	20	24	
V	nm	1.3	2.0	
Collision β^* H	m	0.55	0.70	
V	m	0.065	0.057	
RMS beam angle H	µrad	211	202	
V	µrad	152	187	
Beam-beam parameter ξ H		0.072	0.093	
V		0.100	0.100	
RMS bunch length	mm	7	9	
RMS $\Delta p/p$	10^{-3}	0.58	1.09	
Piwinski angle	rad	2.4	2.1	

Table 3.1: Proton collisions – 275 GeV

Parameter	Unit	Values		Comment
Center-of-mass energy $E_{\rm cm}$	GeV	44.7	63.2	
Proton energy	GeV	100	100	Total particle energy
Electron energy	GeV	5	10	Total particle energy
Luminosity L	$10^{33}{\rm cm}^{-2}{\rm s}^{-1}$	3.68	4.48	
Hourglass factor H		0.88	0.90	
No. of bunches M		1160	1160	
RMS beam size σ_H	µm	125	138	
σ_V	µm	11	12	
$K_x \equiv \sigma_H/\sigma_V$		11.1	11.1	
Protons				
Bunch intensity	10^{10}	4.8	6.9	
Beam current	A	0.69	1.0	
Polarization	%	70	70	Longitudinal and transverse
RMS normalized emittance H	µm	2.7	3.2	
V	µm	0.25	0.29	
RMS emittance H	nm	26	30.0	
V	nm	2.3	2.7	
Collision β^* H	m	0.61	0.63	
V	m	5.5	5.7	
RMS beam divergence H	µrad	206	220	
V	µrad	206	220	
Beam-beam parameter ξ H		0.014	0.012	
V		0.014	0.012	
RMS longitudinal emittance	eV.s	0.021	0.021	
RMS bunch length	mm	70	70	
RMS $\Delta p/p$	10^{-3}	097	0.97	
Maximum space charge ΔQ		0.021	0.026	
Piwinski angle	rad	7.0	6.3	
IBS growth time L	h	3.1	2.5	
H	h	2.0	2.0	
V	h	4.0	4.0	
Electrons				
Bunch intensity	10^{10}	17.2	17.2	
Beam current	A	2.5	2.5	
Polarization	%	70	70	Longitudinal only
RMS normalized emittance H	µm	196	391	
V	µm	18	26	
RMS emittance H	nm	20	20	
V	nm	1.8	1.3	
Collision β^* H	m	0.78	0.61	
V	m	0.12	0.071	
RMS beam angle H	µrad	160	145	
V	µrad	160	105	
Beam-beam parameter ξ H		0.100	0.072	
V		0.100	0.100	
RMS bunch length	mm	7.0	7.0	
RMS $\Delta p/p$	10^{-3}	0.68	0.58	
Piwinski angle	rad	2.0	1.8	

Table 3.2: Proton collisions – 100 GeV

Parameter	Unit	Value	Comment
Center-of-mass energy E_{cm}	GeV	28.6	
Proton energy	GeV	41	Total particle energy
Electron energy	GeV	5	Total particle energy
Luminosity L	$10^{33}\mathrm{cm}^{-2}\mathrm{s}^{-1}$	0.44	
Hourglass factor H		0.93	
No. of bunches M		1160	
RMS beam size σ_H	µm	198	
σ_V	µm	27	
$K_x \equiv \sigma_H/\sigma_V$		7.3	
Protons			
Bunch intensity	10^{10}	2.6	
Beam current	A	0.38	
Polarization	%	70	Longitudinal and transverse
RMS normalized emittance H	µm	1.9	
V	µm	0.45	
RMS emittance H	nm	44	
V	nm	10	
Collision β^* H	m	0.90	
V	m	0.071	
RMS beam divergence H	µrad	380	
V	µrad	220	
Beam-beam parameter ξ H		0.015	
V		0.009	
RMS longitudinal emittance	eV.s	0.011	
RMS bunch length	mm	75	
RMS $\Delta p/p$	10^{-3}	1.03	
Maximum space charge ΔQ		0.05	
Piwinski angle	rad	4.2	
IBS growth time L	h	3.8	
H	h	3.4	
V	h	2.1	
Electrons			
Bunch intensity	10^{10}	13.3	
Beam current	A	1.93	
Polarization	%	70	Longitudinal only
RMS normalized emittance H	µm	196	
V	µm	34	
RMS emittance H	nm	20	
V	nm	3.5	
Collision β^* H	m	1.96	
V	m	0.21	
RMS beam angle H	µrad	101	
V	µrad	129	
Beam-beam parameter ξ H		0.053	
V		0.042	
RMS bunch length	mm	7.0	
RMS $\Delta p/p$	10^{-3}	0.68	
Piwinski angle	rad	1.1	

Table 3.3: Proton collisions – 41 GeV.

Parameter	Unit	Values		Comment
Gold ion energy	GeV/u	110	110	
Electron energy	GeV	10	18	
Luminosity L	$10^{33}\mathrm{cm}^{-2}\mathrm{s}^{-1}$	2.9	0.26	
Hourglass factor H		0.85	0.85	
No. of bunches M		1160	290	
RMS beam size σ_H	µm	199	199	
σ_V	µm	18.0	18.0	
$K_x \equiv \sigma_H/\sigma_V$		11.1	11.1	
Gold ions				
Bunch intensity	10^{10}	0.05	0.05	
Beam current	A	0.57	0.14	
RMS normalized emittance H	µm	3.5	3.5	
V	µm	0.8	0.8	
RMS emittance H	nm	30.	30.	
V	nm	6.8	6.8	
Collision β^* H	m	1.33	1.33	
V	m	0.047	0.047	
RMS beam divergence H	µrad	150	150	
V	µrad	380	380	
Beam-beam parameter ξ H		0.004	0.002	
V		0.002	0.001	
RMS longitudinal emittance	eV.s	0.024	0.024	
RMS bunch length	mm	90	90	
RMS $\Delta p/p$	10^{-3}	0.80	0.8	
Maximum space charge ΔQ		0.002	0.002	
Piwinski angle	rad	5.7	5.7	
IBS growth time L	h	0.6	0.6	
H	h	0.5	0.5	
V	h	14.7	14.7	
Electrons				
Bunch intensity	10^{10}	17.2	6.2	
Beam current	A	2.5	0.227	
RMS normalized emittance H	µm	391	705	
V	µm	14.6	14.6	
RMS emittance H	nm	20	20	
V	nm	0.7	0.4	
Collision β^* H	m	1.98	1.98	
V	m	0.43	0.78	
RMS beam angle H	µrad	100	100	
V	µrad	42	23	
Beam-beam parameter ξ H		0.042	0.023	
V		0.100	0.100	
RMS bunch length	mm	7	7	
RMS $\Delta p/p$	10^{-3}	0.58	1.1	
Piwinski angle	rad	1.3	1.3	

Table 3.4: Gold ion collisions

3.1.1 Luminosity

The luminosity of an electron-ion collider is given as

$$\mathcal{L} = \frac{N_\mathrm{e} N_\mathrm{h}}{4\pi\sigma_x\sigma_y} H f_\mathrm{rep}, \tag{3.1}$$

with N_e and N_h being the electron and hadron bunch intensities, respectively, and σ_x and σ_y the horizontal and vertical RMS beam sizes at the interaction point (IP), which are assumed to be identical for the two beams. H is a factor reflecting the impact of the hourglass effect and the crossing angle; it is near unity if the RMS bunch lengths are smaller than the IP β-functions β^*_x, β^*_y, and the crossing angle is corrected using crab cavities. $f_\mathrm{rep} = N_b f_\mathrm{rev}$ denotes the bunch repetition rate, with N_b the number of bunches per ring and f_rev the revolution frequency of the collider rings.

The numbers of particles per bunch, N_e and N_h are constrained by the beam-beam parameters $\xi_{e,h,x,y}$ induced by each beam on the other, which are computed as

$$\begin{aligned} \xi_{e,h,x,y} &= \frac{r_{e,h}}{2\pi} \frac{N_{h,e}\beta^*_{e,h,x,y}}{\gamma_{e,h}\sigma_{h,e,x,y}(\sigma_{h,e,x} + \sigma_{h,e,y})} \\ &= \frac{r_{h,e}}{2\pi} \frac{N_{e,h}}{\gamma_{e,h}\epsilon_{h,e,x,y}} \frac{1}{1+K_{x,y}}, \end{aligned} \tag{3.2}$$

where we have used

$$\sigma_{x,y} = \sqrt{\epsilon_{h,x,y}\beta^*_{h,x,y}} = \sqrt{\epsilon_{e,x,y}\beta^*_{e,x,y}}. \tag{3.3}$$

$r_{h,e}$ are the classical radii of the hadrons or electrons, $K_x = \sigma_x/\sigma_y$, and $K_y = \sigma_y/\sigma_x$, while $\epsilon_{h,x,y}$ and $\epsilon_{e,x,y}$ denote the horizontal and vertical emittances of the hadron and electron beam, respectively.

Expressing the bunch populations through the beam currents,

$$I_{h,e} = N_{h,e} q f_\mathrm{rep}, \tag{3.4}$$

and combining Equations (3.1) to (3.4) we re-write the luminosity as

$$\mathcal{L} \propto H\sqrt{\gamma_e\gamma_h I_e I_h (1+K_x)(1+K_y)} \left(\frac{\xi_{h,x}\xi_{h,y}\xi_{e,x}\xi_{e,y}}{\beta^*_{h,x}\beta^*_{h,y}\beta^*_{e,x}\beta^*_{e,y}}\right)^{1/4}. \tag{3.5}$$

RHIC has achieved a beam-beam parameter of $\xi_p = 0.015$ in proton-proton collisions; we therefore base the EIC design on the same value. Beam-beam tune shift parameters in excess of $\xi_e = 0.1$ have been reached at the e^+e^- collider KEKB. The main parameters of that machine resemble the EIC electron storage ring as shown in Table 3.5, and can therefore serve as a reference for EIC.

Table 3.5: Key design parameters of CESR-B [**?**], PEP-II [**?**, **?**], KEKB [**?**], and the EIC electron ring. The EIC numbers in parentheses correspond to the version without strong hadron cooling.

	CESR-B	PEP-II LER/HER	KEKB LER/HER	EIC
Circumference C [m]	768	2200	3000	3834
No. of bunches N_b	36	1588	1584	1160
Beam current I [A]	0.365	2.45/1.55	1.3/1.6	2.5
Bunch intensity N_e [10^{10}]	16.2	7.0/4.4	5.0/6.2	15
Beam-beam parameter ξ_e	0.062	0.064/0.055	0.12/0.1	0.1
Transv. damp. decr. δ[10^{-4}]	1.1	1.8/2	2.5	1.25

Taking into account all these constraints, the luminosity is maximized for flat beams with $K_x \gg 1$, as indicated by Equation (3.5). This is realized by both unequal β-functions, $\beta_x^* \gg \beta_y^*$, and unequal emittances, $\epsilon_x > \epsilon_y$. Electron storage rings naturally have a very small vertical emittance; dedicated vertical orbit bumps will be used to increase the electron beam vertical emittance to an appropriate level. Increasing the hadron horizontal emittance may be accomplished by application of horizontal kicker noise to counteract the electron cooling force at injection energy.

The magnitudes of the hadron design emittances are chosen such that the resulting IBS growth time at collision energy is no shorter than 2 hours to ensure reasonable luminosity lifetimes and meaningful physics runs.

To reach an electron beam-beam parameter $\xi_e = 0.1$, comparable to KEKB, sufficient synchrotron radiation damping is necessary. While the transverse synchrotron radiation damping decrement at KEKB was $\delta = 2.5 \times 10^{-4}$, simulation studies indicate that in EIC a transverse damping decrement of $\delta = 1.25 \times 10^{-4}$ is sufficient for stable operation at $\xi_e = 0.1$. This is consistent with the fact that the maximum beam-beam parameter at KEKB reached $\xi_e = 0.12$.

3.1.2 IP β-functions

The minimum achievable IP β-functions β^* are limited by a number of factors. The β-functions and therefore the transverse RMS beam sizes reach their maximum in the low-β quadrupoles which are located at a distance l^* from the interaction point (IP) according to

$$\beta(l^*) = \beta^* + \frac{(l^*)^2}{\beta^*}. \tag{3.6}$$

The EIC Physics program requires a machine-element free space of $\pm 4.5\,\mathrm{m}$ around the IP. In practice, due to required vacuum system elements such as warm-to-cold transitions and bellows, the first magnets cannot be installed closer to the IP than approximately at $l^* > 5\,\mathrm{m}$. The large β-functions resulting from small values of β^* require large apertures in those low-β magnets. As a consequence, for a given gradient requirement in those magnets, the peak field must increase accordingly. In order to reduce the risk and cost associated with building and operating those magnets, the maximum peak field for the EIC IR magnets is kept low enough for conventional NbTi technology. For an electron ion collider IR we must have coil structures that provide large mag-

netic fields in the hadron beam aperture while shielding the electron beam from these fields, and the EIC experimental physics program requires some hadron magnets to have very large apertures.

Large β-functions in the focusing quadrupoles result in large contributions to the chromaticity ζ of the machine lattice,

$$\zeta = \frac{1}{4\pi} \oint k(s)\beta(s)\,\mathrm{d}s, \tag{3.7}$$

where $k(s)$ denotes the quadrupole strength. This chromaticity must be compensated using sextupole magnets in the arcs. Due to the nonlinear nature of those magnets they limit the dynamic aperture of the machine. **Experience at other colliders shows that sufficient dynamic aperture can be achieved as long as the chromatic contribution of the interaction region, ζ_{IR}, does not exceed approximately 1/3 of the chromaticity of the arcs,**

$$\zeta_{\mathrm{IR}} < \frac{1}{3}\zeta_{\mathrm{arcs}}. \tag{3.8}$$

In the EIC electron storage ring (ESR), this condition is fulfilled as long as the maximum β-functions in the low-β quadrupoles do not exceed $\hat{\beta} \simeq 800\,\mathrm{m}$.

Small values of β^* in conjunction with long hadron bunches lead to a geometric reduction of the luminosity. Assuming Gaussian beams, this so-called hourglass effect can be expressed as

$$\begin{aligned} R(t_x, t_y) &= \frac{L}{L_0} \\ &= \int_{-\infty}^{\infty} \frac{\exp(-t^2)}{\sqrt{(1 + t^2/t_x^2)(1 + t^2/t_y^2)}} \frac{\mathrm{d}t}{\sqrt{\pi}}, \end{aligned} \tag{3.9}$$

with

$$t_x^2 = \frac{2({\sigma_{x,p}^*}^2 + {\sigma_{x,e}^*}^2)}{(\sigma_{z,p}^2 + \sigma_{z,e}^2)({\sigma_{x,p}^*}^2/{\beta_{x,p}^*}^2 + {\sigma_{x,e}^*}^2/{\beta_{x,e}^*}^2)}. \tag{3.10}$$

In addition, the finite EIC crossing angle of $\theta = 25\,\mathrm{mrad}$ causes a further reduction of the luminosity despite the use of crab cavities due to the finite wavelength of the 197 MHz crab cavities, which causes a significant residual offset of the head and the tail of the long hadron bunch w.r.t. the electron bunch. In the limit of short electron bunch length and small crossing angle ($\sin\theta \approx \theta$), the luminosity can be expressed as

$$L = \frac{2 f_b N_p N_e}{\sigma_{z,p}(2\pi)^{3/2}} \int_{-\infty}^{\infty} \mathrm{d}z \frac{\exp\left\{ -\frac{(\hat{x}\sin(2kz) - \theta z)^2}{2(\sigma_{x,e}^2 + \sigma_{x,p}^2)} - \frac{2z^2}{\sigma_{z,p}^2} \right\}}{\sqrt{(\sigma_{x,e}^2 + \sigma_{x,p}^2)(\sigma_{y,e}^2 + \sigma_{y,p}^2)}}, \tag{3.11}$$

where k is the crab cavity RF wave number, $k = 2\pi f_{\mathrm{crab}}/c$, $\hat{x}$ is the maximum offset at the IP due

to the crab cavity, and the z dependence of the transverse beam sizes are included. **The luminosity is close to maximum when** $2k\hat{x} = \theta$**.** To limit the geometric luminosity loss due to the hourglass effect and the finite wavelength of the crab cavities, the lowest β^* values should not be significantly smaller than the RMS hadron bunch length. Taking $\sin x \approx x - x^3/6$ the two terms in the exponential of Equation (3.11) are equal at $z = \sigma_{z,p}$ when

$$2\hat{x}k^3\sigma_{z,p}^3 = 3\sqrt{\sigma_{x,p}^2 + \sigma_{x,e}^2}, \tag{3.12}$$

which can be used to judge the relative importance of bunch length and crab wave number as compared to transverse beam size. This puts an upper limit on the wave number of the crab cavity, though other effects, such as synchrobetatron resonances, impose additional constraints.

Lastly, the EIC physics program requires detection of protons with a transverse momentum as low as $p_\perp = 200\,\mathrm{MeV/c}$. At 275 GeV proton beam energy, for instance, this translates into a scattering angle of 0.72 mrad. In order to detect these scattered particles, the divergence angle of the proton beam itself at the IP must be smaller than this scattering angle, so the scattered particles travel outside the proton beam envelope where they can be intercepted by dedicated detectors. Experience at HERA has shown that such "Roman Pots" can be operated safely at a transverse distance of about $10\,\sigma$ from the beam center, where σ denotes the RMS beam size at the location of the Roman Pot. This restricts the RMS proton beam divergence at the IP to a tenth of the minimum scattering angle to be detected, $10\,\sigma' \leq 72\,\mathrm{mrad}$ in at least one transverse plane. For a given proton beam emittance this, in turn, limits the minimum β-function at the IP to

$$\beta^* \geq \epsilon/\sigma'^2 \tag{3.13}$$

The short hadron bunch lengths require small longitudinal emittances in order to limit the resulting momentum spread $\Delta p/p$ for a given bunch length, which would otherwise exceed the off-momentum dynamic aperture of the machine. In conjunction with high bunch intensities, these small hadron beam emittances, on the other hand, result in emittance growth rates of approximately 2 h due to intrabeam scattering (IBS).

3.1.3 Beam heating

While short, intense hadron bunches are desirable to maximize the luminosity, they cause a significant heat load to the 4.6 K cryogenic system due to the resistive wall impedance of the stainless steel beam pipes of the RHIC superconducting magnets, which scales as the product of total beam current, I, and peak bunch current, $\hat{I}$,

$$P_{\mathrm{cryo}} \propto I \cdot \hat{I}. \tag{3.14}$$

We will insert an actuively cooled beam screen with copper on its interior surface throughout the existing RHIC beam pipes to reduce the vacuum chamber resistivity and hence keep the dynamic heat load below 0.5 W/m.

The short bunch spacing of ≈ 10 ns together with the high bunch intensity may give rise to electron clouds in the hadron ring. The threshold for this instability depends strongly on the secondary electron yield (SEY) of the vacuum chamber surfaces. **Simulations show that below an SEY of 1.2 the instability does not occur.** To reduce the secondary electron emission in the hadron ring vacuum chambers to a sufficiently low value, a thin layer of amorphous carbon will be applied on

top of the copper surface of the beam screen.

3.1.4 RF system

Together with the reduced longitudinal emittance achieved by bunch splitting, high RF voltages are required to reach the desired short bunch lengths. It is planned to upgrade the present RF system, which consists of 28 and 197 MHz cavities, with a 591 MHz RF system, thus limiting the required RF voltage due to the higher harmonic number. **24.5 MHz cavities?**

The total electron beam current $I_e = e \cdot N_e \cdot f_b$, where e is the electron charge, is limited by the available RF power required to restore the synchrotron radiation losses. This radiated power can be expressed as

$$P\,[\mathrm{kW}] = 88.46 \cdot \frac{E_e\,[\mathrm{GeV}]^4}{r\,[\mathrm{m}]} \cdot I_e\,[\mathrm{A}]. \tag{3.15}$$

Here E_e is the electron beam energy, and r the dipole bending radius of the storage ring. To limit the required investment cost for the storage ring RF system as well as the operating cost, the synchrotron radiation power has been limited to 10 MW. The RF system in the electron storage ring consists of superconducting 591 MHz single-cell cavities. With a voltage of 3.9 MV per cell, a total of 18 cells are required to provide the necessary voltage at 18 GeV beam energy. The cavities are located in IR10.

Besides the RF power requirement the electron beam intensity is limited by collective effects, namely the coupled bunch instability (CBI) and the transverse mode coupling instability (TMCI). While the plan is to have a damper for longitudinal instabilities, the beam-beam tune spread is a potent source of transverse Landau damping. Any transverse damper would be designed to act only when beam-beam was either weak or absent.

3.1.5 Beam polarization

Both the electron and the proton beam in the EIC require a high degree of polarization. Polarized protons with up to **65% polarization at energies up to 250 GeV** have already been routinely achieved using two Siberian snakes in RHIC. Relocation of the two existing Siberian Snakes from the **unused second ("Blue") RHIC ring** to the hadron storage ring, and converting unused spin rotators into two additional Siberian Snakes for the HSR is expected to increase spin polarization to the 70% level. **Additional improvements planned in the AGS will raise this level to 80%.**

High polarization with arbitrary spin patterns in the electron ring is achieved by injecting bunches with the desired spin orientation at full collision energy. Bunches with their spin orientation parallel to the main dipole field of the storage ring will slowly reverse their polarization direction due to the Sokolov-Ternov effect, and asymptotically reach a polarization level determined by the Sokolov-Ternov self polarization and Derbenev-Kontratenko spin diffusion. It is therefore necessary to replace entire bunches at a rate significantly faster than the Sokolov-Ternov time constant.

The shortest Sokolov-Ternov (de-)polarization time over the entire energy range of the electron storage ring occurs at 18 GeV, where it reaches $\tau_{\mathrm{S-T}} = 28$ min. Replacing individual bunches after approximately 2 min ensures a high level of polarization in either spin orientation. The injection scheme uses "swap-out" injection and extraction with the rapid cycling synchrotron operating at a 1 Hz repetition rate and with one bunch per cycle **(two bunches per cycle at 18 GeV).**

Electron bunches are generated in a polarized electron gun. This gun has routinely generated **11 nC** electron bunches with over **80% polarization**. For EIC operation, 28 bunches of 1 nC each will be generated by the gun at a 30 Hz rate. After pre-acceleration in a 750 MeV normal-conducting S-band LINAC, pulsed at 30 Hz, these bunches will be injected into a Beam Accumulator Ring (BAR) to be merged into a single 28 nC bunch. This bunch will then be extracted from the BAR and injected into the rapid-cycling synchrotron (RCS) in a separate 1.4 km circumference tunnel adjacent to IR4 to be accelerated to full collision energy of up to 18 GeV. The RCS is ramped once per second within 200 ms from 750 MeV to 18 GeV.

In order to preserve polarization during acceleration, the RCS lattice has a high superperiodicity. Together with the appropriate choice of the betatron tune this ensures that no intrinsic spin resonances are encountered during the entire ramp to 18 GeV. **However, spin tracking studies have shown that less than 2% of the initial polarization is lost during the ramp to 18 GeV even with an RMS orbit error of 1 mm. The RF system in the RCS is comprised of multi-cell superconducting 591 MHz cavities with a total voltage of 72 MV.**

Polarized protons are injected from the existing AGS at **24 GeV,** and accelerated to full storage energy in the EIC hadron storage ring. With the maximum design bunch intensity and longitudinal emittance being about half the values presently achieved in RHIC, the required values can be reached by longitudinal bunch splitting.

To achieve the desired transverse emittance ratio of up to $\epsilon_x/\epsilon_y = 11$, a bunched beam electron cooler operating at a Lorentz-γ of **25.5** will be installed in the IR2 straight section. After a cooling time of approximately **30 min**, hadron beams will be accelerated to the desired collision energy.

While the spin orientation in both the electron and the proton beam is vertical in the storage ring arcs, the experiments require longitudinally polarized beams. The necessary spin rotation is accomplished by the existing helical dipole rotators in the proton ring, and by solenoid-based spin rotators in the electron machine. Spin matching is required to preserve spin polarization in the presence of these solenoids.

3.1.6 Interaction Region

The beams are brought into collision in the 6 o'clock interaction region (IR), the present STAR location. A second interaction can be added later in IR8, but is not in the scope of this project. The two beams collide at a total crossing angle of 25 mrad, which provides early beam separation to avoid parasitic collisions, and allows low-β quadrupoles for the two beams to be installed close to the interaction point, with the first magnet located just outside the ± 4.5 long detector. The crossing angle is compensated by sets of crab cavities in each beam. The 197 MHz double quarter-wave crab cavities in the hadron beam line are scaled versions of the 400 MHz HL-LHC prototype crab cavities. A set of 394 MHz crab cavities serves as a second harmonic to straighten out the sinusoidal crab kick of the 197 MHz crab cavities on the hadron bunches. These higher harmonic crab cavities are identical to those used in the electron beam line.

3.1.7 Layout of EIC Accelerator Systems

The EIC accelerator complex is composed of the existing systems that constitute present RHIC and some systems which have been added. The most important existing system is the two RHIC storage rings with their superconducting magnets inside the RHIC tunnel. Only the "Yellow" superconducting ring is needed for EIC as the hadron storage ring (HSR). The ring is composed of

six sextants separated by straight sections. The straight sections are labeled as "2, 4, 6, 8, 10 and 12 o'clock", with 12 o'clock being in the northernmost part of the ring, or, alternatively, as IR2 to IR12. The ring complex also includes the hadron injector chain with the AGS synchrotron, the Booster synchrotron, the injector LINAC and the particle sources. Furthermore there is a large cryogenic 4 K liquid helium plant located near IR6 that feeds the superconducting magnets.

New systems are the electron beam complex consisting of the electron storage ring, the electron injector synchrotron, and the electron injector. The electron storage ring (ESR) is located in the RHIC tunnel, while the rapid cycling electron synchrotron (RCS) is housed in a separate tunnel near IR4. The electron ring is tilted by 200 μrad around the axis through the electron-hadron interaction points in IRs 6 and 8. This results in a vertical separation of the two beam orbits of 102 mm in IRs 4 and 10, and 204 mm in IRs 12 and 2, which greatly eases the design of the cross-over points.

The utility space of the present RHIC complex is not sufficient to host the equipment. A number of new buildings is required. These are described in Sections **??** and **??**.

Figure 3.1 provides an overview of the layout of the EIC facility. The diagram shows the RHIC tunnel and labels indicate which of the new systems are located at or near which straight section. The new systems are summarized as follows:

- IR6:
  IR6 accommodates the EIC colliding beam detector ePIC and the magnetic lattices required for the interaction region. The interaction region also hosts the spin rotators for electron and hadron beams and the crab cavities for both beams. The spin rotators of the hadrons are identical to present RHIC, while the electron spin rotators are based on solenoid and horizontal dipole magnets. The crab cavities require a small 2 K liquid He plant.
- IR8:
  IR8 is to the largest extent possible reserved for a future second interaction region and colliding beam detector. It consists of a simple cross-over of the electron and hadron beam lines. Collisions are avoided by setting the path lengths appropriately.
- IR10:
  IR10 hosts the hadron beam abort and the electron RF systems for storage ring and rapid cycling synchrotron.
- IR12:
  Electrons and hadrons cross over in this section.
- IR2:
  This straight section hosts instrumentation, feedback systems, the electron source, the electron cooler, and the electron beam dump.
- IR4:
  Electron and hadron rings cross over in IR4. Hadrons are transported through a new, normal-conducting transfer line from the end of the present AtR line to the new injection area in IR4, which houses the hadron injection kickers and septa. Electrons are transported from the RCS to their injection area in IR4 via the RCS-to-ESR (RtE) transfer line to be injected into the ESR. Further downstream of the cross-over location and towards the beginning of the arc, the electron collimation system is located. This straight section also accommodates the room temperature RF for hadrons. The hadron storage RF system needs an upgrade for splitting each bunch into 4 bunches and to provide short bunches for collisions. These systems, consisting of 49 MHz and 98 MHz cavities for splitting, and 591 MHz storage cavities, are placed there as well. Hadron polarimeters are also located in this section.

Figure 3.1: update figure and caption Schematic layout of locations of EIC Accelerator Hardware Systems. The yellow lines represent the "Yellow" ring for hadrons. The light blue line represents the electron storage ring, and the red line represents the rapid cycling injector synchrotron. The dark blue line is the unused part of the "Blue" ring which will stay in place. Note that the lattice and simulations described in this document are for the case of a single detector at the 6 o'clock area. Calculations with a second detector at the 8 o'clock area are in progress. Initial studies for the two-detector configuration are described in Sections **??** and 4.5.

3.2 Interaction Region IR6

3.2.1 Electron Storage Ring

3.2.2 Hadron Storage Ring

3.2.3 Machine Detector Interface

3.3 Hadron Storage Ring

3.3.1 Introduction

The hadron beams, heavy ions as well as polarized protons and ^{3}He, will be accelerated and stored in the Hadron Storage Ring which is Yellow ring of present RHIC. The beam in HSR will travel in the counter-clockwise direction, as in present Yellow ring. Here the modifications to the existing RHIC superconducting rings necessary to accommodate requirements for the EIC are listed:

- Raising maximum proton operation energy from 255 to 275 GeV.
- Adding four additional Siberian Snakes to ensure He3 polarization
- Using 12–2 inner arc in order to match electron and hadron revolution frequencies at 41 GeV per nucleon hadron energy.
- New interaction region for electron-hadron collisions.
- Realizing new injection system at 4 o'clock area.
- Using 6–4 inner arc for transferring hadron beam from AtR to the 4 o'clock injection area
- Beam screen for the reused RHIC superconducting magnet beam pipes (see Section **??**).
- Modifications of RF system including a number of new cavities (see Section **??**).
- Upgrading beam instrumentation for high hadron current

3.3.2 Tunnel Layout

The EIC HSR will be constructed from the existing RHIC accelerators with appropriate modifications and additions. The schematic of the Relativistic Heavy Ion Collider (RHIC) accelerators is shown in Figure 3.2. It consists of two rings (called Blue and Yellow) running in opposite direction which intersect with each other at six locations. For RHIC operations, head-on collisions of the Blue (clock-wise) and Yellow (counter clock-wise) beams occur at Interaction Region 6 (IR6) where the STAR detectors are located, and at IR8 where the PHENIX detectors are located.

The beams are brought into head-on collision using a pair of D0 and DX magnets as shown in Figure 3.3. The layout are the same for all six IRs, with the beta function at the Interaction Point (IP) 6 and 8 being squeezed to tens of centimeters for the experiments. One beam travels from the inner ring to the outer ring, while the other beam travels from the outer ring to the inner ring in the opposite direction. The DX magnets near the IP are the only common magnetic elements for both rings. On each side, the D0 magnets and the final focusing triplets (Q1, Q2 and Q3) of the two rings are housed in a common cryostat.

Overview of modifications to the RHIC lattice

We define the RHIC arcs to be everything from quadrupoles Q10 through Q10 inclusive. The IRs will be the remaining magnets between the arcs. The RHIC yellow arcs will be unmodified. The blue arc at 1 o'clock will be used for beams of 41 GeV per nucleon total energy; the polarities of currents in the magnets of that arc will be opposite to what are used in RHIC so as to allow the beam to circulate opposite to its RHIC direction and have the focusing pattern of the quadrupoles

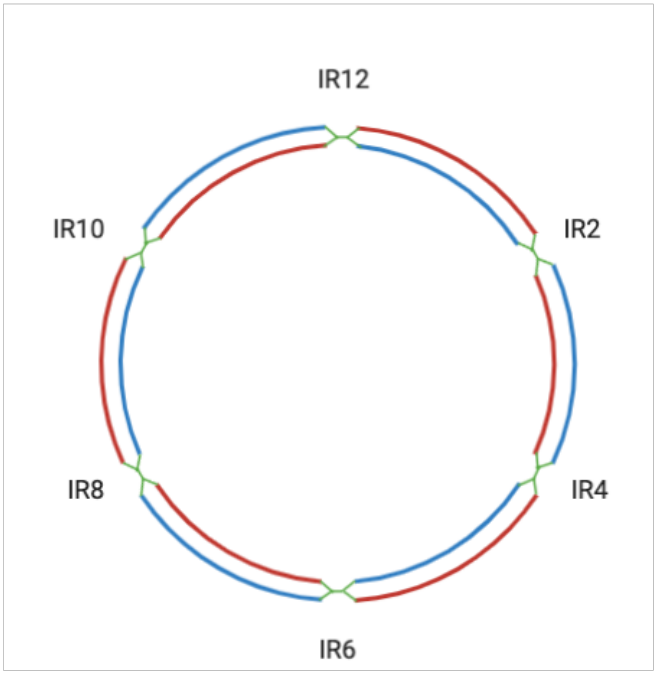

Figure 3.2: The schematic of the RHIC accelerators. The Blue ring is shown in blue while the Yellow ring is shown in red for display purpose. The IRs are shown in green.

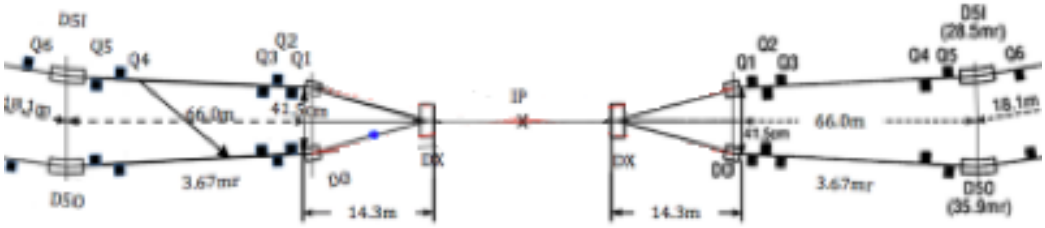

Figure 3.3: The schematic of the RHIC interaction region.

remain as they are in RHIC. In the IRs, all DX and D0 magnets will be removed. Some IRs will be left in a ”standard configuration”:

- Three 2 m long iron dominated dipole magnets will be placed adjacent to the triplet, near where the D0 magnet was, to direct the beam between the triplets.
- Where it does not already exist, a Siberian snake will be placed between Q7 and Q8 on the counter-clockwise side of the IR.
- The remainder of the superconducting beamline will be left in place, except for minor changes as specified below.

The general roles of the IRs are as follows

- IR2 will be used for beam cooling, though the initial lattice configuration (ASR subproject) will not be compatible wit this.
- IR4 will be used for injection, some RF systems, and polarimetry.
- IR6 is where collisions occur in the detector. It will be heavily modified from its RHIC configuraiton, but RHIC magnets will be used where possible.
- IR8 is reserverd as a location for a potential future second detector.
- IR10 contains RF cavities and the beam dump.
- IR12 is where collimation will occur.

HSR layout in the ASR subproject

The IR6 magnet lattice is not part of the ASR subproject. For the remaining IRs:

- IR2 is in the standard configuration.
- IR4 is similar to a standard configuration, except that the iron dipoles will be placed differently, and there only need be two on each side. On the counter-clockwise side, they will be placed between the hydrogen and helium jets and the detectors from the products of those polarimetry measurements, allowing the dipoles to separate collision products. On the clockwise side, RF cavities will be between the triplet and the dipoles. This will necessitate a small change in the location of the triplet magnets on the counter-clockwise side. Injection will occur in this IR. A new set of injection kickers (between the triplets, closer to the counter-clockwise side) and septum magnets (between the clockwise triplet and Q4) will be installed. A new transfer line will be constructed to deliver the hadron beam from the IR6 area to IR4.
- IR8 is in the standard configuration. The spin rotators will be removed, necessitating the replacement of the Q4 modules with magnetically identical modules from RHIC that are no longer needed which have warm to cold transitions.
- IR10 is similar to a standard configuration, except that the iron dipoles on the clockwise side will be placed near the Q4, and there only need be two on each side. This allows a slightly larger separation between the ESR and HSR beamlines in this IR, creating more space between the RF cavities in these rings. This will necessitate a small change in the location of the triplet magnets on the clockwise side.
- IR12 is in the standard configuration. The clockwise side DU7 cold drift between Q7 and Q8 will be replaced with a warm section for collimation, necessitating the replacement of the Q7 and Q8 modules with magnetically identical ones from RHIC IR6 that have warm to cold transitions.

HSR layout in the IR subproject

IR6 is the experimental interaction region where electrons collide with hadrons at a 25 mrad crossing angle. In the IR subproject, the IR6 magnetic structure will be added to the HSR, extending from the Q10 quadrupole on the 5 o'clock side to the Q10 on the 6 o'clock side. It includes newly built magnets in the vicinity of the detector, as well as re-purposed RHIC magnets used in locations different from the standard RHIC lattice.

HSR layout in the ELR subproject

During the ELR subproject, the HSR IR2 area will be reconfigured to provide a very long drift section (170 m) for the Low Energy Cooler. At the same time, the inner arc between the IR12 and IR2 areas will be added for 41 GeV operation. This configuration reduces the 41 GeV beam path length by 94.2 cm to match the revolution frequencies of the electron and hadron beams.

3.3.3 Arc Lattice

Ring Optics and Main Parameters

The hadron storage ring (HSR) is composed of six arcs with eleven FODO cells in each arc. The arcs are connected by five straight sections (SS) and an interaction region (IR) at the 6 o'clock area of the ring with the possibility of a second IR in the 8 o'clock SS. Figure 3.4 is a plot, generated by the computational model engine (CME) [**?**] BMAD accelerator toolkit [**?**], of the β functions and dispersion of the HSR. The interaction point is at the start of the lattice where s equals zero and s increases clockwise around the ring. The HSR is composed of the existing Relativistic Heavy Ion Collider (RHIC) [**?**] yellow ring with the exception of the IR. The path length circumference, without the radial shift, of the ring is 3833.824018 m at full energy. The transit time of the particle,t_p, and the velocity of the particle, v_p are used to calculate the circumference,$C = t_p \times v_p$. For 41 GeV, the blue inner arc between the 12 and 2 o'clock SS will be used for circulating beam which reduces the path length of the beam by approximately 90 cm. The SS are anti-symmetric in quadrupole polarity with respect to the SS midpoint.

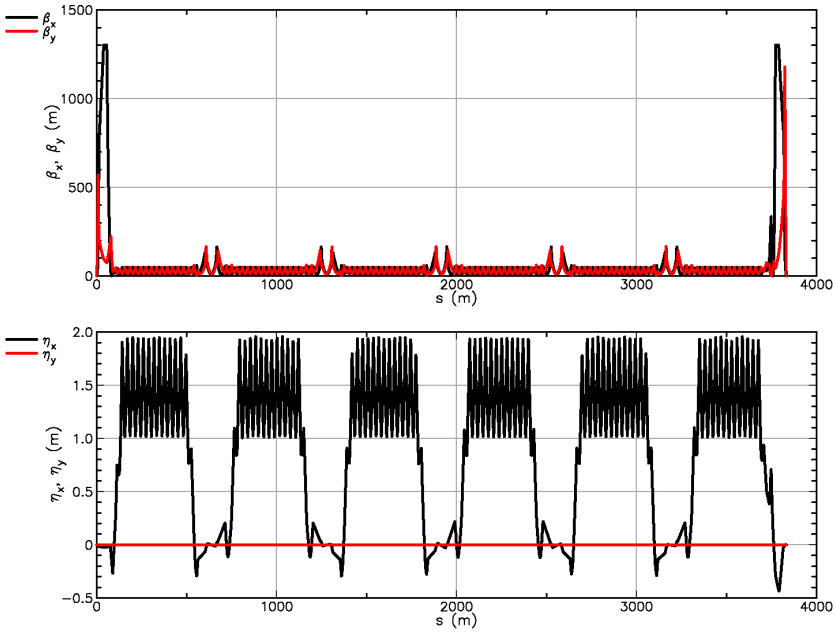

Figure 3.4: Hadron Storage Ring optics from s-coordinate increasing from IP 6 clockwise at top energy 275 GeV protons.

The HSR lattice version 20201208 horizontal and vertical tunes are separated by one unit, $(\nu_x, \nu_y) =$

$(28.228, 27.210)$, with a horizontal and vertical $\beta^* = 10.0$ m at the midpoint of each SS. The absolute value of the horizontal dispersion, η_x, at the SS midpoint is less than 1 cm. Both protons and Au^{79+} ions have the same betatron tunes. The natural chromaticities $(\partial\nu_x/\partial\delta|_{\delta=0}, \partial\nu_y/\partial\delta|_{\delta=0})$ of the 275 GeV proton lattice are (ξ_x, ξ_y) = (-49.09,-72.17), horizontally and vertically. The sextupoles are tuned to a strength that produces a chromaticity of 1 in both planes. Up to 8 sextupole families can be used to correct the first, second, and third order chromaticities [**?**]. The HSR uses the former RHIC arcs and redesigned straight sections. The RHIC DX magnets of the SS are removed because of power supply current constraints and magnet aperture limitations. Since the DX magnets are removed, the D0 magnets are readjusted to a bending angle of ± 5.34 mrad. In the 6 o'clock IR, the interaction point has a $(\beta_x^*, \beta_y^*) = (800, 72)$ mm, horizontally and vertically. The beam travels counter-clockwise in the magnetic lattice. The HSR acts as an accelerator, storage ring, and collider.

The momentum compaction is calculated by using the equation:

$$\alpha_c = \frac{\Delta C/C}{\Delta p/p} = \oint ds(\boldsymbol{g} \cdot \boldsymbol{\eta})/L$$

where $\boldsymbol{g}$ is the curvature vector and equal to (g_x, g_y), the geometric strengths in the horizontal and vertical plane. L is the length of the lattice. The geometric strength is defined as $g = 1/\rho$, where ρ is the radius of curvature. The momentum compaction for the HSR is 2.06×10^{-3}. The gamma transition, γ_t, is therefore $1/\sqrt{\alpha_c}$ which equals 22.02. When the differential of circulation time with respect to $\delta = \Delta P/P$ of the off-momentum particle is zero, transition occurs. Protons are injected above the γ_t at a γ of 25.38 while all other ion species are injected below. Transition crossing in the HSR is handled similar to RHIC. HSR uses a first order matched transition jump so that transition energy at γ_t, rapidly decreases across γ of the accelerating beam with little beam disturbance [**?**].

Arcs

HSR FODO cells in the arcs remain unchanged from RHIC (Figure 3.5). Each FODO cell is composed of two half quadrupoles, one full quadrupole, and two full dipoles. There are sextupoles and dipole correction magnets adjacent to each of the quadrupoles in the arc. The HSR lattice consist of 3 arcs of FODO cell length (inner) 29.5871 m and 3 arcs of FODO cell length (outer) 29.6571 m. Each main dipole has a bend angle of 38.924 mrad with a field of 3.782 T. The bending radius is 242.541 m with a geometric strength $0.004123\,\mathrm{m}^{-1}$. The dipole has a length of 9.441 m with a beam path through the dipole having a sagitta, $\rho - \sqrt{\rho^2 - (L_D/2)^2}$, of 45.932 mm. The beam separation between the center of the 12 to 2 o'clock inner arc to the outer arc is 90 cm. The phase advances and other parameters are listed in Table 3.6 for protons at 275 GeV. Figure 3.7 is a plot of a single outer FODO cell with a horizontal phase advance, ϕ_a, of 78° and a vertical phase advance, ϕ_b, of 81°. At low energy operation, an upper limit is placed on the quadrupole strength to keep γ_t energy below proton injection energy and phase shift below or at 90° [**?**]. The betatron tune adjustment is controlled by the arc focusing, QF, and defocusing, QD, quadrupoles and over a range of ± 1 unit.

The main quadrupole magnets remain constrained by the RHIC power supplies to a current limit of 5500 A which limits the arc quadrupole focusing strength at high energy. The polynomial fit of the current, I , from the main quadrupole bus to the normalized quadrupole strength is:

$$Q_{main}[k_1](I) = I \sum_{j=0}^{10} [cq_j \times I^j]$$

. The equation fits both focusing and defocusing quadrupoles. In the case of the defocusing

Parameter	Inner	Outer
Cell		
Length [m]	29.5871	29.6571
Bending angle [mrad]	77.8481	
Radius of curvature [m]	380.06194	380.9611
Dipole		
Magnetic length [m]	9.441	
Bending radius [m]	242.54058	
Distance between centerlines [m]	0.90	
Geometric strength [1/m]	0.004123	
Angle [mrad]	38.92409	
Quadrupole		
Magnetic length [m]	1.110	
Phase advance per cell, (H, V) [2π]	0.215, 0.223	0.216, 0.224
Horizontal β, (max, min) [m]	49.32, 10.84	49.44, 10.81
Vertical β, (max, min) [m]	48.43, 11.35	48.56, 11.32
Dispersion, (max, min) [m]	1.94, 1.02	1.94, 1.01
Natural chromaticity per cell, (H, V)	-0.046, -0.431	-0.052, -0.423

Table 3.6: Arc FODO cell parameters. The focusing quadrupoles have a field gradient 72.00 T/m and with a rigidity of 917.294 Tm a normalized strength of 0.078443 m^{-2}. The defocusing quadrupoles have a field gradient of -73.53 T/m with a normalized strength of -0.080159 m^{-2}.

quadrupole, the strength is multiplied by negative one. The coefficients of the polynomial are defined as:

$$
\begin{aligned}
cq_0 &= 1.87065957965 \times 10^{-04} \\
cq_1 &= 1.82972358172 \times 10^{-09} \\
cq_2 &= -1.01303041692 \times 10^{-12} \\
cq_3 &= 2.01085282381 \times 10^{-16} \\
cq_4 &= 1.57135850568 \times 10^{-21} \\
cq_5 &= -2.85204046011 \times 10^{-24} \\
cq_6 &= -2.51933991953 \times 10^{-28} \\
cq_7 &= 1.29158861243 \times 10^{-32} \\
cq_8 &= 4.86523477228 \times 10^{-36} \\
cq_9 &= 0.0 \\
cq_{10} &= 0.0.
\end{aligned}
$$

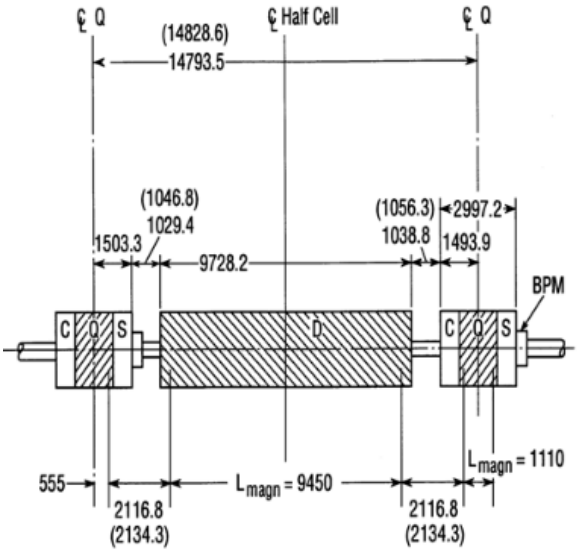

Figure 3.5: Layout of inner (outer) arc half cell.

Each coefficient is multiplied by $(B\rho)_{\text{inj}}/(B\rho)_{\text{full}}$, where the $(B\rho)_{\text{inj}}$ is 79.3667 Tm and $(B\rho)_{\text{full}}$ is the beam rigidity at full energy, 917.2959 Tm for the 275 GeV proton configuration. The units of coefficients are $s/(Qm)$. Figure 3.6 depicts the quadrupole polynomial fit.

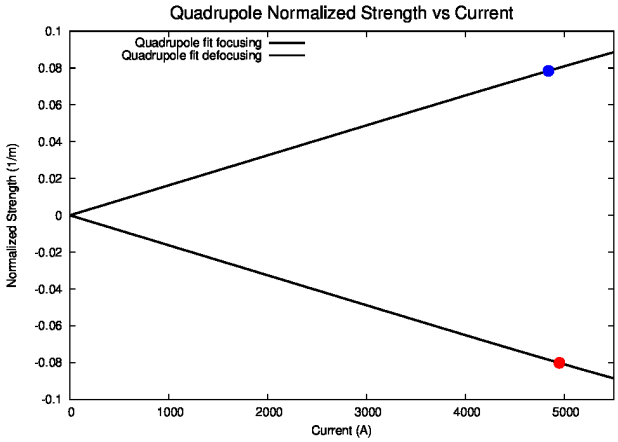

Figure 3.6: Polynomial fit of normalized quadrupole strength versus current. The blue and red points indicate the current and strength in the current HSR lattice

Each quadrupole in the arc has an associate sextupole. The simplest configuration of the sextupole families is to have in dispersive regions, a focusing sextupole by a focusing quadrupole and a defocusing sextupole by a defocusing quadrupole. These chromatic sextupoles are used to control the first order linear chromaticity of the HSR in the following way [**?**]:

$$\xi_x = -\frac{1}{4\pi}\sum_{i=0}^{N}[(b_1 L)_i - 2(b_2 L)_i \eta_{x_i}]\beta_{x_i}$$

$$\xi_y = \frac{1}{4\pi}\sum_{i=0}^{N}[(b_1 L)_i - 2(b_2 L)_i \eta_{x_i}]\beta_{y_i}$$

where the b_1 is the quadrupole field gradient, b_2 is the sextupole field gradient, and L is the length of the moment taken. N is the number of moments taken in the lattice.

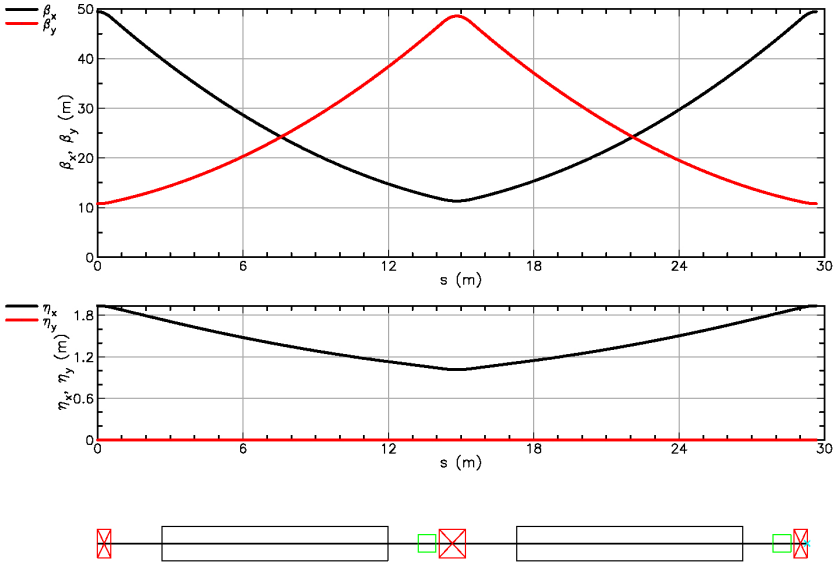

Figure 3.7: Arc FODO cell optics, with tune per cell (H, V) = (0.216, 0.224). Black box:dipole, red box: quadrupole, and green box: sextupole

Straight Section

The SS up to the midpoint has 12 quadrupoles with 5 dipoles. In the dispersion matching section from Q10 to Q4, the space between the Q10, Q9, Q7, Q6, and Q5 half cell insertions are equal in spacing and have the same spacing between the quadrupoles as the arc. The dipoles in this region are used for dispersion control with two of dipoles in the region located at the 6 and 9 positions having a special length of 2.949 m. The Q5 and Q4 doublet with Q3, Q2, and Q1 triplets allow the flexibility of a adjustable waist at the midpoint of the SS. Additional focusing is given in the region from the trim quadrupoles TQ4, TQ5, and TQ6 which are adjacent to the Q4, Q5, and Q6 quadrupoles. The D5 magnetic length is dependent upon the inner or outer configuration, where D5I is 6.916 m and D5O is 8.698 m.

For the insertion quadrupoles, the defocusing QD9 and QD8 have the same normalized strength. The Q7, Q6, Q5, and Q4 have equal but opposite strength to its optical dyad about the midpoint of the SS. The β_{max} values in the SS are 164 m horizontally and 165 m vertically. Figure 3.8 is a plot of the β functions, dispersion, and lattice layout for the 12 o'clock SS. The SS uses the same wiring scheme as the current RHIC where both the dipoles and quadrupoles are powered from the 4 o'clock region with return busses at the 10 o'clock region. Each insertion quadrupole type has a unique current transfer function. Shunt power supplies are used for the insertion quadrupoles with each of pair of the inner and outer QD89, Q7, and Q456 sharing a single power supply. For the 4 o'clock and 10 o'clock SS this is not the case. The trim quadrupoles TQ4, 5, and 6 each have

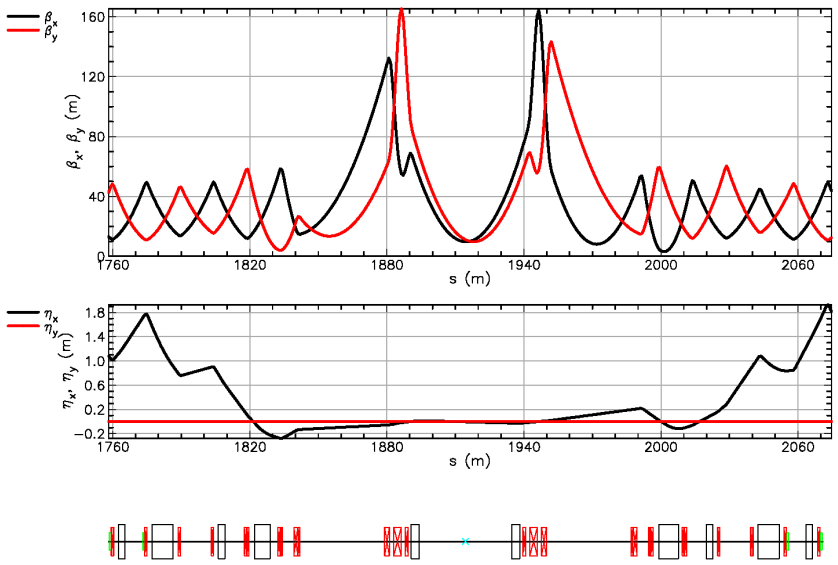

Figure 3.8: Top β functions, middle dispersion, and bottom lattice layout. Black box:dipole, red box: quadrupole, green box: sextupole, and green x: SS midpoint marker

there own auxiliary low current power supply. Table 3.7 is a list of the currents needed from the shunt power supplies in the SS if the wiring configuration remains unchanged from the RHIC. With the current shunt power supplies, the psqad is out of range with its lower and upper limits being between -280 A and +275 A. The trim quadrupoles limits are $\pm$100 A, except in 8 o'clock SS where the limits are $\pm$150. Depending on magnet type, the magnet currents are obtained from 8^{th}, 10^{th}, or 12^{th} order polynomial fits analogous to the equation used for the main quadrupole currents.

Power Supply	Current [A]	Relation
psqad	-469.695	QD89(I)-QD(I)
psqfa	-134.295	-QF9(I)+Q9(I)
psqfb	-241.160	-QF8(I)+Q9(I)
psiqt6	-22.351	Q6IT(I)
psiqt5	97.920	Q5IT(I)
psiqt4	63.743	Q4IT(I)
psoqt6	100.432	Q6OT(I)
psoqt5	-102.620	Q5OT(I)
psoqt4	-35.375	Q4OT(I)
psq7	549.538	Q7(I)-QF(I)
psq456	-33.610	Q456(I)-Q7(I)
psoq3	23.092	QD3(I)-Q456(I)
psoq2	-207.143	QD2(I)-QD3(I)
psqo1	16.765	QD1(I)-QD2(I)
psqi3	-118.862	QF3(I)-Q456(I)
psqi2	67.641	QF2(I)-QF3(I)
psqi1	84.831	QF1(I)-QF2(I)

Table 3.7: Currents needed from shunt power supplies for SS quadrupoles for 275 GeV protons.

Optics Matching

The transition from arc to SS occurs at the Q10 quadrupole magnets of the arc. At these magnets, a set of matching conditions for the beta-functions and dispersion are defined using the following formulas:

$$\begin{aligned} \beta_{\max} &= L\left(\frac{1+\sin(\mu/2)}{\sin(\mu)}\right) \\ \beta_{\min} &= L\left(\frac{1-\sin(\mu/2)}{\sin(\mu)}\right) \\ D_{\max} &= L\Omega\left(\frac{1+\sin(\mu/2)/2}{4\sin^2(\mu/2)}\right) \\ D_{\min} &= L\Omega\left(\frac{1-\sin(\mu/2)/2}{4\sin^2(\mu/2)}\right) \end{aligned} \tag{3.16}$$

where L is the cell length, μ is the phase advance per cell, and Ω is the bending angle of the FODO cell.

3.3.4 Straight Section Modifications

The Utility Straight Sections (also called "straight sections" or "warm sections") host the many beam systems that are listed in Table 3.8 – both hadron and electron.

USS	System
2	24 GeV e-cooling system. Beam instrumentation.
	41 GeV transport & switching magnets.
4	Injection from transfer line from AGS, including injection kickers and septum magnets.
	Warm RF systems
	Polarimeters
6	Detector
8	Place for a future second detector
10	Beam abort kicker and dump.
	Superconducting RF.
	Beam Instrumentation.
12	Collimators

Table 3.8: Beam systems in each utility straight section).

Optics modifications

Figure 3.9 shows the current configuration of one side of a RHIC interaction region, in round-beam collision optics with $\beta^*_H = \beta^*_V = 1.0$ m. All RHIC interaction region layouts are identical, with beam passing from inner-arc to outer-arc, or vice versa. The 6 pairs of (β^*_H, β^*_V) values are all independently tunable. All 6 HSR straight sections are modified from this, each customized to accommodate the systems in that straight. The optical functions are either symmetric or remain anti-symmetric about the (so-called) interaction point, with beam sometimes passing from inner-to-inner or outer-to-outer, in addition to the current inner-to-outer and outer-to-inner layouts.

Magnet changes at a particular straight include some or all of the following, in addition to removing all DX dipoles:

1. Remove D0 dipoles.
2. Remove triplet quadrupole cryostats, or modify them.
3. Remove triplet cold masses from their cryostats, for re-use or storage.
4. Install doublet quadrupole cryostats, re-using some of the triplet quad cold masses.
5. Reconfigure the dispersion suppressor, re-using dipole cryostats or cold masses.

In IR8 and IR2 sections in the ASR subproject the modification of magnetic structure are minimal. The DX and D0 magnets are removed. And new warm dipole magnets are installed The triplet quadrupoles – about 30 m on either side of the interaction point – are still in place. Figure 3.10 shows the optics of IR8 and IR2 areas.

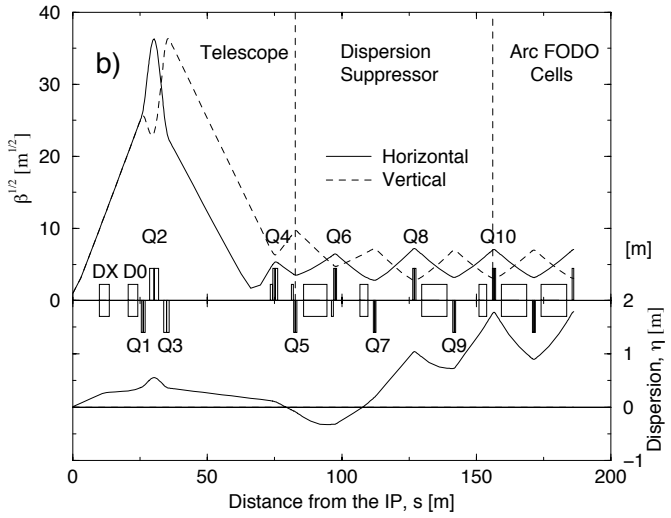

Figure 3.9: RHIC Interaction Region magnets and optics, in round-beam collision optics with $\beta_H^* = \beta_V^* = 1.0$ m. Dispersion suppression is not complete – the slope η'^* is non-zero.

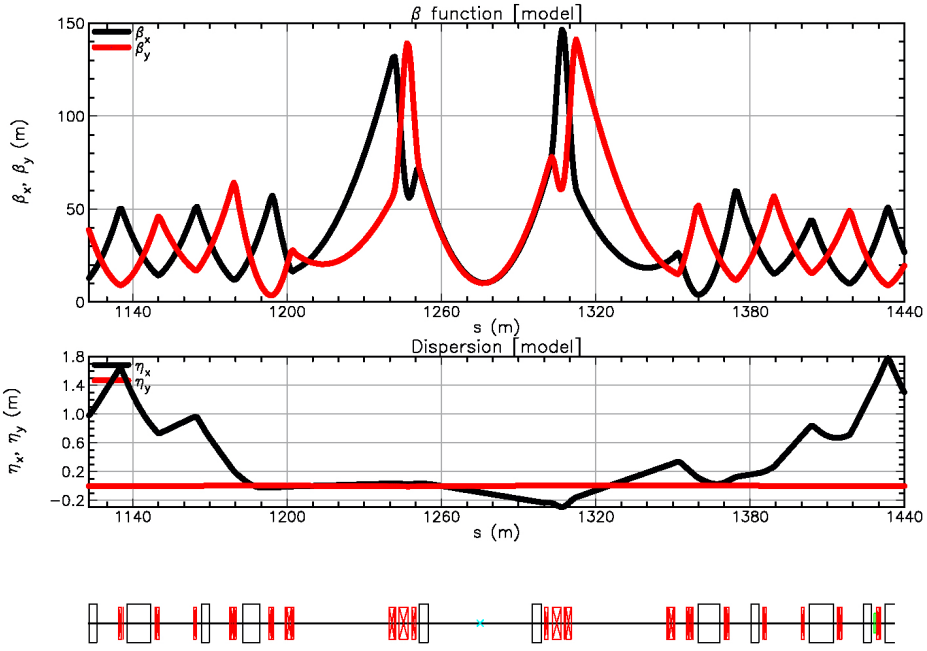

Figure 3.10: The optics of IR8 and IR2 utility section.

Insertion Region IR2 with a long cooling drift

Figure 3.11 shows the schematic layout of the long drift in Insertion Region 2 that is required for low-energy electron cooling, using a permutation of RHIC magnet cryomodules that maximizes the usable drift length. A warm doublet is inserted at both sides of the long drift to provide flxebility to control beam sizes at injection energy. Figures 3.12 shows the IR2 optics at injection.

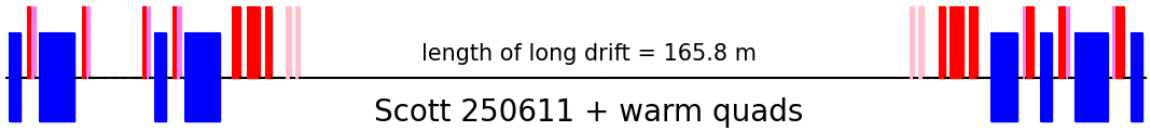

Figure 3.11: IR2 layout optimized to maximize the drift length for low-energy cooling. Blue, red, violet, and pink blocks represent RHIC dipoles, major quadrupoles, trim quadrupoles, and newly added warm quadrupoles, respectively. All quadrupoles are used as tuning knobs for beam optics matching.

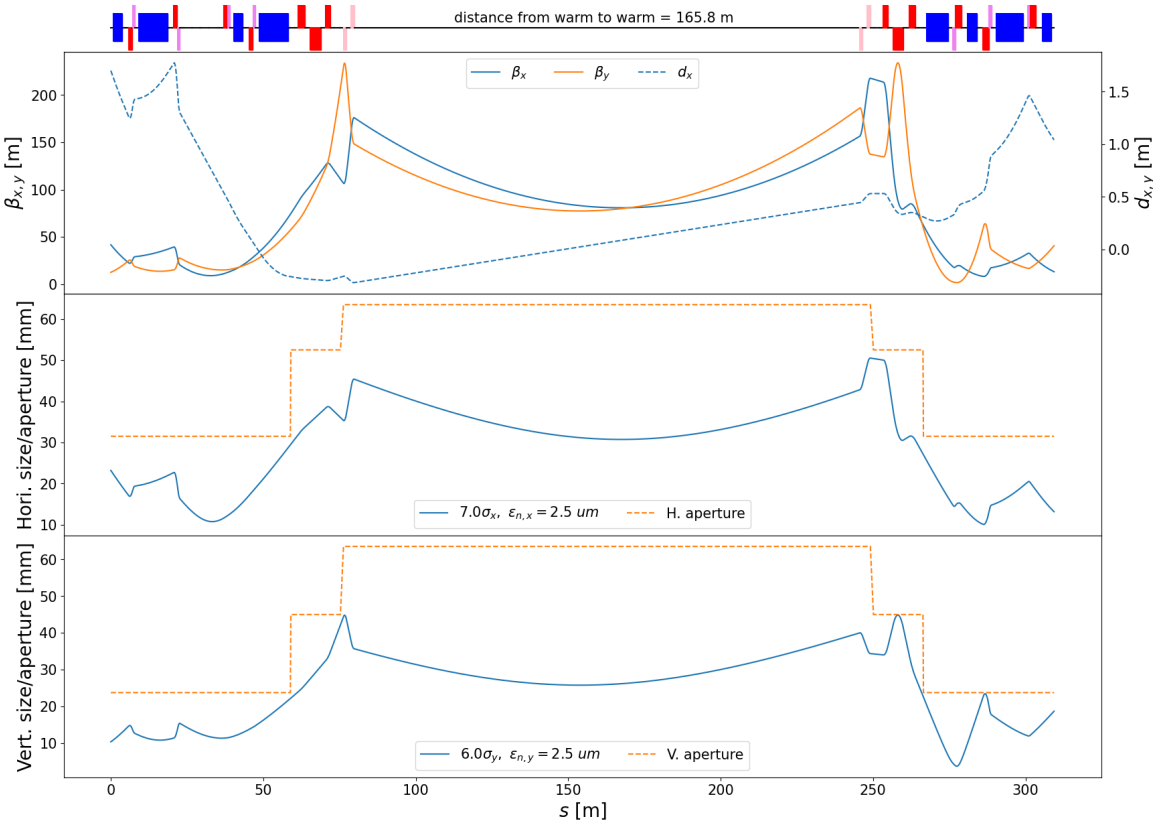

Figure 3.12: IR2 injection optics with increasing s clockwise. The beam direction is from right to left. Top: Beta and dispersion functions. Middle and bottom: Horizontal beam size of 7σ and vertical beam size of 6σ, both with a normalized emittance of $\epsilon_x = 2.5\ \mu$m.

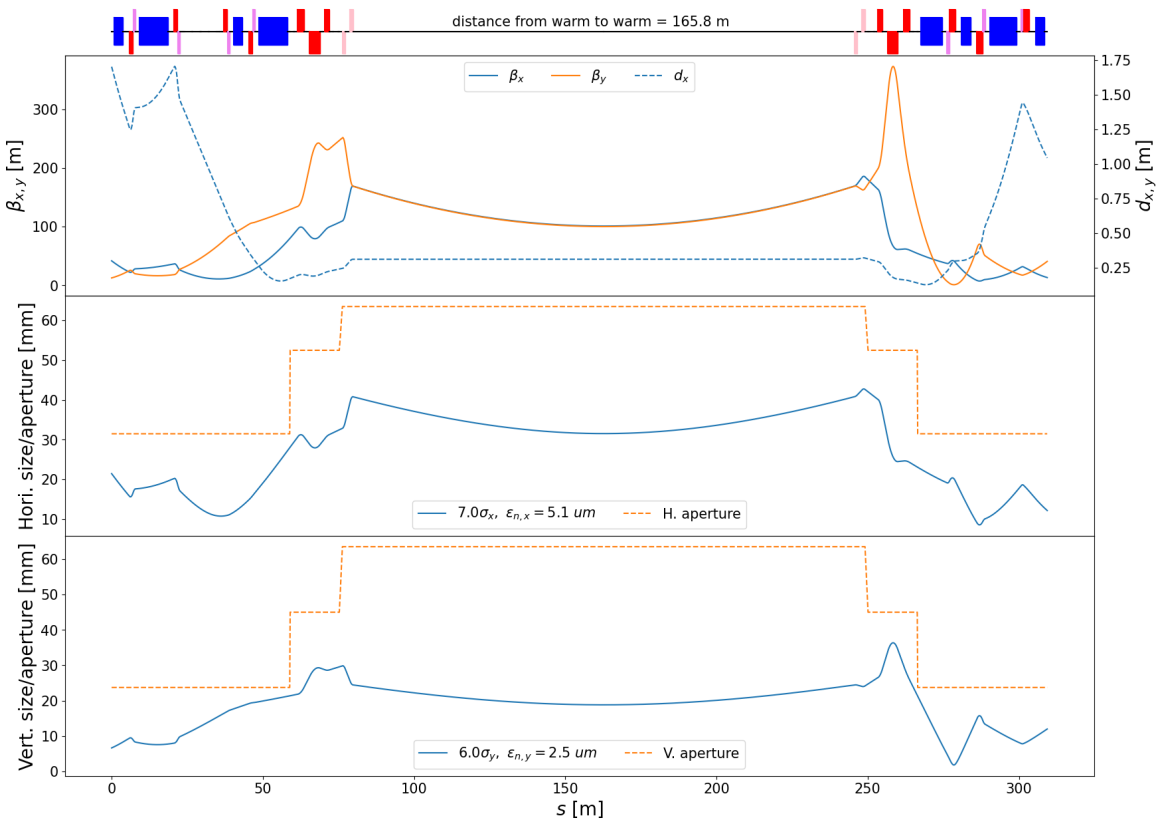

Figure 3.13: IR2 optics for low-energy cooling. The beam direction is from right to left. Top: Beta and dispersion functions. Middle: Horizontal beam size of 7σ with normalized emittance of $\epsilon_x = 5.1$ μm. Bottom: Vertical beam size of 6σ with normalized emittance of $\epsilon_y = 2.5$ μm. In middle and bottom plots, the dashed lines show the physical aperture. Here we assume the horizontal normalized emittance will grow to 5.1 ¯m after cooling.

Figures 3.13 and 3.14 show the IR2 optics for low-energy cooling, and at top energy, with the corresponding quadrupole magnet gradients and strengths listed in Table 3.9. Figure 3.15 shows the ramping curves for IR2 magnets, up to a gold energy of 110 GeV/u.

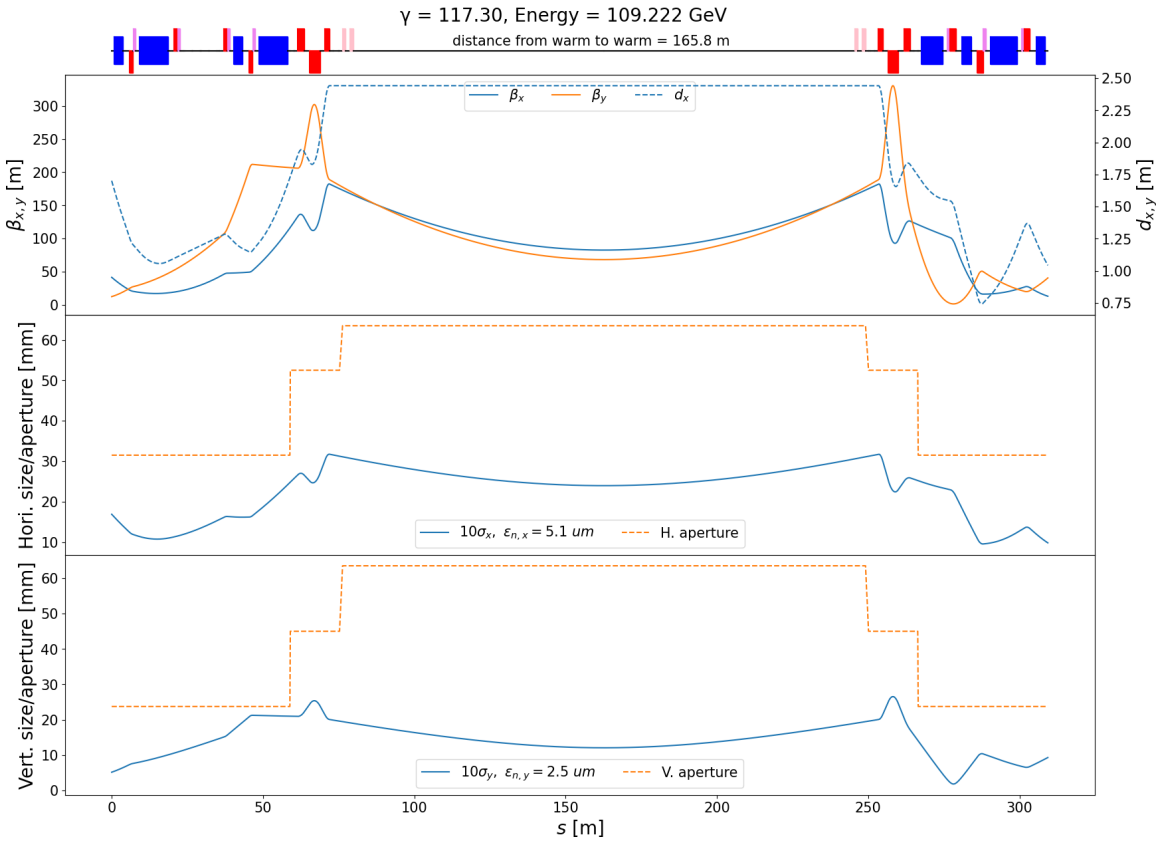

Figure 3.14: IR2 optics for top-energy operation. The beam direction is from right to left. Top: Beta and dispersion functions. Middle: Horizontal beam size of 10σ with normalized emittance of $\epsilon_x = 5.1$ μm. Bottom: Vertical beam size of 10σ with normalized emittance of $\epsilon_y = 2.5$ μm. In middle and bottom plots, the dashed lines show the physical aperture.

Magnet name	Injection		Low energy		Top energy	
	Gradient m^{-2}	Current A	Gradient m^{-2}	Current A	Gradient m^{-2}	Current A
H01O_Q7	-0.189	-1023.09	-0.175	-2291.44	-0.032	-1924.12
H01O_TQ7	0.18	51.65	0.166	115.47	0	0
H01O_Q6	0.261	1414.47	0.149	1950.12	0	12.41
H01O_TQ6	-0.387	-110.87	-0.163	-113	0	0
H01O_Q5	0.003	16.52	0	0.39	0.025	1502.66
H01O_TQ5	0.005	1.48	-0.016	-11.01	0	0
H01O_Q4	0	-1.83	-0.01	-137.17	-0.032	-1929.41
H01O_TQ4	0.005	1.45	0.005	3.41	0	0
BI1_QF3	0.004	37.54	0.032	653.14	0.027	2609.65
BI1_QD2	0	-0.07	-0.02	-421.27	-0.033	-3115.4
BI1_QF1	0.026	217.56	0.014	285.48	0.048	4550.71
WARMA1	-0.138	–	-0.083	–	0	–
WARMB1	0.101	–	0.083	–	0	–
WARMB2	-0.064	–	-0.015	–	0	–
WARMA2	0.063	–	0.033	–	0	–
YI2_QF1	0.07	592.33	0.058	1187.37	0.062	5921.84
YI2_QD2	-0.049	-416.96	-0.043	-889.18	-0.047	-4492.36
YI2_QF3	0.028	235.98	0.011	231.94	0.025	2387.09
H02_TQ4	-0.197	-56.5	-0.125	-87.11	0	0
H02_Q4	0.075	405.89	0.084	1106.45	0.033	2014.14
H02_Q5	-0.181	-978.81	-0.149	-1950.24	-0.08	-4860.64
H02_TQ5	0.31	88.75	0.166	115.47	0	0
H02_TQ6	0.11	31.41	0.12	83.48	0	0
H02_Q6	0	1.63	0.007	89.75	0.048	2882.03

Table 3.9: Quadrupole strengths for the IR2 injection, low energy, and top energy optics. From top to bottom, each row corresponds to a quadrupole in the left-to-right order shown in Fig. 3.12. The transfer functions are 14.983 T/(m·kA) for the major quadrupoles, 9.546 T/(m·kA) for the triplet quadrupoles, and 0.283 T/(m·kA) for the trim quadrupoles.

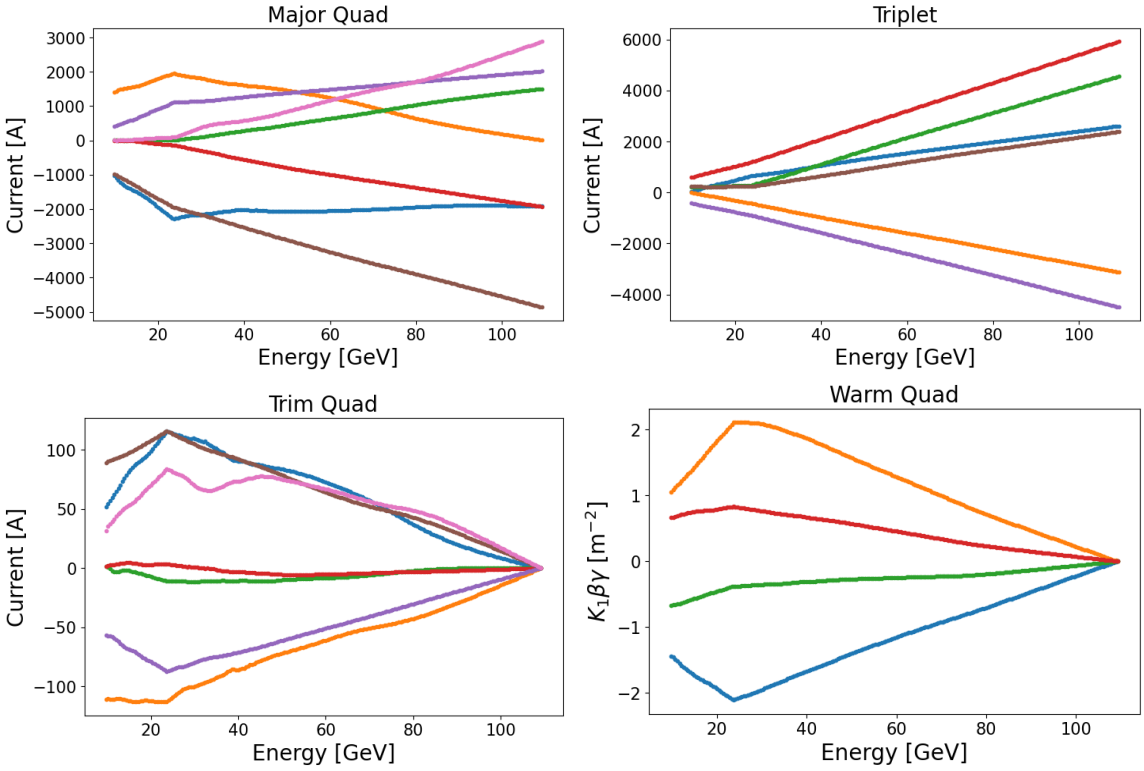

Figure 3.15: Ramping curve for major arc quadrupoles, major triplet, trim quadrupoles, and warm quadrupoles. The transfer function of warm quadrupole is unknown. Therefore, the vertical axis of last plot presents $K_1\beta\gamma$ instead of the current.

3.3.5 Energy Increase to 275 GeV

The proton beam energy of the present RHIC facility is limited to about 260 GeV by the quench limit of the DX separator dipoles in the interaction regions. The next limit, 267 GeV, is due to the RHIC main dipole power supply. Thus, to achieve the energy of 275 GeV one needs to remove DX magnet and replace the main dipole power supply to one capable to provide 5.8 kA current into the magnet bus.

With removed DX magnets, D0 magnets need to be rotated in order to have a sufficient physical aperture for hadron beam. However, it was recognized that a more cost efficient and flexible approach would be to remove the superconducting D0 magnet and install new warm dipoles instead. With warm dipoles one gets considerable flexibility in addressing specific lattice requirements in different IR sections.

3.3.6 Collision Synchronization

Radial Shift

Electrons and hadrons in the ESR and HSR must circulate their respective storage rings with the same revolution period

$$\tau_{\text{hadron}} \;=\; \tau_{\text{electron}} \;\approx\; 12.8\,\mu\text{s} \tag{3.17}$$

during storage, to maximize luminosity and to avoid deleterious beam-beam effects. The electron beam is highly relativistic over the entire EIC energy range from 5 to 18 GeV, so the electron revolution period is practically constant, except for the modest circumference shortening that occurs, by as much as about 8 mm, when super-bends are used to enhance synchrotron radiation at 5 GeV.

In contrast, the hadron relativistic speed β varies significantly over the proton energy range 100 GeV$< E <\sim$275 GeV, with

$$\beta \;=\; \sqrt{1-(m_p c^2/E)^2}$$

where $m_p = 0.9383$ GeV/c^2 is the rest mass of the proton. The design orbit circumference must be

$$C \;=\; \beta C_1 \;=\; C_0 + \Delta C \tag{3.18}$$

where C_1 is the ultra-relativistic circumference and $C_0 = 3833.824$ m is the on-axis reference circumference at a mid-range energy of about 133 GeV. The circumference is adjusted in one or both of two ways, depending on the energy:

- 100 GeV$< E <\sim$275 GeV: A radial shift is induced in all 6 arcs, 3 inner and 3 outer.
- E = 41 GeV: Protons (or ions with the same speed) pass on-axis through 4 inner and 2 outer arcs.

In high-energy operation with a radial shift of ΔR in 3 inner and 3 outer arcs, the total additional circumference is

$$\Delta C \;=\; \int_0^C \frac{\Delta R(s)}{\rho}\,ds \;=\; \int_0^{2\pi} \Delta R\; d\theta \tag{3.19}$$

where the local bending strength $1/\rho$ is zero except in dipoles. The average radial offset therefore spans a range of

$$-11.7\;[\text{mm}] \;<\; \langle \Delta R \rangle \;=\; \Delta C/2\pi \;<\; 11.7\;[\text{mm}] \tag{3.20}$$

KSS

ToDo: Add bend radius value here?]

E_{tot} [GeV]	γ	$1-\beta$ [10^{-3}]	C [m]	ΔC [mm]	$\langle \Delta R \rangle$ [mm]
41.0	43.70	0.26189	3832.9153	-908.7	–
100	106.58	0.04402	3833.7506	-73.4	-11.7
133	141.75	0.02488	3833.8240	0.0	0.0
275	293.09	0.00582	3833.8971	73.1	11.6

Table 3.10: Circumference offsets and average radial shifts for protons at different energies. The very large circumference reduction required in the low energy scenario is achieved by passing hadrons through 4 inner and 2 outer arcs.

Table 3.10 and 3.11 lists the design orbit circumferences C across the high-energy range and at the on-axis low energy value of 41 GeV for protons, and 40.7 GeV/u for gold ions, respectively.

E_{tot} [GeV/u]	γ	$1-\beta$ [10^{-3}]	C [m]	ΔC [mm]	$\langle \Delta R \rangle$ [mm]
40.7	43.70	0.26189	3832.9154	-908.7	–
110	118.09	0.03586	3833.7819	-42.1	-6.7

Table 3.11: Circumference offsets and average radial shifts for gold ions at different energies. The very large circumference reduction required in the low energy scenario is achieved by passing hadrons through 4 inner and 2 outer arcs.

Beam Screen Aperture Constraints

The HSR vacuum beampipe is fitted with a copper beam screen liner coated with a thin film of amorphous carbon, in order to reduce the cryogenic heat load to an average of less than 0.5 W/m in the arc dipoles. The resistive wall effect dominates the electron cloud effect in limiting the maximum practical radial shift, if the Secondary Emission Yield is about 1.0 or less. Quadrupoles and sextupoles are of relatively minor interest for resistive wall heat load considerations, because the arc dipoles occupy most of the HSR circumference. Figure 3.16 shows how the resistive wall heat load increases as a function of the local radial shift in an arc dipole. The heat load is concentrated in the mid-plane where heat conduction to the helium coolant is less than optimum. A radial shift of 20 mm is estimated to enhance the mid-plane heat load by a factor of 13.4 over the average around the perimeter. The total heat load will be about 0.37 W/m in the best case scenario, with high RRR copper at a maximum temperature of 10 K or cooler.

Simulations confirm that sextupoles suffer the worst cryogenic head load from electron cloud. Electron cloud formation can be suppressed by applying amorphous carbon to the beam screen surface with an SEY of less than about 1.0. All the beam screens will be coated with low-SEY amorphous carbon.

Radial offsets as large as 14 mm in quadrupoles do not increase the cryogenic load through electron cloud heating, which is further ameliorated when the amorphous carbon surface has an SEY of less than $\sim$1.0.

The radially shifted closed orbit needs to be smooth and well-matched in the arcs, carefully avoid-

ing peak displacements of more than about 20 mm.

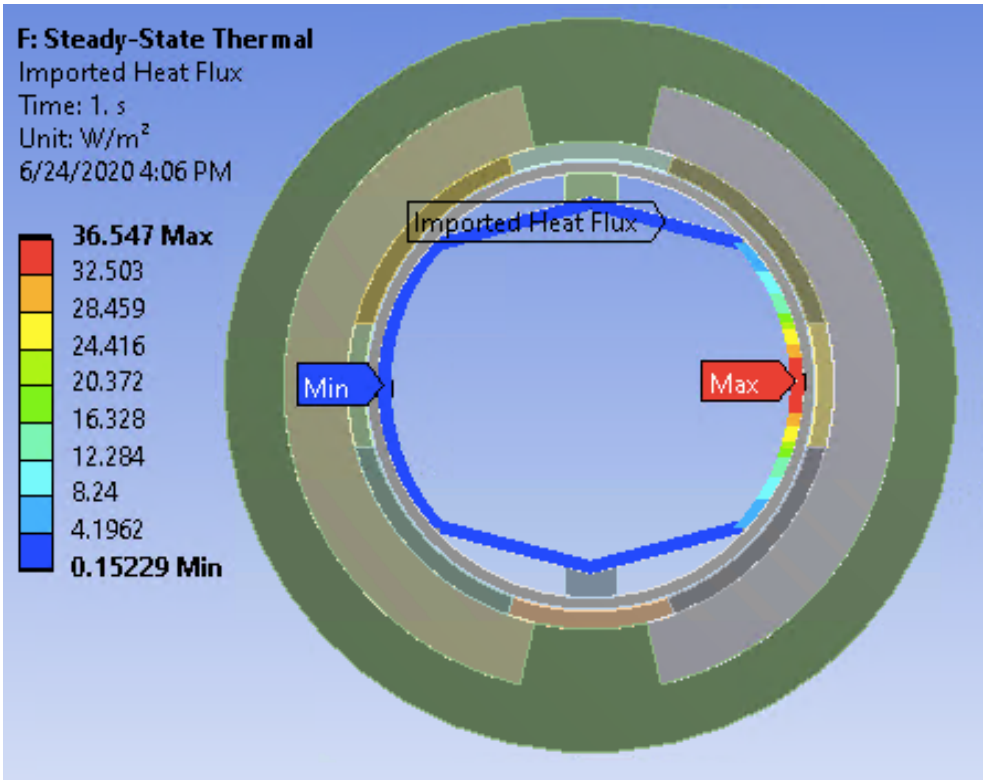

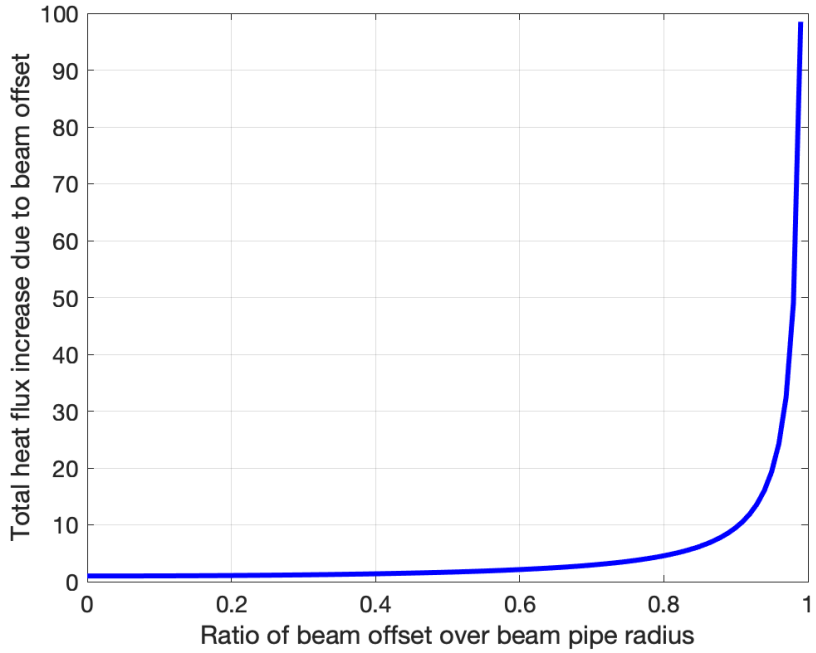

Figure 3.16: Top: resistive-wall heat flux distribution around the perimeter of polygonal beam screen for off-centered beam. Bottom: total heat flux on the beam screen as a function of the beam offset (arbitrary units). The flux increases quickly for offsets of more than about 20 mm.

The Off-field Parameter δ_B and the Geometric Compaction Factor α_B

In all 6 arcs the main dipole strength is adjusted by the *off-field parameter*

$$\delta_B \equiv \frac{\Delta B}{B} = \frac{\Delta(B\rho)}{(B\rho)} \tag{3.21}$$

that also measures the mismatch of beam and arc dipole rigidities. The goal off-axis closed orbit in the body of an arc has a radial offset of

$$x(s) = -D_{\text{matched}}(s) \cdot \delta_B \tag{3.22}$$

where D_{matched} is the dispersion function of a series of matched arc FODO cells, because this minimizes the maximum value of $|x|$ in an arc and makes the best use of the physical aperture. An ideal off-axis closed orbit is generated even when the arc dispersion itself is *not* perfect, by properly launching and capturing it at the beginning and end of each arc.

In the simple approximation that all dipoles (including those between the arcs and in the dispersion suppressors) have the same δ_B, then

$$\Delta C = -\delta_B \int_0^{2\pi} D\, d\theta = -\alpha_{B,\max}\, \delta_B \tag{3.23}$$

where the maximum geometric compaction factor is

$$\alpha_{B,\max} = \frac{C_0}{\gamma_T^2} = 7.18\ [\text{m}] \tag{3.24}$$

and $\gamma_T = 23.12$ is the transition gamma. In practice the geometric compaction factor

$$\alpha_B = -\frac{\Delta C}{\delta_B} \tag{3.25}$$

is somewhat smaller than the maximum, because the closed orbit offset x is zero or small in some dipoles between the arcs. It is maximized by the judicious selection of the 4 (or more) dipole correctors in each arc that launch and capture the off-axis closed orbits.

Figure 3.17 shows how 2 typical alternative sets of dipole correctors – "inner" and "outer" – span 10 or 12 FODO cells in each arc. The "outer" set extends into the partial dispersion suppressors at the interface to the neighboring straights. In the case shown ($\delta_B = -.010$) the extreme radial shift of the closed orbit is about $x_{\text{extreme}} = 18\,\text{mm}$.

Figure 3.18 shows how ΔC depends on the independent parameter δ_B. The outer set is more efficient at generating ΔC, due to the additional 2 FODO cells per arc. Similarly, Figure 3.19 shows the correlation of the circumference change ΔC and the extreme radial offset x_{extreme}.

Table 3.12 shows the geometric compaction factor for each set, and its theoretical maximum, along with the off-field parameter range

$$\frac{\Delta C_{\min}}{\alpha_B} < \delta_B < \frac{\Delta C_{\max}}{\alpha_B} \tag{3.26}$$

that is required to change the circumference by $\Delta C = \pm 73.2\,\text{mm}$.

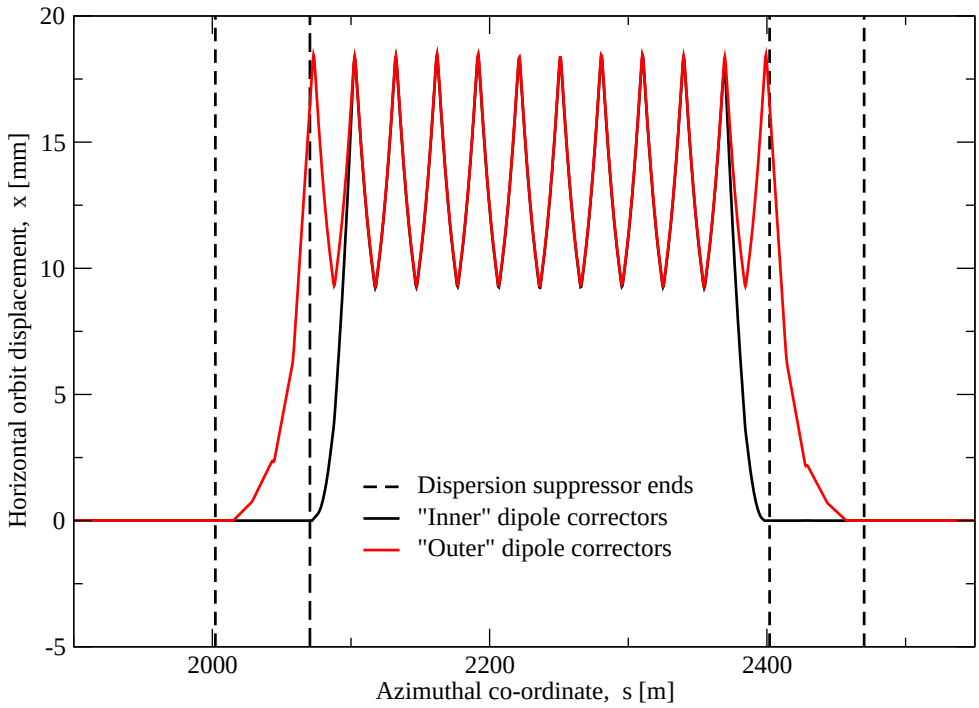

Figure 3.17: The ranges of the 'inner" and "outer" sets of dipole correctors that were studied, with $\delta_B = -0.010$ in a typical HSR arc. The "outer" range is slightly broader, and so is somewhat more efficient in changing the nominal particle circumference.

Name of Dipole Corrector Set	Geometric Compaction Factor α_B [m]	Off-field Parameter Range $\delta_{B,\text{min}}$	$\delta_{B,\text{max}}$
Inner	5.50	-0.0133	0.0133
Outer	7.10	-0.0103	0.0103
Ideal	7.18	-0.0102	0.0102

Table 3.12: Geometric compaction factor and the off-field parameter range required to make $\Delta C = \pm 73.2$ mm, for the "inner" and "outer" dipole corrector sets, and in the ideal case.

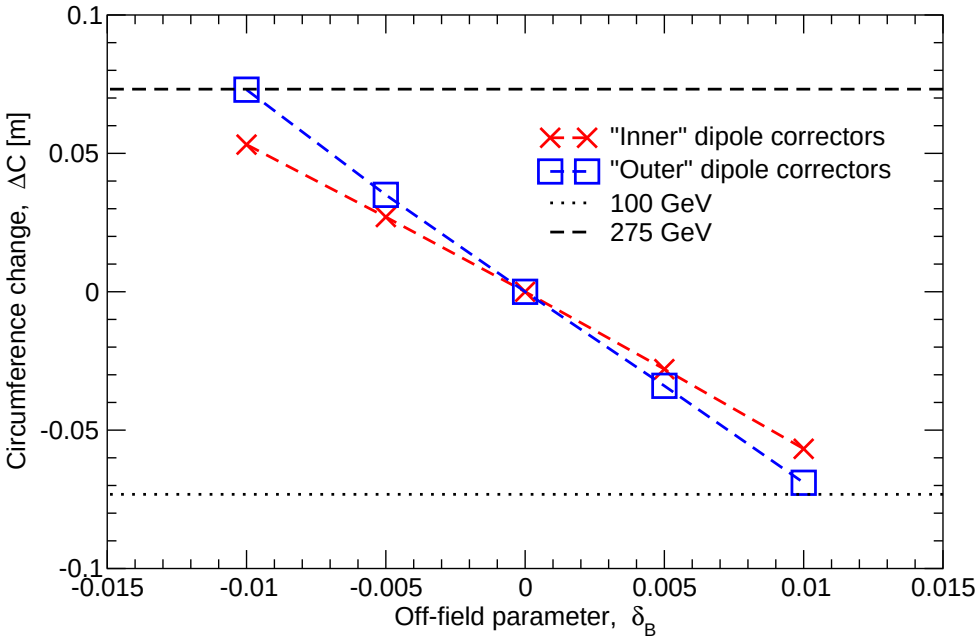

Figure 3.18: The dependence of the change in circumference ΔC on the independent off-field parameter δ_B for two different dipole corrector sets – "inner′ and "outer".

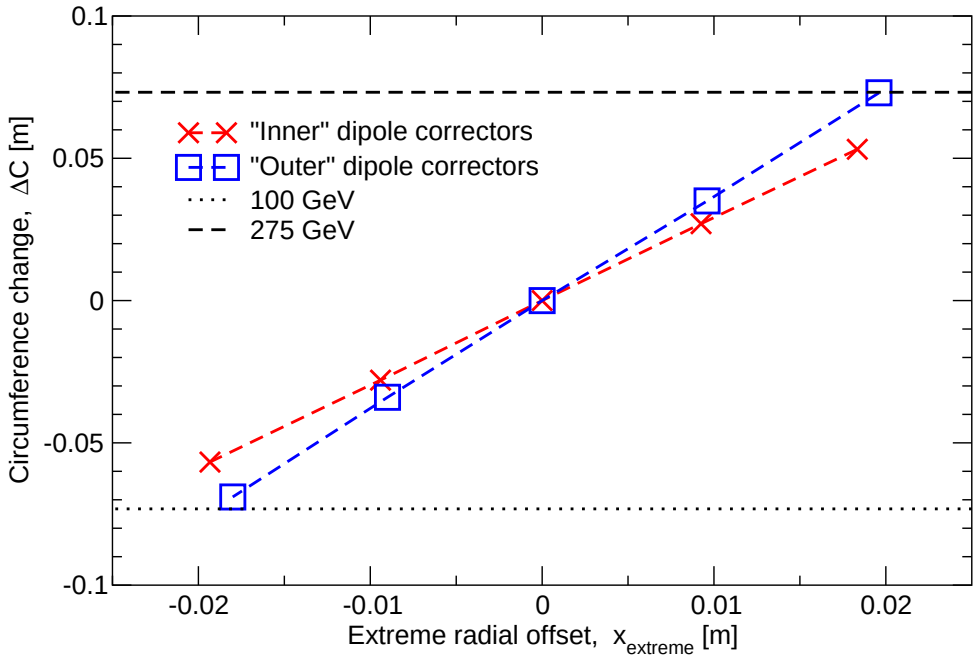

Figure 3.19: The dependence of the change in circumference ΔC on the extreme closed orbit offset for the "inner" and "outer" dipole corrector sets.

Launching and Capturing Off-axis Closed Orbits

The design closed orbit is on-axis in the 6 straights and interaction regions between the arcs. Beam is centered in the experiments, crab cavities, radio frequency systems, et cetera, in spite of the presence of a small number of bending dipoles, and in locations where the dispersion is non-zero. The few dipoles in the interaction regions and utility straights have fields that are matched to the rigidity of the beam.

In contrast, the design closed orbit is off-axis with

$$\begin{pmatrix} x \\ x' \end{pmatrix}_{\text{arc}} = -\begin{pmatrix} D \\ D' \end{pmatrix}_{\text{matched}} \delta_B \tag{3.27}$$

in all 6 arcs. Two dipole correctors in each of the 12 arc-IR and arc-straight interfaces match the on-axis and off-axis orbits, with strengths that depend on the optical functions at their locations. The strengths would be zero if

$$\begin{pmatrix} D \\ D' \end{pmatrix}_{\text{dipole corrector}} = \begin{pmatrix} 0 \\ 0 \end{pmatrix} \tag{3.28}$$

at the correctors – if they were placed outside a full dispersion suppressor at the end of the arc. Their strengths are reduced significantly at locations outside a partial dispersion suppressor.

Table 3.13 lists the "inner" set of dipole correctors used in the study of off-axis optical performance reported below [**?**, **?**, **?**]. Figure 3.20 shows that the currents required to power them are all within the range of ± 70 A, the quench-test acceptance minimum for all dipole correctors. However, most RHIC dipole corrector power supplies are rated at ± 50 A, generating the angular strengths listed in Table 3.14. Ten have been upgraded to 55 A, and two to ± 60 A [**?**]. Thus it is necessary to strengthen the power supplies used to launch and capture off-axis closed orbits, and/or to define a higher-performing set of dipole correctors.

The "outer" set performs somewhat better than the "inner" set (see Figure 3.19), but a few dipole correctors require more than 70 A. A more comprehensive search of potential corrector sets is necessary. *In extremis*, the current could be reduced by using 6 or 8 dipole correctors per arc. The correctors also need some headroom to continue with their original function – correcting the closed orbit.

Sector Numbers	Dipole Corrector Name 1	2	3	4
12-1	YO1_TH10	YO1_TH12	YO12_TH12	YO12_TH10
2-3	BO3_TH10	BO3_TH12	BO2_TH12	BO2_TH10
4-5	BI5_TH11	BI5_TH13	BI4_TH13	BI4_TH11
6-7	YI7_TH11	YI7_TH13	YI6_TH13	YI6_TH11
8-9	BI9_TH11	BI9_TH13	BI8_TH13	BI8_TH11
10-11	BO11_TH10	BO11_TH12	BO10_TH12	BO10_TH10

Table 3.13: The "inner" set of dipole correctors used for off-axis studies.

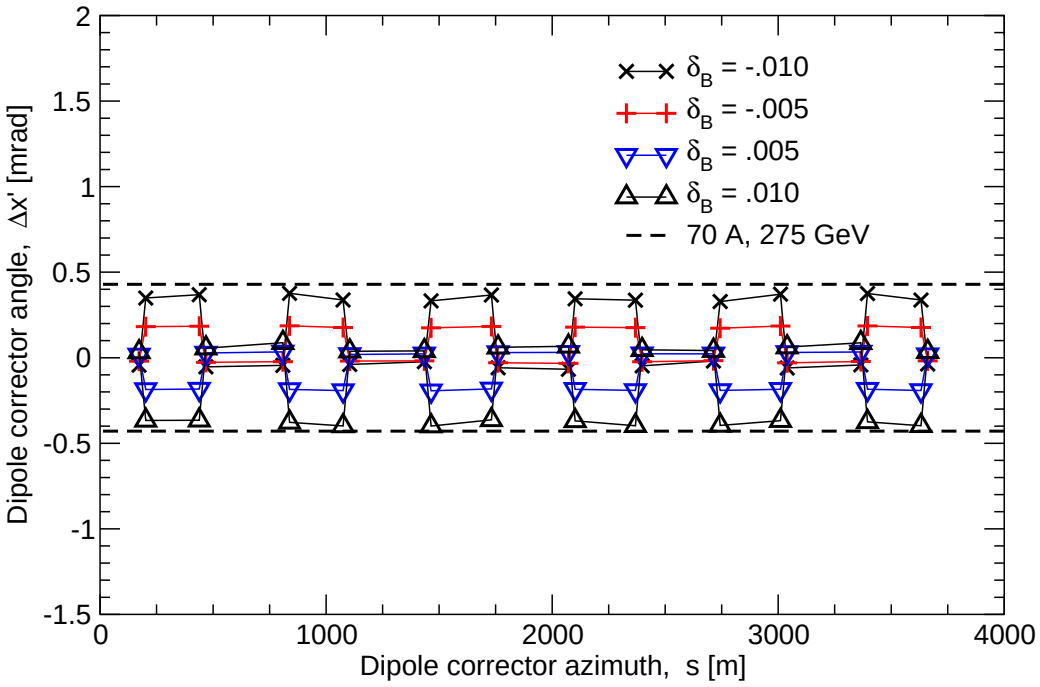

Figure 3.20: The angular strengths required of the "inner" set of dipole correctors.

Warm leads enter cryostats to power individual dipole correctors. Thermal runaway is absent up to 60 A, but needs further testing at 70 A [**?**].

Maximum Current [A]	Integrated Field [Tm]	Maximum Bend Angle [mrad] with proton energy [GeV]: 41	100	133	275
50	0.281	2.055	0.842	0.633	0.306
70	0.393	3.877	1.179	0.887	0.429

Table 3.14: Maximum dipole corrector bend angles, at the nominal maximum RHIC power supply current of 50 A, and at the maximum current of 70 A applied during quench tests.

Parameter	Horizontal	Vertical
Betatron tune Q_H, Q_V	28.228	29.210
Chromaticity C_H, C_V	1.0	1.0
IP2 β^* [m]	6.1	5.8
IP4 β^* [m]	6.2	5.8
IP6 β^* [m]	0.800	0.072
IP8 β^* [m]	6.0	5.9
IP10 β^* [m]	6.1	6.1
IP12 β^* [m]	6.1	6.1

Table 3.15: Primary parameters in off-axis studies of the collision lattice (HSR_200512 lattice).

Off-axis Optical Performance

In addition to setting δ_B to achieve the desired circumference, and setting the dipole correctors to deliver smooth off-axis closed orbits in the arcs, other magnets are tuned to return the optics to a goal state. Tunes and chromaticities are held at the primary values listed in Table 3.15 by adjusting the strengths of the main quadrupoles and main sextupoles in the arcs.

Twiss functions everywhere may then be optimized by small adjustments of individually tuned quadrupoles in the interaction regions and straights. Before that final tuning is performed, the root mean square value of $(\beta(\delta_B) - \beta(0))/\beta(0)$ is $(0.082, 0.064, 0.044, 0.064)$ for δ_B values of (-.010, -.005, .005, .010).

Figure 3.21 shows how the tunes vary with momentum over a $\Delta p/p$ range out to $\pm 8.3\,\sigma_p/p$, for 5 values of the off-field parameter ($\delta_B = -0.010, -0.005, 0.00.005, 0.010$). Although there is significant variation with δ_B, the off-axis cases are comparable in scale with the on-axis case $\delta_B = 0$.

Similarly, Figure 3.22 shows how detuning with respect to horizontal and vertical actions J_x and J_y varies with δ_B. The on-axis case with is typical of all off-axis cases. Straight line fits confirm the expectation that detuning is dominated by second-order chromaticity sextupole effects.

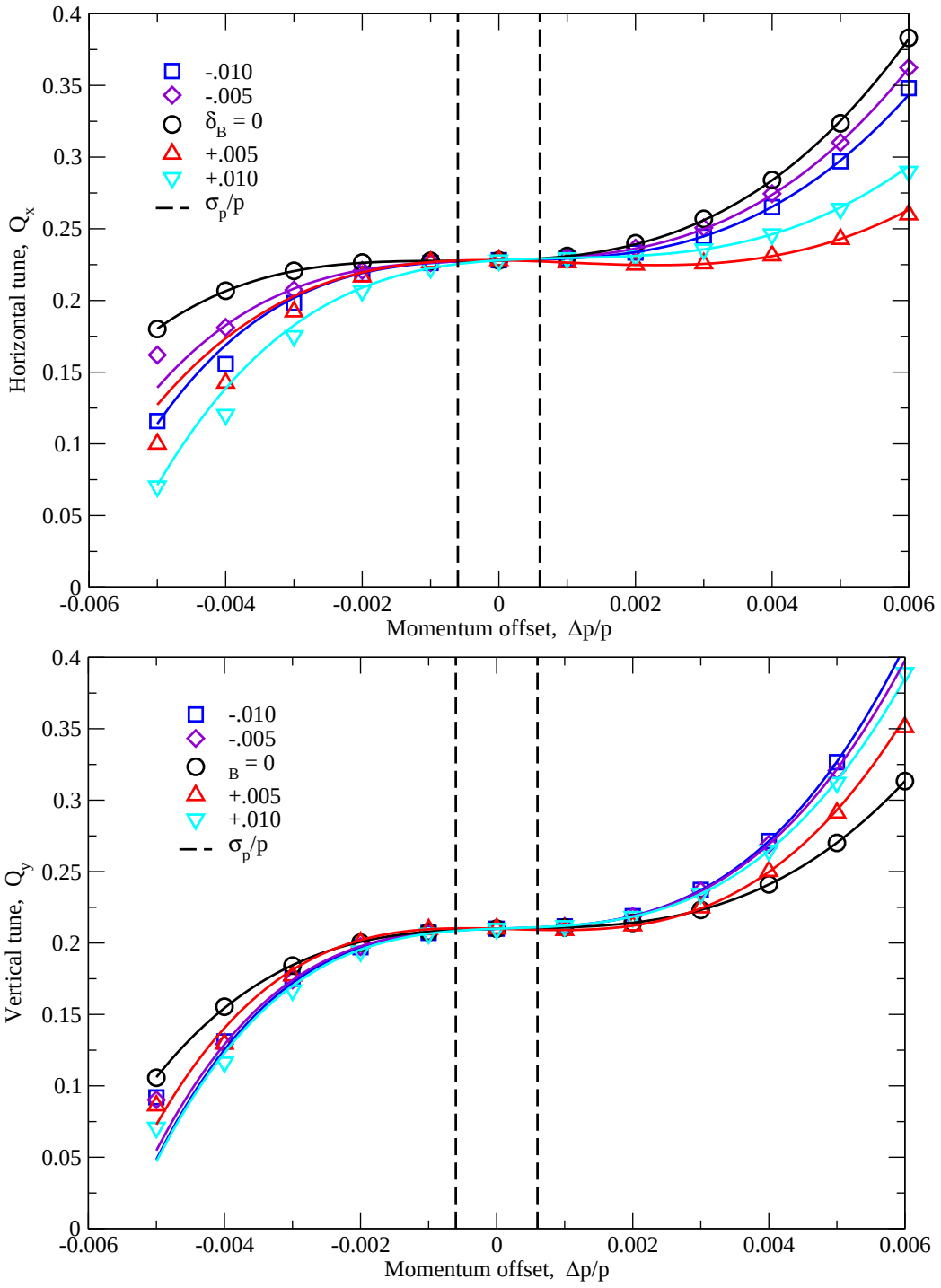

Figure 3.21: Horizontal and vertical detuning versus momentum offset for 5 δ_B values. Curves show quartic polynomial fits, with chromaticities of 1.0 . The vertical dashed lines show the nominal RMS momentum width of $\sigma_p/p = 6 \times 10^{-4}$.

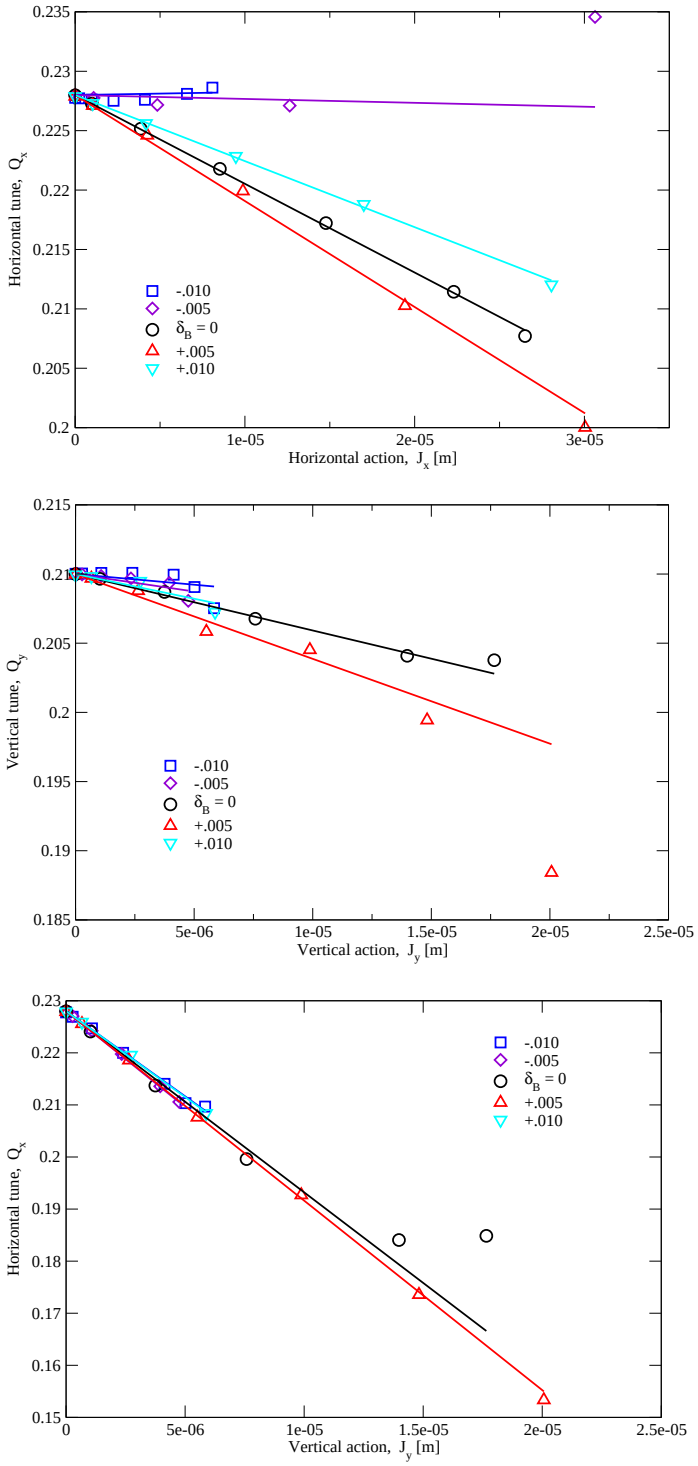

Figure 3.22: Detuning versus action for 5 δ_B values. The on-axis case with $\delta_B = 0$ is typical of all off-axis cases.

Dynamic Aperture

Dynamic aperture studies were performed by Zgoubi [**?**], tracking for 30,000 turns with 5 values of the off-field parameter δ_B, with sextupole multipoles at arc dipole ends but without including any physical apertures. Synchrotron oscillations were included at one of 5 off-momentum amplitudes

$$a_s \;=\; |(\Delta p/p)_{\rm extreme}| \;=\; (0, 0.4, 0.8, 1.2, 1.6, 2.0) \times 10^{-3} \tag{3.29}$$

that scan the bucket of the dual-harmonic RF system, as characterized in Figure 3.23. The (mainly) longitudinal parameters listed in Table 3.16 show that the RF bucket is "full", insofar as the bucket height is 3.0 σ_p/p.

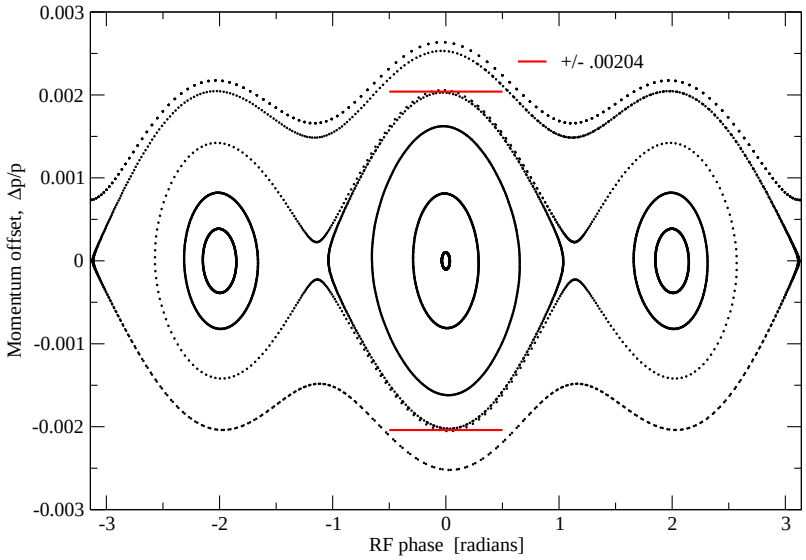

Figure 3.23: RF bucket.

The transverse lattice parameters listed in Table 3.15 show that this is collision lattice, with a dynamic aperture that is reduced by the stronger sextupoles that compensate for the largest natural chromaticities. This conservative perspective is partially offset by using the highest proton energy, shrinking the bean sizes since

$$\sigma \;=\; \sqrt{\frac{\epsilon_N \beta}{(\beta\gamma)}} \tag{3.30}$$

Maximum stable horizontal and vertical betatron amplitudes a_x and a_y are plotted against each other in Figure 3.24, in units of RMS transverse beam sizes σ_x and σ_y. The normalized initial emittance of $\epsilon_N = 2.0\,\mu$m is conservative, since both horizontal and vertical emittances shrink with time due to Strong Hadron Cooling.

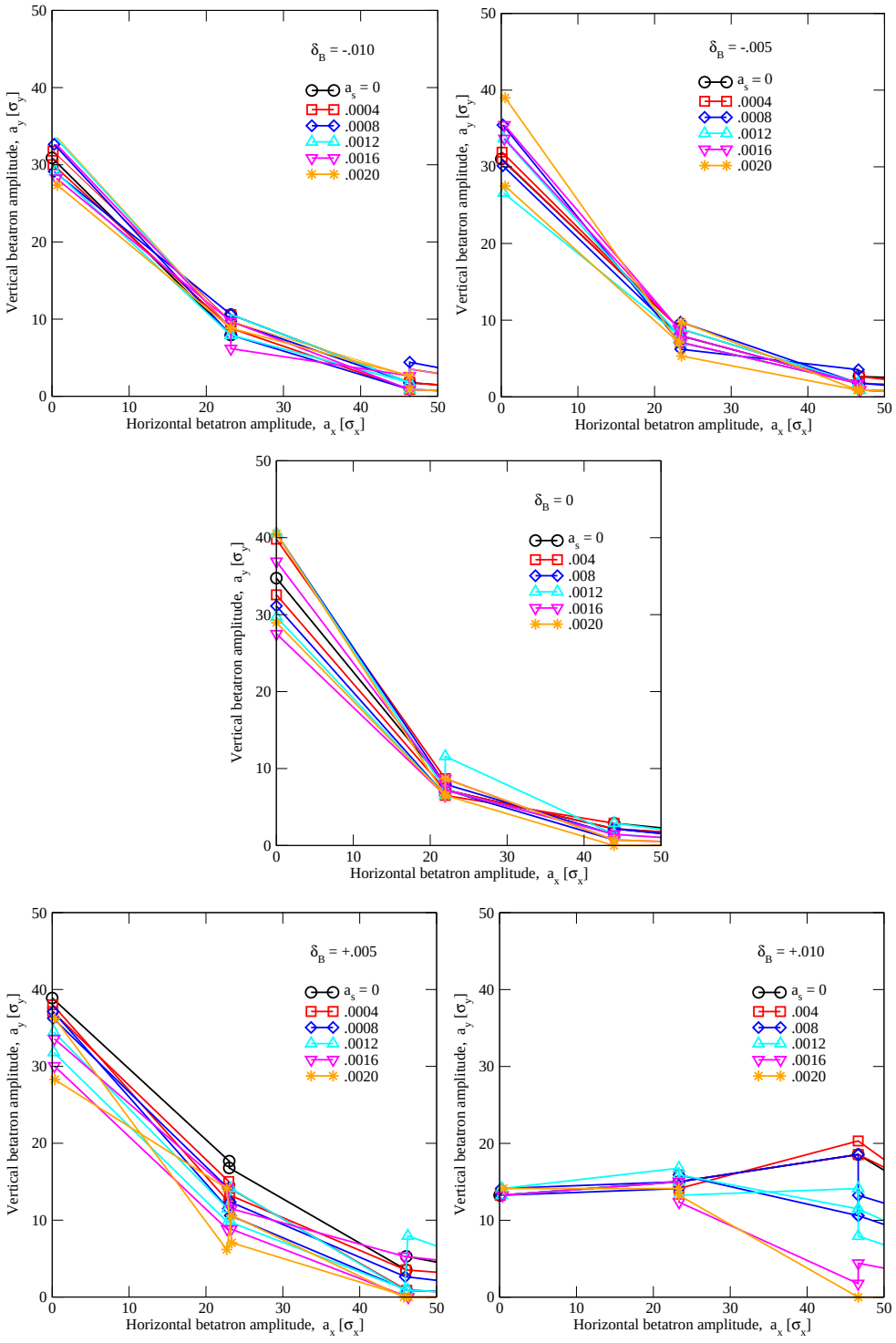

Figure 3.24: Dynamic aperture after 30,000 turns with $\delta_B = (-0.010, -0.005, 0, 0.005, 0.010)$.

Parameter	Value
Proton energy, E [GeV]	275
Normalized emittance (both planes), ϵ_N [µm]	2.0
Synchrotron tune, Q_s	0.0133
RF voltage (h, f)	
at 2520, 197 MHz [MV]	6
at $3 \times 2520, 591$ MHz [MV]	20
RMS momentum spread, σ_p/p [10^{-3}]	0.68
RF bucket height, $(\Delta p/p)_{\max}$ [10^{-3}]	2.04
Scaled bucket height, $\Delta p_{\max}/\sigma_p$	3.0

Table 3.16: Longitudinal parameters used in the Hadron Storage Ring dynamic aperture study.

The dynamic aperture does not vary significantly with δ_B, with stable betatron amplitudes of at least 11 σ through all of the RF bucket. The dynamic aperture varies with the synchrotron amplitude a_s, but without a simple dependency.

Beam Experiments and Operational Experience

In 2016 RHIC operations the pre-fire protection bump gave a maximum horizontal displacement of 20 or 21 mm to gold beam with an energy of 100 GeV/u and an emittance of 2.0 µm, at a location with $\beta_x = 40$ m and RMS beam size $\sigma = 0.9$ mm [**?**,**?**,**?**]. Larger displacements generated unacceptable beam losses. Gold ion losses include the generation of Au^{78+} through pair production and recombination, and the generation of $196Au^{79+}$ through electromagnetic dissociation. Both Au^{78+} and $196Au^{79+}$ are off-momentum with respect to $197Au^{79+}$. Protons do not generate such halo and have a slightly smaller beam size – for example $\sigma_x = 0.6$ mm at the same rigidity. In this way gold ion studies are more critical and informative than proton studies.

In 2018 RHIC Accelerator Physics EXperiments (APEX) studies were performed by storing a large emittance gold beam at an injection energy of 10 GeV/u, with an RMS beam size of about $\sigma = 2.8$ mm [**?**]. A ramp from off-axis to on-axis operations was developed to maintain clean off-momentum optics, and to minimize the ratio of $|x|_{\max}$ / $\langle \Delta R \rangle$ by careful control of the closed orbit. Performance with an average radial shift of $\langle \Delta R \rangle = -8.6$ mm was mostly satisfactory, but significant beam losses were seen with $\langle \Delta R \rangle = -11.0$ mm. An extreme displacement of -25.4 mm was observed, maintaining a 4.5 mm clearance with an assumed inner beampipe radius of 34.5 mm, including a 6σ envelope. Calculations extrapolating from these low-energy results at 10 GeV/u to high-energy gold beam operations at 100 GeV/u suggest that $\langle \Delta R \rangle$ could be reduced to about -15 mm, significantly outside the required range of $\langle \Delta R \rangle = \pm 11.7$ mm.

In 2020 a brief study took data at 26.5 GeV during an energy scan for Coherent electron Cooling. The RF frequency was held constant while the waveform manager was used to vary the value of the rigidity. Tune feedback was on, and closed orbit feedback was used as needed. Data showed spikes in Yellow ring losses, first on the outside when $x_{\max} \approx 12$ mm, and later on the inside when $x_{\min} \approx -14$ mm.

In 2021 dedicated high-energy studies are possible, with off-axis proton or gold ion lattices prepared following the HSR strategy:

1. Beam is on-axis in the 6 straights and off-axis in the 6 arcs
2. Non-zero δ_B is applied to all dipoles on the main dipole bus
3. One or more alternative sets of 24 dipole correctors are powered to launch and capture displaced closed orbits in the 6 arcs
4. Tunes and chromaticities are maintained at nominal values in a δ_B-ramp

Goals and implementation plans for these high-energy studies are in preparation at the time of writing.

A Mitigation Strategy to Reduce the Extreme Displacement

The extreme radial shift in the arcs depends on the maximum dispersion

$$|x|_{\max} \;=\; D_{\max}\;|\delta_B| \tag{3.31}$$

while the change in circumference depends on $\langle D \rangle$, the average off-axis dispersion. If

$$Y \;=\; D_{\max}/D_{\min} \tag{3.32}$$

is the ratio of maximum and minimum dispersions in the arcs, then the extreme and average displacements are approximately related through

$$|x|_{\max} \,/\, \langle \Delta R \rangle \;\approx\; Y^{1/2} \tag{3.33}$$

The extreme displacement could therefore be reduced at constant ΔC by reducing Y, which is a function of $\Delta\phi$, the phase advance per arc FODO cell. The results from Figure 3.25 recorded in Table 3.17 show that the extreme displacement could be reduced by almost 3 mm, by reducing the phase advance per cell to 40°.

$\Delta\phi$ [deg]	Y	$\langle \Delta R \rangle$ [mm]	$\lvert x \rvert_{\max}$ [mm]
82	2.0	14.0	19.8
82	2.0	11.5	16.3
40	1.4	11.5	13.6

Table 3.17: The potential reduction of the extreme displacement $|x|_{\max}$ by lowering $\Delta\phi$, the phase advance per arc FODO cell, from 82° to 40°.

However, Intra-Beam Scattering times decrease for smaller $\Delta\phi$ values, for both gold ions and protons. Reducing the phase advance per cell is therefore reserved as a potential mitigation strategy, to be adopted only if unexpected radial shift difficulties are encountered.

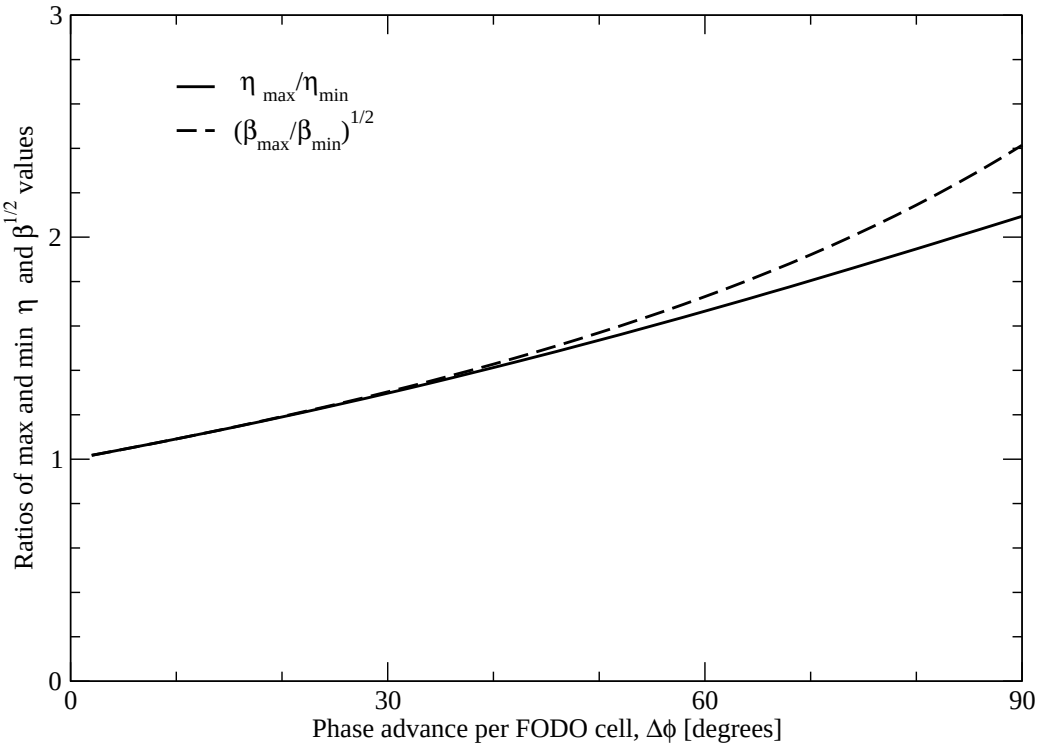

Figure 3.25: The dispersion ratio $D_{\max}/D_{\min}$ as a function of $\Delta\phi$, the phase advance per cell (in both planes) for FODO cells with thin quadrupoles. The ratio reduces significantly, from 2.0 to 1.4, when $\Delta\phi$ is reduced from the nominal RHIC value of 82° per cell to 40° per cell.

41 GeV Bypass

3.3.7 Z-line injection

Beamline layout and lattice

The new "Z-Line" beamline from the AGS to the HSR extends from the end of YD27 bending magnet to the end of the HSR injection septum system. The complete transfer line system includes the currently existing AGS-to-RHIC (AtR) transport beamline segments. The AtR X-Arc (RHIC Blue Arc) is removed. The magnets and other beamline components are redeployed for the Z-Line. Figure 3.26 describes the segments of the entire.

Periodic cells

Combined function magnets provide a fixed bend angle with a quadrupole component in 9 periodic cells in most of the length of the Z-line add references to BNL-225059-2023-TECH and EIC-ADD-TN-079. Each structure consists of the two combined function magnets and two quadrupole magnets. Two types of combined function magnets are re-used from the AtR beamline, with the parameters listed in Table 3.18, and as illustrated in Figure 3.27. Figure 3.28 shows the optical functions for the periodic cells. Table 3.19 counts the magnets and instruments that used in the periodic

Figure 3.26: Schematic of the Z-line layout. Green: AtR U-Line. Blue: AtR W-Line. Yellow: AtR Y-Arc, to the end of YD27. Orange: Z-Line upstream matching section. Dark Blue: Z-Line Sector-5 periodic arc cells. Red: Z-Line downstream matching section.

cells.

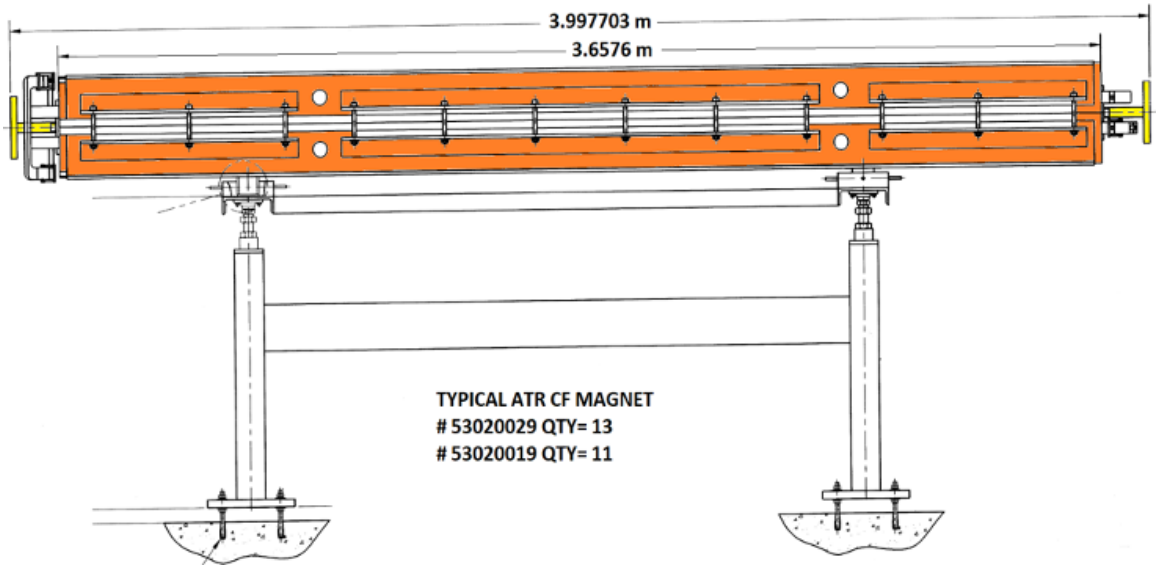

Figure 3.27: A Z-line combined function magnet.

Parameter	Units	Value
LONG		
Magnetic length	m	3.6579
Bend angle	deg	2.7591
	mrad	48.155
Quadrupole strength	m^{-2}	0.038082
Integrated strength	m^{-1}	0.1393
Focusing magnet count		12
Defocusing magnet count		13
SHORT		
Magnetic length	m	2.9465
Bend angle	deg	2.2224
	mrad	38.788
Quadrupole strength	m^{-2}	0.038079
Integrated strength	m^{-1}	0.1122
Focusing magnet count		4
Defocusing magnet count		2

Table 3.18: Z-line combined function magnet parameters

Item	Count
Long focusing combined function	9
Long defocusing combined function	9
Quadrupole	18
Dual plane corrector	18
Dual Plane BPMs	27

Table 3.19: Count of Z-line magnets and instrumentation in periodic cells

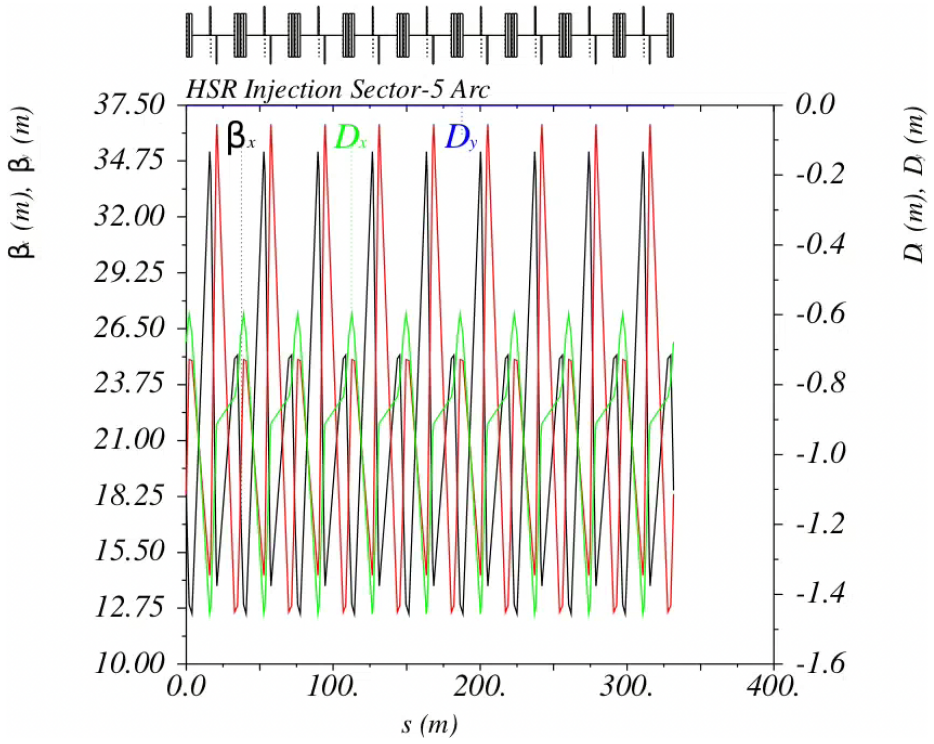

Figure 3.28: Optics of the 9 periodic cells in the Z-line

Upstream and downstream matching sections

The upstream matching section starts at the end of the Y-Arcand, and establishes a straight section to guide the beam into the beginning of the periodic cell section of the beamline. It is also responsible for adjusting the elevation by 0.0477 m, using two pitching magnets re-purposed from from that AtR X-Arc and Y-Arc. Optics for both upstream and downstream sections are shown in Figure 3.29, while the magnets and instruments used are counted in Table 3.20.

Item	Count
UPSTREAM	
Long focusing combined function	2
Long defocusing combined function	2
Quadrupole	10
Pitching dipoles	2
Dual plane corrector	5
Dual plane BPM	5
DOWNSTREAM	
Long focusing combined function	1
Long defocusing combined function	2
Quadrupole	10
Horizontal dipole	2
Dual plane corrector	7
Dual plane BPM	7
Current septum	1
Induction septum	1
Beam profile flag	3

Table 3.20: Count of Z-line magnets and instrumentation in matching sections

The downstream matching section is responsible for matching the optics for the injection into the HSR. It uses three of the remaining X-Arc CF magnets from the inventory. In addition, there will be two newly built horizontal dipoles ("Warm D0" equivalents), located in the middle of this beamline. Three beam profile flags are also installed in this beamline, enabling 6D beam profile diagnostics.

3.3.8 Transition crossing

While the RHIC arcs are preserved in the HSR, the insertion regions (IR) are rearranged with the exception of IR6 being fully replaced. Due to the complexity of the optics in the refurbished IRs, the placement of the γ_T quadrupoles destroys the symmetry of the First Order Matched (FOM) that is used in RHIC. Formulated as:

$$\Delta\gamma_T = \frac{\gamma_T^3}{2C_0}\sum_i (k_1 l)_i \eta_i^2 \tag{3.34}$$

where $k_1 l$ is the integrated normalized strength of the i^{th} jump quadrupole. It is clear to see that the change in $\delta\gamma_T$ is linear to the strenght of the jump quadrupole.

Figure 3.31 is the FOM when applied to the RHIC lattice. The scheme is designed to correct the local tune shift and wave generation driven by the arc jump quadrupoles. The lattice defined γ-transition, γ_T, is a direct feature of a closed geometry periodic lattice that at transition energy, affects the particle bunch by decreasing the bunch length and simultaneously increasing the momentum spread forcing the synchrotron tune to approach zero which causes the particle beam motion to become unstable [**?**].

$$\gamma_T = 1/\sqrt{\alpha_0} \tag{3.35}$$

, where the momentum compaction, α_0

$$\alpha_0 = \oint ds(\eta_x/\rho_x) \tag{3.36}$$

The quantities η_x and ρ_x, horizontal dispersion and radius of curvature is gathered from the electromagnetic lattice of the accelerator.

The G-family, which is the quadruplet of quadrupoles in the arc, distort the optics and dispersion when excited in such a way that the γ_T of the lattice becomes dynamic and for HSR, this is a change of ± 0.5 units. The Q-family, which are pairs of doublets that reside around the arc in minimum dispersion areas, compensate for the tune shift driven by the G-family by ramping with the opposite polarity. To optimize the effectiveness of the jump quadrupoles the horizontal and vertical β-functions and phase advances at the jump quadrupoles must be as close as possible to identical and 90°.

The HSR lattice breaks the symmetry of the standard RHIC layout with the redesign of IR2 and IR6. Figure 3.32 shows the layouts of RHIC and the HSR. RHIC contains 24 G-family jump quadrupoles and 24 Q-family jump quadrupoles (G24Q24) where as the HSR contains 24 G-family, and 16 Q-family jump quadrupoles (G24Q16). For the HSR, 16 Q-family quadrupoles are not evenly spread throughout the lattice. The standard FOM scheme is broken for the arcs adjacent to IRs 2 and 6. This presents a challenge in the minimization of the wave generation when the jump quadrupoles are at there maximum or minimum excitation.

Designing the γ_T Jump

The β-beat and η-wave at the peak absolute excitation of the jump quadrupoles can be written as [**?**]

$$\frac{\Delta\beta_H}{\beta_H} = \frac{1}{2\sin(2\pi Q_H)} \sum_i (k_1 l)_i \beta_{Hi} \cos(2|\phi - \phi_i| - 2\pi Q_H) \tag{3.37}$$

and

$$\frac{\Delta\eta}{\sqrt{\beta}} = \frac{1}{2\sin(\pi Q_H)} \sum_i (k_1 l)_i \eta_i \sqrt{\beta_{Hi}} \cos(|\phi - \phi_i| - \pi Q_H) \tag{3.38}$$

where the difference in phase advance $\Delta\phi = |\phi - \phi_i|$ is taken at the jump quadrupole from a phase advance upstream of the doublet or quadruplet. The relationship between the strengths of the two

jump quadrupole types, G and Q, is [**?**, **?**]:

$$q_G = kq_Q \tag{3.39}$$

where k is the proportionality constant that relates the integrated normalized strength, q_Q, of the Q family to the integrated normalized strength, q_G, of the G family. The value of k is determined by sensitivities associated with the jump quadrupole families. A response matrix, T, that aids in establishing the strength ratio in the two-knob Q and G scheme, can be obtained from these sensitivities

$$T = \begin{pmatrix} T_{GG} & T_{GQ} \\ T_{QG} & T_{QQ} \end{pmatrix} = \begin{pmatrix} \sum S_{G,p} & \sum S_{G,p} \\ \sum S_{Q,p} & \sum S_{Q,p} \end{pmatrix} \tag{3.40}$$

The ratio of the $(-T_{QG}/(T_{QQ}) = k$. A "stay clear" area is needed to safely cross transition if $T_{NL} \gg T_c$

$$\Delta\gamma_T \approx 4\dot{\gamma}T_{NL} \tag{3.41}$$

Figure 3.30 is a schematic of a change in γ_T with respect to time with a jump and without a jump. The jump duration is 40 ms which in HSR is approximately 3300 turns. During the jump the γ_T value changes by -1 unit.

Jump quadrupole sensitivities

Other metrics that are used in determining the effectiveness of the jump quadrupoles are the sensitivities to the phase advance within a given jump quadrupole family. Derived from Equ. 3.37 and 3.38, we write the sensitivity to the β- and η-wave generation, S_{bw} and S_{hw} as:

$$S_{bw} = \frac{\Delta\beta_H}{\beta_H}/(k_1 l)_i = \frac{\beta_{Hi}\cos(2|\phi - \phi_i| - 2\pi Q_H)}{2\sin(2\pi Q_H)} \tag{3.42}$$

and

$$S_{hw} = \frac{\Delta\eta}{\sqrt{\beta}}/(k_1 l)_i = \frac{\eta_i\sqrt{\beta_{Hi}}\cos(|\phi - \phi_i| - \pi Q_H)}{2\sin(\pi Q_H)} \tag{3.43}$$

From S_{bw} and S_{hw}, it is clear to see that the difference in the phase advance of the jump quadrupoles increase the wave sensitivities as the phase advance moves away from 90°. To better illustrate the point, Fig. 3.33 shows the effect of the increasing the difference in the phase advance from 75° to 90°.

Hadron Storage Ring optics

The HSR transition optics, shown in Fig. 3.34, are designed to place the phase advance per cell in the arcs as close to 90° as possible while constraining γ_T below the γ needed for hadron beam cooling. The beam direction in plot is from right to left, counterclockwise in the HSR ad in the direction of decreasing s-position. The optics of IR2, approximately 2400 to 2700, at transition maintain a relatively flat β-function and fully suppress dispersion for cooling purposes. The injection region, IR4, maintains the triplet optics of RHIC however, the dipole layout has changed. The warm dipoles that are the final bend before the midpoint of the IR in the RHIC-like IRs (IR8,

IR10, and IR12) are between the triplets where as in IR4 the downstream warm dipoles are located downstream of the second set of triplets in the IR. They not only set the geometry of the lattice but also are used as spectrometer dipoles for tagging particle fragments generated by the polarization jets in the IR. Table 3.21 gives that parameters associated with transition lattice (trans-ef2e8c3:hsr-au-trans-8786phi-071725.var) **without** a transition jump. For simplicity, during the jump only the transition quadrupoles are excited to distort the optics.

Parameter	**Value**
Atomic Weight, A	196.97
Atomic Number, Z	79
Transition Energy, E_T [GeV]	22.9
Lattice Fractional Tunes $Q_{x,y}$	0.235, 0.232
RF Voltage, [kV]	200
Stable Phase, ϕ_s [rad]	0.074
Gamma Transition, γ_T	24.6
Harmonic Number, h	315
γ' [s^{-1}]	0.5
Circumference, C [m]	3833.802
Nonadiabatic Time, T_c [ms]	71
Maximum Momentum Spread, δ_{max}	0.0041
Nonlinear factor, α_1	-5.4$\times 10^{-4}$
Nonlinear Time, T_{NL} [ms]	302
Bunch Intensity, [10^{10}]	0.2
Peak Current, I, [A]	19.322

Table 3.21: Non-adiabatic and nonlinear parameters necessary to determine transition crossing efficiency in the HSR

The G24Q16 and G24Q16 configurations

Without introducing additional jump quadrupoles in IR2 or IR6, the performance through transition will suffer due to increased β-beating which causes scraping in the apertures of the magnet. The reduction of jump quadrupoles allows the β-wave to propagate around the ring. Table **??** show the various sensitivities discussed in Equs. 3.37, 3.38, 3.42, and 3.43 for the existing jump quadrupoles and the sum of the sensitivities on a given power supply. From the S_G and S_Q power supply columns, the ratio of the strengths of the G and Q, Equ. 3.39, are found to be $k_{inner} = -1.24$ and $k_{outer} = -1.61$ where inner and outer denote the position of the arc. The wave sensitivities are show that at 87$\circ$ the arc sensitivity remains close to zero while the straight section jump quadrupoles have great influence on the β-wave generation.

The horizontal tune before the jump is 28.226 and the vertical is 29.235. After the jump, the tunes are 28.209 and 29.227, horizontal and vertical, respectively. The post jump horizontal tune is close to the 5^{th} order betatron tune, 0.2 fractional, which an cause beam loss which crossed. The wave generation for the G24Q16 configuration is shown in Fig. **??** where Fig. **??** is the pre-jump wave generation and Fig. **??** is the post-jump.

The G24Q20 configuration introduces jump quadrupoles in the IR6 region. Though the phase ad-

Configuration	G24Q16-Pre	G24Q20-Pre	G24Q16-Post	G24Q20-Post
Hor. β-wave RMS	0.2876	0.2171	0.1804	0.2217
Ver. β-wave RMS	0.0894	0.1102	0.0922	0.0986
Hor. η-wave RMS $\sqrt{m}$	0.0393	0.0752	0.0888	0.1332

Table 3.22: Optical wave RMS sizes with 16 and 20 Q-family jump quads.

vances and dispersion do not meet the standard requirement for the γ_T jump quadrupoles, the quadrupoles are used for tune compensation. These quadrupoles aid in the enforcement of the moving the working point post jump further away from any strong tune resonance. The challenge in the placement of the jump quadrupoles is that in IR6 there is a limited number of available modules. The γ_T jump quadrupoles use corrector packages associated with IR quadrupoles and in IR6 slot for the jump quadrupoles are in competition with the skew quadrupoles.

3.3.9 Subproject 1 Scope

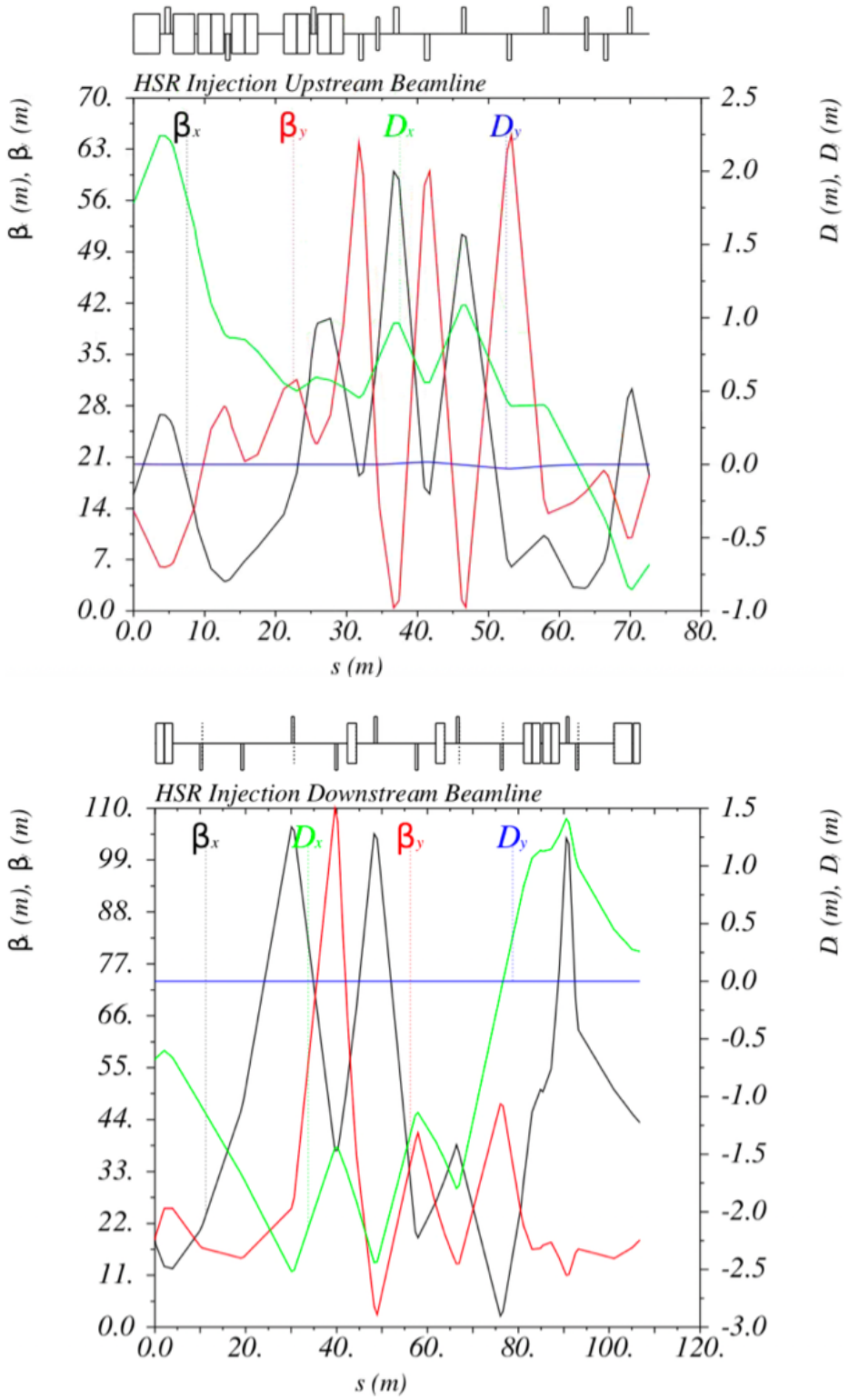

Figure 3.29: Optics of the Z-line matching sections. Top: upstream. Bottom: downstream.

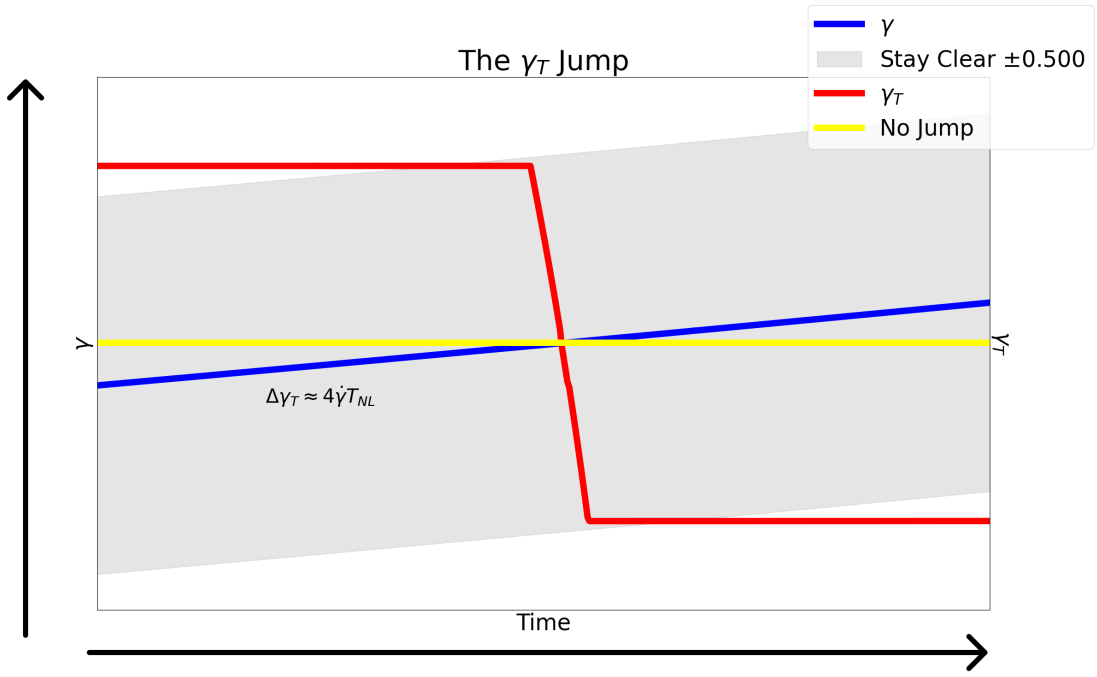

Figure 3.30: A schematic of the transition jump of -1 unit. The blue curve is the increase of energy through transition where the yellow curve is the γ_T without the jump and the red curve is γ_T with the jump. The "stay clear" region is marked in gray with the formula for the region.

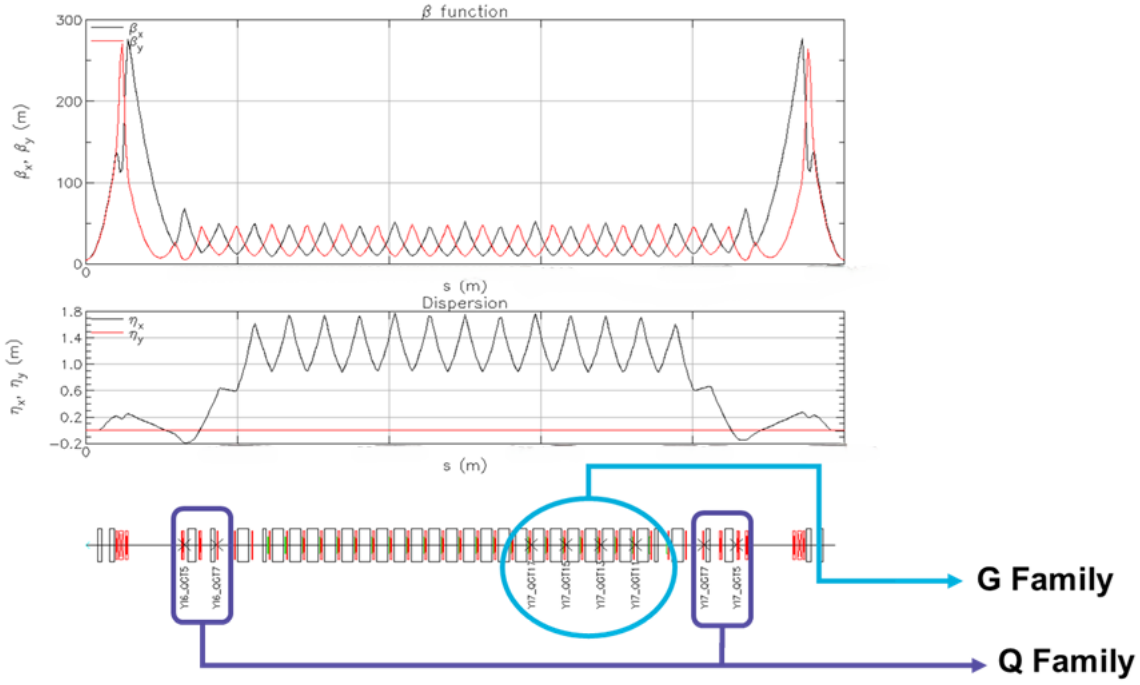

Figure 3.31: The FOM when applied to a typical sextant of RHIC. The circled G-family jump quadrupoles are in the dispersive section and the pair of doublets that surround the arc, Q-family, are in absolute minimal dispersive areas.

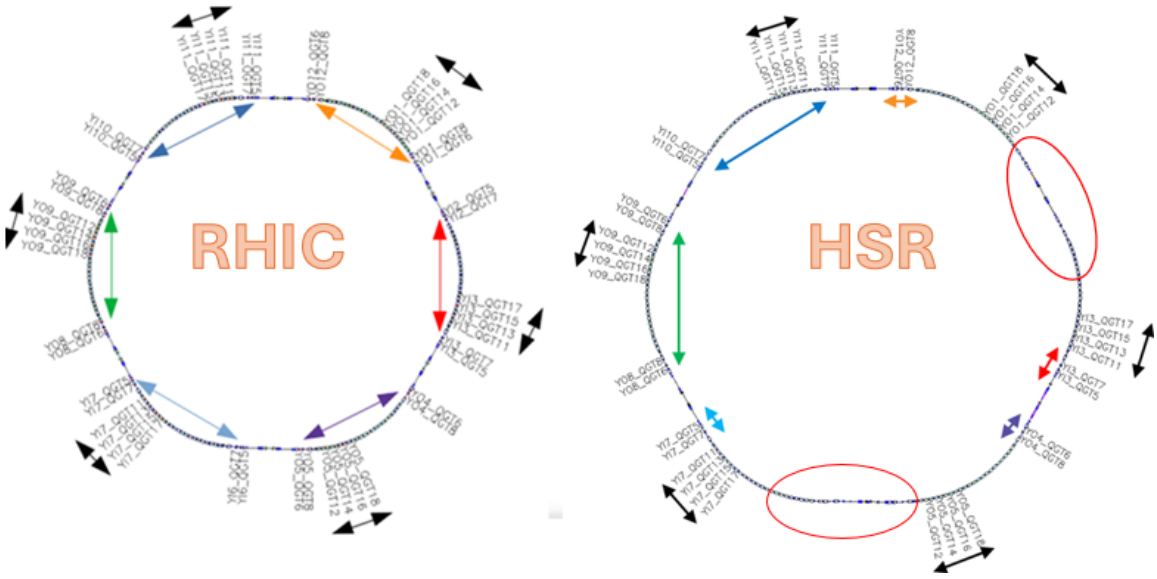

Figure 3.32: A comparison of the jump quadrupoles placement in RHIC and the HSR. The number of jump quadrupoles in RHIC is 48 where there are 24 jump quadrupoles for the G-family and 24 jump quadrupoles for the Q-family. The HSR has 24 G-family jump quadrupoles of 16 Q-family jump quadrupoles that are in the correct placement and phase advance.

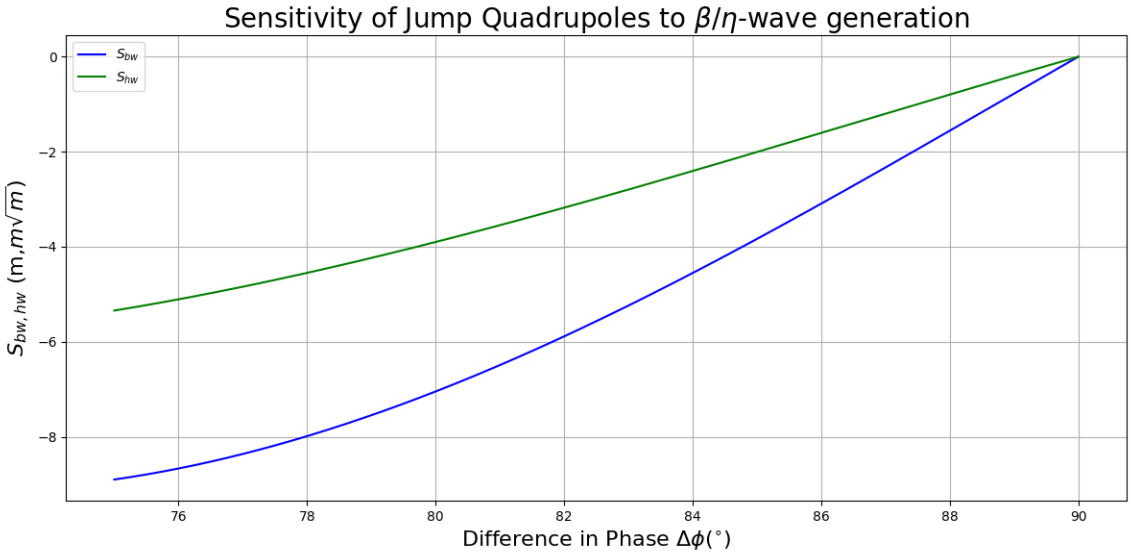

Figure 3.33: The sensitivities S_{bw} and S_{hw} absolute value decreases as the phase advance moves closer to 90°. For S_{bw} doublets are considered and for S_{hw} quadruplets

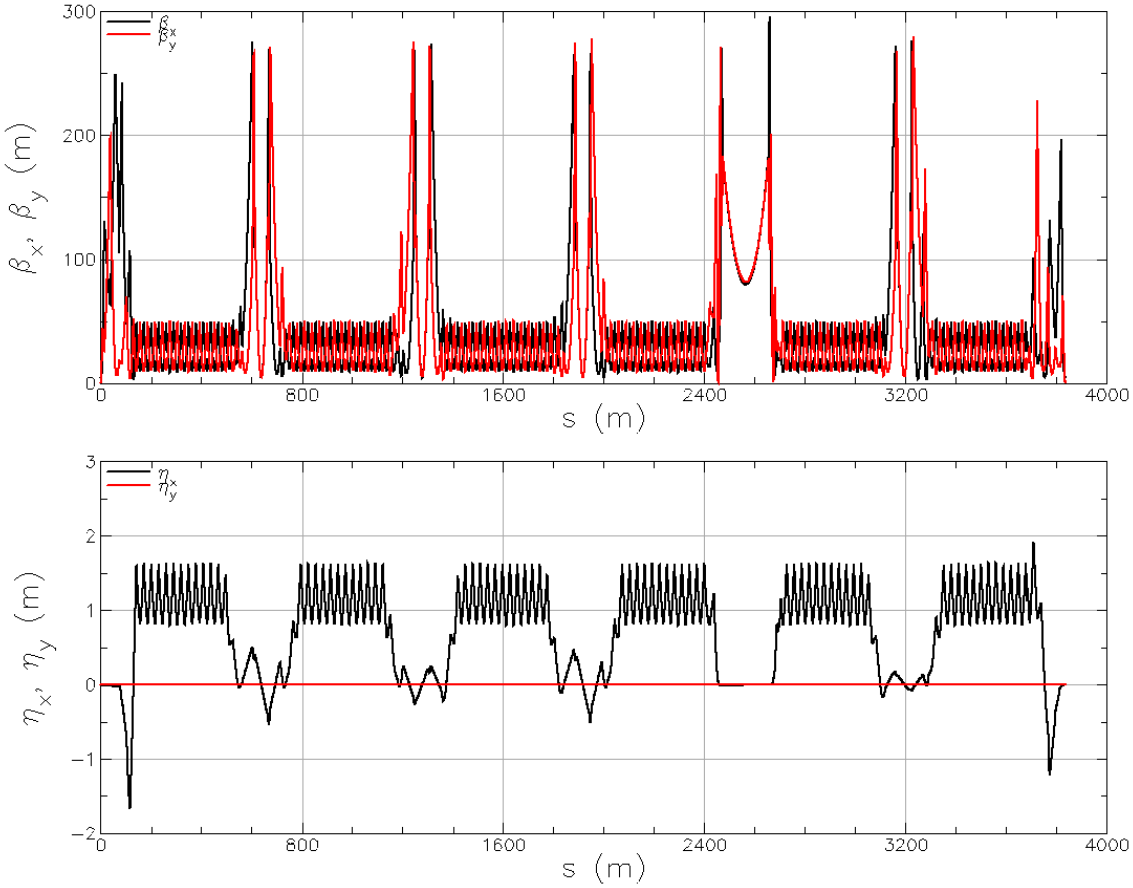

Figure 3.34: The HSR transition optics starting at IP6 with increasing s clockwise. The beam direction is from right to left in the two plots. Top: Twiss parameters with black the horizontal plane and red the vertical plane. Bottom: Dispersion with black the horizontal plane and red the vertical plane.

3.4 Hadron injector

The hadron beams for the EIC will be provided by the existing BNL Collider-Accelerator Department injector complex (Fig. 3.35), which has provided a wide range of heavy ions and polarized protons for the RHIC program for the last twenty five years. The hadron injector complex will be used 'as is' for the EIC operation for heavy ion and polarized proton operation. In the following sections we outline the basic operation of the injectors for those operations modes. The EIC's polarized ^{3}He program requires the development of a new source, which is discussed in subsection 3.7.2. The preservation of the polarization of both protons and helium is discussed separately in Chapter 5.

Three ion sources are routinely used to provide beam to the injectors. Heavy ions are provided by both an Electron Beam Ion Source (EBIS) and a Tandem van de Graaf (TVDG) [**?**]. Polarized protons of up to 10^{12} particles per pulse are provided by an Optically Pumped Polarized Ion source (OPPIS) [**?**]. A fourth source, which produces high intensity unpolarized protons ($> 10^{14}$ protons per pulse), is principally used for isotope production at the BLIP facility and occasionally for high intensity beam studies.

The heavy ion beams from EBIS and the Tandem are accelerated near the beam source to energies that depend on the specific species charge states and then delivered to the Booster. Polarized protons are accelerated from the source in a 200 MeV Linac (as H^-) and then strip-injected into the Booster through a carbon foil. From there, all species used for EIC will be accelerated in the Booster, transferred to the Alternating Gradient Synchrotron (AGS) and then extracted for delivery to the Hadron Storage Ring. Typical transfer energies are shown in Table **??**. Multiple Booster pulses can deliver beam for each AGS acceleration cycle. The repeat period of the AGS is anywhere from 4-6 seconds.

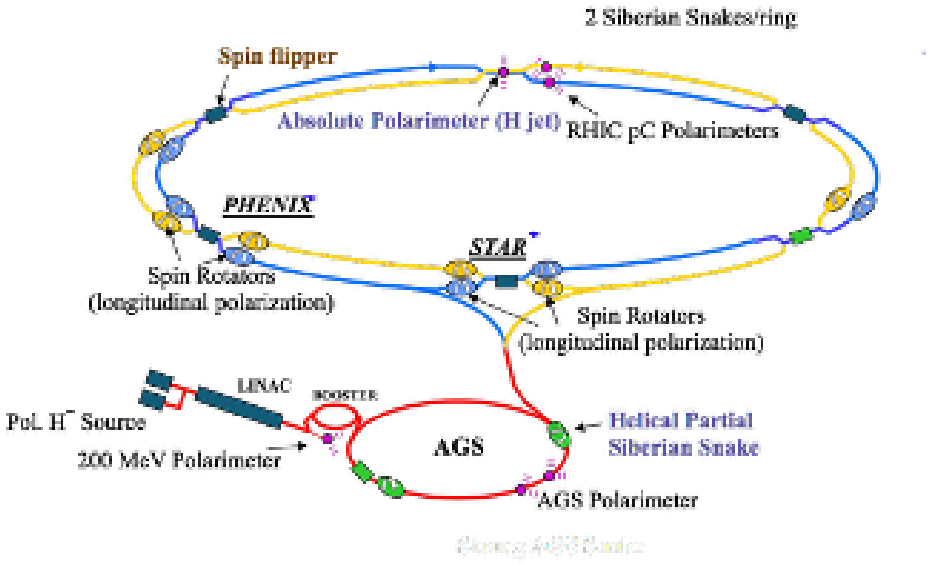

Figure 3.35: The RHIC collider and its injector complex.

	Energy (Total,GeV/N)	
	gold	protons
Source+Linac	n/a	1.14
Booster	1.03	2.36
AGS	9.8	23.8

Table 3.23: Typical top energies of hadron injector complex accelerators

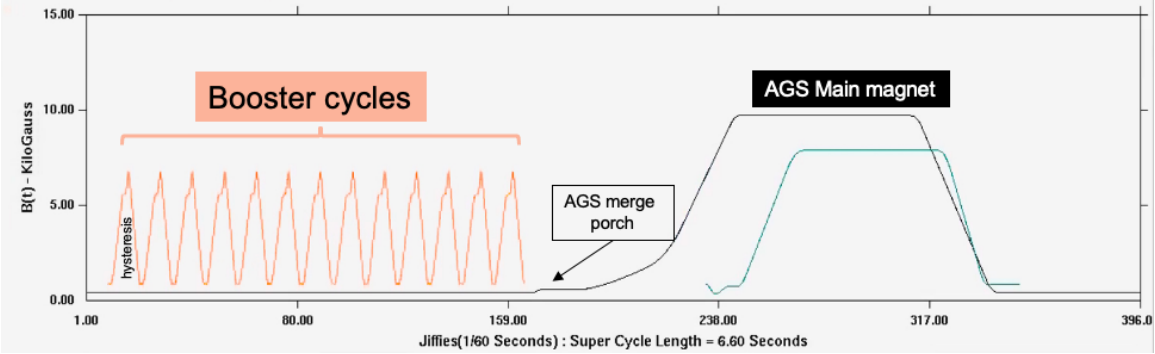

Figure 3.36: An injector supercycle showing 12 Booster pulses per AGS cycle.

3.5 Heavy ion acceleration

In addition to gold beams, the hadron injector complex has successfully delivered ion beams of d (deuterons), ^{3}He (helions, unpolarized), Al (aluminum), Cu (copper), O (oxygen), Ru (ruthenium), Zr (zirconium), and U (uranium) ion beams to RHIC. A full listing of all past hadron operating parameters for RHIC is in Ref. [**?**]. The EBIS and Booster also suppport the NASA Space radiation program, which has used a wider range of ions including: C,Ne,Si,Ar,Ti,Fe,Nb and Bi [**?**].

Heavy ions produced by EBIS and Tandem are not fully stripped of electrons. Further stripping is accomplished by passage through foils in the Booster-to-AGS transfer line (BtA) ad the AGS-to-RHIC transfer line. Foil materials and thicknesses are selected based on species to maximize yield in the desired charge state and minimize beam growth via scattering. Gold beam, for example, is accelerated in the Booster as Au^{32+}, stripped by a carbon/aluminum foil to Au^{77+} after the Booster and stripped again to a bare Au^{+79} nucleus by a titanium foil after extraction from AGS. The stripping efficiency of the foil at the Booster to AGS transfer energy is a strong determinate of the maximum intensity achievable. For stripping $Au^{32+} \rightarrow Au^{77+}$ this efficiency is 60-65%. The efficiency of the AtR stripping is typically >99% [**?**].

Per bunch intensity for heavy ions is maximized by using the RF to longitudinally merge multiple pulses from the sources into single bunches for extraction to the collider. Filling for the HSR will be the same asa filling for RHIC. Up to 12 Booster cycles of beam can be delivered to each AGS ramp. A typical arrangement of Booster and AGS cycles (called the injector "supercycle" is show in Figure 3.36. The 12 bunches provided to the AGS are then merged in two stages from 12 to 6 bunches and then from 6 bunches to 2 which can then be extracted to the HSR (Fig. 3.37. The filling rate for heavy ions is therefore planned to be up to 2 bunches every 4 seconds.

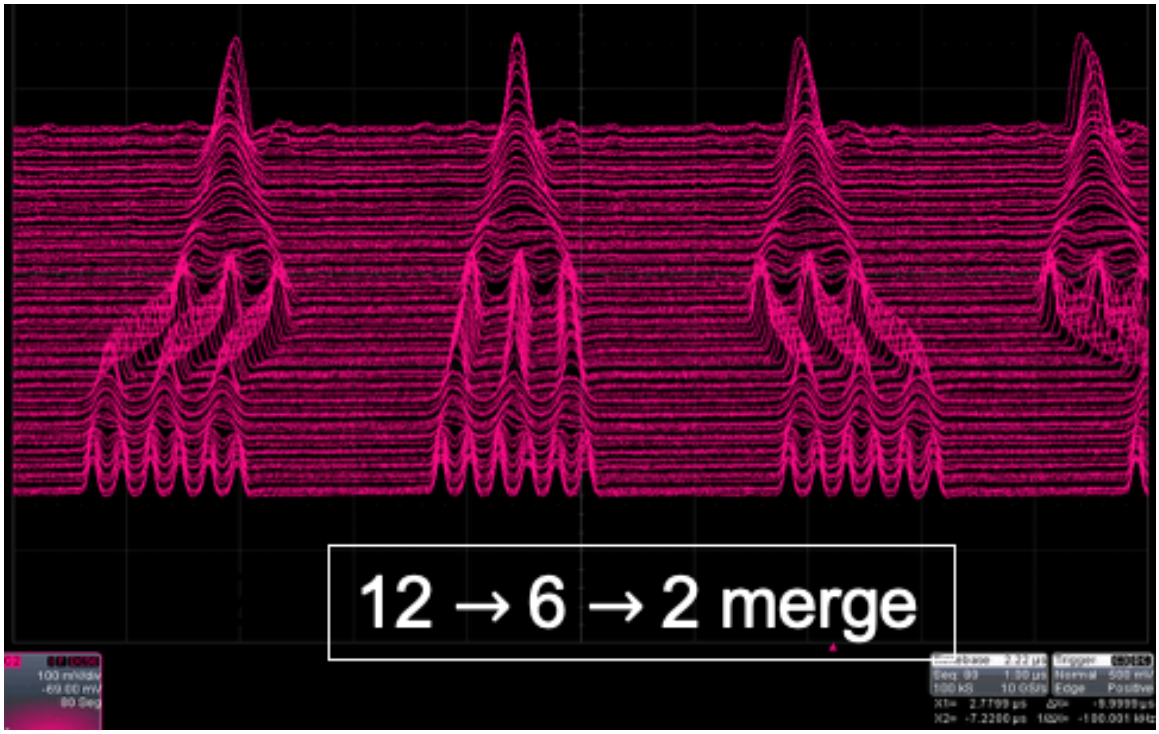

Figure 3.37: Wall current monitor measurement showing gold bunches in the AGS being merged from groups of 6 to 3 to 1 (time goes from bottom to top).

3.6 Polarized proton acceleration

In this section we treat only the general scheme for providing proton beam to AGS extraction energies. The polarization specific issues are elaborated in Chapter 5. The OPPIS delivers a single pulse of up to 10^{12} H^- ions to Booster injection (kinetic energy of 200 MeV). In typical operation, the source is configured to deliver 6-7$\times 10^{11}$ ions. The H^- is passed through a carbon foil inside the Booster aperture to produce a proton beam. During acceleration in the Booster, the bunch is scraped down against apertures in both transverse planes to an intensity and emittance required for the collider program. The scraping scheme is depicted in Figure 3.38. The proportion of beam scraped away is determined by empirical optimization of beam brightness and polarization downstream (see, e.g. [**?**]).

The polarized proton beam is transferred to the AGS at 2.25 GeV ($G\gamma = 4.5$) and accelerated to 23.8 GeV ($G\gamma = 45.5$). In normal operation, there is one Linac pulse (and one Booster cycle) for each AGS cycle resulting in one bunch for the collider every 4-6 second supercycle.

3.7 Intensity, Emittance and Space Charge

The proton intensity required by EIC is within the demonstrated capability of the injector complex and 10% higher than that required for RHIC operation (3.0×10^{11} compared to 2.7×10^{11}). Space charge tune shifts for polarized protons at AGS injection for a per bunch intensity of 2.5×10^{11} are as high as -0.17 and -0.25 (horizontal and vertical, respectively). It was observed in RHIC Run 17

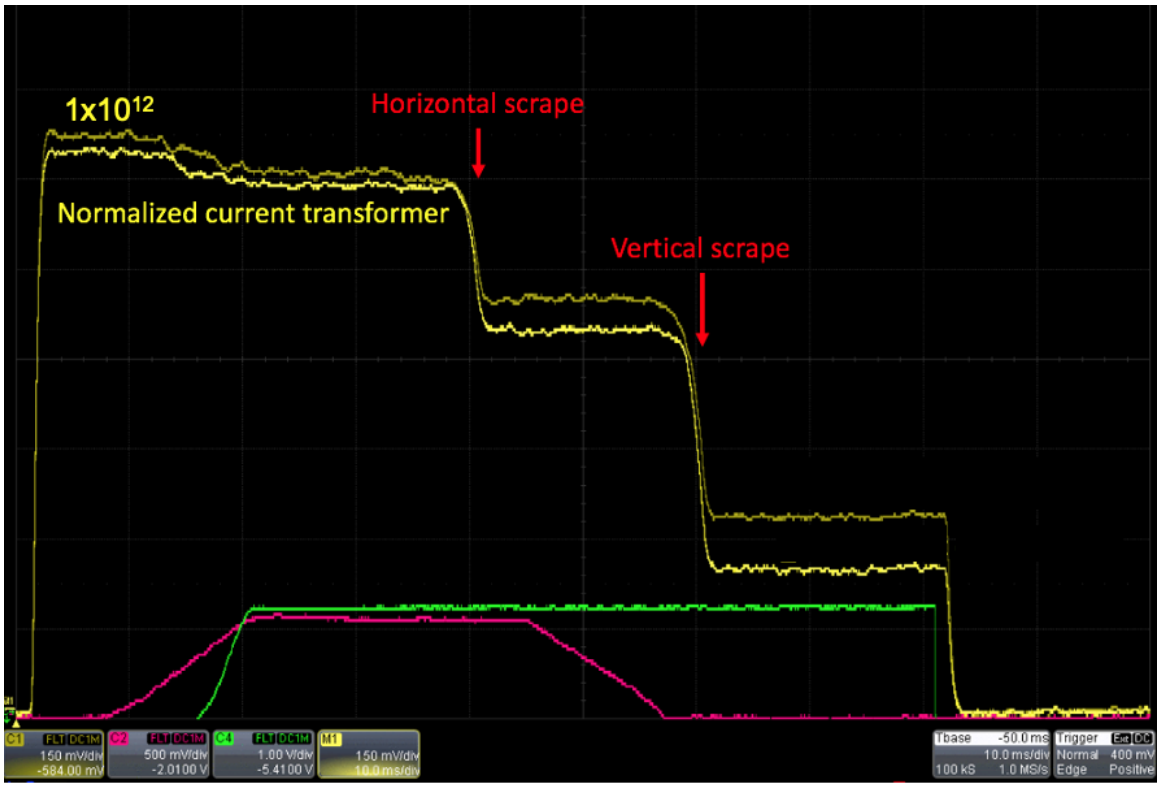

Figure 3.38: Evolution of intensity in Booster during a polarized proton cycle. Beam is transversely scraped to optimize brightness and polarization.

.

that reducing the peak current at AGS injection using defocusing RF voltage to lengthen the bunch longitudinally reduced the transverse emittance, consistent with space charge induced emittance growth [**?**]. A 20% reduction in the peak current produced a 15% reduction in the transverse emittances. Figure 3.39 shows the remaining dependence of the transverse emittances of the polarized beam at AGS extraction energy on the per bunch intensity in the presence of the defocusing RF.

The peak current at AGS injection can be lowered further by introducing a longitudinal bunch splitting scheme in the Booster. Longitudinally splitting the proton pulse in two reduces both the intensity and longitudinal emittance of each AGS bunch by a factor 2, resulting in a $\sqrt{2}$ reduction in the peak current.

Longitudinal merging of bunches in the Booster and AGS is common for RHIC heavy ion operations. In order to make bunches suitable for EIC the split bunches need to be merged again at AGS flattop, once space charge effects are much smaller. The long synchrotron period at that energy (12 ms) requires a longer merge time. Simulations indicate that a merge can be performed that preserves the longitudinal emittance in 500 ms, which fits on the AGS extraction porch. This bunching scheme uses only existing equipment and was commissioned during RHIC Run 24. Further developments can thus be tested in the injectors in advance of EIC construction.

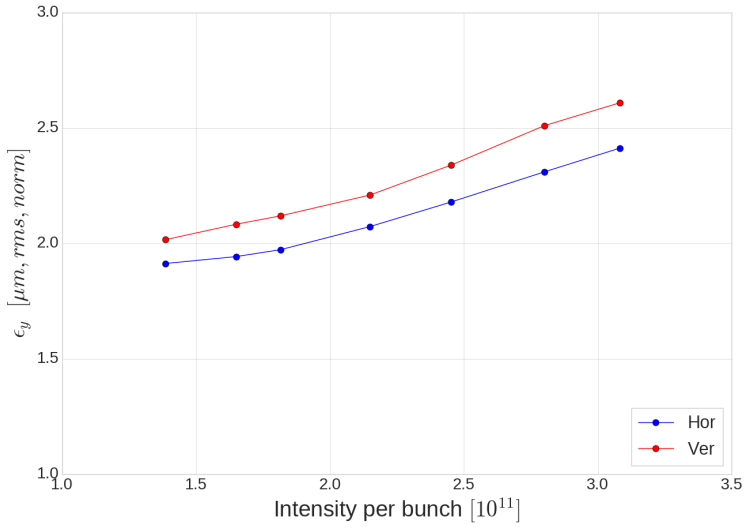

Figure 3.39: Normalized transverse emittances of polarized proton beam at AGS extraction energy ($\gamma = 25.5$) as a function of intensity.

3.7.1 Performance summary

Table 3.24 shows the beam parameters required for polarized proton and gold beams in the EIC, and the demonstrated beam parameters from the injector complex. From the various EIC operating modes the case for highest bunch intensity is selected for both polarized proton and gold beams. A hadron bunch injected into the EIC is either not split longitudinally, split once, or split twice. To define the required parameters at injection we make the following assumptions for the parameter evolution from the AGS extraction to EIC storage energy:

1. Up to 10% intensity loss (transfer and ramp)
2. Up to 10% transverse emittance increase (transfer and ramp)
3. Up to 10% longitudinal emittance increase (transfer, ramp and bunch splits)
4. No polarization loss

For the highest bunch intensity cases the hadron beams required for EIC injection have already been demonstrated in the RHIC injectors.

Parameter	proton		Au ion	
	EIC design	RHIC demonstrated	EIC design	RHIC demonstrated
Energy [GeV/nucleon]	23.8	23.8	9.80	9.80
Particle per bunch [10^{10}]	30	30	0.22	0.22
RMS norm. emittance, h/v [µm]	3.0/3.0	2.3/3.0	1.8/1.8	1.8/1.8
RMS long. emittance [10^{-3}eV·s]	130	75	670	120
RMS bunch length [cm]	63	48	172	140
RMS $\Delta p/p$ [10^{-4}]	8	6	9.8	8.5
Polarization [%]	70	65	—	—

Table 3.24: Comparison of required EIC hadron beam parameters at AGS extraction, and demonstrated beam parameters. Shown are the EIC cases with the highest bunch intensity demand from the AGS. The proton case (left) is for 275 GeV protons on 10 GeV electrons. The gold ion case (right) is for 110 GeV/nucleon gold on 10 GeV electrons.

3.7.2 Polarized ^{3}He Ion Source

EBIS and ^{3}He Source Overview

The EIC will require about 2×10^{11} ion in the source pulse and about 10^{11} ions in the EIC bunch. To deliver this intensity in a 20 micro-second pulse duration for the booster, the source peak current must be about 2 mA, which is $\times$ 1000 higher than ever achieved in previous ^{3}He ion source. The polarized ^{3}He ion source will be an upgrade to the existing EBIS [**?**], which currently provides high charge state ions to RHIC and will remain the primary source of charged ions from D to U for the EIC. At one end of the EBIS an electron beam is produced, and then radially compressed by a 5 T solenoidal magnetic field before being dumped into an electron collector at the other end. The EBIS ion trap region is a series of cylindrical electrodes in the 5 T field. Ions are radially confined by the space charge of the electron beam and longitudinally confined by electrostatic barriers at the ends of the trap region. Ions are held in the trap until the desired charge state is reached, and then extracted by raising the potential of the trap and lowering the barrier. In the upgraded EBIS, there are two 5 T solenoids. ^{3}He gas will be injected and ionized in the upstream solenoid, and ^{3}He ions will be trapped and breed to the $^3He^{++}$ state in the downstream solenoid. Parameters for the EBIS production of polarized $^3He^{++}$ are shown in Table 3.25. Modifications that need to be made for polarized ^{3}He production include the polarization of ^{3}He at 5 T fields, gas injection into the EBIS electrostatic trap, construction of a ^{3}He spin-rotator, and ^{3}He polarimeters. A conceptual illustration of primary components of the ^{3}He ion source inside the upstream end of the EBIS is shown in Figure 3.40.

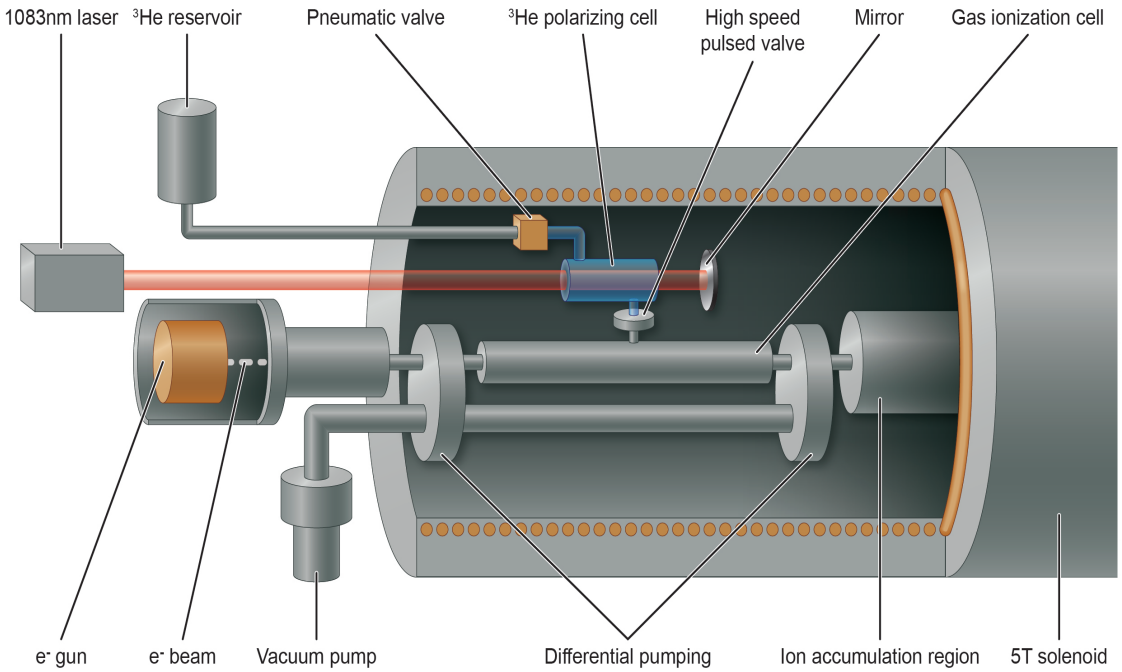

Figure 3.40: Conceptual illustration of the ^{3}He ion source components inside EBIS.

Parameter	Value
e-beam current [A]	10
e-beam energy [keV]	20
e-beam density [A/cm^2]	$\sim$575
^{3}He ion trap length [m]	1.5
Extracted beam pulse length [µs]	$\leq$ 20
Trap capacity (charges)	1×10^{12}
^{3}He^{++} yield	2.5–5$\times 10^{11}$
^{3}He^{++} polarization	70%

Table 3.25: EBIS parameters for ^{3}He^{++}.

^{3}He Polarization and Purification

The ^{3}He gas needs to be polarized before ionization such that a ^{3}He^{++} polarization of 70% is achieved in the EIC. ^{3}He gas at 1-5 Torr will be polarized in a cylindrical glass cell ($\sim$30 cm^3) inside the 5 T magnetic field of the EBIS solenoid using the technique of metastability exchange optical pumping (MEOP) [**?**]. An RF excitation of the ^{3}He gas will be created to populate the 2^3S metastable state, which will be optically pumped by a Keopsys 1083 nm fiber laser, and the nuclear polarization will be simultaneously polarized by hyperfine coupling. The ^{3}He polarization can be absolutely measured in the pumping cell by monitoring the transmission spectrum of a weak probe beam

created by a 1083 nm Toptica diode laser. The maximum ^{3}He polarization is achieved in a time scale of about 10 minutes with some variation for ^{3}He pressure and purity. Continuous 5 Hz operation of the EBIS will require injection of $\sim 4 \times 10^{17}$ ^{3}He atoms per day, which corresponds to a 0.4 Torr pressure drop in the 30 cm^3 polarizing cell. Therefore, a 10 minute refill and polarize period will take place at most once a day to maintain a polarized ^{3}He reservoir for gas injection into EBIS. In between refills of the polarizing cell, the ^{3}He gas will be purified with a specialized 46 K cryopump to remove contaminants.

Gas Injection and Ionization

The ^{3}He gas will be ionized by the 20 keV, 10 A electron beam in a thin drift tube structure connected to the polarized ^{3}He reservoir by a high speed pulsed valve. A high vacuum is required outside the region of ^{3}He injection to produce a large $^3He^{++}/^3He^{+}$ ratio and for source recovery to generate other ion species after the 1 s switch time.

In the present configuration, the gas ionization cell is a 1 cm diameter 30 cm long drift tube with 0.5 cm constrictions at the ends and differential pumping. The small diameter will limit the amount of gas that needs to be injected into the EBIS to neutralize the electron beam, and the constrictions will limit gas flow from the gas ionization cell to the EBIS high vacuum regions. Polarized ^{3}He injection is implemented with a high speed pulsed valve that opens by the Lorentz force when a current is pulsed through a conductive plate in a high magnetic field. Such a valve has been in successful operation in the OPPIS source for couple of decades. The pulsed valve opens on a time scale of $\sim$500 µs and will have to inject $\sim 10^{12}$ ^{3}He atoms to produce a uniform pressure of 10^{-6} Torr inside the gas ionization cell. The pressure is limited to 10^{-6} Torr for high vacuum EBIS performance. After ^{3}He is ionized to $^3He^{+}$, the $^3He^{+}$ ions quickly move downstream in less than 1 ms where conversion to $^3He^{++}$ will take place along the 1.5 m length of the ion trap in the downstream EBIS magnet.

Spin Rotator

The $^3He^{++}$ polarization state in the EIC will be set with a spin rotator in the HEBT (High Energy Beam Transport) line after the EBIS LINAC, which will align the $^3He^{++}$ polarization to the transverse vertical direction at 6 MeV beam energy.

Layout for the spin direction alignment system is shown in Figure 3.41. The ^{3}He longitudinal polarization is first rotated to the transverse direction by the 21.5° bending magnet. Then the solenoid spin-rotator rotates the spin to the vertical direction. The spin-rotator will be a pulsed solenoid with a reversible field to enable spin flip of EBIS pulses on a pulse-by-pulse basis. The vertically polarized beam will be returned back to the straight HEBT line by the system of three dipole magnets after the spin rotator solenoid. Beam quality will be preserved with a number of focusing quadrupoles, steering magnets, and beam diagnostics. A low-energy $^3He^{++}$ polarimeter can be installed in the straight beam line section after the dipole magnet.

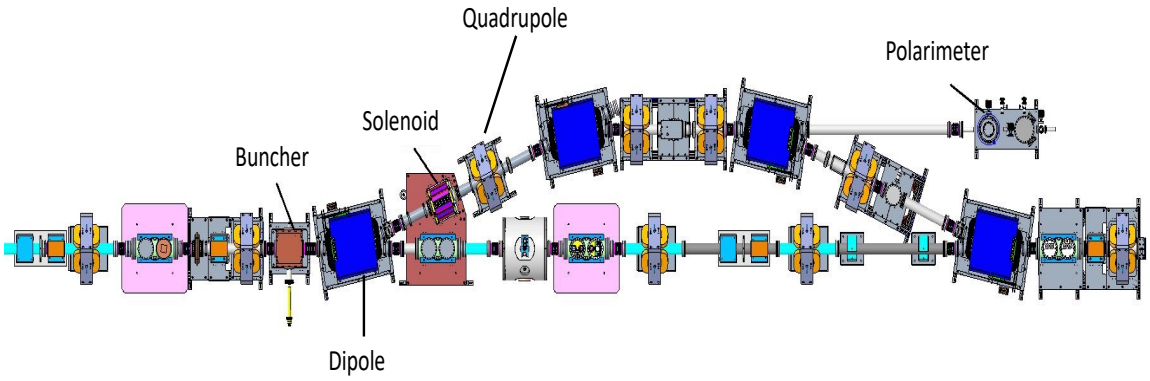

Figure 3.41: ^{3}He spin rotator.

Low-Energy Polarimetry

The $^3He^{++}$ polarization will be measured at 6 MeV after acceleration through the EBIS LINAC via scattering on an unpolarized ^{4}He gas target. A low-energy polarimeter design is shown in Figure 3.42. The analyzing power for elastic scattering of polarized ^{3}He on unpolarized ^{4}He is ideally $A_N = 1$ at a beam energy of ∼5.3 MeV and $\theta_{CM} \approx 91^\circ$ [**?**,**?**]. For the 6 MeV polarized $^3He^{++}$ beam emitted from the EBIS LINAC, there is a local maximum at $A_N > 0.9$ and $\theta_{CM} \approx 96^\circ$ where the polarization can be determined by measuring the spin correlated asymmetry from scattered ^{3}He and ^{4}He. Silicon photodiode strip detectors will detect the scattered ^{3}He and ^{4}He over a range of center of mass scattering angles ($69^\circ < \theta_{CM} < 100^\circ$) and recoil particle energies (2.6-4.2 MeV for ^{3}He and 1.5-2.4 MeV for ^{4}He). Simultaneous detection of scattered ^{3}He and ^{4}He provides a coincidence signal to reduce background.

To produce an absolute polarization measurement, the polarimeter will be calibrated at 5.3 MeV either by decelerating the $^3He^{++}$ beam after the EBIS LINAC with a buncher or by detuning the EBIS LINAC to increase the energy spread. The ^{4}He gas target will be at 5 Torr with an effective target length of 1 cm. The statistical error for the ^{3}He polarization measurement is estimated at $(\delta P/P)_{stat} \approx 1.1\%/\text{min}$. Methods for high energy ^{3}He beam polarimetry farther down the accelerator chain are discussed in Section **??**.

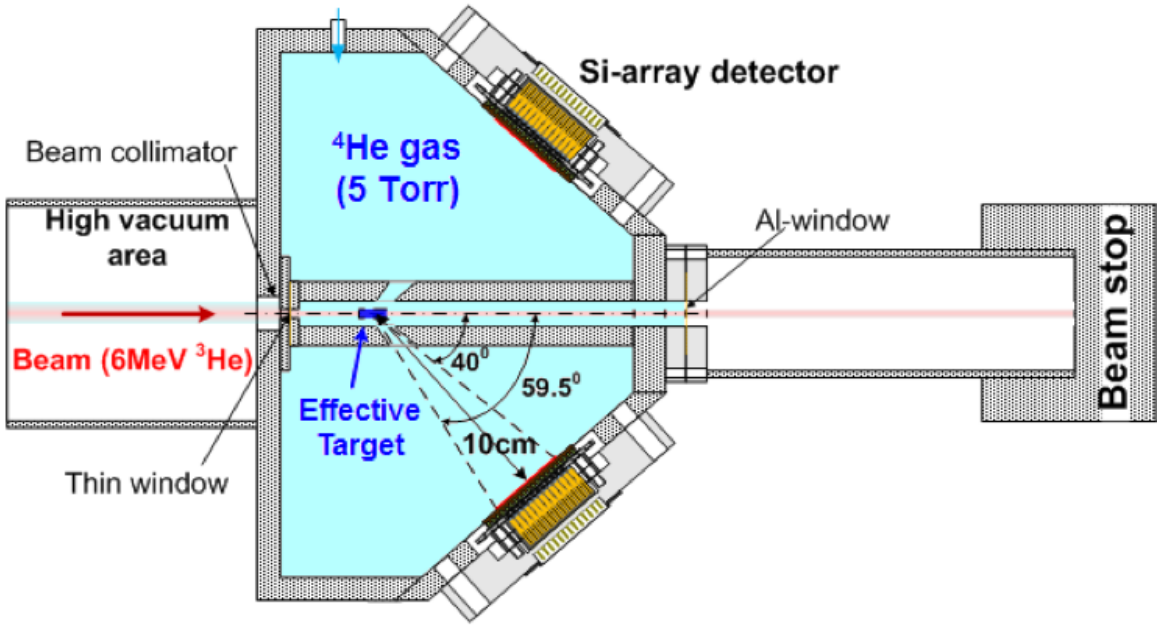

Figure 3.42: Layout of low-energy ^{3}He polarimeter.

Summary

Extensive R&D efforts have systematically addressed the technical challenges, progressing from 90% polarization in sealed samples to 80% with open-cell gas handling systems, and developing a minimal optical layout achieving 60% polarization within the tight geometric constraints. The development of the ^{3}He polarizing apparatus, the spin-rotator, and the nuclear polarimeter at the $^3He^{++}$ ion beam energy 6 MeV (in the high-energy beam transport line after the EBIS IH Linac) has now been successfully realized. Current work involves testing the optical system in a full-scale EBIS solenoid replica while finalizing the gas handling design, with complete installation scheduled during the 2025 EBIS shutdown and commissioning planned for 2026 using both the absolute polarimeter and existing AGS CNI carbon polarimeter.

3.8 Electron Storage Ring

3.8.1 Introduction

The electron storage ring with its 3834 m circumference will be installed in the existing RHIC accelerator tunnel. The elevation of the ring will be identical to that of the hadron ring in the IR6 and IR8 crossing points. To avoid vertical bends at the IR12 and IR4 cross-over points that would be detrimental to polarization, the entire ESR is tilted by 200 μrad around the axis through IPs 6 and 8, such that its elevation is above the HSR by 104 mm in IR4, and by 208 mm in IR12. Similar to the hadron storage ring, the electron ring consists of inner and outer arcs as well in order to provide the required circumference.

The six arcs consist of 16 regular FODO cells with a cell length of around 18.5 m. To generate the required equilibrium emittances at different beam energies, appropriate betatron phase advances per FODO cell are chosen. At 5 and 10 GeV, the phase advance per FODO cell is 60 degrees, while at 18 GeV it is set to 90 degrees. The vertical emittance is adjusted by vertical dispersion bumps [**?**]. Chromatic correction is accomplished by a scheme of sextupole families, using 3 families per arc and per plane for the 60 degree optics, and 2 families for the 90 degree optics. Although the baseline plan is to use only sextupoles in the regular arc cells for chromatic correction, additional 11 pairs of sextupoles in the regions immediately neighboring the arcs will be installed but not connected in case they are needed to maximize the dynamic aperture for future upgrades.

The main bending dipoles consist of three segments each, with a short 0.89 m dipole in the center in-between the two 2.7 m long magnets. At 5 GeV beam energy, this center dipole is powered with reverse polarity in order to generate additional synchrotron radiation, thus increasing the equlibrium emittance as well as the synchrotron radiation damping decrement, therefore enabling large beam-beam tuneshift parameters over the entire energy range. At beam energies of 10 GeV and above, all dipoles have the same bending direction, thus maximizing the bending radius and therefore minimizing the synchrotron radiation losses. Figure 3.44 illustrates the resulting orbits at different energies.

The EIC detector ePIC will be located in IR6. This straight section will be equipped with a low-β section around the collision point, using superconducting magnets. The electron and ion beam collide at the IP under a total crossing angle of 25 mrad. Spin rotation from the vertical orientation in the arcs to the longitudinal direction at the IP is accomplished by solenoid-based spin rotators. Two solenoids with subsequent horizontal bends are required on each side of the IP in order to provide longitudinal polarization at the IP over the entire beam energy range from 5 to 18 GeV.

The ESR RF system (See Section **??**) provides a total installed voltage of 68 MV and is located in IR10. Bunches from the Rapid-Cycling Synchrotron (RCS) will be injected into the storage ring in IR4. The bunch extraction and injection occur on the same turn using fast kickers. While the emittance and charge of the injected and extracted bunches are not identical, they are very close. This minimizes the discontinuity in the beam-beam force on the hadrons.

The vacuum system uses **CuCrZr** alloy beam pipes with a cross section of 80 mm $\times$ 36 mm. In the arcs the edges of the pipe are equipped with water cooling channels to counteract the 10 MW of synchrotron radiation power impinging on the inside of the tube. This material has been chosen for its superior tensile strength and radiation shielding properties, as compared to both pure copper and aluminum.

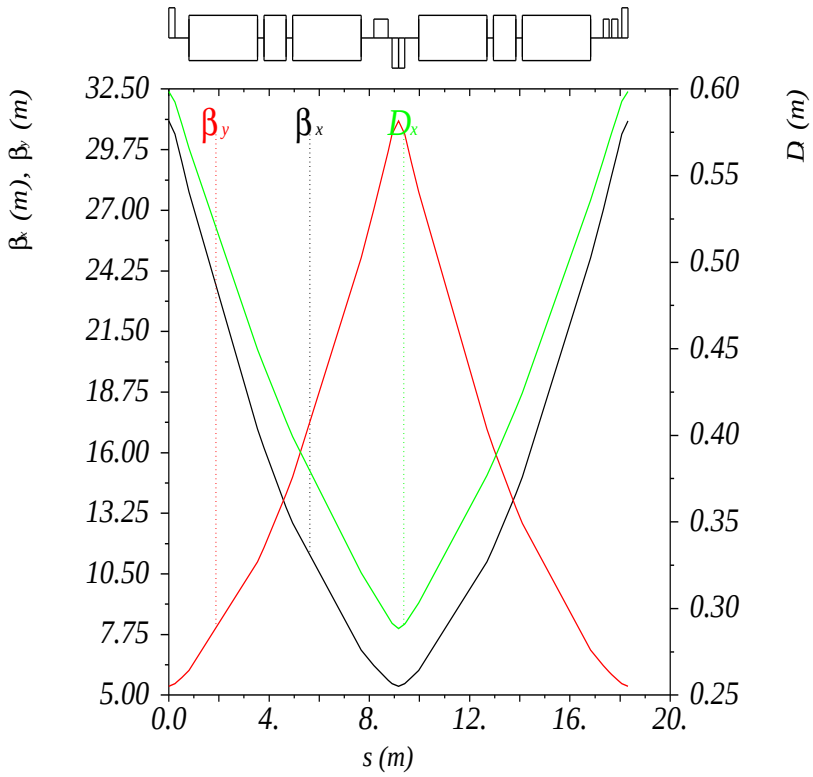

Figure 3.43: One FODO cell of the Electron Storage Ring arc, tuned to 90 degrees betatron phase advance.

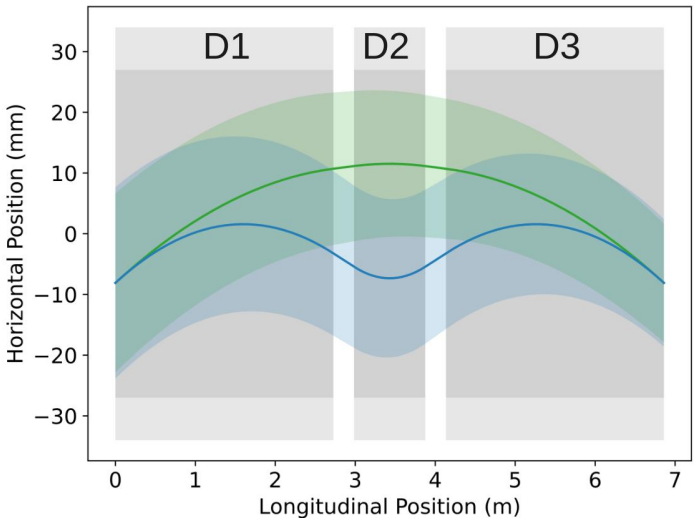

Figure 3.44: Superbend dipole assembly. The trajectory at 10 and 18 GeV is shown in green, and the trajectory at 5 GeV is shown in blue. The beam envelopes shown correspond to 15σ.

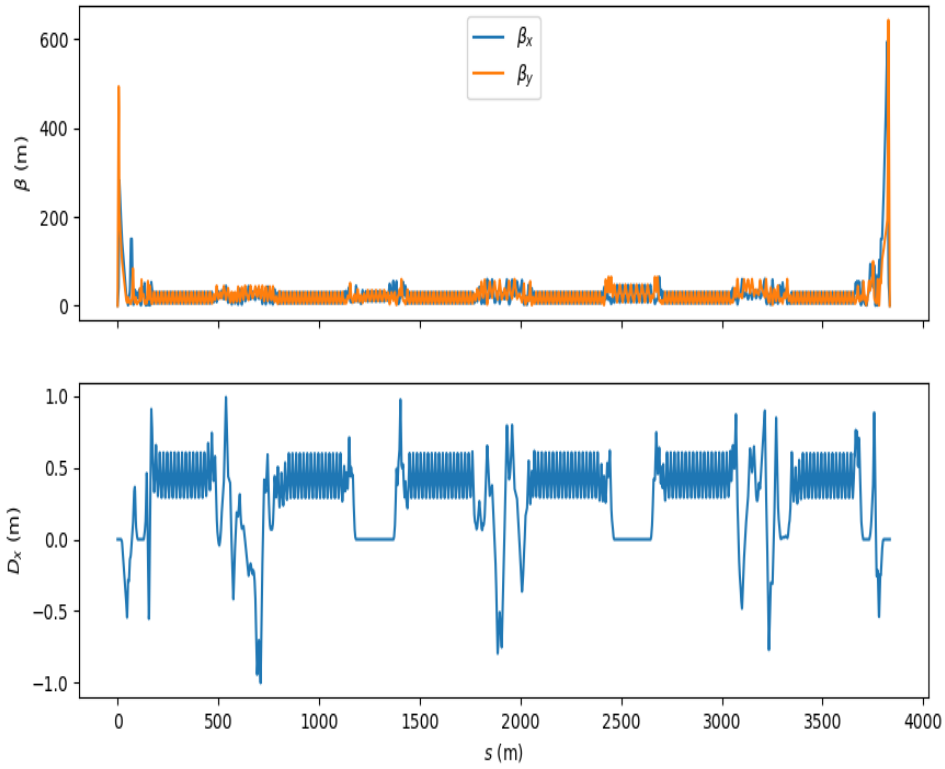

Figure 3.45: ESR optics at 18 GeV starting at IP6 and progressing clockwise.

3.8.2 Tunnel Layout

The ESR will be installed in the existing RHIC tunnel, adjacent to the HSR. Like the HSR, it consists of three "inner" and three "outer" arcs to match the circumference of the HSR. However, unlike the HSR, which alternates between "inner" and "outer" arcs at all six straight sections around the perimeter of the ring, the ESR crosses over in only four locations, namely IRs 6, 8, 12, and 4. Crossing points in IRs 6 and 8 are pre-determined by the need to provide collisions between electrons and hadrons in the ePIC detector in IR6 and a potential second detector in IR8. For the 1IR lattice, the crossing point location in IR8 is set to achieve maximal separation in arrival times between electron and hadron bunches. To maximize the longitudinal space for SRF cryomodules in IR10 and for the electron cooler in the HSR in IR2, there are no crossing points between ESR and HSR and these two straight sections. This leaves the two remaining crossing points in IRs 12 and 4. Figure 3.46 shows the layout of the ESR in the tunnel, relative to the tunnel center line and the two RHIC rings.

To facilitate crossing between ESR and HSR in IRs 12 and 4, the entire ESR is tilted with respect to the HSR by 200 μrad around the axis through the crossing points in IRs 6 and 8. As a result, the elevation of the ESR orbit is 104 mm above the HSR orbit in IR4, and 208 mm above in IR12, while in the two collision (or crossing) points in IRs 6 and 8 the elevation of the two rings is identical.

3.8.3 Arc Lattice

3.8.4 ESR Arc Sections

The three goals for the design of the storage ring arcs is to

1. ensure emittance values consistent with the design values,
2. minimize radiation from the dipoles,
3. and fit in the existing tunnel.

The first two goals work against each other. To reduce the amount of radiation, a cell with a high packing factor is desired. To reduce the electron emittance, there are specialized cell designs to achieve this, but with reduced packing factor. Some cell designs – FODO cell, TAL (Triplet Achromat Lattice) and TBA (Triple Bend Achromat) [**?**,**?**] – have been considered. Furthermore, the lower dispersion in the low emittance cells requires larger sextupole strengths for correction. This could lead to smaller dynamic and momentum aperture. To reduce the cost of operation by minimizing the electron radiation, the FODO cell approach was chosen for its high packing factor. This design achieves the desired equlibrium emittance.

The main bending element is a super-bend consisting of three rectangular dipole magnets, see Figure 3.44. The super-bends allow us to increase the emittance at lower energies. Correctors, BPMs and sextupoles are kept next to the quadrupole.

There are 16 FODO cells per arc with 6 arcs total. Figure 3.48 shows a schematic of the entire ring. IRs and straight sections, shown, will be matched to these arcs. With a betatron phase advance of 60 degrees per FODO cell, these cell dimensions provide an emittance of about 22 nm in the ring at 10 GeV. At 18 GeV the emittance is about 28 nm with the phase advance increased to 90 degrees. At 5 GeV beam energy, the short center dipole in the super-bends is powered with reverse polarity. This increases the euqilibrium emittance to the desired value of 20 nm at that energy. Using a small radial shift, the emittance can be fine-tuned at all energies in order to maximize the luminosity.

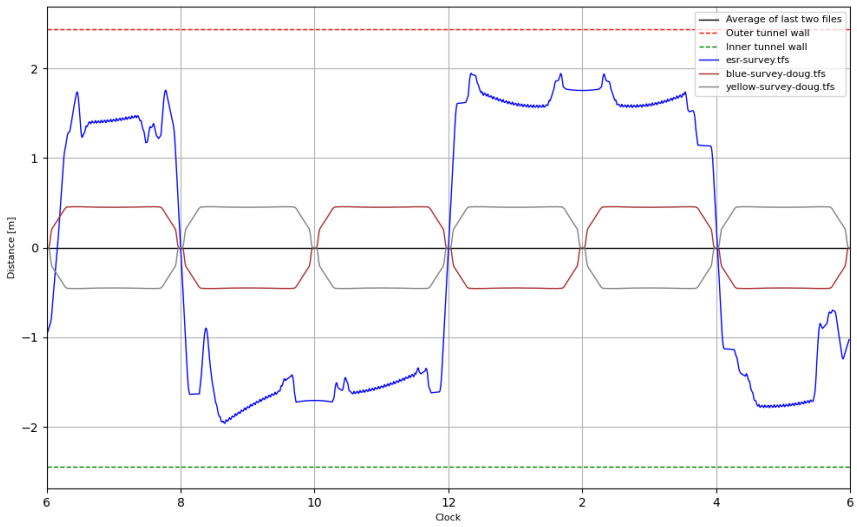

Figure 3.46: Schematic layout of the ESR in the RHIC tunnel, relative to the tunnel center line. The ESR beam line center is shown as a blue line, while the brown and gray lines correspond to the "Blue" and "Yellow" RHIC rings. The tunnel walls are shown as red and green dashed lines.

Parameter	Value
Cell length [m]	18.23 - 18.50
Dipole Ends length [m]	2.7
Dipole Center length [m]	0.89
Dipole bend angle [mrad]	24.2
Dipole bending radius [m]	262.2
Quadrupole length [m]	0.5
Sextupole length [m]	0.24
Corrector length [m]	0.2

Table 3.26: Dimensions for the arc FODO cell. The BPMs will fit in the 20 cm space between the quadrupole and sextupole. The super-bend dipole consist of three dipoles separated with a 15 cm space, see Figure 3.44

In a FODO cell storage ring, the required integrated strength per sextupole in the vertical plane is about twice as large as in the horizontal one. This is reflected by the arrangement of sextupoles in the ESR. In arcs 11, 1, and 3, a single 24 cm long sextupole will be installed next to each horizontally focusing quadrupole, while next to each vertically focusing quadrupole two identical, 24 cm long sextupoles will be placed. Dynamic aperture optimization with two fully built-out interaction regions (collision points) has shown that in the three arcs adjacent to the IRs 6 and 8 more integrated sextupole strength is required than in the other three arcs. Therefore two identical 24 cm long sextupoles will be installed in the horizontal plane, while new, long sextupoles will be used for the vertical plane. The overall length of these long sextupoles will be identical to that of two 24 cm long sextupoles adjacent to each other, but since the gap between the two will be filled with steel the overall yoke length is 57 cm, which is sufficient to provide the required integrated sextupole field.

Figure 3.49 shows the layout of the electron ring relative to the two RHIC rings and the tunnel walls.

3.8.5 Straight Sections

The utility straight sections where the beams do not collide are used in the ring for RF cavities, injection, extraction etc. Each section has a bending angle of 273 mrad, made up of 24 dipoles with 11.4 mrad. In IRs 4, 8 and 12, additional dipoles of the same type will be used to provide additional bending for crossover. These dipoles will all have the same 11.4 mrad bending angle, though some will bend in the opposite direction.

In IRs 2 and 10, there is no crossover, which leaves a longer section in the central section, where a FODO-like lattice is used. The dispersion is also suppressed by matching the quadrupole strengths. The straight sections should also have minimal impact on the dynamic aperture of the ring.

IR8

The IR8 straight section will eventually house a second EIC detector. However, since this detector and the associated IR magnets are not in the project scope, the lattice will be kept as simple as possible at this time. The electron and hadron beam lines need to cross in IR8, as they would in a

future interaction region. To avoid collisions between the two species the location of that cross-over point is chosen such that due to the pathlength between this cross-over point and the interaction point in IR6 electron and hadron bunches arrive at the crossing point at different times, with the time between electron and hadron bunch passes close to 5 nsec, which is half the bunch spacing in either ring. Figure 3.50 shows the lattice and optics of IR8 between the two ends of the periodic arcs in ARC7 and ARC9.

IR10

The RF cavities will be installed in IR10, which must be dispersion free to avoid synchrobetatron resonances. Nine SRF cryomodules with two single-cell cavities are located in the 90 m long wide tunnel section. This section is realized as a strictly periodic FODO cell structure with one cryomodule installed in-between each pair of quadrupoles. To accommodate the large 180 mm ID beam pipe of those cryomodules, dedicated large-aperture quadrupoles and dipole correctors have been designed for this section. CAD modelling has ben employed to ensure that all elements can be fit into the 90 m long section without interferences with other installations such as components in the HSR. Figure 3.51 depicts the lattice and optics of IR10 between the two ends ot the periodic arcs in ARC9 and ARC11.

IR12

The IR12 straight section provides a cross-over between the ESR and HSR.

IR2

In IR2, the ESR is located along the outer tunnel wall in order to provide as much space for the HSR with its electron cooling facility.

IR4

IR4 houses the swap-out injection system, consisting of a number of stripline kickers, a DC injection septum, and an internal dump for the ejected, spent bunch. The ESR crosses over the HSR in the center of the group of the HSR injection kickers. Betatron collimators will also be located in this IR, downstream of the crossover point.

3.8.6 Injection

3.8.7 RF Requirements

The RF requirements for the ESR have been developed via interaction between accelerator physics and the RF group. The RF system developed supplies stable beams of adequate lifetime that provide the design luminosity. Table 3.28 shows the RF parameters for the 3 main operating energies in the ESR. These parameters work well for bunch length, instabilities, transient beam loading and luminosity production.

parameter	5 GeV	10 GeV	18 GeV
e^-/bunch 10^{10}	17.2	17.2	6.2
number of bunches	1160	1160	290
γ_t	29.66	29.28	40.72
V_{synch} (MV)	1.150	3.708	38.972
$\sigma(E)/E$ (10^{-4})	4.86	5.40	9.72
α_z (s^{-1})	17.94	29.02	169.2
σ_z(mm)	7	7	9
number of focusing cells	10	12	18
focusing voltage (MV)	34	43	58
number of defocusing cells	8	6	0
defocusing voltage (MV)	29	21	0
RF bucket height $\Delta E/E$ %	0.91	1.09	0.81

Table 3.27: Acceptable RF parameters for the final configuration.

parameter	5 GeV	10 GeV	18 GeV
e^-/bunch 10^{10}	17.2	17.2	6.2
number of bunches	1160	1160	290
γ_t	29.66	29.28	40.72
V_{synch} (MV)	1.150	3.708	38.972
$\sigma(E)/E$ (10^{-4})	4.86	5.40	9.72
α_z (s^{-1})	17.94	29.02	169.2
σ_z(mm)	7	7	9
number of focusing cells	10	12	18
focusing voltage (MV)	34	43	58
number of defocusing cells	8	6	0
defocusing voltage (MV)	29	21	0
RF bucket height $\Delta E/E$ %	0.91	1.09	0.81

Table 3.28: Acceptable RF parameters for the final configuration.

Figure 3.55 shows the Touschek lifetime for the low energy beams as a function of RF bucket height for 28 nC bunches. The minimum occurs for 5 GeV and is more than 8 hours.

3.8.8 Aperture Requirements

3.8.9 ESR Aperture Requirement

The vacuum chamber of the EIC electron storage ring (ESR) must provide sufficient aperture to ensure a beam lifetime of several hours under realistic operational conditions. Besides providing a minimum aperture of 15σ around the design orbit, horizontal and vertical orbit errors Δx_{orbit} and Δy_{orbit} have to be accommodated. In addition, the horizontal design orbit varies as a function of beam energy due to the super-bends, as shown in Figure 3.44.

The requirements on the horizontal and vertical aperture radii can therefore be expressed as

$$A_x \geq 15\sqrt{\sigma_{\beta_x}^2 + \sigma_\delta^2} + \Delta x_{\text{orbit}} + \Delta x_{\text{superbends}} \tag{3.44}$$

$$A_y \geq 15\sqrt{\sigma_{\beta_y}^2} + \Delta y_{\text{orbit}}. \tag{3.45}$$

When calculating the horizontal and vertical RMS beam sizes σ_{β_x} and σ_{β_y}, we take into account the uncoupled horizontal emittance ϵ_x and the fully coupled vertical emittance $\epsilon_y = \epsilon_x/2$ despite the fact that the design vertical emittance is significantly smaller. This ensures sufficient vertical aperture even under less-than-ideal conditions, as typically occurs during machine commissioning.

Table 3.29 lists the parameters and resulting aperture requirements for the two most extreme cases, 5 GeV and 18 GeV, of electron beam energy.

Table 3.29: Aperture requirements for 5 and 18 GeV electron beam energy.

Parameter	5 GeV	18 GeV
uncoupled ϵ_x [nm]	20	22
fully coupled ϵ_y [nm]	10	11
$\hat{\beta}_x$ [m]	30	30
$\hat{\beta}_y$ [m]	30	30
$\hat{D}_x$ [m]	1.0	0.5
$\Delta p/p$	1×10^{-3}	1×10^{-3}
Δx_{orbit} [mm]	10	10
Δy_{orbit} [mm]	5	5
$\Delta x_{\text{superbends}}$ [mm]	11	11
A_x [mm]	40	35
A_y [mm]	13	14

It is worthwhile mentioning that the maximum orbit excursion due to the superbends, $\Delta x_{\text{superbends}}$, occurs in the center of the dipole section, while both the RMS beam sizes and the orbit errors reach their maximum in the quadrupoles in-between those dipole sections. The minimum aperture radii listed are therefore slightly pessimistic by a few millimeters. A horizontal aperture radius of 40 mm is sufficient.

These general aperture requirements may be violated in a few locations, for instance at the injection septum, the replacement dump, or at the IR magnets. In this case, a minimum aperture of $13.5\sigma_x$ and $23.5\sigma_y$ is required, with the vertical RMS beam size based on the vertical design emittance, not a fully coupled beam.

3.8.10 Magnet Requirements

3.8.11 Power Supply Ripple and Stability Requirements

3.8.12 Emittance Control (horizontal, or also BAGELS?

3.8.13 ESR Emittance Control Scheme

The horizontal equilibrium emittance of an electron beam in a storage ring is determined by the Twiss parameters around the perimeter of the ring, and mathematically expressed by a set of synchrotron radiation integrals. One important feature is that for a given lattice and optics functions of a storage ring the emittance scales quadratically with the beam energy. However, for highest possible luminosity over the entire center-of-mass energy range of the the EIC, the horizontal emittance of the electron beam has to be kept approximately constant at **20 to 24 nm** over the entire ESR energy range from 5 to 18 GeV. This is accomplished by adjusting the betatron phase advance per arc FODO cell as well as by invoking the "super-bends" (Section **??**).

With the betatron phase advance in the arc FODO cells set to 60 degrees at 10 GeV, and to 90 degrees at 18 GeV, the horizontal emittance at these two energies is kept nearly the same, with **20 nm** at 10 GeV and **29 nm** at 18 GeV. Further reduction of the betatron phase advance to generate a similar emittance at 5 GeV is impractical. Instead, we modify the dipole bending sections in the arcs to generate additional synchrotron radiation via reverse bends. This is realized by placing three dipoles, instead of a single dipole, between the arc quadrupoles. At high energies of 10 to 18 GeV, all three dipoles will have the same field in order to produce a smooth, nearly uniform bend that minimizes synchrotron radiation. At 5 GeV, the central dipole will be powered in reverse with a high field, higher than even the field for the high energy beam. By chosing the relative lengths and strengths of the individual dipoles in this "super-bend", an equilibrium emittance of 20 nm is achieved at 5 GeV. Figure 3.44 shows the dipole configuration and orbits at different energies.

This dipole design produces a transverse damping decrement (energy loss per turn divided by $2\beta^2 E$, where β is the relativistic β and E is the total beam energy) of 2.5×10^{-4} for the 5 GeV beam. This damping decrement approximately equals the value used in KEK-B [**?**] where a vertical beam-beam parameter similar to the one envisioned in the ESR was reached. Table **??** gives dipole field values, radiation loss, and the Sokolov-Ternov (de-)polarization time [**?**] at the design energies.

Total Energy	5 GeV	10 GeV	18 GeV
Inner Bend Field [T]	-0.456	0.138	0.248
Inner Bend Angle [mrad]	-12.2	1.8	1.8
Outer Bend Field [T]	0.113	0.138	0.248
Outer Bend Angle [mrad]	18.0	11.0	11.0
Energy Loss per Turn [MeV]	1.3	3.7	38
Sokolov-Ternov Time [h]	12.4	9.8	0.5
Inner Dipole Length [m]		0.59	
Outer Dipole Length [m]		3.25	
Orbit Width [mm]		14	

Table 3.30: replace this table withAppA/ESR/top_level.tex and/or lattice+orbit.tex

3.8.14 Subproject 1 Scope

Figure 3.47: Arc FODO cells: F-Cell (top) and G-Cell (bottom). To increase the packing factor, the quadrupole is not centered between the dipoles. G-Cell is the mirror image of the F-Cell to retain overall ring symmetry.

Figure 3.48: Schematic of the electron storage ring showing the arc FODO cell arrangement. The colliding IRs are at IP6 and IP8. The other IRs are straight sections.

Figure 3.49: Fitting the electron storage ring (blue) into the tunnel. This shows the electron storage ring relative to the existing Blue ring (brown), Yellow ring (gray) and center line (black). The inner and outer tunnel walls are shown with dashed lines. This picture doesn't show the IR housing which extends beyond the tunnel walls, such as in IR2. The angle increases positively in the clockwise direction starting at IP6.

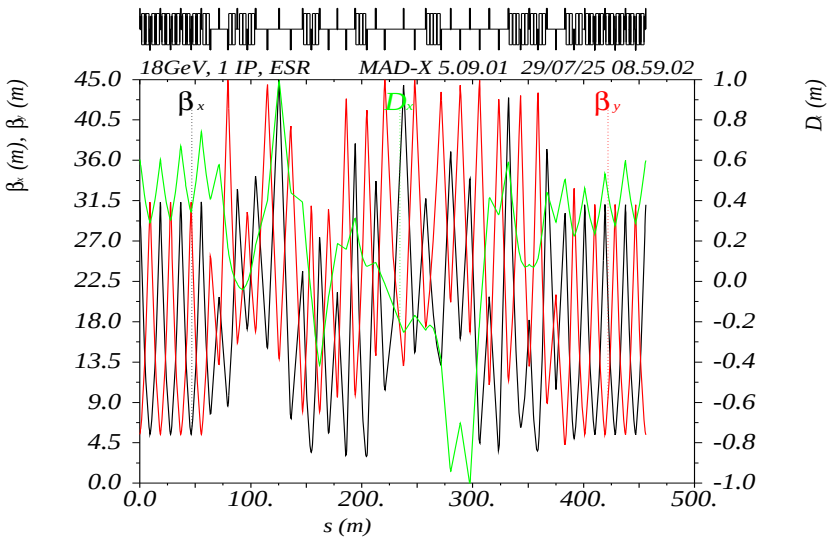

Figure 3.50: Optics of the IR8 straight section. The cross-over point with the hadron storage ring is located at s = 228.285 m.

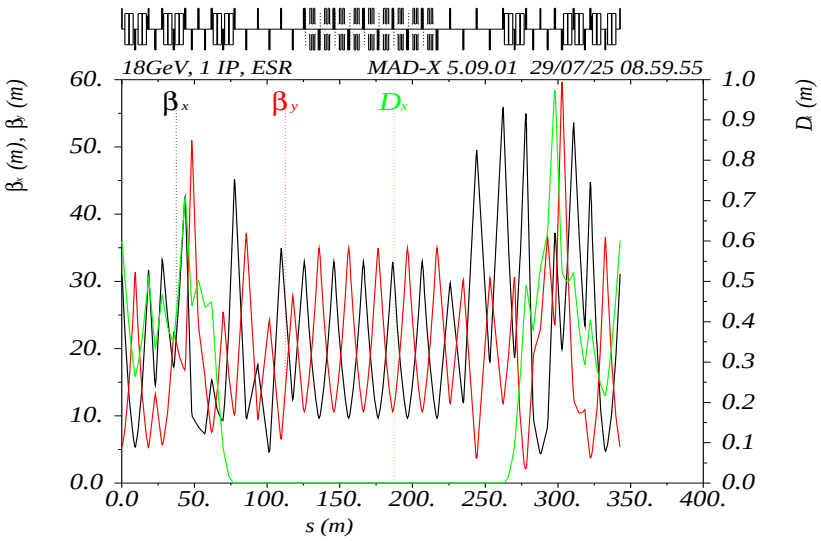

Figure 3.51: Optics of the IR10 straight section. Dispersion is fully corrected for the RF cavities.

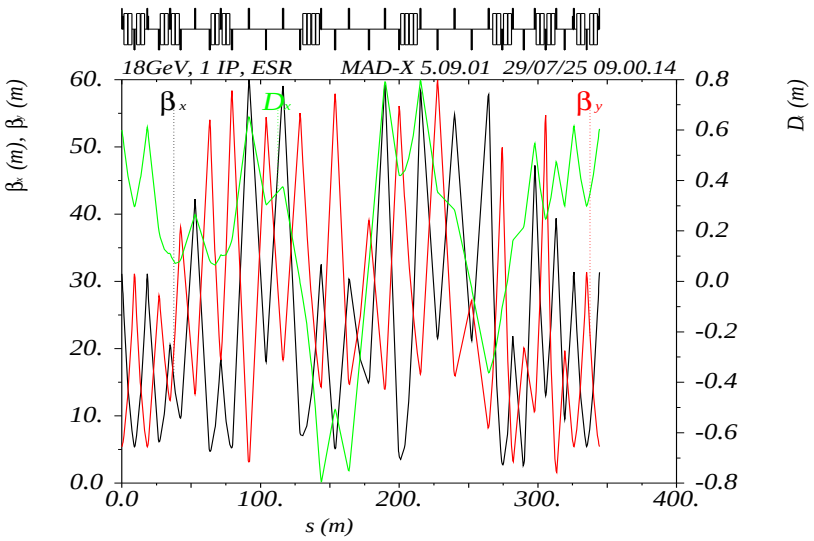

Figure 3.52: Optics of the IR12 straight section. Four dipoles on each side of the IP introduce a 45.5 mrad crossing angle to avoid the hadron cryostat chamber.

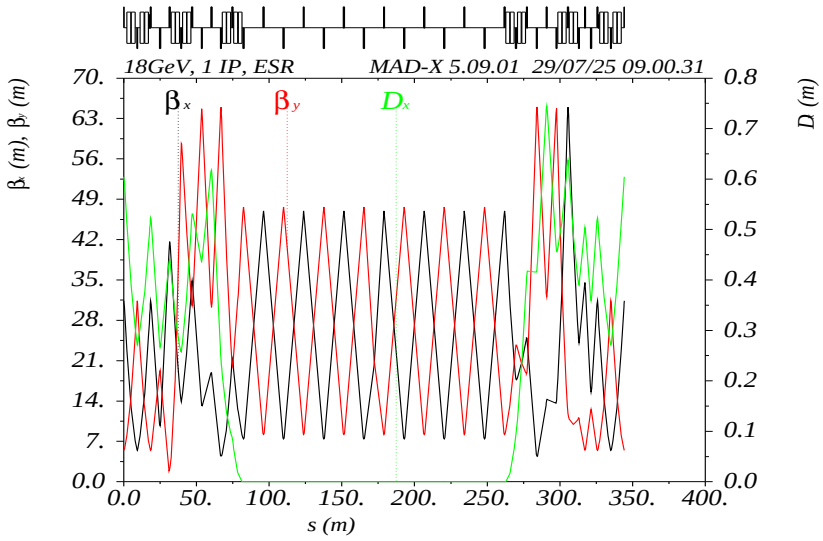

Figure 3.53: Optics of the IR2 straight section.

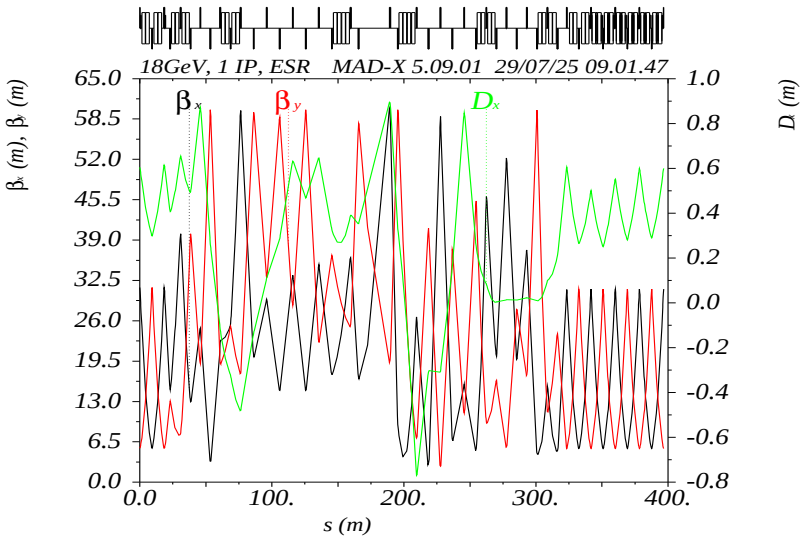

Figure 3.54: Optics of the IR4 straight section, which houses the swap-out injection area. The dispersion is suppressed at the collimator location. Four dipoles on each side of the IP introduce a 45.5 mrad crossing angle to avoid the hadron cryostat chamber.

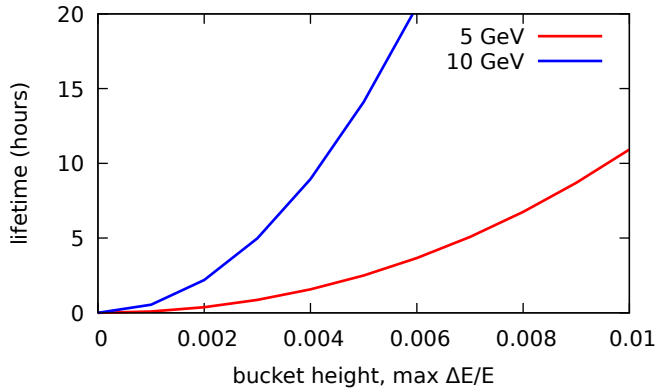

Figure 3.55: Touschek lifetimes for 28 nC electron bunches at 5 and 10 GeV as a function of RF bucket height.

3.9 Electron Injector

3.9.1 Introduction

The **Electron Injector** complex is a ramping, pulsed accelerator system designed to generate, accumulate, accelerate, and inject polarized electron bunches into the ESR. It operates both to fill the ESR before collisions and to perform single-bunch swaps during collisions, maintaining the required average polarization over time.

As a pulsed machine handling polarized beams, the Electron Injector places particular emphasis on preserving polarization throughout the entire process, from source to injection, while also minimizing intensity losses and ensuring reliable, high repetition rate operation.

The beam delivery requirements for the ESR are summarized in Table 3.31. The final injected bunch parameters are defined by the ESR electron beam specifications documented in the EIC-controlled Master Parameter Tables for the EIC (EIC-SEG-RSI-005).

ESR injection energy	GeV	5	10	18
Repetition rate	Hz		1	
Number of bunches			1	
Max bunch charge	nC	28	28	11
RMS emittance (norm; x,y)	µm	196, 18-34	391, 26	845, 71
RMS energy spread	10^{-3}	0.68	0.58	1.09
RMS bunch length	mm, ps	7,23	7,23	9,30
Bunch polarization	%		$\geq$85	

Table 3.31: Summary of the Electron Injector System requirements

To accomplish this, the EIC electron injector is comprised of two accelerators, an accumulator storage ring, and associated transfer lines:

- The **Preinjector**, consisting of a polarized electron source and 750 MeV S-band linac
- The **Beam Accumulator Ring** (BAR), a storage ring for high-intensity bunch accumulation and 6D emittance equilibration
- The **Rapid Cycling Synchrotron** (RCS), a synchrotron designed to preserve beam polarization while ramping high-intensity bunches to GeV-scale ESR injection energies at 1 Hz

A schematic overview of this new electron injector complex in the 4 o'clock region of the EIC complex is shown in Fig. 3.56.

The preinjector delivers electron bunches with charges up to 1 nC at a repetition rate of 30 Hz, and accelerates them to 750 MeV. It comprises a High Voltage Direct Current (HVDC) polarized electron gun, a spin rotator, a ballistic bunching section with a buncher and drift space, a capture cavity, and a traveling wave (TW) linear accelerator. The system also includes a gun diagnostics beamline, a spin diagnostics beamline equipped with Mott polarimetry, and energy spectrum diagnostics. Details of the preinjector are found in Section **??**.

Polarized electron bunches at 750 MeV are injected into the BAR and accumulated into single high-intensity bunches with charges up to 28 nC. The BAR is a compact accumulator ring, conceptually

similar to the original NSLS VUV ring [**?**] and the APS PAR accumulator ring [**?**]. It provides strong damping to support both charge accumulation and emittance equilibration. Details of the BAR are found in Section **??**.

The Linac to RCS (LTR) transport line connects the preinjector to the RCS, with a branch that enables beam transport to and from the BAR. This flexible configuration supports direct delivery of low-intensity bunches from the preinjector to the RCS for commissioning and low-intensity operations, while enabling high-intensity operations that require accumulation in the BAR. Details for the LTR transport line are found in Section **??**.

The RCS accepts vertically polarized, accumulated electron bunches from the BAR or lower-intensity polarized bunches directly from the preinjector, and accelerates them for delivery to the ESR via the RCS-to-ESR (RTE) transport line. Details of the RCS are found in Section **??**; details of the RTE are found in Section **??**.

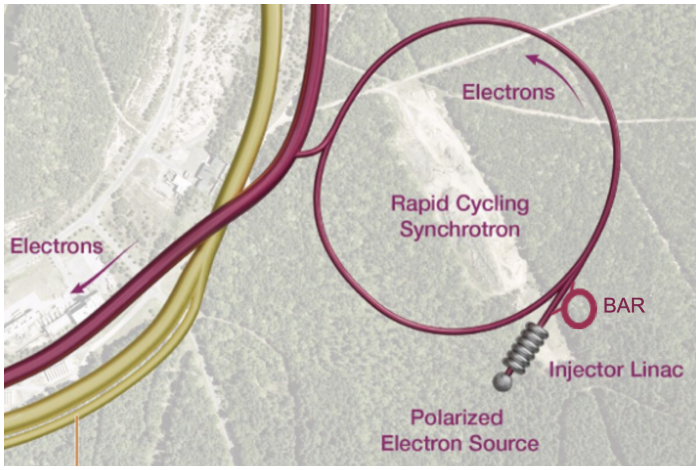

Figure 3.56: Overview of the EIC electron injector systems. The EIC Electron Storage Ring (ESR) is the thick dark magenta line with the electron direction indicated on the left.

.

3.9.2 Electron preinjector

Requirements

The Electron Pre-Injector plays a critical role in delivering highly polarized electron bunches with consistency and reliability. The polarized electron gun must support continuous operations for at least a week between cathode replacements while maintaining polarization above 87 % to support the experimental program effectively.

Beam Performance

The pre-injector must provide electron bunches with a charge of 1 nC, but it should also have the flexibility to reach up to 1.7 nC per bunch at a repetition rate of 30 Hz or higher. At extraction, the beam energy is designed to be 750 MeV. Additionally, the energy spread must be well-controlled, with an rms value kept below 0.5 % to ensure beam quality.

Polarization

Maintaining and manipulating the electron beam polarization is essential. The pre-injector requires a spin rotator to transition the spin orientation from longitudinal to vertical, preserving polarization throughout transport.

Furthermore, to meet the demands of the physics program, the pre-injector must allow for variable polarization patterns within a single store. This capability ensures that the beam can be tailored dynamically to different experimental requirements.

By meeting these requirements, the Electron Pre-Injector will provide a stable, high-quality, and adaptable electron beam, supporting the broader scientific objectives of the collider.

Layout and interfaces

The electron pre-injector consists of three major sections:

Front-end: polarized electron source and spin rotator

The photo electron source produces 1 to 1.7 nC electron bunches at a repetition rate of 30 Hz. Initial acceleration is achieved using a high-voltage DC source, bringing the electrons to an energy of 320 keV before further manipulation. Directly following the electron gun, the spin rotators rotate the electron spin from the longitudinal direction to the vertical direction.

Bunching section

To prepare the beam for efficient acceleration, a 197 MHz RF bunching cavity compresses the electron bunches to ensures fitting into linac longitudinal acceptance.

Linac section

The Lband capture cavities accelerate the bunches to 13 MeV before the main acceleration linac.

A spin diagnostic beam line using Mott polarimeter is placed in between the Lband capture cavities, to measure the polarization and spin direction.

The final stage of the pre-injector is the 2.856 GHz main accelerating linac, where the electron bunches are accelerated to 750 MeV.

This beam is then extracted and directed into the Linac-to-RCS (LTR) transfer line, where the phase-space parameters are carefully matched to ensure efficient injection into the accumulator ring.

The 1 to 1.7 nC electron bunches from the pre-injector must be efficiently injected into the Beam Accumulator Ring (BAR) with minimal losses. To ensure successful injection, the energy spread must be tightly controlled to remain within the energy acceptance limits of the BAR.

3.9.3 Preinjector beamline design

The preinjector accelerates 1 to 1.7 nC polarized electron bunch from the HVDC gun up to 750 MeV using a normal conducting RF (NCRF) Linac at 30 Hz. It consists of:

- An HVDC gun to generate polarized electron bunches
- Two Wien filters to rotate the beam polarization direction from longitudinal to transverse
- One 197 MHz buncher to provide a longitudinal chirp, with drift space as a ballistic compression

- One 1300 MHz NCRF taper cavity to capture the compressed bunch and accelerating to relativistic velocity
- One 1300 MHz NCRF standing wave cavity to increase the energy to 13 MeV
- 14 sections of 3 m S-Band linac to accelerate beam to 750 MeV.
- Three diagnostic beamlines: a gun commissioning diagnostic beam line, a dispersive beamline at 3 MeV, and a spin diagnostic beamline

The preinjector from the gun to the end of linac is shown in Fig. 3.57. We use PARMELA 3.4 to track the beam through the entire preinjector with space charge and longitudinal wakes.

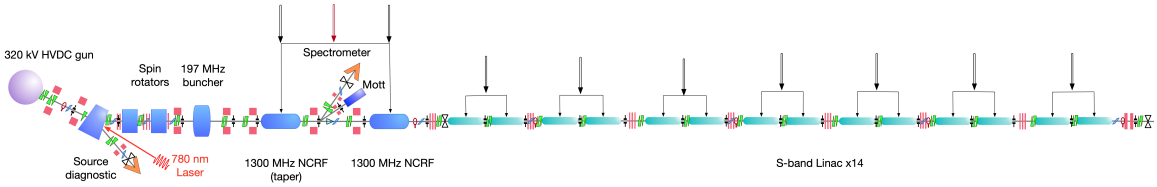

Figure 3.57: Preinjector schematic layout

The initial laser pulse duration of 300 ps (half maximum full width) is established by minimizing the bunch length at the entrance to the buncher. The buncher imparts a chirp, resulting in a RMS energy spread of 5 %. The buncher phase is positioned at the zero phase crossing, followed by an approximately 2-meter drift as a ballistic compression. A single 1300 MHz tapered cavity accelerates the beam energy to 3.8 MeV while compressing the bunch length to approximately 1 mm. In polarization measurement mode, the beam energy is adjusted to 3 MeV to enhance the detection rate. The solenoid fields from the gun to 1300 MHz cavity are optimized to minimize the transverse emittance. Subsequently, the beam is further accelerated to 13 MeV using an additional 1300 MHz cavity. This elevated beam energy enables injection into the S-band linac without the superposition of solenoidal and accelerating fields, thereby preventing spin rotation. A triplet quadrupole configuration is employed to match the beam into the S-band linac. Triplet quadrupoles are utilized between the S-band groups as well, configured as one of two units and three of four units. The electron beam envelope, from the gun to the end of the linac, is illustrated in Fig. 3.58. The RMS bunch length, beam energy, normalized transverse emittance and RMS beam size along the preinjector are shown in Fig. 3.59. The parameters of beam at the 40 cm of the exit of the last S-Band linac are listed as the Table 3.32. The longitudinal wake impact on the bunch is included.

Description	Norminal	High charge
Bunch charge	1.2 nC	1.7 nC
RMS bunch length	2.2 ps	3.1 ps
RMS dp/p	0.19%	0.23%
Energy	750 MeV	750 MeV
RMS normalized emittance (x/y)	29.87/18.06 mm-mrad	80/50 mm-mrad
Length	80 m	80 m
Rep. rate	30 Hz	20 Hz

Table 3.32: Summary of beam parameters at the end of the electron Linac

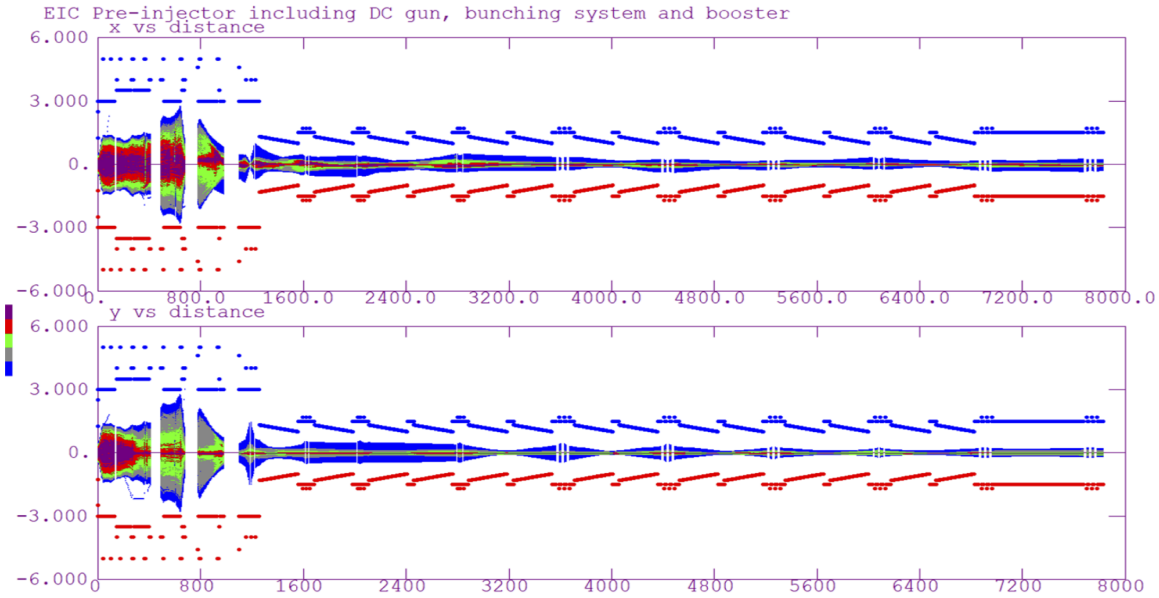

Figure 3.58: Beam envelope from the gun to the end of the linac at 1.7 nC of maximum bunch charge.

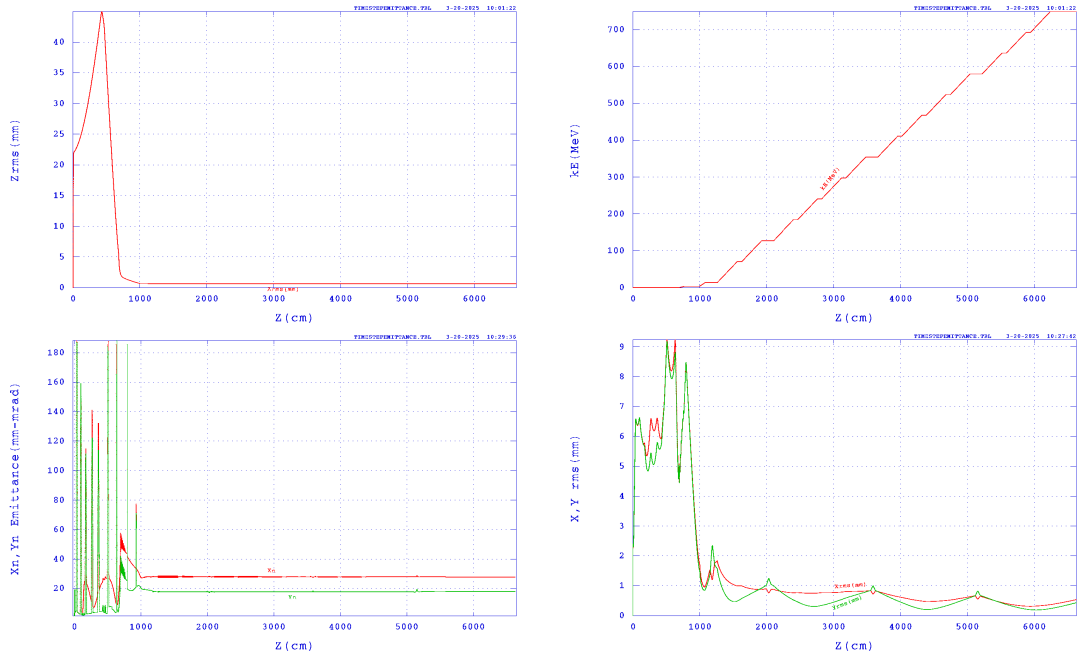

Figure 3.59: The beam performance along the pre-injector when the bunch charge is 1.2 nC. Upper left: RMS bunch length. Upper right: Beam energy. Lower left: RMS normalized emittance. Lower right: RMS horizontal and vertical beam sizes.

The transverse wake will cause the beam emittance growth due to single bunch beam breakup if the beam go through the linac off centered. We use an analytical formula to evaluate the impact of

transverse misalignment of the linac [?, ?]. In the case where the accelerator structures' misalignment errors are random about a smooth trajectory but systematic between a pair of quadrupole magnets (as it may happen when consecutive quadrupoles are used for alignment reference), we have

$$\Delta(\gamma\varepsilon) \approx \Delta_{\mathrm{str}}^2 \left[\pi\varepsilon_0\varepsilon N_e w_\perp(2\sigma_z)\right]^2 \frac{L_{\mathrm{str}} L_{\mathrm{cell},i}\bar{\beta}_i}{4\alpha\Delta\gamma_{\mathrm{str}}} \left[\left(\frac{\gamma_f}{\gamma_i}\right)^{2\alpha} - 1\right] \tag{3.46}$$

Then, we consider one-to-one trajectory correction where one minimizes the reading of BPMs located close to quadrupoles. BPM misalignment by a quantity Δ_{BPM} forces the beam to pass off axis in the quadrupoles and in the accelerating structures and one has:

$$\Delta(\gamma\varepsilon) \approx \Delta_{\mathrm{BPM}} \left[\pi\varepsilon_0\varepsilon N_e w_\perp(2\sigma_z)\right]^2 \frac{\cos\left(\frac{\Delta\mu_{\mathrm{cell}}}{2}\right) i L_{\mathrm{str}} L_{\mathrm{cell},i}}{\sin^3\left(\frac{\Delta\mu_{\mathrm{cell}}}{2}\right) 16\alpha\Delta\gamma_{\mathrm{str}}} \left[\frac{\gamma_f}{\gamma_i}\right]^{2\alpha} - 1 \tag{3.47}$$

The emittance growth calculated for this linac is shown in Fig. 3.60.

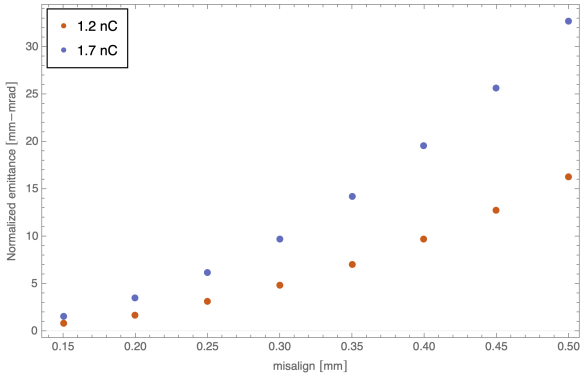

Figure 3.60: The emittance growth due to the misalignment of BPM and Linac. The x-axis is the Linac misalignment. BPM misalignment is linac misalignment minus 100 µm

3.9.4 High voltage DC polarized photogun

The polarized electron source must provide high polarization, high bunch charge electron beam — requirements are listed in Table 3.33. The polarized electron source section consists of a cathode growth system, cathode transfer section, HVDC gun, and a 16° switch dipole magnet that either brings the beam to the preinjector or the diagnostic beam line. A drift space between the gun and the dipole chamber is instrumented with diagnostics to check the beam performance such as position, profile and charge.

Polarized electron source R&D was carried out from 2018 to 2024. An inverted 300 kV large cathode gun (Fig. 3.61) was developed and commissioned in the R&D stage. The polarized electron source R&D project has its goals and EIC requirements in December 2023 [?, ?]. The achieved R&D parameters are shown in Table 3.33. To summarize R&D achievements:

- Distributed Bragg reflector superlattice (DBR-SL-GaAs) cathodes were grown with metal-organic chemical vapor deposition (MOCVD) method within an ODU/BNL/JLab collaboration. The cathode Electron Spin Polarization (ESP) was measured up to 91 % at its peak QE

Parameter	EIC R&D Goal	Achieved in Stable Operation	EIS Requirements
Bunch charge [nC]	7	7.5 (12)	1
Peak current [A]	3.8	4.8 (No SCL)	NA
Frequency [Hz]	1 (4 bunches)	1 (9000 bunches)	30
Voltage [kV]	300	320	320
Average Current	28 nA	30 µA	30 nA
Polarization [%]	>85 %	88 %	86 %

Table 3.33: Comparison of EIC R&D Goals, Achieved Values in Stable Operation, and EIC EIS Requirements

range.

- We suppressed the surface charge limit by optimizing the surface doping level and cathode surface cleaning procedure.
- a wavelength-tunable laser was developed to address varying peak QE wavelengths due to various factors.
- DBR-SL-GaAs photocathodes were successfully tested in an HVDC gun. We achieved a maximum of 11.6 nC bunch charge, 30 µA of average current, and lifetime exceeding 2 weeks.
- We observed and explained the laser wavelength's impact on the cathode lifetime, and proposed an optimal operational laser wavelength range for the DBR-SL-GaAs photocathode.

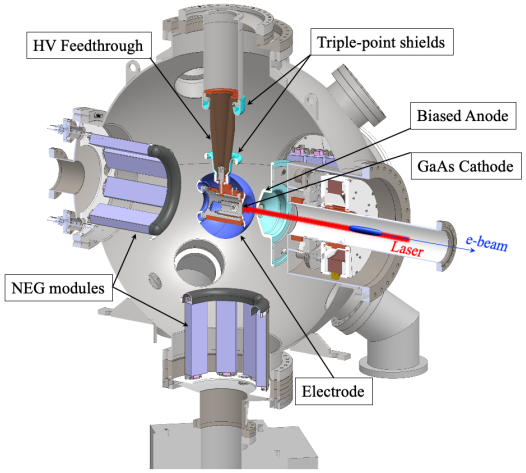

Figure 3.61: HVDC polarized gun cross view

Towards an long-term operation gun, the following upgrade is planned.

- change the NEG pumps which used for more than 10 years and shows the pumping rate degradation.
- Upgrade the cathode growth system, including alignment, automatic temperature control system, and wavelength scan system.
- Simplify the anode position mechanism which was dedicated for R&D purpose.

- Remove the cathode storage chamber due to mitigate the high current requirement, and make the gun cathode system simpler and more stable.

The photocathodes used to generate the polarized electrons are super lattice, strain-compensated GaAs/GaAsP (SL-GaAs) crystals [**?**]. Applying the Distributed Bragg Reflector(DBR) layer underneath the superlattice layer can enhance the QE. As of 2025, there are no commercial vendors for these crystals. BNL is collaborating with multiple institutes to develop reliable high quality DBR-SL-GaAs cathode production. The structure of the cathode has been well-studied by the photocathode community. Figure 3.62 illustrates the detailed layered structure of the DBR-SL-GaAs photocathode we are using. Figure 3.63 illustrates its quantum efficiency (QE) as a function of polarization during R&D measurements. The SL-GaAs crystals will be activated in Extremely High Vacuum (XHV) using O_2 and Cs to lower the surface work function.

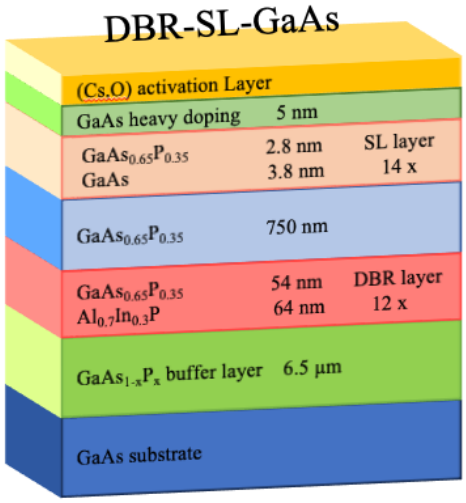

Figure 3.62: DBR-SL-GaAs photocathode structure

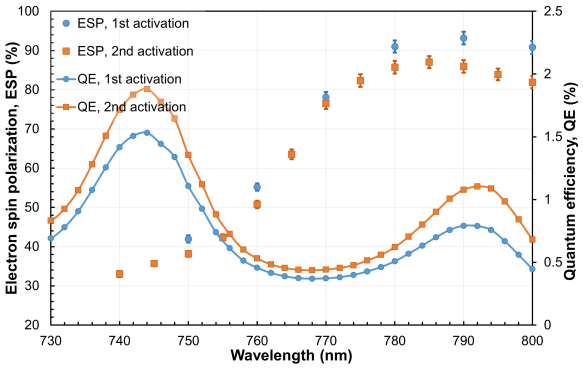

Figure 3.63: Cathode quantum efficiency and polarization as the function of wavelength. Two iterated activations were used.

We will use a Glassman LH-OS High Voltage Power Supply (HVPS) at a maximum of 400 kV. This HVPS can provide a maximum current of 6 mA at this voltage. To avoid the use of environmentally adverse Sulfur hexafluoride (SF_6) or oil, the power supply is in air within a grounded cage. This

places the HVPS about four meters from the gun. To avoid the cable storage energy damage to the gun, we will use a semiconducting layer as the shield of the cable with a resistivity of $1 \times 10^{-10}\,\Omega -$ cm. The resistivity is low enough to keep the cable from building charge but high enough to limit the delivery of stored energy from the cable in the DC gap. During conditioning, external 100 MΩ resistors will be used in series, between the power supply and gun, to avoid damage to the polished electrode by a strong discharge. The vacuum pressure in the gun and beamline towards the first dipole is in o(10^{-12} Torr). A week-long bake is needed at 300°C. The dipole chamber has the NEG bumps installed and the drift tube between the dipole and gun will be NEG coated. The gun commissioning beam dump, similar as the R&D beam dump, will be placed after the first 16° dipole.

3.9.5 Circular polarized laser

To achieve the required beam parameters from the gun, we designed a laser to meet the requirements shown in Table 3.34. The proposed laser system is a high-performance, tunable source designed to deliver precisely controlled pulses to drive the polarized photocathode gun of the EIC injector. This system is designed for stability, adaptability, and reliability. It consists of four primary stages:

1. a wavelength-tunable seed laser
2. a regenerative Alexandrite-based amplifier
3. a beam conditioning module
4. a free-space beam transport system

Figure 3.64 shows the stage 1 to 3.

Parameter	**Value**
Wavelength tunable	760 to 790 nm
Pulse energy on cathode	up to 6 µJ
Pulse frequency	30 Hz
Polarization	>99 %
Power stability (pulse to pulse)	1 % rms
Pulse Shape	Beercan (long); trunc-Gaussian 1 sigma (trans)
Pulse Duration	200 to 350 ps (FWHM)
Timing Jitter (pulse to pulse)	<3 ps rms
Pulsed Mode Contrast	> 50 dB
Polarization	left/right circular
Polarization switch speed	1 Hz rate in <30 ms

Table 3.34: Circular polarized laser parameters

Wavelength-Tunable Seed Laser

The seed laser covers a wavelength range of 760 to 790 nm and is based on a fiber resonator with a total reflector at one end and a free-space optical grating for wavelength tuning at the other. A

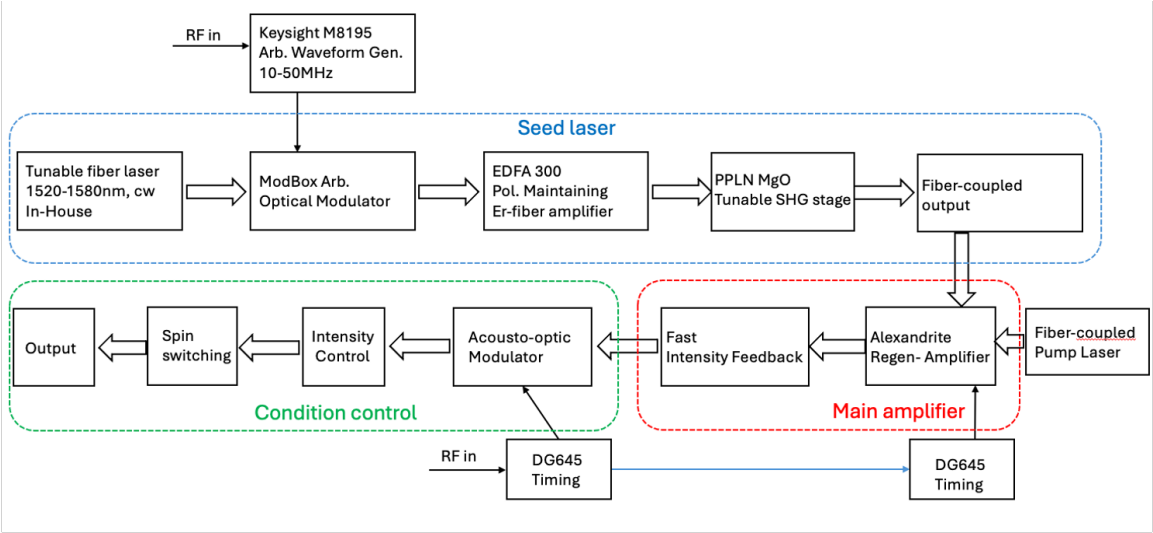

Figure 3.64: Schematic drawing of conceptual high intensity polarized laser

traveling-wave amplifier chip serves as the gain medium, and a 90:10 fiber splitter outputs 10 % of the circulating power. The laser produces a polarized, continuous-wave (CW) beam, which is modulated into pulses using an electro-optic modulator (EOM) driven by an arbitrary waveform generator with a 30 ps rise time. The pulse duration is tunable from 100 ps to 2 ns. To increase power, the pulsed beam is amplified using an Erbium-doped fiber amplifier (EDFA) to ∼23 dBm (∼200 mW) before undergoing frequency doubling in a periodically poled MgO-doped lithium niobate (PPLN) crystal. With a conservatively estimated 25 % conversion efficiency, the final output at 760 to 790 nm delivers ∼50 nJ per pulse. The system operates at 30 Hz to 1 MHz, synchronized to the experiment's RF clock. The output is delivered via single-mode, polarization-maintaining fiber, ensuring excellent beam quality. The main laser parameters are listed in Table **??**

Regenerative Amplifier

The regenerative amplifier is a custom-built, Alexandrite-based solid-state system, using fiber-coupled laser diodes for end-pumping. The gain crystal is mounted in a temperature-controlled heatsink for optimal efficiency and is placed within a cavity utilizing a Pockels cell for pulse injection and ejection. The cavity has a round-trip time of ∼8 ns, allowing for the amplification of pulses up to 2 ns. The amplifier provides 33 dB of gain, yielding output pulse energies of ∼100 µJ. The repetition rate of the amplifier is chosen for maximum stability, as a multiple of 30 Hz (likely 10 to 20 kHz). A downstream pulse picker will adjust the repetition rate to match experimental needs. Due to the nature of regenerative amplifiers, the output beam quality is excellent ($M^2 < 1.2$).

Beam Conditioning

After amplification, an interference-based intensity feedback system, developed in-house, reduces pulse energy fluctuations to below 1 % RMS, ensuring experimental stability requirements are met. Pulse selection is performed by an acousto-optic modulator (AOM) pulse picker. Additionally, a pair of opposed polarizing beam splitters with a remotely operated half-wave plate (HWP) al-

lows user-controlled intensity adjustment for further flexibility. A Pockels cell enables polarization switching between pulses, providing additional configurability for experimental requirements.

Free-Space Beam Transport

The beam is transported over a 15 m evacuated optical path, enclosed in tubes with AR-coated wedged windows at both ends to eliminate unwanted reflections. Piezo-controlled mirrors allow for remote beam alignment and steering, with an optional camera-based feedback system to compensate for slow drifts due to building shifts. The beam is relayed using dielectric mirrors and directed into an optical enclosure near the experiment. Inside the enclosure, the beam overfills a circular aperture, which is imaged 1:1 onto the photocathode to ensure uniform illumination. The beam believe to the gun through the dipole chamber window. The 1st YAG viewer has a hole in the center to make sure the laser beam can go through. A parallel translation stage enables precise beam positioning on the photocathode.

System Diagnostics and Safety Measures

Diagnostics such as power sensors, photodiodes, and cameras are distributed throughout the system for remote performance monitoring of each stage. A custom laser protection system (LPS) monitors critical infrastructure using flow, temperature, and dry contact sensors and operates independently to ensure the system remains in a healthy state. The LPS reports its readings and status to the control system for remote monitoring. The laser system is fully interlocked inside the laser room to ensure personnel safety during operation.

3.9.6 Spin rotator

Wien filters are widely used for rotating polarized electron spin orientations [**?**, **?**]. A Wien filter is comprised of perpendicular electric and magnetic fields that exert forces on the particles as they pass through. When the forces from the electric field and magnetic field balance each other, only particles with a specific velocity travel straight through without deflection. Both electric field and magnetic field are involves rotate the electron's spin direction.

Existing Wien filters have operated only with beams below 200 keV and with electron bunch charges of tens of pC [**?**, **?**]. For the EIC beam of 320 keV and up to 1.7 nC bunch charge, a longer Wien is required due to limitations in the required high voltage feedthrough. However, this conflicts with the need for a close placement of the focusing element to address high space charge. We are designing two Wien filters, each rotating the spin by 45°. Given the large beam size, a significant gap between the two electrical plates is necessary to maintain a uniform field and matched E-B fringe fields to minimize beam deflection. We designed a Wien filter for 7 nC bunch charge at 2024. We use this design for 1.7 nC bunch charge spin rotation. The design parameters for the high charge high energy Wien filter are shown in Table 3.35 and the preliminary design is shown in Fig. 3.65.

A Rogowski profile is employed at the end of the electrode plate to achieve a uniform entrance field. The electric and magnetic fields have different decay characteristics, so nickel plates suppress the B-field in the fringe region, ensuring proper matching with the E-field in that region. Opera 3D electrostatic and magnetostatic solvers are used separately to simulate the electric and magnetic fields of the Wien filter, and results are exported in grid format for use in Parmela and General

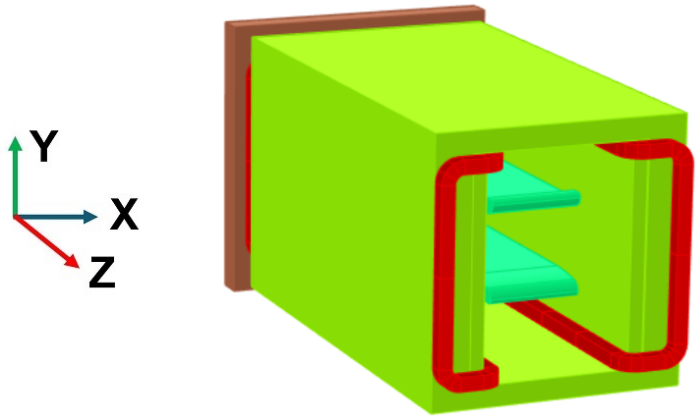

Figure 3.65: Perspective view of the Opera 3D model of the Wien filter. Nickel plates are used on both sides to shape the fringe B-field. The front-side Nickel plate is not shown here to make the electrodes visible.

Parameter	Value
Bunch charge	1.7 nC
Energy	320 keV
L	45.92 cm
E_x	1.44 MV m^{-1}
B_y	60.88 G
Electrode gap	7 cm
Feedthrough	50.5 kV each

Table 3.35: Wien filter parameters.

Particle Tracer (GPT). Figure 3.66 shows well-matched E_y and B_x components along the center line. The electrode plate width and the transverse shaping of the iron core are optimized to achieve field matching along the center line and in the transverse direction.

Beam dynamics simulations with two Wien filters were carried out in Parmela and further checked with GPT. Numerous optimization steps for the electrodes and magnets of the Wien filters were performed to minimize beam deflection in the Wien filter region. Thin quadrupole lenses in a triplet configuration were used before and between the Wien filters. Figure 3.67 shows the beam envelope through the Wien filter.

The bunch length of the beam from the cathode was 450 ps, with a bunch charge of 1.7 nC, and in beam simulation, the space charge effect was included. These simulations indicate that a 1.7 nC beam with peak current of 3.77 A can pass through both Wien filters. A 7.0 nC bunch charge with 1.3 ns bunch length beam was also studied in GPT. While there is a slight increase in emittance, it does not appear to significantly affect the overall performance. A 1.2 nC bunch charge will have additional margin.

One of the challenging aspects of the Wien filter is constructing the electrode and magnet to meet the precise specifications required for maintaining uniform electric and magnetic fields. Even a minor misalignment during commissioning or the bake-out process can affect the beam trajectories.

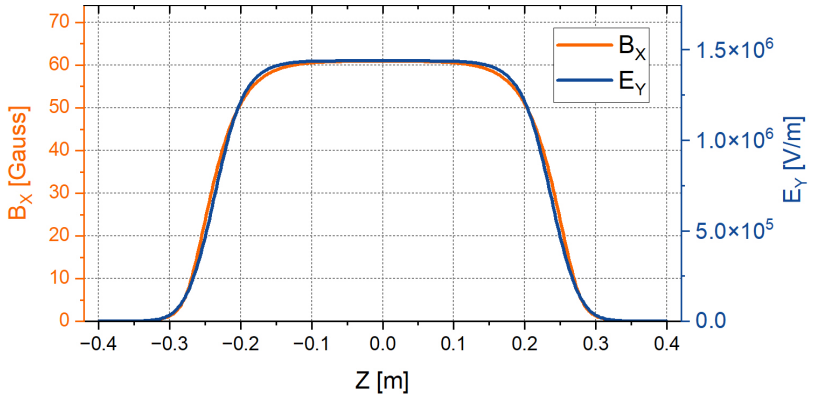

Figure 3.66: Simulated electric and magnetic field generated from Opera 3D at the centerline.

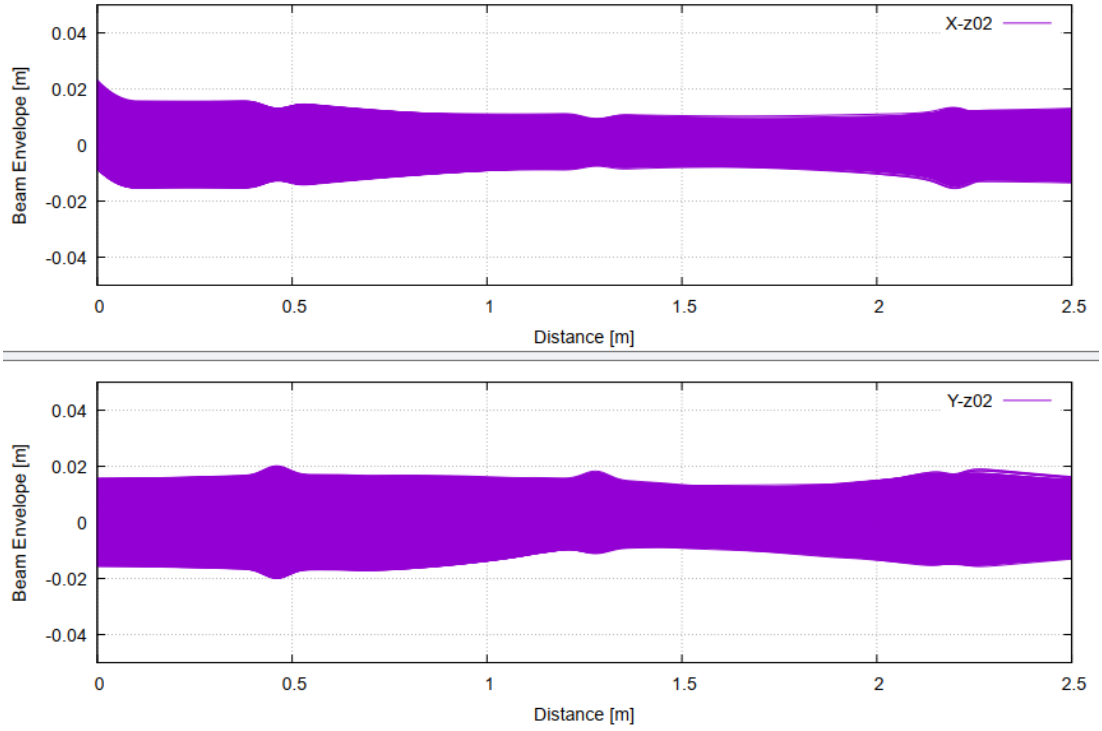

Figure 3.67: Simulated beam envelope of a 1.7 nC space charge-dominated beam through Wien filters 1 and 2, obtained using GPT. From dipole bend to the end of the Wien are shown here.

Additionally, our analysis indicates that the combined ripple from the electrode high-voltage power supply and the magnet power supply needs to remain below 100 ppm. Therefore, developing a prototype is essential to validate this unique high-charge, high-voltage Wien filter configuration.

We analytically calculated the impact of 7 nC space charge on spin polarization both in the Wien filter section and downstream of it [**?**]. The longitudinal space charge, which causes energy spread in

the bunch, contributes to an ESP degradation of about 4×10^{-4} in the Wien filter range. The transverse space charge causes the following ESP degradations: 4×10^{-4} for the Gun to Wien section, 4×10^{-6} during through the Wien filter, 1×10^{-3} for ballistic compression, and 3×10^{-6} for chicane compression [**?**]. The overall ESP degradation is between 1×10^{-3} and 2×10^{-3}. These analyses show that the space charge force of 7 nC bunch charge impact on spin polarization degradation is negligible, same conclusion is applied to 1.2 nC bunch charge

GPT simulation, including 3D space charge and spin tracking, shows the spin degradation through the Wien filter is 0.0016 %. This confirms this effect is negligible. The vacuum in the Wien filter will be on(10^{-11} Torr).

3.9.7 Bunching section and capture section

The bunch from the gun is about 50 mm. We use 197 MHz cavity to generate energy chirp. A drift after the buncher cavity to compress the bunch length to 2 mm. A 1.3 GHz taper cavity as the capture section to accelerating beam to 3 MeV, while the bunch length keep reducing to 0.7 mm in the capture cavity. The energy spread at the exit of capture cavity is 3 MeV with energy spread 0.5 %. Two diagnostic beam lines are designed for spin measurement and energy spectrum measurement.

The 197 MHz normal conducting cavity using the CERN/RHIC 197 MHz cavity geometry. It is using in the RHIC in the CW mode. One of the back up cavity is considered to be used in the preinjector, operating at 30 Hz pulsed mode, The cooling channel will be reduced, the damping couplers will be removed. The cavity gap voltage is 400 kV, provide beam a energy chirp with energy spread of 5 %. With drift of 2.3 m, the RMS bunch length is compressed to 5 mm and inject into a tapered 1.3 GHz cavity. The Taper cavity is modified from the Argonne Wakefield Accelerator (AWA) 1.3 GHz, 7-cell cavity. The cavity choose a π-mode, iris-loaded cavity. In addition, a z-slot rf coupler was used , and the width of the rf coupler equalled the width of standard WR650 waveguide. To match the velocity, The first, second, and third cell lengths are reduced to 7.11, 10.89, and 11.26 cm respectively. Rest of the cell length is 11.53 cm as $\beta = 1$. The cavity geometry is illuminated in Fig. 3.69. The iris thickness is 32.75 cm and radius is 4.6 cm. The input power is 2.2 MW to make the cavity gap voltage about 5.5 MV. The bunch was dechirped in the taper cavity and bunch length is reduced to 1.2 mm, while energy goes up to 3.8 MeV.

After the AWA taper cavity, there is a 2 m drift space to accommodate a spin diagnostics beamline which will be described in the next section. To inject the beam into S-Band linac without superposition solenoidal focusing, we further accelerate beam to 13.8 MeV by an standard AWA cavity with gap voltage of 11 MV with input power of 8.7 MW [**?**]. At exit of the 2nd capture cavity, the bunch length is reduced to 0.7 mm with an energy spread of 0.6 %. The cavity geometry is illuminated in Fig. 3.70. The longitudinal wake from both Bane's analytical formula and ABCI simulation are shown in Figure 3.71. The 5% different is caused by the iris geometry difference used in the Bane's analytical and more realistic ABCI simulation. The ABCI generated one is included in the beam tracking. Both 1.3 GHz capture cavities are powered by two of E37507 Klystrons with peak power up to 12 MW.

In the bunching and capture section with energy up to 3.8 MeV, the spin direction is vertical. To avoid solenoid longitudinal magnetic field rotate the spin direction, we use solenoid with clockwise and countclock-wise coils using identical current. The spin direction will swing to the left into half of the solenoid and swing back to vertical at exit of solenoid. The longitudial B field has satisfy $\int_{-\infty}^{\infty} B_z dz = 0$. Figure 3.72 shows the solenoid modeling and field profile along the center. Two power supplies will be power two coils simultaneously. The Mott polarimetry at 3.8 MeV will be used to measure the spin direction. Separated power supply could provide a knob to tune the spin

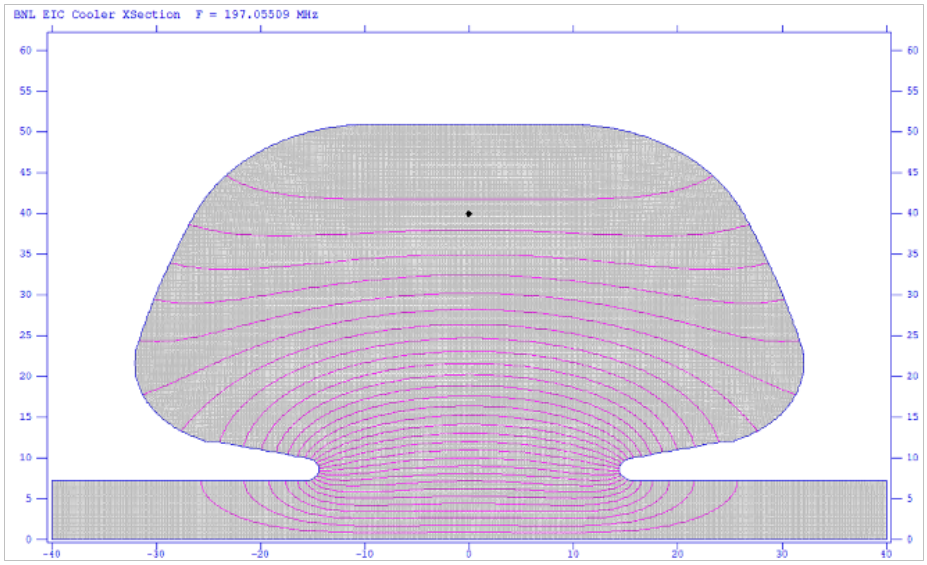

Figure 3.68: Superfish model of 197 MHz cavity

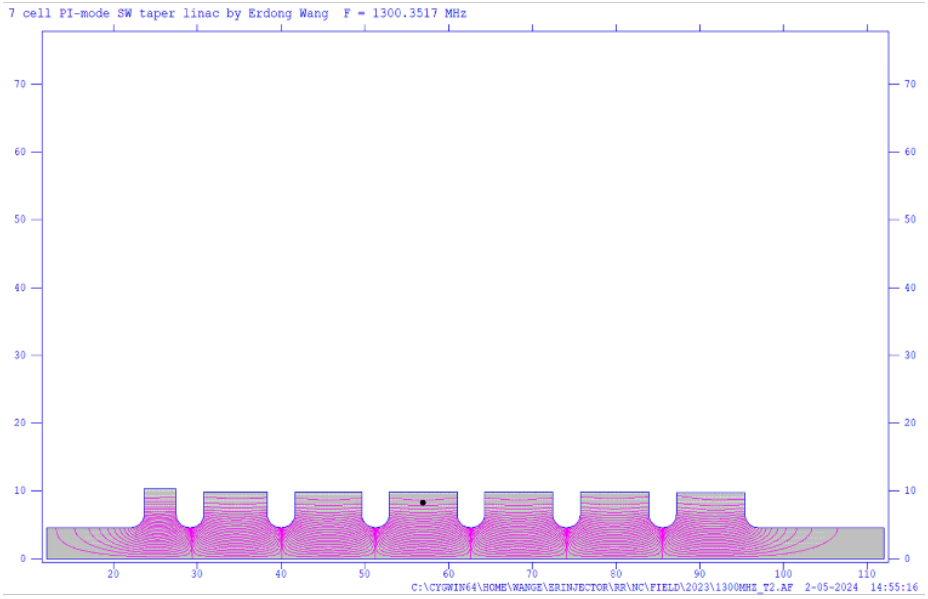

Figure 3.69: Superfish model of tapered 1.3 GHz cavity

direction.

3.9.8 Linac

The EIC preinjector linac section is composed of fourteen 3 m S-Band linac units. The fourteen units will be powered as follows:

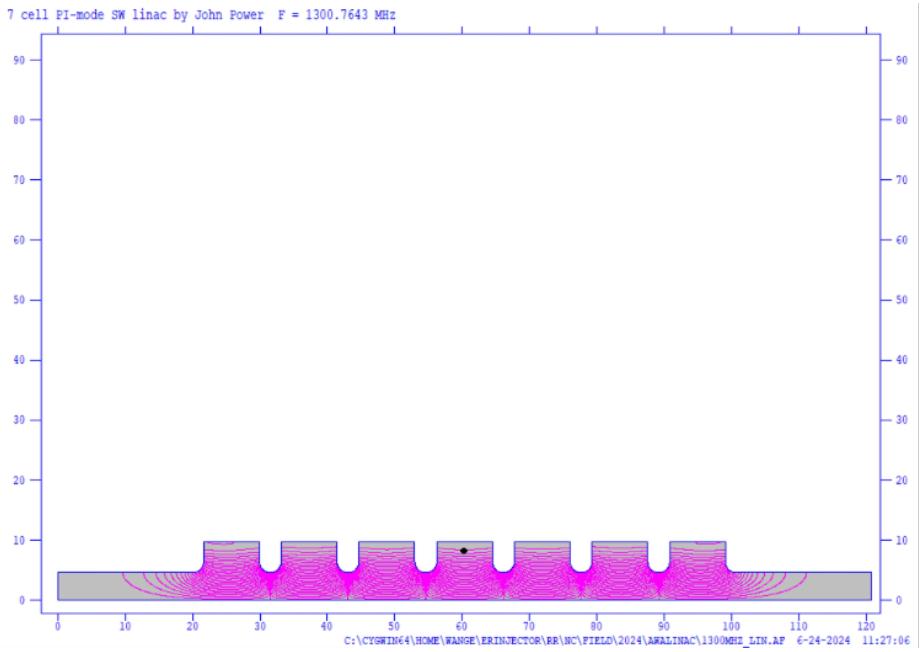

Figure 3.70: Superfish model of 1.3 GHz cavity

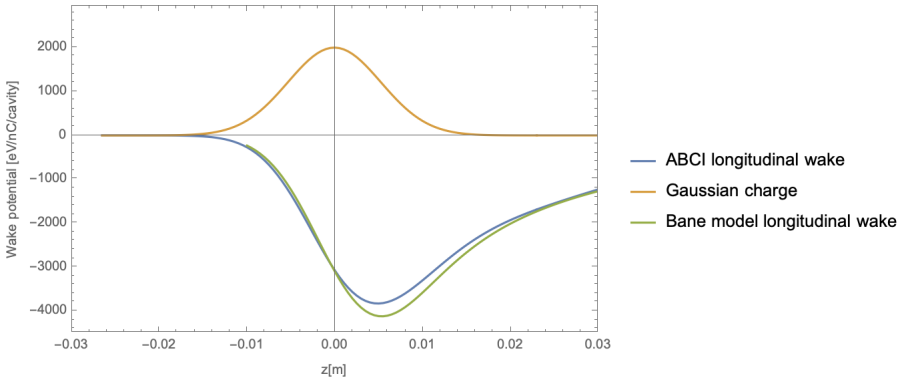

Figure 3.71: AWA longitudinal wake potential generated by a Gaussian beam. Bane's model and ABCI results are compared

- Seven sections, each consisting of four (2x) 3 m unit.

The average field gradient of the units is 20 MV/m. Between each section, we have triplets quadruple to focus the beam.

The groups of two 3 m Linac unit will be powered from a single high-power, short-pulse klystron with a maximum peak output power of 50 MW, A SLED type pulse compression system will provide nominal power gain of 4.Similar to other set up [**?**,**?**]. A section has an energy gain of 120 MeV.

The S-band SLED consists of a 3 dB power hybrid and two identical over-coupled cavities resonant at the 2856 MHz as shown in Fig. 3.73. A fast-acting triggered π-phase-shifter, which reverses the RF phase of the klystron output power, is inserted into the klystron drive line. For a 4 µs,by

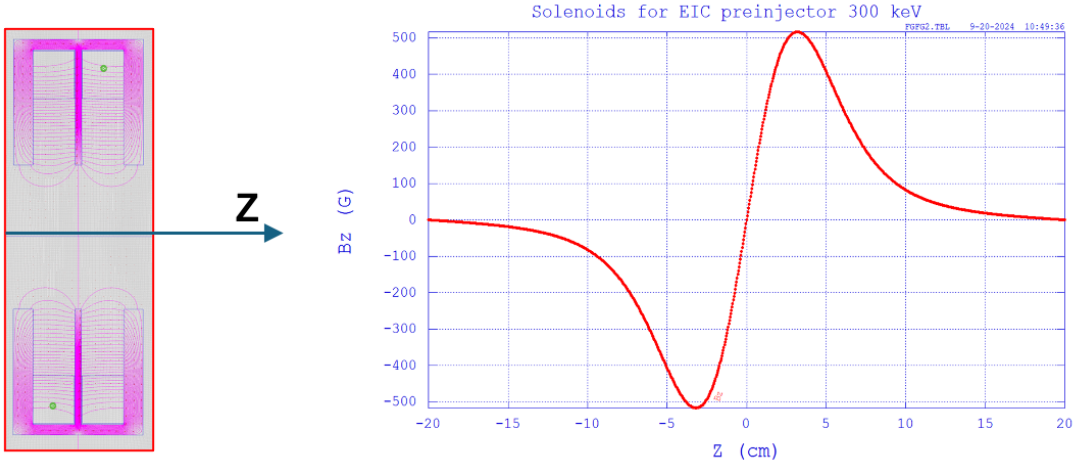

Figure 3.72: Preinjector solenoid model and longitudinal field along the axis

reversing the phase at 3 µs, the power from klystron combined with emit power from SLED cavity, can enhance the power the factor of 4. The emit peak power of each SLED system is up to 122 MW These linac units are 3m long, constant gradient, S-band 2856 MHz accelerating structures. Cell number is 84 regular cells and 2 coupler cells. To get the constant gradient, the iris radius narrowing from 13.11 mm to 9.95 mm along the length of the linac. Quasi- symmetrical type coupler cell have wave guide of 1/4-wave length in iris opposite side in order to compensate asymmetry of electromagnetic field in the coupler cavity. The longitudinal and transverse wake of the S-Band linac are shown in the Fig. 3.74, which are used in the beam tracking [**?**].

To stabilize the phase between two structures powered by the single klystron, we have to maintain the phase error under 2 degrees in a maintained the structure at around 105-115 F depends on tuning to the center frequency of 2856 MHz.

3.9.9 Spin diagnostics

There are two Mott polarimeters for measuring the electron beam polarization in the pre-injector, one on the cathode preparation system and the other one on the preinjector beam line at 3 MeV. The cathode preparation polarimeter will be used for checking the beam from the SL-GaAs wafer after activation. BNL already developed this low energy Mott polarimeter and in the routing operation as shown in Fig. 3.75. It will be used for the EIC. The pre-injector beam line needs a high energy Mott polarimeter which is similar to the one used in the CEBAF injector [**?**, **?**].

The spin-coupling inelastic Coulomb scattering, also called Mott scattering, results in a spatial asymmetry by Coulomb-scattering of electrons off heavy atom nuclei. The calculated Sherman function and differential cross section for scattering with gold nuclei are shown in Fig. 3.76. The detectors are installed at the scattering angle with maximum Sherman function. In the spin measurement mode, the 1300 MHz taper cavity reduce the gap voltage, control the beam energy up to 3 MeV. For a kinetic energy of the electron beam of 3 MeV, the scattering angle at the maximum Sherman function is $\theta = 169^\circ$, with the extreme value of Sherman function being $S(\theta) = 0.52$.

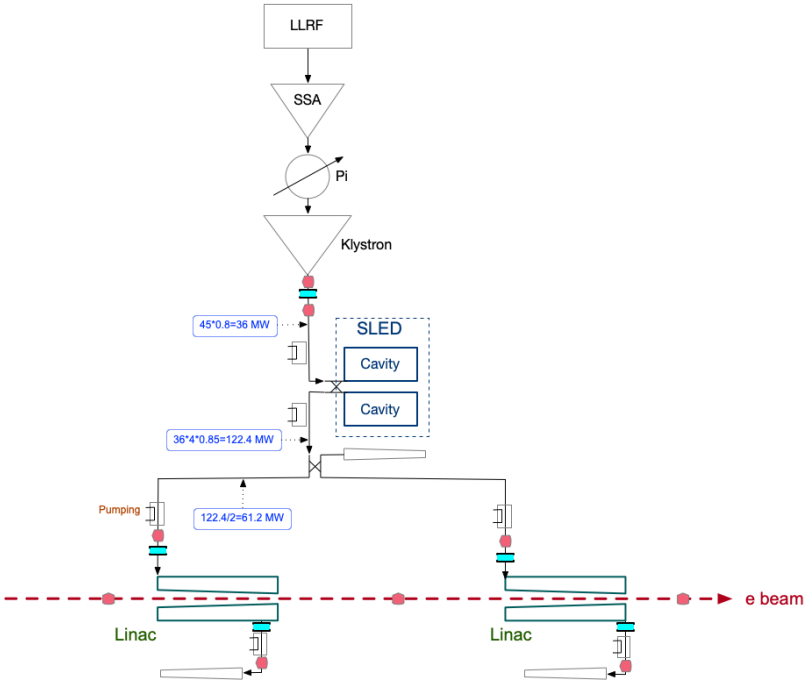

Figure 3.73: Schematic diagram of a four unit S-band linac system with SLED

Description	S-band
Operating Frequency (GHz)	2856
Type	TW, Cons. Grad.
Mode (phase per cell)	$2\pi/3$
Q	13,000–14,000
Shunt Impedance ($M\Omega\,m^{-1}$)	53
Attenuation Factor (neper)	0.58
RF pulse length (μs)	1
Filling Time (μs)	0.83
Input peak power (MW)	33.4
Accelerating gradient (MV/m)	20
Water Temperature (°C)	38 ± 0.1
Rep. rate (Hz)	30
Avg. Power (kW)	1
Coupler cell Type	Quasi-Symmetry

Table 3.36: Specifications of a 3 m S-band accelerating unit

Using a 15° bend magnet, the beam will be kicked into the Mott diagnostic beamline. With the same bend magnet, a 30° dispersive diagnostic beamline with a Faraday cup will be used to determine the charge, energy and energy spread. These parameters will be as the input value for the Mott polarization measurement. The Mott polarimeter will have four detectors. Two on the vertical plane, and other two on the horizontal plane, therefor, the spin direction and polarization can

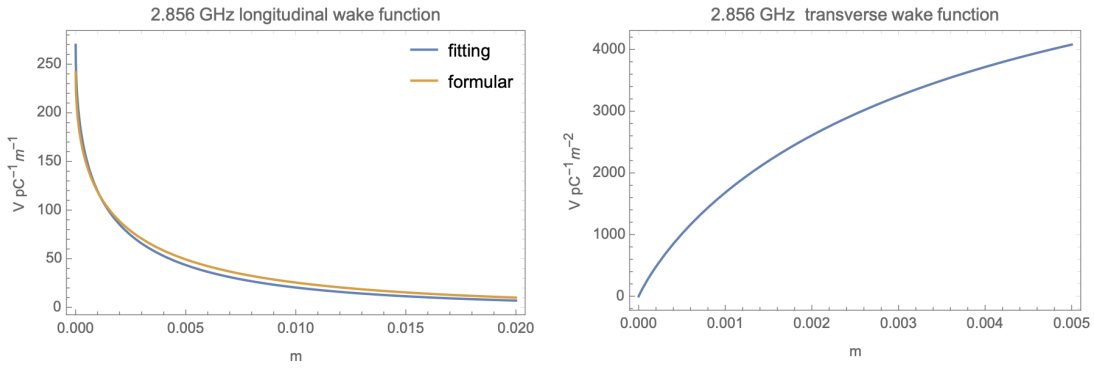

Figure 3.74: Longitudinal and Transverse wake function of S-Band linac

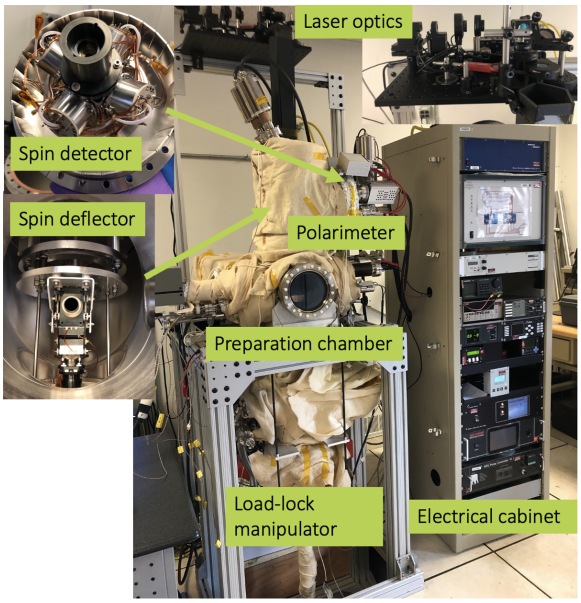

Figure 3.75: Mini-Mott for the cathode polarization measurement

be both determined. This Sherman function $S(\theta)$ is only known for single scattering, however the practical Sherman function S_{eff} is always smaller than $S(\theta)$ because of the effects of multiple scattering in the target foil which is sensitive to the thickness of that foil. Thus, the practical effective Sherman function will be determined by the series of different thickness of the target foil. We compared target material of Th, Au, Ag and Cu. Th is can give the maximum detector rate due to its high Z. But considering the safety, we choose Gold film with seven different thickness from 100 nm up to 1 um.

Figure 3.77 shows the detect time to achieve 0.5% static error with various target thickness and average current. The gun to the Mott section is designed to operated up to 30 Hz, charge up to 7 nC. In the commissioning, it will take about 1–2 hours to get the Sherman function. Once we know the Sherman function, in the routing operation, we can switch to thicker sample and use the effective Sherman function to evaluate the polarization in 10 minutes.

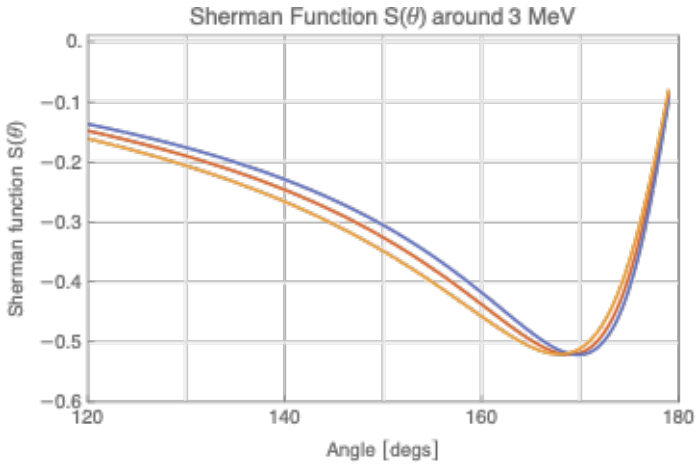

Figure 3.76: The Mott polarimetry Sherman function as a function of scattering angle. Three energies are evaluated: 2.7 MeV, 2 MeV and 3.3 MeV

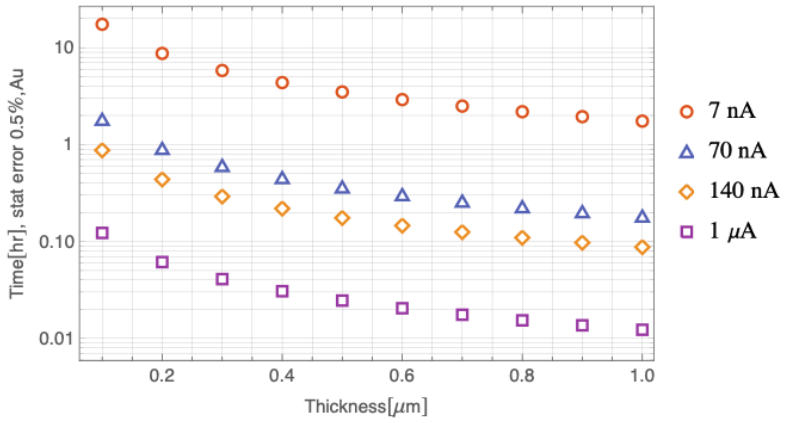

Figure 3.77: The detector time to achieve 0.5% uncertainty with various average current

3.9.10 Beam Accumulator Ring

3.9.11 Introduction

The Beam Accumulator Ring (BAR) is a 750 MeV electron storage ring, designed to accumulate o(1 nC) polarized electron bunches from the S-band linac into a single bunch of intensity up to 28 nC before transfer to the RCS. The BAR provides sufficiently aggressive damping for accumulation and emittance equilibration. A pre-conceptual design for the BAR is provided in [?] in a separate document; highlights are included here for completeness.

The pre-conceptual BAR design is similar to the original NSLS VUV ring [?] and the APS PAR accumulator ring [?]. Table 3.37 summarizes the BAR parameters including injection and extraction beam parameters. The NSLS VUV ring original design parameters are strikingly similar to the BAR requirements, particularly the 750 MeV operating beam energy, so it is used as the pre-conceptual design basis described in this section. Original design documentation for the VUV ring is also

located at BNL and accessible for design iteration.

General		
Number of bunches		1
Bunch length	mm	43
Injection		
Energy	MeV	750
Bunch charge	nC	1
Repetition rate	Hz	30
Horizontal RMS emittance (norm)	µm	$\sim$30
Vertical RMS emittance (norm)	µm	$\sim$50
RMS energy spread		0.0045
Extraction		
Energy	MeV	750
Bunch charge	nC	28
Repetition rate	Hz	1
RMS transverse emittance (norm)	µm	$<$170
RMS energy spread	10^{-3}	0.5–5.0
RMS bunch length	mm	20–70
RF		
Frequency	MHz	52.88
Voltage	kV	100
Magnet		
Main dipole number		8
Main dipole effective length	m	1.5
Main dipole field	T	1.3099
Quad number		24
Quad effective length	m	0.3
Quad field gradient	T/m	4.6/-2.9/4.7

Table 3.37: Summary of Beam Accumulator Ring parameters

3.9.12 Optics design

The BAR, like the original NSLS VUV ring, consists of four 90°, six-quadrupole double-bend achromats (DBAs), as illustrated in Fig. 3.78. Cell lengths are 12.756 m, and the total circumference is 51.024 m.

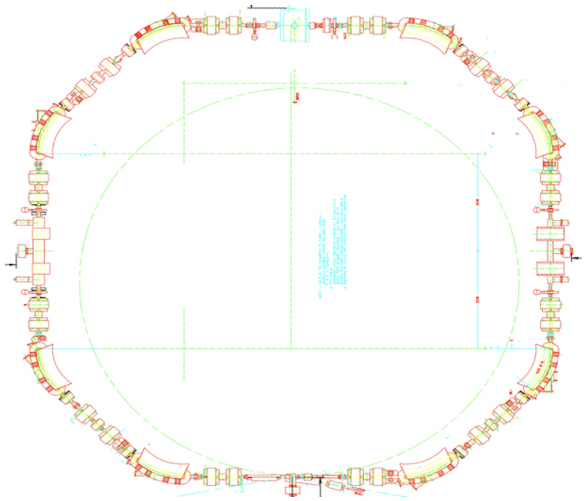

Figure 3.78: A pre-conceptual layout of the 51 m circumference BAR ring, with four 90° DBAs and four straight sections for injection/extraction, RF, and diagnostics.

Parameter	Value
Energy (GeV)	0.75
Circumference (m)	51.024
Hor. emittance (nm)	128.476
Hor./Vert. tune	3.14035 / 1.25914
Hor./Vert. chromaticity	-3.57507 / -2.65412
Momentum compaction	0.0235138
Rad. integral 1 / 2	1.19977 / 3.28987
Rad. integral 3 / 4	1.72257 / -0.246102
Rad. integral 5	0.550337
Hor./Vert. damping time (s)	0.0162073 / 0.0174197
Hor. damping partition	1.07481 / 1
Long. damping time (s)	0.00904829
Long. damping partition	1.92519
Energy spread	4.738×10^{-4}
Energy loss per turn (keV)	14.6556
Revolution frequency (Hz)	5.88×10^{6}

Table 3.38: Beam Accumulator Ring optics parameters

3.9.13 Magnets

Since the pre-conceptual design is based on the NSLS VUV ring at the same energy and similar, VUV ring magnet designs are used as a design and cost basis. These magnet designs will be iterated as required in conceptual design based on start-to-end tracking, 3D field calculations, and BAR damping and emittance requirements. Power supply requirements for these magnets are also similar to those in the VUV ring; these requirements are well-established and should be commercially available at reasonable cost.

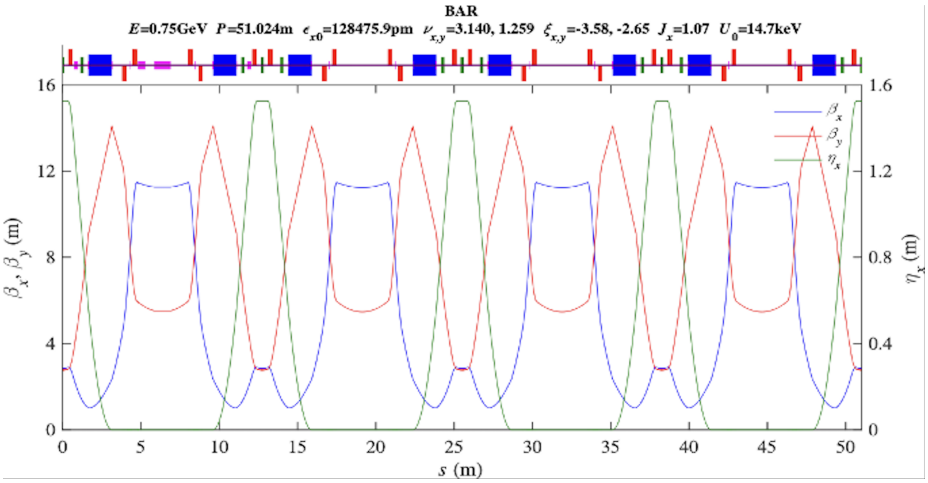

Figure 3.79: Pre-conceptual Twiss parameters of the 51 m circumference BAR ring, showing four characteristic DBA cells.

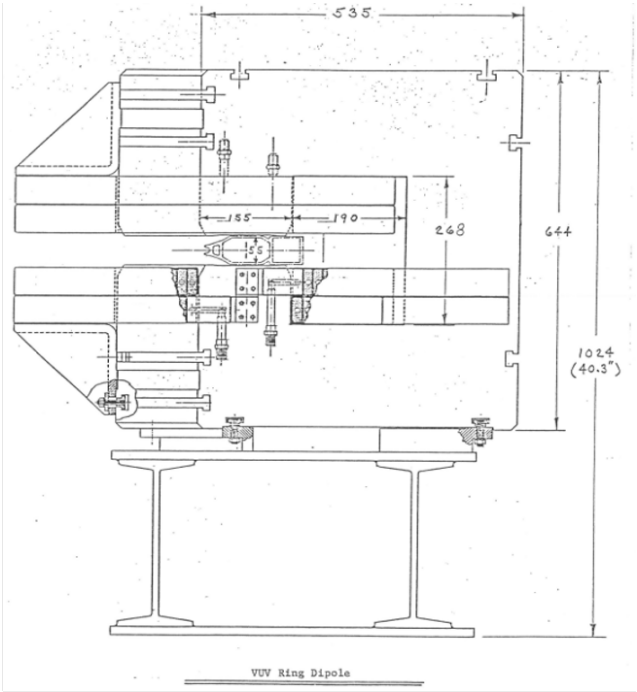

Figure 3.80: A pre-conceptual cross section and scale of the BAR dipole, based on the NSLS VUV ring dipole. Dimensions are in mm.

The pre-conceptual design of the eight BAR dipole magnets follows that of the VUV ring dipole design. The pre-conceptual dipole cross section is illustrated in Fig. 3.80, and the dipole magnet pre-conceptual parameters are shown in Table 3.39. One dipole power supply is necessary with 1470 kW load power, providing 256 A at 87 V.

The pre-conceptual design of the 24 BAR quadrupole magnets follows that of the VUV ring

Parameter	Value
Number of Magnets	8
Magnetic Field (T)	1.223
"Good field" Region (mm)	34
Magnetic Radius (m)	1.91
Magnetic Arc Length (m)	1.445
Bend Angle (deg)	45
Pole Width (mm)	155
Gap Height (mm)	55
Core Weight (kg)	3400
Turns per Pancake	10
Conductor Dimensions (mm^2)	44.5 x 16
Cooling Hole Diameter (mm)	9.5
Amp Turns	58800
Current (A)	1470
Current Density (A/mm^2)	2.3
Inductance (mH)	10.4
Power (kW)	11.2

Table 3.39: Beam Accumulator Ring dipole magnet pre-conceptual parameters

quadrupole design. The pre-conceptual quadrupole cross section is illustrated in Fig. 3.81, and the quadrupole magnet pre-conceptual parameters are shown in Table 3.40. Six quadrupole power supplies are required, each with 256 kW load power, providing 256 A at 87 V.

Parameter	Value
Number of Magnets	24
Gradient (T/m)	9
Quadrupole "Good Field" Radius (mm)	30
Pole Tip Field (T)	0.45
Magnetic Length (m)	0.3
Core Weight (kg)	240
Turns per Pole	38
Conductor Dimensions (mm^2)	9.3 x 9.3
Cooling Hole Diameter (mm)	5.2
Amp Turns	9730
Current (A)	256
Inductance (mH)	13.73
Power (kW)	10.75

Table 3.40: Beam Accumulator Ring quadrupole pre-conceptual parameters

The pre-conceptual design of the 12 BAR sextupole magnets follows that of the VUV ring sextupole design. The pre-conceptual sextupole cross section is illustrated in Fig. 3.82, and the sextupole mag-

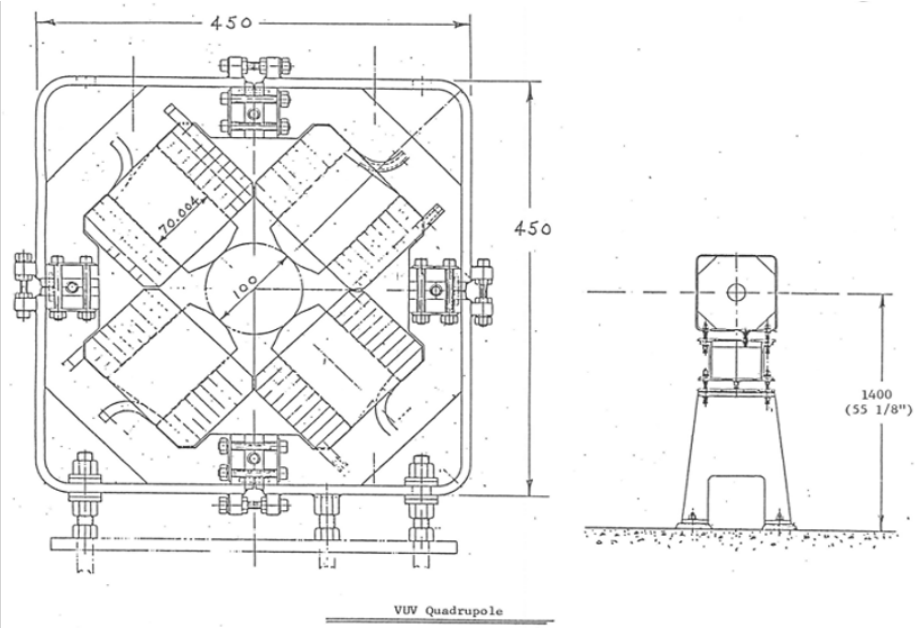

Figure 3.81: A pre-conceptual cross section and scale of the BAR quadrupole, based on the NSLS VUV ring quadrupole. Dimensions are in mm.

net pre-conceptual parameters are shown in Table 3.41. Six sextupole power supplies are required, each with 256 kW load power, providing 205 A at 32 V.

Parameter	**Value**
Number of Magnets	12
2nd Derivative (T/m^2)	100
Sextupole "Good Field" Radius (mm)	30
Pole Tip Field (T)	0.13
Magnetic Length (m)	0.2
Core Weight (kg)	66
Turns per Pole	18
Conductor Dimensions (mm^2)	7.4 x 7.4
Cooling Hole Diameter (mm)	4
Amp Turns	1812
Current (A)	100
Inductance (mH)	7.1
Power (kW)	4.3

Table 3.41: Beam Accumulator Ring sextupole pre-conceptual parameters

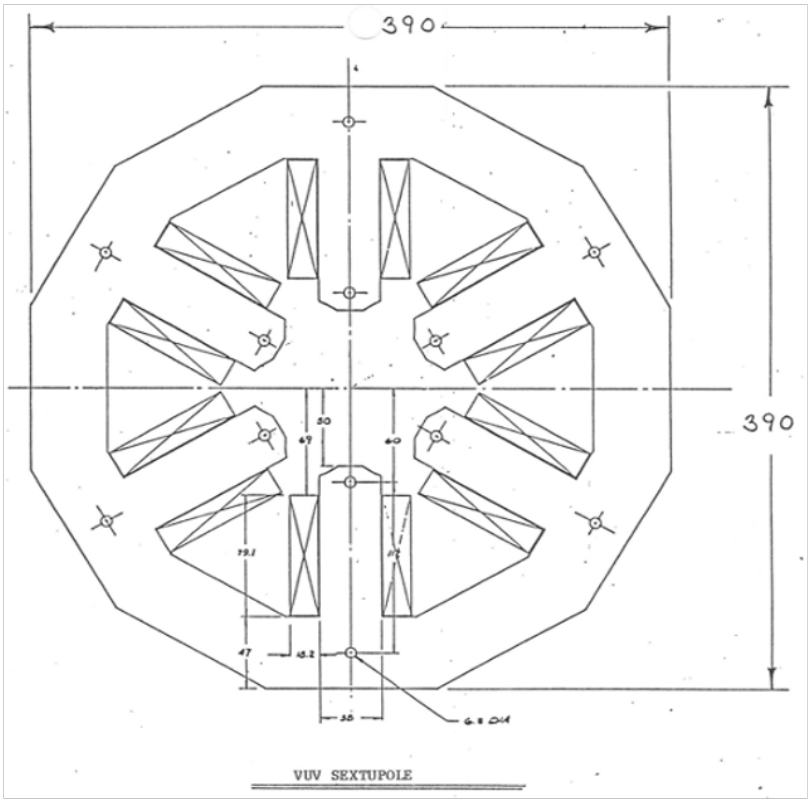

Figure 3.82: A pre-conceptual cross section and scale of the BAR sextupole, based on the NSLS VUV ring sextupole. Dimensions are in mm.

3.9.14 RF, Vacuum, and Longitudinal Dynamics

RF and longitudinal dynamics parameters are outlined in Table 3.42.

Parameter	Value
Beam current (mA)	212
Momentum compaction	0.0245
Energy loss / turn (MeV)	0.014727
RF frequency	52.8797
RF voltage (kV)	100
Accelerating voltage (MV)	0.1
Synchronous phase (rad)	2.99378505
Synchrotron tune	0.00215174
Harmonic number	9
Momentum acceptance (%)	1.73229688
Detuning angle (°)	-46.322403
Detuning frequency (kHz)	-6.7664357
Bunch length (mm)	42.9265

Table 3.42: Beam Accumulator Ring RF and longitudinal pre-conceptual parameters

The VUV vacuum chamber has a rectangular cross-section of 80 × 40 mm, where single-bunch charges up to 68 nC were demonstrated. Equilibrium bunch length and energy spread are affected by the microwave instability, but fit within acceptable bounds as shown in Fig. 3.83. The TMCI threshold is above the expected current of the extracted beam if bunch lengthening is included.

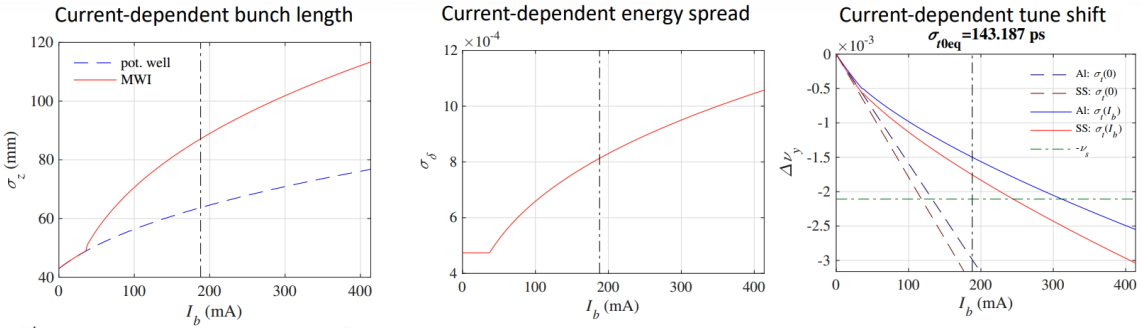

Figure 3.83: The BAR current-dependent bunch length (left), energy spread (center), and tune shift (right), including the effects of the microwave instability (MWI).

3.9.15 Injection Septum and Kicker

The BAR injection and extraction septum magnets follow that of the APS PAR septum, which has proven to be reliable at high bunch charges and over repetitive operations. Parameters for this type of septum magnet are shown in Table 3.43, and the cross section of the APS PAR septum is illustrated in Fig. 3.84.

Parameter	Value
Physical length (m)	0.48
Effective length (m)	0.4
Field strength (T)	0.75
Max septum thickness (mm)	2
Magnetic field aperture (cm)	7× 2
Bending angle (mrad)	199.6
Peak current (kA)	12.057
Peak power (kW)	29
Repetition rate (Hz)	60
Pulse length (half-sin, μs)	275
Average power (kW)	0.574

Table 3.43: Beam Accumulator Ring injection and extraction septum parameters

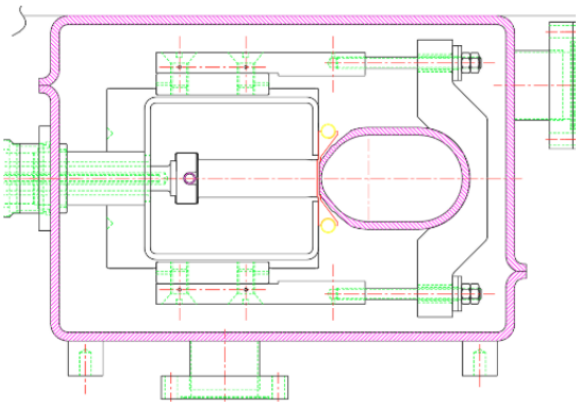

Figure 3.84: The BAR pre-conceptual septum magnet cross section, modeled after the well-established APS PAR septum.

The BAR injection and extraction septum magnets also follow that of the APS PAR kickers. Parameters for this type of kicker magnet are shown in Table 3.44. The repetition rates and charge times are sufficient for rapid bunch accumulation of 1 nC bunches from the linac in the BAR to eventual total bunch charge of 28 nC.

3.9.16 LTR and BAR Transport Lines

The Linac to RCS (LTR) transfer line must match 750 MeV linac extraction to RCS injection, and support two insertions: a straight "bypass" insertion that permits direct transport of o(1 nC) vertically polarized electron bunches from the linac to the RCS, and shunting into and out of the BAR (Section **??**) for accumulation of up to 28 nC vertically polarized electron bunches for delivery to the same RCS injection area.

The interface point between the linac and LTR is a point 40 cm downstream of the end of the last traveling wave linac section. Expected 1.2 nC bunch parameters at the end of the linac are given

Parameter	Value
Length (m)	0.3
Gap (cm)	5
Pole width (cm)	7
Angle (mrad)	7
Turns	2
Conductor cross section (cm^2)	4
Current (kA)	1.2
Resistance (Ω)	55
Inductance (μH)	2
Current ramp time (ns)	100
Voltage (kV)	25
Repetition rate (Hz)	30
Charge time (ms)	25

Table 3.44: Beam Accumulator Ring injection and extraction kicker parameters

in Table 3.32. Preliminary injector particle tracking from the cathode to the end of the linac give interface bunch parameters shown in Table 3.45.

Parameter	Value
Beam energy	750 MeV
Twiss $\beta_{x,y}$	15.34 m, 15.46 m
Twiss $\alpha_{x,y}$	-1.41, -2.04
RMS beam size $\sigma_{x,y}$	540 µm, 435 µm
RMS geometric emittance $\epsilon_{x,y}$	19 nm, 12 nm
RMS bunch length	2.2 ps, 0.7 mm
RMS momentum spread	0.19 %

Table 3.45: Linac-To-Ring interface bunch parameters

The layout, twiss functions, dispersion, and orbit of the LTR line into RCS injection are shown in Fig. 3.85. The LTR is designed in three sections:

- Four quadrupoles immediately following the S-band linac for matching into the bypass diagnostic straight (dipoles D1 and D2 off), or into BAR transport (dipoles D1 and D2 on);
- A $\sim$20 m long bypass straight between dipoles D1 and D2, configured as a low-beta insertion for preinjector beam characterization with multiple profile beam size measurements;
- A betatron and dispersion match dogleg section from the exit of bypass dipole D2 to the injection septum IS entry.

Dipole D1 and D2 strengths are determined by BAR injection and extraction requirements, and geometry constraints to maintain adequate separation between the BAR and bypass line. Dipoles D3 and D4 provide horizontal dispersion in the matching quadrupoles to also close RCS injection

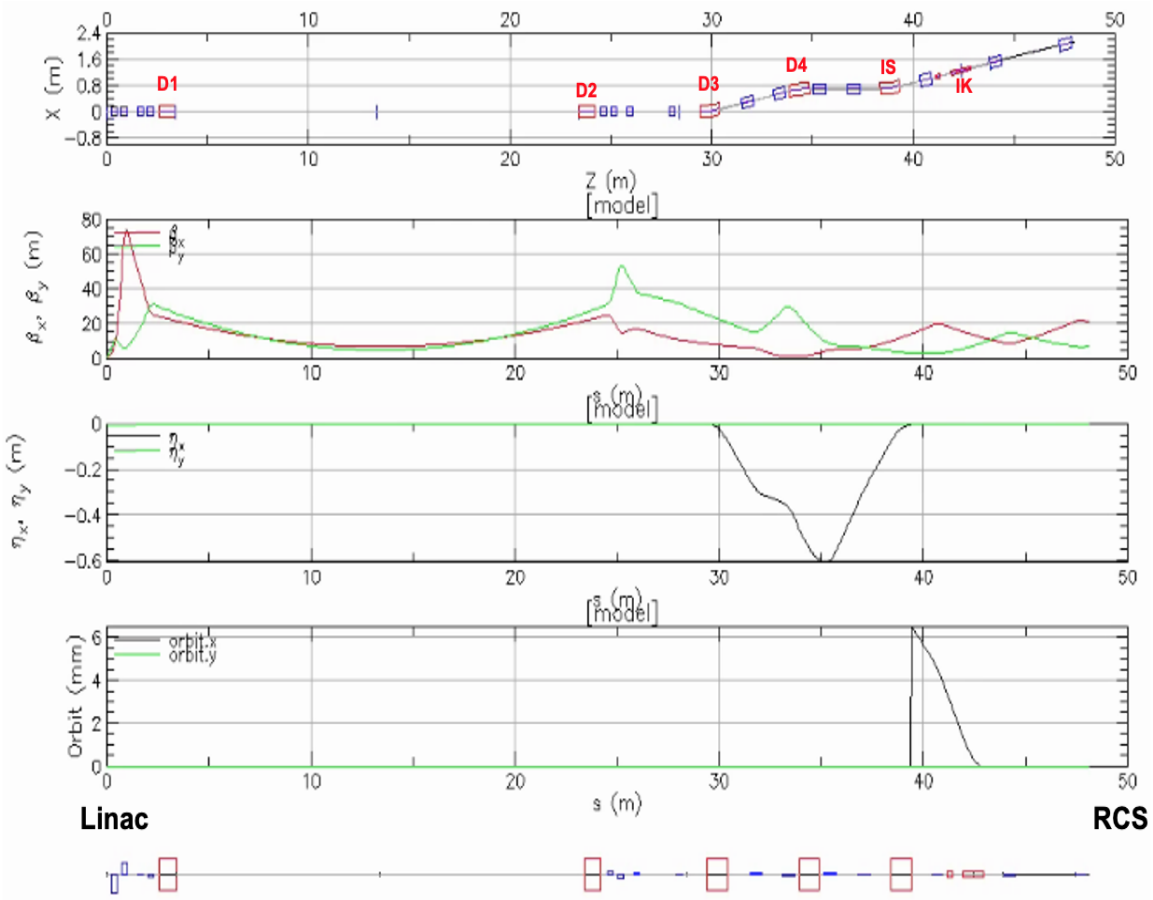

Figure 3.85: Top to bottom: floor plan, beta functions, dispersion, and orbit of the LTR line to RCS injection. Dipoles D1–D4, the RCS injection septum (IS), and RCS injection kicker (IK) are included. The orbit center reference changes from the transfer line to RCS at s =39 m, the exit of the injection septum.

septum and kicker horizontal dispersions as described in Section **??**. This matching may also be used to correct residual horizontal dispersion from the preinjector or BAR.

3.9.17 RCS

3.9.18 Requirements and design concept

The Rapid Cycling Synchrotron (RCS) will be used to accelerate, and inject one polarized electron bunch into the EIC electron storage ring (ESR) per second. In the low current regimes, the RCS will take one 1 nC bunch per LINAC cycle. In the peak current regimes, the RCS will take one 28 nC bunch from the Beam Accumulator Ring (BAR). We have chosen to limit the radiative loss per turn at 18 GeV to about 100 MeV/turn. This is dictated by the desire to limit the cost for the RF and the length of the straight sections. We also want to ensure that the strength of the lowest fields are not much lower than 300 G since this is the level at which dipole magnets should be able to achieve decent field quality. Figure 3.86 shows that using injection energy of 800 MeV with a

bending radius of 90 m we will keep loss per turn at 100 MeV. Based on this we set our injection energy to 750 MeV and our bending radius at 91.67 m.

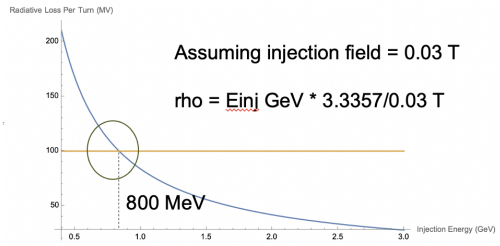

Figure 3.86: Plot of energy loss per turn at 18 GeV versus injection energy for bending radius which gives 300 G at injection.

The current design uses a spin resonance free lattice which recovers the high arc periodicity by requiring the vertical phase advance across any straight section that breaks periodicity to be an integer multiple of 2π **[?]**. Such an accelerator will provide spin polarized electrons accelerated up to 18 GeV. The accelerator will have a 'racetrack' geometry with two straight sections and two 180 degree arcs. It will employ standard technology, and accelerate an electron bunches using a peak ramp rate of 0.1725 GeV/ms. In the past it was believed that such a device would cause profound polarization loss due the combined effects of many depolarizing resonances. However we have devised a lattice that by virtue of the symmetry of construction and high operating tunes, avoids all significant depolarization sources in the energy range of its operation. This is due to the fact that all the strong spin resonance are a function of the tune and periodicity. These spin resonance occur at energies corresponding to $a\gamma = nP \pm Q_y$, where $a = \frac{g-2}{2}$ is the anomalous magnetic moment coefficient for an electron (0.001159), and γ is the relativistic factor, n is an arbitrary integer, P is the periodicity of the lattice, and Q_y is the vertical betatron tune.

Thus ramping from 750 MeV to 18 GeV the spin tune $a\gamma$ will range from 1.702–41. This sets the lower limit on our vertical tune to be $Q_y > 41$.To keep the lattice compact it is also important to minimize the periodicity while also keeping the phase advance per cell not much greater that 120 degrees in order to maintain good dynamic aperture performance, thus $Q_y/P < 1/3$. Together both limits require that our minimum periodicity is $41 \times 3 = 123$. Additionally studies have shown that generally the remaining weak imperfection spin resonances are reduced with larger tune and peridocity (discussed in chapter 5). To balance the size, cost, polarization and dynamic aperture performance, we chose $P = 160$, and constrained the integer part of the vertical arc betatron tune to be 52.

The main parameters of the RCS are summarized in Table 3.46.

3.9.19 Lattice geometry

The RCS will use a 'racetrack' geometry with two 180° arcs and two straight sections. Each arc will be made up of 80 FODO cells and each straight will consist of 8 FODO cells with a total length of 83.136 m. The 'racetrack' design has a natural periodicity of 2. However, since the spin precession, which advances $a\gamma$, occurs in the dipoles, one can maintain the periodicity of 160 from the point of view of $a\gamma$ precession by designing the straight sections such that each has a betatron phase advance equal to $2\pi n$. In this way the straight sections will not contribute to the integral that

Parameter	Value
Injection energy [MeV]	750
Top energy [GeV]	18
Momentum compaction α_c	0.00065
Max relative pol. loss	3%
Circumference [m]	1490.386
Ramping repetition rate [Hz]	1
Acceleration time [ms], [turns]	100, 21000
Total number of "spin effective" superperiods	160
Integer horizontal tune	35-41
Integer vertical tune	56
Number of arc Cells	160
Number of straights	2
Number of dipoles	320
Number of quadrupoles	352
Number of sextupoles	312
Round beam pipe inner diameter [mm]	36.32
beam pipe thickness [mm]	0.89
Number of bunches	1
Charge per bunch [nC]	1–28
Radio frequency [MHz]	591
Total Cavity peak Voltage [MV]	136

Table 3.46: Basic parameters of the Rapid Cycling Synchrotron injector

defines the strength of the spin resonance (see Figure 3.87). Thus we can maintain the 160 superperiodicity from the point of view of the spin precession.

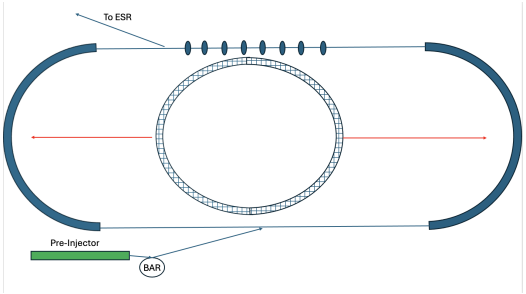

Figure 3.87: Projecting the pure ring lattice with 160 super-periodicity onto the 2-fold periodic 'racetrack' ring.

Arcs

Each of the two arcs are made up of 80 FODO cells. These cells with rectangular bending magnets is outlined in the Table **??**. Here D represents drift space, QF0/D0 focusing and defocusing

quadrupoles respectively and RBEND the rectangular bend magnet. In the drift spaces 2 families of sextupoles are inserted (not shown). The horizontal phase advance can vary such that the horizontal arc tune is set to an integer. The range of quadrupole and sextupole strengths permit this arc tune to vary from 16–20 units (i.e. 16/80 to 20/80 phase advance per arc cell). Fixing the arc tunes to be an integer helps keep the dispersion close to zero in straight sections. While the fractional horizontal tune is set by the straight section phase advance. The vertical phase advance per cell is typically set to ensure at least 26 tune units in each arc or 26/80=0.325 or 117°.

QD0/2	D	RBEND	D	QF0	D	RBEND	D	QD0/2

Table 3.47: Rapid Cycling Synchrotron arc FODO cell sequence

Straight sections

The straight sections are composed to two different FODO cells with 3 m drifts between the quadrupoles placed at the beginning and end of each straight section. This section matches the arc into the straight, followed by 4 FODO cells in the central area. The central FODO cells have quadrupole to quadrupole drifts of 6.3 m. The layout is shown in Table 3.47. Here DM and DML are drift spaces of 3 m and 5 m respectively. While QFm(1-2) and QDm(1-2) represent focusing and defocusing quadrupole families for the matching quadrupoles. QFS and QDS are the focusing and defocusing quadrupole families for the central FODO cells with DS representing the 6.3 m drift between them. This drift space should be sufficient to accommodate up to eight 591 MHz, 5-cell cryo-modules. The RF will be installed on the straight section closest to the RHIC tunnel to provide closer access to the cryogenic lines.

The breaking of the spin transport symmetry caused by these insertions are managed by tuning the quadrupoles to achieve a vertical phase advance of 4π while the horizontal phase advance is adjusted to achieve the desired fractional tune.

QF0	DM	QDm1	DML	QFm1	DM	QDm2	DM	QFm2	DS	QDS	DS
3 × (QFS DS QDS DS)					QFm2	DM	QDm2	DML	QFm1	DM	QDm1

Table 3.48: Rapid Cycling Synchrotron straight section sequence

With the straight sections the fractional part of the horizontal tunes can be adjusted using the horizontal phase advance. So for example with the horizontal arc tunes set to 20 units the phase advance in the straight can be tuned to contribute 1.6 units each to achieve a total tune of $Q_x = 43.2$. However for the vertical tune the fractional part will be controlled by setting the vertical phase advance in the arcs while fixing the phase advance in the straight sections set to 4π or 2 vertical tune units each. For example setting the phase advance for each FODO cell in the arc to 0.326 units (117.36°) will achieve a total machine tune of $Q_y = 56.16$. However the total vertical arc tunes of 52.16 and periodicity of 160 will determine spin resonance structure. The beta and dispersion functions are plotted in Figure 3.88. The straight section is shown in Figures 3.89. Here the maximum vertical and horizontal beta function is about 25 m, while the maximum dispersion in the arcs is 0.53 m.

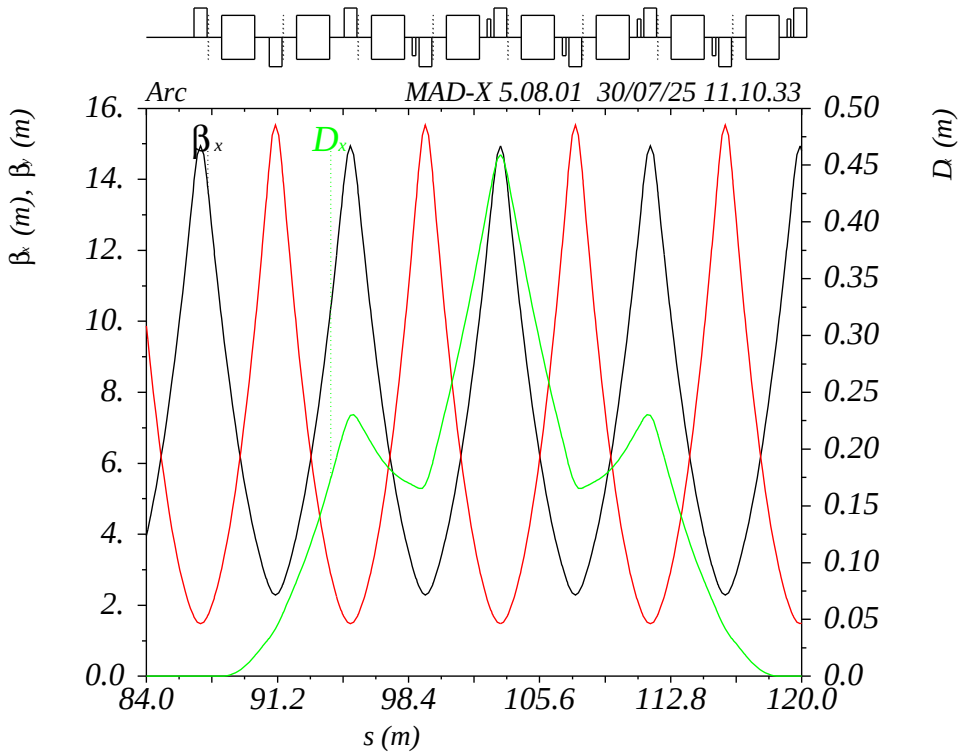

Figure 3.88: Twiss functions in RCS arc-cell.

3.9.20 Injection

The RCS injection transport will support injection of single bunches at up to 1 Hz directly from the linac or the BAR. RCS injection requirements are shown in Table 3.49.

RCS injection will employ single-bunch, on-axis horizontal injection to avoid vertical kicks that may perturb the vertical beam polarization. On-axis injection is achieved using a conventional septum followed by a single kicker, located in consecutive dispersion-free straight sections at the beginning of the southeast straight section.

The layout of the RCS injection section is shown in Fig. 3.90. Similar to mergers of energy recovery linacs, this injection line assumes a non-dispersive incoming beam and consists of two dipoles followed by the injection septum; while only two quadrupoles are needed to close dispersion and dispersion prime, two additional quadrupoles are included to allow for better control of the maximum beta values while matching into the RCS.

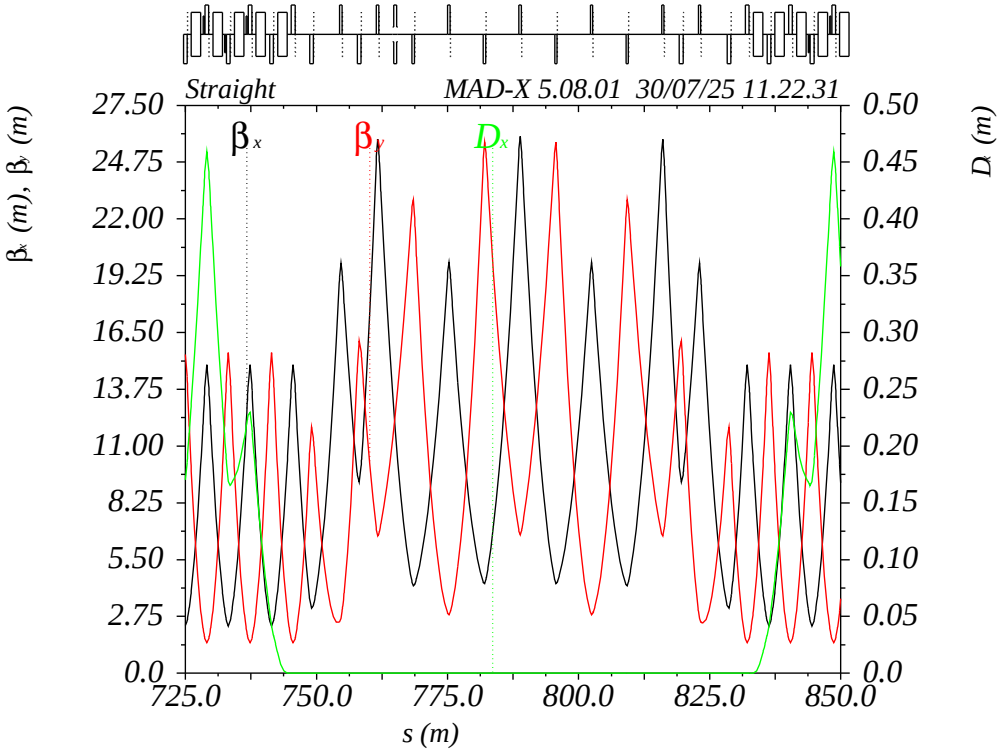

Figure 3.89: Twiss functions in RCS around the straight section with dispersion kept to zero.

Injection septum

The injected beam is set to exit the septum at an offset of 6.5 mm from the center of the RCS beampipe. The septum is 1 m long, with a field of 0.389 T, corresponding to a bending angle of 156 mrad, and non-standard edge angles. The upstream dipoles have a similar magnetic field, though the edge angles are different.

Injection kicker

The injection kicker is placed in the straight on the other side of the RCS quadrupole downstream of the septum. It is 1 m long, with a field of 6.50 mT, corresponding to a kick angle of 2.60 mrad.

Injection matching

The optics at the beginning of the injection line and the four quadrupoles before the RCS allow for matching into the RCS; the twiss functions, dispersion, and orbit of the injection line through

Parameter	Min	Max	Units
Energy E	750	750	MeV
Rigidity $B\rho$	2.5	2.5	T – m
Bunch charge q	0.1	28	nC
Bunch intensity N	6.25×10^8	1.75×10^{11}	–
Injection rate	1	1	bunch/s
Geometric rms emittance $\epsilon_{x,y}$	-/-	300/120	nm
Normalized rms emittance $\epsilon_{nx,ny}$	-/-	440/176	µm
rms bunch length σ_t	40	233.5	ps
rms bunch length σ_z	0.6	7.0	cm
rms fractional momentum spread σ_p/p	5	50	10^{-4}
Polarization direction		vertical	

Table 3.49: Rapid Cycling Synchrotron injection requirements

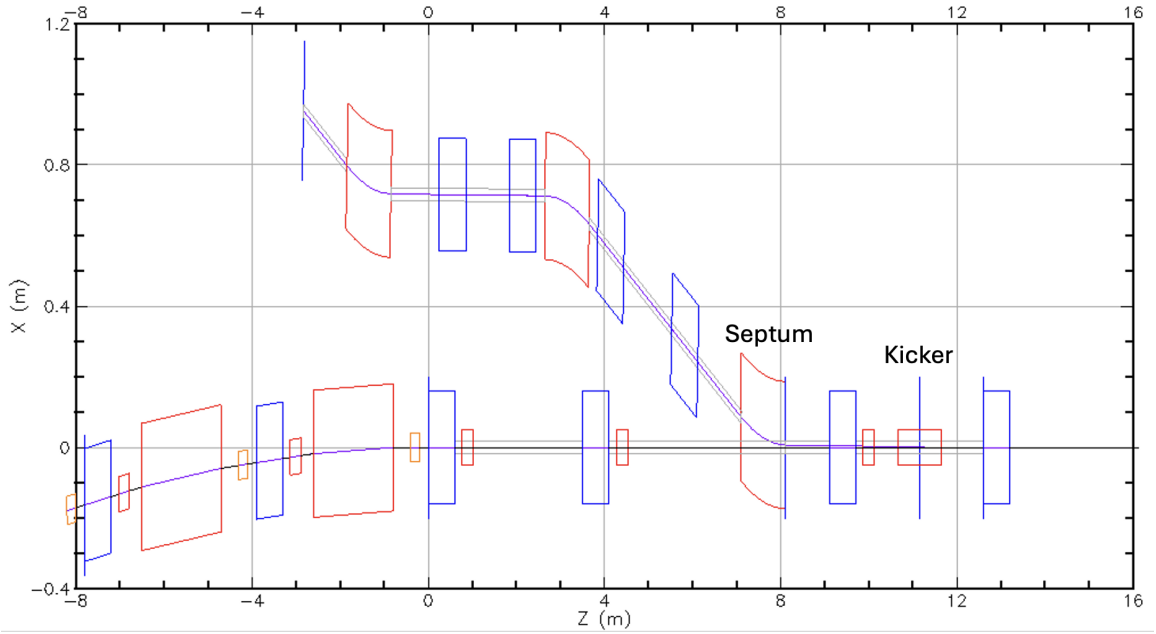

Figure 3.90: Physical layout of RCS injection line and end of the RCS west arc; injected beam starts at the upper left (outside the RCS ring) and moves to the right.

the RCS straight are shown in Fig. 3.91. The maximum quadrupole field of the four injection line quadrupoles is 1.95 T m^{-1}, similar to the maximum gradient in the arc.

3.9.21 Magnets

Tables 3.50 contain a list of the specifications and numbers of magnets required for the RCS. This lattice will require a total of 330 long L =0.71 m quadrupoles with a peak k1 strength of 0.661 m^{-2},

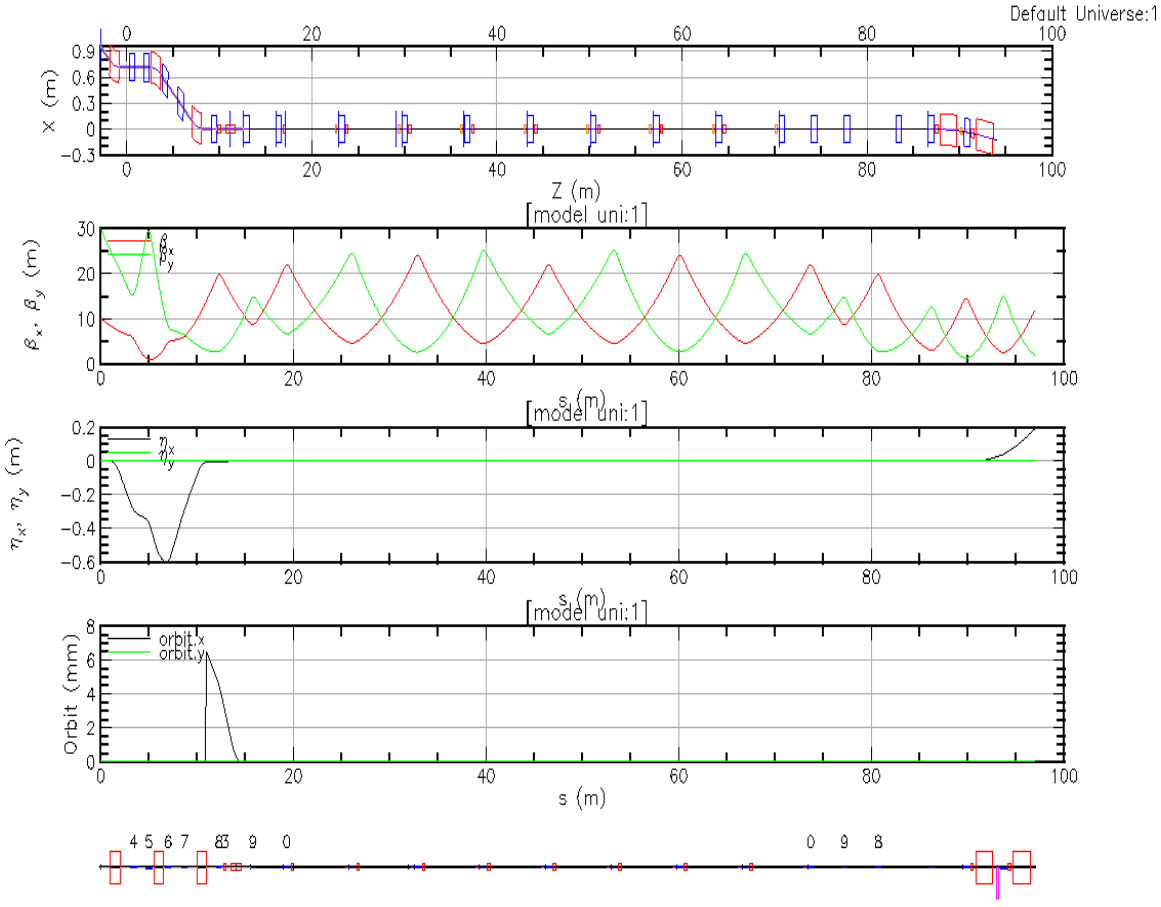

Figure 3.91: Top to bottom: floor plan, beta functions, dispersion, and orbit of the injection line through the RCS straight section.

22 short quadrupole L =0.47 m with a peak k1 also of 0.661 m^{-2}. It will also require 320 L =1.816 m rectangular dipole magnets with bending angles of 0.01963 rad, 312 L =0.2 m sextupoles with peak k2 design strengths of 28 m^{-3} and 352 dual plane correctors with peak deflection angles of 0.125 mrad.

All the quadrupole magnets will also be built with extra windings to carry an additional current necessary to vary the quadrupole strength by 0.2% of its peak strength (about $\pm$ 5 Amps). This will enable a beam-based alignment system.

These sextupole peak strengths permit the chromaticity to be controlled to within one unit in both planes using two families of arc sextupoles. This is also sufficient to achieve good off-momentum dynamic aperture out to $\pm$1.0% in δ beyond 4σ of an injected rms geometric beam emittance of up to 170 nm $-$ rad in both the horizontal and vertical planes, as is discussed in section **??**.

These magnets will need to maintain these strengths while energies are ramped from 750 MeV to 5 GeV, 10 GeV, and ultimately 18 GeV over 100 ms. For the dipole field this can be estimated using

$$\frac{dE}{dt}\frac{3.3357}{\rho} = \frac{dB}{dt}$$

Name	Type	Length m	Number	k1 m^{-2}	k2 m^{-3}	Angle mrad
QF0	Arc Focusing Quad	0.71	162	0.5 to 0.661	–	–
QD0	Arc Defocusing Quad	0.71	160	0.5 to 0.661	–	–
QFS	Str. Focusing Quad	0.47	6	0.3 to 0.661	–	–
QDS	Str. Defocusing Quad	0.47	8	0.3 to 0.661	–	–
QFm1	Str. Focusing Quad	0.47	4	0.3 to 0.661	–	–
QDm1	Str. Defocusing Quad	0.71	4	0.3 to 0.661	–	–
QFm2	Str. Focusing Quad	0.47	4	0.3 to 0.661	–	–
QDm2	Str. Defocusing Quad	0.71	4	0.5 to 0.661	–	–
Dipole	Rbend	1.816	320	0	0	19.63
SF	Sextupole	0.2	156	0	8 to 18	0
SD	Sextupole	0.2	156	0	17 to 27	0
Cor	Kicker	0.2	352	0	0	0 to 0.125

Table 3.50: Rapid Cycling Synchrotron magnet families, counts, and typical strength ranges

$$\frac{(18 - 0.75)\ \text{GeV}}{0.1\ \text{s}} \frac{3.3357}{(91.67\ \text{m})} \quad = \quad 6.27695\ \text{T/s} \tag{3.48}$$

This is below our estimate of the peak ramp rate of 28 T/s that DESY II achieved. DESY II ramped electrons from 450 MeV to 6 GeV using a 12.5 Hz cycle with a bending radius of 27.12 m.

3.9.22 Vacuum and Impedance

The RCS vacuum system provides adequate aperture and friendly environment during the acceleration of the electron beam from the injection energy of 750 MeV to the extraction energy ranging from 5 to 18 GeV. The RCS will accelerate a single bunch of electrons, with maximum current up to 5.9 mA for 5 to 10 GeV and 2.32 mA for 18 GeV. For 18 GeV extraction, the beam will be accelerated over a magnet ramp-up time of about 100 ms. To reduce the impedance in the beam pipe which can drive collective instabilities the use of copper is preferable due to its low resistivity however this low resistivity will help the creation of significant eddy currents in the vacuum chamber wall which can create multipolar fields, however for a round beam pipe these are mostly canceled due to symmetry though a phase lag in response is induced. But at the magnets, the fields will break this symmetry and help created significant multipolar fields. As a compromise the use of a stainless steal beam pipe with a 30 µm copper coating will be used. This will have the effect of both reducing the eddy currents and keeping the resistive wall impedance low.

Eddy Currents

For the eddy current effect, the most significant multipolar field will be due to the sextupole contribution at the dipoles, which can be expressed,

$$S_{\text{dipole}} = \frac{\pi^4}{15} \frac{dB}{dt} \frac{t_d R^3 \mu_0}{\rho_c g^4}. \tag{3.49}$$

Here t_d=0.89 mm is the pipe thickness, R=18.16 mm is the beam pipe radius, g=40 mm is the magnet gap, and ρ_r is the resistivity of the beam pipe metal. In our case ρ_r will be the combined resistivity of the stainless steal with the 30 µm copper coating. For eddy currents flowing along the plane of layers with different resistivity, the stainless steel and copper layers are electrically parallel over the same cross-sectional area in the plane. One convenient way to handle "sheet-like" conductors is to use sheet resistance or sheet conductance. For a single layer of thickness t and bulk resistivity of ρ this can be estimated using the following:

$$R_s = \frac{\rho}{t} \tag{3.50}$$

Combining them in parallel,

$$R_T = \frac{1}{\frac{1}{R_{s,SS}} + \frac{1}{R_{s,Cu}}} \tag{3.51}$$

From this a $\rho_{c-s} = R_T(t_{SS} + t_{Cu})$ gives $3.17 \times 10^{-7}\,\Omega - \mathrm{m}$ now using Eq. 3.49 the sextupole field becomes $0.349\,\mathrm{T/m^2}$ and the effect of each of the 320 dipoles would contribute ≈0.629 T/m integrated sextupole field in each plane. This compares to the smallest fields of our sextupoles which is $k_2 = 10{\times}2.5\,\mathrm{T\,m}{\times}0.2\,\mathrm{m}{=}5\,\mathrm{T/m}$ or about 12% of each of our 320 sextupoles, yielding a chromatic change of about 4-5 units at injection. There will also be a tune feed-down effect from these sextupole fields due to the sagitta in the dipole which we can estimate to be $\frac{L_{\mathrm{dipole}}}{8\rho}$=4.45 mm giving an average horizontal orbit offset of 1/3 of this or $x_{0,dipoles}$=1.5 mm.

$$\begin{aligned}
\Delta Q_x &\approx \frac{1}{4\pi B\rho}\int \beta_x(s)B_2(s)x_0(s)ds \\
&\approx \frac{N_{\mathrm{dipoles}}}{4\pi B\rho} < \beta_{x,\mathrm{dipoles}} > S_{\mathrm{dipole}} L_{\mathrm{dipole}} x_{0,\mathrm{dipoles}} \\
&\approx 0.07
\end{aligned} \tag{3.52}$$

Here the average horizontal beta function is $< \beta_{x,\mathrm{dipoles}} >$=7.37 m and the number of dipoles in the lattice is N_{dipoles}=320. Thus the field effects due to eddy currents appear to be easily corrected using the sextupoles and quadrupoles during the early part of the acceleration ramp.

Collective Effects

Section details RCS simulation with collective effects. The principle effects are due to the Transverse Mode Coupling Instability (TMCI) and the Longitudinal Microwave Instability can both be estimated using approximate formulas.

TMCI

The TMCI has an analytical approximation of the stability threshold in terms of current, bunch length and momentum spread. This approximation is given by assuming that the ratio of the transverse tune shift to synchrotron tune is less than 0.7.

$$\frac{\Delta\nu_\perp}{\nu_s} = \frac{eI_{th,0}}{2E\nu_s\omega_0}\sum_j \beta_\perp k_{\perp j} \approx 0.7$$

$$\sum_j \beta_\perp k_{\perp j} \approx \beta_{avg} k_\perp \approx 0.58 \frac{c Z_0 C s_0 \beta_{avg}}{\pi R^4} \sqrt{\frac{s_0}{\sigma_s}}$$
$$s_0 = \sqrt[3]{\frac{2R^2}{Z_0 \sigma_c}} \tag{3.53}$$

Here $I_{th,0}$ is the current, E energy ν_s synchrotron tune, ω_0 angular revolution frequency, $\beta_\perp$ is the beta function in the plane of the instability, k the kick. While C is the circumference, Z_0 the impedance of free space R the beam pipe radius, σ_s the bunch length and σ_c the conductivity of the beam pipe. Solving for the threshold current:

$$I_{th,0} = \frac{0.7 E \nu_s 2\omega_0 \pi R^4}{0.58 e \beta_{avg} Z_0 C c} \sqrt{\frac{\sigma_s}{s_0^3}} = 2.413 \frac{E \nu_s \omega_0 \pi R^3}{e \beta_{avg} C c} \sqrt{\frac{c \sigma_\tau \sigma_c}{2 Z_0}} \tag{3.54}$$

Using the linear approximation for the synchrotron tune:

$$\nu_s = \frac{\eta \sigma_\delta}{\omega_0 \sigma_\tau} \tag{3.55}$$

We obtain an expression for the instability threshold in terms of the bunch length and bunch energy spread:

$$I_m < 2.413 \frac{E \eta R^3 \pi}{e C \beta_{avg}} \sqrt{\frac{\sigma_c}{2 Z_0}} \frac{\sigma_\delta}{\sqrt{c \sigma_\tau}} \tag{3.56}$$

At injection energy $E = 3$ GeV, η =0.000647988, $Z_0 = 120\pi$, /Ω, c is the speed of light, the circumference of the RCS ring C =1421.257 m, the beam pipe radius R =18.16 mm, and the conductivity of the beam pipe σ_c =40×10^6 S m^{-1}. For the injected beam of 28 nC the current I_m =0.0059062 A, the average beta function β_{avg} =8.15 m and e the electric charge. Plotting the TMCI threshold as a function of bunch length and energy spread as shown in Fig. 3.92 shows that if we inject with a bunch length of about 10 ps (3 mm), the bunch is longitudinally stable with a σ_δ above 1.0×10^{-3} and above 3.0×10^{-3} with a bunch length of 150 ps (45 mm). The region stability only grows with energy.

Longitudinal Microwave Instability

To estimate the microwave instability, the Boussard extension can be evaluated using,

$$I_{th} = 9.4 \frac{E \nu_s^2}{e \alpha (\frac{\Im Z}{n})_0} (\omega_0 \sigma_\tau)^3, \tag{3.57}$$

with α the momentum compaction factor. In terms of bunch length and energy spread we get,

$$I_{th} = 9.4 \frac{E \eta^2 \sigma_\delta^2 \omega_0 \sigma_\tau}{e \alpha (\frac{\Im Z}{n})_0} \tag{3.58}$$

The following equation has the same form as Boussard's extension to the Keil-Schnell formula but with the factor of 9.4 replacing Boussard's $2\pi \approx$2.5. For the RCS we assume that $(\Im Z/n)_0 = 0.1\Omega$. The longitudinal stability region is also plotted in Fig. 3.92 and together with the TMCI region shows that a 28 nC bunch in the RCS should be stable between an rms σ_δ of 3.15×10^{-3} and above at 10 ps (3 mm) to 3.0×10^{-3} and above at 150 ps (45 mm).

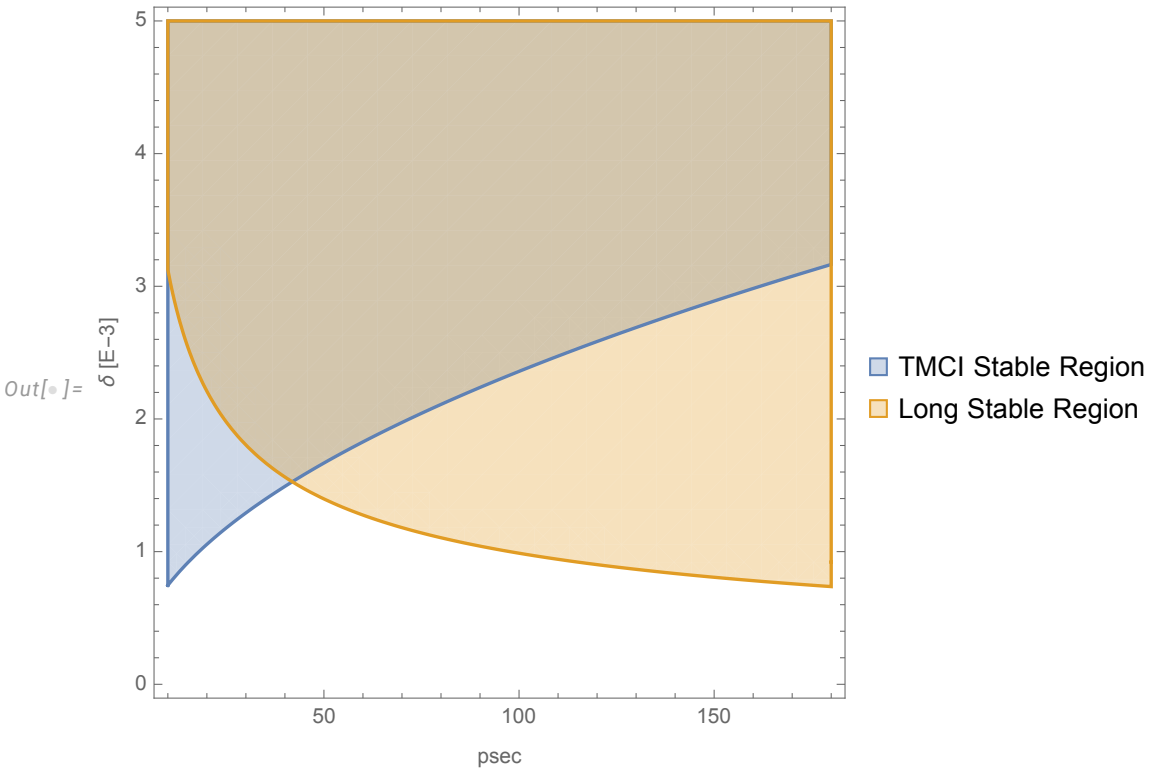

Figure 3.92: Plot of Stable TMCI region and Longitudinal Microwave Stable Region for a 28nC bunch as a function of bunch length and energy spread.

3.9.23 Orbit Distortion Estimates and Correction

The major contribution to depolarization for the RCS is imperfection spin resonances. To correct the residual imperfections below $a\gamma = 41$, correctors are used. The primary drivers of vertical orbit distortions are due to misalignments through quadrupole fields.

The effect of this type of misalignment (Δy) is to deliver an effective angular kick $\Delta\theta$ at each quadrupole field location given by

$$\Delta\theta = K_1 L \Delta y. \tag{3.59}$$

where K_1 is the quadrupole strength in m^{-2} and L is the length over which the quadrupole field operates. Placing the corrector adjacent to the quadrupoles permits the immediate correction of kicks due to misalignments, so they do not propagate around the ring. The strength needed to correct for the misalignments is estimated by considering the tolerance when aligning the quadrupoles in the ring, which currently are 0.1 mm rms. Using a 2.0σ cut off, gives a maximum quadrupole kick of Δy =0.2 mm. Considering the maximum integrated quadrupole strength, $K_1 L$ =0.471 m^{-1} we can estimate that our correctors should need to be able to compensate most of the effects of quadrupole misalignments with a maximum kick strengths of 0.0942 mrad. This dictates the maximum corrector strength.

A statistical estimate of the rms closed orbit is given by

$$\begin{aligned} y_{\mathrm{co,rms}} &\approx \frac{\beta_{\mathrm{avg}}}{2\sqrt{2}|\sin \pi Q|}\sqrt{N_q}\Delta\theta_{\mathrm{rms}} \\ &\approx \frac{\beta_{\mathrm{avg}} K_1 L \sqrt{N_q}}{2\sqrt{2}|\sin \pi Q|}\Delta y_{\mathrm{rms}} \end{aligned} \tag{3.60}$$

With a tune of $Q_y = 56.128$, the number of quadrupoles, $N_q = 352$, β_{avg} =6.8 m, and $K_1\, L_{\mathrm{avg}}$ =0.25 m^{-1}, we find the estimated rms vertical orbit to be 2.88 mm. This estimate is somewhat smaller than our estimate of 3.56 mm given by the direct application of random misalignments to the RCS lattice for 100 random seeds including 0.4 mm RMS rolls.

Studies with calculated spin resonances and spin-orbit tracking to 10 GeV indicate that imperfection resonances should not contribute more than 3 % loss with with quadrupole rms misalignments of 0.1 mm and dipole rolls of 0.4 mrad. This yields a vertical orbit errors less than 3.56 mm rms (see Tables 5.1 in Section 5.3.4). Above 10 GeV the situation becomes more challenging. In this case the 3 % Polarization loss occurs with uncorrected quadrupole misalignments and rolls of 10 µmand 10 µrad. This determines our minimum desired BPM resolution of 0.01 mm. Section 5.3.4 also includes a detailed discussion of our orbit tolerances and correction scheme.

Beam-based alignment

In addition to maintaining tight alignment tolerances the RCS will maintain a beam-based alignment system. This will involve designing our quadrupole magnets with the ability to individually power an extra-current carrying coil to vary the field slightly and thus help identify the magnetic center of the quadrupole relative to the electrical center of the BPMs to within 10 µm, BPM one turn resolution is expected to be 10 µm, which over 1000 turns should average to 0.316 µm. Considering the arc quadrupoles and BPMs the lowest beta values are at 1.7 m. Fig. 3.93 shows the response of the orbit at the BPM for different misalignments. From this we can conclude that quadrupole k1 variation of 0.03 $m^{-}1$ would be necessary to resolve a 10 µm misalignment. This is about 0.2% of the peak current or about 5 Amps.

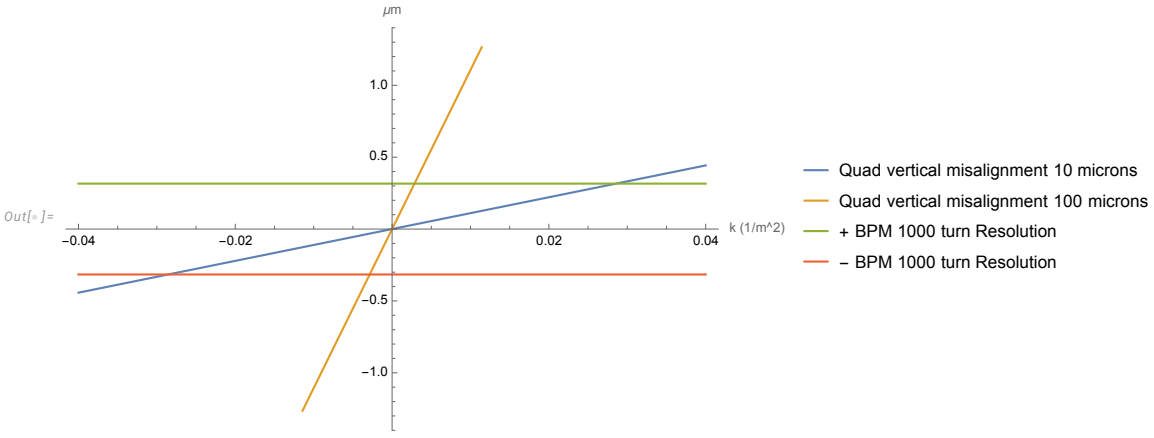

Figure 3.93: Variation of vertical arc quadrupole strength versus orbit deflection at the attached BPM for 10 and 100 micron misaligned quadrupole.

3.9.24 3-D Emittance Control Scheme

Table. 3.51 shows the acceptable range of emittances for the ESR at each extraction energy and the current RCS's equilibrium values.

Required by ESR	**5 GeV**	**10 GeV**	**18 GeV**
Eh (nm-rad)	16-50	16-50	19-50
Ev (nm-rad)	1.4-10	1.4-10	1.6-10
Long. Emit (eV-s)[E-4]	0.8-5	1-5	0.624-5.8
RCS Equilibrium	**5 GeV**	**10 GeV**	**18 GeV**
Eh (nm-rad)	3	12	39
Ev (nm-rad)	5.75e-6	5.75e-6	5.75e-6
σ_δ	4.49e-4	8.96e-4	1.61e-3
Transverse Damping time (msec)	83	10	1.7
Ramp Avg. with Errors	**5 GeV**	**10 GeV**	**18 GeV**
Eh (nm-rad)	20.2±1.6	9.6±0.4	39.5±3.3
Ev (nm-rad)	1.4±0.8	0.4±0.5	1.5±2.4

Table 3.51: Electron Storage Ring acceptance and Rapid Cycling Synchrotron equilibrium emittances and average emittance from tracking up ramp with errors from 10 different seeds assuming injected emittance of 170 nm-rad and 5 nm-rad for horizontal and vertical geometric emittance respectively.

For all extraction energies the RCS's equilibrium vertical emittances are smaller than the acceptable ESR values. Likewise the horizontal equilibrium emittance at 5 GeV is also too small. Thus these emittances at extraction will need to be enlarged to match ESR injection requirements. We plan to replicate an approach similar to that used in the SPS. During the last 2000 to 5000 turns, vertical kickers will trigger multiple times to deflect the beam to approximately $\sigma_y/2$. Nonlinear fields ensure filamentation of the phase space and a controlled increase of the effective vertical emittance. The horizontal equilibrium emittances at 18 GeV will need to be reduced to match the ESR acceptance; this can be accomplished by introducing a $-0.6\,\%$ δ momentum offset using radial loop steering. This will bring the equilibrium horizontal emittance down to $27\,\mathrm{nm}-\mathrm{rad}$ while increasing the equilibrium energy spread to 2×10^{-3}.

==========

3.9.25 RCS Extraction and Transport

RCS extraction and transport will support extraction of single bunches at up to 1 Hz for delivery to the ESR during fill or collisions. RCS extraction and transport requirements to the ESR are shown in Table 3.52. The interface to the ESR is at the upstream (entry) flange of the first ESR injection septum.

RCS extraction and transport will employ single-bunch, on-axis extraction in the horizontal plane to avoid vertical kicks that may affect beam polarization. Extraction is achieved using a three kickers followed by thin and thick septa to support the full extraction energy range to 18 GeV. RCS

Parameter	Min	Max	Units
Energy E	5	18	GeV
Rigidity $B\rho$	16.6	60	T − m
Bunch charge q	0.1	28	nC
Bunch intensity N	6.25×10^8	1.75×10^{11}	–
Extraction rate	1	?	bunch/s
Geometric rms emittance 5 GeV $\epsilon_{x,y}$	16/1.4	24/2.2	nm
Normalized rms emittance 5 GeV $\epsilon_{nx,ny}$	156.5/13.7	235/21.5	µm
Geometric rms emittance 10 GeV $\epsilon_{x,y}$	16/1.4	24/2.2	nm
Normalized rms emittance 10 GeV $\epsilon_{nx,ny}$	313/27.4	470/43	µm
Geometric rms emittance 18 GeV $\epsilon_{x,y}$	19/1.6	29/2.4	nm
Normalized rms emittance 18 GeV $\epsilon_{nx,ny}$	669.3/56.36	1021.5/84.5	µm
rms bunch length 5 GeV σ_t	7.8	70	ps
rms bunch length 5 GeV σ_z	0.23	2.1	cm
rms bunch length 10 GeV σ_t	7.8	70	ps
rms bunch length 10 GeV σ_z	0.23	2.1	cm
rms bunch length 18 GeV σ_t	10	90	ps
rms bunch length 18 GeV σ_z	0.3	2.7	cm
rms fractional momentum spread 5 GeV σ_p/p	0.22	2.04	10^{-3}
rms fractional momentum spread 10 GeV σ_p/p	0.2	1.74	10^{-3}
rms fractional momentum spread 18 GeV σ_p/p	0.36	3.27	10^{-3}
Polarization direction		vertical	

Table 3.52: RCS extraction requirements; maximum bunch parameter requirements are consistent with ESR 10 GeV collision parameters.

extraction is located in the consecutive dispersion-free straight sections at the end of the RCS north straight section, downstream of the RCS SRF cryomodules.

The net extraction angle from the RCS is 52.36 mrad (3°) to provide sufficient separation for the transport to avoid downstream RCS magnets. RCS extraction also overlaps an RCS focusing quadrupole, so all pulsed elements must provide a total horizontal angular kick of 57.37 mrad (3.29°).

Two L =0.8 m pulsed extraction kickers will each kick by 1.35 mrad, a L =1.5 m thin septum will kick by 18.32 mrad, and a L =2.0 m thick septum will provide the remaining 35.0 mrad kick. Kicker angles are chosen to provide a 3 cm displacement at the thin septum entrance to provide required septum clearance. The overall extraction geometry is shown in Fig. 3.95.

Following the completion of the conceptual design, the RCS lattice has been revised. In this revised version, two separate quadrupole families are introduced for focusing and defocusing, with lengths of 0.71 m and 0.47 m, respectively. The drift spaces in between them are not equal. The drift section where pulsed kickers are placed in the conceptual design has to be changed, to accommodate RF cold trap. The kickers are shifted to the drift section downstream of the next quadrupole magnet (MQD11). Three shorter kickers with 0.7 m and a fourth kicker with 0.8 m are used with maximum bend angles to achieve a reasonable beam separation at the thin septum entrance with respect to the downstream RCS line. However, to achieve a sufficient separation in between RTE line and

downstream RCS magnets, a longer straight section between MQD21 and the first arc quadrupole is required, as illustrated in figure 3.94. The kick angle is 3.0 mrad for short kickers and for longer

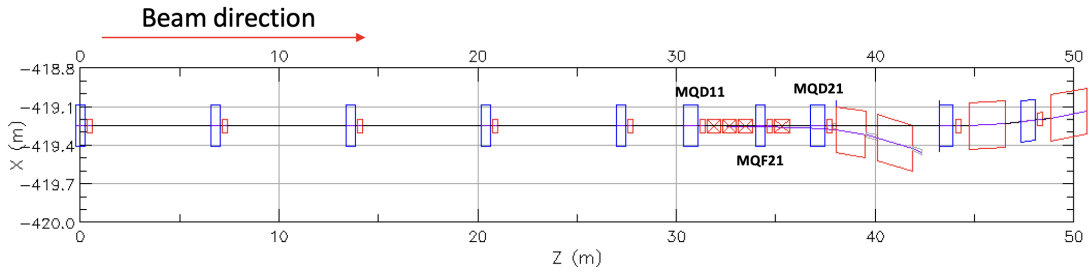

Figure 3.94: Placement of pulsed magnets in the updated RCS lattice

kicker it is 3.1 mrad.

The thin septum now follows the APS booster septum magnet design, with length 1.493 m and a maximum kick angle of 33 mrad, and shorten the length of thick septum to 1.75 m, to achieve an overall extraction angle of 3°. The pulsed septum magnet parameters are defined with referencing APS septum designs [**?**]. The extraction lattice layout is shown in figure 3.94.

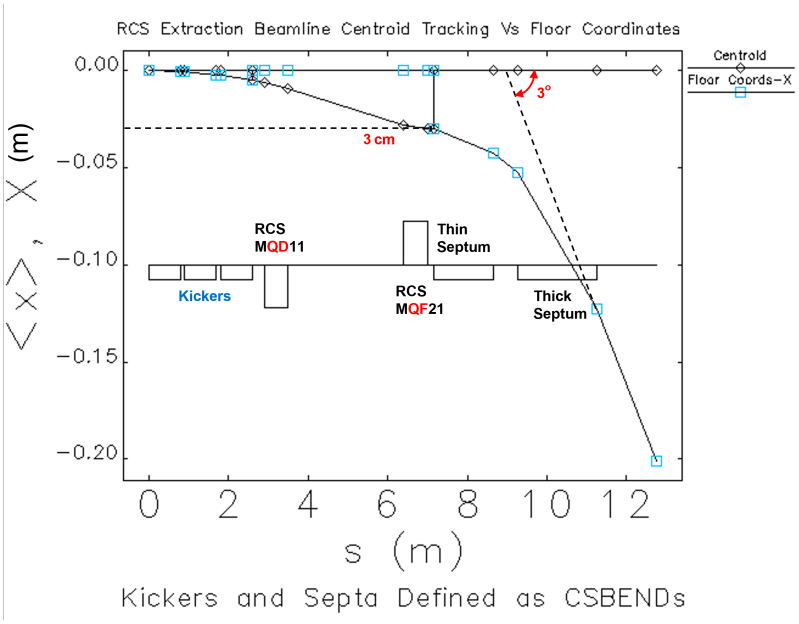

Figure 3.95: RCS extraction region, showing locations of kickers, septa, and orbit calculations using elegant. The 0.29° angle is the kick from the focusing quadrupole MQF21 that must be compensated.

3.9.26 Extraction Kickers

Though one might consider duplication of the ESR kickers, their requirements (low impedance for up to 2.5 A circulating current, profile of ESR vacuum chamber, single-bunch rise and fall times, high voltage feedthroughs) are more constraining than the RCS single-bunch extraction kicker requirements. We therefore plan for the RCS extraction kickers to be traditional.

Both traditional ferrite H- and C-style L =0.8 m ferrite window frame kickers over ceramic beampipe similar to APS booster kickers [**?**] are being considered for the extraction kickers, with 1-turn conductors to minimize inductance and rise time. Maximum magnetic field is 1010 G with rise time of 1 µs. The current and inductance for these type of kickers are given by,

$$B = \frac{\mu_\circ I}{g} \tag{3.61}$$

$$L = \frac{\mu_\circ w l}{g} \tag{3.62}$$

where I is the required beam current to support the field B, g is the magnet gap, l is the magnet length and w is the magnet width. Based on the load resistance in [**?**] of 4Ω we can calculate the approximate voltage required for the desired risetime of $1.0\mu s$ according to,

$$V = L\frac{dI}{dt} + RI \tag{3.63}$$

$$\frac{dI}{dt} \approx \frac{I_\circ}{t_r} \tag{3.64}$$

where $I_\circ$ is the current required to support the kicker field B and t_r is the desired risetime. Conceptual extraction kicker parameters are shown in Table 3.53. The table indicates the minimum kicker voltage required since the inductance will be larger than calculated in 3.62 due to cables and parasitic inductance from capacitors and the 4Ω load and damping resistors. Three kickers of this type should be sufficient for RCS extraction requirements.

Parameter	**Value**	**Units**
Turns	1	
Length	0.8	m
Gap Height	40	mm
Gap width	40	mm
Rise Time	1.0	µs
Field Strength	1010	G
Required Current	3224	A
Inductance	>0.05	µH
Required Voltage	>13.1	kV
Resistance	4.0	Ω

Table 3.53: Rapid Cycling Synchrotron extraction kicker parameters

3.9.27 Pulsed Septum

A thin pulsed induction-type septum has been conceptually designed (Fig. 3.96) with a 3.4 mm thick copper plate as at the septum nose. This separation supports the required thin septum field of 7.6 kG over L =1.5 m necessary to provide the required kick of 18.32 mrad at 18 GeV.

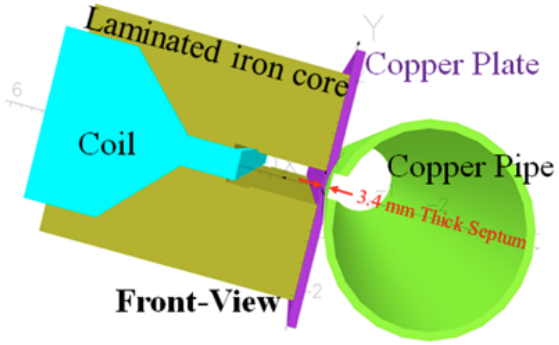

Figure 3.96: RCS thin extraction septum conceptual design.

3.9.28 DC Septum

The thick extraction septum will be a traditional DC extraction septum of L =2.0 m and field B =1.05 T. Comparable DC septa exist at the ANL APS, BNL AGS, FNAL Main Injector, and at J-PARC.

The thin septum adopts the APS booster septum of 1.493 m length, and for 18 GeV the magnetic field is 1.01 T. The length of the thick septum is decreased to 1.75 m with a field of 0.72 T.

3.9.29 Transport Line Optics

The RCS to ESR (RTE) line must match RCS extraction to transport, transport high-intensity, vertically polarized bunches with minimal intensity and polarization loss with ≈ -1.68 m of vertical displacement from the RCS to the ESR, and match into ESR injection. It accomplishes this with extraction and injection matching sections, and an intermediate vertically achromatic dogleg with FODO transport.

The lattice layout and optics of the RTE line design updated with revised RCS design are illustrated in figure 3.97. The total length of this transport line is $\approx$ 133 m The conceptual design indicates horizontal dispersion leakage within the vertical bend achromat. The matching sections are constructed using FODO cells, with three cells used to match to the RCS extraction and four cells to match into the ESR injection.

The upstream portion of the RTE line must interlace matching quadrupoles with downstream magnetic elements in the RCS. This is conceptually illustrated in Fig. 3.98 where the first four RTE extraction match quadrupoles are placed at locations consistent with the RCS lattice and expected magnet dimensions. RCS extraction optics matches at the downstream end of the DC septum are also included.

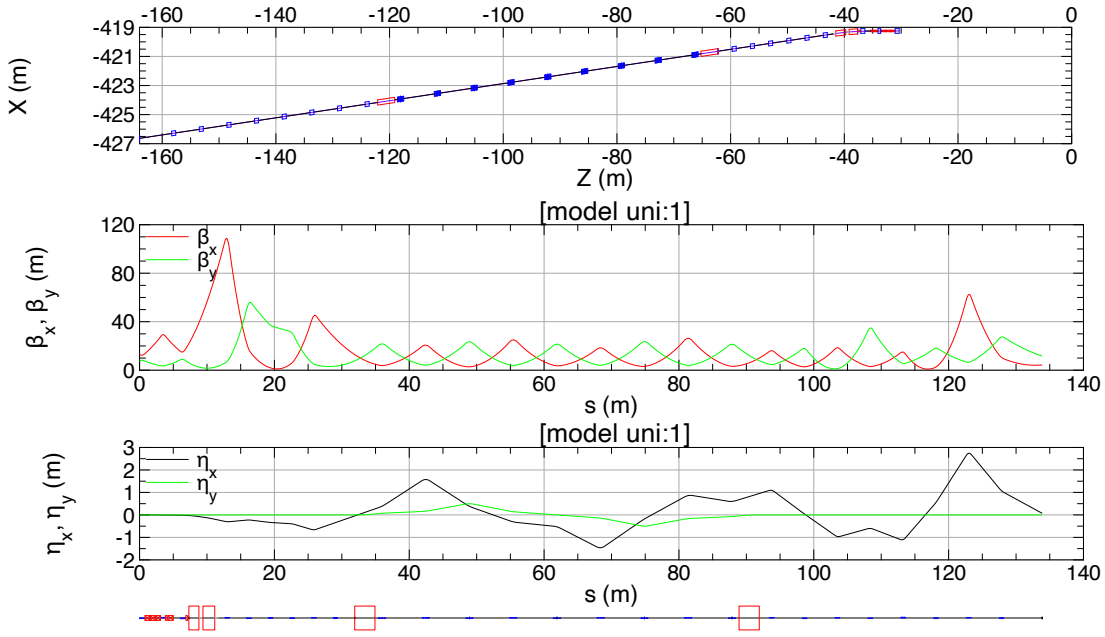

Figure 3.97: RCS to ESR transport line conceptual optics.

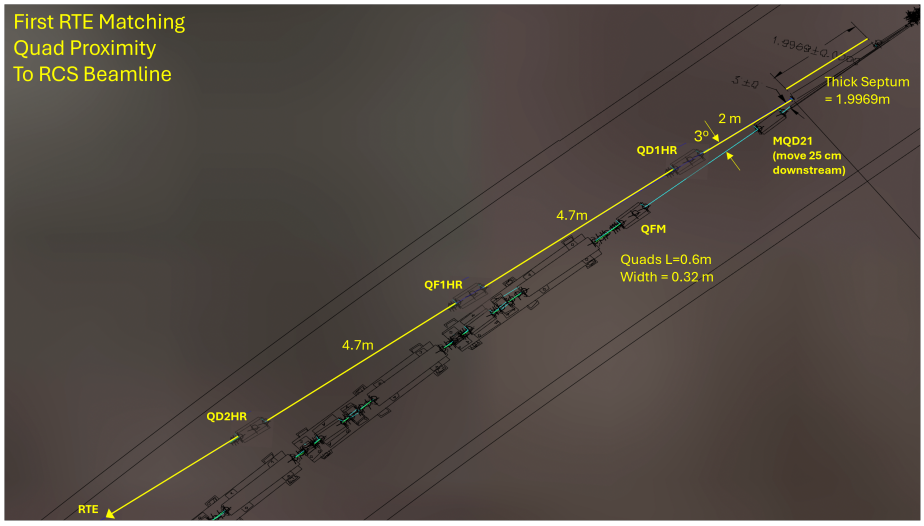

Figure 3.98: Conceptual drawing of RTE line near RCS, illustrating quadrupole placement to avoid magnet interference.

3.9.30 Magnets

Matching quadrupole magnets utilize the longer RCS quads with length 0.71 m, with a total of 14 quadrupole magnets. The vertical bend section is designed to reuse the MIT bates quadrupole magnets with length 0.3 m. However, a set of three bates magnets separated by a 0.1 m drifts are used to form a single quadrupole unit required in this section as the focusing strengths are lower

in bated magnets due to their larger aperture. The arrangement is shown in figure 3.99, where now a single quadrupole unit in the vertical FODO section is 1.1 m long.

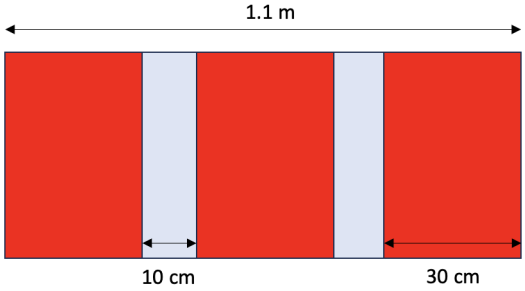

Figure 3.99: Layout of a single quadrupole unit re-using MIT-bates magnets. Three magnets with 0.3 m are used for a single quadrupole unit.

3.9.31 Diagnostics

Beam diagnostics for the RTE transport line is fairly standard. We wish to perform a multi-screen OTR emittance measurement in the FODO section and have BPMs at each quadrupole. A bpm between the thin and thick septa will allow for precise measurement of position near the extraction point of the RCS to aid commissioning and steering the extracted beam into the RTE. Bunch charge monitoring near extraction of the RCS and at injection into the ESR will allow for precise monitoring of charge transport (in addition to calibration of BPM sum signals). Fiber-optic loss monitors along the line will monitor direct loss of the electron beam. Total counts are as follows: 7 OTR screens, 17 bpms, two charge monitors (ie. ICTs) and 3 fiber-optic loss monitors.

3.10 Low Energy Cooler

The Low Energy Cooler (LEC) uses conventional electron cooling technique to decrease the vertical emittance of proton bunches just after they are injected into the Hadron Storage Ring. The design of the LEC is based on RF-accelerated electron bunches, similar to LEReC [**?**], but scaled to higher energy. Schematic layout of the LEC accelerator is shown in Fig. 3.100.

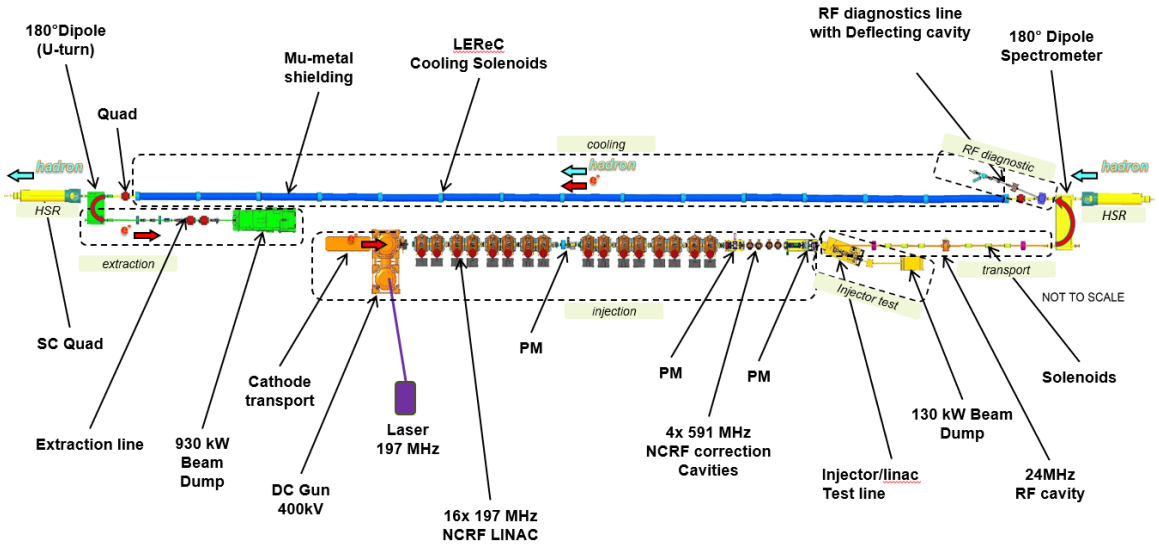

Figure 3.100: Schematic layout of the Low Energy Cooler.

Electron beam will be generated by illuminating a multi-alkali CsK2Sb photocathode with green light (532 nm) from a laser. The photocathode is inserted into a DC gun with design operational voltage of around 400 kV. The 197 MHz laser will produce bunch trains with individual electron bunches of about 400 ps full length at 24.6 MHz bunch train repetition frequency. The bunch train repetition rate will be the same as the repetition rate of proton bunches in the HSR at injection energy. The 3rd harmonic 591MHz RF cavities will be used for energy correction.

After acceleration to 13 MeV, an electron beam is transported to the cooling section in the HSR ring, propagates together with proton beam through 160 meters of cooling section, turned around and transported to the beam dump.

In the HSR, a second harmonic RF system is used to alleviate space-charge effects on protons during cooling, producing a longitudinally flattened proton bunch distribution with peak current that is reduced by a factor of two. The 197 MHz repetition rate of electron bunches, corresponding to 5.1 ns spacing, allows us to place up to three electron bunches with 1.0 nC charge each (as shown in Figure3 3.101) on a single proton bunch to provide total required charge of electrons of 3 nC per proton bunch.

After cooling, the proton bunches are accelerated to the collision energy, and are each split into four bunches.

For faster cooling, it is beneficial to provide cooling of both horizontal and vertical emittances simultaneously, as shown in Fig. 3.102. However, if needed for stability of cooled beams, horizontal emittance can be heated and maintained at a required level at the expense of the cooling time. As an example, Figure 3.103 shows expected cooling performance for the vertical emittance while horizontal emittance is being heated from the start.

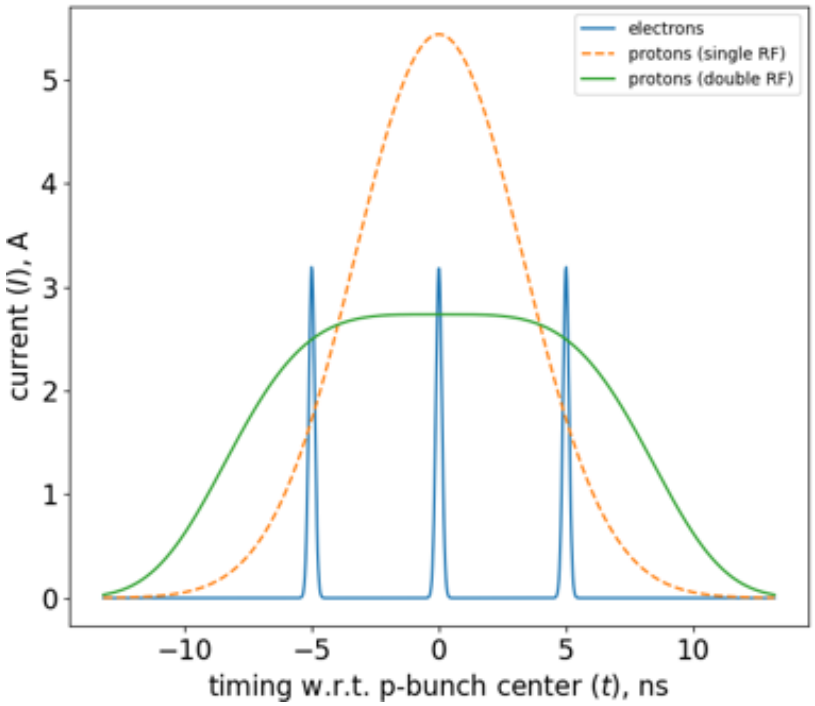

Figure 3.101: Time structure of three electron bunches (blue color) synchronized with a single proton bunch for cooling at 23.8 GeV. Vertical axis: peak current [A]. Horizontal axis: time [nsec]. Orange trace shows proton bunch only with 24 MHz RF. Green trace shows proton bunch with second harmonic RF (48 MHz).

Parameter	**Unit**	**Value**
Relativistic gamma	–	25.4
Proton energy	GeV	23.8
Electron kinetic energy	MeV	12.5
Length of cooling section	m	170
Proton repetition rate	MHz	24.6
Proton bunch length, RMS	m	1.0
Proton beta function in the cooling section	m	150
Electron beta function in the cooling section	m	150
Total electron charge per proton bunch	nC	3
Single electron bunch charge (3 electron bunches)	nC	1
Average electron current	mA	74
Electron emittance in cooling section, normalized RMS	µm	$<$1.5
Electron angular spread in cooling section, RMS	µrad	25
Electron energy spread in cooling section, RMS	–	4×10^{-4}
Electron bunch length in cooling section, RMS	mm	40

Table 3.54: Proton cooling at injection

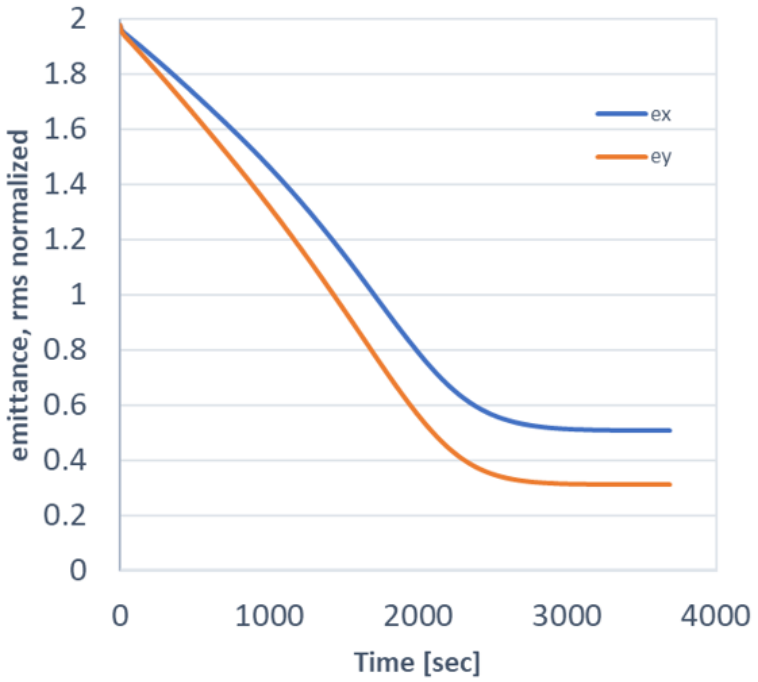

Figure 3.102: Normalized rms emittances (blue: horizontal emittance; orange: vertical emittance) during cooling at 23.8 GeV, with electron beam parameters from Table **??**.

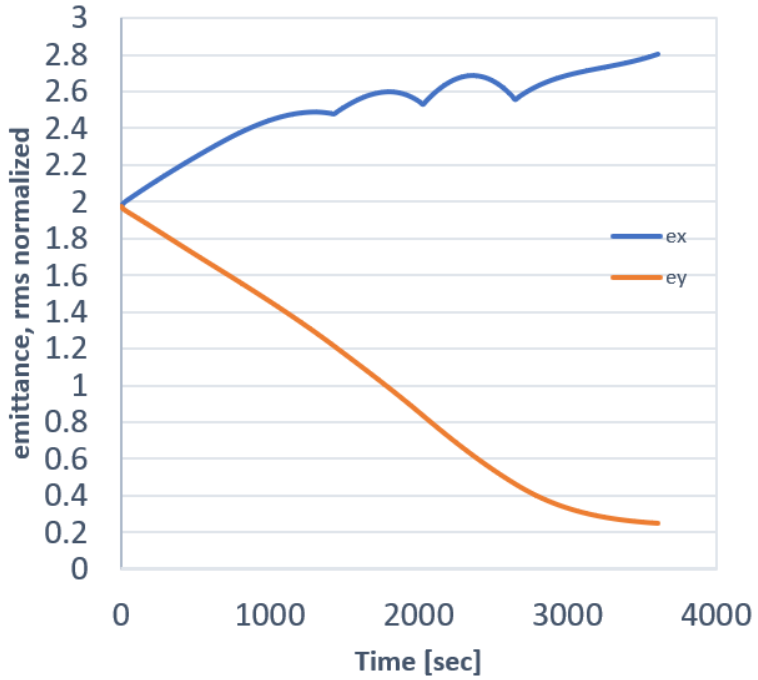

Figure 3.103: Normalized rms emittances (blue: horizontal emittance; orange: vertical emittance) during cooling at 23.8 GeV, with electron beam parameters from Table **??**. Horizontal emittance was heated while vertical emittance was being cooled.

Parameter	Unit	Value
DC gun voltage	kV	400
Final electron kinetic energy	MeV	12.5
Main RF bunch frequency	MHz	197
Number of 197MHz NCRF cavities		17
Voltage per 197MHz RF cavity	kV	850
Energy correction RF frequency	MHz	591
Number of 591MHz NCRF correction cavities		4
Voltage per 591MHz cavity	kV	375
Number of 591MHz deflecting cavities		1
Voltage of deflecting cavity	kV	150
Number of 24.6MHz cavities		1
Voltage of 24.6MHz cavity	kV	10
Bunch train repetition rate	MHz	24.6
Photocathode material		CsK_2Sb
Laser wavelength	nm	532
Electron bunch full length on cathode	ps	400
Average electron current	mA	74
Beam dump power	kW	925

Table 3.55: Low Energy Cooler parameters

3.11 Stochastic cooling for heavy ions

A stochastic cooling system for a bunch spacing corresponding to the h=315 is feasible in the HSR. We will need to put kickers from both existing RHIC rings into the HSR to allow for the 40ns. bunch spacing. Also, the HSR has a larger momentum spread than RHIC and it is necessary to use two longitudinal pickups, on in the 4 o'clock straight section and one in the two o'clock straight section and take the difference of these signals to drive the longitudinal kicker in 12 o'clock. The fiber optic links for the transverse kickers will be the same as used currently.

The value of such a system depends on the initial operating parameters. If the RF power in the ESR is initially limited then, by using the maximum 28 nC. bunch charge in 290 bunches, it is likely that stochastic cooling for heavy ions will be highly beneficial.

Chapter 4

Beam Dynamics (editors: Blaskiewicz & Blednykh)

Beam dynamics introductory words go here ...

4.1 Collective Effects

Collective effects in the Electron-Ion Collider (EIC) present critical challenges for both beam stability and vacuum system performance. One of the most demanding operational requirements is the accumulation of an average bunch current of I_{av} =2.5 ampere distributed over M=1160 bunches in the Electron Storage Ring (ESR). Achieving this goal necessitates rigorous control of single-bunch instabilities driven by broadband impedance, coupled-bunch instabilities arising from narrow-band impedance — primarily from RF cavities — as well as ion-induced instabilities under insufficient vacuum conditions, and beam-induced heating.

Beam-induced heating is a key consideration in the vacuum system design, particularly for the Electron Storage Ring (ESR) and Hadron Storage Ring (HSR), where significant radial beam offsets occur at high energies. Under such conditions, the beam may approach the vacuum chamber wall or cryogenic components, increasing the risk of localized power deposition. Power loss and thermal load calculations have been carried out for individual components, guiding the implementation of active cooling systems where needed — especially in the ESR — and assessing compliance with the overall thermal budget in the HSR.

To characterize and mitigate collective effects, comprehensive wakefield and impedance analyses have been conducted across the EIC accelerator complex using simulation tools such as CST [ref], ECHO3D [ref], and GdfidL [ref]. These studies evaluate longitudinal, transverse dipole, and quadrupole wakefield contributions from vacuum discontinuities (e.g., BPMs, bellows, flanges), RF cavities, resistive-wall effects, and geometric transitions. Particular emphasis has been placed on minimizing the total wake potential through optimized mechanical design and material selection.

A centralized impedance and vacuum component database has been developed for each accelerator ring — RCS, ESR, and HSR — and is continuously updated to reflect the evolving maturity of the vacuum system design. The impedance budget is regularly revised in accordance with these updates.

Beam dynamics simulations have been performed using the ELEGANT code, with cross-validation against the TRANFT code and analytical approximations. For the HSR, where beam stability at injection energy during low-energy cooling is particularly critical, simulations incorporate nonlinear space-charge effects and Landau damping mechanisms via chromaticity and octupole fields. Recent advances in simulation capabilities — including the implementation of nonlinear space-charge algorithms in ELEGANT and benchmarking with TRANFT — have significantly improved the accuracy and reliability of beam stability predictions.

4.1.1 Impedance and single bunch instability in RCS

The longitudinal, vertical dipole, and quadrupole wakefields are calculated for a 0.5 mm rms bunch length (pseudo Green function) and are presented in Figure 4.1. The contribution of each individual component is accounted for and multiplied by the number of such components distributed around the ring. The resistive wall contribution is calculated separately using the analytical Bane and Sands approximation [Ref]. The standard RCS vacuum chamber is made of stainless steel, has a circular profile with a radius of b=18.16 mm, and features a 30 µm Cu coating.

To perform beam dynamics simulations and estimate instability thresholds, the obtained wakefields were used in the ELEGANT code [Ref] for particle tracking during the linear energy ramp from 750 MeV to 5 GeV over approximately 50 ms. The RF voltage in the RCS increases exponentially from 1 MV to 4 MV. The ramp profile is subject to optimization, and we used the current ramp configuration for the preliminary stability analysis. As a first step, we used preliminary beam parameters extracted from the Beam Accumulator Ring (BAR) at the injection energy of 750 MeV and evaluated the Transverse Mode Coupling Instability (TMCI) threshold at zero chromaticity, excluding longitudinal wakefield. Due to the RF system mismatch between the BAR and RCS, the beam experiences a transient period during the first few hundred turns. Energy spread (σ_δ), bunch length (σ_t), horizontal and vertical emittances ($\varepsilon_{x,y}$) dependence as a function of turns are shown in Figure 4.2. The numerically simulated TMCI threshold is 12 mA, compared to 9 mA calculated analytically at an energy of E_0 = 750 MeV, RF voltage V_{RF} = 1 MV, energy spread σ_δ = 2.5e-3, bunch length σ_s = 20 mm, and average beta function β_y = 9.4 m.

4.1.2 Impedance and single bunch instabilities in ESR

One of the most challenging tasks in the EIC project is to accumulate an average bunch current of $I_{av} = 2.5$ mA within $M = 1160$ bunches in the electron storage ring. Beam-induced heating, single-bunch instabilities (broad-band impedance), coupled-bunch instabilities (narrow-band impedance), and ion instabilities are the main focus in the vacuum system design. Currently, we have some designs for the main vacuum components, and their impedance have been eventuated according to their current design and will be updated based on their new status.

To increase the ESR beam current instability threshold and reduce the heat load on vacuum components, it is important to minimize the total impedance of all components in the ESR. In parallel, a detailed examination of trapped modes in each vacuum element — particularly those modes that can persist for a long time — is also critical.

The total impedance and wakefield in the ESR ring can be classified into three categories: geometric wakefield and impedance, resistive-wall wakefield and impedance, and coherent synchrotron radiation (CSR) wakefield and impedance. In the following sections, we will describe each of them separately.

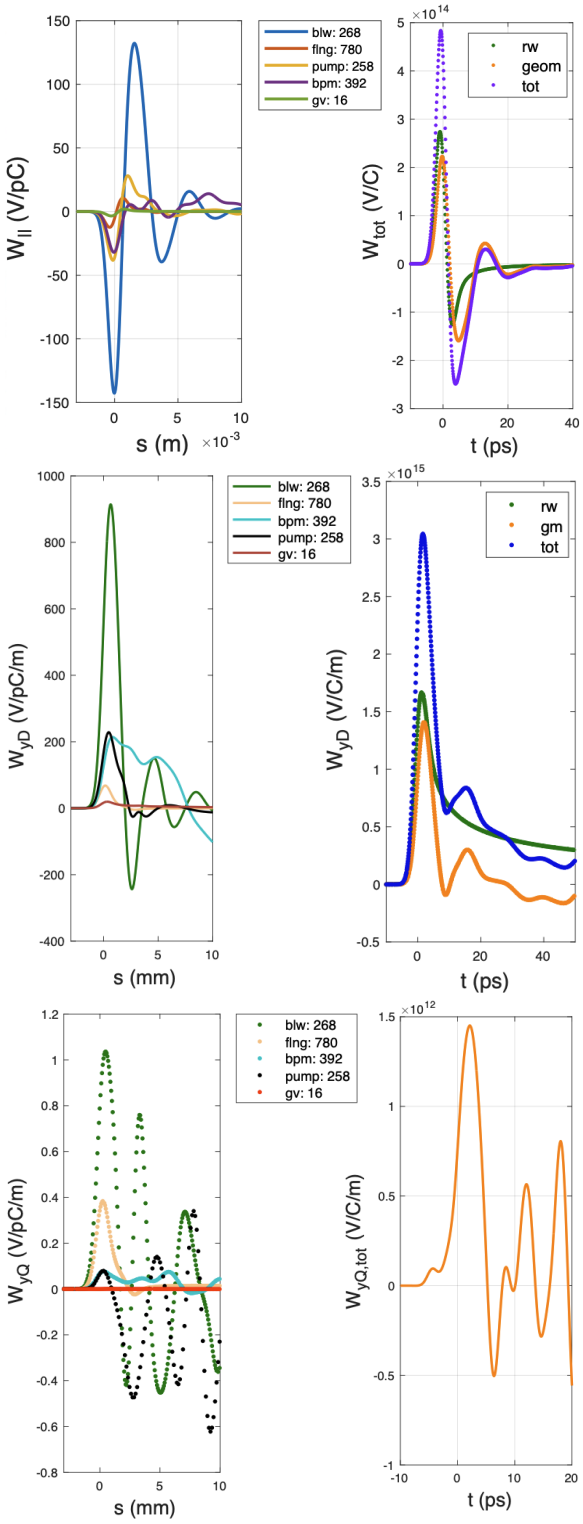

Figure 4.1: Wakefields in the Rapid Cycling Synchrotron, from individual vacuum components and the total combined contribution. (Top) Longitudinal wakefields. (Middle) Vertical dipole wakefields. (Bottom) Quadrupole wakefields.

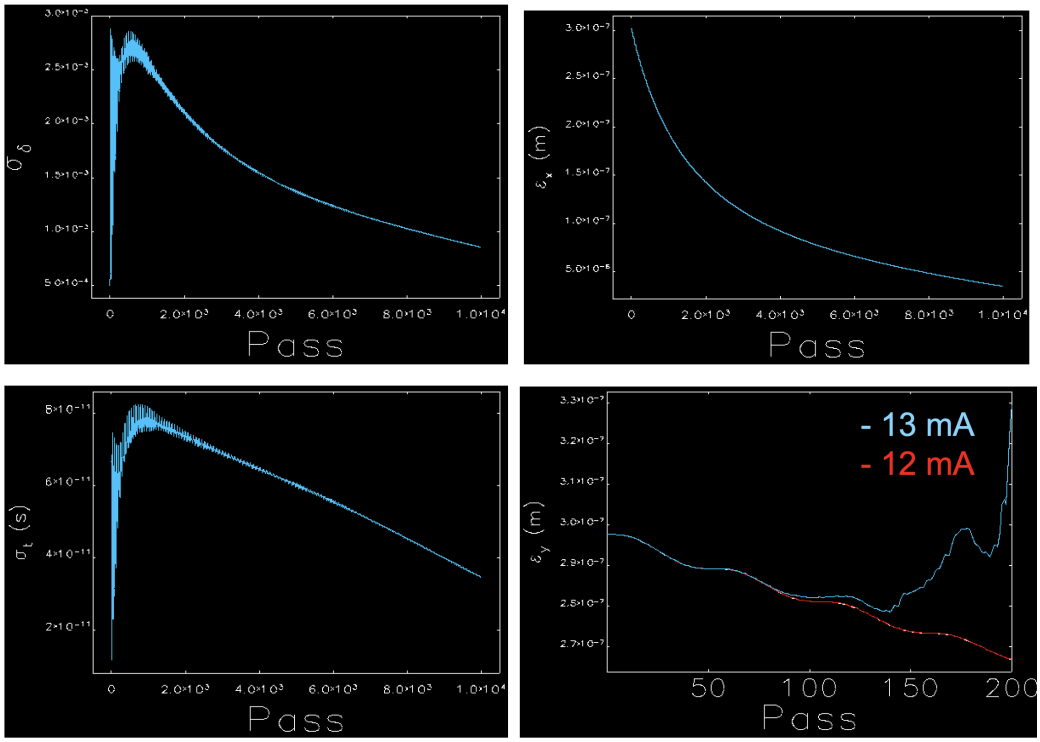

Figure 4.2: Beam parameters evolution in the RCS as a function of the number of turns simulated by the ELEGANT code. Top Left (σ_δ vs. Pass): Energy spread showing an initial rapid growth due to RF systems mismatch, followed by a gradual decrease as the beam stabilizes. Top Right (ε_x vs. Pass): Horizontal emittance (ε_x) decreases monotonically, indicating beam damping. Bottom Left (σ_t vs. Pass): Bunch length (σ_t) exhibits a similar trend to energy spread, with early oscillations and a subsequent steady decline. Bottom Right (ε_y vs. Pass): Evolution of vertical emittance (ε_y) for two single-bunch currents (12 mA and 13 mA). The 13 mA case shows beam blow-up near 200 turns, indicating the onset of transverse mode coupling instability (TMCI), while the 12 mA case remains stable.

Geometric Wakefield and Impedance

The impedance budget and the overall characteristics of the geometric impedance of the ESR are evaluated through numerical simulations of the ESR vacuum components using GdfidL and ECHO3D, with a Gaussian electron beam of 0.5 mm rms bunch length. To ensure accurate and reliable impedance evaluation and to avoid potential errors in time-domain simulations, two methods are employed. First, the wakefield and impedance results from any numerical method must be verified across different mesh sizes to confirm convergence. Second, consistency between different simulation codes, such as GdfidL and ECHO3D, must be demonstrated.

Although the individual impedance of vacuum components in the ESR arc may be small, their cumulative contribution can be significant due to the large number of such elements. These components include RF-shielded bellows, vacuum flanges, beam position monitors (BPMs), vacuum pump ports, photon absorbers, etc. In contrast, while the number of vacuum elements in the interaction region (IR) is smaller, their impedance can be large. These IR elements include RF cavities, collimators, injection/abort kickers and septa, tapers, and other critical devices.

Parameter	Unit	Value
Energy, E	GeV	5
Average Current, I_{av}	A	2.5
Revolution Period, T_0	µs	12.79
Gamma$_t$		29.6
Momentum Compaction, α		1.14×10^{-3}
Number of Bunches, M		1160
Energy Loss, U_0	MeV	1.2
RF Voltage, V_{RF}	MV	12
RF Acceptance	%	1.2
Synchrotron Tune, ν_s		0.057
Damping Time, $\tau_{x,y}$, τ_s	ms	54, 27
Energy Spread, σ_δ		4.93×10^{-4}
Bunch Length, σ_s	mm	6.0

Table 4.1: Electron Storage Ring machine parameters

Parameter	5 GeV	10 GeV	18 GeV
Num. of electrons per bunch, N	1.72×10^{11}	1.72×10^{11}	6.25×10^{10}
Bunch Charge, Ne	28 nC	28 nC	11 nC
Number of Bunches, M	1160	1160	290
Single Bunch Current, $I_0 = \frac{Ne}{T_0}$	2.2 mA	2.2 mA	0.8 mA
Bunch Length, σ_τ	22.7 ps	25.4 ps	30 ps
Peak Bunch Current, $I_p = \frac{Ne}{\sqrt{2\pi}\sigma_\tau}$	484 A	433 A	155 A
Average Current, I_{av}	2.5 A	2.5 A	0.23 A

Table 4.2: Electron bunch and current parameters at different beam energies.

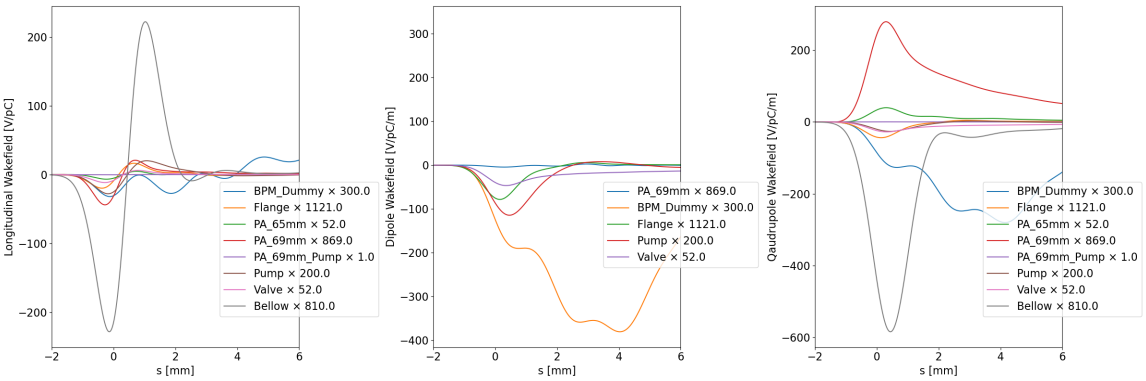

Figure 4.3: Total geometric wakefield in ESR for longitudinal (left), dipole (middle) and qaudrupole (right)

Resistive-wall Wakefield and Impedance

The resistive-wall longitudinal wakefield in a storage ring with circuference length L is defined as:

$$W_{\text{long}}(s) = P_{\text{long}} \cdot f_{\text{bessel,long}}\left(\frac{s}{\sigma_z}\right) \quad \left[VC^{-1}\right]$$
$$W_{\text{trans}}(s) = P_{\text{trans}} \cdot f_{\text{bessel, trans}}\left(\frac{s}{\sigma_z}\right) \quad \left[VC^{-1}m^{-1}\right] \tag{4.1}$$

Element	Qty	sum(kloss) [V/pC (7mm)]	sum(ImZ/n) [mΩ]	sum(ky) [V/pC/m]	betax [m]	betay [m]
RF shielded bellows (80x36mm)	810	2.5489e-01	5.8088e+02	9.3602e+00	—	—
PA (69mm min gap)	869	1.2561e-01	6.4325e+02	-1.0860e-01	—	—
PA (65mm min gap)	52	1.1281e-02	9.8474e+01	-1.5587e-03	—	—
PA (69mm) with pump	200	4.9660e-02	4.4315e+02	-1.1317e-01	—	—
Vacuum chamber (80x36mm)	3400	—	—	—	—	—
80mm flange step	1121	4.6304e-03	3.4774e+02	-3.0421e-01	—	—
Pump port (80mm)	200	2.1468e-02	3.5508e+02	7.2232e-01	—	—
RF shielded gate valve (80mm)	52	9.9922e-02	1.7640e+02	3.5861e+00	—	—
BPM (80blank)	300	7.7898e-03	3.5704e+02	-1.2343e+00	—	—
BPM (80mm) 20mm	300	2.7815e-01	5.2254e+02	—	—	—
591 MHz RF Cavity	18	—	—	—	—	—
Bellows, 274 mm	18	—	—	—	—	—
Bellows, 180 mm	40	—	—	—	—	—
Tapered Transition	2	—	—	—	—	—
Gate Valve, 180 mm	20	—	—	—	—	—
Beam Line Absorbers, 274 mm	9	—	—	—	—	—
Beam Pipes, 180 mm, L∼5 m	10	—	—	—	—	—
Beam Pipes, 150 mm, L∼2.5 m	8	—	—	—	—	—
Cold Trap	—	—	—	—	—	—
Gate Valve, 88 mm	—	—	—	—	—	—
Crab Cavity taper	4	2.7653e-01	4.8025e+02	—	—	—
80-60 Taper	2	—	—	—	—	—
60-80 Taper	2	—	—	—	—	—
Horizontal Collimators	—	—	—	—	—	—
Vertical Collimators	—	—	—	—	—	—
Pump port (60mm)	14	—	—	—	—	—
PA (49mm min gap)	72	—	—	—	—	—
PA (60mm min gap)	—	4.8774e-02	5.3894e+02	—	—	—
60mm flange step	72	2.0031e-03	1.9363e+01	4.3278e-02	—	—
Vacuum chamber (60x36mm)	140	—	—	—	—	—
RF shielded bellows (60x36mm)	28	—	—	—	—	—
RF shielded bellows (100x36mm)	4	—	—	—	—	—
Vacuum chamber (100x36mm)	25	—	—	—	—	—
IPA (85mm min gap)	8	—	—	—	—	—
BPM (60mm)	10	—	—	—	—	—
BPM (60blank)	0	—	—	—	—	—
Stripline kickers (IR4)	—	—	—	—	—	—
Septum - RCS to ESR	1	—	—	—	—	—
Crab Cavities	2	—	—	—	—	—

Table 4.3: Electron Storage Ring component list with impedance and optics parameters

Where the pre-factor is:

$$
\begin{aligned}
P_{\text{long}} &= \frac{r_e\, E_0\, N_p}{2b\sqrt{2\mu_r Z_0 \sigma}} \cdot \frac{1}{\sigma_z^{3/2}} \cdot L \\
P_{\text{trans}} &= \frac{2r_e\, E_0\, N_p}{b^3\sqrt{2\mu_r Z_0 \sigma}} \cdot \frac{f_2}{\sqrt{\sigma_z}} \cdot L
\end{aligned}
\tag{4.2}
$$

Here, r_e denotes the classical electron radius, and E_0 is the rest energy of the electron. The number of particles per bunch is given by N_p. The parameter b represents the beam pipe radius, while μ_r is the relative permeability of the wall material. The vacuum impedance is denoted by Z_0, and σ stands for the electrical conductivity of the wall material (for example, copper). The RMS bunch length is represented by σ_z, and L is the physical length of the resistive wall section under consideration.

And $f_{\text{bessel,long}}(u)$ and $f_{\text{bessel,trans}}(u)$ are the Green's function defined via a Bessel-based form, and

are defined piecewise as:

$$f_{\text{bessel,long}}(u) = |u|^{3/2} \cdot e^{-u^2/4} \times \begin{cases} I_{1/4}\left(\frac{u^2}{4}\right) - I_{-3/4}\left(\frac{u^2}{4}\right) - I_{-1/4}\left(\frac{u^2}{4}\right) + I_{3/4}\left(\frac{u^2}{4}\right), & u < 0 \\ I_{1/4}\left(\frac{u^2}{4}\right) - I_{-3/4}\left(\frac{u^2}{4}\right) + I_{-1/4}\left(\frac{u^2}{4}\right) - I_{3/4}\left(\frac{u^2}{4}\right), & u \geq 0 \end{cases}$$
$$f_{\text{bessel,trans}}(u) = \begin{cases} |u|^{1/2}\, e^{-u^2/4} \left[I_{-1/4}\left(\frac{u^2}{4}\right) - I_{1/4}\left(\frac{u^2}{4}\right) \right], & u < 0 \\ |u|^{1/2}\, e^{-u^2/4} \left[I_{-1/4}\left(\frac{u^2}{4}\right) + I_{1/4}\left(\frac{u^2}{4}\right) \right], & u \geq 0 \end{cases} \tag{4.3}$$

where $u = \frac{s}{\sigma_z}$ and $I_\nu(x)$ is the modified Bessel function of the first kind.

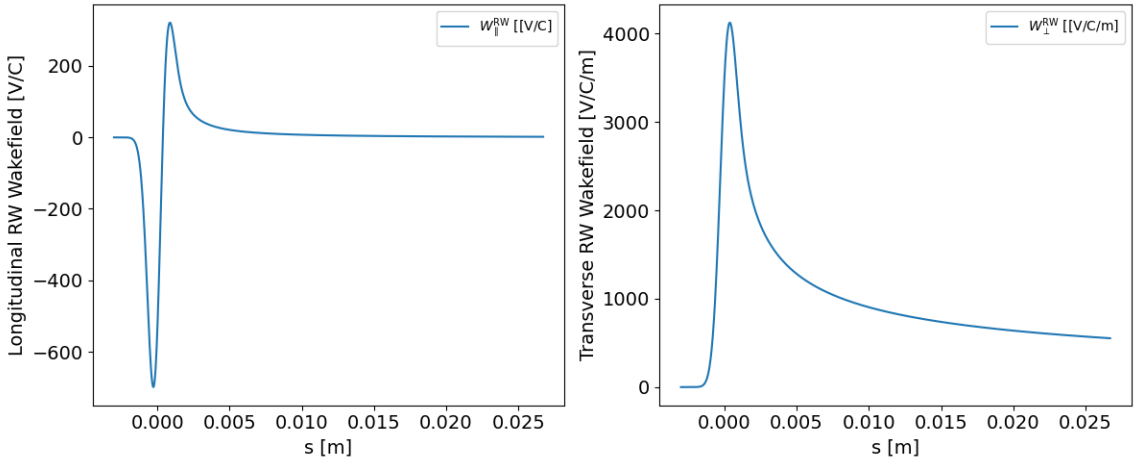

Figure 4.4: Resistive-wall wakefield

The longitudinal and transverse resistive-wall impedances per unit length are [Ryutaro]:

$$\begin{aligned} \frac{Z_\parallel^{\text{RW}}(\omega)}{L} &= \frac{e^{-i\pi/4}}{2\pi} \cdot \frac{1}{b} \left(\frac{Z_0 \rho\, \omega}{c} \right)^{1/2} \quad \left[\Omega\,\text{m}^{-1}\right] \\ \frac{Z_\perp^{\text{RW}}(\omega)}{L} &= \frac{e^{-i\pi/4}}{2\pi} \cdot \frac{2}{b^3} \left(\frac{c Z_0 \rho}{\omega} \right)^{1/2} \quad \left[\Omega\,\text{m}^{-2}\right] \end{aligned} \tag{4.4}$$

For a Gaussian bunch, the effective longitudinal resistive-wall impedance represents how the bunch "samples" the frequency-dependent longitudinal impedance. It is a weighted average of the impedance spectrum over the bunch spectrum. They can be expressed as below.

$$\begin{aligned} \left| \frac{Z^{\text{RW}}\parallel(\omega)}{n} \right| \text{eff} &= \Gamma(1/4) \cdot \left(\frac{\sigma_z Z_0 \rho}{2\pi b^2} \right)^{1/2} \quad [\Omega] \\ \left| \frac{Z^{\text{RW}}\perp(\omega)}{L} \right| \text{eff} &= \frac{\Gamma(1/4)}{\pi b^3} \cdot \left(\frac{\sigma_z Z_0 \rho}{2\pi} \right)^{1/2} \quad [\Omega \cdot \text{m}^{-2}] \end{aligned} \tag{4.5}$$

where $\Gamma(1/4) = 3.6256$. These expressions are approximations valid for a Gaussian bunch and account for the bunch length-averaging effect in impedance interaction.

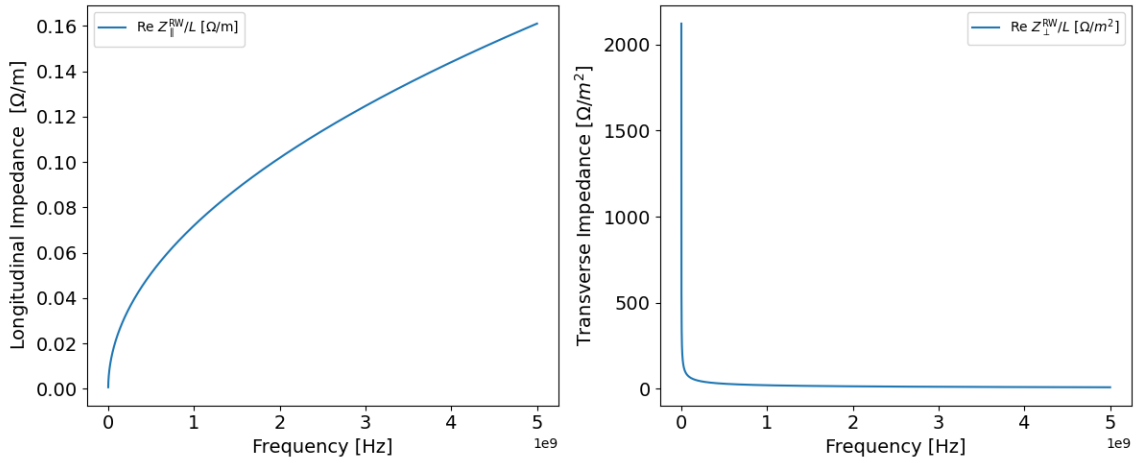

Figure 4.5: Resistive-wall impedance

Coherent Synchrotron Radiation Wakefield and Impedance

In a electron storage ring like ESR, coherent synchrotron radiation (CSR) can induce longitudinal microwave instability.

Microwave Instability

When a relativistic beam circulates in a storage ring or propagates through a linac, and it interacts with its own wakefields or impedance, longitudinal instabilities such as the Microwave Instability (MWI) in storage rings or the Microbunching Instability (MBI) in FELs and linacs may occur.

In a storage ring, when the longitudinal impedance couples to high-frequency components of the bunch, small initial fluctuations (e.g., shot noise, coherent synchrotron radiation) can be amplified by the beam's own wakefields. This leads to energy and density modulations along the bunch, resulting in increased energy spread and potential beam degradation. Since these effects occur over very short longitudinal scales, MWI is categorized as a single-bunch instability.

MWI is primarily caused by longitudinal broadband impedance, typically arising from geometric discontinuities in the vacuum chamber. Although broadband impedance peaks at low frequency, it has non-zero components across a wide frequency spectrum and thus can couple to high-frequency beam fluctuations responsible for microbunching. In contrast, narrowband impedance affects only discrete frequencies and is significant only when a beam harmonic resonates with its narrow frequency band.

MWI can affect both coasting and bunched beams. The theory originally developed for coasting beams can be extended to bunched beams if two conditions are met:

- The bunch length is much longer than the wavelength of the instability mode.
- The instability growth time is much shorter than the synchrotron oscillation period.

The Boussard-modified Keil-Schnell criterion provides a threshold condition for the onset of MWI in a bunched Gaussian beam with effective longitudinal impedance per harmonic Z/n. It is given

by:

$$\begin{aligned} \frac{Z_n(n\omega_0+\Omega)}{n} &< \frac{2\pi\beta_0^2 E_0|\eta|\sigma_\delta^2}{eI_{\text{peak}}} \\ I_{\text{peak}} &= \frac{eN_b c}{\sqrt{2\pi}\delta_z} \\ \frac{dp}{p} &= \beta^{-2}\frac{d\gamma}{\gamma} = \beta^{-2}\frac{dE}{E} \\ \frac{Z_n(n\omega_0+\Omega)}{n} &< \frac{2\pi E_0|\eta|\sigma_{\Delta E}^2}{\beta_0^2 eI_{\text{peak}}} \end{aligned} \tag{4.6}$$

Here:

- N_b: number of particles per bunch,
- E_0: nominal beam energy (excluding rest mass),
- δ_z: rms bunch length,
- η: slip factor,
- σ_δ or $\sigma_{\Delta E}$: rms relative energy spread.

the mode number n is the frequency in unit of the revolution frequency $n = \frac{\omega}{\omega_0} = \frac{f_r}{f_0}$. While the the frequency $f_r = \sigma_t^{-1}$ is used sometimes.

Equation (4.7) provides an estimate of the threshold peak current above which the beam becomes unstable due to microwave effects. The total impedance MWI threshold is estimated as 0.2 Ohm.

$$\left|\frac{Z_\perp^{\text{th}}}{n}\right| = \frac{4\sqrt{2\pi}\,|\eta|\,E\,\sigma_\varepsilon}{\langle\beta\rangle\, I_{\text{pk}}} \tag{4.7}$$

With $\langle\beta\rangle = 25$ meter, we can get the limit for transverse microwave instability is $2.4\Omega/m$

Some Elegant simulation plots from Alexei Blednykh here.

For bunch beam, the threshold current for only CSR caused Microwave instability is [Yunhai Cai, Mbtrack2]:

$$I_{\text{th1}} = I_A \alpha_c\, \gamma\, \sigma_\delta^2 \cdot \frac{\sigma_z^{1/3}}{R^{1/3}} \cdot \xi_1 \tag{4.8}$$

and the shielding parameter χ and empirical factor ξ, are defined as:

$$\begin{aligned} \chi &= \sigma_z \cdot \left(\frac{R}{h^3}\right)^{1/2} \\ \xi_1 &= 0.5 + 0.34 \cdot \chi \end{aligned} \tag{4.9}$$

- $I_a = \frac{4\pi\varepsilon_0 m_e c^3}{e}$ — Alfven current [A]
- α_c — Momentum compaction factor (dimensionless)

- $\gamma = \frac{E_0}{m_e c^2}$ — Lorentz relativistic factor
- σ_δ — RMS relative energy spread (dimensionless)
- σ_z — RMS bunch length [m]
- h — gap between the parallel plates [m]
- R — Bending radius of the dipole [m]
- $\chi = \sigma_z \sqrt{\frac{R}{h^3}}$ — Shielding parameter
- $\xi = 0.5 + 0.34\chi$ — Empirical fitting factor

ESR, we can get 9.44 mA. Another move conservative threshold comes from the steady-state parallel-plates theory for Coasting Beam [Yunhai Cai] and it give us 6.82 mA which is also higher than our requirement of 2.15 mA per bunch.

$$I_{\text{th2}} = I_A \alpha_c \gamma \sigma_\delta^2 \cdot \frac{3\sqrt{2}\sigma_z}{\pi^{3/2} h} \tag{4.10}$$

Using the FF-SS CSR model and the dispersion relation equation for the stability of a coasting beam,

Using the wake function for the CSR instead of the impedance, there is another similar scaling law for CSR instability with parallel-plates shielding [Sara Dastan],

$$\begin{aligned} I_{\text{th3, 4}} &= \frac{4\pi(E/e)\eta_0 \sigma_\delta^2 \sigma_z^{1/3}}{Z_0 \rho^{1/3}} \xi_{3,4} \\ \xi_3 &\approx 0.5 + 0.12 \cdot \chi \\ \xi_4 &\approx 0.384 \cdot \chi^{2/3} \end{aligned} \tag{4.11}$$

Comparing with Eq. 4.8 4.10, the shielding parameter in Eq. 4.11 has different definition which $\chi = \sigma_z \sqrt{\frac{R}{b^3}}$ and b is half of height h. ξ_3 is bunch beam with parallel-plates shielding, while ξ_4 is for high-frequency impedances or with coasting beam assumption. We can get the 6.87 mA and 9.4 mA for ξ_3 and ξ_4 respectively.

Transverse Mode Couple Instability (TMCI)

The transverse Mode-Coupling Instability (TMCI), also known as the strong (or fast) head-tail instability, is a transverse instability that occurs *within* a bunch. For a long bunch, different longitudinal slices can oscillate transversely with different phases. For example, the head and the tail of the bunch may oscillate 180° out of phase.

The TMCI threshold can be derived using the two-particle model and the TMCI threshold is:

$$\begin{aligned} \Upsilon = \frac{\pi e^2 N_b W_\perp^1 \hat{v}^2}{4E_0 C \omega_\beta \omega_s} &= \frac{\pi e^2 N_b W_\perp^1}{4 m_0 C \omega_\beta \omega_s} < 2, \\ N_{b,\text{thr}} &= \frac{8}{\pi e^2} \cdot \frac{p_0 \omega_s}{\beta_y} \cdot \left(\frac{C}{W_\perp^1} \right) \\ \sin\left(\frac{\phi}{2}\right) &= \frac{\Upsilon}{2} \end{aligned} \tag{4.12}$$

Transverse Head-tail instability

In the previous section, the strong head-tail instability was discussed using a two-particle model, under the assumption that the betatron and synchrotron motions are decoupled. In this section, we introduce the coupling between longitudinal and transverse motions, which is essential for a more complete understanding of transverse and longitudinal head-tail instabilities.

Following a similar mathematical procedure as in the previous section, but now accounting for the coupling between betatron and synchrotron oscillations, the two eigenvalues for small Y are given by:

$$\begin{aligned} \lambda_{\pm} &= e^{\pm i\mathrm{Y}} \\ \mathrm{Y} &= \frac{e^2 N_b W_{\perp}^1 \beta_{\perp}}{8RE_0 C\nu_s}\left(1 - i\frac{4\phi_{\xi}}{\pi}\right) \\ \phi_{\xi} &= \frac{2\pi\xi\tau}{\eta T_0} \end{aligned} \tag{4.13}$$

The growth rates of the two modes are $\pm\mathrm{Im}(\mathrm{Y})$ per synchrotron oscillation, or:

$$\frac{1}{\tau_{\pm}} = \mp\frac{e^2 N_b \xi\tau\omega_0^2}{4\pi^2 E_0\eta} W_{\perp}^1 \beta_{\perp} \tag{4.14}$$

The transverse head-tail instability arises due to nonzero chromaticity, i.e., when the betatron tune varies with the particle energy.

Incoherent quadrupole tune shift

Incoherent Laslett tune shift is caused by the wake fields which do not depend on the offset of beam betatron motion or there is no β item in the formula as below:

$$\frac{d\nu_{x,y}}{dI} = \pm\left(\frac{\pi r}{48Q_{x,y}}\right)\left(\frac{Z_0}{E/e}\right)\left(\frac{R}{b}\right)^2\left(\frac{L}{C}\right)$$

describes the incoherent tune shift per unit current. In this expression, $\nu_{x,y}$ denotes the horizontal or vertical betatron tune, and I is the beam current. The quantity $Q_{x,y}$ is the corresponding transverse tune, Z_0 is the vacuum impedance (approximately 377 Ω in SI units), and E is the total beam energy in electronvolts (eV), with e being the elementary charge. The term R is the average machine radius, and b is the half-height of the vacuum chamber. The factor $\frac{L}{C}$ represents the fractional length of the ring occupied by the dipole vacuum chamber. The geometric factor is defined as

$$r = 1 + \left(\frac{b}{d}\right)^2,$$

where d is the half width of the vacuum chamber. This formula assumes a rectangular chamber cross-section.

The ESR tune shift slopes caused by resistive wall for horizontal and vertical are $\frac{d\nu_x}{dI} = 0.0733\frac{1}{A}$ and $\frac{d\nu_y}{dI} = -0.0834\frac{1}{A}$. With 2.5A total beam current, the tune shift caused only by RW will be $d\nu_x = +0.18$ and $d\nu_y = -0.20$.

There is another Laslett tune shift formula for the electron storage ring and it is given by

$$\Delta Q_x = \frac{Z_0 I_{\text{avg}} q R^2}{2\pi Q_x E_T} \left\{ f_{\text{flat}} \frac{\epsilon_1}{h^2} + f_{\text{mag}} \frac{\epsilon_2}{g^2} \right\}, \tag{4.1}$$

where $Z_0 = 377\,\Omega$, I_{avg} is the average current, q is the particle charge, R is the machine radius, Q_x is the horizontal tune, E_T is the total particle energy, $h = 18mm$ is the half vertical aperture of the vacuum chamber, $g = 26mm$ is the half aperture of the dipole magnets, f_{flat} is the fraction of the ring with a flat vacuum chamber and f_{mag} is the fraction of the ring filled with dipole magnets. For flat chambers the coefficients are $\epsilon_1 \approx \pi^2/48$ and $\epsilon_2 \approx \pi^2/24$. For the vertical tune shift substitute the vertical tune and multiply by -1. We assume the vacuum chamber is flat throughout so $f_{\text{flat}} = 1$. The dipole magnets only fill a fraction of the arc so $f_{\text{mag}} = 0.42$. For 5 GeV operation the beam current is 2.5 A. The respective tune shifts are $\Delta Q_x = 0.242$. These tune shifts are due to smoothly distributed focusing and can be easily corrected with the quadrupole magnets. It will be necessary to adjust the quadrupoles as bunches are injected. The one second interval between injections is long compared to the few millisecond eddy current penetration time.

Parameter/Result	**A. Chao**	**K Y, Ng**		
		parallel plate	**rectangular**	**elliptical**
h (m)	0.018	0.018	0.018	0.020
w or d (m)	0.040	N/A	0.040	0.045
g (m)	N/A	0.026	0.026	0.026
ϵ_{1H}	N/A	0.206	0.201	0.181
ϵ_{1V}	N/A	-0.206	-0.201	-0.181
ϵ_{2H}	N/A	$\pi^2/24$	$\pi^2/24$	$\pi^2/24$
ϵ_{2V}	N/A	$-\pi^2/24$	$-\pi^2/24$	$-\pi^2/24$
$\Delta\nu_x$ **or** ΔQ_x	**0.1833**	**0.242**	**0.238**	**0.192**
$\Delta\nu_y$ **or** ΔQ_y	**-0.2084**	**-0.275**	**-0.270**	**-0.218**

Table 4.4: Comparison of Laslett tuneshift input parameters and results, with all negative signs removed. All three values of $\epsilon_{1H,V}$ are very similar.

Parameter	**PEP-II HER**	**FCC-ee**	**KEKB HER**	**EIC ESR**
E_{beam} [GeV]	9.0	80.0	8.0	5.0
Tune ν_x	24.62	389.0	44.514	41.08
Tune ν_y	24.64	391.0	41.58	36.14
Half-Height b [m]	0.025	0.035	0.025	0.018
Half-Width d [m]	0.0354	0.060	0.052	0.040
L/C	0.59	0.71	0.71/-	0.442
Circumference C [m]	2199.32	97750.00	3016.00	3833.00
Bending radius R [m]	350.03	15557.40	480.01	610.04
Theoretical $d\nu_x/dl$ [1/A]	0.0193	0.1491	0.0223/0.02259	0.0733
Theoretical $d\nu_y/dl$ [1/A]	-0.0193	-0.1491	-0.0223/-0.02259	-0.0834
Measured $d\nu_x/dl$ [1/A]	0.018	–	0.026 (1st), 0.02806 (2nd)	–
Measured $d\nu_y/dl$ [1/A]	-0.018	–	-0.037 (1st), -0.01383 (2nd)	–

Table 4.5: Comparison of parameters and tune slopes for various electron storage rings.

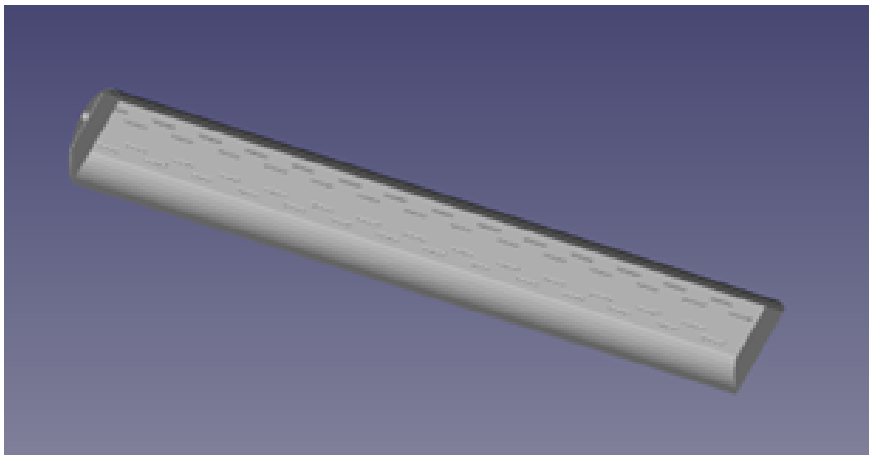

Figure 4.6: 3D model of the beam screen to be installed in the arcs of the HSR

4.1.3 Impedance and single bunch instabilities in HSR

Geometric wake potential and impedance of the HSR

In order to predict the stability condition of the hadron beam in the hadron storage ring (HSR), one of the major challenges is to have an accurate calculation of the wake field induced by the beam in the vacuum components. The HSR comprises of 6 straight sections connected by 6 arcs. Depending on the location of the straight section, they are named IR2, IR4, IR6, IR8, IR10 and IR12. The sub-systems, such as the detectors, the RF cavities and the low energy cooler are located in these straight sections. Since different sub-system has different requirements for the aperture of the vacuum chamber, each IR has to be analyzed individually. The major contributors to the wake field in the arc section are the beam screen and the bpms. To ensure that reliable results are obtained, we have used multiple codes for cross-checking, including GdifidL, ECHO3D, ECHOz1, ECHOz2 and CST. Once satisfactory agreement are reached among various codes, the results are provided to the engineers for further optimization of the design and to the instability simulations. The shortest proton bunches in the HSR have a rms bunch length of 60 mm. To compute the pseudo-Green function, a pilot bunch with an rms length of 4 mm is used for all calculations of the wake potential.

Beam screen

For reduced beam-induced resistive wall heating and to suppress electron cloud buildup, a copper-coated stainless steel beam screen chamber with a thin film of amorphous carbon will be installed in the beamline of the superconducting magnets of RHIC used for the HSR. A section of the screen is shown in Fig. 4.6. There are four rows of pumping slots on both upper and lower walls of the screen. The length of the pumping slot is 17 mm and the width is 2 mm. The longitudinal separation of two adjacent slots is 18 mm. The total length of the considered model is 50 cm.

The longitudinal wake potential computed by three different codes, CST , ECHO3D and GdfidL, is shown in Fig. 4.7. The short-range wake potential obtained from ECHO3D and GdfidL are in good agreement. However, the longitudinal wake potential calculated by CST is significantly different from that calculated by the other two codes, especially in the long range, as shown in the right plot of Fig. 4.7, which suggests that a convergence study for the CST simulation is needed.

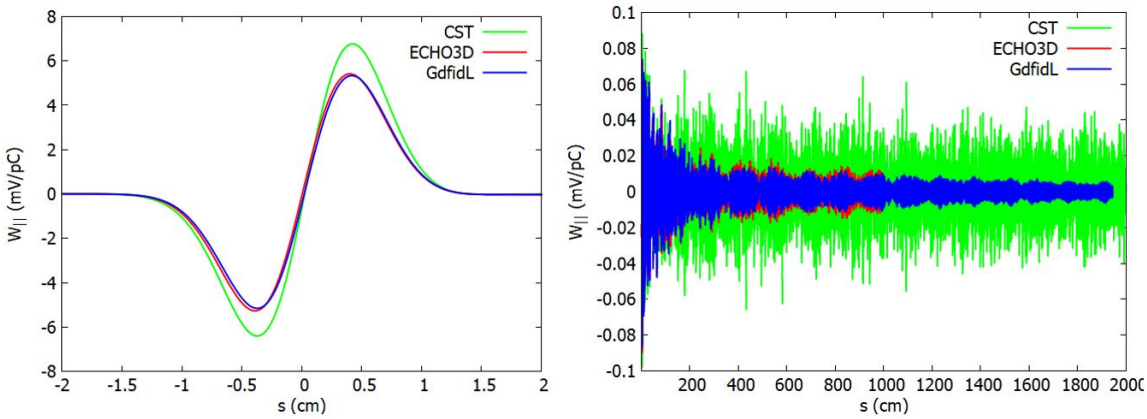

Figure 4.7: The longitudinal wake potential induced by a pilot proton bunch with an RMS. bunch length of 4 mm as it passes through the beam screen

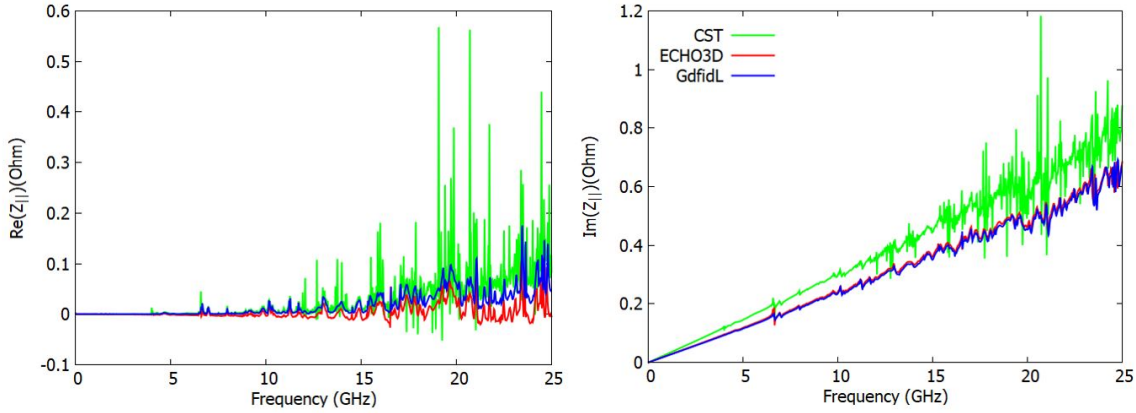

Figure 4.8: The longitudinal impedance of the beam screen with pumping slots as calculated from CST (green), ECHO3D (red) and GdfidL (blue). The wake length used for calculating the impedance is 20 meters for CST, 19.5 meters for GdfidL and 10 meters for ECHO3D.

Figure 4.8 shows the longitudinal impedance calculated from the wake potential. The impedance spectrum calculated from CST finds higher Q, narrower-band resonances than those from the other two codes, as one would expect from the different amplitude for long-range wake potential shown in Fig. 4.8 (right). Since the wake lengths used to compute the impedance are not dramatically different, the discrepancy is not due to the resolution in frequency domain.

Figure 4.9 shows the vertical dipole wake potential induced by a proton bunch passing through the screen with a vertical offset. The results have been obtained from GdfidL and ECHO3d respectively. There is about 10 percents discrepancy between results obtained from the two codes. Further investigations are needed to understand the sources of the discrepancy.

Results shown in Fig. 4.7 and Fig. 4.9 are calculated for a 50 cm long screen. A total length of 2733 meters of such screen will be installed in the HSR and consequently, the HSR screen become the largest contributor to the longitudinal and vertical dipole geometric wake potential among all the vacuum components calculated so far for the HSR.

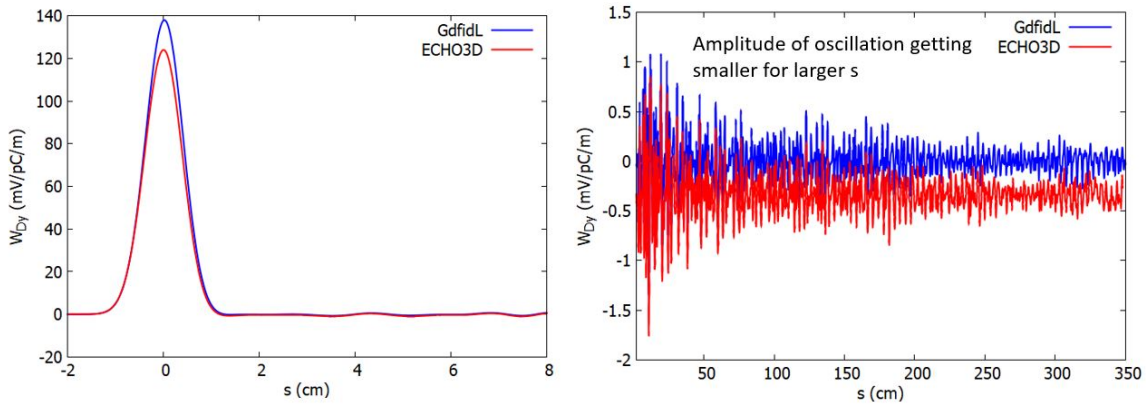

Figure 4.9: The vertical dipole wake potential induced by a proton bunch with RMS bunch length of 4 mm as it passes through the beam screen.

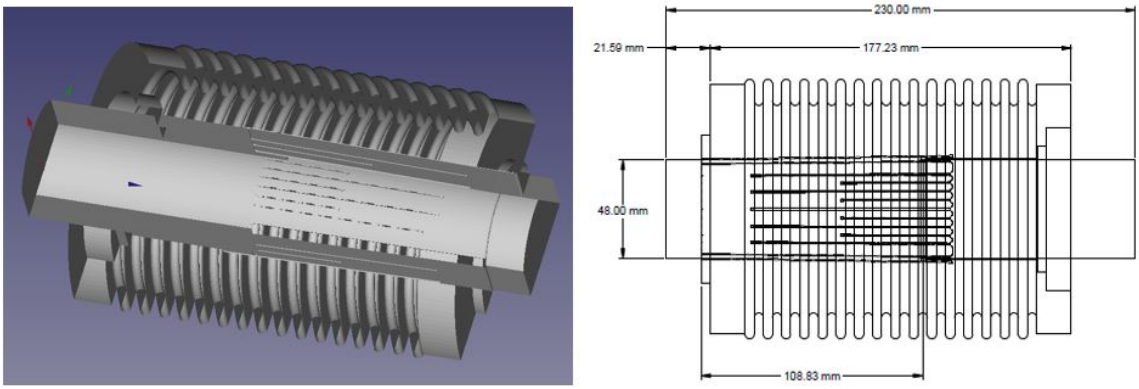

Figure 4.10: The 3D model and the drawing of the interconnect module of the beam screen.

Beam screen interconnect module

The beam screen will be manufactured into sections and an interconnect module will be used to connect two successive sections. There will be 402 interconnect modules installed in the HSR. Figure 4.10 shows the 3D model and the drawing of the interconnect module.

Figure 4.11 shows the longitudinal and vertical dipole wake potential induced by a proton bunch in the interconnect module. The interconnect module is one of the major contributors to the wake potential, especially to the vertical dipole wake potential.

Bellows in the straight sections

Figure 4.12 shows the 3D model of the warm bellows currently installed in the RHIC straight sections. For the HSR, a total number of 200 such bellows are planed to be installed in the straight sections.

Figure 4.13 shows the longitudinal and the vertical dipole wake potentials induced by a proton bunch passing through the bellow. As shown in fig. 4.14, these bellows are the major contributor

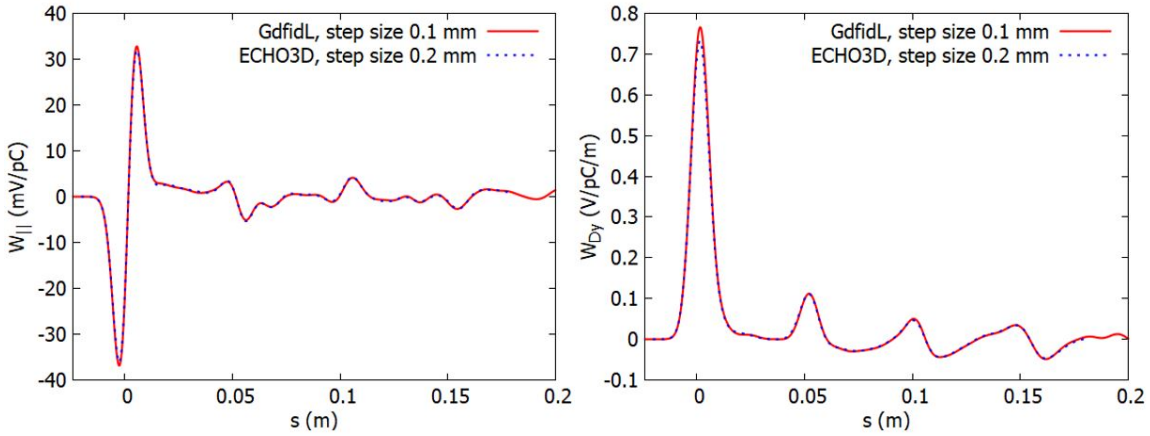

Figure 4.11: The wake potential induced by a proton bunch with RMS bunch length of 4 mm as it passes through a screen interconnect module.

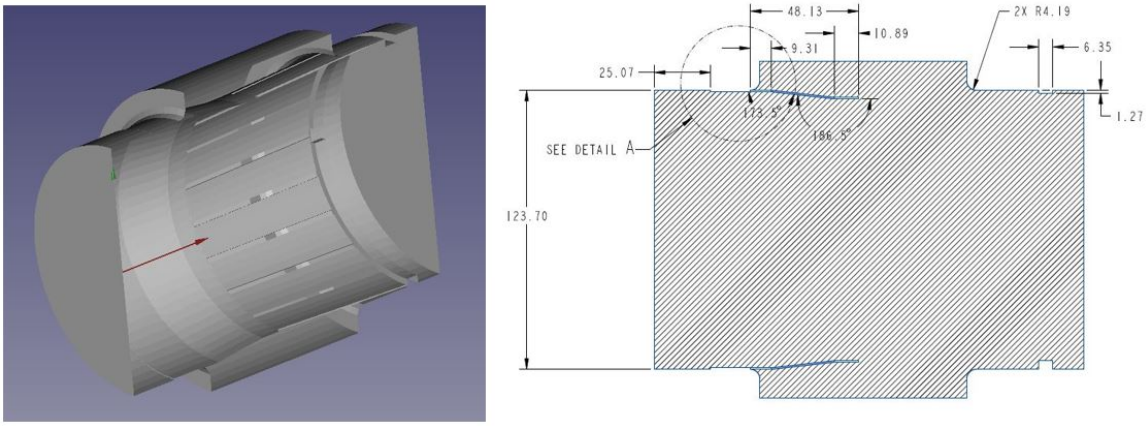

Figure 4.12: The 3D model and the drawing of the bellows to be installed in the straight sections of the HSR.

to the longitudinal and vertical dipole geometric wake potential in the straight section of the HSR.

Summary of the wake potential calculation for the HSR

The overall longitudinal wake potentials calculated for the vacuum components in the HSR are shown in Fig. 4.14. The major contributors to the longitudinal geometric wake potential are arc beam screen, the interconnect module of the arc beam screen and the bellows in the straight section. In the previous design of the arc beam screen, there were two steps of 3 mm width located at the each side of the interconnect module, which was one of the largest contributors to the longitudinal wake potential. In the latest design, the width of the steps is reduced to below 1 mm and consequently, their contribution to the longitudinal wake potential decreased significantly as shown in Fig. 4.14.

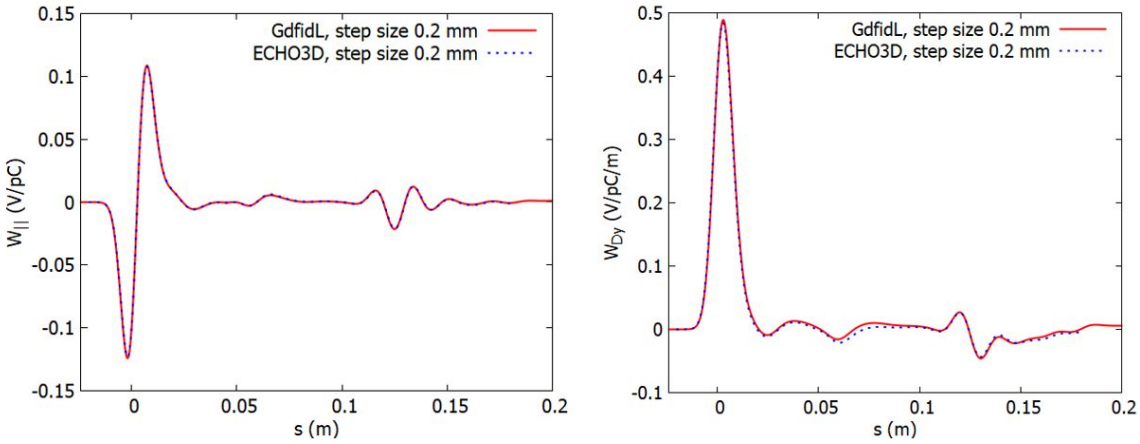

Figure 4.13: The wake potential induced by a proton bunch with RMS bunch length of 4 mm as it passes through a bellow installed in the straight section.

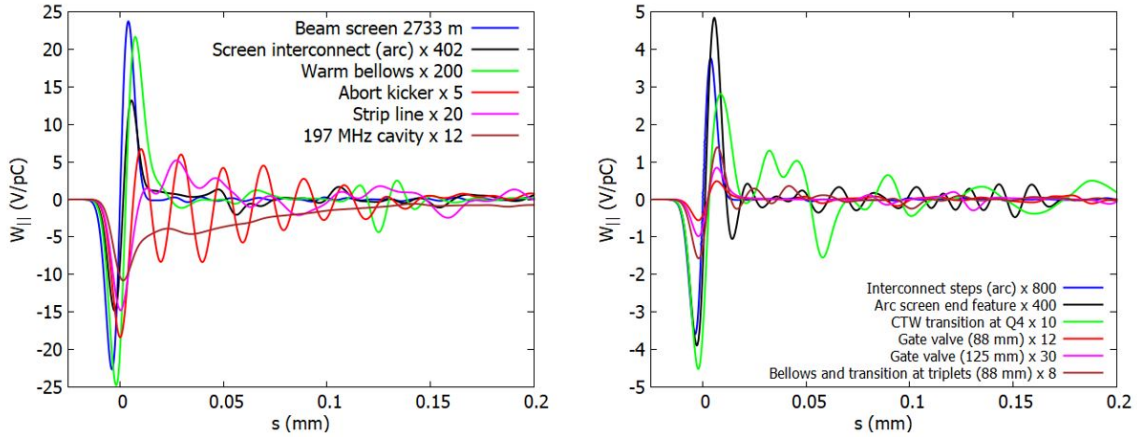

Figure 4.14: The overall wake potential calculated for the vacuum components in the HSR

Single bunch instabilities in HSR

At injection energy (23.8 GeV for protons), a single bunch in the EIC hadron storage ring experiences a relatively strong space charge field that can facilitate the onset of deleterious instabilities, particularly in the transverse plane, in conjunction with other wake sources. In order to guard against this possibility, a systematic study of the underlying beam dynamics under the influence of the relevant collective effects is required. In particular, special emphasis needs to be placed on the impact of the transverse component of the space charge force, which is intrinsically nonlinear in character and can potentially reduce the stability margin for a given machine impedance. In what follows, we present the outline of a short, simulation-based study of the above-mentioned effects, with the aim of clarifying the fundamental single-bunch stability behavior of the protons.

Transverse Beam Dynamics

To start with, a straightforward means of quantifying the impact of (linear) wakefields upon the transverse dynamics of the hadrons is through the familiar concept of the transverse impedance. The latter quantity includes both dipole and quadrupole-type contributions, signifying dependence of the corresponding wake with respect to the transverse coordinates of the leading and trailing particles (respectively). Assuming a Gaussian transverse profile for the beam, it can be shown that, for the case of linear transverse space charge, the beam-induced component of the dipole impedance per unit length is given by [**?**, **?**]

$$\hat{Z}_{x,y}^{(d)}(\omega) = Z_{x,y}^{(d)}/L_R = -\frac{Z_0}{4\pi\gamma_0^2\Sigma_{x,y}^2}\,, \tag{4.15}$$

where $Z_0 \approx 377\,\Omega$ is the vacuum impedance, L_R is the ring circumference, γ_0 is the average relativistic factor and $\Sigma_{x,y} = (\sigma_{x,y}(\sigma_x + \sigma_y)/2)^{1/2}$ - with $\sigma_{x,y}$ being the proton beam transverse sizes, assumed constant in the simplified, smooth focusing model under consideration. As far as the corresponding quadrupole impedance per unit length is concerned, it is simply given by $\hat{Z}_{x,y}^{(q)}(\omega) = -\hat{Z}_{x,y}^{(d)}(\omega)$. An additional, but sometimes overlooked, source of dipole space charge impedance can be visualized by considering the image charges induced by an off-axis hadron beam upon the vacuum chamber, which (because of their asymmetrical distribution) cause a net deflection to an on-axis test particle. The relevant contribution to the dipole impedance is expressed by

$$\hat{Z}_{x,y}^{(d,i)}(\omega) = \frac{Z_0}{2\pi\gamma_0^2 b^2}\,, \tag{4.16}$$

where b is the vacuum chamber radius. Both the dipole and the quadrupole contributions to the transverse impedance can be fed directly into a particle tracking code such as ELEGANT [**?**]. Specifically, the latter code facilitates a transverse impedance input by means of the intrinsic ZTRANSVERSE element.

The dynamics impact of the above-described linear space charge impedances can be elucidated by means of the corresponding tune shifts, which are given by

$$\Delta\nu_{x,y}^{\text{linear}} = -\nu_{x,y}\beta_{x,y}^2\frac{Ne^2cZ_0\lambda(z)}{8\pi\gamma_0^3 m_h c^2\Sigma_{x,y}^2}\,, \tag{4.17}$$

where $\nu_{x,y} = L_R/(2\pi\beta_{x,y})$ are the original tunes of the ring, $\beta_{x,y}$ are the (constant) beta function values, Ze and m_h the charge and mass of the hadrons (respectively), N is the total number of hadrons and $\lambda(z)$ is the scaled longitudinal profile of the beam (normalized according to $\int dz\lambda(z) = 1$, where z is the position within the bunch). As expected for the defocusing space charge force, the tune shifts are negative and vary along the bunch according to the local current value.

All the results mentioned so far have assumed that the transverse space charge force is linear in nature. However, for the Gaussian model under consideration, this is merely an approximation. A more rigorous analysis reveals that the effect of the neglected nonlinear terms is to add a dependence of the particles tunes with respect to the transverse action variables $J_{x,y}$, so that the tune shifts now become $\Delta\nu_{x,y} = \Delta\nu_{x,y}^{\text{linear}}F(J_x, J_y)$. In fact, the modification factor F is such that the transverse actions only *reduce the absolute value of the tune shifts*. Moreover, it can be shown that the action-averaged values of the tune shifts can be approximated by $\langle\Delta\nu_{x,y}\rangle \approx 0.5\Delta\nu_{x,y}^{\text{linear}}$ [**?**]. Accordingly, one can simply halve the beam-induced components of the linear-model dipole and quad space charge impedances (though not their image counterpart) in order to take some account of the nonlinearity. Apart from this rather heuristic way of dealing with this complication, a more self-

Parameter	Value
Energy spread σ_δ	7.4×10^{-4}
RMS bunch length σ_{z0} (m)/double RF system	1.5
RF voltage V_0 (kV)	40
RF frequency f_{RF} (MHz)	24.61
Transition gamma γ_t	22.7
Injection gamma γ_0	25.36
Momentum compaction factor $\alpha_c = 1/\gamma_t^2$	1.94×10^{-3}
Proton normalized emittance $\gamma_0 \epsilon_{x,y}$ (mm-mrad)	3.0 / 0.3
Proton average beta function $\beta_{x,y}$ (m)	22.4 / 23.3
Proton transverse rms beam size $\sigma_{x,y}$ (mm)	1.62 / 0.52
Ring circumference L_R (km)	3.83
Average beam pipe radius b (mm)	24

Table 4.6: Proton stability study parameters

consistent analysis involves the use of the Basseti-Erskine formula ([**?**]) in order to rigorously calculate the transverse fields of the hadron beam, assuming the latter remains Gaussian in profile. This particular method is implemented in the ELEGANT tracking code via the SCMULT element [**?**], which facilitates the automatic insertion of transverse space charge into a lattice.

Numerical data

Confining our attention to protons from now on - the main parameters for the configuration under study are listed in Table 4.6. Given a Gaussian energy profile, a double RF system is being considered with the aim of generating a longer bunch and raising the stability threshold (for a more detailed discussion of the longitudinal dynamics, based on the Haïssinski solution, we refer the reader to Ref. [**?**]). Using the stated parameters, the left panel of Fig. 4.15 plots the real and imaginary parts of the external (i.e. geometric plus resistive wall-related) transverse impedance $Z_d(\omega)$, while also comparing them to the dipole space charge impedance component due to the image charges. As is evident, these contributions are of a similar magnitude (a few MΩ/m), but they are dwarfed by the beam-related dipole and quad impedances, which are given by $Z_x^{(q)} = -Z_x^{(d)} = 90$ MΩ/m and $Z_y^{(q)} = -Z_y^{(d)} = 330$ MΩ/m. On the other hand, the right-hand-side panel of Fig. 4.15 plots the scaled longitudinal profile of the bunch under consideration. For the latter, we note that one must use all sources of longitudinal impedance (resistive, geometric and space charge) in order to generate the distorted super-Gaussian profile shown here.

Before we move on to the main simulation results, it is instructive to consider the output of some simple tracking studies that aim to provide a benchmark for the intrinsic ELEGANT algorithm for transverse space charge calculation. In particular, Fig. 4.16 plots the extracted horizontal and vertical particle tunes for three consecutive turns, assuming tracking under the influence of nonlinear transverse space charge alone (the external dipole impedance is excluded here). As expected from our earlier discussion, the simulated tunes lie predominantly within the area defined by the original tune values and the linear space charge tune shifts, the latter defined by Eq. (4.17).

Having verified the space charge algorithm, we examine the stability of the parameter set under consideration by performing parallelized ELEGANT simulations. Unlike the previously-mentioned benchmark runs, the full-scale simulations take into account all sources of trans-

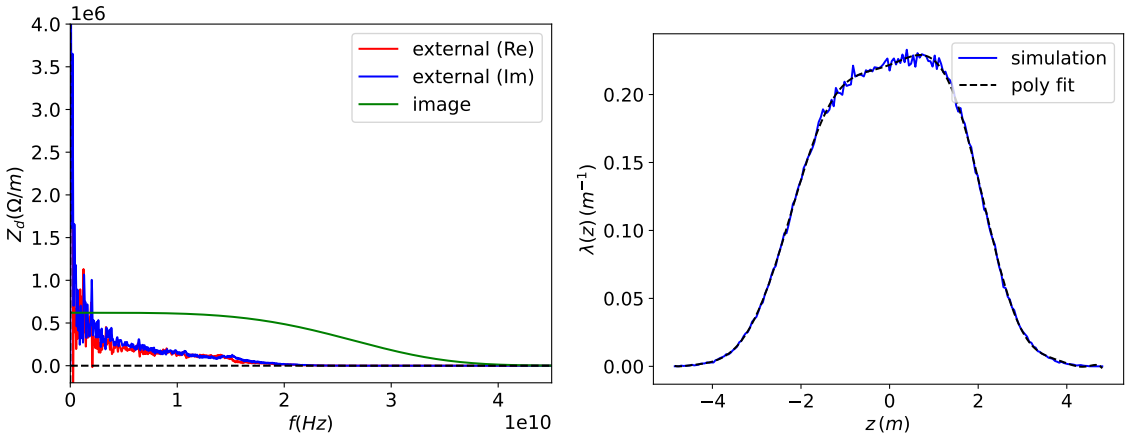

Figure 4.15: Various components of the dipole impedance (left) and scaled longitudinal profile of the proton bunch for an average current of 4.5 mA (right).

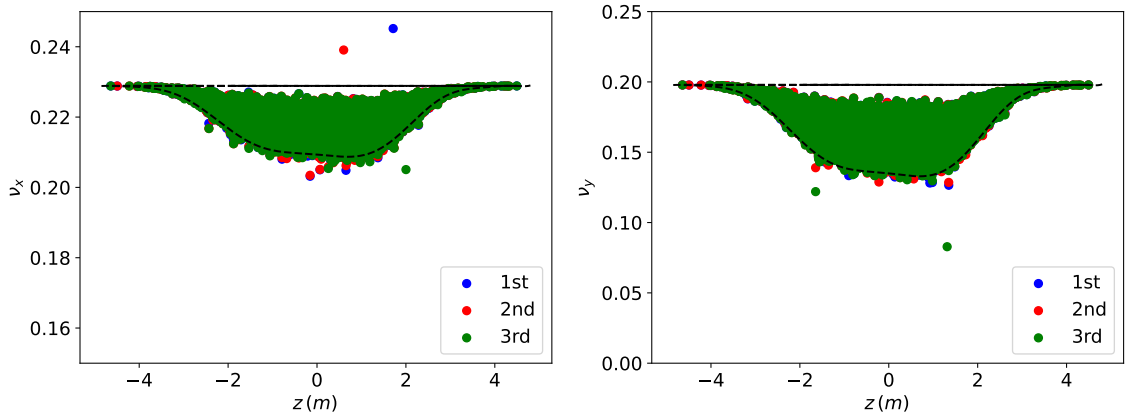

Figure 4.16: Fractional particle tunes for three consecutive turns, for ELEGANT tracking under the influence of nonlinear transverse space charge (4.5 mA current). The flat lines represent the original tunes, while the dashed curves correspond to the linear space charge limits.

verse impedance. Specifically, we follow two different approaches: for both, the external dipole impedance and its image charge-related counterpart are fed directly into the code as tabulated impedance files. However, as far as the remainder is concerned, we either a) also feed it directly into the code in the form of dipole and quad impedance files, generated with the aid of Eq. (4.15) and incorporating the previously-discussed factor of $1/2$ or b) model it explicitly through the SCMULT ELEGANT element. In both cases, to facilitate the transverse stabilization of the beam, an array of 80 octupoles (uniformly-distributed around the ring) is assumed, each with a 30 cm length and a strength of $K_3 = -150$ m^{-4} ([**?**]). Finally, a lattice chromaticity of $\xi_{x,y} = d\nu_{x,y}/d\delta = 6.0$ has also been used in the simulations. The tracking extends up to 4×10^4 turns for 5×10^5 macroparticles, and key quantities such as the rms bunch duration, energy spread and the hadron transverse emittances are monitored in order to check for longitudinal and transverse instabilities. From the combined results, which are presented in Figs. 4.17-4.18, one observes i) a typical fluctuation of the longitudinal quantities due to the synchrotron motion and ii) a slow, relatively modest growth

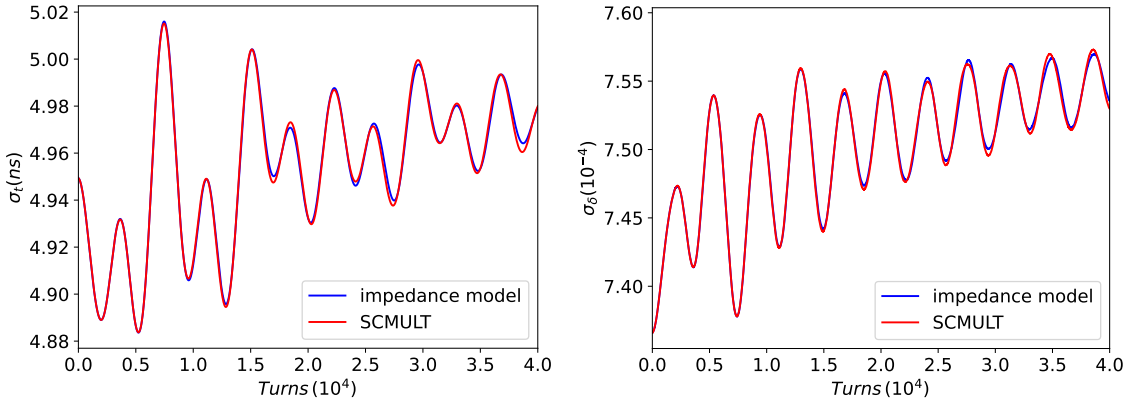

Figure 4.17: ELEGANT simulation data for an average current of 3 mA/double RF system: the left-hand panel shows the variation of the rms bunch duration σ_t over many revolutions, while the right-hand panel plots the evolution of the rms energy spread.

in terms of the transverse emittances, possibly numerical in nature. Overall, one may reasonably conclude that this system configuration is both longitudinally and transversely stable for average currents up to 3 mA. Of course, more optimization work remains to be done in order to push the stability threshold to higher current values.

4.1.4 Multi-bunch instabilities and feedback requirements in RCS,ESR and HSR

RCS

The Rapid Cycling Synchrotron RF control loops will damp any rigid bunch longitudinal instability. A rigid bunch transverse damper will control any instability from the narrow band transverse

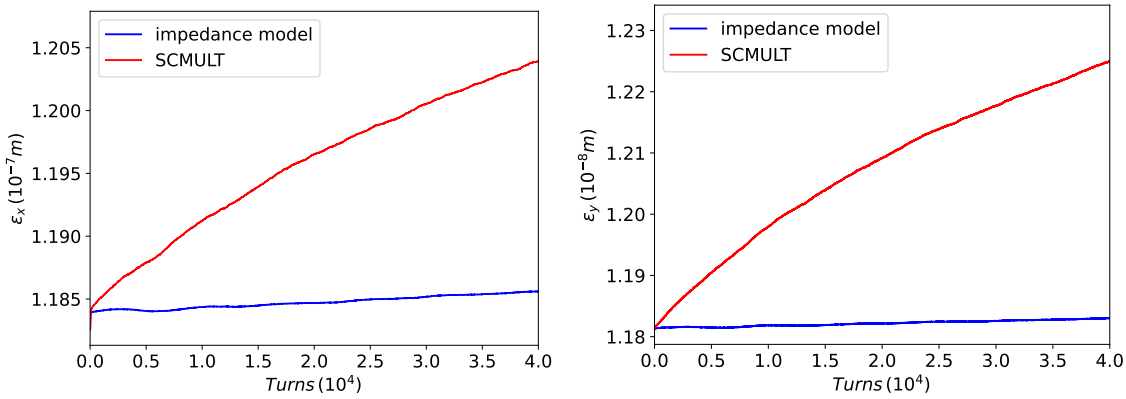

Figure 4.18: ELEGANT simulation data for an average current of 3 mA/double RF system: the left-hand panel shows the variation of the horizontal emittance ε_x over many revolutions, while the right-hand panel plots the evolution of its vertical counterpart.

impedance. Such a damper will be needed to damp injection oscillations so there is no additional hardware needed. As of now there is no reason to believe that either a longitudinal or transverse head-tail mode will be an issue.

ESR

Unstable longitudinal coupled bunch modes are expected in the ESR and a longitudinal damper is planned. Calculations based on the Wang formalism are shown in Figures 4.19 and 4.20. While the required damping is robust it is well within the state of the art.

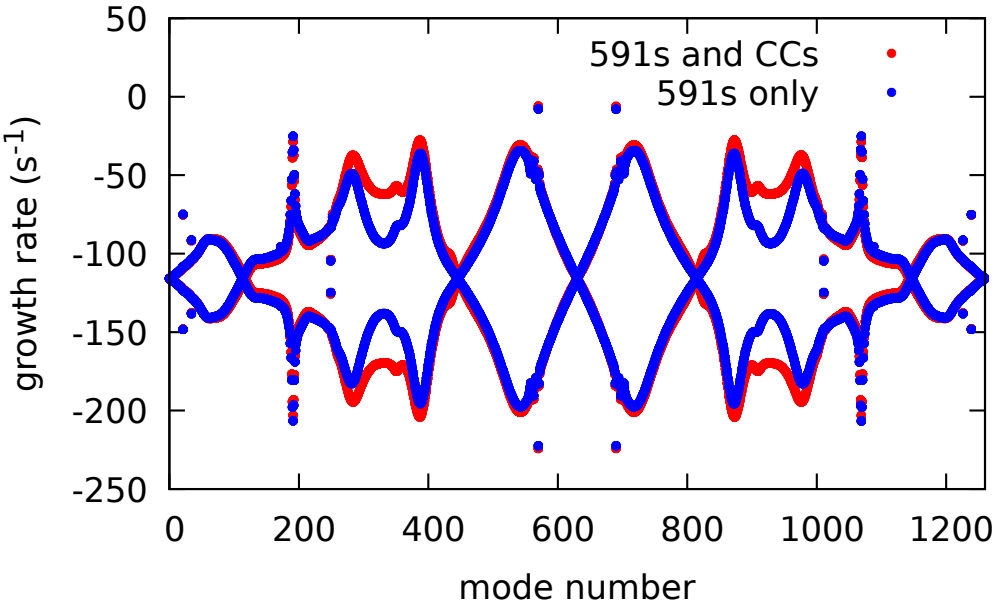

Figure 4.19: ESR coupled bunch growth rates at 5 GeV with self consistent damper applying $98s^{-1}$. The growth rates with only the 591 MHz RF cavities are shown in blue. The red dots include the effect of the crab cavities.

HSR

At injection in HSR the space charge forces are significant. In this section we consider the linear model discussed in section 4.1.3. Transverse coupled bunch modes driven by the fundamental

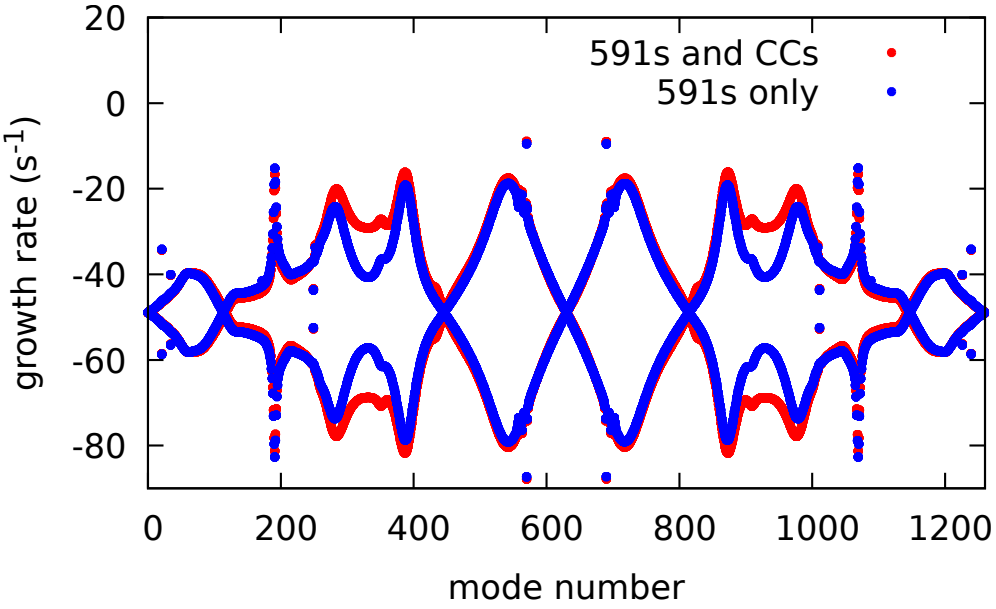

Figure 4.20: ESR coupled bunch growth rates at 10 GeV with self consistent damper applying $20s^{-1}$. The growth rates with only the 591 MHz RF cavities are shown in blue. The red dots include the effect of the crab cavities.

mode of the crab cavities (CCs) are important in the HSR [**?**]. It was found that RF feedback on the crabbing mode is needed to stabilize the beam. Recent published work has focused on the behavior at store energy [**?**, **?**] where it was found that the beams in both the electron and ion rings should be passively stabilized by the beam-beam tune spread. Here we turn to proton injection, see Table 4.7. Between the long bunch length and strong space charge it was decided that simulations with realistic crab feedback are needed.

The crab cavity transverse voltage is related to the dipole moment by

$$\ddot{V}_x + \omega_r^2 V_x + 2\alpha \dot{V}_x = \frac{R_x}{Q}\omega_r^2 D_T(t), \tag{4.18}$$

where V_x is the transverse voltage on the cavity, ω_r is the angular resonant frequency of the cavity, R_x is the transverse shunt impedance, Q is the loaded quality factor of the cavity, $\alpha = \omega_r/2Q$, and D_T is the total dipole moment driving the cavity. The dipole moment is given by

$$D_T(t) = D_B(t) + x_0 I_{LL}(t) - \frac{1}{\omega_r R_{eff}}\frac{d}{dt}\left(V_x(t - T_d) + V_{notch}(t)\right). \tag{4.19}$$

In equation (4.19) D_B is the beam dipole moment at the cavity as a function of time, $x_0 I_{LL}$ is the drive derived from the setpoints of the RF system, R_{eff} is the effective transverse shunt impedance for the feedback gain, T_d is the time delay for wide-band feedback which is equal to an integer number of RF periods. The time derivative operating on the voltages is automatic if one couples to the electric field of the cavity. The voltage V_{notch} is output from narrow band notch filters centered at the betatron sidebands.

Both the low level RF system and TRANFT assume that a typical voltage varies like $V(t) = Re[\hat{V}\exp(j\hat{\omega}t)]$. For typical parameters, $M = 315$ updates per turn works well. This is the RF harmonic during injection and ramping. We take $\hat{\omega} = 2520\omega_{rev}$ which makes $\omega_r - \hat{\omega}$ small while keeping an integer number of carrier oscillations per update. The CC voltage update on a given turn begins with creating the drive signal from the beam,

$$\hat{V}_B(n) = -j\frac{R_x}{Q}\frac{\omega_r^2}{\hat{\omega}}\int_{(n-1)\tau}^{n\tau} D_B(t)\exp(j\hat{\omega}t)dt \tag{4.20}$$

where $\tau = T_{rev}/M$ and the dipole moment for the turn resides in the interval $[0, T_{rev}]$. The wide-feed back drive is

$$\hat{V}_{eff}(n) = \frac{\omega_r\tau}{2Q_{feed}}\left[f_-\hat{V}_{cav}(n-n_-) + f_+\hat{V}_{cav}(n-n_+)\right]\exp(-j\hat{\omega}T_d), \tag{4.21}$$

where $n_- \leq T_d/\tau \leq n_+$ bound the true delay, Q_{eff} is the quality factor associated with feedback and $f_- = n_+ - T_d/\tau = 1 - f_+$. For the notch filters there are two stages of processing. First, the notches are formed

$$\hat{V}_\pm(n) = (1-\epsilon)\hat{V}_\pm(n-M)\exp(\mp j2\pi Q_x) + \epsilon\hat{V}_{cav}(m-K)\exp(\mp j2\pi Q_x), \tag{4.22}$$

where $K < M$ is an input delay, ϵ controls the width of the notch, and Q_x is the betatron tune. Next a low pass filter is applied.

$$\hat{V}_{notch}(n) = \frac{1}{1+\alpha_{notch}}\left\{\frac{\omega_r\tau}{2Q_{feed}}G_{notch}(\hat{V}_+(n) + \hat{V}_-(n)) + \alpha_{notch}\hat{V}_{notch}(n-1)\right\}, \tag{4.23}$$

where G_{notch} is the notch filter gain and α_{notch} controls the bandwidth of the notch filter. With all the various inputs defined the cavity voltage is updated via

$$\hat{V}_{cav}(n) = \exp[j(\omega_r - \hat{\omega})\tau - \alpha\tau]\hat{V}_{cav}(n-1) - \hat{V}_{eff}(n) - \hat{V}_{notch}(n) + \hat{V}_B(n). \tag{4.24}$$

The voltage is applied using linear interpolation. For particles in interval $[(n-1)\tau, n\tau]$ this is $V_x(t) = Re[(f_-V_{cav}(n-1) + f_+V_{cav}(n))\exp(j\hat{\omega}t)]$ where t is the particle arrival time and $f_- = n - t/\tau$. After the forces are updated one shifts $\hat{V}(n) \to \hat{V}(n-M)$ and the process is repeated.

The feedback system for the CCs is operating whenever beam is present. Just before collisions begin the cavities are brought up to voltage. Before that they are on with a setpoint of zero. The effective transverse impedance for all eight CCs at proton injection is shown in Figure 4.21. The Fourier transform of the voltage calculated using TRANFT with delta function excitation is compared with analytic formulas from [**?**]. Note that the peak of the impedance is above the nominal harmonic number since the revolution frequency at injection is less than the revolution frequency at store and the resonant frequency of the crab cavity does not change. During the ramp the notches for the betatron lines will shift smoothly keeping the impedance low.

parameter	value
protons/bunch	$N_p = 2.8 \times 10^{11}$
Lorentz factor	$\gamma = 25.37$
angular revolution frequency	$\omega_{rev} = 490940\text{s}^{-1}$
transition	$\gamma_t = 22.75$
betatron tunes	$Q_x = 29.23$, $Q_y = 30.25$
chromaticity	$\Delta Q_x/(\Delta p/p) = +0.5$
number of bunches	$N_b = 290$
voltage (h=315)	$V_{315} = 40$ kV
voltage (h=630)	$V_{630} = 20$ kV
rms bunch duration	$\sigma_t = 5.10$ns
rms energy spread	$\Delta E/E = 7.7 \times 10^{-4}$
β function at CCs	$\beta_x = 100$m
normalized rms emittance	$\epsilon_x = 3.0\,\mu$m, $\epsilon_y = 0.3\,\mu$m
space charge impedance	$< \beta_x Z_{sc,x} >= 1.00\text{G}\Omega$, $< \beta_y Z_{sc,y} >= 3.66\text{G}\Omega$
octupoles	$a_{xx} < J_x >= \pm 0.0112$, $a_{xy} < J_y >= \mp 0.0010$

Table 4.7: Simulation parameters for protons at injection. The space charge impedance corresponds to that for a constant density beam with the same rms radii as the actual beam.

Octupolar detuning is critical to maintain stability. The tune shift as a function of betatron action is $\Delta Q_x = a_{xx} J_x + a_{xy} J_y$. For the parameters in Table 4.7 both signs of the octupolar detuning lead to horizontal stability when simulated over 20,000 turns at injection. To test boundaries we increased $\beta_x Z_x$ for the crab cavities by a factor of 5. In this case one needed $a_{xx} < J_x >= +0.0112$ for the beam to be stable. With the other sign the beam was unstable. Figure 4.22 shows the horizontal offset as a function of longitudinal position for the first bunch in the train for the unstable beam. The blue dots show the 6000 macroparticles used in the simulation and the red trace is the smoothed offset of the bunch centroid. More than one coupled bunch mode went unstable. This can be seen in Figure 4.23. If only a single coupled bunch mode went unstable then the voltage would correspond to a single frequency and the heterodyned amplitudes, V_c and V_s would be purely sinusoidal. Given the safety margin we close this discussion concluding that instabilities due to the crabbing mode will be passively damped at injection.

While the crab cavities do not lead to coherent instabilities, noise in the RF system leads to long term emittance growth. Noise in the vicinity of the betatron sidebands is particularly dangerous. Specifications for noise levels in the CC RF system are very tight but in addition an active horizontal feedback system to damp any small residual kicks is planned [**?**, **?**].

The higher order modes in the crab cavities and the other RF cavities might also lead to instabilites....

4.1.5 Electron-ion instability in ESR

Beam-ion instability is one of a few collective effects in the ESR which is not driven by the impedance but by the residual ions in the vacuum chamber. This instability was predicted [**?**] to be of concern to the ESR because any coherent motion of the electron beam will be imprinted into ions in the HSR, reducing the luminosity and increasing the detector backgrounds. For accurate instability threshold predictions, the simulations must include all relevant physics, such as the

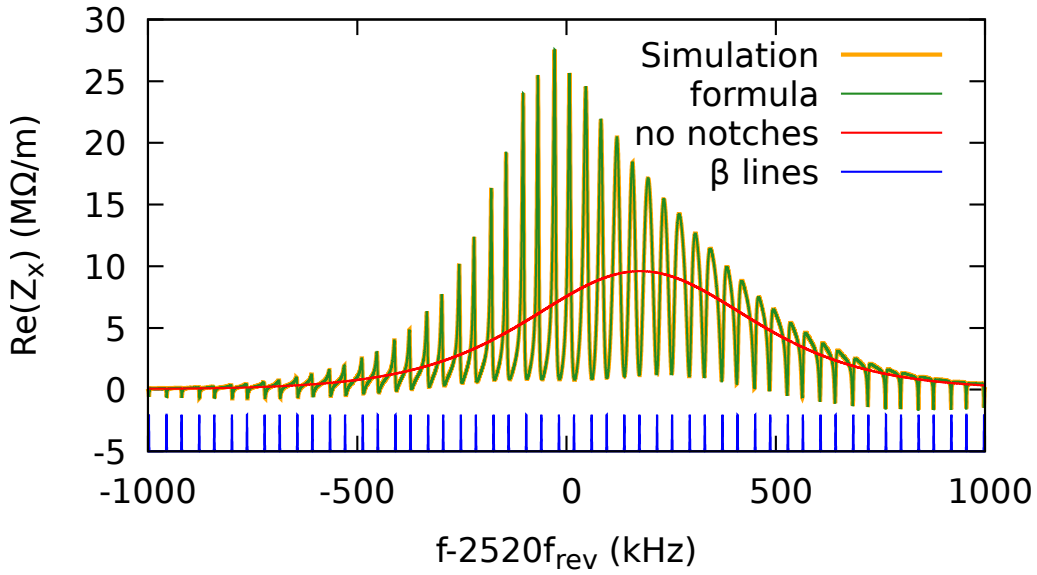

Figure 4.21: Transverse resistance for eight crab cavities. The yellow curve shows the impedance calculated within the simulation code using the algorithm planned for the actual machine. The green curve, which overlies the yellow one, is the impedance calculated using the analytic formula in [**?**]. The red curve shows the impedance one gets by turning off the notch filters. The blue lines show the locations of the betatron sidebands.

beam-beam-induced tune spread, the actual ring lattice, realistic fill pattern, multiple ion species, etc. Some features of the ESR, especially the long bunch train, large circumference, and large variation of beta functions, make these simulations extremely computer-intensive and require parallel computations.

The parallel version of Elegant [**?**] is especially well-suited for these simulations because its instability modeling was extensively benchmarked against other codes and experimental observations. However, applying this code to the ESR had only become possible recently, after the new BEAMBEAM element was added to the code. This element allows one to introduce the appropriate amount of transverse tune spread in the electron beam, which would normally come from the beam-beam interaction. This tune spread, in turn, allows for accurate modeling of the Landau damping, which provides significant instability suppression. After some debugging and cross-checking studies, it was confirmed that beam-ion instability simulations with BEAMBEAM provide reliable results. Detailed simulations for the ESR confirmed the original concern about the instability at the predicted residual ion pressure.

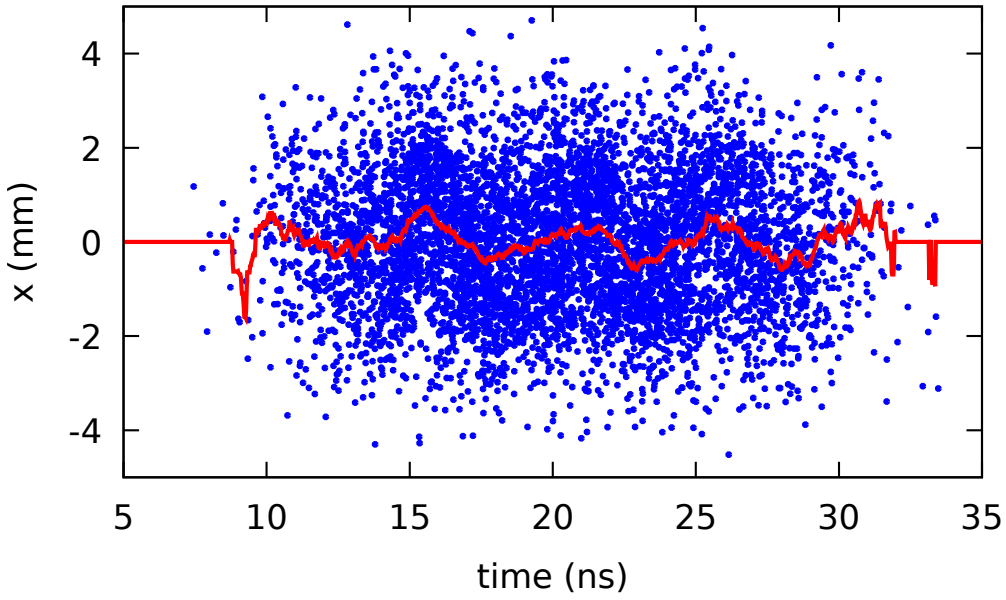

Figure 4.22: First of 290 bunches for unstable beam at injection. The value of $\beta_x Z_x$ was five times nominal and the octupolar detuning had $< a_{xx} J_x >$ = -0.0011

The need to suppress this instability motivated, at least partially, the updated ESR vacuum system design. The present design has greatly expanded the use of NEG coating throughout the ring. This resulted in at least a factor of 5 reduction in the expected ring-average residual ion pressure, from 5.6 nTorr to 1.12 nTorr.

At these pressures, simulations with Elegant and other analyses performed to date predict stability for colliding beams. This is very different from the results obtained for the previous vacuum system design, where strong instabilities were predicted. This is illustrated in Fig. (4.24), which shows that at 5.6 nTorr and higher ion pressures, there is a strong instability-induced peak centered on the ion oscillation frequency. In contrast, at the pressure corresponding to the new vacuum system design, there is no instability-induced peak, and the residual beam oscillations are statistically indistinguishable from the case without ions.

Additional studies included driven beam oscillations, when below the instability threshold but still under the influence of collective forces. While these forces increase the amplitude of the residual beam oscillations, it was confirmed to be comfortably small, at least for the shot noise excitation.

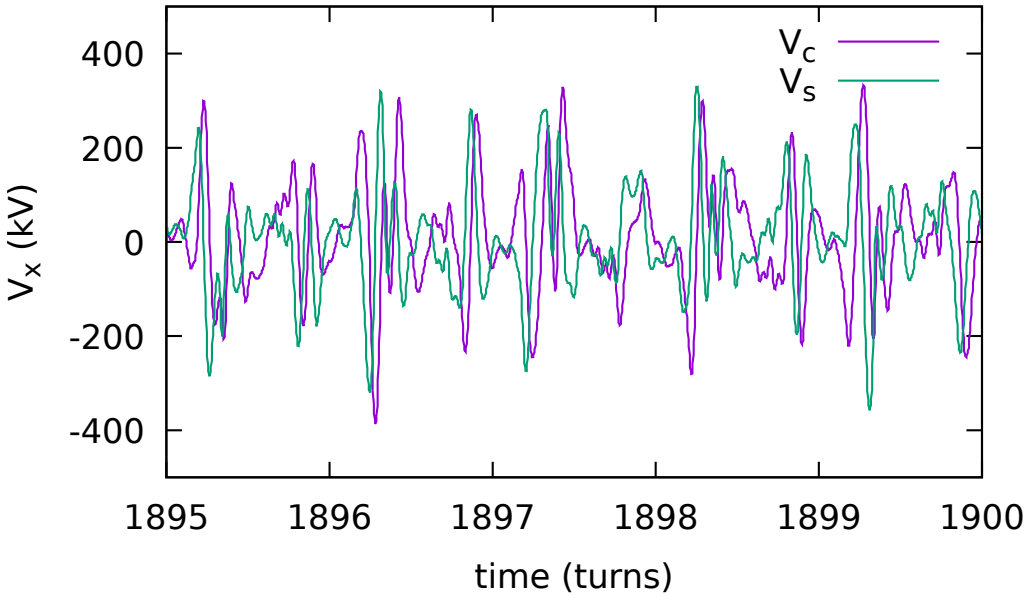

Figure 4.23: Crab cavity voltage during the last 5 turns of the simulated instability. The actual transverse voltage is $V_x(t) = V_c(t)\cos(\hat{\omega}t) + V_s(t)\sin(\hat{\omega}t)$ with $\hat{\omega} = 2520\omega_{rev}$

.

4.1.6 RF beam physics

Bunch splitting Simulation in HSR

4.8.

Parameters	Symbol	Value
Intensity	N_p	$6.9e^{10} * 4$
Bunch Length	σ_z[m] / [ps]	0.75 / 2.5
Bunch Number	N_b	290
Energy	E [GeV]	275
Energy Spread	δ_p / p	$2.0e^{-4}$
Slip Factor	a_c	$1.8e^{-3}$

Table 4.8: Bunch parameters used in bunch splitting simulations

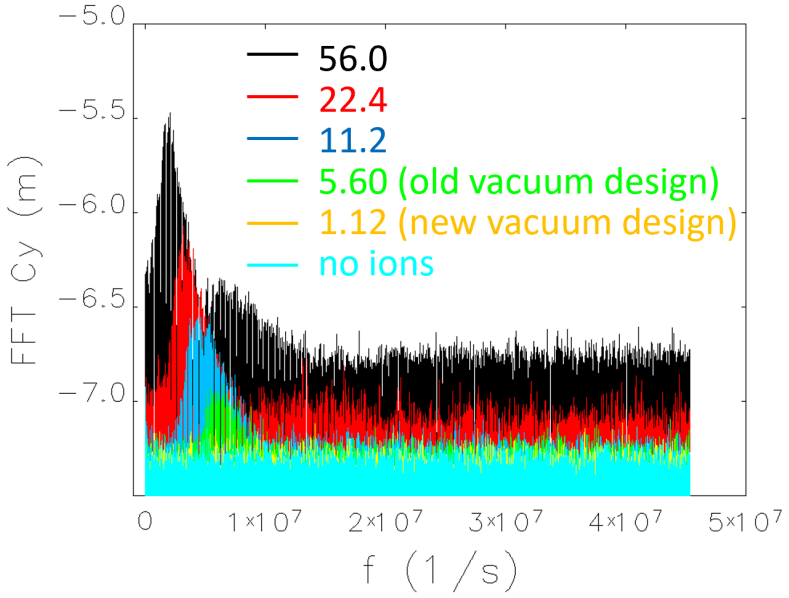

Figure 4.24: FFT (log scale) of the vertical beam centroid at the IP at several residual ion pressures for the nominal 1160 bunch fill at 10 GeV. The pressures are marked in the legend in nTorrs.

According to the EIC design parameters, the number of bunches in the HSR at 275 GeV is 1160. Injection and acceleration will be performed with 290 bunches. At 275 GeV storage mode, the bunches will be adiabatically split in two steps/stages, from 290 bunches into 580 bunches, then again from 580 bunches into 1160 bunches.

These bunch splittings involve manipulating various harmonic RF systems, such as combining fundamental and higher harmonic RF systems, to alter the bunch structure, and intensity within a high-intensity synchrotron ring. For example, splitting one bunch into two bunches (1:2 bunch splitting) is obtained using simultaneously some RF fundamental (m=1) cavities and some second order (m=2) harmonic RF cavities.

To implement this method for EIC HSR, hadron bunches in HSR will be captured and accelerated to 275 GeV with an RF system of operational frequency of 24.6 MHz (h=315). Therefore, to optimize bunch train formation for maximum luminosity as required above, a two-stage two-fold bunch split scheme (1:2:4) will be implemented to adiabatically split the hadron bunches into four bunches. This will require another two normal-conducting bunch splitting cavities at 49.3MHz (h=630) and 98.5MHz (h=1260). The cavity parameters used in the paper are presented in Table 4.9.

Figure 4.25 illustrates the result of the bunch split without beam-loading effects. The top left figure shows the initial longitudinal centroid position of the 290 bunches (580 after splitting). No longitudinal beam position deviation is observed. The middle left plot displays the induced voltage from the two cavities, which is 0 due to the absence of beam current. The bottom left plot depicts the voltage evaluation during the voltage ramp for these two cavities.

The top right and middle right plots present the phase space and macro-particle number of the two small bunches after splitting from the initial bunch and the last bunch in the bunch train. We observe that after bunch splitting, the bunches are evenly split into left and right small bunchlets,

Cavity	Parameters	Value
$m = 1$	Q	14000
	Q_L	4700
	RoQ	42
	h	315
	Phase [degree]	180
	Frequency [MHz]	24.8
	Total Voltage [MV]	0.10 (0.15)*4
	Cavity Quantity	4
$m = 2$	Q	12200
	Q_L	3350
	RoQ	26.2
	h	630
	Phase [degree]	0
	Frequency [MHz]	49.2
	Total Voltage [MV]	0.25*2
	Cavity Quantity	2
$m = 4$	Q	9500
	Q_L	2780
	RoQ	28
	h	1260
	Phase [degree]	0
	Frequency [MHz]	98.6
	Total Voltage [MV]	0.2*3
	Cavity Quantity	3

Table 4.9: RF cavity parameters used in bunch splitting simulations

with their macro-particle numbers being very close. The bottom right plot illustrates the energy spread distribution of the first and last bunches at 80k turns.

However, there are two critical issues during these bunch-splitting processes for the high-intensity beam in HSR which may affect luminosity significantly. First, the RF parameters should be optimized to keep a minimum longitudinal emittance growth during the bunch splitting. Second, the beam loading effect should be considered because of the high-intensity beam in HSR. The beam loading effect tends to make the bunch-splitting process asymmetric, which will result in two unequal bunch intensities.

To address the first issue which is to have a minimum longitudinal emittance growth, the cavity voltages and their ramp times are optimized via particle tracking studies. To address the second issue, which is to keep the split bunches equal or uniform particle partition, the phase of these two harmonics RF cavities should also change accordingly.

Therefore, to find a good adiabatic condition during the bunch split and to simulate the beam loading effect caused by significant high beam intensity during the bunch splitting, two Python codes named mbtrack2 and BLonD are employed for this study.

Figure 4.26 depicts the three modes of RF cavity voltages as the function of simulation turns during

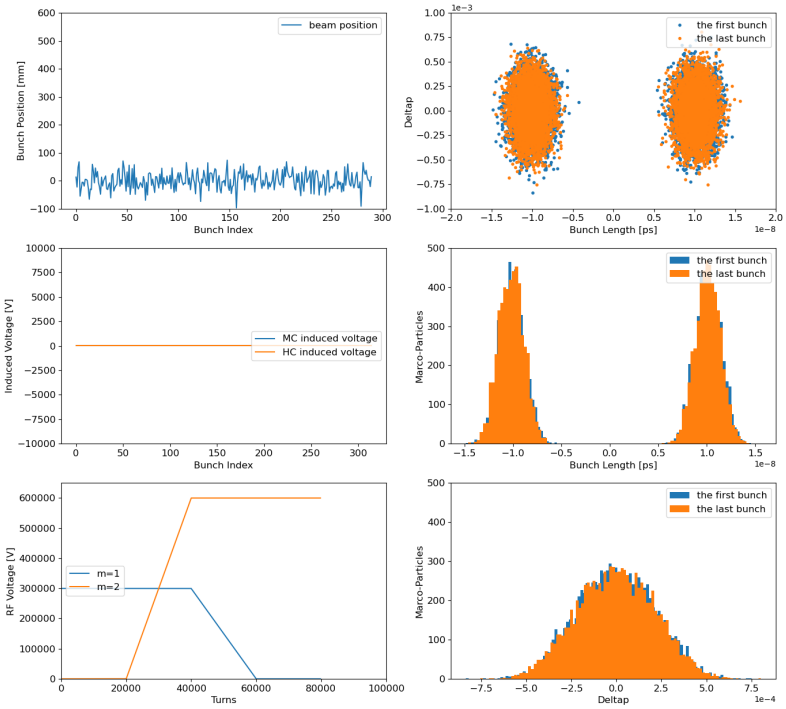

Figure 4.25: Bunch splitting without beam loading, with 24 Mhz and 49 MHz Cavity.

the two stages bunch split simulation. The horizontal axis represents the number of revolution turns in the HSR. T_1 and T_2 are the ramp time of the 49.2 MHz and 98.6 MHz cavities, while V_1, V_2, and V_3 are the cavity voltages of the 24.8 MHz, 49.2 MHz, and 98.6 MHz cavities. Meanwhile for the cavity voltage ramp, from Fig. 4.26, one can find that all three cavities ramp separately. That means, only one of the three cavities ramps up or ramps down voltage while the other two cavities's voltage keeps constant.

Figure 4.27 depicts the split longitudinal emittance as a function of ramp time T_1 (top plot) and T_2 (bottom plot) for the first and second stage respectively. From Fig. 4.27, one can find that to have a minimized emittance growth, the ramp time T_1 should be greater than 50 thousand turns which is about 0.64 second, while the ramp time T_2 in the second stage should be greater than 30 thousand turns which is 0.38 second.

The three cavity voltages also play an important factor during the two-stage bunch split. To evaluate the effects of the cavity voltages on the longitudinal emittance, they are scanned for the two stages bunch split separately. Figure 4.28 depicts the split longitudinal emittance as a function of cavity voltage V_1 and V_2 during the first stage of bunch split. One can find that with the voltage of 24.8 MHz cavity voltage $V_1 = 0.32$ MV, the longitudinal emittance can have a minimum emittance. While the voltage of 49.2 MHz cavity voltage V_2 seems to have less effect on the emittance growth during the first stage bunch split.

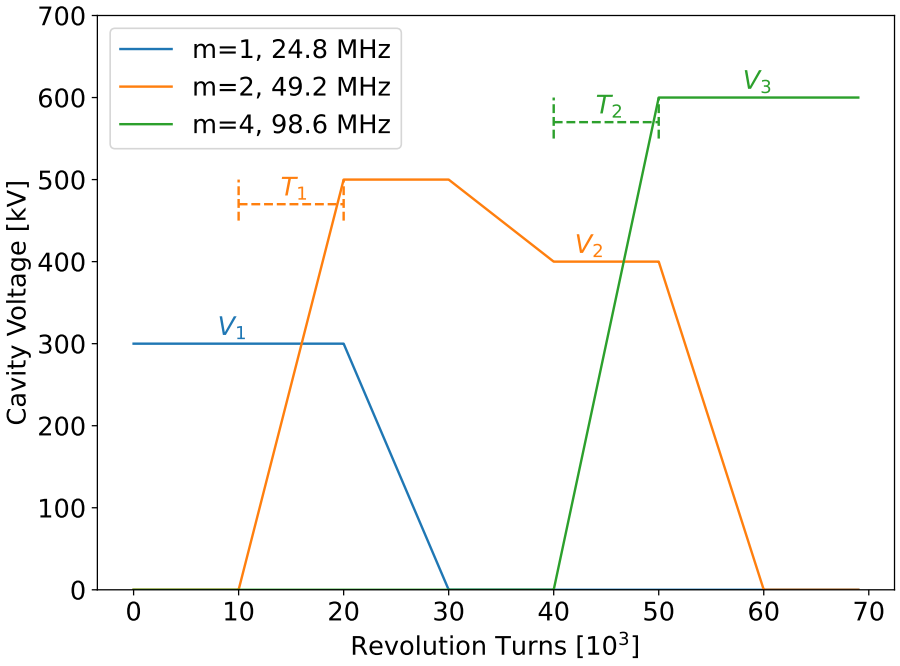

Figure 4.26: Cavity voltage as function of turning number during 1-to-2 bunch splitting.

During simulation, we assume that the cavities could have a feedback system, and the Q for all cavities can be reduced to $\frac{1}{300}$ of their initial value, or the feedback loop gain factor $f_{max} = 300$.

After simulation, one proton bunch is split into two bunches, as shown in Fig. 4.30. The top plot of the figure displays the phase space of the first (blue) and last (orange) bunches, while the bottom plot illustrates the macro-particle count for these two bunches after splitting. Examining the bottom figure in Fig. 4.30, we notice that after splitting, the number of macro-particles in the left and right bunches differs for the first and last bunches in the 290 bunch train. The right bunches contain more macro-particles than the left bunches.

Referring to the top figure in Fig. 4.30, we can determine the bunch length and energy spread after splitting for the left and right bunches for all the bunches along the 290 bunch train.

The top plot of Fig. 4.31 displays the split bunch lengths (left and right, after splitting) as a function of the index of bunches (before splitting) in the bunch train. We observe that the bunch lengths for the left and right bunches post-splitting are very close, showing no significant differences.

The bottom plot of Fig. 4.31 shows the macro-particle number for the split bunch lengths (left and right) as a function of the index of bunches in the bunch train. We note a disparity in the macro-particle bunch numbers between the left and right bunches (4800 vs. 5200), especially evident in the initial 50 bunches prior to the 290-bunch splitting.

Figure 4.29 depicts the split longitudinal emittance as a function of cavity voltage V_2 and V_3 during the second stage of bunch split. The longitudinal emittance can have a minimum emittance with $V_2 = 0.425$ MV. Similar to the first stage of bunch split, the voltage of 98.6 MHz cavity voltage V_3 has less effect on the emittance growth during the second stage of bunch split.

To mitigate this uneven distribution of macro-particles, attributed to the beam loading effect, opti-

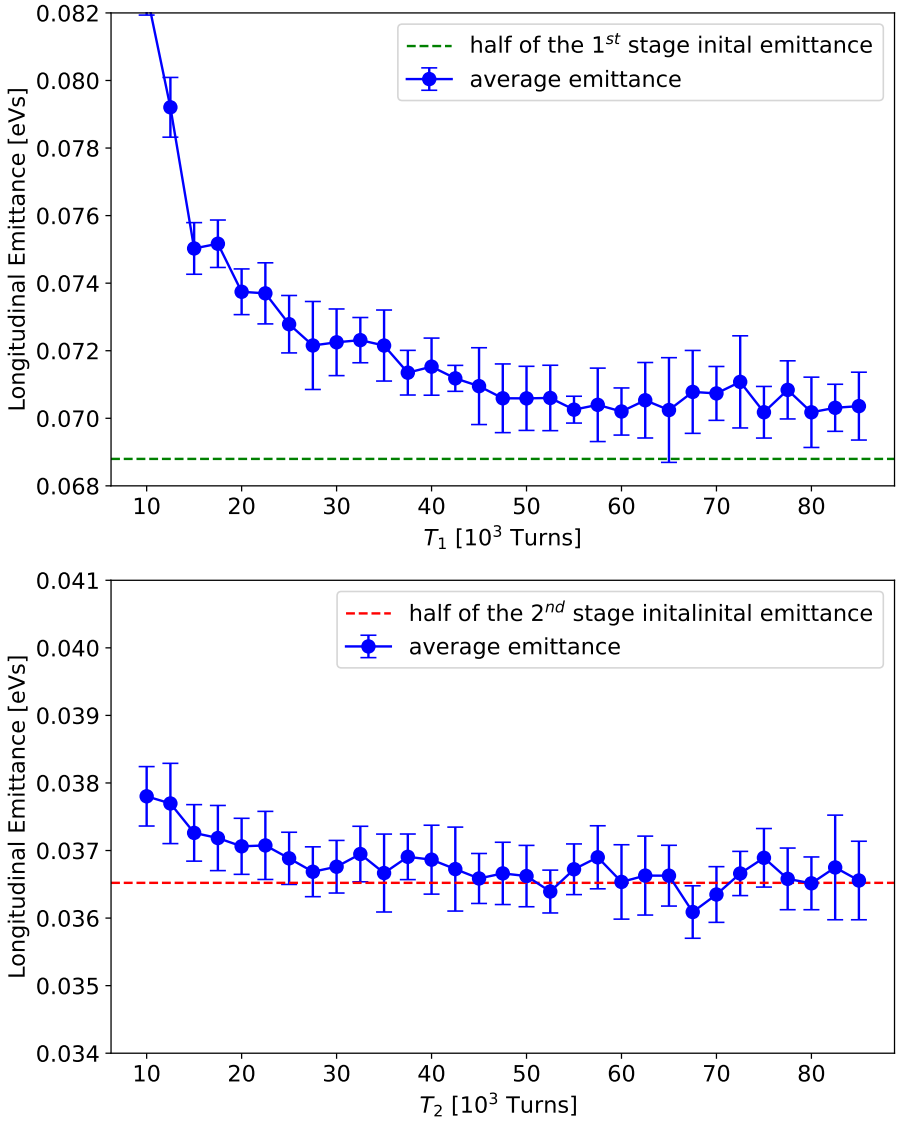

Figure 4.27: Longitudinal emittance as function of ramp times T_1 and T_2.

mization could be pursued using phase adjustments for the fundamental cavity. Figure 4.32 illustrates how different fundamental RF cavity phases can affect the macro-particle ratio between the left and the right bunches after splitting.

With a phase adjustment of 0.2 degrees, Fig. 4.32 (the top right plot) shows that the macro-particles in the left and the right bunch are very close, indicating an even splitting for the bunches in the later part of the bunch train. However, the bunches at the beginning of the bunch train, they are still split unevenly.

Meanwhile, in Fig. 4.32, the bunch length, energy spread, and emittance are also plotted for the right and left bunches.

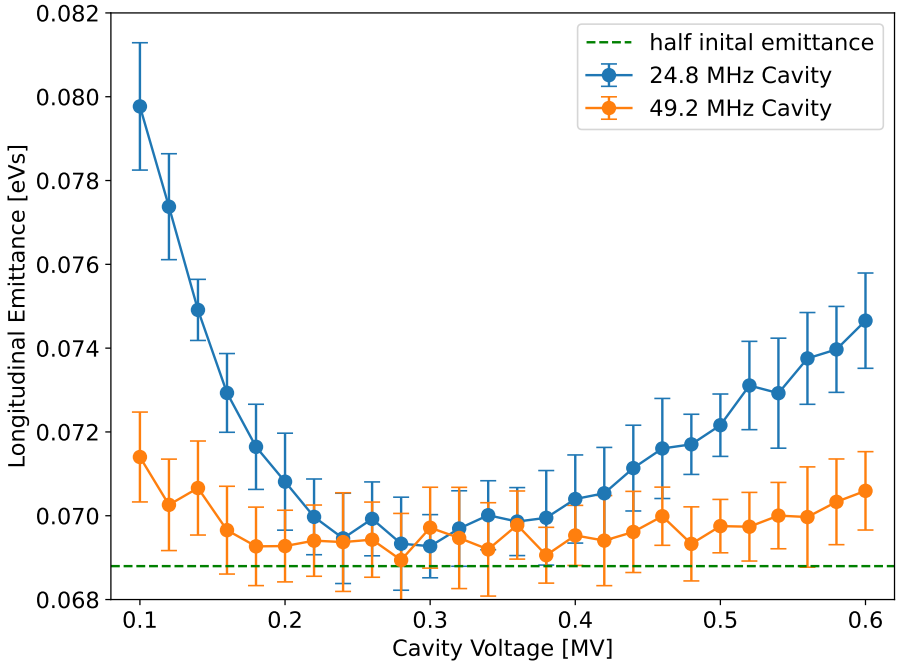

Figure 4.28: Longitudinal emittance as function of cavity voltage for $m = 1$ and $m = 2$.

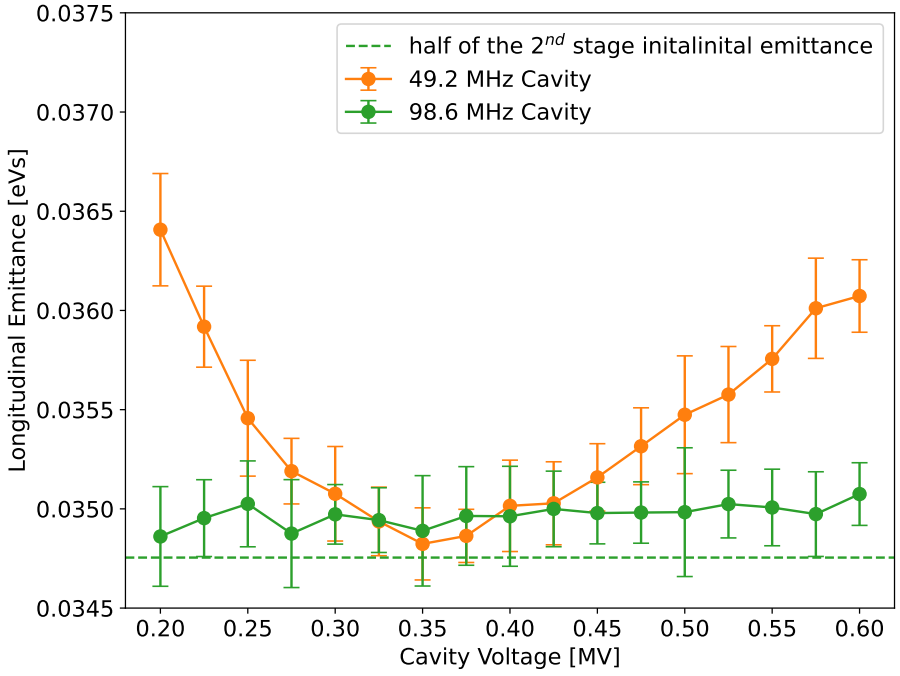

Figure 4.29: Longitudinal emittance as function of cavity voltage for $m = 2$ and $m = 4$.

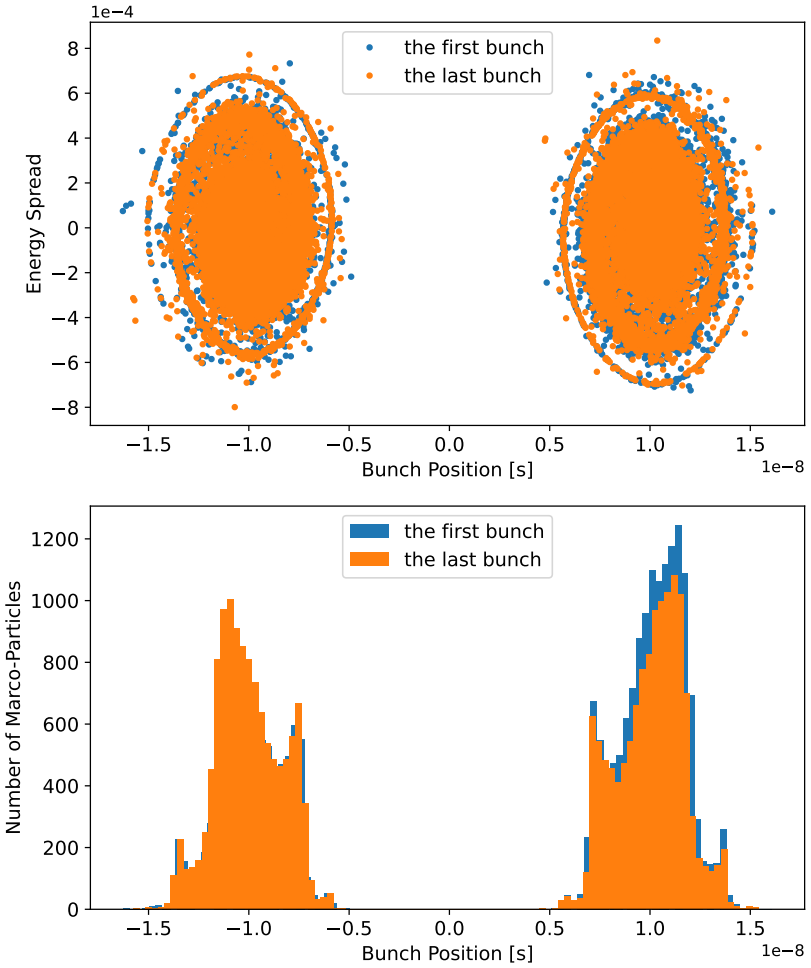

Figure 4.30: longitudinal bunch position and Macro-particle distribution for the 1 to 2 bunch Split with 24 Mhz and 49 MHz Cavity.

To mitigate this uneven distribution of macro-particles, attributed from the beam loading effect, optimization can been pursued using both cavity voltage and phase adjustments for the fundamental cavity.

The Reverse Phase Configuration in ESR

The ESR of the EIC requires a high-power (∼10 MW power) RF system to compensate losses due to synchrotron radiation and beam-induced wakefields for the 2.5 A average current or $M = 1160$ bunches. With the RF voltage of VRF =12 MV at 5 GeV and VRF =24 MV at 10 GeV, the required

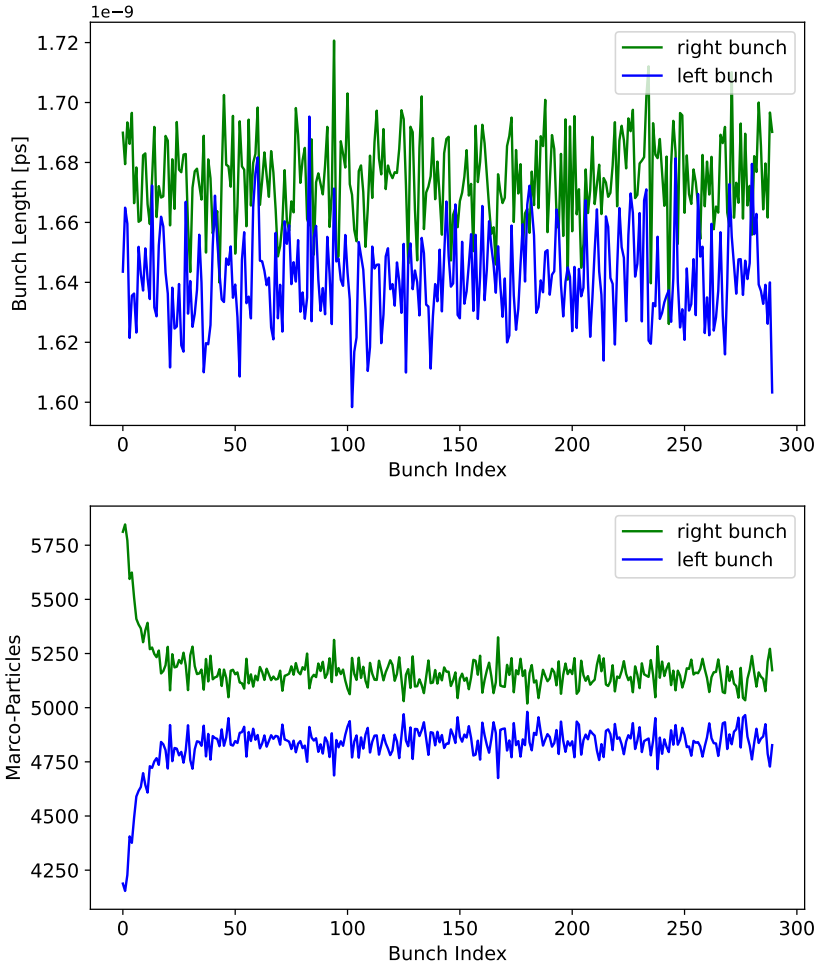

Figure 4.31: Bunch Length and Macro-particle as a function of the bunch index for the 1 to 2 bunch Split with 24 Mhz and 49 MHz Cavity.

detuning frequency becomes so large that the beam can be Robinson unstable. To avoid this issue, the concept of the reversed phasing RF system is considered as a viable option for stable beam operation. It is a well-known concept, when two groups of cavities are set up with the same RF cavity voltage and different synchronous phases. Experimentally, the RF system with the reversed phasing was tested with a beam in KEK B-Factory [**?**] and no issues during operation were found.

The ESR RF system with reversed phasing is simulated via Elegant and mbtrack2 code, using the lattice version of 5.3 at 5 GeV energy. This study provides valuable insights into the feasibility and effectiveness of the reversed phasing RF system for stable beam operation in the ESR at the EIC. The full beam dynamics results, including energy spread, bunch length, and centroid offset as a function of bunch number in the train are presented here.

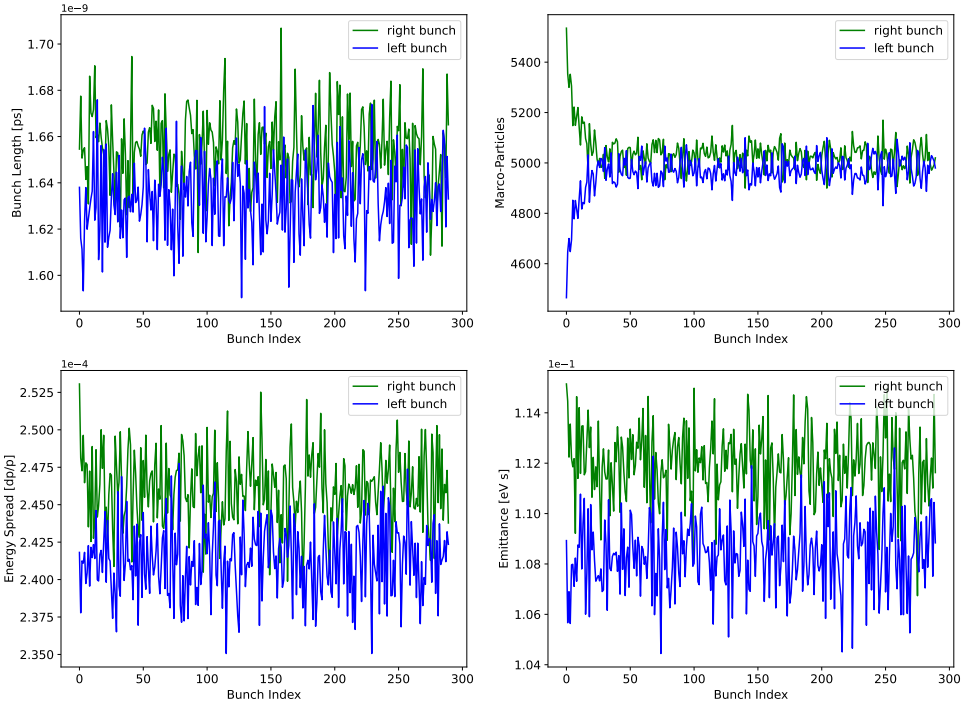

Figure 4.32: Bunch Length and Macro-particle ratio (between right and left) as a function of the bunch index for the 1 to 2 bunch Split with Beam Loading.

The main electron beam and the RF system parameters are listed in Table 4.10 and Table 4.11. The beam parameters are related to the 5.3 lattice version. With the updated parameters, the RF system with 10 focusing and 7 defocusing cavities has been simulated. The detune frequencies are much lower than the revolution frequency $f_0 = 78.194kHz$ with a counter phasing scheme. The total number of macroparticles used in ELEGANT is 5k. The results of the particle tracking simulations are presented in Figs. 4.33. The bunch length dependence has a parabolic shape (Fig. 4.33). The bunches at the end of the train have a significantly larger length than the bunches early in the train. The time evolution of the bunch of centroids shows something close to a cotangent behavior along the train with their zero offset in the middle of the train. The energy spread $\sigma_\delta(M_i)$ dependence on the number of bunches looks a bit noisy due to a less number of macroparticles used during the simulations, but we don't observe an explicit parabolic dependence as in the case of the bunch length. The present simulations have been performed with the RF system only, including the RF cavity impedance. Since the bunch length is varied along the train, it may affect the Robinson threshold with the presence of the beam-induced wakefields and impedances (leading to a tune shift). The minimum bunch length in the middle of the train is $\sigma_s \approx 6mm$. The bunch length spread in the train is $\sim 1mm$.

By employing the parameter setup as presented in Table 4.12 for the 10 focusing cavities and 5 defocusing cavities, we can obtain the bunch length distribution, bunch longitudinal position, and energy spread along the bunch train with such reverse phase configuration.

Energy, E_0	5	GeV
Average Current, I_0	2.5	A
Momentum Compaction, α_c	1.33e-3	
Number of Bunches, M	1160	
Energy Loss per turn, U_0	0.95	MeV
RF Voltage, V_{RF}	10.1	MV
Bunch Length, σ_s	6.8	mm
Energy Spread, σ_δ	5.16e-4	

Table 4.10: Main Electron Storage Ring beam parameters (lattice v5.3).

Number of focusing & defocusing cavities	10 & 7	
RF Frequency, f_r	591.150	MHz
Quality Factor, Q	334364	
R/Q	37	
Voltage per Cavity, V_c	3.35	MV
Synchronous Phase, φ_s	179.05&0.95	deg
Detune Frequency (foc.)	-16240	Hz
Detune Frequency (def.)	16240	Hz
Total Cavity Voltage of foc. & def. cavities, $V_{c,tot,foc}$ / $V_{c,tot,def}$	33.52 & 23.47	MV
Total Generator Voltage of foc. & def. cavities, $V_{g,tot,foc}$ / $V_{g,tot,def}$	6.39 & 4.47	MV
Generator Phase of foc. & def. cavities, φ_g	158.1 & 21.9	

Table 4.11: Electron Storage Ring RF parameters.

Figure 4.34 presents the results of simulations with 290 bunches, 50k macro-particles, and 20k turns. The single cavity voltage is 3.35 MV, and the synchrotron phase is 88.86 degrees (178.86 degrees for cosine conversion).

The theoretical design values for bunch length and energy spread are indicated by the red solid lines in the figure. The bunch length is also evaluated using the equilibrium profile (represented by the red dashed line). The theoretical longitudinal bunch position for the two RF systems is calculated based on the equilibrium state formula. The energy spread is determined by the lattice itself.

The top plot of Fig. 4.34 shows that the bunch length exhibits an asymmetric parabolic shape for different bunch indices in a bunch train. The bunch length at the end of the bunch train is slightly larger than at the beginning. This result is consistent with the findings from the Elegant simulations above. The middle plot reveals that the centroid of the bunch train has a shift of 17.68 mm, displaying a linear distribution for the different bunches in the train. Additionally, the bunch energy spread is 5.5×10^{-4}, which is very close to the design value of 5.2×10^{-4}.

Similarly, the 12 focusing cavities and 6 defocusing cavities setup is also simulated and the results are shown in Fig. 4.35 and Fig. 4.36. Fig. 4.37 shows the bunch profile of the first bunch, the middle bunch and the last bunch in the bunch train and comparison between the mbtrack2 calculated equilibrium profile. The equilibrium profile agrees with the middle bunch very well.

From these plots, we observe that the simulated bunch length, longitudinal bunch centroid, and bunch energy spread closely match their theoretical values. Hence, we demonstrate that the mb-

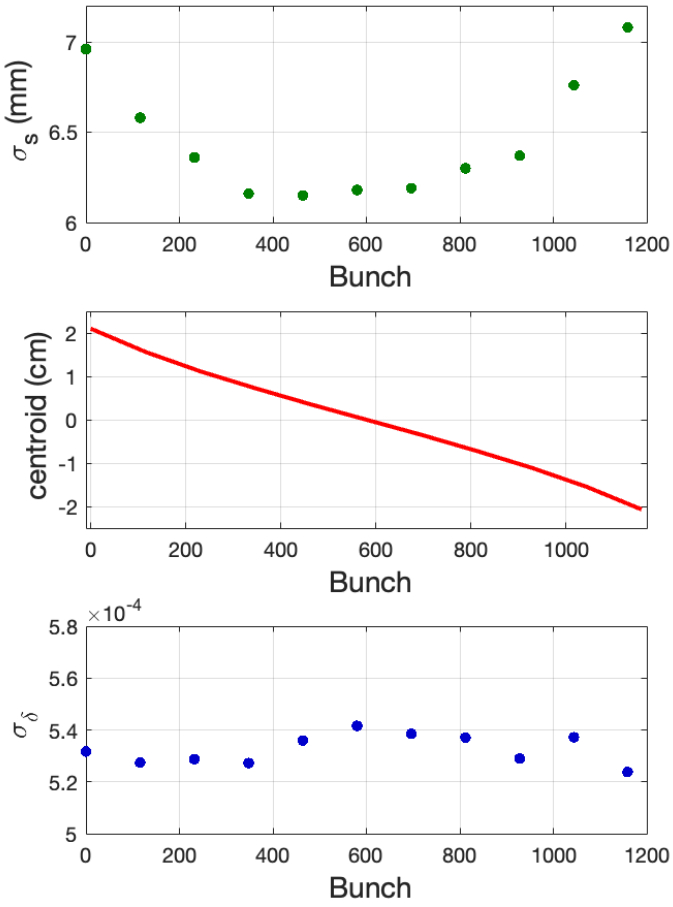

Figure 4.33: The bunch length σ_s (top), bunch centroid offset (middle) and energy spread (bottom) dependence on the bunch number M_i, $\sigma_s(M_i)$.

track2 code accurately simulates these parameters, including the beam loading effect.

Meanwhile, from Fig. 4.34 and Fig. 4.35, we can find the reverse phase configuration can be used for different cavity setup, in case of some cavity modules are off.

Parameter	10 Focusing Cavity	5 Defocusing Cavity
m	1	1
N_{cav}	10	5
Q	2e+10	2e+10
RoQ	37	37
$R_{s\_per\_cavity}$ [Ω]	7.4e+11	7.4e+11
R_s [Ω]	7.4e+12	3.7e+12
β	2.19784e+04	2.19784e+04
Q_L	9.09944e+05	9.09944e+05
R_L	33667928	33667928
$detune$ [Hz]	-1.63399e+04	1.63404e+04
f_c [Hz]	5.91134e+08	5.91167e+08
ω_c [rad/s]	3.71421e+09	3.71441e+09
ψ [deg]	-88.86	88.86
V_c [V]	3.35e+07	1.675e+07
θ_s [deg]	88.86	-88.86
V_g [V]	1.33158e+06	6.65788e+05
θ_g rad	1.80814e-06	-1.80829e-06
V_{gr} [V]	6.6997e+07	3.34985e+07
θ_{gr} [deg]	88.86	-88.86
V_b [V]	3.35e+07	1.675e+07
V_{br} [V]	1.68552e+09	8.42759e+08
P_g [W]	1.66657e+06	8.33285e+05
P_c [W]	7.58277e+01	3.79139e+01
P_b [W]	1.66649e+06	8.33247e+05
P_r [W]	2.51703e-10	9.43601e-12
n_{bin}	200	200
Filling time [s]	4.89980e-04	4.89953e-04
Loss factor [V/C]	6.87128e+11	3.43583e+11

Table 4.12: The initial 10F-5D reverse phase configuration RF parameters before mbtrack2 tracking

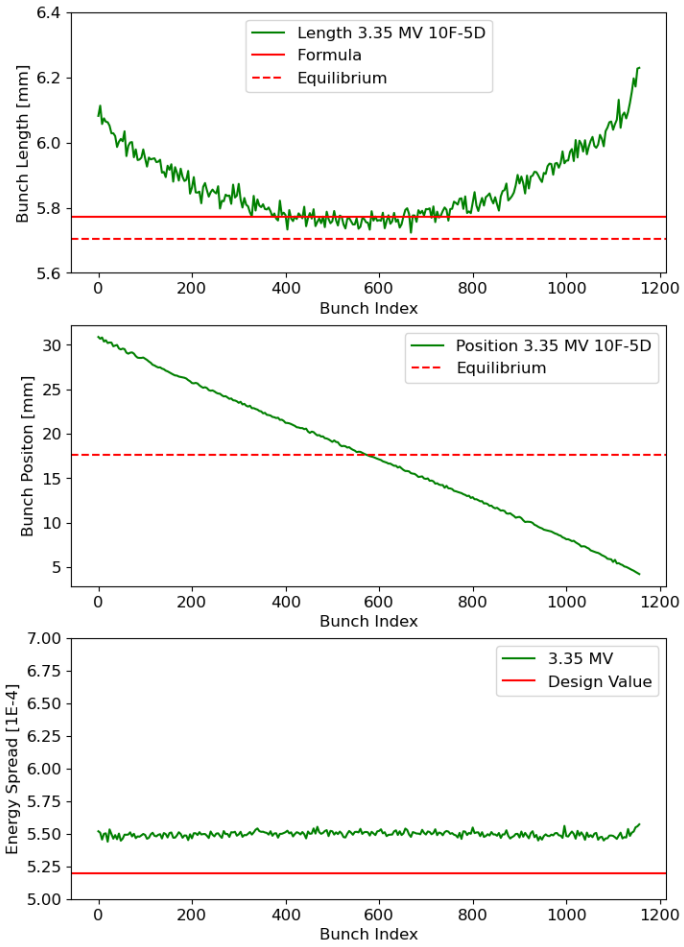

Figure 4.34: The bunch length (top), bunch position (middle), and energy spread (bottom) depend on the index of the bunch within a bunch train.

Parameter	12 Focusing Cavity	6 Defocusing Cavity
m	1	1
N_{cav}	12	6
Q	2e+10	2e+10
RoQ	37	37
$R_{s\_per\_cavity}$ [Ω]	7.4e+11	7.4e+11
R_s [Ω]	8.88e+12	4.44e+12
β	1.84899e+04	1.84899e+04
Q_L	1.08161e+06	1.08161e+06
R_L	4.80388e+07	4.80388e+07
$detune$ [Hz]	-1.63409e+04	1.63413e+04
f_c [Hz]	5.91134e+08	5.91167e+08
ω_c [rad/s]	3.71421e+09	3.71441e+09
ψ [deg]	-89.05	89.05
V_c [V]	4.02e+07	2.01e+07
θ_s [deg]	89.05	-89.05
V_g [V]	1.34427e+06	6.72135e+05
θ_g rad	1.80816e-06	-1.80840e-06
V_{gr} [V]	8.03957e+07	4.01978e+07
θ_{gr} [deg]	89.05	-89.05
V_b [V]	4.02e+07	2.01e+07
V_{br} [V]	2.40421e+09	1.20210e+09
P_g [W]	1.68246e+06	8.41228e+05
P_c [W]	9.09932e+01	4.54966e+01
P_b [W]	1.68237e+06	8.41183e+05
P_r [W]	-1.63610e-10	1.51026e-10
n_{bin}	200	200
Filling time [s]	5.82419e-04	5.82387e-04
Loss factor [V/C]	8.24554e+11	4.12300e+11

Table 4.13: The initial 12F-6D reverse phase configuration RF parameters before mbtrack2 tracking

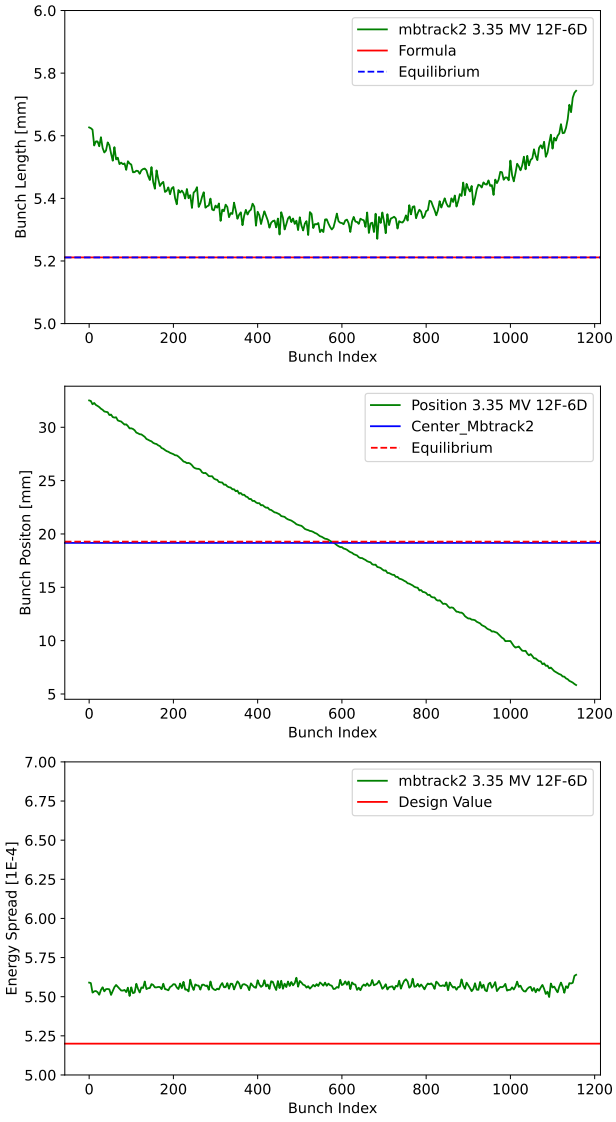

Figure 4.35: The bunch length (top), bunch position (middle), and energy spread (bottom) depend on the index of the bunch within a bunch train.

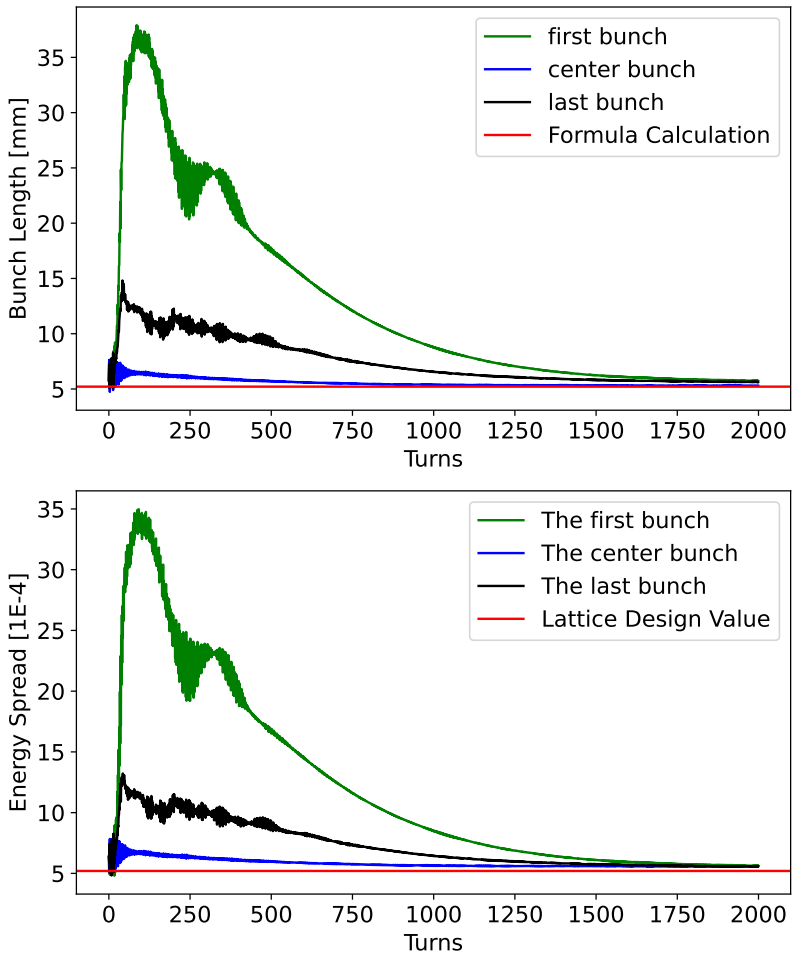

Figure 4.36: The bunch Bunch length, and energy spread as function of simulation turns.

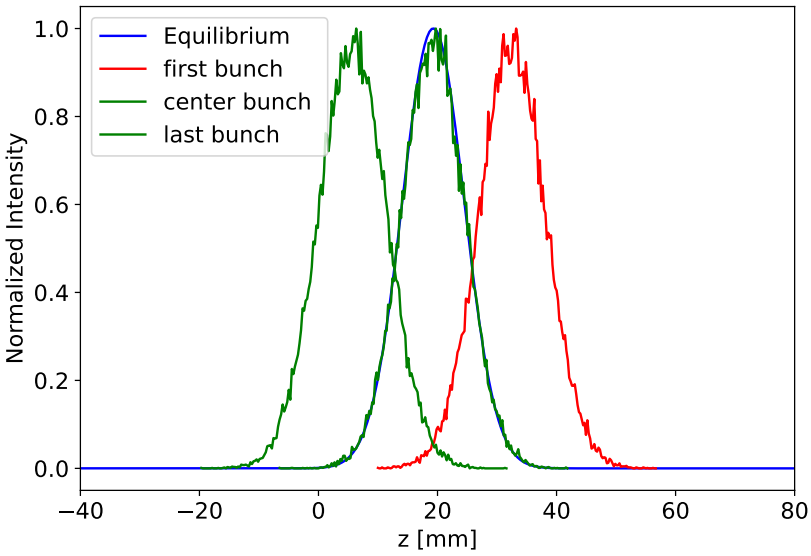

Figure 4.37: The bunch profile of the first bunch, the middle bunch and the last bunch in the bunch train and comparison between the mbtrack2 calculated equilibrium profile.

4.2 Dynamic Aperture in the Electron Storage Ring

4.2.1 High energy – 18 GeV

Dynamic aperture and sextupole configuration.

4.2.2 Low and medium energy – 5 (or 6) GeV to 10 GeV

Dynamic aperture and sextupole configuration.

4.2.3 Magnet multipole tolerances

quantity	unit	proton	electron
Beam energy	GeV	275	10
Bunch intensity	10^{11}	0.668	1.72
(β_x^*, β_y^*) at IP	cm	(80, 7.2)	(45, 5.6)
Beam sizes at IP	μm	(95, 8.5)	
Bunch length	cm	6	0.7
Energy spread	10^{-4}	6.8	5.8
Transverse tunes		(0.228, 0.210)	(0.08, 0.06)
Longitudinal tune		0.01	0.069

Table 4.14: Machine and beam parameters for the HSR dynamic aperture studies.

4.3 Dynamic Aperture in the Hadron Storage Ring

4.3.1 Introduction

Dynamic aperture studies are an essential tool in the design and operational tuning for proton and ion circular accelerators. They can contribute to the choice of design parameters, verify the long-term stability of a design, and be used to guide performance improvements.

The Hadron Storage Ring (HSR) of EIC will re-use the existing RHIC arcs. Based on RHIC operational experience **[?]**, simulated dynamic aperture in 10^6 turns with beam-beam interaction and IR nonlinear field errors should be larger than 5 σ with 3 $(dp/p_0)_{rms}$ to guarantee an acceptable beam lifetime at physics store. The beam-beam parameter for the proton beam in HSR is comparable to RHIC, therefore we require that the minimum dynamic aperture for the HSR should be larger than 5 σ for particles with 3 $(dp/p_0)_{rms}$.

The EIC will collider polarized high energy electron beams with hadron beams with luminosities up to $1 \times 10^{34}\text{cm}^{-2}\text{s}^{-1}$ in the center mass energy range of 20-140 GeV. We focus on the collision mode involving 275 GeV protons and 10 GeV electrons since at this collision mode both protons and electrons reach their highest beam-beam parameters in the EIC. Table 4.14 lists the beam-beam related design parameters for the HSR dynamic aperture study. The proton ring's working point is (0.228, 0.210). The RMS bunch sizes are (95um, 8.5um) at the interaction point (IP). (β_x^*, β_y^*) are (80 cm, 7.2cm) respectively.

Crossing Collision with Crab Cavities

There are a few new features for the HSR than the RHIC. First, the EIC adopts a full crossing angle of 25 mrad at IP. To compensate the geometric luminosity loss due to the crossing angle, crab cavities are used to tilt the proton and electron bunches in the $x - z$ plane by half of the full crossing angle to restore head-on collision condition. For the EIC, local crabbing scheme is adopted.

For dynamic aperture calculation, we assume that the electron bunch is rigid and it is perfectly crabbed. To simulate the crossing angle collision, we install crab cavities into the HSR lattice on both sides of IP. At IP, Lorentz Boost is used to transfer the coordinates of protons from the laboratory coordinate frame to a head-on collision frame, where the beam-beam kicks are applied. The electron bunch is split into 5 longitudinal slides in our studies. After beam-beam interaction, the co-

ordinates of particles are transferred back to the laboratory frame and continue element-by-element tracking through the rest of ring.

Radial Shifted Orbit

Another main feature of the HSR lattice is the radial shifted orbit. To match the revolution frequency of ESR, HSR needs to be able to adjust its path length, which is achieved with a radial shift orbit in arcs. The required path length change and average radial orbit shift vary at different collision energies. The radial shift orbit is created with a field deviation from the nominal design value by a fraction of $\Delta B/B_0$ to all the arc bending dipoles. However, the design orbit should always be centered in the interaction region.

With radial shift orbit, on-momentum design orbit will not go through the centers of arc main dipoles as most accelerators do. The phases of RF cavities, crab cavities should be synchronized with on-momentum particle. Also, due to the large radial orbit shift for some collision modes, we need to pay extra attention to the impacts of magnetic field errors in arc magnets, which is normally ignored in the RHIC dynamic aperture calculation.

Since the HSR lattice design with the radial shifted orbit is ongoing, their effects are not included in the following HSR dynamic aperture studies.

HSR Lattices

For the EIC design, it is recommended to accommodate two experiments or two interaction regions. For the HSR lattice design, lattice designs are grouped into two categories : one with a single interaction point at IP6, another with two interaction points at IP6 and IP8. In the following, we will focus on the HSR lattice with a single collision at IP6. The lattice design with two interaction regions is in progress. Its dynamic aperture studies will start when the lattices are ready.

The HSR will re-use some of existing RHIC arcs. Same as each ring of RHIC, the HSR contains six arcs made up of FODO cells. Each arc quadrupole has an adjacent sextupole, denoted by "focusing" or "defocusing" based on which types of quadrupoles they are adjacent to. The phase advances in each cell are approximately 90°, chosen to reduce the second order chromaticity and cancel the geometric resonance driving terms due to the arc sextuples. The sextupoles are powered together in interleaved "families," of which there are four per arc, two of focusing sextupoles and two of defocusing sextupoles. The arcs are connected by utility straights, and for these studies only one (IR6) contains an interaction region.

Based on the strong-strong beam-beam simulations, the tunes chosen for these dynamic aperture studies are $(28.228, 29.210)$. To correct chromaticity, we first use two sextupole families: all focusing sextupoles and all defocusing sextupoles have the same strengths. Chromaticity was corrected to be +1 in each plane. The resulting second order chromaticities are about $(40, -600)$, which from RHIC experience are acceptable. Figure 4.38 shows the off-momentum tunes as a function of the relative momentum deviation $\delta = dp/p_0$. For the EIC design, $3(dp/p_0)_{rms} = 2 \times 10^{-3}$, which is the horizontal range shown in that figure. The third order chromaticity clearly dominates the tune variation with momentum deviation, and will be corrected in the future.

Figure 4.39 shows the off-momentum $\beta^*_{x,y}$ as a function of relative momentum deviation. The β^* variation with energy is clearly dominated by the second order β^* variation with δ.

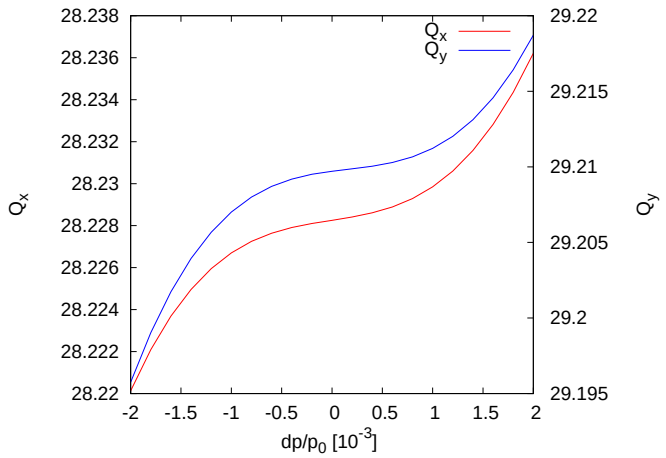

Figure 4.38: Off-momentum tunes Q_x, Q_y versus the relative momentum deviation δ, with 2 families of sextupoles.

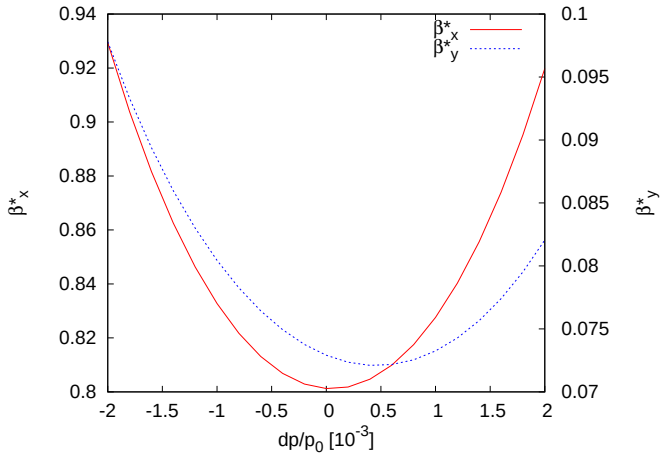

Figure 4.39: Off-momentum $\beta^*_{x,y}$ versus the relative momentum deviation δ, with 2 families of sextupoles.

Unclosed Crab Dispersion Bump

For the current version of the EIC HSR lattice, the horizontal phase advance between IP6 and the crab cavities are not exact 90 degrees. The phase advances between IP and crab cavities are about 87 degrees in the forward side and 88 degrees in the rear side in the IR6. The total phase advance between two side crab cavities is about 175 degrees, which is 5 degrees off 180 degrees. Therefore,

the crab dispersion bump is not locally closed in the interaction region IR6. The crab dispersion or dx/dz will introduce an additional horizontal offset which depends on the particle's longitudinal position from the bunch center. The particles with non-zero z will feel more nonlinear fields in the IR magnets and also in the arc sextupoles, which may reduce the proton's dynamic aperture.

Figure 4.40 shows the crab dispersion along the HSR ring due to the unclosed crab dispersion bump. The horizontal axis is the path length starting from IP6 and going in the clockwise direction. The design crossing angle at IP6 is 12.5 mrad. From the plot, the amplitude of the leaked crab dispersion in the arcs is about 5 mrad.

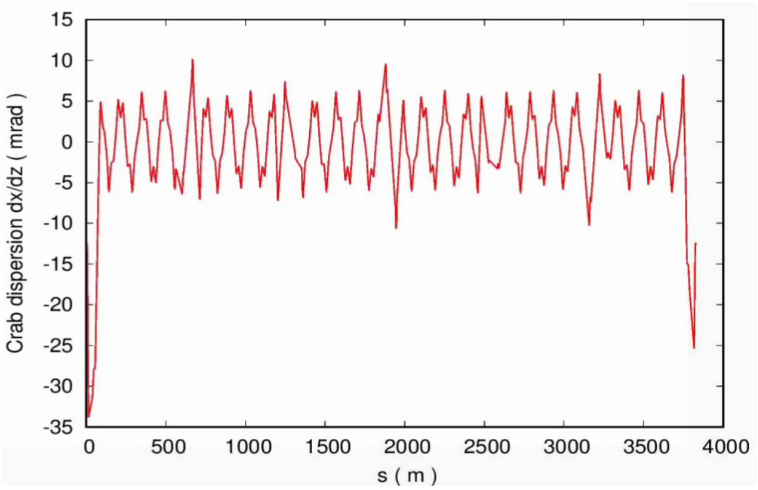

Figure 4.40: Crab dispersion along the HSR ring due to the unclosed crab dispersion bump in the interaction region.

IR Magnet Field Errors

Based on RHIC experience, IR magnetic field errors play an important role in dynamic aperture reduction. At the the EIC design phase, we will artificially assign high order field errors to all IR dipoles and quadruples within 160 m from IP6. Dynamic aperture calculations are used to evaluate the impacts of IR field errors on the dynamic aperture and to determine their tolerances.

Magnet field errors are defined as

$$(B_y L) + i(B_x L) = B(R_r)L\left[10^{-4}\sum_{n=0}^{N_{max}}(b_n + ia_n)\frac{(x+iy)^n}{R_r^n}\right]. \tag{4.25}$$

Here L is the magnet length, R_r is the reference radius where the magnetic field is measured, $B(R_r)$ is the main field at R_r, b_n and a_n are the normal and skew magnetic components. For dipoles, $b_0 = 10^4$. For upright quadrupoles, $b_1 = 10^4$. Components other than the design ones are field errors.

Both systematic and random field errors can be assigned in the tracking code. Here we focus on the random field errors. The random error distribution can be uniform or Gaussian. In the following dynamic aperture calculation, we mostly used uniform distribution due to the small number of IR magnets. Comparison between uniform and Gaussian distributions of field errors will be discussed later.

We ignored the allowed multipoles for dipoles and quadrupoles during the error assignment. From the actual measurements of IR magnets of the KEK-B factory, we did not see such strong correlations. Therefore, all orders of field errors will be assigned in the same way in our current dynamic aperture studies. For example, for an uniform distribution with 1 unit field errors, all orders of field errors up to 22th poles will be randomly assigned between -1 and 1. Of course, if we have a better knowledge of realistic EIC IR magnetic field errors in the future, we will incorporate those information into the field error assignment in our dynamic aperture studies.

For our previous dynamic aperture studies for the HSR, we set the reference radius 60 mm for all IR dipoles and 40 mm for all IR quadrupoles. With the progress in the EIC IR magnet design, we have more information on realistic reference radius. They will be applied in the future HSR dynamic aperture studied.

After installing magnetic field errors, we noticed sizable changes in the orbits and tunes. Orbit offsets at the interaction point IP6 and crab cavities should be avoided. We install 4 local beam position monitors and 4 dipole orbit correctors around IP to correct the orbits at IP and crab cavities. After that, we will re-match the lattice tunes to their design values. We then install the beam-beam interaction at IP and crab cavities. They are not included during above orbit and tune corrections due to the IR magnetic field errors.

Dynamic Aperture Tracking Setup

To evaluate the proton dynamic aperture, we use the symplectic particle tracking code SimTrack [**?**], which has been used for the dynamic aperture calculation for RHIC. It provides 6-D symplectic orbit tracking with 4th order symplectic integration for magnet elements and a 6-D symplectic synchro-beam map for the beam-beam interaction. RHIC studies indicated that 10^6 turns of tracking are sufficient for its dynamic aperture studies.

For each study condition, test particles are launched in the first quadrant of phase space (x/σ_x, y/σ_y) in 5 equidistant phase angles. Test particles are tracked up to 1 million turns. We search the minimum dynamic aperture in each direction of those phase angles by slowly increasing the test particle's initial amplitude step by step until the test particle gets lost in 10^6 turns. We focus on the minimum dynamic aperture found among all the phase angles. In the future, we plan to increase the tracking phase angles.

For each dynamic aperture calculation condition, 10 sets of random IR magnetic field errors are used in our current studies. More seeds will be used in the future dynamic aperture studies.

4.3.2 Dynamic Aperture Results

Without Magnetic Field Error

First we calculate and compare the proton dynamic aperture without any field error in the HSR lattice. Figure 4.41 shows the dynamic aperture in 5 phase angles with head-on and crossing angle collision with crab cavities. The proton's relative momentum deviation is 20×10^{-4}. In the plot, the dynamic aperture is larger close to 90 degrees in phase space. The reason is that the design vertical RMS beam size is about 10 times smaller than the horizontal one. Without magnetic field error, the minimum dynamic aperture among 5 phase angles is about 20 σ with head-on and crabbed collisions.

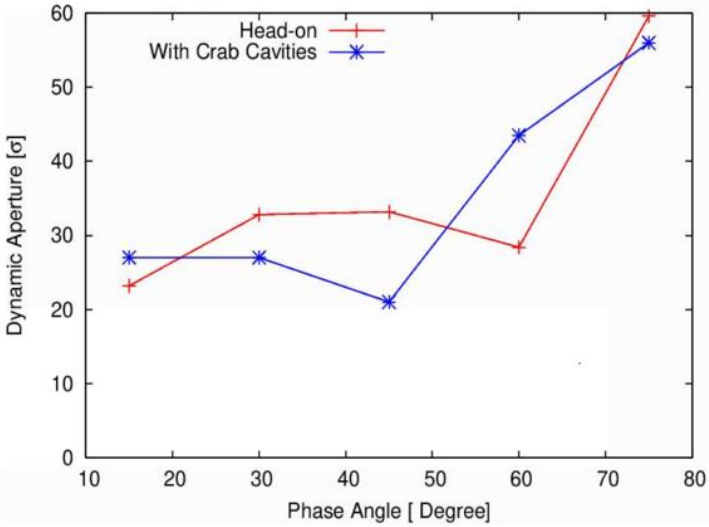

Figure 4.41: Dynamic aperture without IR magnetic field errors: head-on and crabbed collisions.

With Magnetic Field Errors

Figure 4.42 shows the dynamic aperture with beam-beam and with IR magnetic field errors. The shown dynamic aperture is the minimum dynamic aperture among 10 seeds in all phase angles. From the plot, the dynamic apertures for both head-on and crossing angle collisions decrease with increase in IR magnetic field errors. For 1 unit of magnetic field errors, the dynamic aperture with crossing angle collision is about 6 σ, which is sufficient for the proton beam's lifetime according to the RHIC operational experience. Currently we set the tolerances of nonlinear field errors for all orders below 1 unit for all the IR magnets in the HSR.

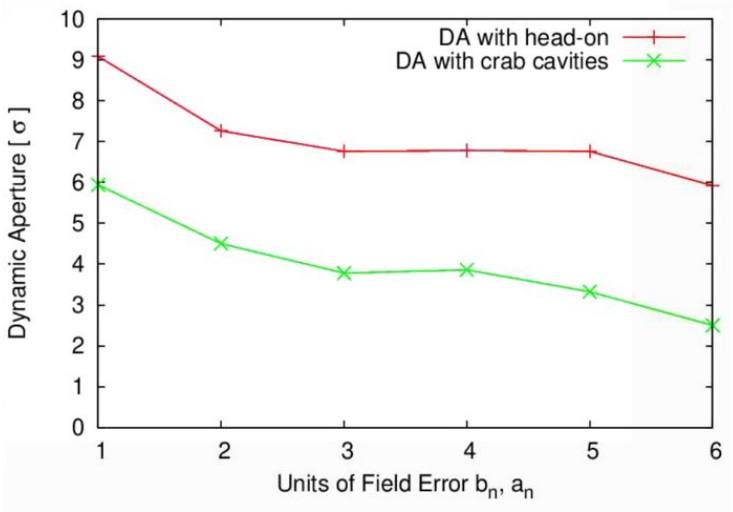

Figure 4.42: Dynamic aperture with the IR magnetic field errors: head-on and crabbed collisions.

Reason for DA Drop with Crossing Angle Collision

From the plot, we notice that there is about 3 σ drop in the dynamic aperture from head-on collision to crossing angle collision. In principle, head-on collision is restored with crab cavities. Figure 4.43 compares the dynamic apertures for head-on and crossing angle collisions without IR nonlinear field errors. The horizontal axis is the particle's relative momentum deviation from zero up to 20×10^{-4}. From the plot, there are not much difference in the dynamic apertures between them for the shown dp/p_0 range. Therefore, we suspect the dynamic aperture drop is related to the IR magnetic field errors.

Figure 4.44 compares the dynamic apertures for head-on and crossing angle collisions with IR nonlinear magnetic field errors. The maximum IR field errors is 1 unit for all b_n and a_n. From the plot, the dynamic aperture for head-on is higher than that from crossing angle collision. When the relative momentum deviation increases, especially from 10×10^{-4} to 20×10^{-4}, the difference in the dynamic apertures between those two cases gets bigger. With $dp/p_0 = 20 \times 10^{-4}$, the difference is 3σ as we saw in Figure 4.42.

From above comparisons, we learned that the dynamic aperture reduction from head-on collision to crossing angle collision is related to IR nonlinear magnetic field errors. As we know, with local crabbing scheme, particles with non-zero longitudinal offset z will have an additional horizontal offset $\Delta x = \zeta \times z$ in the interaction region, where $\zeta = dx/dz$ is the crab dispersion.

For example, Figure 4.45 shows a test particle's horizontal trajectories across the interaction region with different combinations of initial z and dp/p_0. Test particles are launched from one side crab cavities and travel toward other side crab cavities. From the plot, particles with non-zero z will have a sizable horizontal orbit in the interaction region as predicted.

Particles with non-zero z will sample larger IR field errors than particles at the bunch center with $z = 0$. Considering the synchrotron motion, it is true too for particles with non-zero dp/p_0. The larger the momentum deviation is, the greater IR magnetic field errors they will feel. To minimize the dynamic aperture drop from head-on collision to crossing angle collision, we need to reduce

and have a good control of IR magnetic field errors.

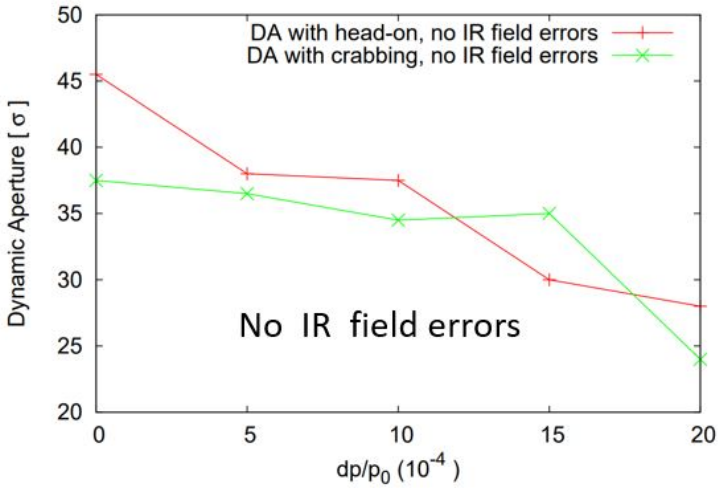

Figure 4.43: Dynamic aperture as function of dp/p_0 without IR field errors.

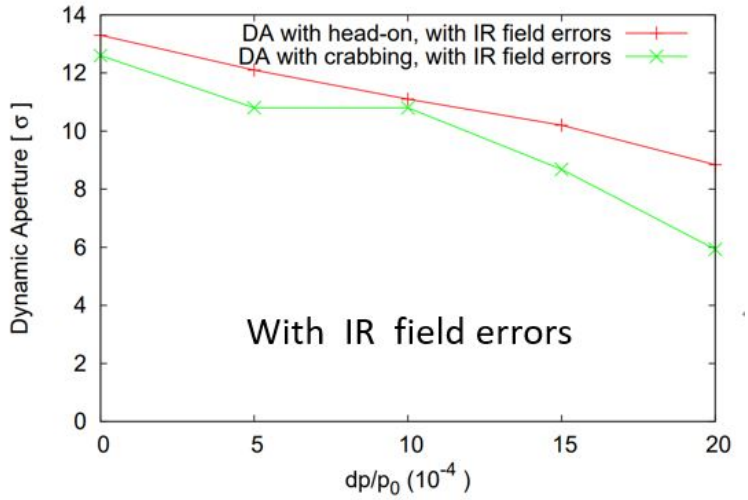

Figure 4.44: Dynamic aperture as function of dp/p_0 with IR field errors.

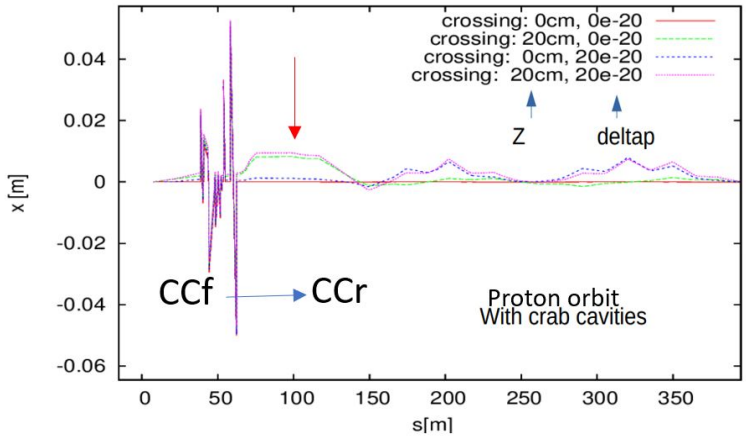

Figure 4.45: Horizontal trajectories across IR with different combinations of z and dp/p_0.

Predominant Magnetic Field Errors

We carry out some contrast comparisons for the HSR IR field errors, as shown in Figure 4.46. First we compare the dynamic aperture with field errors assigned to all IR magnets within 160m (red curve) and 80m (green curve) from IP6. In the plot, the horizontal axis is units of IR field errors and vertical axis is the dynamic aperture from 10 seeds of random IR field errors. There is no big difference in dynamic aperture when we assign field errors to magnets within 160 m instead of 80 m from IP. This means that the important field errors to dynamic aperture are those closer to IP6.

In the next test, we exclude sextupole field errors (blue curve) from all the IR magnets. Compared to the green curve with them in the plot, the dynamic aperture improves marginally. This means that the sextupole component of field errors may not be the predominant field error for the HSR dynamic aperture. Impacts from other component of field errors should studied carefully too.

For the last comparison, we intentionally do not assign field errors to IR dipoles with design offsets, IR dipoles without design orbit offset, and IR quadruopoles. From Figure 4.46, dynamic aperture increases when field errors not assigned to quadrupoles (yellow curve) and dipoles with design orbit offsets (purple curve). This means that field errors in the IR quadrupoles and in the IR dipoles with design orbit offsets are more important to dynamic aperture reduction. More detailed studies about individual IR magnet's impact on dynamic aperture are planned.

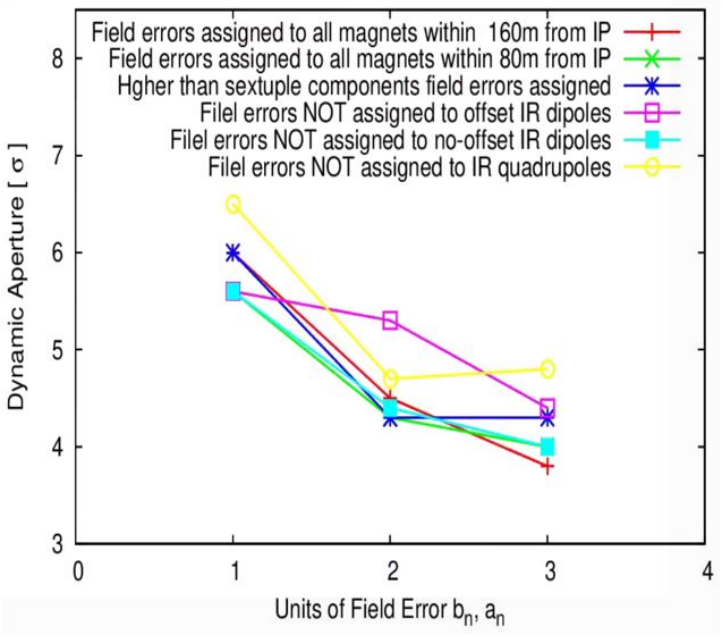

Figure 4.46: Dynamic aperture comparison with different IR field error assignment scenarios.

Updated Reference Radius

Based on Eq. 4.25, IR magnetic field error coefficients b_n and a_n depend on the reference radius R_{ref}. In the previous dynamic aperture studies for the HSR, we set the reference radius to be 60 mm for all IR dipoles and 40 mm for all IR quadrupoles. With the progresses in the HSR magnet design, we have a better knowledge of the reference radius. Table 4.15 shows the updated reference radius that should be used from now on. In the table, near side or farther side means the two ends of magnets facing IP or away from IP.

Magnet	R1 (mm)	R2 (mm)	R_{ref} (mm)
Name	near side	farther side	used in simualton
B0pF	IP	non-IP	60
B0ApF	43	43	43
Q1ApF	44	33.5	44
Q1BpF	55	32	55
Q2pF	73	73	73
B1pF	40	55	55
B1ApF	63	63	63
Q1ApR	26	26	26
Q1BpR	28	28	28
Q2pR	54	54	54

Table 4.15: Updated reference radius for interaction region magnets.

Different Random Number Generation

In the previous dynamic aperture calculation, we assigned IR field errors with an uniform random number generator. For example, for 1 unit of b_n or a_n, their values from random number generator can vary from -1 to 1. As noted above, currently we use 10 seeds of random IR field errors for each simulation condition.

We compared the dynamics apertures with different random number generators. For example, for a Gaussian random number generator, with 1 unit of field errors of b_n and a_n, the actual values of errors can be more than 1 unit but the statistical standard deviation will stay 1 unit for many seeds.

Table 4.16 compares the dynamic apertures with uniform and Gaussian distribution generators for IR nonlinear magnetic field errors. The dynamic aperture is normally larger with an uniform random number generator than with a Gaussian generator. The reason is that the random filed errors with Gaussian distribution can go higher than the uniform distribution. For the EIC, considering a small number of IR magnets, we prefer uniform distribution of IR field errors in simulation.

	Uniform Distr.			Gaussian Distr.		
unit	min	ave	rms	min	ave	rms
0.0	19.4	19.4	0	17.8	19.2	0.5
0.3	5.8	9.1	1.6	6.8	9.5	1.4
0.6	5.8	8.1	1.5	3.4	7.18	1.9
0.9	6.2	7.9	0.7	3.8	6.88	1.6
1.2	4.8	6.7	1.3	5.0	7.22	1.0
1.5	4.8	7.1	1.4	5.2	6.58	0.8
1.8	4.0	7.3	2.0	3.8	5.56	1.3
2.1	5.6	7.0	1.1	5.0	6.76	1.3
2.4	4.8	6.0	0.7	3.2	5.32	1.2
2.7	4.2	6.2	1.1	2.2	5.36	1.3

Table 4.16: Dynamic aperture comparison with uniform and Gaussian random number generation.

Field Tolerances for a Large Aperture Magnet B2PF

There are some large physical aperture magnets in the IR6 of HSR. Magnetic field errors may get bigger away from the center of beam pipe. We paid particular attention to a large aperture dipole B2PF, which is just in front of the crab cavities in the forward side of IP6. We set its reference radius to 50 mm. In the dynamic aperture calculation, we set B2PF's field errors for all b_n and a_n the same from sextupole component to 11th pole. Table 4.17 shows the simulated dynamic aperture with B2PF field errors. To have dynamic aperture not less than 6σ for the HSR lattice, B2PF's field errors b_n and a_n should be below 1 units.

Unit	DA-Min	DA-Max	DA-Ave	DA-RMS
1	5.0	7.6	6.2	0.8
2	2.2	5.4	3.9	0.8
3	2.6	4.2	3.6	0.5
4	1.8	3.4	2.5	0.5
5	1.4	2.8	1.8	0.4

Table 4.17: Dynamic aperture versus field errors in magnet B2PF.

Field Tolerances for Shared IR Magnet B0PF

With the recent progress in the EIC B0PF magnet design, we learned that the sextupole component could reach 20-30 units when the ESR is operating at 18 GeV and 5 GeV. B0PF is a two-hole shared magnet next to IP6 by both HSR and ESR. It will provide a main dipole field to the protons and a main quadrupole field to the electrons. The current B0PF design focused to optimize all the higher order field errors in the HSR to be lower than 1 unit when the EIC is operating in the collision mode involving 275 GeV protons and 10 GeV electrons. However, the field errors when the ESR is operating at 18 GeV and 5 GeV are much larger and need further optimization.

Here we carried out proton dynamic aperture calculation to evaluate the effects of those large sextupole field error in B0PF for the collision mode with 275 GeV protons and 18 GeV electrons. For this studies, we used 40 seeds for random field errors for other IR magnets except B0PF. Figure 4.47 shows the histogram of the calculated dynamic aperture. The minimum dynamic aperture is 9.2 σ among these 40 seeds. The average minimum dynamic aperture is 11.2 σ. Based on this quick study, the large sextupole error in B0PF does not significantly reduce the proton dynamic aperture for this collision mode. The reason is that the beam-beam parameter for the proton beam is only 0.003, which is about a factor of 4 smaller than the collision mode involving 275 GeV protons and 10 GeV electrons.

Next we will evaluate the effects of the large sextupole field errors of current B0PF design for the collision mode involving 100 GeV protons and 5 GeV electrons when the 100 GeV HSR lattice ready. For this collision mode, the beam-beam parameter for the protons is about 0.015 and we expect to see dynamic aperture drop due to the large sextupole error in the current B0PF magnet design.

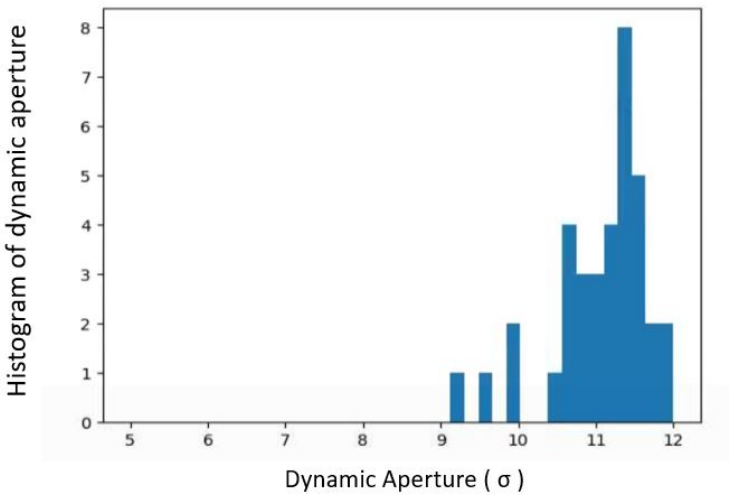

Figure 4.47: Histogram of the calculated dynamic aperture with a large sextupole component in the B0PF design.

4.4 Dynamic Aperture in Rapid Cycling Synchrotron

4.4.1 Emittances and charge

Injection.

The current RCS optics should be able to accept a single 28 nC electron bunch with horizontal emittance up to 170 nm-rad, vertical emittance up to 65 nm-rad, bunch length up to 30 mm, and fractional energy spread up to 2×10^{-3}.

Extraction.

4.4.2 Physical aperture: max σ's in all planes.

We assume a round RCS beampipe with radius 18.16 mm. The maximum horizontal beta function is 26.0-m and the maximum vertical beta function is 25.7 m. For an injected beam with 170 nm-rad horizontal emittance and 65 nm-rad vertical emittance, this corresponds to a physical aperture of 8.6-σ in the horizontal plane and 14.1-σ in the vertical.

4.4.3 Collective effects: Bunch charge, impedances.

4.4.4 RF bucket aperture: Max $\delta p/p$ and max frequency change on ramp.

4.4.5 Optical aperture: DA optimization sextupole settings, effect of errors.

We use two sextupole families to bring the chromaticities to near unity. This is already sufficient to give us a DA of roughly 6 σ in both planes with fractional energy offsets up to 1%, as seen in Fig. 4.48.

In order to understand the impact of errors, we provide all magnets with Gaussian random offsets, rolls, and multipole errors, as detailed in Tab. 4.18, with a 2.5σ cutoff. For the multipoles, we define systematic errors as those which are the same for all dipoles, quadrupoles, sextupoles, or correctors, and random errors as those which vary between individual magnets. The multipoles are scaled relative to the magnet's nominal magnetic field 15 mm off-axis, and extend up to 10^{th} order, with the notation that 0^{th} order is a dipole, 1^{st} order is a quadrupole, etc. Magnets only receive multipoles of orders equal to or greater than the order of their nominal field (eg, sextupoles will not get quadrupole or dipole errors). Additionally, they do not receive a systematic normal error of the same order as their nominal field because that can be trivially fixed by adjusting the power supply.

Once the errors are applied, we make a suite of corrections to the lattice. First, we zero the orbit relative to the quadrupole centers, with 100 µm resolution. Then, we set the tunes to their nominal values and the chromaticities to unity. After these corrections are applied, we introduce power supply errors to the dipoles, quadrupoles, and sextupoles by providing a 300 part-per-million Gaussian random error with 2.5σ cutoff to the strengths of the independent magnet families. Since the power supplies are assumed to fluctuate with time, this error cannot be corrected.

Parameter	**RMS Value**
Roll Errors (μrad)	400
Magnet x/y Offests (μm)	100
Normal Systematic Multipoles	10^{-3}
Normal Random Multipoles	10^{-4}
Skew Systematic Multipoles	10^{-4}
Skew Random Multipoles	10^{-5}
Normal Systematic Multipoles for Correctors	10^{-2}
Normal Random Multipoles for Correctors	10^{-2}
Skew Systematic Multipoles for Correctors	10^{-2}
Skew Random Multipoles for Correctors	10^{-2}
BPM x/y Offsets Relative to Quadrupoles (μm)	100
Power Supply Errors	3×10^{-4}

Table 4.18: Random errors for Rapid Cycling Synchrotron dynamic aperture estimates

We run this procedure with 10 random seeds and evaluate the dynamic aperture using BMAD [**?**]. The results are shown in Fig. 4.48. With errors and corrections, the dynamic apertures tend to lie between the 4 and 6-σ acceptance curves. Note that our correction scheme is still fairly simple at this stage, and can likely be improved in the future.

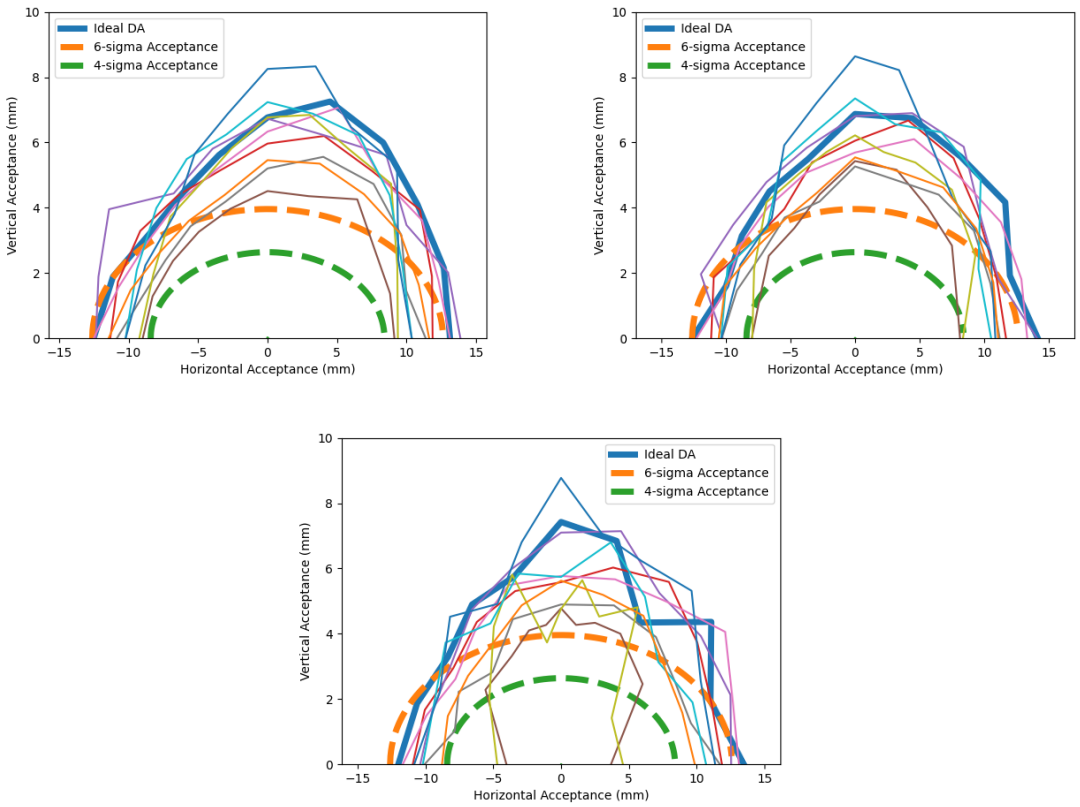

Figure 4.48: Dynamic apertures in the RCS for an injected beam which is off-energy by 0% (upper left), 0.5% (upper right), and 1% (bottom). Of the ten random seeds, one was unable to be corrected by our simple scheme, but the other nine have apertures beyond 4σ out to 0.5% energy error, and most are still beyond this limit at 1%.

4.5 Beam-Beam Effects

4.5.1 Introduction

Luminosity and the Beam-beam Interaction

The luminosity characterizes the number of physics events produced per unit cross section per second during the collision between two beams. For beams with a transverse Gaussian distribution, the luminosity is

$$L = \frac{N_p N_e f_c}{2\pi\sqrt{\sigma^{*2}_{p,x} + \sigma^{*2}_{e,x}}\sqrt{\sigma^{*2}_{p,y} + \sigma^{*2}_{e,y}}} H(\beta^* s, \sigma_l s, ...) \tag{4.26}$$

Here N_p and N_e are the proton and electron bunch intensities, f_c is the bunch collision frequency per second, and $\sigma^*_{e,p,x,y}$ the electron and proton bunches' RMS horizontal and vertical beam sizes at the interaction point (IP). H is a luminosity reduction factor arising from the hour-glass effect, crossing angle, and other effects.

During the collision, the motion of charged particles from one bunch will be affected by the electric and magnetic fields from the opposite bunch. The beam-beam parameter characterizes the strength of the beam-beam interaction force. For Gaussian beams, the beam-beam parameter is defined as

$$\xi_{e,p,z} = \frac{N_{p,e} r_{e,p}}{\gamma_{e,p}} \frac{\beta^*_{e,p,z}}{2\pi\sigma^*_{p,e,z}(\sigma^*_{p,e,x} + \sigma^*_{p,e,y})}, \tag{4.27}$$

where $z = x, y$ denotes the horizontal or vertical plane, $r_{e,p}$ the classical radius of the electron or proton, $\gamma_{e,p}$ the relativistic Lorentz factor of the respective beam, $\beta^*_{e,p,z}$ the electron and proton *beta*-function at the IP, and $\sigma^*_{e,p,z}$ the RMS beam sizes at the IP.

To increase the luminosity, we can increase the bunch intensities $N_{e,p}$, decrease the beam sizes $\sigma^*_{e,p,z}$ at the IP, or increase the bunch collision frequency. As Equation 4.27 shows, the first two methods will increase the beam-beam parameter. The beam-beam interaction leads to

- The dynamic β effect, where the β-function and size change due to focusing provided by the oncoming beam;
- The incoherent beam-beam tune shift, where particles at the core of the beam see additional focusing from the oncoming beam, while particles in the transverse tails see no additional focusing;
- Nonlinear beam-beam resonances, because the highly nonlinear nature of the beam-beam force results in strong nonlinear driving terms in the forces experienced by individual particles;
- Coherent beam-beam motion, because each beam is effected by the other and therefore must be seen as a single system of the two beams, the eigenmodes of which are potentially unstable.

Beam-beam effects can lead to particle loss, emittance blow-up, and coherent beam-beam instabilities, all of which can lead to luminosity reduction and poor luminosity lifetime.

For the EIC design, we set the maximum beam-beam parameter ξ to be 0.1 for the electron and 0.015 for the proton beam. The choice of the maximum beam-beam parameter for the electrons in

teh Electron Storage Ring (ESR) is based on the successful operational experience of the electron-position collider KEKB, where it was achieved with a transverse radiation damping time of 4000 turns. The maximum beam-beam parameter for the protons in the Hadron Storage Ring (HSR) is based on the successful operational experience during the RHIC polarized proton runs, where a beam-beam parameter of $\xi_p = 0.015$ was routinely achieved. However, such large beam-beam parameters together have never been demonstrated simultaneously in previous electron-proton colliders. The main goal of numerical beam-beam simulation studies for the EIC is to verify the feasibility of our design parameters to help guide changes in those parameters that might further improve the machine performance.

Crossing Collision with Crab Cavities

From Equation 4.26, the luminosity can also be increased by raising the frequency of bunch collisions. This is realized by increasing the number of bunches in each ring, which will decrease the longitudinal distance between adjacent bunches for a given ring circumference. To avoid parasitic collisions and to minimize the distance of the final focusing elements from the IP for both beams, the beams cross at a horizontal angle of 25 mrad at the IP.

To compensate the luminosity loss due to the non-zero crossing angle, crab cavities tilt the proton and electron bunches in the z-x plane by half of the full crossing angle to restore head-on collisions at the IP. Ideally, the crabbing force should be proportional to the longitudinal position of each individual particle in the bunch. For each ring, two sets of crab cavities are to be installed, ideally in a non-dispersive location, one on each side of the IP. The horizontal betatron phase advance between the IP and the crab cavities should be $\pi/2$ to close the z-x orbit bump. Figure 4.49 shows the local crabbing compensation scheme.

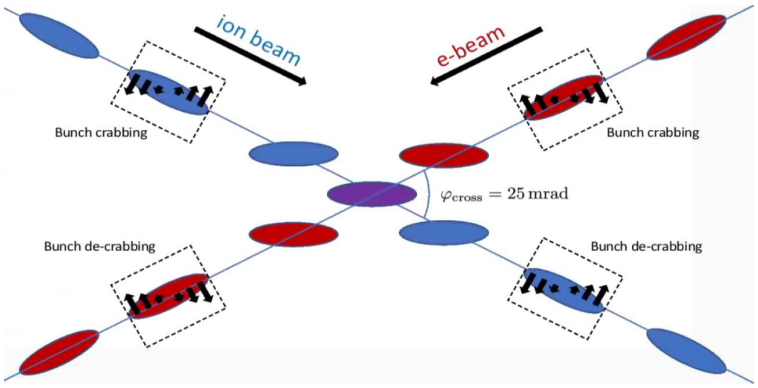

Figure 4.49: Schematic overhead view of collision between bunches separated by a crossing angle and optimized by crab cavities.

The crab cavities on each side of the IP will tilt the protons or electrons by 12.5 mrad in the z-x plane. The total voltage required in the RF cavities on each side of the IP is given by

$$\hat{V}_{\text{RF}} = -\frac{cE_s}{4\pi f_{\text{RF}}\sqrt{\beta_x^*\beta_{cc}}}\theta_c. \tag{4.28}$$

Here c is the speed of light, E_s is the particle energy in eV, f_{RF} is the crab cavity frequency, and θ_c is the full crossing angle. β_x^* and β_{cc} are the β-functions at the IP and the crab cavity, respectively. From Equation 4.28, raising the crab cavity frequency lowers the required crab cavity voltage, and

larger horizontal β-functions at the IP and/or the crab cavity location reduce the required crab cavity voltage as well.

For crabbed crossing collision, when the bunch length is comparable with the wavelength of the crab cavity, the sinusoidal waveform of the crab cavity voltage generates a horizontal offset at the IP as function of longitudinal position of individual particles. As a result the entire bunch will not be crabbed perfectly onto the z axis along its entire length. A lower crab cavity frequency would provide a more uniform crabbing than a higher frequency, but a lower frequency crab cavity has a larger physical size and would require a higher crabbing voltage for a given crabbing angle.

At present, we are considering two crab cavity frequencies for the EIC: 197 MHz and 394 MHz. Based on beam-beam simulation studies, a 197 MHz crab cavity frequency is required for the HSR to maintain an acceptable proton beam lifetime in collision. 394 MHz cavities can be added to further flatten the proton bunch at the IP and improve the proton beam lifetime. Due to the short electron bunch length, only 394 MHz crab cavities are required in the ESR.

394 MHz is close to the 400 MHz frequency of the crab cavities used for the LHC High Luminosity Upgrade program. Brookhaven National Laboratory originally designed these crab cavities and actively participated in beam tests of the cavities in the PS accelerator at CERN. We benefit from the experience gained at CERN with the 400 MHz crab cavity design, manufacture, and commissioning. The 197 MHz crab cavity requires a larger physical size than 394 MHz crab cavity.

Beam-beam Related Design Parameters

In the EIC, there are several different configurations that have different combinations of electron and ion beam energies. In the following, we will only discuss collisions between 275 GeV protons and 10 GeV electrons, which is the configuration with the highest luminosity, reaching $1 \times 10^{34}\,\mathrm{cm}^{-2}\,\mathrm{s}^{-1}$. This combination also requires the highest beam-beam parameter for both the proton and electron beams among all configurations. For other configurations, the required beam-beam parameters are smaller than for this combination. The beam-beam interaction at those other collision energies will be studied later.

There are several constraints on the choice of machine parameters:

- The proton and electron beam currents are limited to 1 A and 2.5 A, respectively;
- The proton and electron beam-beam tune shifts must not exceed 0.015 and 0.1, respectively;
- A maximum electron beam divergence of 220 µrad
- For the proton beam, $\beta_x^* \geq$90 cm, $\beta_y^* \geq$5 cm
- For the electron beam, $\beta_x^* \geq$35 cm, $\beta_y^* \geq$4 cm
- A minimum intrabeam scattering (IBS) growth time for the protons of 2 h.

We use the luminosity, its degradation rate, and the proton beam growth rates to evaluate performance for a given set of machine parameters. Due to radiation damping, the electron beam reaches a stable equilibrium distribution, with a transverse damping time of 4000 turns for our machine design. Growth rates in the electron beam are thus ignored, and the above parameters are evaluated well after the electron beam has reached equilibrium. Our studies showed that flatness, defined as the ratio of the vertical to the horizontal RMS beam sizes at the IP, is an important parameter characterizing the impact of the beam-beam interaction. A smaller value of the flatness at the IP will

lead to a higher instantaneous luminosity, but will also lead to a more rapid growth in the vertical beam size.

There are two main approaches to optimize the beam-beam related design parameters to reach the maximum design luminosity of $1 \times 10^{34}\,\mathrm{cm}^{-2}\,\mathrm{s}^{-1}$. For Apprach I: we started with a larger beam flatness 0.012 which delivers a luminosity $0.72 \times 10^{34}\,\mathrm{cm}^{-2}\,\mathrm{s}^{-1}$ but with a relatively low proton beam size growth rate. We then slowly reduced the flatness at IP step by step and at each step we carefully adjusted the electron equilibrium beam sizes to be close to or slightly larger than the proton beam sizes at IP. To match the transverse sizes of electron and proton beams at IP, we normally adjusted $\beta^*_{x,y}$-functions at IP and the vertical emittance for the ESR. By doing in this way, we were able to reach the design maximum luminosity with an acceptable proton emittance growth rate.

For Approach II, we maintained a beam flatness 0.12 at IP but reduce the horizontal beam size at IP to reach the maximum design luminosity of $1 \times 10^{34}\,\mathrm{cm}^{-2}\,\mathrm{s}^{-1}$. By doing in this way, β^*_x in the HSR was reduced from 90 cm to about 65 cm and the electron horizontal emittance was slightly increase to 22 nm. The biggest challenge for this approach is that the maximum design voltage of crab cavities have to be increased by about 30%. Therefore, in the following we will focus on the design parameters from Approach I if not specifically mentioned.

Besides the beam-beam parameters and the beam flatness at IP, we also noticed that synchro-betatron resonance affects the proton emittance growth rate due to crossing angle collision. For 275 GeV protons, the design RMS bunch length is 6 cm and the wavelength of 197 MHz crab cavities is 1.5 m. Protons in the bunch head and tail will not be perfectly crabbed onto the z axis and will feel offset beam-beam interaction at IP, which leads to synchro-betatron resonance and causes poor proton beam lifetime. To minimize the effects of synchro-betatron resonances, we moved the HSR working point down along the diagonal in the tune space from the orginal tunes (0.310, 0.305) to (0.228, 0.210). We also increased the fraction tune split to minimize the effects from linear betatron coupling resonance.

Table 4.19 lists the beam-beam related design parameters for the EIC collision mode between 275 GeV protons and 10 GeV electrons. For this collision mode, the luminosity reached the maximum design luminosity $1 \times 10^{34}\,\mathrm{cm}^{-2}\,\mathrm{s}^{-1}$ in the EIC. To match the beam sizes of proton and electron bunches at the IP, including the effects of the beam-beam interaction and synchrotron radiation effects, we adjusted $\beta*_{x,y}$ of the electrons at IP to be (55 cm, 6.5 cm) and the initial vertical emittance of the electrons from 1.3 to 1.1 nm. These corrected values are used in strong-strong beam-beam simulations and for the ESR lattice design. However, in the weak-strong simulations, where the size and shape of the electron distribution is not affected by the beam-beam interaction, we use the electron beam parameters as shown in Table 4.19.

Parameter	proton	electron
Ring circumference [m]	3833.8451	
Particle energy [GeV]	275	10
Lorentz energy factor γ	293.1	19569.5
Bunch population [10^{11}]	0.688	1.72
RMS emittance (H,V) [nm]	(11.3, 1.0)	(20.0, 1.3)
β^* at IP (H, V) [cm]	(80, 7.2)	(45, 5.6)
RMS bunch size σ^* at IP (H, V) [µm]	(95, 8.5)	
RMS bunch length σ_l at IP [cm]	6	0.7
Beam-beam parameters (H, V)	(0.012, 0.012)	(0.072, 0.1)
RMS energy spread [10^{-4}]	6.8	5.8
Transverse tunes (H,V)	(29.228, 30.210)	(51.08, 48.06)
Synchrotron tune	0.01	0.069
Longitudinal radiation damping time [turn]	-	2000
Transverse radiation damping time [turn]	-	4000
Luminosity [$10^{34}\text{cm}^{-2}\text{s}^{-1}$]	1.0	

Table 4.19: Machine and beam parameters used for the beam-beam interaction study.

Challenges to EIC beam-beam interaction

There are several challenges for the EIC beam-beam interaction:

- Large beam-beam parameters: as mentioned above, the maximum beam-beam parameters about 0.1 in the ESR and 0.015 in the HSR are used for the EIC design. However, combination of these two large beam-beam parameters had never been experimentally demonstrated in the previous electron-ion collider HERA. The beam-beam parameter for the HEAR-p is about 0.0014, which is about 10 times smaller than the EIC design maximum beam-beam parameter. The beam-beam parameter for the HERA-e is about 0.12 but with two experiments.
- Large crossing angle 25 mrad: although a 22 mrad full crossing angle had been used in the lepton collider KEK-B, such a large crossing angle had never been used in a hadron collider. For the upgrade project of LHC, or HL-LHC, the full crossing angle is only about 0.5mrad.
- Crab cavities in the both rings: a single crab cavity had been used in the KEK-B but it did not double the luminosity as planned. Also, for the EIC interaction region, the effects of the detector solenoids are not locally compensated close to IP. The combined effects from the detector solenoid and the nearby crab cavities need to be carefully compensated. Our early simulation studies showed that the tolerable for the residual vertical crossing angle at IP is less than 25 µrad.
- Near-integer tunes for the electron beam: near-integer tunes will generate dynamic-beta effect or pinch effect. The electron beam beam sizes are IP will be squeezed by the beam-beam force and therefore increases the luminosity. However, near-integer tunes do give difficulties for online optics controlling and correction, especially for the vertical beam orbit and the betatron coupling correction which is critical to the polarization.
- Flat beam at the interaction point: flat beams at IP are required to achieve the maximum design luminosity in the EIC. However, from the beam-beam simulation studies, a flatter

beam will cause a larger proton vertical beam size growth rate. For comparison, the ratio of the vertical to the horizontal beam sizes at IP is 0.09 for the EIC, while it is 0.27 for the HEAR. For hadron colliders, normally round beams at IP are used.

- 10:1 emittance ratio in the HSR: to obtain a flat beam at IP, the proton emitance ratio about 10:1. For hadron colliders, the transverse emittances are normally the same. To achieve a 10:1 emittance ratio in HSR, the betatron and synchro-betatron coupling resonances should be strictly compensated to eliminate any sizeable increase in the vertical emittance. Strong hadron cooling is aimed to counteract the intra-beam scattering (IBS) at store. Any other mechanism to cause additional emittance growth, such as beam-beam interaction, space charge effect, beam instabilities, crab cavity noises, and power supple current ripple should be minimized at store.

Simulation Methods and Tools

Both strong-strong and weak-strong beam-beam simulation methods have been used for EIC beam-beam interaction studies. The goal of these studies is to verify that the chosen machine parameter achieve the design luminosity with an acceptable luminosity lifetime, and to further adjust the machine parameters to improve performance. For the strong-strong simulation, we mostly use BeamBeam3D [**?**] and BBSS [**?**]. Weak-strong simulations were performed using SimTrack [**?**].

BeamBeam3D is a parallel three-dimensional particle-in-cell code to model beam-beams effects in high energy colliders. This code includes a self-consistent calculation of the electromagnetic forces from two colliding beams, a linear transfer map model for beam transport between collision points, a stochastic map to treat radiation damping and quantum excitation, and a single map to account for chromaticity effects. The beam-beam forces are calculated by solving the Poisson equation using a Green's function based algorithm.

BeamBeam3D also includes a soft-Gaussian model to speed up strong-strong simulations. It can also model a crab cavity. The code can handle multiple bunches in each beam and collisions at multiple interaction points. The parallel implementation is done using a particle-field decomposition method to achieve a good load balance. BeamBeam3D has been applied to studies of the beam-beam effect at RHIC, the Tevatron, the LHC, PEP-II, and KEK-B.

SimTrack is a compact C++ library for 6D symplectic element-by-element particle tracking in high energy accelerators. It was originally designed for head-on beam-beam compensation simulation studies in RHIC. The code uses 4th order symplectic integration to perform 6D orbit tracking through magnetic elements. Both 4D and 6D symplectic beam-beam interaction models are implemented. Collisions with a crossing angle and simulation of crab cavities were recently implemented in the code. Since SimTrack is a library-based code, it is straightforward to use and modify it to study various physics problems. SimTrack has been extensively used for linear and nonlinear optics calculations, single particle orbit tracking, particle loss map calculations, dynamic aperture computation, and beam-beam interactions and compensation in RHIC.

In a weak-strong beam-beam model, the strong bunch is assumed rigid and the weak beam is represented by macro-particles. Therefore, weak-strong beam-beam simulation is not self-consistent because the force of the weak beam on the strong beam is ignored. Normally, the rigid beam is assumed as a 6D elliptical Gaussian distribution and the beam-beam force of the strong beam on each particle in the weak beam is calculated using an analytical solution. In a strong-strong beam-beam model, both beams are represented by large numbers of macro-particles. The beam-beam forces are calculated by solving the Poisson equation using the particle-in-cell method. In contrast to a weak-strong simulation method, a strong-strong beam-beam model is self-consistent. However, it needs

much more computing time and is inherently subject to numerical noise. Strong-strong simulations are mostly used to determine luminosity and beam sizes after equilibrium is reached. It is an indispensable tool to study coherent beam-beam motion and instability. For the study of long-term proton beam stability and dynamic aperture, in the absence of coherent beam-beam effects, we use weak-strong beam-beam simulations to reduce simulation time and the impact of numerical noise.

Besides strong-strong and weak-strong beam-beam simulation model, we also used a so-called frozen model. The purpose of using this model is to minimize the numerical noise seen in the strong-strong simulation. For this method, we first carry out a regular strong-strong simulation until the electron beam reaches its quasi-equilibrium beam sizes. We then freeze the electron bunch's charge distribution and space charge potential by averaging them in the following 1000 turns. Next we perform a long-term weak-strong simulation with these electron bunch's space charge potentials. By doing it this way, the proton bunch will see more realistic electron bunch distribution than the simple weak-strong simulation. The numerical noises from the strong-strong simulation will be largely reduced since there is no turn-by-turn variation in the particle distribution or space charge potentials. The simulated proton beam size growth rate with the frozen model will be much smaller than that from the strong-strong simulation, but still a few times larger than that from the weak-strong model. More detailed studies on the numerical noises in the EIC beam-beam simulation will be presented later.

4.5.2 Beam-Beam Simulation with Crabbed Collision

Dynamic β^* Effect with Linear Crabbing

As mentioned above, the beam size of the electron beam changes during the beam-beam collision; we refer to this as the dynamic β^* effect. Because the focusing from the beam-beam collision is different depending on where a particle passes through the opposite beam, there is a strong variation of the focusing strength with particle position, leading to a large increase in tune spread in the beam. In this section we present calculations of these two effects with crab crossing, but where the crabbing effect of the crab cavity is perfect linear (not taking into account the finite RF wavelength). In strong-strong simulations, we did not observe any difference in the results when we used this perfectly linear crabbing from the results for head-on collisions. We will show the tune footprint and frequency map analysis using crab cavities with a finite RF wavelength in the next section.

The dynamic β^* effect can be computed to first order by treating the beam-beam interaction as a thin-lens focusing element; this will change the one-turn linear map from what it was without the beam-beam element, and thereby change the ring tune and the β^* at the IP. Figure 4.50 shows the perturbed β^* and tune changes of the perturbed ESR versus the lattice tunes when the beam-beam element is absent. When the design tunes are very close to an integer, the actual β^* in the presence of the beam-beam interaction will become smaller than the design values of the bare lattice. The unperturbed electron $\beta^*_{e,x,y}$ are 45 cm and 5.6 cm, respectively. For electron tunes of $(0.08, 0.06)$, the beam-beam interaction modifies $\beta^*_{e,x,y}$ to 29 cm and 2.9 cm, resp. The tune shifts caused by the beam-beam interaction are smaller than the beam-beam parameter computed with Equation 4.26 as well. For the electron tunes $(0.08, 0.06)$, the design beam-beam parameters $\xi_{e,x,y}$ are $(0.072, 0.10)$. With beam-beam interaction, the actual beam-beam tune shifts are much smaller, $(0.056, 0.067)$.

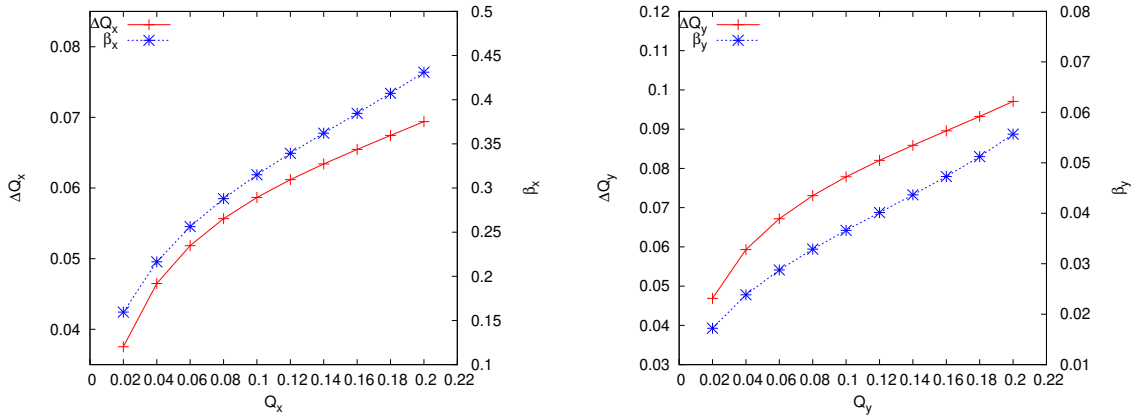

Figure 4.50: β^* and tune changes when the beam-beam effect is added to the lattice, plotted as a function of the tune values without the beam-beam interaction. The beam-beam interaction is treated as a thin focusing element.

Tune Footprints with Linear Crabbing

Since the field gradient a particle sees when passing through the opposite beam depends on position, the beam-beam effect creates a large tune dependence on transverse amplitude. The particles at the bunch core experience a large tune shift, while the particles with a larger amplitude will have a smaller tune shift. If we plot the tunes of all the particles in a bunch in a 2D tune diagram, they will occupy an area which is called a tune footprint. The width of the tune footprint or tune distribution is the tune spread. The tune spread is dominated by the contribution from the beam-beam interaction.

Figure 4.51 shows the tune footprints of the proton and electron beams when the beam-beam interaction is included. The bare lattice tunes are $(0.228, 0.210)$ for the HSR and $(0.08, 0.06)$ for the ESR. In the plot, different colors indicate different orders of magnitude of tune diffusion during 2048 turns of particle tracking for test particles launched in the $(x/\sigma_x, y/\sigma_y)$ plane up to 6σ. The tune diffusion is defined as

$$\Delta Q = \sqrt{\Delta Q_x^2 + \Delta Q_y^2}, \tag{4.29}$$

where $\Delta Q_{x,y}$ are the differences between the tune averages in the first 1024 turns and the last 1024 turns. Electrons with large transverse amplitude have tunes close to the integer and a large tune diffusion. Large tune diffusion is an indicator of chaotic particle motion. One can also observe resonance lines crossing the electron tune footprint in the plot. The resonance structure for the proton beam is discussed in Section 4.5.2.

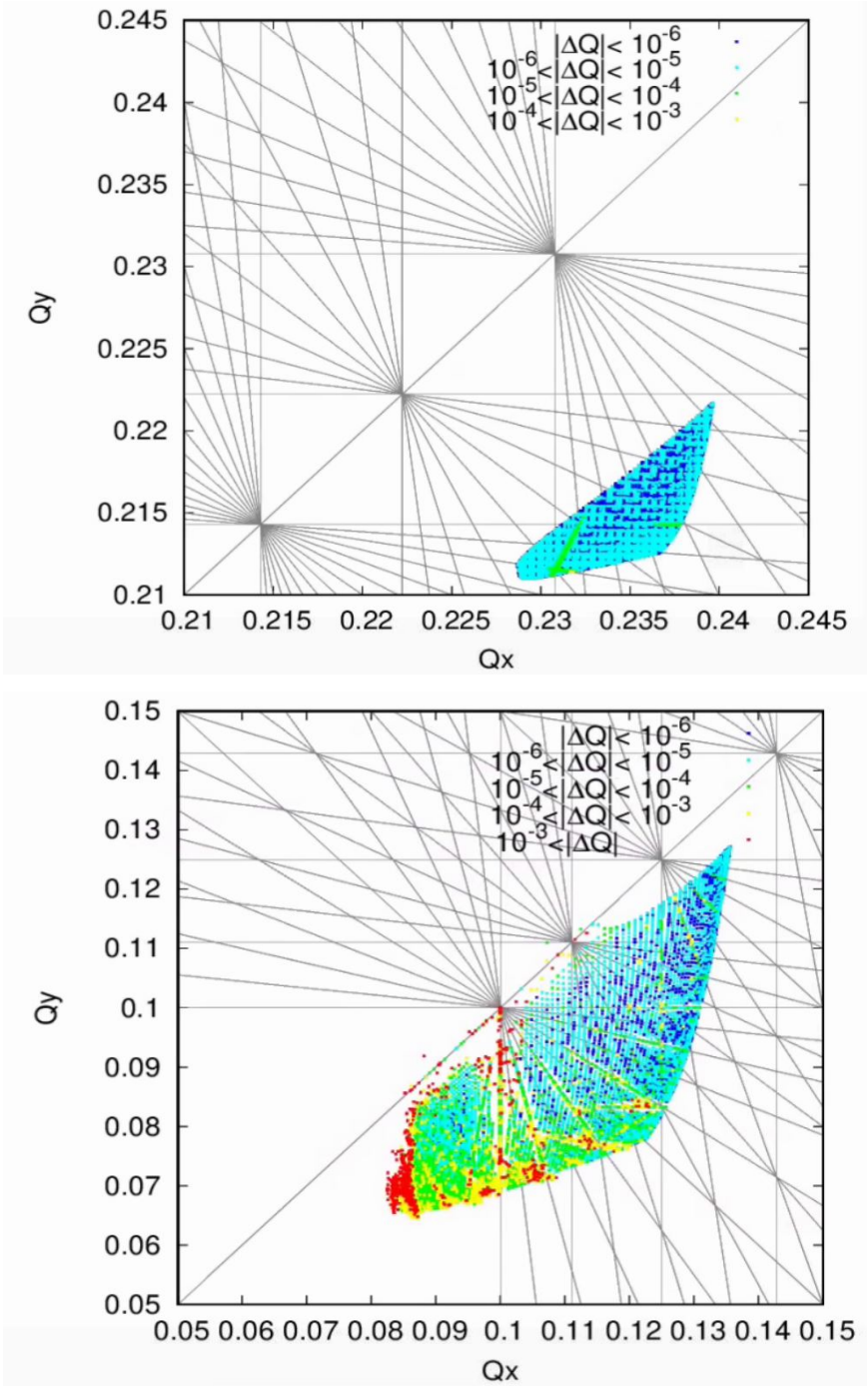

Figure 4.51: Tune footprints of (a) proton beam and (b) electron beam.

Luminosity and Beam Size Evolution

Figure 4.52 shows an example of particle distributions in the z-x plane at the IP from a strong-strong beam-beam simulation. The design beam parameters in Table 4.19 were used. For this calculation, we used both 197 MHz and 394 MHz crab cavities for the HSR and 394 MHz crab cavities for the ESR. The horizontal β-functions at the crab cavity locations are 1300 m for the protons and 150 m for the electrons. The required total crab cavity voltages on each side of IP are 36.2 MV and -5.2 MV for 197 MHz and 394 MHz crab cavities in the HSR. The required crab cavity voltages on each side of IP are 1.7 MV for the ESR.

The proton tunes $(0.228, 0.210)$ and the electron tunes $(0.08, 0.06)$ were used in this example. AS mentioned early, we deliberately match the electron transverse beam size be close to that of the proton beam to obtain a lower vertical proton beam size growth rate. The luminosity after reaching equilibrium is about $1 \times 10^{34}\,\mathrm{cm}^{-2}\,\mathrm{s}^{-1}$. Figures 4.53 to 4.55 show the evolution of the beam sizes over 50,000 turns.

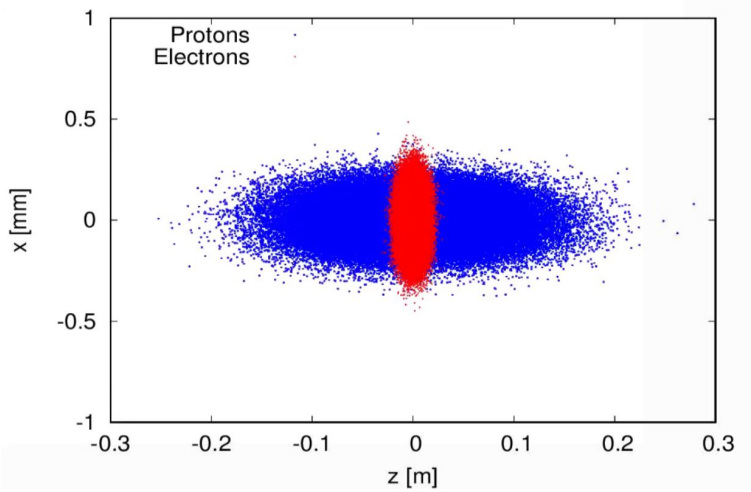

Figure 4.52: Proton (blue) and electron (red) particle distributions in the z-x plane at the IP.

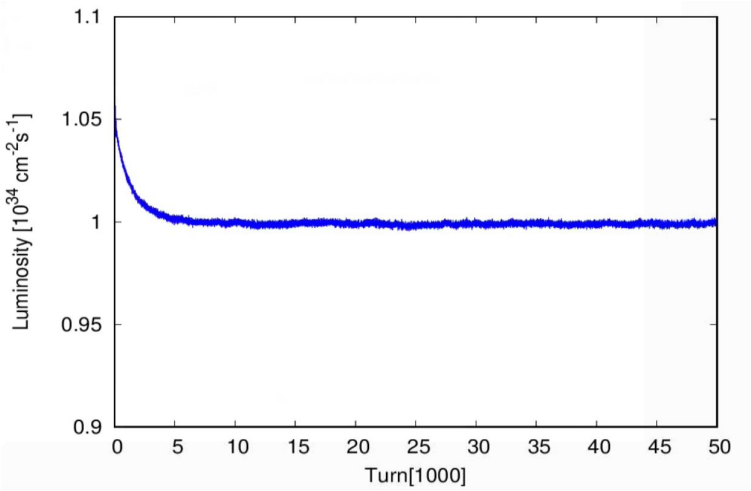

Figure 4.53: Luminosity evolution from a strong-strong beam-beam simulation.

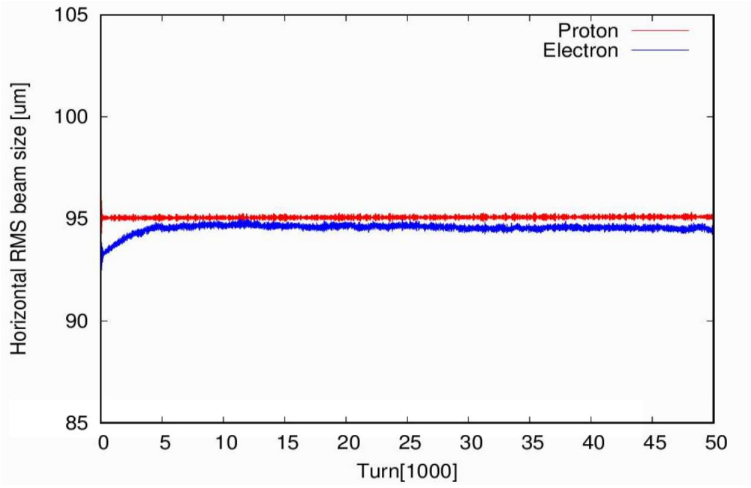

Figure 4.54: Evolution of horizontal beam sizes of both beams from a strong-strong beam-beam simulation.

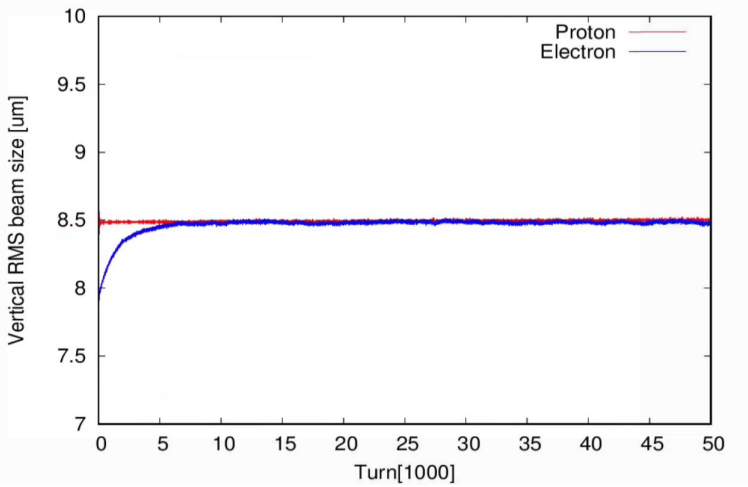

Figure 4.55: Evolution of vertical beam sizes of both beams from a strong-strong beam-beam simulation.

Proton Crab Cavity Frequency Choice

In Figure 4.56, we show the centerline of the proton bunch at the IP after passing through the crab cavities for three frequency combinations for the crab cavities: 197 MHz alone, 394 MHz alone, and a combination of 197 MHz and 394 MHz cavities. For the latter case, to achieve the 12.5 mrad crab angle, the voltage in the 197 MHz cavities is set to create a crab angle of 1.4×12.5 mrad, while the voltage in the 394 MHz crab cavities is set to create a crab angle of -0.4×12.5 mrad. The horizontal offset at $\pm 3\sigma_l$ longitudinally is reduced by a factor of 3.7 when using a 197 MHz crab cavity frequency relative to the offset for a frequency of 394 MHz. With both frequencies, the horizontal offset is reduced by another factor of 14 from the case where there are only 197 MHz cavities, leading to an offset at $\pm 3\sigma_l$ of only 14 µm, which is small compared to the design horizontal RMS beam size at the IP of 95 µm.

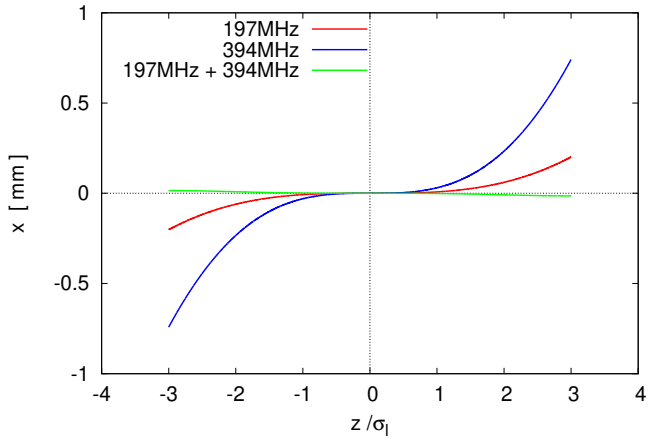

Figure 4.56: Proton bunch shapes in the z-x plane with different crab cavity frequency combinations.

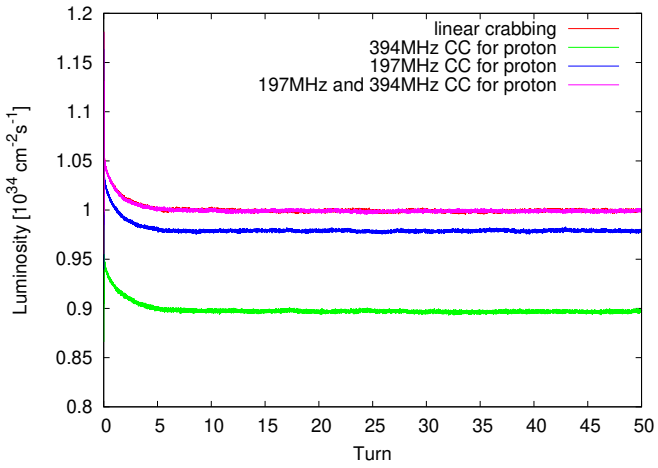

Figure 4.57: Luminosity evolution with different proton crab cavity frequency combinations.

Figure 4.57 shows the luminosity evolution from strong-strong simulations for the three different

proton crab cavity frequency combinations described above. In this study, the electron beam is always crabbed with 394 MHz crab cavities. With 394 MHz proton crab cavities, the equilibrium luminosity is 88% of that with linear crabbing. With 197 MHz crab cavities, the luminosity is 97% of that with linear crabbing or head-on collision. With both 197 MHz and 394 MHz combined, the luminosity is almost the same as for the linear crabbing case.

Necessity of second harmonic crab cavities in HSR

In addition to recovering the luminosity by a few percent, the combination of 197 MHz and 394 MHz helps to mitigate the proton emittance growth. When only 197 MHz is used, the beam centroid is

$$< x(z) >= -\theta_c \left[\frac{1}{k_c} \sin(k_c z) - z \right] \approx \frac{k_c^2 z^3 \theta_c}{6} \tag{4.30}$$

When the both frequencies exist, the beam centroid turns into

$$< x(z) >= -\theta_c \left[\frac{4}{3k_c} \sin(k_c z) - \frac{1}{6k_c} \sin(2k_c z) - z \right] \approx \frac{k_c^4 z^5 \theta_c}{30} \tag{4.31}$$

where k_c is the wave number of 197 MHz crab cavity, and θ_c is the half crossing angle. The non-zero centroid for particles with large longitudinal offset z will drive high-order synchro-betatron resonances [**?**] which lead to proton emittance growth. As shown in Equation (4.31), the z^3 term can be removed when both frequencies are used. The proton emittance growth is therefore mitigated.

Figure 4.58 compares the weak-strong tracking with and without harmonic crab cavity. The vertical emittance growth rate is largely mitigated when the harmonic crab cavity is used. Figure 4.59 shows the tracking by the frozen model. In the first $60,000$ turns, the simulation is done by strong-strong model. Then the electron beam distribution is frozen and memorized. The beam-beam kick on the proton particles is calculated by the Green's function method with the charge density distribution smoothed by a spectral filter. In the latter $500,000$ turns, the simulation is performed by the weak-strong simulation. The PIC noise is removed in the latter weak-strong simulation. However, there is still longitudinal interpolation noise in the frozen model. That explains why the growth rate in the frozen model as shown in Fig. 4.59 is larger than the weak-strong simulation in Fig. 4.58. With the second order harmonic crab cavity, the electron beam vertical size reaches a smaller equilibrium value, which gives us about 3% more luminosity. The proton vertical emittance growth rate is also reduced by half. Both weak-strong and frozen model prove that the harmonic crab cavity benefit the luminosity and the proton emittance growth. As a result, the second order harmonic crab cavity is necessary for the EIC.

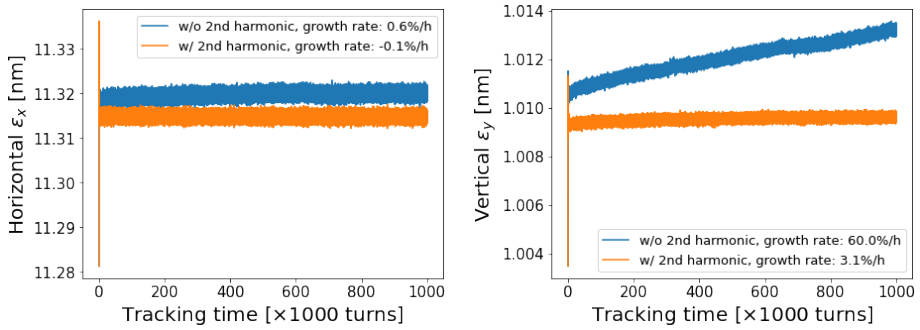

Figure 4.58: The emittance evolution tracked by weak-strong simulation with and without harmonic crab cavity. The growth rates are linearly fitted by the last 60% tracking turns. The proton working point is $(0.228, 0.210, 0.010)$.

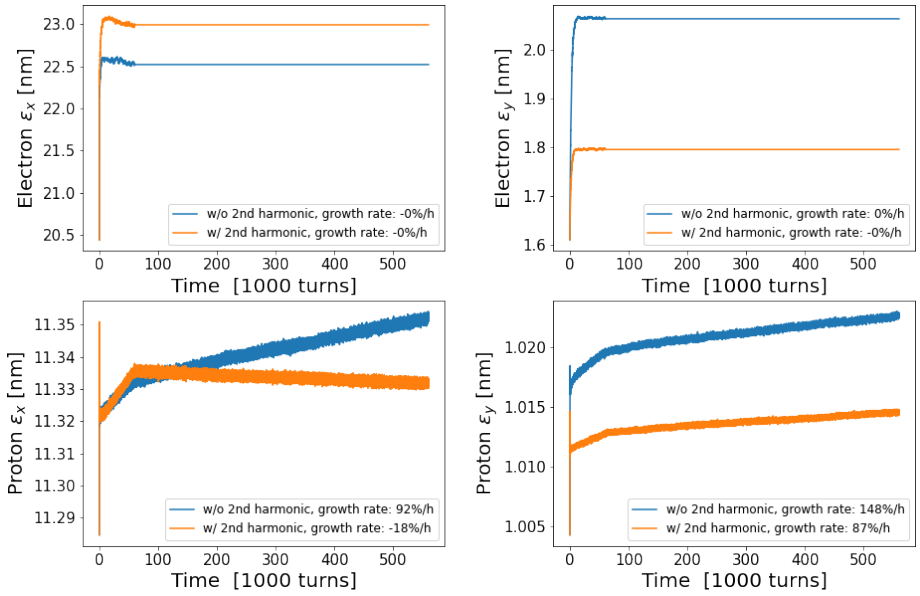

Figure 4.59: The emittance evolution with and without harmonic crab cavity. The simulation is tracked by frozen model. In the first 60, 000 turns, the simulation is done by strong-strong model. In the later 500, 000 turns, the electron beam distribution is frozen, and the simulation is performed by weak-strong simulation. The growth rates are linearly fitted by the last 60% tracking turns. The proton working point is $(0.206, 0.209, -0.010)$.

Electron Crab Cavity Frequency Choice

In the present design, the RMS electron bunch length is 0.7 cm, which is about 9 times shorter than the RMS proton bunch length of 6.0 cm. Figure 4.60 shows the luminosities with and without 394 MHz crab cavities in the ESR. In this calculation, we usedd both 197 MHz and 394 MHz crab cavities in the HSR. Crab cavities for the ESR are clearly needed, as without them the luminosity would be reduced to $0.8 \times 10^{34}\,\mathrm{cm}^{-2}\,\mathrm{s}^{-1}$.

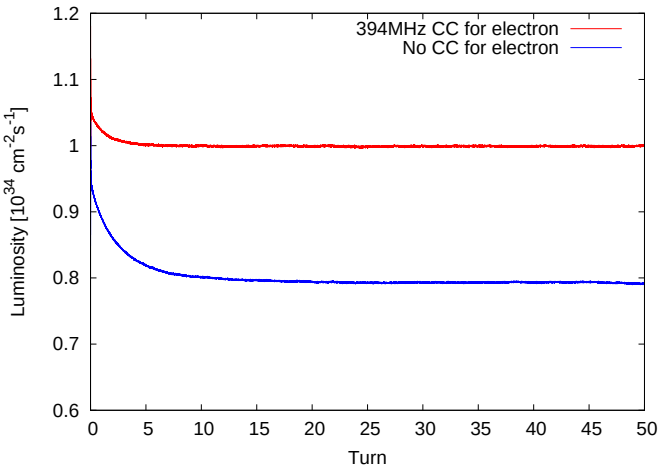

Figure 4.60: Luminosity evolution with and without electron crab cavities. Two different crab cavity frequencies are shown, and the lines for those two frequencies almost coincide. Chapter4/figs/red replaced.

Beam-beam Limit

The beam-beam limit is defined as the maximum beam-beam parameter that a collider can achieve and sustain over long periods of time. After the beam-beam limit is reached, the luminosity will no longer increase linearly with the bunch intensity since the beam emittance blows up due to the strong nonlinear beam-beam interaction.

Figure 4.61 shows the luminosity as function of the proton bunch intensity N_p. The proton bunch intensity is scanned from 0.41×10^{11} up to 1.25×10^{11}. As the plot shows, the luminosity will deviate from its scaling linearly with the proton bunch intensity when the proton intensity exceeds 0.9×10^{11}, which is about 30% larger than the design proton bunch intensity of 0.688×10^{11}.

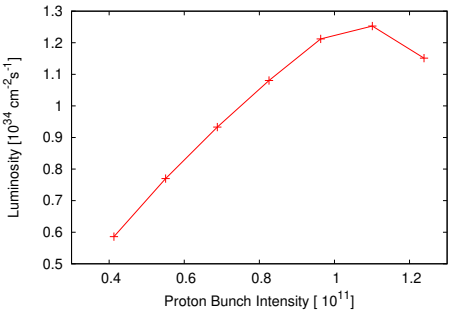

Figure 4.61: Luminosity as function of proton bunch intensity from strong-strong simulations.

Figure 4.62 shows the luminosity as function of the electron bunch intensity N_e. The electron bunch

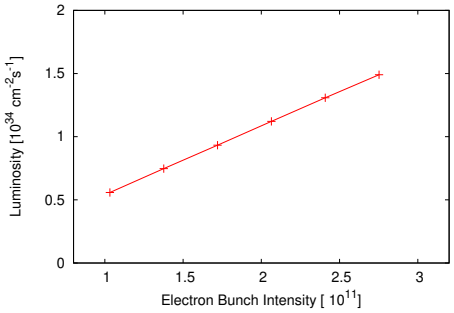

Figure 4.62: Luminosity as function of electron bunch intensity from strong-strong simulations.

intensity is scanned from 1.0×10^{11} up to 2.7×10^{11}. As shown, the luminosity increases almost linearly with the electron bunch intensity in this range. The design electron bunch intensity is 1.72×10^{11}. However, with increased electron bunch intensity, we observed an elevated proton emittance growth rate. Since there is no radiation damping in the HSR, any sizable proton emittance growth should be avoided.

Electron Working Point Considerations

To determine optimal design tunes for the ESR in the presence of beam-beam interaction, we performed electron tune scans with both weak-strong and strong-strong simulation models. In the weak-strong tune scan, we assume that the proton bunch is rigid and the electron bunch is represented by 50,000 macro-particles. Both the horizontal and vertical electron tunes are scanned between 0.02 and 0.25 with a step size of 0.02. Electrons are tracked to 50,000 turns, which is 10 times longer than the transverse synchrotron radiation damping periods. In this study, we focus on the luminosity and the electron bunch sizes after the electron bunch reaches its quasi-equilibrium.

Figure 4.63 shows the final luminosity averaged over the last 1000 turns in the weak-strong simulation. From the plot, luminosity is higher when the electron beam's horizontal tune is below 0.10, especially with a higher vertical tune. The results can be explained by the pinch effect of beam-beam interaction when the horizontal tune is close to an integer.

In the strong-strong electron tune scan, both bunches are represented by 500,000 macro-particles and are tracked to 50,000 turns. The proton tunes are fixed to (0.228, 0.210). Both the horizontal and vertical tunes of electron beams are scanned from 0.02 through 0.20 in steps of 0.02. Figures 4.64 shows the average luminosity in the last 1000 turns as function of electron tunes. The luminosity is higher with a smaller horizontal tunes together with a higher vertical tune, which is in agreement with the results from the above weak-strong tune scan.

Figures 4.65 and 4.66 show the relative variation of the horizontal and vertical proton beam sizes at the beginning and at the end of tracking. A larger proton beam size growth presents when the horizontal tune is around 0.06 and around 0.14. Our explanation is that the beam-beam interaction introduced tune footprint overlaps the 10th order resonance line at 0.1 and the 5th order resonance at 0.2. We also observe larger beam size changes along the diagonal in the tune space, which is due to the linear betatron coupling resonance.

We originally chose the fractional design tunes $(0.08, 0.06)$ for the ESR. With this working point,

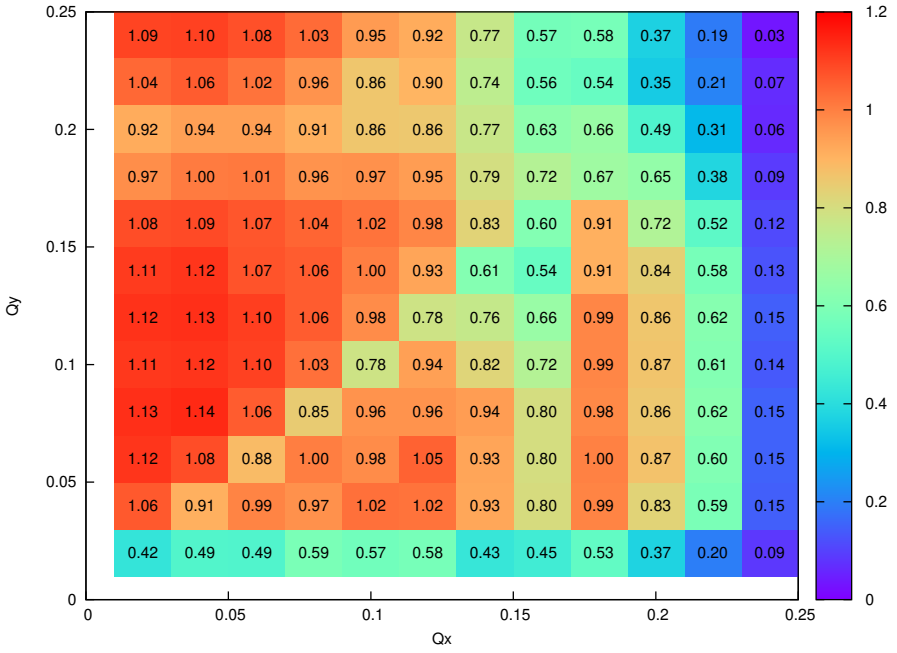

Figure 4.63: Luminosity, averaged over the last 1000 turns, as a function of electron tunes in the first pass weak-strong simulation. Values are in units of $10^{34}\,\mathrm{cm}^{-2}\,\mathrm{s}^{-1}$.

the maximum design luminosity can be reached with a relatively smaller proton vertical beam size growth rate than these working points in the upper-left corner in Figures 4.64.

However, during the polarization simulation studies for the ESR, we noticed that a low vertical tune of electron beam makes it difficult to correct vertical closed orbit and betatron coupling which are vital for polarization. Recently we did a fine electron tune scan in the upper-left corner of Figures 4.64 and found that a working point (0.08, 0.14) also delivers an acceptable proton vertical beam size growth rate in the strong-strong beam-beam simulation. Currently we are carrying out dynamic aperture and polarization simulation studies to verify this working point. The final optimal design tunes for the ESR should be accepted by beam-beam, dynamic aperture, polarization, and instabilities.

Proton Working Point Considerations

The proton working point for the routine RHIC polarized proton operation is between 2/3 and 7/10. For the EIC, since colliding beams have charges with opposing signs, the working point can be selected as (0.310, 0.305), which mirrors the tunes of the RHIC proton tunes below the half integer. However, there are many distinguishing features of the EIC, e.g. the large synchrotron tune of the ion beam, flat beams at the IP, and the crab crossing scheme. These features motivate the detailed tune scans shown in the previous section.

The crabbing tail of the proton beam may excite the synchro-betatron resonance. For working points around $(0.31, 0.305)$, the leading resonance for the horizontal motion is $3\nu_x + p\nu_z = 1$, where p is a positive integer. Theoretical studies and simulations suggest that the degradation improves if the tune moves to $(0.228, 0.224)$, between 2/9 and 1/4, where the leading resonance is $4\nu_x + p\nu_z =$

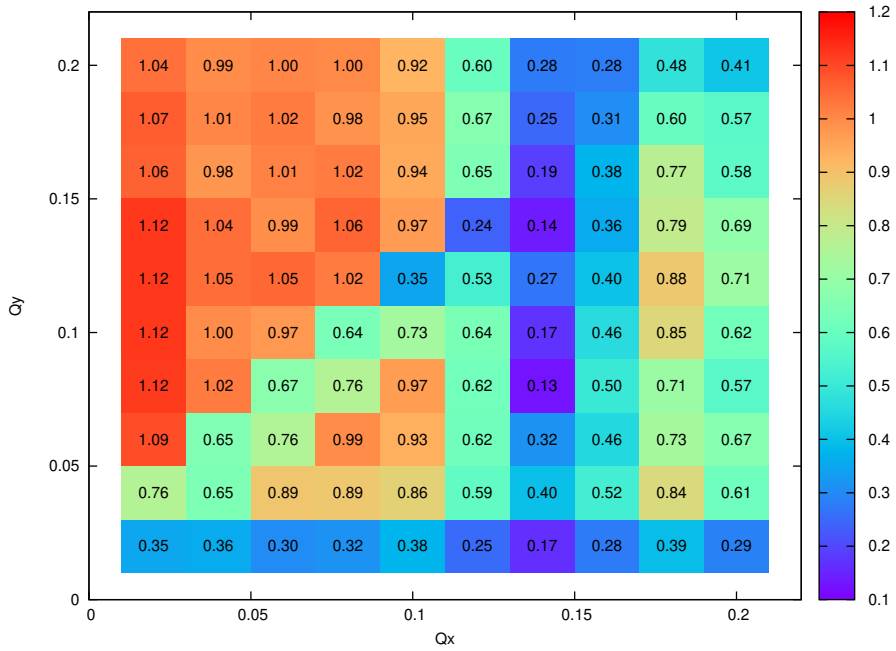

Figure 4.64: Luminosity averaged over the last 1000 turns of a strong-strong simulation as function of electron tunes. Values are in units of $10^{34}\,\mathrm{cm}^{-2}\,\mathrm{s}^{-1}$.

1.

In addition, the flatness of both beams (defined as σ_y/σ_x) at the IP is as low as 0.09 to achieve higher luminosity. The very flat beam makes the vertical direction more vulnerable to degradation due to synchro-betatron couplings as a result of the intrinsic nonlinear coupling effect of the beam-beam force as well as the hour-glass effect. The leading resonance for the vertical motion is $2\nu_x - 2\nu_y - p\nu_z = 0$. A typical working point close to the diagonal line, e.g. $(0.228, 0.224)$, excites low order, $p = 1$, synchro-betatron coupling resonances. Simulations have verified that moving the working point away from the diagonal line helps to improve the dynamics in the vertical plane. As a result, the working point $(0.228, 0.210)$ is proposed, where the resonance order increases to $p = 4$.

Figure 4.65: Relative proton horizontal beam size change in percent, computed as the fractional difference between the average size in the first 1000 turns and the last 1000 turns, as a function of electron tunes, from strong-strong simulations.

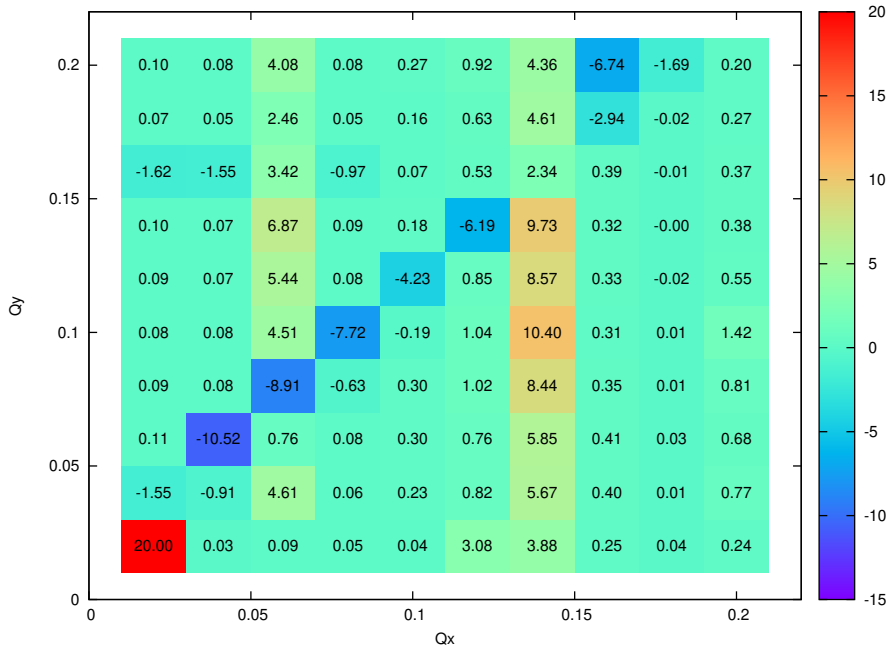

Figure 4.66: Relative proton vertical beam size change in percent, computed as the fractional difference between the average size in the first 1000 turns and the last 1000 turns, as a function of electron tunes, from strong-strong simulations.

Proton Stability with Crabbed Collision

For crabbed crossing collisions, when the bunch length is comparable with the wavelength of the crab cavity, the sinusoidal waveform of the crab-cavity voltage generates transverse offsets at the IP as function of the longitudinal position of individual particles within the bunch.

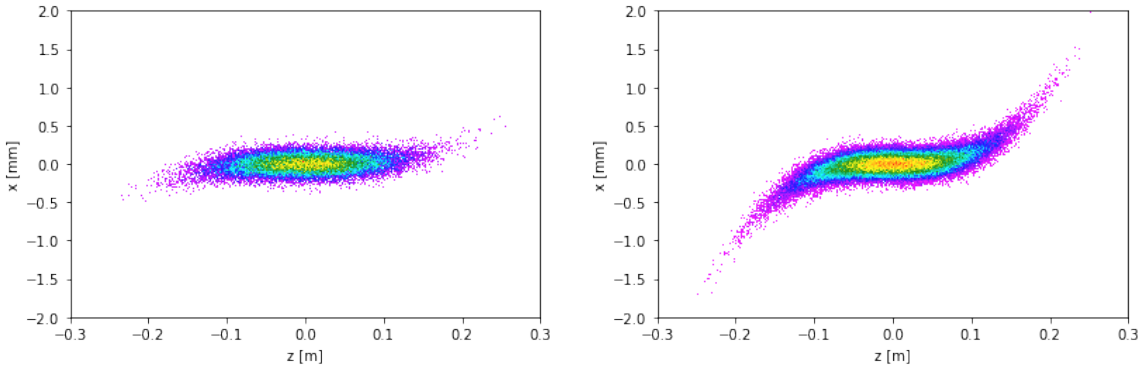

Figure 4.67: Proton beam $x - z$ distribution with 197 MHz (left) and 394 MHz (right) crab cavities.

A lower crab cavity frequency results in a more linear crabbing than a higher frequency. However, the low frequency crab cavity has a bigger physical size and requires a higher crabbing voltage. Figure 4.67 shows the comparison of the proton beam distribution (projection in x-z plane) with 197 MHz and 394 MHz crab cavity systems. The tails will excite synchro-betatron resonances via the nonlinear beam-beam interaction. To avoid excessive beam quality degradation, massive beam-beam simulations have been performed in order to understand the resonances and to optimize the design parameters.

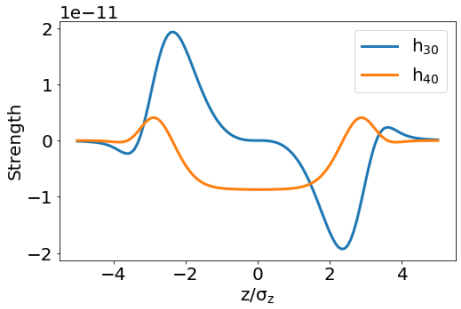

Figure 4.68: Spectrum of the horizontal centroid motion of the proton bunch with three different proton crab cavity frequencies.

- *Synchro-betatron Resonance*

  Many higher-order synchro-betatron resonances are excited in the crab-crossing collision scheme with a large crossing angle. This causes luminosity degradation and should be avoided or mitigated in the design. If we choose the unperturbed working point around the diagonal resonance line $\nu_x - \nu_y = 0$, a family of synchro-betatron resonances $m\nu_x + p\nu_z = 0$ will be excited. The driving term strength h_{m0} can be calculated from the beam-beam Hamil-

tonian in the presence of the crab cavity, as shown by Figure 4.68. It shows that a larger m is preferable, which supports the tune change from below $1/3$ to below $1/4$.

- *Frequency Map Analysis*

  Frequency map analysis (FMA) is a powerful technique to visualize the impact of nonlinear resonances. This technique is applied after tracking test particles and recording their turn-by-turn positions for N turns. For each record, the data is split into two time windows, each of which has length $N/2$. The first time window starts from the beginning; while the second window starts from i^{th} turn, with $i \in [0, N/2]$. The frequency diffusion of horizontal motion is defined as:

$$dQ_x = \log_{10} \max_i \left| Q\left(x\left(0, \frac{N}{2}\right)\right) - Q\left(x\left(i, \frac{N}{2} + i\right)\right)\right| \tag{4.32}$$

  where Q is the frequency calculated by NAFF using the sequence in the argument. Similarly diffusion for vertical motion is also calculated.

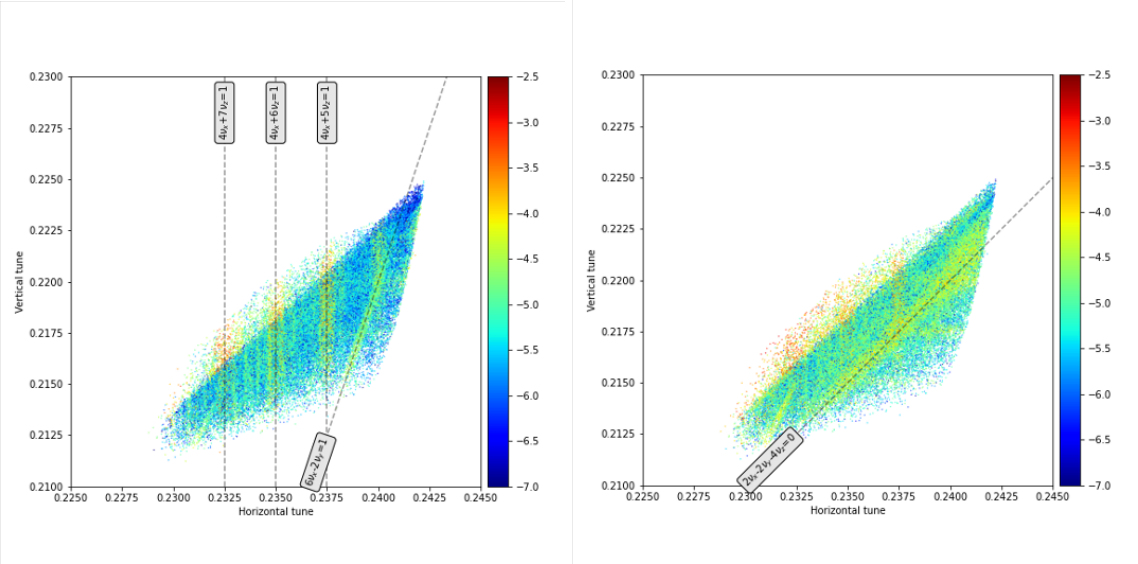

Figure 4.69: Frequency map analysis of proton beam with working point (0.228, 0.21). Left: horizontal diffusion; right: vertical diffusion

Figure 4.69 shows FMA plots of horizontal and vertical motion of working point $(0.228, 0.21)$. The data is calculated by the strong-strong simulation code BeamBeam3D using 1024 consecutive turns. This clearly shows that the horizontal motion has a dominating resonance at $4\nu_x + 5/6/7\nu_z = 1$, while the vertical motion has a resonance at $2\nu_x - 2\nu_y - 4\nu_z = 0$, a reduced strength compared with $2\nu_x - 2\nu_y - \nu_z = 0$ if the working point $(0.228, 0.224)$ is chosen.

Coherent Beam-beam Instability

The electromagnetic beam-beam interactions between the counter rotating electron beam and proton beam can cause coherent instabilities of the colliding beams. Those instabilities depend on the

working points, i.e. tunes, of the collider. In this report, we carried out a systematic tune scan of the electron beam with the fixed tunes of the proton beam.

Figure 4.70 shows evolutions of the proton beam horizontal centroid (red) and the electron beam horizontal centroid (green) as a function of tune scan. It is seen that there is a major instability stopband in the electron horizontal tune space between 0.1 and 0.14.

An initial spectral analysis of the centroid motion of both beams shows the presence of proton beam mode in the electron beam centroid motion and vice versa. This suggests strong coupling between the electron beam mode and proton beam mode during the beam-beam interactions. The instability associated with the 0.1 to 0.14 stopband could be due to the coupling sum resonance between the electron beam mode and the proton beam mode. Such an instability can be avoided by moving the proton beam working tunes away from the original tunes.

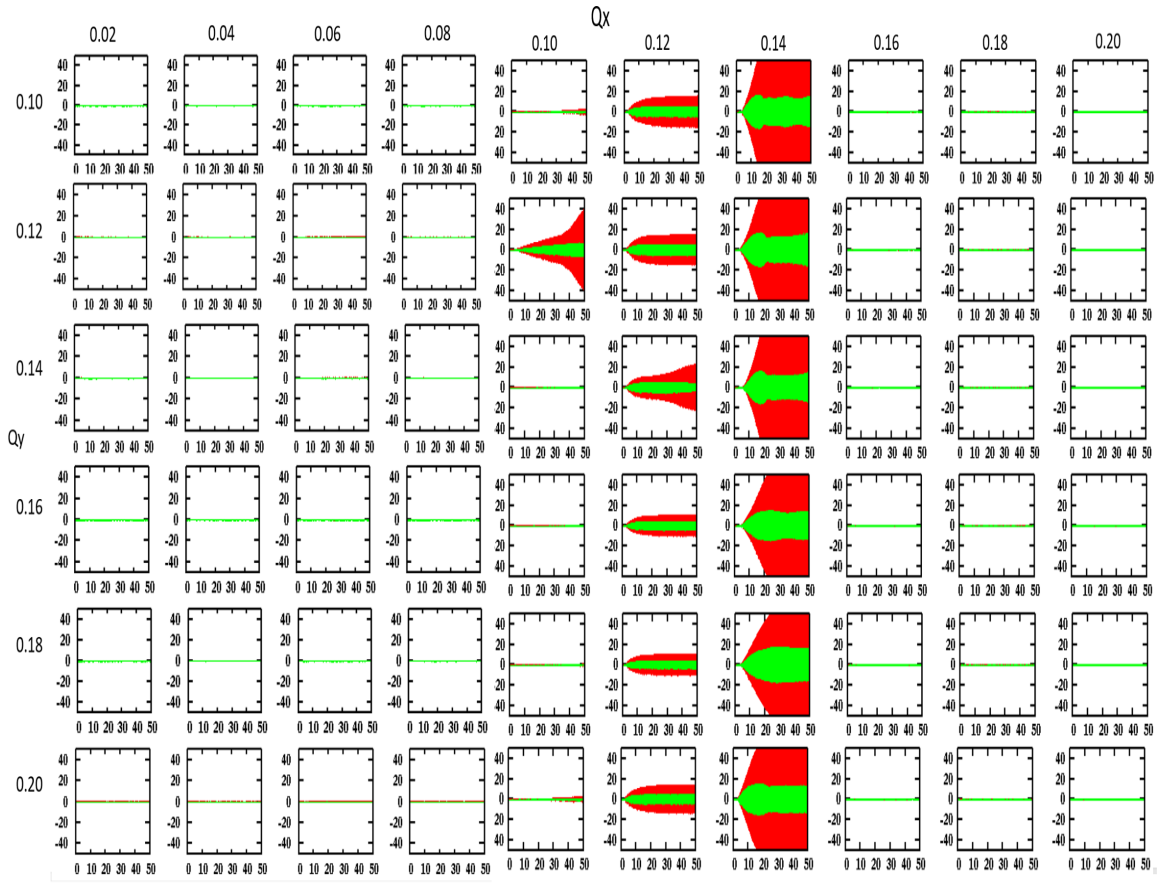

Figure 4.70: Evolutions of the proton beam horizontal centroid (red) and the electron beam horizontal centroid (green) as a function of tune scan.

4.5.3 Imperfections with Crabbed Collision

In the previous sub-sections, the beam-beam studies presented assume that the crab cavities have exact voltages with precise timing with respect to the beam arriving time, and are located at lo-

cations with ideal optics properties. The properties include the $\pm(2n+1)\,\pi/2$ betatron phase advance from IP and zero dispersion functions. In this section, the effect of imperfections of the crabbing scheme is presented. In the linear model used in this subsection, the 4D phase space refers to (x, x', z, δ).

Effect of Phase Advance Error

In the realistic lattice, the phase advance between the crab cavity and the interaction point is not $(2n+1)\,\pi/2$. We define $\delta\psi_i$ as the phase difference of the i^{th} cavity from the ideal phase. The phases of the two crab cavities will be $\psi_1 = -\pi/2 - \delta\psi_1$ and $\psi_2 = \pi/2 + \delta\psi_2$. The 'one-turn' map at the interaction point including the crab cavity is

$$M = \tilde{M}_{CC_1}\tilde{M}_{IP}\tilde{M}_{CC_2} \tag{4.33}$$

where $\tilde{M}_{IP}$ is the one-turn map of IP with the head-on scheme without crab cavity. $\tilde{M}_{CC}$ is the matrix for linearized crab cavity kick, measured at IP:

$$\tilde{M}_{cc_{1/2}} = M_{CC_{1/2}\to IP}(-\psi_{1/2})M_{cc}M_{IP\to CC_{1/2}}(\psi_{1/2}) \tag{4.34}$$

By varying the voltage of the crab cavity, the beam may have ideal crab dispersions θ_c with vanishing derivative, same as the case without phase advance error. This requires the voltage of the crab cavity becomes:

$$\begin{pmatrix} V_1 \\ V_2 \end{pmatrix} = \begin{pmatrix} \frac{-\sin(\delta\psi_2)+\sin(\delta\psi_2-2\pi\nu_x)}{\sin(\delta\psi_1+\delta\psi_2-2\pi\nu_x)} \\ \frac{-\sin(\delta\psi_1)+\sin(\delta\psi_1-2\pi\nu_x)}{\sin(\delta\psi_1+\delta\psi_2-2\pi\nu_x)} \end{pmatrix} V_0 \tag{4.35}$$

where V_0 is the crab cavity's voltage when no phase advance error is present. However, in the presence of the crab phase error, the crab dispersion will leak outside the pair of crab cavities and cause additional synchro-betatron coupling. This effect is more important for the electron beam since the betatron tune and synchrotron tune are close which induces large oscillation of the transverse beam size. Therefore the phase advance between the crab cavity will be kept π, or $\delta\psi_1 = -\delta\psi_2$, so that the crab dispersion leakage vanishes. For the proton beam, such cancellation is hard to achieve. The simulation showed that a 5-degree deviation from π is tolerable when the voltages of the crab cavities are set correctly, as shown in Figure 4.71.

Horizontal Dispersion at Crab Cavity

In the interaction region design of the EIC, dispersion is helpful for the energy resolution of detecting the collision products. The location of the crab cavities is designed to have finite dispersion, especially on the forward side of the IP in the proton lattice and the rear side in the electron lattice. When the dispersion and/or its derivative at the crab cavity do not vanish, the longitudinal position-dependent energy kick will have a residual effect on both the longitudinal and the transverse plane. The crab dispersion will couple with the momentum distribution, therefore a coherent treatment is necessary, as in Ref **[?]**

When a finite dispersion presents at the crab cavity (d, d'), both the crab dispersion and the mo-

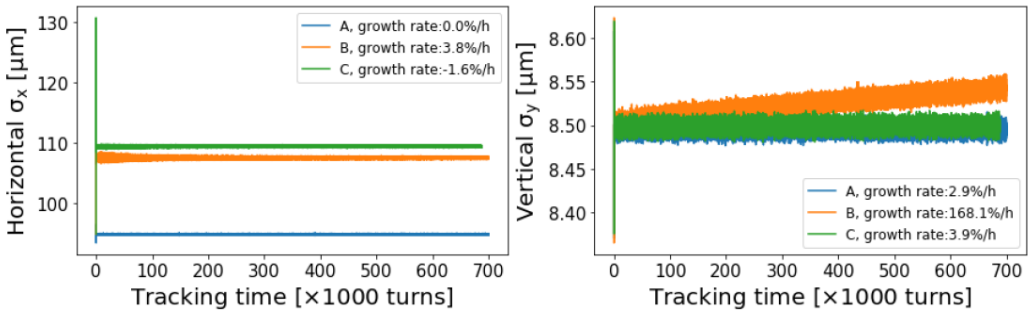

Figure 4.71: Horizontal and vertical beam size evolution by the weak-strong simulation. Case A: Crab crossing with ideal phase advance, $\delta\psi_1 = \delta\psi_2 = 0$, Case B and C have phase advance error $\delta\psi_1 = -2^\circ$, $\delta\psi_2 = -3^\circ$. Case B has an incorrect voltage setting while Case C set the voltage according to the equation 4.35

mentum distribution are not vanish at IP, which are

$$\begin{aligned} \zeta_b &= \left(-\frac{\Lambda\lambda_b}{1+\lambda_b d}, 0\right)^{\mathrm{T}}, \\ \eta_b &= (1+\lambda_b d)\lambda_b d \left(\Lambda d', -\frac{d}{\Lambda}\right)^{\mathrm{T}} + r_{56}(1-\lambda_b d)\left(\Lambda\lambda_b, 0\right)^{\mathrm{T}} \end{aligned} \tag{4.36}$$

where ζ_b and η_b represent the crab dispersion and momentum dispersion respectively. $\Lambda = \sqrt{\beta\beta^*}$ and λ_b is the normalized strength of the crab cavity, which should be set to θ_c/Λ. From the theory, it is clearly to see that the effect at IP is second order with respect to the d and d'

Nonlinear beam-beam tracking is performed to ensure the beam quality is preserved with the design dispersion at the crab cavity. As shown in Figure 4.72, the luminosity of the current design is not sensitive to the dispersion function at crab cavity up to values of 5 m. The current lattice has about 0.5 m dispersion at the crab cavities in both the proton and electron lattice. Simulations also show that the luminosity will not be negatively affected by the derivative of the dispersion if the value is less than 0.1. The current design has a safety margin of 10 below the threshold.

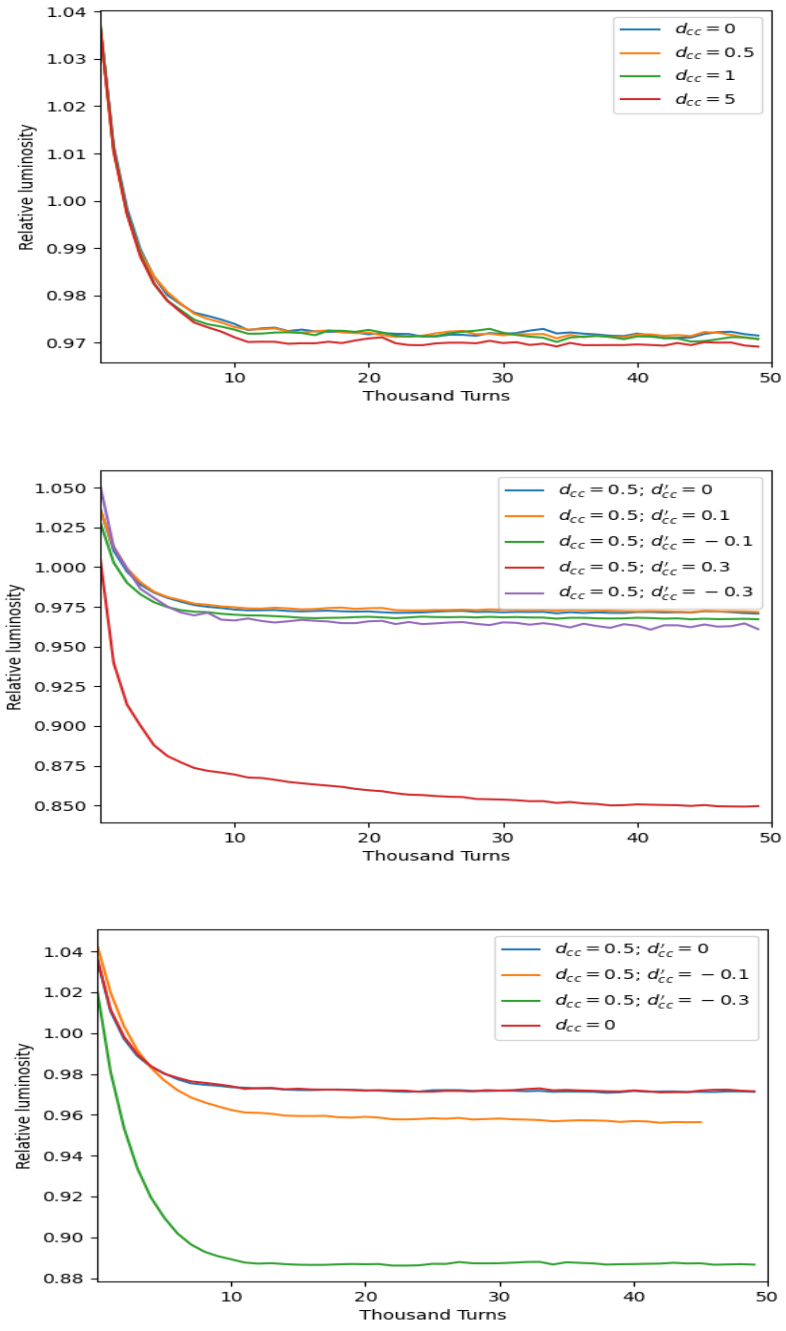

Figure 4.72: Luminosity comparison of, top figure: different dispersion function at crab cavity in hadron beam, with zero derivative of dispersion; middle figure: different derivative of dispersion function at crab cavity in hadron beam, with 0.5 m dispersion function; bottom figure: different derivative of dispersion function at crab cavity in electron beam, with 0.5 m dispersion function.

Effects of Detector Solenoids in the Crab-crossing Scheme

The crab crossing scheme for the electron beam will be affected by the detector solenoid. The 4 m long detector solenoid is designed to provide up to 3 T longitudinal magnetic field aligned with the electron trajectory.

The rotation angle θ_s caused by the detector solenoid can be approximated using a hard-edge solenoid model,

$$\alpha_s = \frac{B_\parallel L_s}{2P_0}, \tag{4.37}$$

where $B_\parallel$ is the solenoid field, L_s is the length of the hard-edge model and P_0 is the momentum of the charged particle. The rotation combined with horizontal crab cavity will create an effective vertical crossing angle

$$\theta_{cv} = \theta_c \sin\left(\frac{\alpha_s}{2}\right) \ . \tag{4.38}$$

The effective vertical Piwinski angle Θ_{pv} is

$$\Theta_{pv} = \frac{\sigma_z}{\sigma_y}\theta_{cv} = \frac{\Theta_P}{r}\sin\left(\frac{\alpha_s}{2}\right) \ , \tag{4.39}$$

where Θ_P is the original Piwinski angle (horizontal) without detector solenoid and $r = \sigma_y/\sigma_x$ is the transverse beam size ratio at the IP.

As shown in Table 4.20, the effective vertical Piwinski angle clearly indicates that the rotation effect of the detector solenoid must be compensated for the electron beam due to the adoption of flat beam collision scheme ($r = 0.09$). Otherwise, a significant luminosity loss will occur. The compensation may be either a local scheme (in-between the pair of horizontal crab cavities) or a global version with vertical crabbing kicks to correct the vertical crossing angle θ_{cv}. The local compensation is the cleanest method, however may not be practical since the space between the IP and the crab cavity is fully occupied. One approach could adopt global coupling compensation; the effective vertical crossing angle could be compensated by vertical crabbing kicks with voltage

$$\hat{V}_{CC,y} = \pm\frac{cE_s}{4\pi f_{\rm RF}\sqrt{\beta_y^*\beta_{cc,y}}}\theta_{cv} \ . \tag{4.40}$$

Since the detector solenoid is aligned with the electron beam trajectory, the proton beam enters the same solenoid at a horizontal angle, equal to the crossing angle. As a consequence, the proton beam receives a vertical kick by the solenoid. This vertical kick could be corrected by nearby vertical

	Proton	Electron
Energy [GeV]	275	10
RMS bunch length [cm]	6	2
RMS horizontal beam size [μm]	95	95
Transverse ratio, σ_y/σ_x	0.09	0.09
Piwinski angle, Θ_P	7.9	2.6
Vertical Piwinski angle, Θ_{pv}	0.29	2.6

Table 4.20: Vertical Piwinski angle caused by the detector solenoid.

correctors to achieve a vanishing closed orbit at the IP.

When both the rotation and the closed orbit are corrected in the IP, the interplay between the detector solenoid and the beam-beam effect can be estimated in the Lorentz boost frame where the beam-beam interaction is equivalent to a head-on collision. In this frame, the proton would experience a vertically deflecting force

$$F_y = 2qB_{\parallel}c\sin\left(\frac{\theta_c}{2}\right) . \tag{4.41}$$

The longitudinal collision position is $s = \left(z_e + z_p\right)/2$. With a 5σ cutoff, the maximum location for this interaction is at s =0.2 m. Detector solenoid modeling is being implemented in strong-strong and weak strong simulation codes to simulate the long term effect on the beam dynamics.

Effects of Tilted ESR Plane

The ESR is proposed to be tilted by $\sim$ 0.2 mrad to resolve the interference between rings and transfer line in IR2. Figure 4.73 illustrates this concept. The rotating axis goes through both interaction points: IP6 and IP8. The ESR and HSR are vertically separated at IR2 without any vertical dipoles.

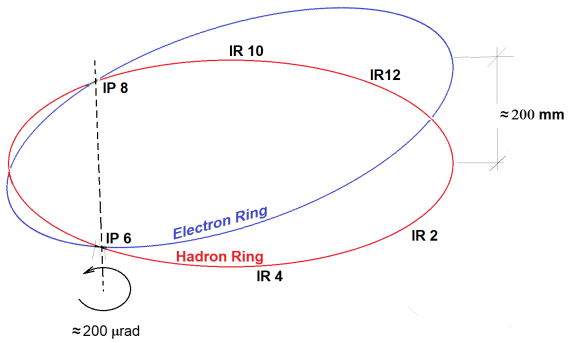

Figure 4.73: Schematic diagram of tilted ESR in EIC.

When two beams collide with a crossing angle, it is convenient to consider the beam-beam interaction in the boost frame [**?**], as shown in Fig. 4.74. Although the rotation angle is small, the longitudinal axis has been changed. The new Lorentz Boost map is concatenated by the rotation map and the Hirata map

$$\mathcal{L}' = \mathcal{R}(\chi) \circ \mathcal{L}(\theta_c') \tag{4.42}$$

The new crossing angle $\theta_c' \approx$ 12.5 mrad, and the pure rotation angles for electron and ion beam are $\chi_e \approx \chi_i \approx -4$ mrad [**?**]. The rotation couples the vertical and longitudinal plane which can be corrected by skew quadrupoles between the crab cavities and IP [**?**] or vertical crab cavity.

Figure 4.75 resents the vertical size evolution of the proton beam by weak-strong simulation. The left plot shows the tracking result without second order harmonic crab cavity, and the right plot shows the tracking data with second order harmonic crab cavity. With vertical crabbing and harmonic crab cavity, the vertical growth caused by tilted ESR is compensated. Without vertical crabbing, no matter if harmonic crab cavity is present, the vertical size growth caused by tilted ESR is

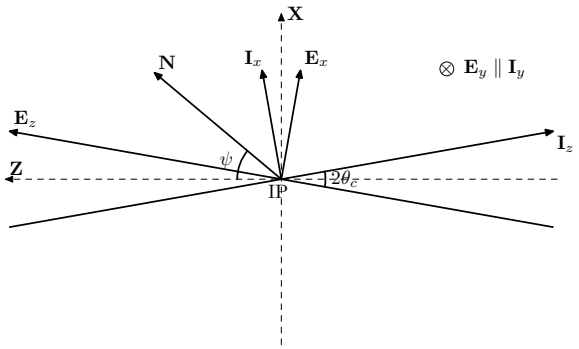

Figure 4.74: The boost frame with a large crossing angle before the ESR is tilted. **N** points from IP6 to IP8. $\theta_c = 12.5$ mrad is the half crossing angle, and $\psi = \pi/6 + \theta_c$. The right-handed $(\mathbf{E}_x, \mathbf{E}_y, \mathbf{E}_z)$ are the basis vectors for the Frenet-Serret frame of the ESR, and the left-handed $(\mathbf{I}_x, \mathbf{I}_y, \mathbf{I}_z)$ are of the ion ring.

unacceptable

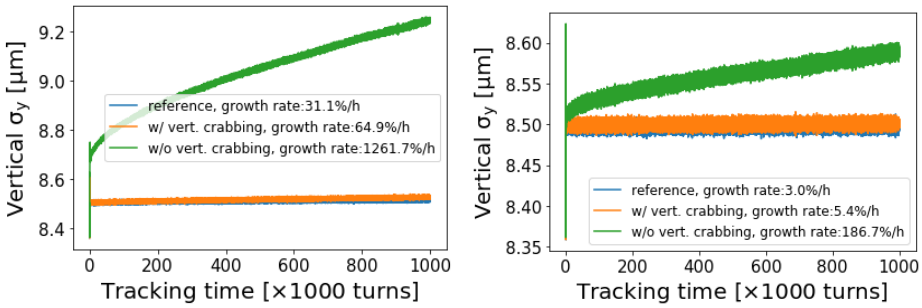

Figure 4.75: Beam size evolution by weak-strong simulation, left: without 2nd-order harmonic crab cavity, right: with 2nd-order harmonic crab cavity.

Tolerance of vertical crossing angle at IP

In the EIC, the horizontal crab cavities will create a z-dependent horizontal offset along the bunch length at IP. Here z is the longitudinal offset w.r.t. the bunch center. Conventionally, we define dx/dz as the horizontal crab dispersion. There are other three terms of first order crab dispersion: $dx'/dz, dy/dz, dy'/dz$. dy/dz is the vertical crab dispersion. We normally also call dx/dz and dy/dz at IP as horizontal and vertical crabbing angles.

Due to the detector solenoid and tilted ESR plane w.r.t. the HSR plane in the interaction region (IR), horizontal crab dispersion may be coupled to the vertical plane and generates non-zero vertical crab dispersion at IP. Vertical crab dispersion or vertical crabbing angle at IP will generate a z-dependent vertical offset along the bunch length. Offset beam-beam interaction in either horizontal or vertical plane may cause the proton beam emittance blow up and leads to a bad proton beam life.

We carried out strong-strong, weak-strong beam simulation, and dynamic aperture calculations to determine the tolerances of crab dispersion at IP, in particular, we will focus on the vertical crab dispersion dy/dz. The design beam and machine parameters for the collision between polarized

dy/dz **at IP** (µrad)	**DA-Min** (σ)	**DA-Max** (σ)	**DA-Ave** (σ)	**DA-RMS** (σ)
0	6.2	10.2	8.0	1.2
5	6.2	9.8	7.5	1.0
10	5.6	10.8	8.2	1.4
20	5.2	11.6	7.8	1.9
30	5.6	10.4	8.0	1.4
40	4.8	11.4	7.8	1.8
50	5.8	10.4	7.9	1.1
60	4.8	8.6	6.7	1.3

Table 4.21: Dynamic aperture versus vertical crab dispersion at the Intersection Point.

10 GeV electrons and 275 GeV protons are used. As an example, Table 2 shows the calculated 10^6 turn dynamic aperture in a vertical crab dispersion scan. For each vertical crab dispersion setting, we track with 10 seeds of IR nonlinear magnetic field errors. We list the minimum, maximum, and average dynamic apertures for each dy/dz setting. Based on the simulation results with weak-strong model and quick dynamic aperture calculation, the vertical crab dispersion tolerance at IP is about 20-25 µrad, which requires an accurate and robust online correction system in the future EIC operation.

Betatron coupling and crab dispersion correction in IR

There are several aspects of the coupling effect induced by the detector solenoid at the IP of each IR. They include generation of betatron coupling as well as of vertical momentum and crabbing dispersions and their slopes at the IP. All of these effects must be compensated at each IP. The complete coupling compensation scheme is described in the IR design section, Section **??**. Here we only briefly reiterate the part of the coupling correction solution relevant to the crabbing scheme.

The main impact of the detector solenoid on the crabbing dynamics is rotation of the crabbing plane, or, in other words, coupling of the horizontal crabbing dispersion $(dx/dz, dx'/dz)$ into the vertical plane $(dy/dz, dy'/dz)$. If uncorrected it has adverse effects on the beam stability and luminosity. Correction is done using skew quadrupoles. This is the only feasible option given the lack of space for anti-solenoids.

Lack of betatron phase advance variation does not allow for correction of all coupling effects between each crab-cavity set and the IP. However, it is not needed, since the only necessary requirements are correction of $(dy/dz, dy'/dz)$ at the IP and closing of the vertical crabbing dispersion between the crab-cavity sets. In terms of the transfer matrix elements, the former condition (namely, $(dy/dz, dy'/dz)_{IP} = 0$) can be expressed as

$$M_{yx'}^{FC\to IP} = 0,\ M_{y'x'}^{FC\to IP} = 0, \tag{4.43}$$

where the transfer matrix M is from the Forward Crab cavity set (FC) to the IP. The condition on localizing the crabbing dispersion between the forward and rear crab cavity sets is given by

$$M_{yx'}^{FC\to RC} = 0,\ M_{y'x'}^{FC\to RC} = 0, \tag{4.44}$$

where M is the transfer matric from FC to the Rear Crab cavity set (RC).

The conditions of Equation 4.43 are satisfied by adjusting the strengths of two skew quads placed between the FC and IP. The quad locations are optimized from their orthogonality point of view. Given the betatron phase advance from the FC to IP, one of the skew quads is placed near the crab cavity section on its IP side while the other one is placed near the final focusing quads (FFQs). In case of the ESR, the second quad is combined with one of the FFQs as . Closing of the vertical crabbing dispersion according to Eq. 4.44 requires two additional knobs and is accomplished using two additional skew quads on the rear side of the IR between the IP and RC. For the same reason as on the forward side, one of the skew quads is placed close to the rear FFQs while the second one is near the RC on its IP side. The ESR FFQ design allows for combing the first skew quad with one of the FFQs.

Correction of the vertical momentum dispersion at the IP and control of transverse betatron coupling is done using additional skew quads that are located outside of the beam line region enclosed by the FC and RC. These details can found in Section **??** describing the IR design.

Crab Cavity Voltage Miscalibration

The crab voltage may be have a calibration error, which differ from the ideal voltage. A higher voltage may have have benefit in the geometric luminosity when the proton bunch is long, compared with the crab cavity wavelength (Figure 4.76). However, an increased or decreased voltage from the calculated value leads to a linear correlation between the horizontal and longitudinal direction, therefore may enhances the synchro-betatron resonance as described earlier.

Figure 4.77 shows the simulation results with slightly modified crab cavity voltage. The impact of luminosity due to ion beam's finite bunch length can be partially compensated by the increased crab cavity voltage. However, the long-term luminosity degradation also slightly increases due to the over crabbing. (observed in the case of 2% voltage increment, which is the optimized value for the geometric luminosity). The voltage of the crab cavity of electron beam should be set to its design value, since there is no benefit on any modification.

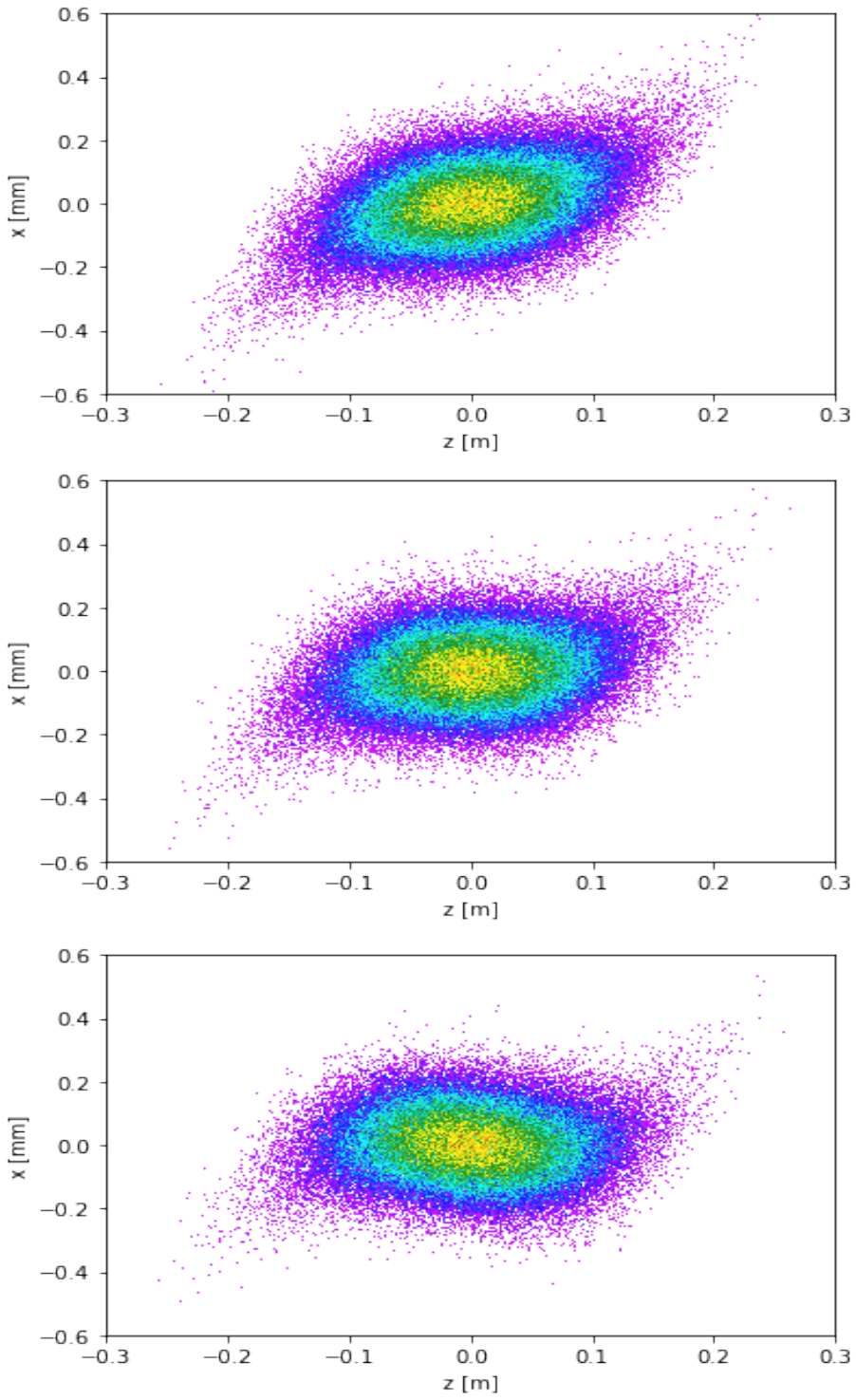

Figure 4.76: Horizontal-longitudinal distribution of protons at IP in the Lorentz frame under different crab cavity voltage, top: 3% less than design value; middle: design value; bottom: 3% larger than design value.

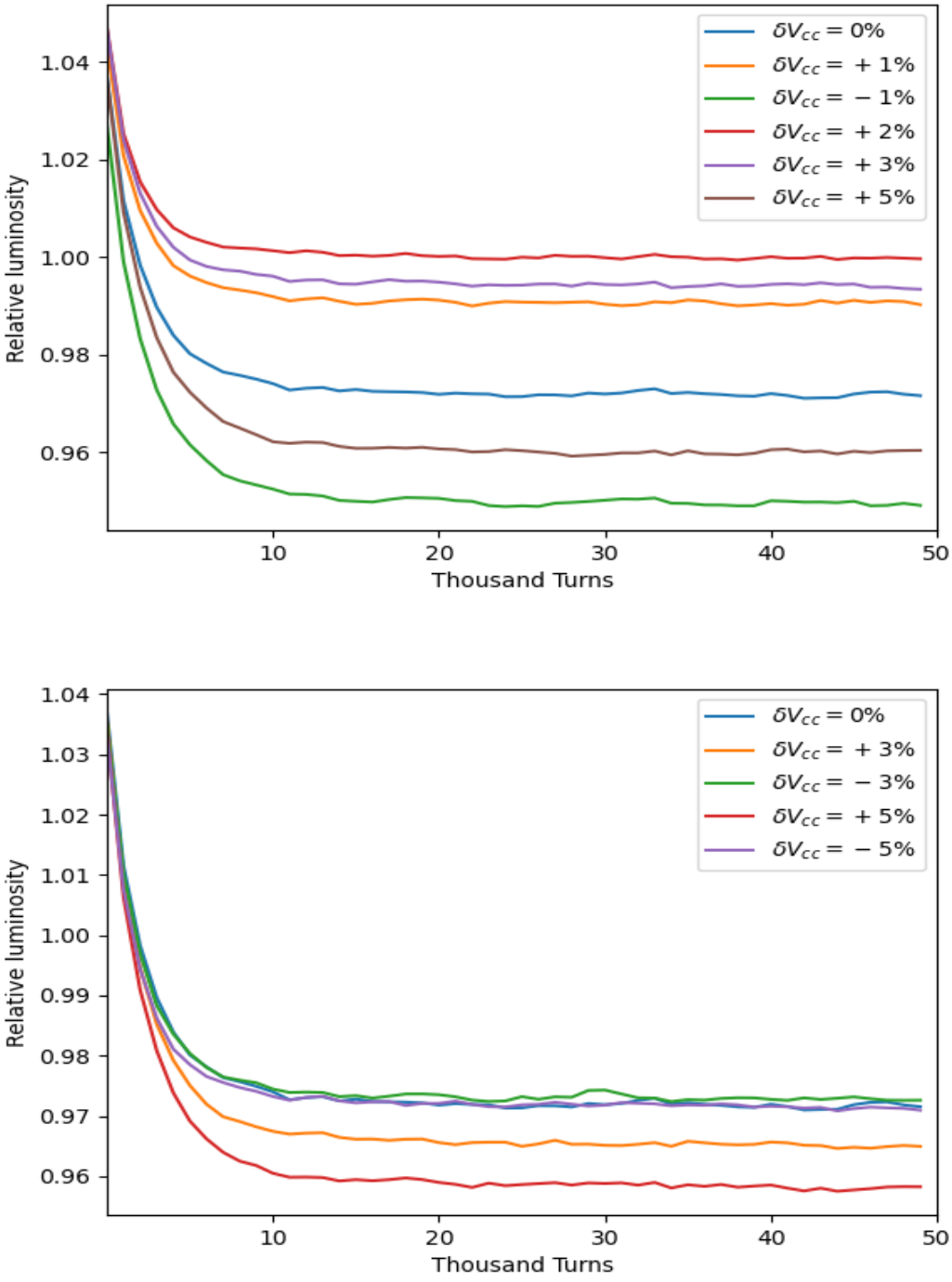

Figure 4.77: Luminosity comparison of different voltages at crab cavity. Top: in the HSR. Bottom: in the ESR.

4.5.4 Noises with Crabbed Collision

ESR Position Ripples at IP: Derong, text to be reduced

Beam-beam considerations directly affect many technical systems of the EIC, including magnet power supplies in both colliding rings. This section presents key findings for the ESR main magnet power supplies, summarizing more detailed analysis from [**?**].

Beam-beam requirements:

The luminosity reduction due to imperfect transverse beam overlap at the IP can be estimated by the factor $e^{-\frac{1}{4}(\delta_x^2+\delta_y^2)}$, where $\delta_{x,y}$ are the distances between the colliding beam centers in each plane in units of the corresponding rms beam size. For instance, assuming equal δ_x and δ_y and allowing no more than 5% luminosity reduction requires the relative orbit jitter at the IP to be below 32% of the corresponding rms size.

A much more stringent requirement for beam positional stability at the IP comes from dynamical aspects of beam-beam interaction, specifically the beam-beam kick modulation leading to the emittance growth of the hadron beam. For instance, as was shown analytically [**?**] as well as by means of weak-strong beam-beam simulations, to keep the emittance growth within 10% per hour, the amplitude of electron beam centroid oscillations at the proton betatron frequency needs to be limited to about 10^{-4} fraction of the rms beam size.

Even at much lower frequencies, the positional stability the electron beam must be maintained at a percent level of the beam size in each plane. This is illustrated in Fig. 4.78 which shows the proton beam size evolution when the electron beam centroid is oscillating near 60 Hz. Unacceptably high emittance growth occurs at higher oscillation amplitudes. Importantly, while the growth mainly occurs in the vertical plane, it is driven both by the horizontal and vertical orbit ripple. Even the cases of purely horizontal ripple (studied separately) result in the vertical growth via beam-beam-induced betatron and synchro-betatron coupling.

Fig. 4.78, as well as the more detailed analysis [**?**], suggest that to keep the vertical emittance growth within 10% per hour, the motion at the IP must be maintained within 1% of the beam size in both

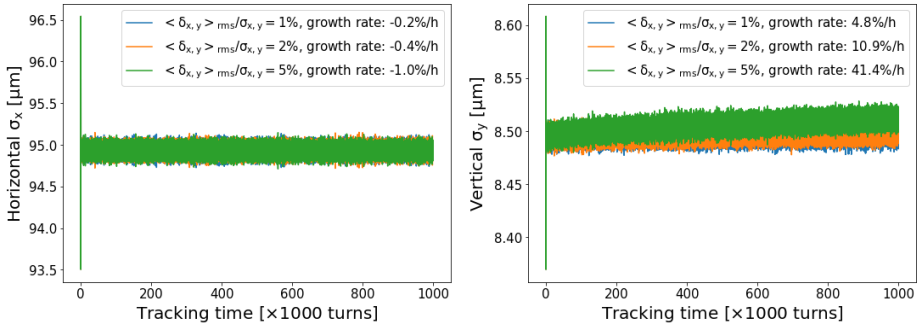

Figure 4.78: Proton beam size evolution from weak-strong simulation when the electron beam is undergoing positional oscillations amounting to 1, 2, or 5% of the rms beam size in each plane. The oscillations are band-limited to [55 65] Hz range, with uniform magnitude and random phase. Fitted beam size growth rates are shown in the legend.

planes. (Alternative configurations with somewhat higher noise in one plane at the expense of the other could also be acceptable.)

In addition to the beam centroid stability at the IP, beam-beam considerations impose limits for the maximum allowable electron beam size variation. These limits also depend on the frequency of the variation, with frequencies near the hadron betatron tune being the most dangerous. Quantitatively, however, these limits turn out not to be very restrictive, so they do not end up defining any power supply specifications. Instead, the quadrupole power supply ripple specifications largely follow from the required tune stability, i.e. something not directly related to beam-beam.

The rest of this section describes 1) how $\approx 10^{-2}$ of beam size level of positional stability could be achieved at low frequencies; 2) how $\approx 10^{-4}$ level stability will be achieved at high frequencies; and 3) how both of these affect the ESR dipole power supply current ripple specifications. In the rest of the section the low-frequency range is defined as [1-4000] Hz, and the high-frequency range as [4 40] kHz, corresponding to the tune range of [0.05-0.5].

Power supply ripple at frequencies 1-4000 Hz:

Here the two primary causes of the electron beam orbit jitter at the IP are the dipole magnet power supply ripple and the quadrupole magnet vibrations (treated in [**?**]). The yet-to-be-designed IP orbit feedback system should be able to significantly reduce the orbit ripple, especially at lower frequencies, and therefore potentially relax the specifications for the power supply ripple. However, because the PS systems have not been fully designed yet, the expected PS ripple spectrum is unknown and the expected residual orbit ripple with the feedback cannot be accurately estimated. Therefore, at this stage of the design, we conservatively specify the PS ripple without crediting the orbit feedback system. This will be iterated upon in the future.

Closed orbit perturbation due to rippling dipoles can be described analytically. In the simplest case of large number of dipoles, $N >> 1$, with an uncorrelated ripple of the fractional strength $\delta\theta/\theta$, the rms orbit ripple at the IP is given by

$$\left\langle \Delta x \right\rangle_{\rm rms} = \frac{\pi\sqrt{\bar{\beta}\,\beta^*}}{\sqrt{2N}\,|\sin(\pi\nu)|}\delta\theta/\theta, \tag{4.45}$$

where $\bar{\beta}$ is the average beta function, θ is the nominal bend angle, $\delta\theta =< \theta >_{\rm rms}$. Estimating this for the typical ESR lattice parameters (e.g. $\bar{\beta}$=30 m, β^*=0.4 m, $N = 670$, $\nu = 0.12$) results in about one-micron rms per $\delta\theta/\theta = 10^{-6}$ fractional ripple. This suggests that to passively maintain the orbit to within 1% of $\sigma \approx$100 µm horizontal beam size, the dipole power supply current ripple $\delta I/I \approx \delta B/B = \delta\theta/\theta$ on the order of one part-per-million (ppm) would be required. Note that here the ripple is assumed normalized to the operating current value.

More accurately, the orbit ripple for a given amount of dipole field ripple can be calculated with lattice codes. Simulations of the IP orbit ripple for a large number of dipole field error sets were performed in Elegant and MAD-X for v.5.6 1- and 2-IP lattices at 6, 10, and 18 GeV. Cases of uncorrelated magnet errors as well as the ones with equal errors for the magnets sharing a common dipole PS were simulated. For the fractional field strength error of 10^{-4} and the lattice tunes $\nu_x = 0.12, \nu_y = 0.1$, the values of IP orbit ripple were found to be in the range from 30 to 200 microns, generally in good agreement with Eq. (4.45) or similar expressions which account for the magnet families. Conservatively assuming that the horizontal tune could end up as low as 0.05, the results were additionally scaled by $\sin(\pi\ 0.12)/\sin(\pi\ 0.05) \approx 2.35$.

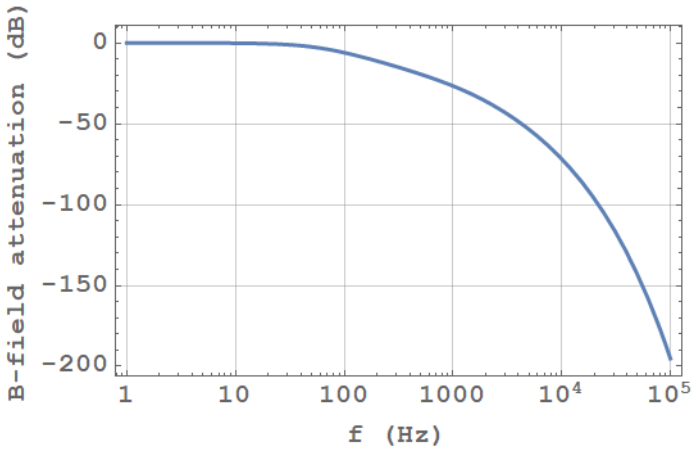

Figure 4.79: Dipole field ripple attenuation for a copper chamber with a circular cross-section of 18 mm inner radius and 4 mm wall thickness.

The final ripple specifications need to be normalized to the maximum power supply current. With the exception of short arc bends, the dipole bend angles remain constant across all operating energies, while their maximum power supply currents scale proportionally to the energy. Therefore, the lattice with the largest ratio of the simulated IP jitter to the beam energy (6 GeV 2-IP) was taken to define the ripple specifications. Requiring the IP orbit jitter to be at 1% of the rms beam size resulted in 0.1 ppm current ripple normalized to the values from 18 GeV operation. The short arc bend supply ends up with a more relaxed, 0.3 ppm specification. For reference, the dipole power supply ripple specifications for the HL-LHC [**?**] and SuperKEKB [**?**] are 1 ppm rms.

Power supply ripple at frequencies 4-40 kHz:

High-frequency centroid beam motion at the IP also primarily comes from the dipole power supplies although it could be additionally caused by the main [**?**] and crab-cavity [**?**] RF system noise.

At these frequencies the amplitude of beam oscillations coming from the magnet power supply current ripple is significantly attenuated by the eddy currents in the vacuum chamber walls and the magnets themselves. Apart from minor details related to the cooling channels and ante-chamber, the copper vacuum chamber cross-sections will be identical at the dipole and multipole magnets [reference to figure similar to CDR Fig. 6.125], and can be described by an ellipse with 4-mm thick wall and with the inner semi-axes of 40 mm and 18 mm. For the purposes of this analysis the chambers were conservatively approximated with a circular cross-section with 18-mm inner radius and then the electromagnetic shielding was calculated with exact analytical expressions, which allow arbitrary wall thickness to skin depth ratio. The resulting attenuation factor for the dipolar field is shown in Fig. 4.79.

A dipole kick, located at $s = 0$, oscillating at the betatron frequency would cause resonant oscillations of beam centroid with the amplitude

$$\hat{x}(s) = \frac{\hat{\theta}_0 \sqrt{\beta(0)\beta(s)}}{2\alpha T_0}, \tag{4.46}$$

where $\hat{\theta}_0$ is the kick amplitude and $(\alpha T_0)^{-1} \gg 1$ is the damping time in turns.

The effect of multiple kicks can be found by summation, which, in addition, must include the relative betatron phases, the oscillation phases, and other factors, which are impossible to accurately estimate for the ESR magnets at this time. The most conservative estimate is therefore to assume that the oscillating kicks from all rippling dipoles add in phase. Then, for the required $x_{\rm rms} = 10^{-4}\sigma$ at the IP, the rms field ripple can be estimated as

$$\delta B/B = 10^{-4}\sigma \frac{\alpha T_0}{\pi\sqrt{\bar{\beta}\beta^*}}. \tag{4.47}$$

Taking 100-turn damping (with beam-beam) results in $\delta B/B \approx 9.2 \times 10^{-12}$. (A numerically equivalent estimate in terms of the field spectral power density at the tune frequency was also obtained for the case of white-noise variation of the field).

Even this very conservative estimate implies that, for instance, 1 ppm dipole power supply current ripple at the tune frequency would be acceptable, as long as 5 orders of magnitude of additional attenuation is coming from elsewhere. As is clear from Fig. 4.79, the vacuum chamber shielding results in this much attenuation at frequencies exceeding 22 kHz. The switching frequencies for the ESR magnet power supplies are expected to be substantially higher, so the high-frequency ripple requirement is not too restrictive.

In reality, the dipole ripples will not add in phase, and at least $N^{-1/2}$ additional cancellation can be safely assumed. With this assumption, and taking the relevant width of the tune line to be on the order of the beam-beam parameter, $\Delta\nu$=0.01, the maximum spectral power density of the field ripple becomes

$$P_{\delta B/B} = \frac{T_0}{\Delta\nu}\left(10^{-4}\sigma\sqrt{N}\frac{\alpha T_0}{\pi\sqrt{\bar{\beta}\beta^*}}\right)^2. \tag{4.48}$$

Dividing this expression by the attenuation factor shown in Fig. 4.79, and accounting for the 5/18 factor for the ESR energy variation one finally gets the maximum allowable dipole PS current ripple plotted in Fig. 4.80.

ESR Beam Beam Size Ripples: Derong

Figure 4.81 presents the results of a frequency scan with an electron beam size ripple of 0.5%. The ripple amplitude is defined as the RMS variation of the electron beam size, normalized to the nominal beam sizes at the interaction point (IP). The proton working point is $\nu_x = 0.228$, $\nu_y = 0.210$, and $\nu_z = -0.01$. The ripple is modeled as narrow-band noise with a bandwidth of 1000 Hz, which is slightly larger than the beam-beam tune spread. The center frequency of this ripple is scanned from 0 up to half the revolution frequency.

In the horizontal plane, the dominant peak appears at $f_3 = 2\nu_x$, corresponding to envelope oscillations of the proton beam. Due to the beam-beam tune spread $\xi_x \sim 0.01$, this peak spans from $2\nu_x$

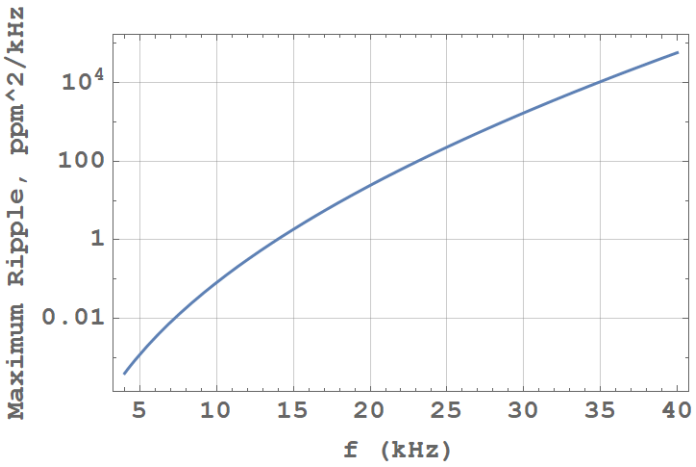

Figure 4.80: Maximum dipole PS rms current ripple normalized to 18 GeV operational current. This requirement applies only in the frequency range shown, corresponding the tune range of [0.05-0.5].

to $2\nu_x + 2\xi_x$. This resonance occurs because the external ripple frequency aligns with the envelope oscillation frequency of the proton beam, which is twice the horizontal betatron frequency.

The second strongest peak occurs at $f_1 = 4\nu_x - 4\nu_y$, which is interpreted as a harmonic of the cross-plane coupling resonance $2\nu_x - 2\nu_y$. Since the beam-beam potential is an even function of transverse coordinates $V_{bb} = V(x^2, y^2)$, and the size ripple drives envelope oscillations at twice the betatron frequency, this resonance drives a large emittance growth when the external frequency coincides with it.

The third peak, located at $f_2 = f_3 - f_1$, may correspond to a sideband arising from the interference between the primary envelope mode and the nonlinear coupling mode.

Similarly, in the vertical plane, the highest peak appears at twice the vertical betatron frequency, $f_4 = 2\nu_y$, corresponding to vertical envelope oscillations. Since the vertical emittance is much smaller than the horizontal one, the vertical emittance evolution is also sensitive to horizontal resonances due to nonlinear beam-beam coupling. As a result, a secondary peak emerges at the horizontal envelope frequency, $f_3 = 2\nu_x$.

A more complex pattern arises near the low-frequency region, where multiple peaks are observed. These can be attributed to synchro-betatron resonances of the form

$$f_5 = 4(\nu_x - \nu_y) + p\nu_z$$

where p is an integer. These resonances are intrinsic to the nonlinear beam-beam interaction and represent synchro-betatron sidebands of the betatron coupling. When the external ripple frequency matches one of these sidebands, vertical emittance growth can be resonantly excited.

To evaluate the impact of low-frequency ripple, Figure 4.82 presents a frequency scan using a finer step size of 60 Hz in the range up to approximately 1200 Hz. The ripple amplitude is set to 5% of the electron beam's RMS size in both transverse planes.

The simulation results show that vertical emittance growth is accompanied by a corresponding decrease in horizontal emittance. The most severe emittance transfer occurs near 60 Hz, while its

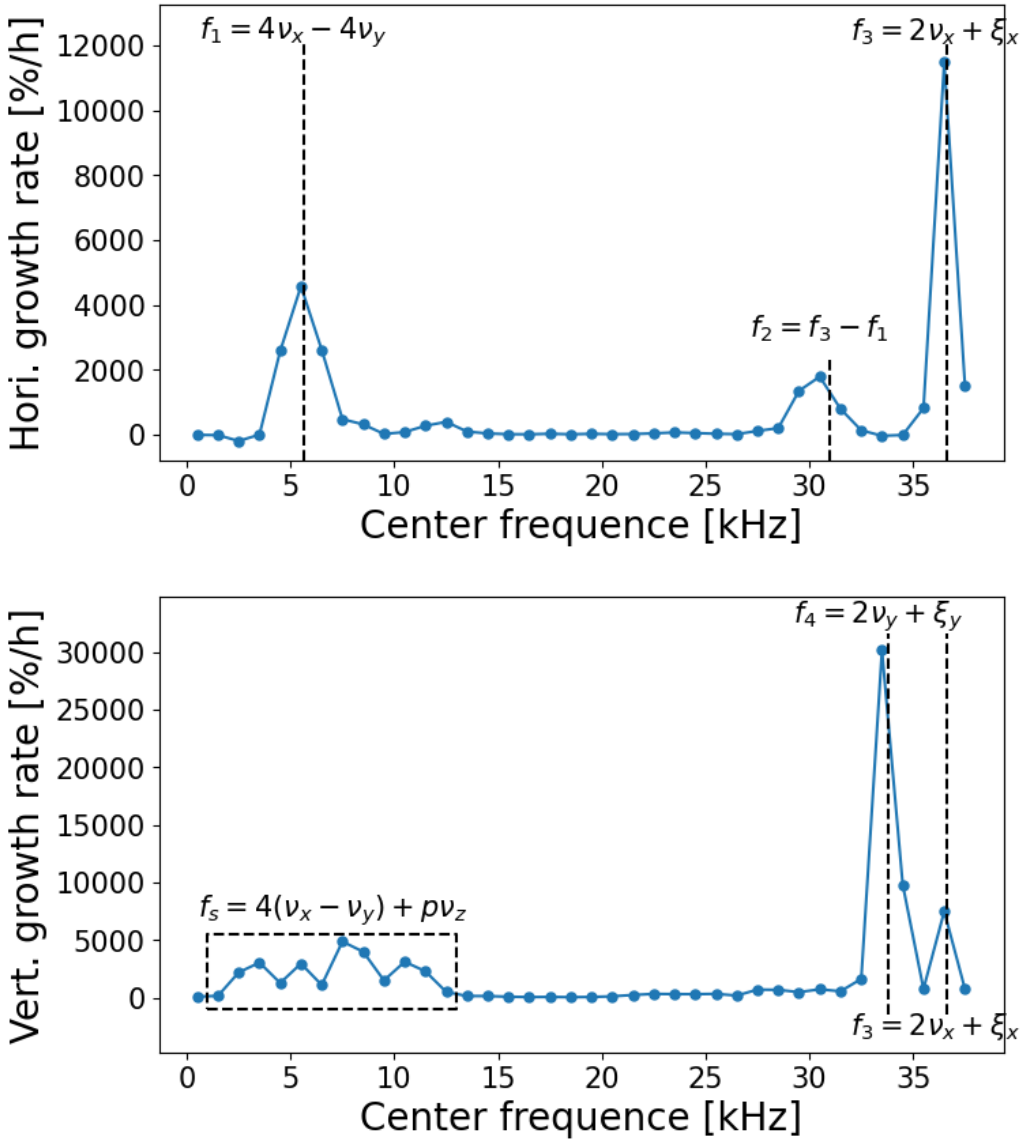

Figure 4.81: Proton horizontal (top) and vertical (bottom) emittance growth rates as a function of ripple frequency, with a fixed electron size ripple amplitude of 0.5%$\sigma_{x,y}$. The vertical lines and labeled numbers indicate resonance conditions (frequencies normalized by the revolution frequency). Simulations are tracked for 10^6 turns.

impact diminishes rapidly at higher frequencies.

The strong response observed around 60 Hz is particularly concerning, as the standard AC power line frequency in the US is 60 Hz.

Figure 4.83 illustrates the horizontal and vertical emittance growth rates as a function of the electron size ripple magnitude. The center frequency and the bandwidth are set to 60 Hz. The figure also presents the combined growth rate, defined as the summation of horizontal and vertical emittance growth (H+V). While the horizontal and vertical emittance growth rates show significant variation

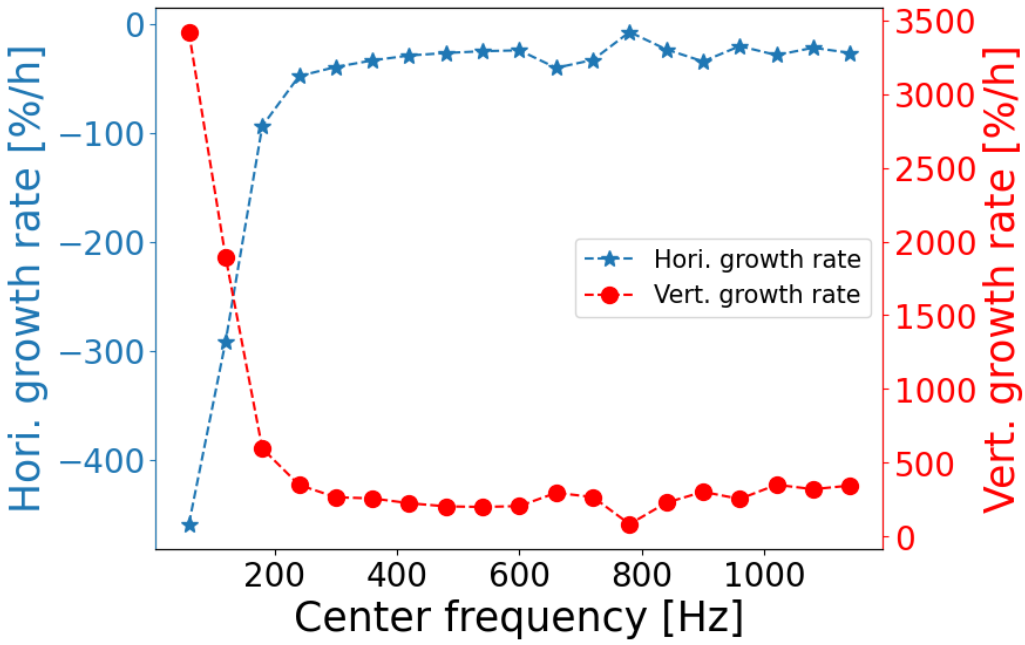

Figure 4.82: Emittance growth rates under a 5% electron beam size ripple within the range of 1200 Hz.

with increasing ripple magnitude, the combined growth rate remains much more stable across all cases. This stability indicates that there is emittance transfer between the horizontal and vertical planes. The conservation of the total emittance (H+V) highlights its role as a better conserved quantity in the presence of electron size ripple.

Assuming an emittance growth threshold of 10%/h, the allowable electron size ripple is estimated to be in the range of $0.1\% - 0.2\%$. This sets a stringent requirement on quadurpole power supply.

Unequal transverse emittances and electron size ripple are essential ingredients for driving emittance transfer. The emittance transfer induced by electron size ripple also depends on the transverse working point. Figure 4.84 shows the proton emittance growth rates across various transverse working points under a 0.5% electron size ripple. A clear diagonal pattern emerges in the tune space: working points along the same diagonal line exhibit similar emittance growth rates. This pattern directly indicates that emittance growth and transfer are driven by synchro-betatron resonances, specifically those of the form $2\nu_x - 2\nu_y + p\nu_z = 0$. The results also reveal that vertical emittance growth rates are more sensitive to the transverse working point, highlighting the possibility of optimizing the working point to suppress vertical emittance growth.

Figure 4.85 illustrates the proton emittance growth rates as a function of proton bunch length and momentum spread in the presence of a 5% electron size ripple. Reducing either the bunch length or the momentum spread decreases emittance transfer between the horizontal and vertical planes. Among the two strategies, shortening the bunch length proves to be more effective. This is because shorter bunch lengths not only reduce the longitudinal action but also mitigate the hour-glass effect.

Compared to electron orbit ripple, electron size ripple of the same amplitude induces significantly larger emittance transfer. This distinction arises because electron size ripple not only causes proton diffusion through beam-beam interactions but also modulates the proton betatron tunes.

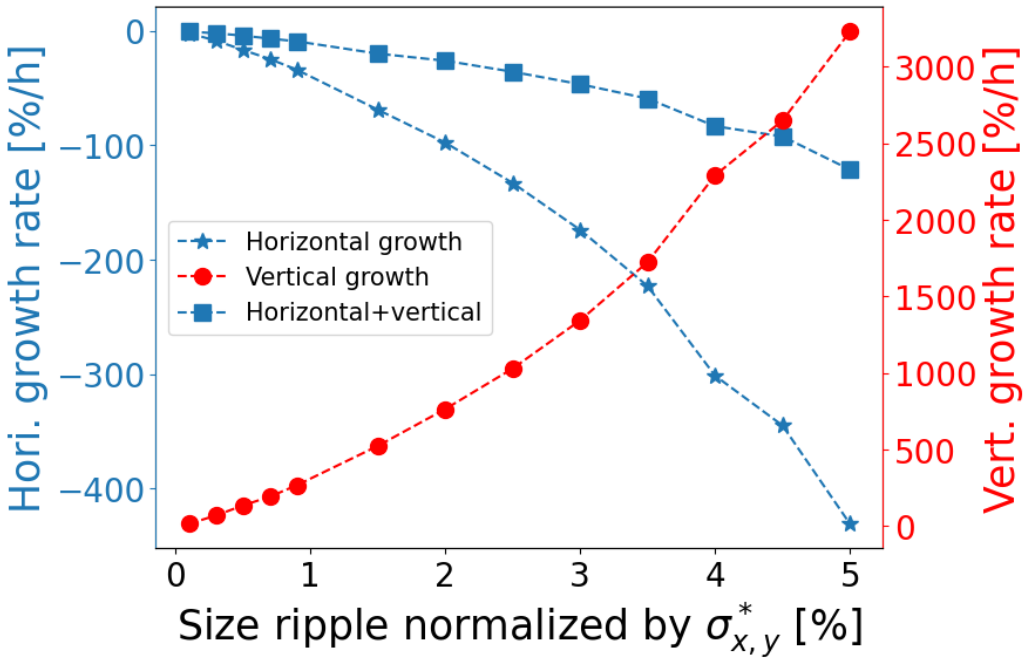

Figure 4.83: Proton emittance growth rates for different magnitudes of electron size ripple. The horizontal and vertical emittance growth rates are shown separately, along with the combined growth rate for the summation of horizontal and vertical emittance (H+V).

To understand why ripple near 60 Hz is particularly harmful, and to explore how tune modulation enhances emittance growth, we introduce a simplified model to study beam dynamics near a synchro-betatron resonance.

The effective Hamiltonian governing the coupled motion near the synchro-betatron resonance is given by:

$$h = \mu_x J_x + \mu_y J_y + \mu_z J_z + \frac{\lambda \mu_t}{\sin \mu_t} J_x J_y J_z^2 \sin\left(2\phi_x - 2\phi_y + 4\phi_z + \mu_t\right) \tag{4.49}$$

where $\mu_t = \mu_x - \mu_y + 2\mu_z$ denotes the detuning from the resonance condition.

The vertical action J_y is resolved using a symplectic ODE solver. Figure 4.86 shows the fitted growth of J_y when μ_t is modulated by a cosine function. A fractal-like structure emerges when scanning the modulation frequency and amplitude, indicating the onset of chaotic behavior.

Notably, the frequency 60 Hz lies within the center of the chaotic layer. This explains why the strongest emittance growth in the presence of electron size ripple occurs at low frequencies, particularly around the AC line frequency.

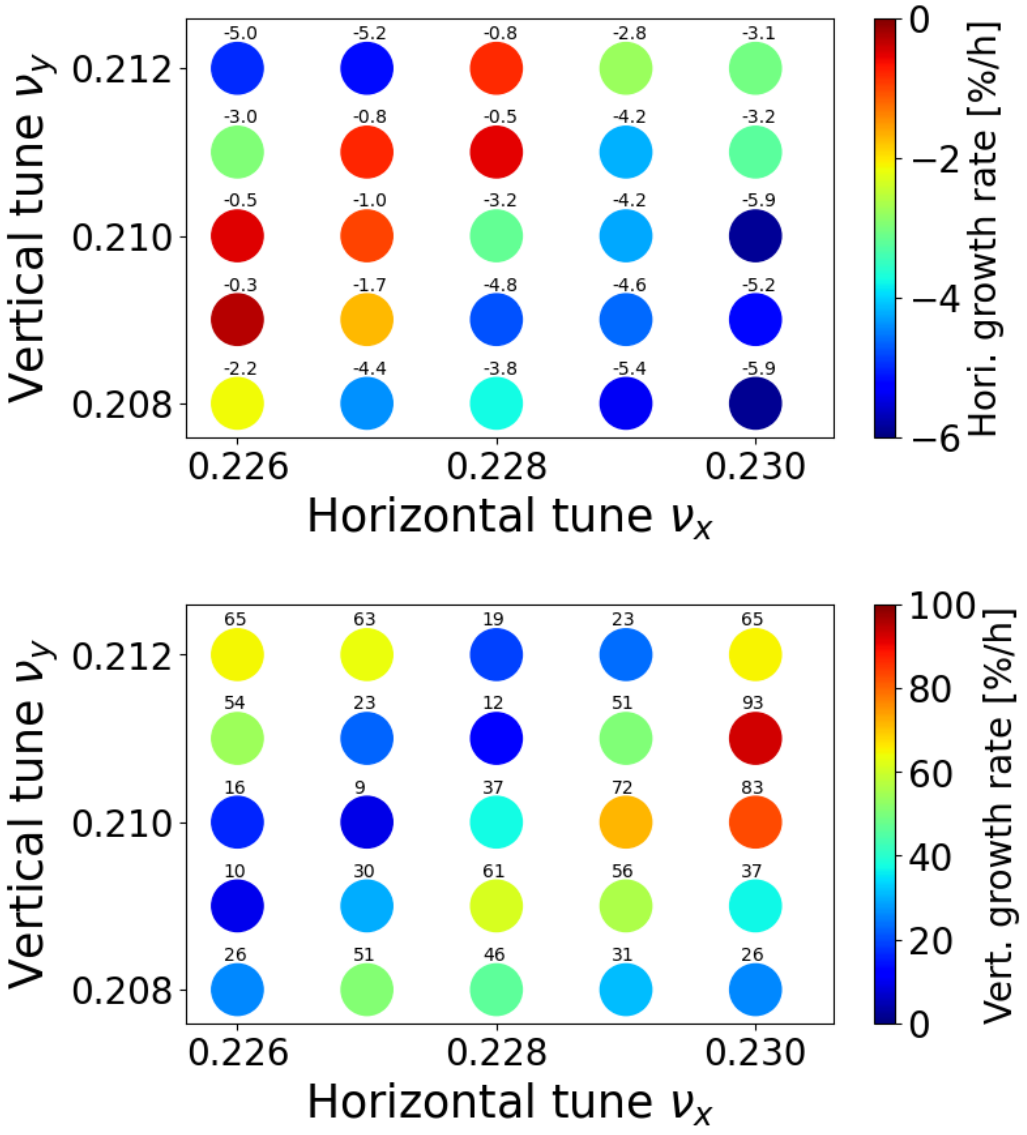

Figure 4.84: Proton emittance growth rates at different working points with a 0.5% electron size ripple. The fitted growth rates, in units of %/h, are labeled on the plot.

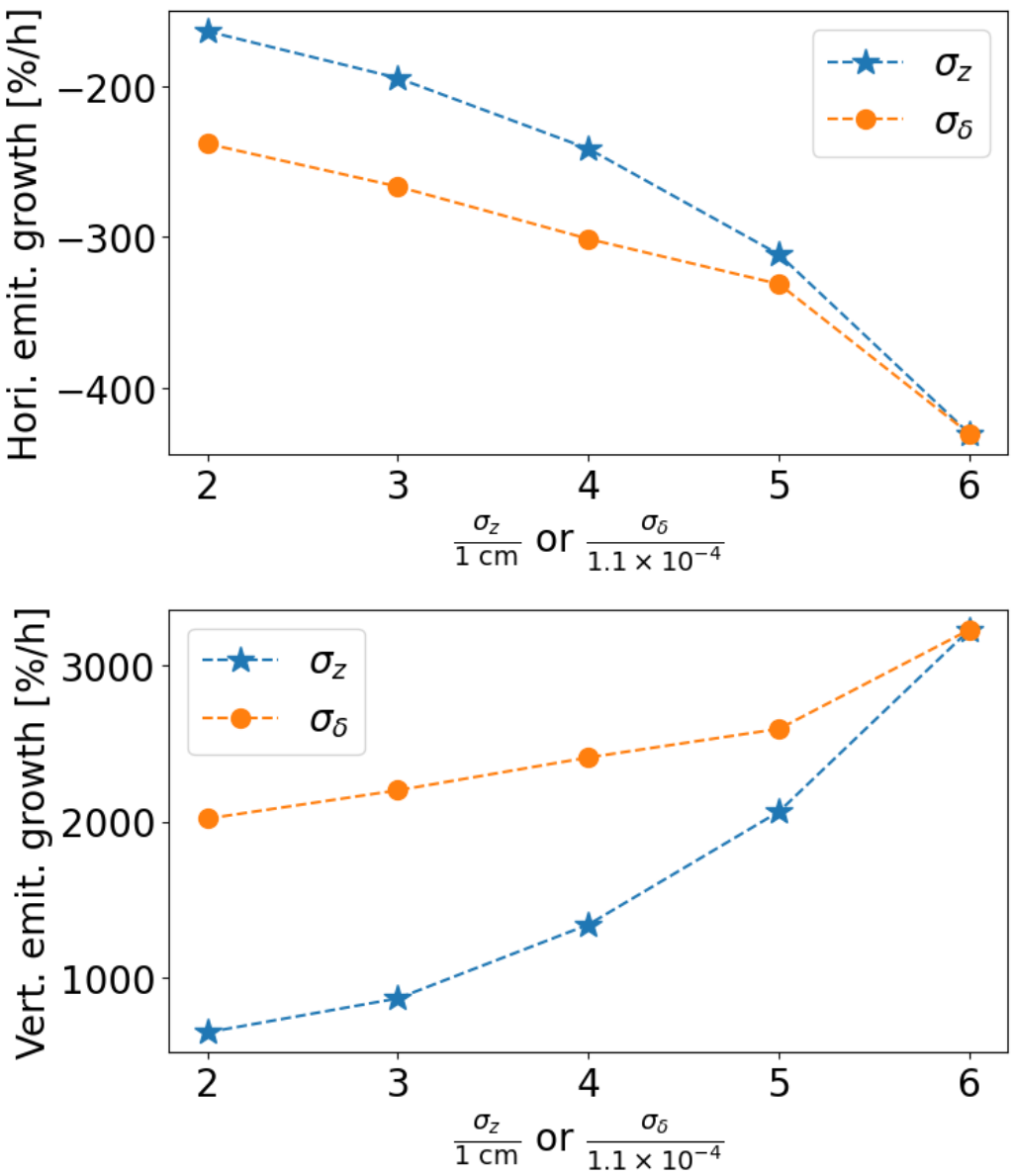

Figure 4.85: Proton emittance growth rates for different proton bunch lengths and momentum spreads under a 5% electron size ripple. The impact of reducing the bunch length and momentum spread on mitigating emittance transfer is illustrated.

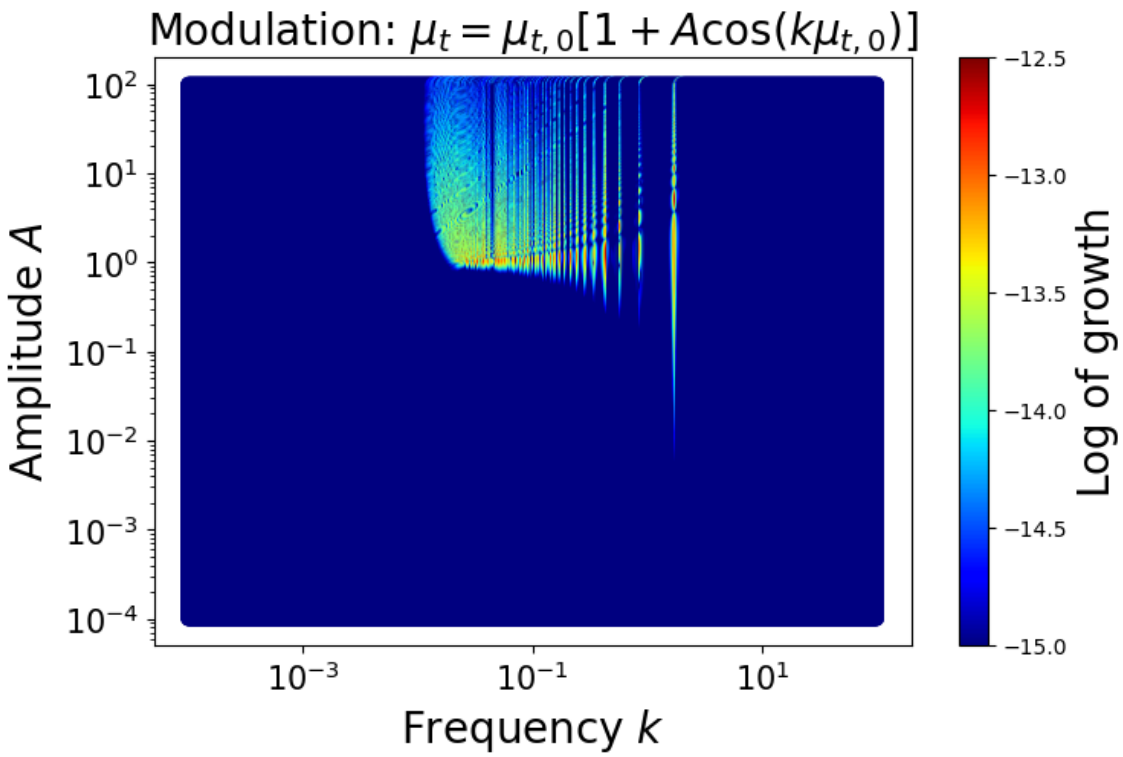

Figure 4.86: Growth of vertical action under tune modulation near the synchro-betatron resonance. The nominal working point is used, and $\mu_{t,0} = 2\pi\left(\nu_x - \nu_y + 2\nu_z\right) = -0.004\pi$, corresponding to 156 Hz. The initial action is chosen as $J_x = \epsilon_x, J_y = \epsilon_y$.

Crab Cavity Voltage and Phase Noise

Noise of the cavity voltage will produce a crossing angle error of the two opposing beams, while cavity phase noise creates a transverse offset at the interaction point. A theoretical approach can be found in Ref. [**?**].

A reliable approach for estimating the requirement of the cavity phase and voltage stability is to use the measured power spectrum density (PSD) of the low level RF controller for the crab cavity in the beam-beam simulation. Currently, the PSD information on the Low Level RF (LLRF) controller for the EIC crab cavity is not available. The exact requirements can be obtained from simulations using the PSD as input for the noise signal generation.

Noise components in the amplitudes and phases of the crab cavities cause the growth of the transverse beam emittance over time. This is not an issue for the electron beam whose emittance is dominated by strong synchrotron radiation effects but is of concern for the hadron beam, which lacks a sufficiently fast damping mechanism. The resulting hadron emittance growth in turn leads to luminosity degradation. To keep the luminosity loss at an acceptable level over the store time, the emittance growth rate must be limited to less than 10%/hour. This requirement then translates into a combination of the noise level limit and feedback system efficiency.

With beam-beam interaction and action of a feedback system ignored, the emittance growth rates due to crab cavity amplitude ($\Delta A \equiv \Delta V/V$) and phase ($\Delta\phi$) noise can be obtained analytically. They are respectively given by

$$\left.\frac{d\varepsilon_x}{dt}\right|_{\Delta A} = N_{cav}\beta_x^{cc}\left(\frac{eV_{cav}f_c}{2E_b}\right)^2 C_{\Delta A}(\sigma_\phi)\sum_{k=-\infty}^{+\infty} S_{\Delta A}[(k\pm\bar{\nu}_b\pm\bar{\nu}_s)f_c], \tag{4.50}$$

$$\left.\frac{d\varepsilon_x}{dt}\right|_{\Delta\phi} = N_{cav}\beta_x^{cc}\left(\frac{eV_{cav}f_c}{2E_b}\right)^2 C_{\Delta\phi}(\sigma_\phi)\sum_{k=-\infty}^{+\infty} S_{\Delta\phi}[(k\pm\bar{\nu}_b)f_c], \tag{4.51}$$

where N_{cav} is the total number of crab cavities including both the upstream and downstream sets and the noise from each is assumed independent, β_x^{cc} is the Twiss beta function at the crab cavities, V_{cav} is the voltage amplitude of each crab cavity, f_c is the beam circulation frequency, and E_b is the beam energy. $C_{\Delta A}$ and $C_{\Delta\phi}$ are the coefficients correcting for the bunch length. They are analytic functions of the rms crab cavity RF phase σ_ϕ occupied by the bunch. The asymptotic behaviors of $C_{\Delta A}$ and $C_{\Delta\phi}$ for short bunches are

$$\lim_{\sigma_\phi\to 0} C_{\Delta A} = 0, \quad \lim_{\sigma_\phi\to 0} C_{\Delta\phi} = 1. \tag{4.52}$$

Since the EIC bunches are relatively short, emittance growth is dominated by phase noise.

$S_{\Delta A}$ and $S_{\Delta\phi}$ in Equations 4.50 and 4.51 are the amplitude and phase power spectral densities (PSD), respectively. k is an integer. $\bar{\nu}_b$ and $\bar{\nu}_s$ are the average betatron and synchrotron tunes, respectively. A PSD falls off rapidly with frequency. Therefore, the summation in Equation 4.50 is dominated by the four lowest-frequency harmonics $\pm|\min(|k\pm\nu_b|)\pm\nu_s|\,f_c$ while the sum in Equation 4.51 is dominated by the two lowest-frequency harmonics $\pm|\min(|k\pm\nu_b|)|\,f_c$.

It is reasonable to assume that the amplitude and phase noise distributions are Gaussian. The PSD of white Gaussian noise is constant over the entire frequency domain. Since this is clearly not physical we consider pink Gaussian noise whose PSD is the same as that of white Gaussian at the lowest-frequency harmonics discussed above and becomes negligible at higher frequencies. The PSDs of the amplitude and phase noise distributions at the lowest-frequency harmonics are then

respectively given by

$$S_{\Delta A} = \frac{\sigma_{\Delta A}^2}{f_c}, \quad S_{\Delta\phi} = \frac{\sigma_{\Delta\phi}^2}{f_c}, \tag{4.53}$$

where $\sigma_{\Delta A}$ and $\sigma_{\Delta\phi}$ are the standard deviations of the amplitude and phase noise distributions, respectively.

The crab cavity voltage V_{cav} required at a beam crossing angle φ_{cr} is given by

$$\frac{N_{cav}}{2} V_{cav} = \frac{cE_b}{e2\pi f_{cr}\sqrt{\beta_x^{cc}\beta_x^*}} \tan\frac{\varphi_{cr}}{2}, \tag{4.54}$$

where f_{cr} is the crab cavity frequency and β_x^* is the horizontal Twiss β function at the IP. Under the pink Gaussian noise assumption of Equation 4.53, substituting Equation 4.54 into Equations 4.50 and 4.51, we find the following respective expressions for the contributions of the amplitude and phase noises to the horizontal emittance growth rates

$$\left.\frac{d\varepsilon_x}{dt}\right|_{\Delta A} = \frac{f_c}{N_{cav}\beta_x^*}\left(\frac{c\varphi_{cr}}{2\pi f_{cr}}\right)^2 C_{\Delta A}\sigma_{\Delta A}^2 , \tag{4.55}$$

$$\left.\frac{d\varepsilon_x}{dt}\right|_{\Delta\phi} = \frac{f_c}{2N_{cav}\beta_x^*}\left(\frac{c\varphi_{cr}}{2\pi f_{cr}}\right)^2 C_{\Delta\phi}\sigma_{\Delta\phi}^2 . \tag{4.56}$$

Using Equations 4.55 and 4.56 and requiring the relative emittance growth rate due to each type of noise to be less than 10%/h, i.e.,

$$\frac{1}{\varepsilon_x}\frac{d\varepsilon_x}{dt} < \left(\frac{1}{\varepsilon_x}\frac{d\varepsilon_x}{dt}\right)_{\max} = 0.1\ \mathrm{h}^{-1}, \tag{4.57}$$

one can specify the following constraints on the amplitude and phase noise levels, respectively,

$$\sigma_{\Delta A} < \frac{2\pi f_{cr}}{c\varphi_{cr}}\sqrt{\frac{N_{cav}\beta_x^*\varepsilon_x}{f_c C_{\Delta A}}\left(\frac{1}{\varepsilon_x}\frac{d\varepsilon_x}{dt}\right)_{\max}}, \tag{4.58}$$

$$\sigma_{\Delta\phi} < \frac{2\pi f_{cr}}{c\varphi_{cr}}\sqrt{\frac{2N_{cav}\beta_x^*\varepsilon_x}{f_c C_{\Delta\phi}}\left(\frac{1}{\varepsilon_x}\frac{d\varepsilon_x}{dt}\right)_{\max}}. \tag{4.59}$$

For the EIC hadron beam parameters (namely, $f_c = 78.2$ kHz, $N_{cav} = 8$, $\beta_x^* = 0.8$ m, $\varphi_{cr} = 25$ mrad, $f_{cr} = 197$ MHz, $\varepsilon_x = 11.3$ nm, $\sigma_z = 6$ cm, $\sigma_\phi = 0.248$ rad, $C_{\Delta A} = 0.029$, and $C_{\Delta\phi} = 0.942$), Equations 4.58 and 4.59 give the following limits on the crab cavity amplitude and phase noise levels, respectively,

$$\sigma_{\Delta A} < 4.9\cdot 10^{-6}\ , \quad \sigma_{\Delta\phi} < 1.2\,\mu\mathrm{rad}\ . \tag{4.60}$$

Note that the tolerance in Equation 4.60 were obtained ignoring the beam-beam interaction and nonlinear beam dynamics around the ring. These effects are accounted for using numerical simulations as discussed below.

Simulations have been performed to verify the analytical prediction from the linear theory (Eq.4.55 and 4.56). The simulation can include the nonlinear effects that are not included in the linear theory. The nonlinear effects include:

- beam-beam effect at IR

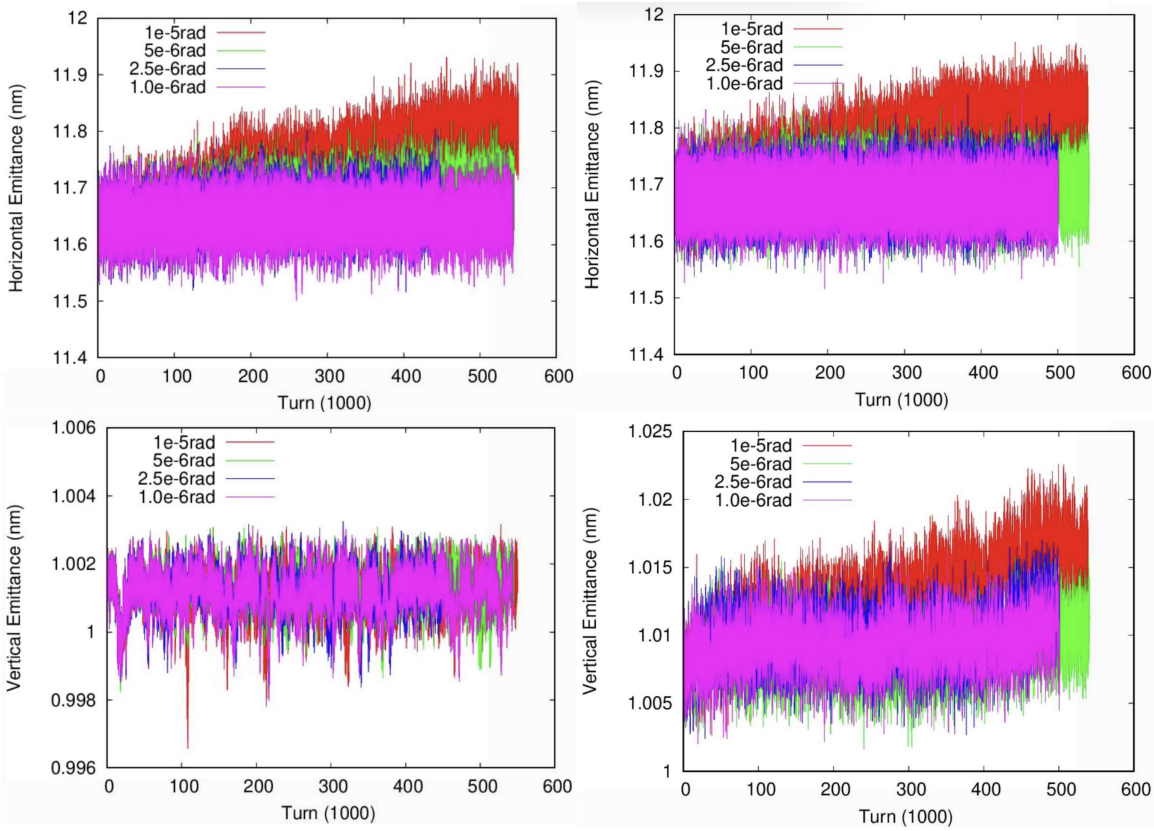

Figure 4.87: Emittance growth of proton beam induced by crab cavity RF phase noise. Top left: Horizontal direction without beam-beam effect; Top right: Horizontal direction with beam-beam effect; Bottom left: Vertical direction without beam-beam effect; Bottom right: Vertical direction with beam-beam effect;

- nonlinear magnetic field in the ring

The emittance growth rate in the crabbing plane (horizontal plane) calculated from the simulation is similar to the linear prediction. The top row of Figure 4.87 shows that the horizontal emittance growth is similar with or without the beam-beam interaction. If the beam size growth is fit linearly, 1e-6 rms phase stability is required to achieve 10%/hour growth rate.

It can be clearly seen that the beam-beam interaction induce the emittance growth in the non-crabbing plane, from the bottom row of Figure 4.87. The effect can be understood as the nonlinear beam-beam coupling effect that couples the horizontal noise to the vertical direction. Currently there are no theoretical analysis to estimate the growth rate of the vertical growth due to the crab cavity RF noise in the horizontal plane. The noise of beam-beam simulation also prevent achieving precise crab noise 's requirement for limiting the vertical growth rate less than 50%/hour. However, it it is clear that the RF phase error of crab cavity must be small than 1e-5 rad, which corresponding to 400%/hour growth in vertical plane. Therefore, further studies are required to set clear threshold for the RF noise

Simulation can also provide several insights on the vertical emittance growth due to RF noise, which are useful for the countermeasures. First, the beam centroid of the vertical direction does not

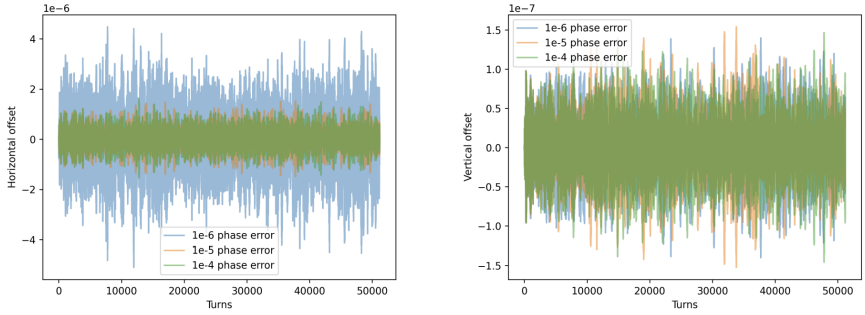

Figure 4.88: Comparison of horizontal (left figure) and vertical (right figure) offset of the proton beam for various phase noise amplitude of the crab cavity.

grow, as that of the horizontal direction as shown in Figure 4.88. Therefore, the vertical centroid of the proton beam can not be used as a feedback signal.

Second, a scaling study can be done to explore the relation between the emittance growth rate and the flatness $r \equiv \sigma_y/\sigma_x$. In the scaling process, the beam-beam parameter of both plane are kept constant. Therefore the design emittance of the vertical direction will be scaled as $\epsilon \sim r/(1+r)$. Figure 4.90 show that the vertical emittance growth rate inversely scales with the emittance of the vertical direction

$$\frac{1}{\epsilon_y}\frac{d\epsilon_y}{dt} \sim 1 + \frac{1}{r} \sim \frac{1}{\epsilon_y} \tag{4.61}$$

which indicates that the effect will be only important for a flat beam.

Third, while the feedback system can be very effective in suppress emittance in the crabbing plane, it is challenging to apply it in the vertical plane. Figure 4.90 shows that the horizontal growth rate can be effectively decreased. However, the vertical growth rate does not show significant improvement in the feedback process. The results indicates that an alternative countermeasure is needed in future studies.

Storage RF Noises: added by Yun

To detect small proton beam size growth rates on the order of a few percent per hour, we employ a weak-strong beam-beam simulation model. Unlike the electron beam, the proton beam does not benefit from synchrotron radiation damping, making it more susceptible to emittance growth, particularly in the vertical plane. In our model, the proton beam is represented by macro-particles, while the electron bunch is modeled as a rigid six-dimensional Gaussian charge distribution. The proton ring is modeled using a 6D linear uncoupled matrix. Simulations typically track the protons for up to one million turns.

For the RF phase and voltage noise spectra, we assume white noise, with a uniform power spectral density over the chosen frequency range. The revolution frequency of the EIC storage rings is approximately 78 kHz. Noise signals are generated in the frequency domain and then transformed to the time domain using inverse FFT to produce turn-by-turn noise profiles. The RMS value of the time-domain signal is used to characterize the phase noise strength, while for voltage noise, we use the RMS value of the relative voltage variation.

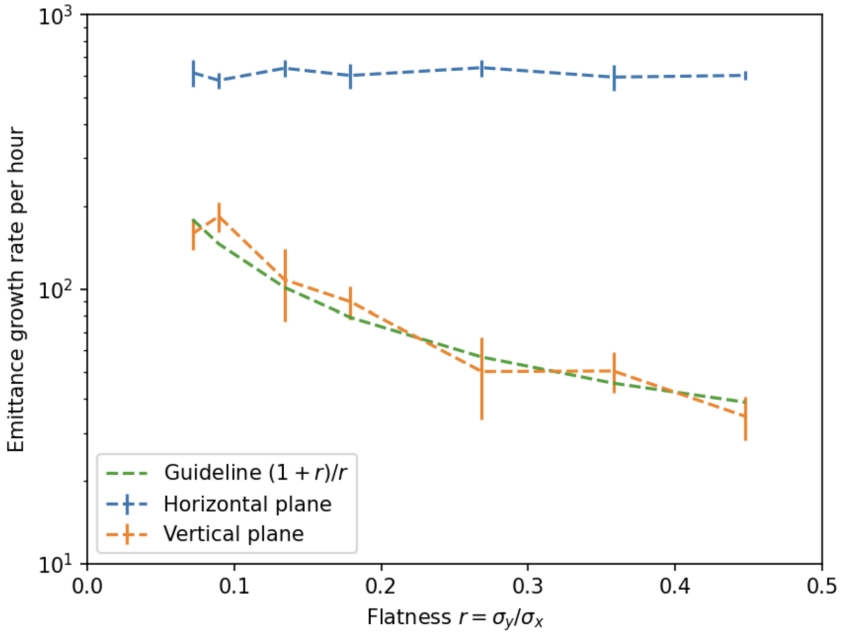

Figure 4.89: The horizontal and vertical emittance growth rate as function of the flatness of the beam transverse size at IP.

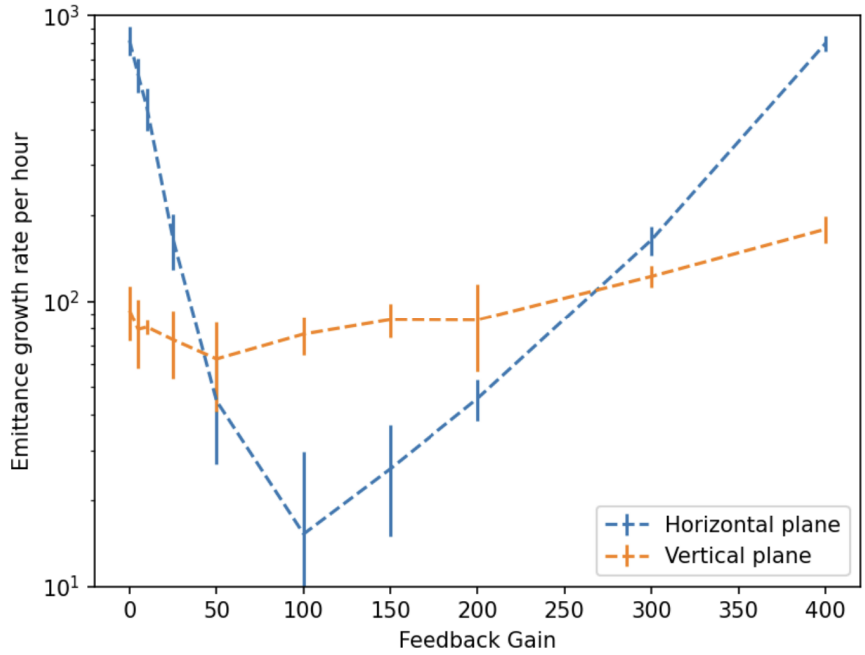

Figure 4.90: The horizontal and vertical emittance growth rate as function of the gain in the feedback system.

We adopt the parameters corresponding to the highest peak luminosity collision mode: 10 GeV electrons colliding with 275 GeV protons. In this configuration, both beams reach their maximum beam-beam parameters in the EIC. As shown in the table, the vertical beam size at the IP is approximately 11 times smaller than the horizontal one, making it particularly vulnerable to beam-beam perturbations and machine noise.

1) Simulation With ESR RF Noises

As mentioned earlier, in our weak-strong simulation model, the electron bunch is assumed to be rigid, and the simulation code does not support explicit modeling of RF cavities. Instead, we simulate the effects of RF noise by applying random perturbations to the electron bunch's arrival time and bunch length at the interaction point (IP). Phase noise in the RF cavities leads to arrival time jitter of the electron bunch at the IP, while voltage noise affects the bunch length. We are currently developing an analytical framework to map the electron bunch arrival time jitter and bunch length variations back to the corresponding ESR RF phase and voltage noise levels.

Table 4.22 presents the simulated proton beam size growth rates for different levels of electron bunch arrival time jitter. The RMS values of the arrival time noise are scanned from 5×10^{-13} s to 1×10^{-14} s in six steps. From the results, it is observed that the proton horizontal beam size growth is negligible across this range, while the vertical beam size growth is significant. The tolerable RMS electron bunch arrival time jitter is approximately 1×10^{-13} s for head-on collisions, and about 5×10^{-14} s for collisions with crab crossing. Given the RF frequency of the ESR is 591 MHz, an arrival time jitter of 5×10^{-14} s corresponds to a phase error of roughly 0.02 degrees.

RMS of noises (10^{-12} second)	head-on collison (%/hour, %/hour)	crab collision (%/hour, %/hour)
0.5	(-1.9, 181)	(1.4, 227)
0.2	(0-.48, 30)	(-0.45, 34.6)
0.1	(-0.49,9.6)	(-0.35, 19.5)
0.05	(0.36, -0.87)	(-0.21, 4.5)
0.02	(-0.24,2.9)	(-0.50, 3.4)
0.01	(-0.21,0.95)	(-0.13, 1.4)

Table 4.22: Proton beam size growth rates with electron bunch arrival time noise

Next, we apply white noise to the electron bunch length at the IP to simulate the effect of RF voltage fluctuations. Table 4.23 shows the simulated proton beam size growth rates under varying levels of electron bunch length fluctuations. In this study, the relative variation of the electron bunch length is scanned from 0.1 to 1.0×10^{-6} of its design RMS value. As shown in the table, the resulting proton beam size growth rates are negligible across the full range of simulated bunch length variations. All simulated growth rates remain well below the acceptable threshold of 10% per hour.

2) Simulation With HSR RF Noises

To determine the tolerances for RF phase and voltage noise in the HSR, we include RF cavities directly in the simulation model. The HSR contains two types of RF cavities: 591 MHz and 197 MHz, with total voltages of 20 MV and 6 MV, respectively. In the simulation, we model a single 591 MHz cavity and a single 197 MHz cavity, each carrying their full total voltage to simplify implementation.

relative electron bunch length noises (100%)	proton horizontal growth rate (%/hour)	proton vertical growth rate (%/hour)
0.1	-0.12	1.8
0.01	-0.04	1.5
1×10^{-3}	-0.15	3.9
1×10^{-4}	-0.11	3.1
1×10^{-5}	-0.08	5.1
1×10^{-6}	-0.51	3.9

Table 4.23: Proton beam size growth rates with relative electron bunch length noise

We observed that protons with longitudinal coordinates beyond $3\sigma_l$ or momentum deviation exceeding $3\sigma_{\delta p/p_0}$, as defined in the EIC CDR, fall outside the stable region of the RF bucket. Therefore, in calculating proton beam size growth rates, we include only protons within $2.8\sigma_\ell$ in the longitudinal phase space.

Table 4.24 presents the simulated proton beam size growth rates under various levels of HSR RF phase noise. The phase noise is quantified as arrival time jitter at the RF cavities. To convert this to RF phase, we multiply the arrival time noise by $2\pi f_{\mathrm{RF}}$, where f_{RF} is the RF cavity frequency. The arrival time jitter is scanned from 5×10^{-13} s to 1×10^{-14} s.

The HSR RF phase noise affects both horizontal and vertical proton beam sizes: typically reducing the horizontal beam size and increasing the vertical size. For the crab crossing collision configuration, the tolerable RF phase noise level corresponds to an arrival time jitter of approximately 2×10^{-14} s.

RMS of noises (second)	head-on collison (%/hour, %/hour)	crab collision (%/hour, %/hour)
5×10^{-13}	(-12, 173)	(-10.2, 162)
2×10^{-13}	(0.6, 20.6)	(-2.8, 41.4)
1×10^{-13}	(-3.6, 21.7)	(-1.7,12.7)
5×10^{-14}	(-1.2, 5.5)	(-2.3, 11.3)
2×10^{-14}	(-1.1, 3.9)	(-0.71, 4.25)
1×10^{-14}	(-0.46. 4.4)	(-0.59, 2.45)

Table 4.24: Proton beam size growth rates with Hadron Storage Ring RF phase noise

Table 4.25 presents the simulated proton beam size growth rates under different levels of relative RF voltage noise in the HSR. In this study, the relative RF voltage noise is scanned from 1×10^{-2} to 1×10^{-7} of the nominal design voltage. From the simulation results, we find that the tolerance for relative RF voltage noise is approximately 1×10^{-4} for both head-on and crab crossing collision scenarios.

3) Simulation With Banded RF Noises

Since RF noise components near the synchrotron motion frequencies are expected to have the strongest impact on beam dynamics, we simulate banded RF noise centered at one or two times

RMS of noises (second)	head-on collison (%/hour, %/hour)	crab collision (%/hour, %/hour)
1×10^{-2}	(-61.5, 4220)	(-240, 3950)
1×10^{-3}	(-4.2, 52)	(-3.6, 53.3)
1×10^{-4}	(-0.44, 6.4)	(-0.91, 10.1)
1×10^{-5}	(-0.23, 7.4)	(-0.52, 3.7)
1×10^{-6}	(-0.46, 3.7)	(-0.17, 1.1)
1×10^{-7}	(-0.17, 18)	(-0.65, 3.2)

Table 4.25: Proton beam size growth rates with Hadron Storage Ring RF voltage noise

the synchrotron frequency Q_s. The synchrotron tunes for the ESR and HSR are 0.069 and 0.01, respectively. We assume the width of the banded spectrum to be equal to the synchrotron frequency in each case. The banded noise is generated in the frequency domain and then transformed into the time domain using an inverse FFT to produce turn-by-turn RF phase or voltage noise signals.

Table 4.26 summarizes the RF phase and voltage noise tolerances obtained from early simulations using white noise. Table 4.27 presents the corresponding tolerances for simulations with banded noise spectra. The tolerances for the banded noise are generally within a factor of 2 of those determined for white noise. From both tables, it is evident that the tolerances related to electron bunch length variations are relatively large.

RF noises	Unit	White Noise
HSR RF phase	second	2×10^{-14}
HSR RF voltage	100%	1×10^{-4}
e-bunch arrival time	second	5×10^{-14}
e-bunch length	100%	huge

Table 4.26: Tolerances on RF phase and voltage white noise

RF noises	Unit	$Q_s \pm Q_s/2$	$2Q_s \pm Q_s/2$
e-bunch arrival time	second	1×10^{-13}	5×10^{-14}
e-bunch length	100%	huge	huge
HSR RF phase	second	5×10^{-14}	5×10^{-14}
HSR RF voltage	100%	1×10^{-4}	1×10^{-4}

Table 4.27: Tolerances on banded RF phase and voltage noise, centered at Q_s or $2Q_s$

IBS Diffusion: Derong

Intra-beam scattering (IBS) refers to a diffusion process arising from multiple small-angle Coulomb scatterings between particles within the same beam. While small emittances are essential for achieving high luminosity, the high phase space density of hadron beams makes them particularly

susceptible to IBS-induced emittance growth. As a result, IBS is a major performance limitation in hadron colliders.

This section focuses on the additional vertical emittance growth induced by the beam-beam interaction in the presence of IBS diffusion. The beam-beam force is highly nonlinear, and the hourglass effect introduces a dependence on the longitudinal position, making synchro-betatron resonances unavoidable. We study how horizontal and longitudinal diffusion driven by IBS can couple into the vertical plane through these resonances, leading to vertical emittance growth and potential degradation of the flat-beam configuration.

We employ a custom-developed weak strong simulation code to study the interplay between beam-beam interaction and IBS diffusion. The strong electron beam is modeled as a rigid Gaussian distribution, while the weak proton beam is represented by dynamically evolving macro-particles subject to beam-beam kicks and external perturbations. The beam parameters used in the simulation are consistent with the EIC design values.

In our simulations, particles are tracked for one million turns, corresponding to approximately 12.8 seconds. Over this timescale, it is reasonable to assume that the IBS growth and cooling times remain constant. Therefore, the IBS diffusion and potential cooling effects are modeled using a lumped element located at the interaction point (IP).

$$\lambda_u = \exp\left(-\frac{-T_{\text{rev}}}{\tau_u}\right) \tag{4.62}$$

$$u_{n+1} = \lambda_u u_n + R_u \sigma_u \sqrt{1-\lambda_u^2} \tag{4.63}$$

By turning off cooling, the diffusion equations simplify further:

$$u_{n+1} = u_n + R_u \sigma_u \sqrt{1-\lambda_u^2} \approx u_n + \frac{T_{\text{rev}}}{\tau_u} \sigma_u R_u \tag{4.64}$$

where $u = x, p_x, y, p_y, z, p_z$ represents the phase space coordinate, T_{rev} the revolution time, τ_u the characteristics time of IBS diffusion, σ_u the RMS size of corresponding dimension, and R_u the random number following standard Gaussian distribution.

Figure 4.91 shows that vertical emittance growth occurs when horizontal diffusion is present. Specifically, a horizontal IBS growth time of $\tau_x = 1$ h drives a vertical emittance growth rate of 100%/h, requiring vertical cooling time as short as 0.5 h to suppress this substantial growth. However, implementing such strong vertical cooling is not part of the current EIC design. In contrast, longitudinal diffusion does not induce any horizontal or vertical emittance growth.

The effective cooling technique for high energy hadron beams are still under development. Here, we assume artificial cooling in the simulation. Figure 4.92 presents simulation results including both IBS growth and artificial cooling. In the absence of beam beam interaction, IBS growth is fully balanced by cooling, as expected. When the beam beam force is included, horizontal and longitudinal emittance growth remain suppressed, indicating successful mitigation in these planes. However, vertical emittance continues to grow due to horizontal IBS diffusion, even with horizontal cooling applied. This result demonstrates that horizontal cooling alone is insufficient to suppress vertical emittance growth driven by horizontal diffusion through the beam beam interaction. Additional mitigation strategies are required to control vertical emittance growth in this regime.

The vertical emittance growth observed in this study presents a significant challenge to high energy cooling. Unlike dispersion-based mechanisms that allow diffusion or damping to redistribute

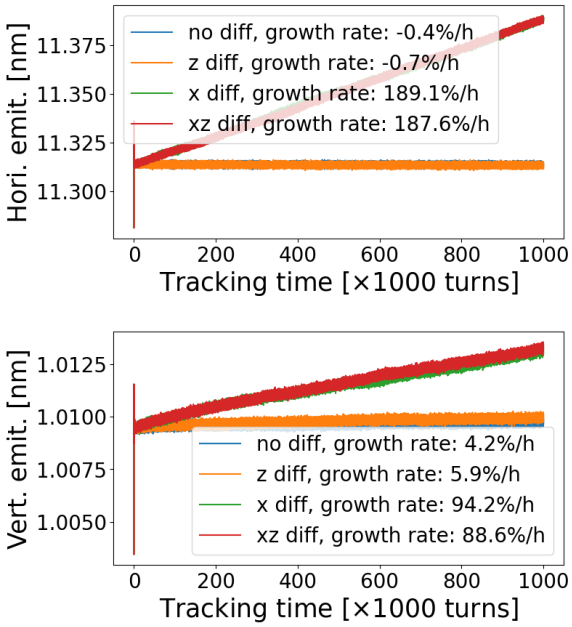

Figure 4.91: Proton emittance evolution for different horizontal ($\tau_x = 1$ h) or longitudinal ($\tau_z = 2$ h) IBS growth time: top (horizontal), bottom (vertical). The growth rates are linear fitted from the last 60% tracking data. Here τ_x and τ_z are IBS growth time in terms of beam size, as shown by Eq. (4.64). The blue curve, shadowed by other curves, serves as a reference, showing no emittance growth in both planes.

between planes, this phenomenon induces a unidirectional emittance transfer from the horizontal to the vertical plane, without enabling cross-plane cooling. As a result, dedicated vertical cooling is necessary. To preserve the flat hadron beam profile, the cooling system must be sufficiently strong in all three planes to counteract IBS-driven emittance growth.

The similar growth in vertical plane has also been observed in the study of electron orbit and size fluctuations. The frequency map shows that the synchro-betatron resonance $2\nu_x - 2\nu_y + p\nu_z = 0$ crossing the beam-beam footprint. This resonance amplifies the external noise and drive the emittance flows from the horizontal into the vertical plane.

The tune scan is performed to confirm that the vertical emittance growth due to the horizontal IBS diffusion also relates to this resonance. Figure 4.93 presents the tune scan results with horizontal IBS diffusion $\tau_x = 1$ h . A clear diagonal pattern is observed. Minimal vertical emittance growth is observed at $\nu_x - \nu_y \approx 0.011$ or 0.016. The vertical emittance growth rate is highly sensitive to the working point, as demonstrated in the bottom plot of Figure 4.93, where the growth rate ranges from 25%/h to 250%/h. This sensitivity suggests that optimizing the working point could be an effective strategy for mitigating vertical emittance growth.

The strength of the beam-beam interaction is directly proportional to the bunch intensities. As the electron bunch intensity decreases, the beam-beam kick received by the proton beam is reduced, which mitigates or even eliminates vertical emittance growth. Figure 4.94 shows the dependence of vertical emittance growth rate on the electron bunch intensity under fixed horizontal IBS diffusion with $\tau_x = 1$ h. Notably, the vertical growth rate does not scale linearly with electron intensity. When the intensity is sufficiently low, the vertical emittance growth is negligible. However, once the intensity exceeds a certain threshold, the growth rate increases rapidly, exhibiting an approximately

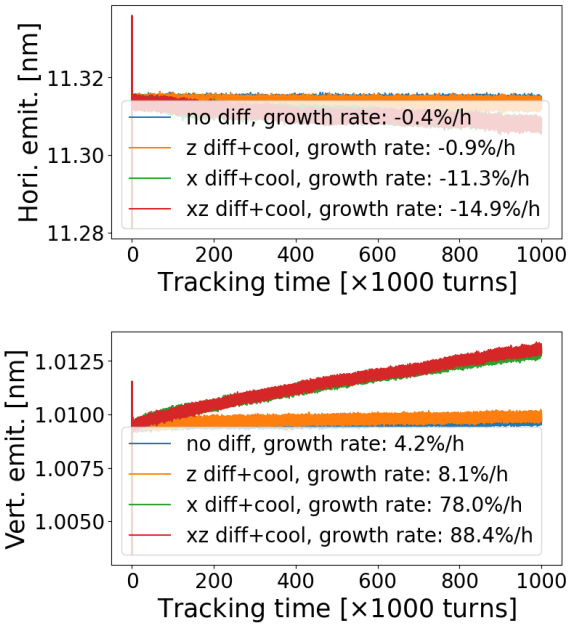

Figure 4.92: Proton emittance evolution for different horizontal ($\tau_x = 1$ h) or longitudinal ($\tau_z = 2$ h) IBS/cooling time: top (horizontal), bottom (vertical). Without beam-beam, the IBS growth is balanced by cooling.

exponential dependence on the electron bunch intensity.

This behavior has important implications for early EIC operation, where the electron bunch intensity is expected to be reduced to one fourth of the nominal design value. In this regime, the vertical emittance growth is negligible.

Another key observation is that the vertical growth rate is nearly identical in both head-on and crab-crossing collision scenarios. This is because the underlying synchro-betatron resonance is driven by the hourglass effect, which introduces a longitudinal dependence into the beam-beam force. In the EIC design, a second-order harmonic crab cavity is employed to compensate for the nonlinear crabbing, effectively restoring the overlap area of colliding beams.

Reducing the longitudinal action effectively weakens the synchro betatron resonance strength, as demonstrated in Fig. 4.95. Among the longitudinal parameters, reducing the bunch length is more effective than reducing the momentum spread. This is consistent with the earlier observation that the synchro betatron coupling originates from the hourglass effect. A shorter bunch length mitigates the hourglass effect directly, thereby suppressing the resonance that drives vertical emittance growth.

Dynamic Focusing: Derong

Unequal transverse emittances, synchro-betatron resonance, and physical fluctuations collectively form the essential ingredients that drive emittance transfer. Among these, the emittance asymmetry is fundamental to achieving high luminosity in flat-beam collisions and cannot be sacrificed. On the contrary, maintaining the transverse emittance ratio is a core design objective, as it underpins the luminosity enhancement in the EIC.

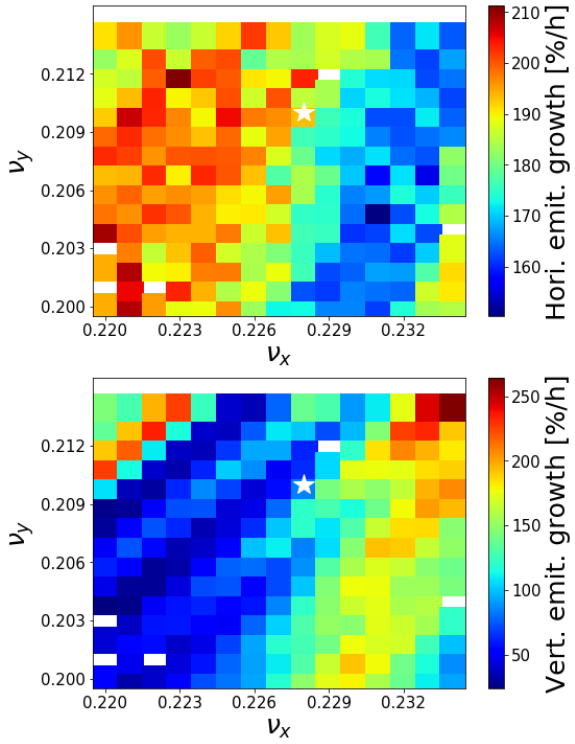

Figure 4.93: Proton emittance growth rates at different working points with horizontal IBS diffusion $\tau_x = 1$ h: top (horizontal), bottom (vertical). The pentagram shows the nominal working point in the EIC CDR [**?**].

One straightforward mitigation strategy is to reduce the amplitudes of known fluctuation sources. While effective in principle, this approach often incurs higher cost in accelerator subsystems and may even demand technologies beyond the current state of the art. Although dedicated feedback systems could help relax such constraints, unknown or unpredictable noise sources during machine operation remain a persistent challenge to beam stability.

Another strategy to mitigate emittance transfer is working point optimization. Since the emittance transfer is driven by synchro-betatron resonances, carefully choosing the betatron tunes can help suppress the associated diffusion. This approach has proven effective in simulations, where specific working points significantly reduce vertical emittance growth.

However, the flexibility of working point selection is constrained by several practical factors. First, the working point must be compatible with dynamic aperture requirements. Although our simplified model allows the identification of an optimal tune, operational experience at RHIC indicates that the hadron beam can be sensitive to resonances of order ten and higher. As a result, the viable tune space is narrow. Second, the interplay between beam-beam effects and collective wakefields further restricts the allowable tune range. In certain tune regimes, coherent beam-beam modes may couple with wakefields, potentially triggering beam instabilities. These considerations underscore the challenge of finding a working point that simultaneously avoids high-order resonances, maintains dynamic aperture, and mitigates collective effects.

These considerations highlight the need for an active strategy to suppress emittance transfer. To this end, we propose a dynamic focusing scheme that directly targets the underlying resonance

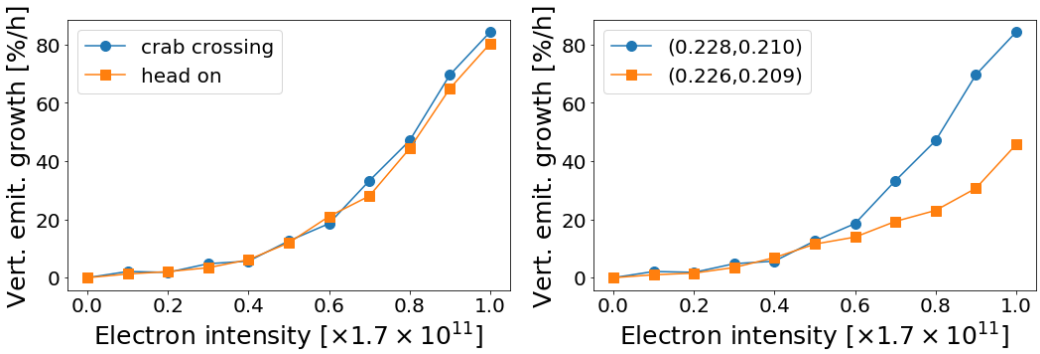

Figure 4.94: Proton vertical emittance growth rates for different electron intensities, with fixed proton horizontal IBS diffusion $\tau_x = 1$ h. Note here τ_x stands for beam size growth time, which is twice of emittance growth time. The typical IBS emittance growth time for EIC baseline design is $2-3$ hours. The diffusion is several times smaller than the value used in the simulation.

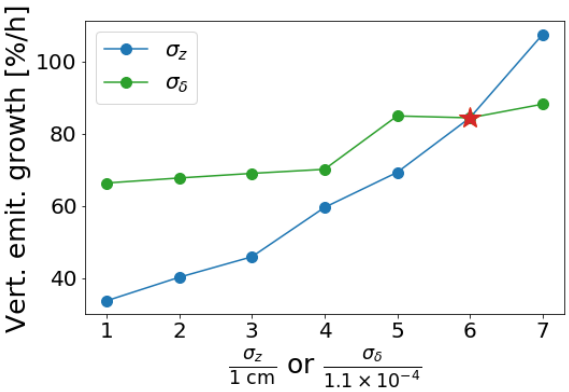

Figure 4.95: Proton vertical emittance growth rates for different bunch lengths and momentum spreads.

mechanism. Figure 4.96 illustrates the relative position in a crab crossing scheme to generate dynamic focusing. A horizontal local crab crossing scheme is assumed, in which the crab dispersion is confined between the upstream and downstream crab cavities around the IP. The horizontal phase advance between crab cavities and the IP is $\pi/2$ mod π.

To compensate for the vertical IP-to-CP shift, a sextupole is inserted between the crab cavity and the IP with the vertical phase advance of $\pi/2$ mod π. The required integrated sextupole strength is given by:

$$K_2 L = \frac{\sqrt{\beta_x^* / \beta_{s,x}}}{4\theta_c \beta_{s,y} \beta_y^* \cos\psi_x} \tag{4.65}$$

Here, θ_c is the half crossing angle, ψ_x is the horizontal phase advance from the sextupole to the IP, and $\beta_{s,x}$ and $\beta_{s,y}$ are the beta functions at the sextupole.

To cancel the second-order geometric terms introduced by the sextupole, another sextupole is placed outside the crab cavities, such that the two sextupoles form a $-I$ transformation. This cancellation is imperfect because the crab dispersion vanishes at the second sextupole. As a result, the

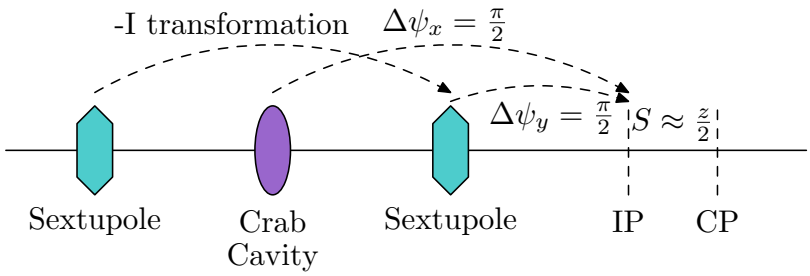

Figure 4.96: Locations of sextupoles and crab cavities to generate dynamic focusing. The other side of the IP is omitted for clarity, assuming symmetry and a locally closed crab crossing scheme. The values of $\Delta\psi_{x,y}$ represent the remainders of the corresponding phase advances modulo π.

residual horizontal kick at the CP is:

$$\Delta p_x = -\frac{\beta_{s,x}}{\beta_x^* \beta_{s,y} \beta_y^*} \left(\frac{\theta_c z_0^2}{4} + \frac{x_0 z_0}{2} \right) \tag{4.66}$$

where x_0 and z_0 are the horizontal and longitudinal phase space coordinates at the IP. This residual term can be minimized by reducing the ratio $\beta_{s,x}/\beta_{s,y}$, thereby ensuring that the perturbation to horizontal dynamics is negligible.

By combining crab cavities with sextupoles in a carefully phased lattice configuration, this approach introduces a time-dependent focusing that counteracts the drift space between the IP and collision point (CP). Unlike passive strategies such as noise suppression or working point optimization, dynamic focusing modifies the beam optics to cancel the resonance-driving terms at their origin. This suppression mechanism is demonstrated in Fig.4.97, and its effectiveness in improving noise tolerance is quantified in Tab.4.28.

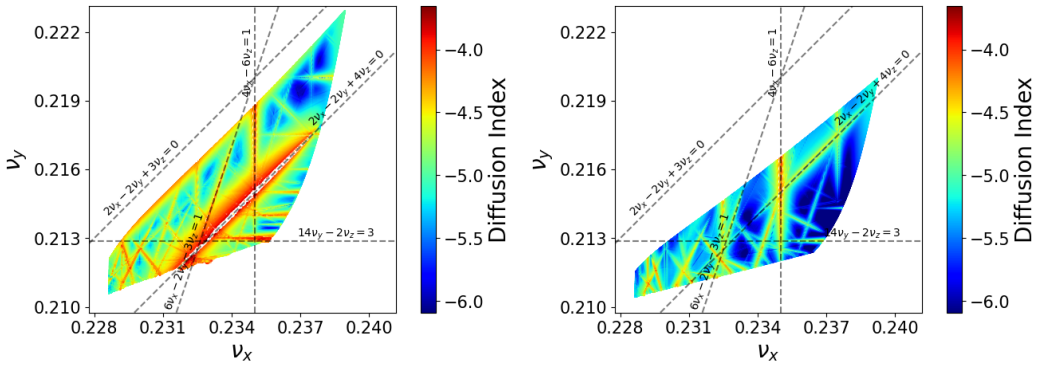

Figure 4.97: Frequency maps for particles launched at $z_0 = 3\sigma_z$, left: EIC baseline, right: dynamic focusing. The dynamic focusing scheme clearly suppresses the synchro-betatron resonance.

Implementing this scheme in the EIC interaction region presents challenges, as the ideal phase advance shown in Fig. 4.96 cannot be precisely realized. A similar compensation scheme with an adjusted phase is under development to address this constraint. The impact of this implementation on beam dynamics is currently being assessed.

Parameter	Unit	EIC Baseline	Dynamic Focusing
$\beta^*_{y,e}$	cm	5.6	7.2
Luminosity	$10^{34}/\text{cm}^2\text{s}$	0.93	0.97
Electron orbit ripple	$\sigma^*_{x,y}$	2.5%	5.0%
Electron size ripple	$\sigma^*_{x,y}$	0.3%	1.0%
Hadron IBS time	hour	4.5	1.5

Table 4.28: Comparison of tolerances under 20%/h vertical emittance growth for the EIC baseline and dynamic focusing scheme. Note that a smaller IBS time means a larger threshold of IBS diffusion.

4.5.5 Additional Beam-beam Studies

Beam-beam Effects with Two Experiments

One of the key requirement for the EIC is the capability to support two detectors. In the beam-beam interaction studies described earlier, we focus on one beam-beam interaction per turn. In the following, we assume there are two IPs at IR6 and IR8 and study the related beam-beam concerns.

F illing Pattern and Beam-Beam Pattern

To deliver collisions to two experiments at IP6 and IP8 simultaneously, with each bunch colliding only once per revolution in order to not exceed the beam-beam limit, we adopt a dedicated filling scheme. To achieve this, the following conditions have to be met:

- Fill proton bunches in every HSR bucket;
- The ESR filling pattern is (210*6 + 3 + 209*6 + 3)* 3. That is, fill the ESR with 3 identical bunch trains. Each train includes two batches. The first batch has 210 electron bunches, the second batch has 209 electron bunches. The gap between adjacent electron bunches in each batch is 6 ESR buckets. The gap between the first and the second batch is 3 ESR buckets, while the gap between the second batch to the next train is 3 ESR buckets.
- The detector at IP8 is to be moved counter-clockwise, or towards IP6, by 1.5 electron buckets, or 0.76 m.
- 197 MHz RF cavities for the HSR with 1260 buckets, 591 MHz RF cavities for the ESR with $1260 \times 6 = 7560$ buckets.

Here we temporarily ignore the abort gap.

With the above bunch shift scheme, there are totally 1260 proton bunches in the HSR and 1257 electron bunches in the ESR. Each electron or proton bunch only collides once per turn, at either IP6 or IP8. There are a total of 630 collisions at IP6 and 627 collisions at IP8 per turn. The integrated luminosity per experiment is therefore half of that with single experiment. Figure 4.98 shows the collision pattern. The horizontal and vertical axes are the bunch index of the proton and electron bunches. The red dots indicate collisions taking place at IP8, and the green dots show collisions occurring at IP6. In this plot, the abort gap has not been taken into account at this moment.

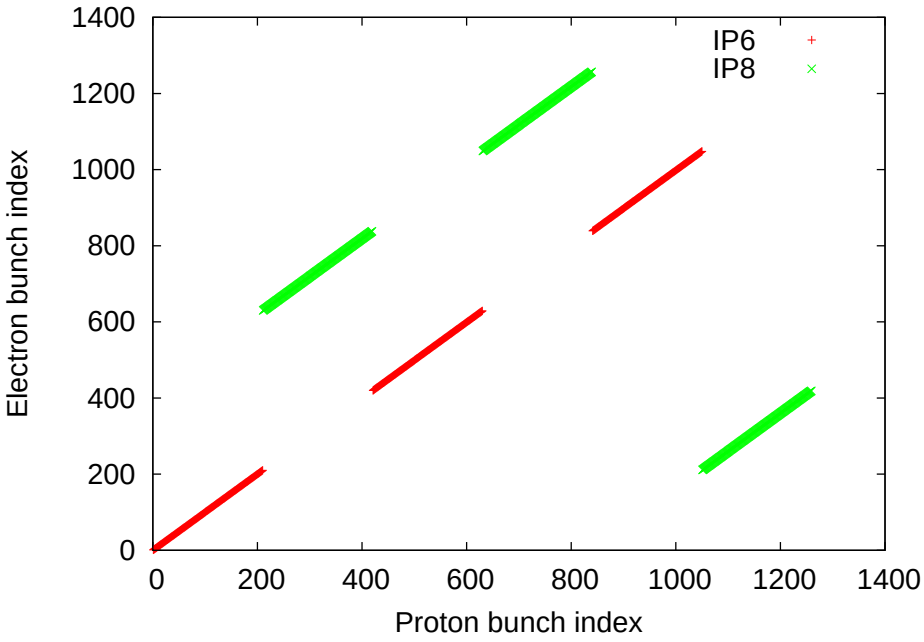

Figure 4.98: Bunch collision pattern with the bunch shift scheme.

L ong-range Beam-beam Interaction

In the present interaction region design, the common beam pipe is 9 m long with the interaction point at the center. With a single experiment, the bunch spacing of the proton and electron beams are equal. Each bunch will experience 6 long-range beam-beam interactions, 3 on either side of the IP. The nearest long-range beam-beam interaction takes place 1.52 m from the IP.

With two experiments and the above bunch shift scheme, each bunch will undergo 12 long-range beam-beam interactions, with 6 long-range beam-beam interactions at each experiment.Figure 4.99 shows the locations of these long-range beam-beam interactions for protons at the interaction region IR8. The nearest long-range beam-beam interaction is 0.76 m away from the IP.

Table 4.29 shows the horizontal separation between the electron and the proton bunch at the nearest interaction points for the cases with one and two experiments. The horizontal crossing angle between the ESR and HSR at the interaction point is 25 mrad. The horizontal separation at the nearest long-range beam-beam interaction point corresponds to 146 σ_p or 211 σ_e. Therefore, the long-range beam-beam effect is negligible for the present EIC design.

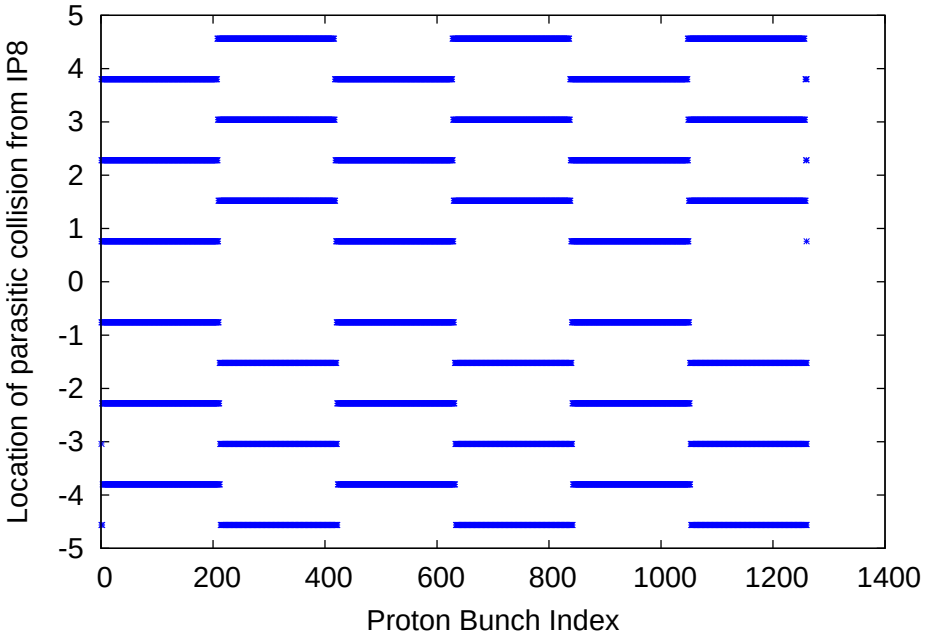

Figure 4.99: Locations of long-range beam-beam interactions with two experiments and bunch shift scheme.

Parameter	1 experiment	2 experiments
Number of long-range BB interactions	6	12
Nearest distance to IP [m]	1.52	0.76
Horizontal separation d [mm]	38	19
Local beam sizes σ_p, σ_e [mm]	0.20, 0.31	0.13, 0.18
Separation in beam sizes $\frac{d}{\sigma_p}$, $\frac{d}{\sigma_e}$	186, 123	145, 106

Table 4.29: The long-range beam-beam interaction with 1 and 2 experiments.

Transient Beam-Beam Effect During Electron Bunch Replacement

To maintain high electron bunch polarization in the ESR, we will replace each electron bunch in about every five minutes. The full bunch charge is about 50 ns. When an electron bunch is kicked out, another electron bunch will be injected into the same electron bucket on orbit and on energy from the RCS. Transient beam-beam effect during electron bunch replacement needs to be studied, especially possible proton emittance growth during this process.

The proton beam emittance growth due to the optics mismatch caused by a newly injected electron

bunch can be expressed as a function of the β-function of the bare lattice, β_0, and the β-function as modified by the beam-beam interaction with the electron bunch, β_1, as

$$\epsilon_1 = \frac{\epsilon_0}{2}\left(\frac{\beta_1}{\beta_0} + \frac{\beta_0}{\beta_1}\right), \tag{4.67}$$

where ϵ_0 is the unperturbed emittance, and ϵ_1 the resulting emittance after filamentation. The analytical calculated relative emittance growth is less than 10^{-3} for each bunch replacement.

The transient effects from the electron beam replacement injection was studied using a self-consistent strong-strong beam-beam simulation using the BeamBeam3D code. In these simulations, the accelerator lattice is approximated by a linear one-turn map. Macro-particles representing the proton and electron beams are tracked, and the beam-beam force between them is calculated numerically by solving Poisson equation with particle-in-cell method. A new electron bunch was injected on the axis after 20,000 turns where the old electron bunch in the ESR already attained an equilibrium.

The upper two plots of Figure 4.100 show the proton bunch's emittance evolutions with one electron bunch replacement. The lower two plots shows the electron bunch's emittance evolutions. It is seen that the electron beam attained the equilibrium emittance after a few thousand turns. The proton beam emittances increased by less than 0.1% in horizontal dimension and about 0.2% in vertical plane after the electron beam injection. The trend of the proton beam evolution stays about the same.

As we can see, both electron bunches have similar emittance evolution with beam-beam interaction. For the proton bunch, although there is an increase of emittance less than 10^{-3}, the proton emittance growth rates keep the same before and after a new electron bunch is injected.

In the above simulation, we assumed an ideal injection scenario. In the real accelerator, there will be imperfections during the injection. Those imperfections include initial centroid positions, angles, and energy offset, and electron beam size and intensity fluctuations.

As an example, Figure 4.101 shows the proton beam emittance growth after electron beam replacement as a function of the electron beam offset amplitude. It is seen that the resulting proton beam emittance growth is small (less than 1%) even with 1 sigma vertical injection offset. The proton beam horizontal emittance growth is not sensitive to those offset errors. The vertical emittance growth shows weak dependence on the offset error below 0.8 sigma. Here, one sigma corresponds to about 8 um of vertical rms beam size.

Figure 4.102 shows the proton beam emittance growth after electron beam replacement as a function of the initial electron beam vertical emittance mismatch. The proton beam emittance growth is small as long as the electron beam mismatch factor is above 0.6. The horizontal emittance growth is not sensitive to the electron beam vertical emittance mismatch during the electron beam replacement injection.

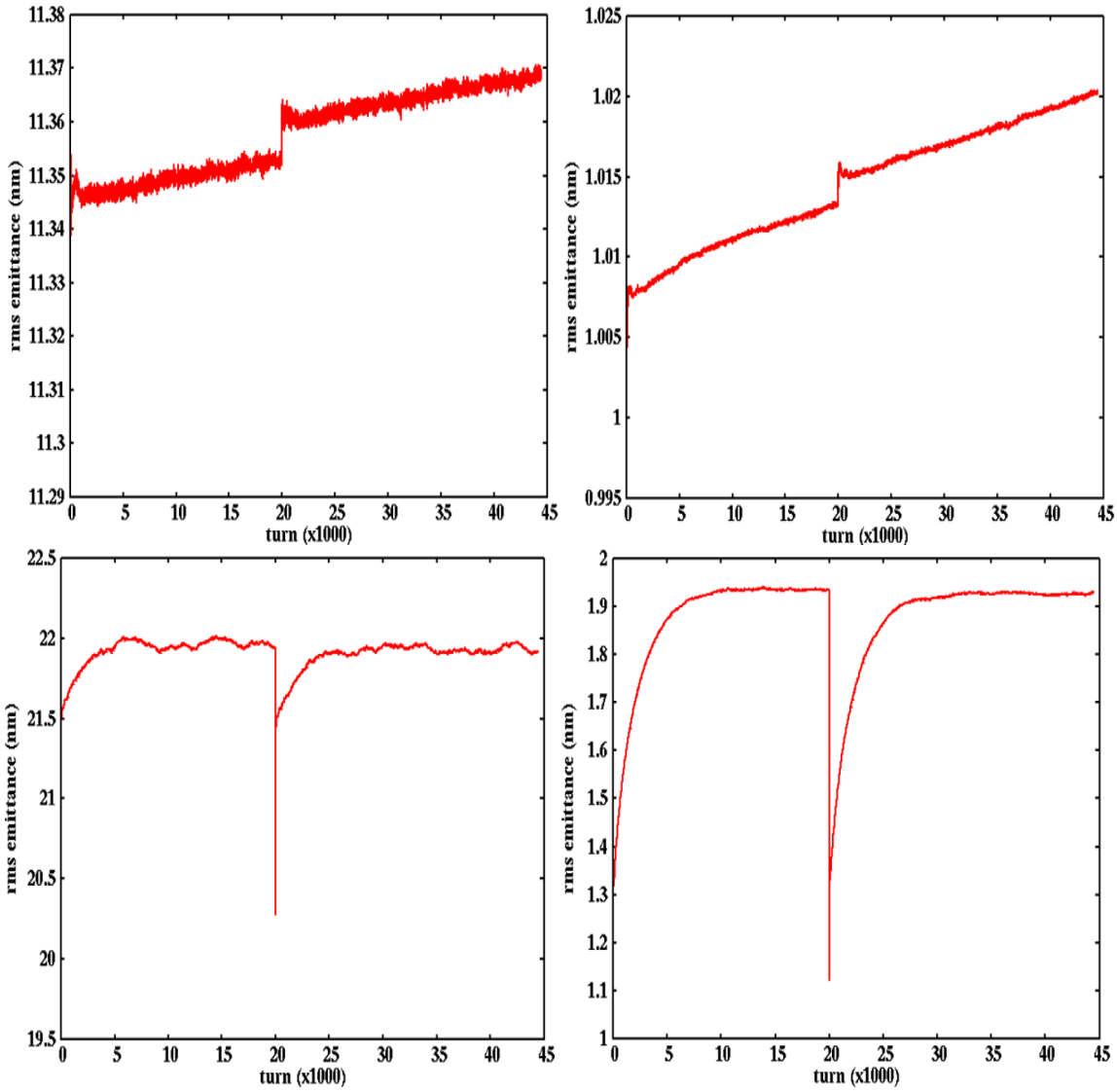

Figure 4.100: Simulated emittance evolution of the proton bunch during 100 electron bunch replacement. Injection error is not included.

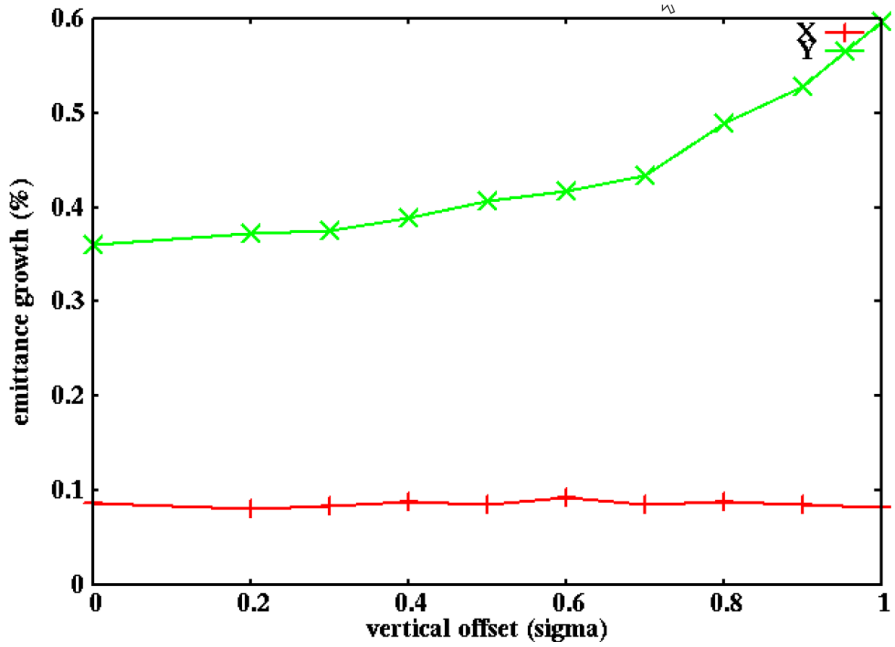

Figure 4.101: The proton beam emittance growth after electron beam replacement as a function of the electron beam offset amplitude.

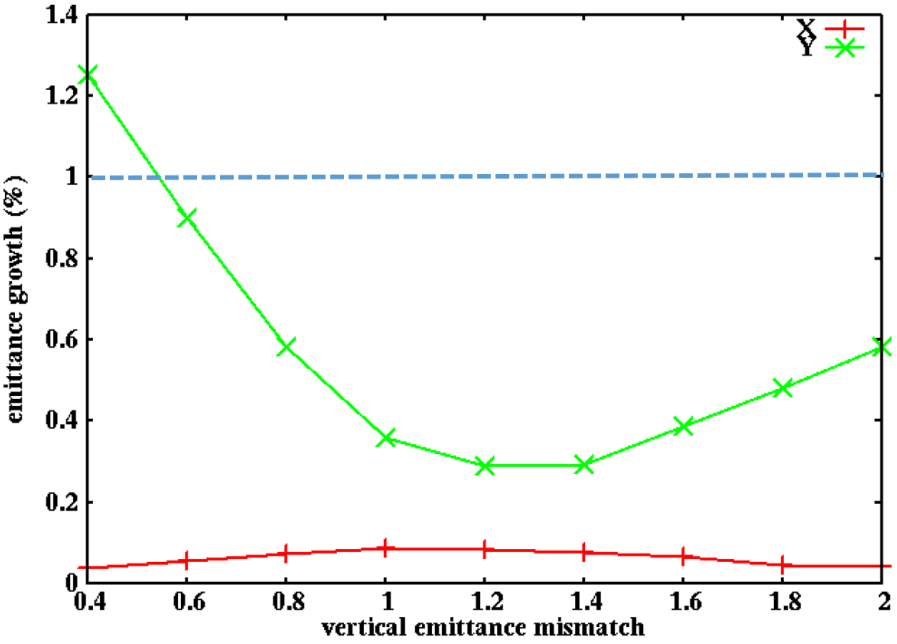

Figure 4.102: The proton beam emittance growth after electron beam replacement as a function of the initial electron beam vertical emittance mismatch.

Radiation Damping Decrement and Beam-beam Interaction

To reach a beam-beam parameter of $\xi = 0.1$ in the ESR, a transverse radiation damping decrement of $\delta = 1/4000$, or a radiation damping time of 4000 turns, is required, based on the experience at KEKB.

To achieve the same radiation damping time at the low electron beam energies, the ESR lattice uses super-bends in the arcs. The purpose of these super-bends is to generate additional synchrotron radiation at low electron energies to increase the radiation damping rate. Since the relation between the damping decrement and the achievable beam-beam parameter is empirical, we carried out beam-beam simulations to study the beam performance with different radiation damping decrements.

As an example, Figure 4.103 shows the evolution of the horizontal beam size of the electron beam with different radiation damping times. In this simulation study, we did not observe any significant difference in the coherent beam-beam motion and luminosity over the damping time range under study. With a longer damping time, it takes a longer time to reach the electron equilibrium beam size. However, there is not much difference in equilibrium beam size and luminosity as long as the radiation damping time is shorter than 16,000 turns, or 4 times the design value. This study of the beam-beam interaction shows that we may relax the requirement on the damping decrement at low energy collisions so we may reduce the radiation power of the super-bends, and the required magnet current.

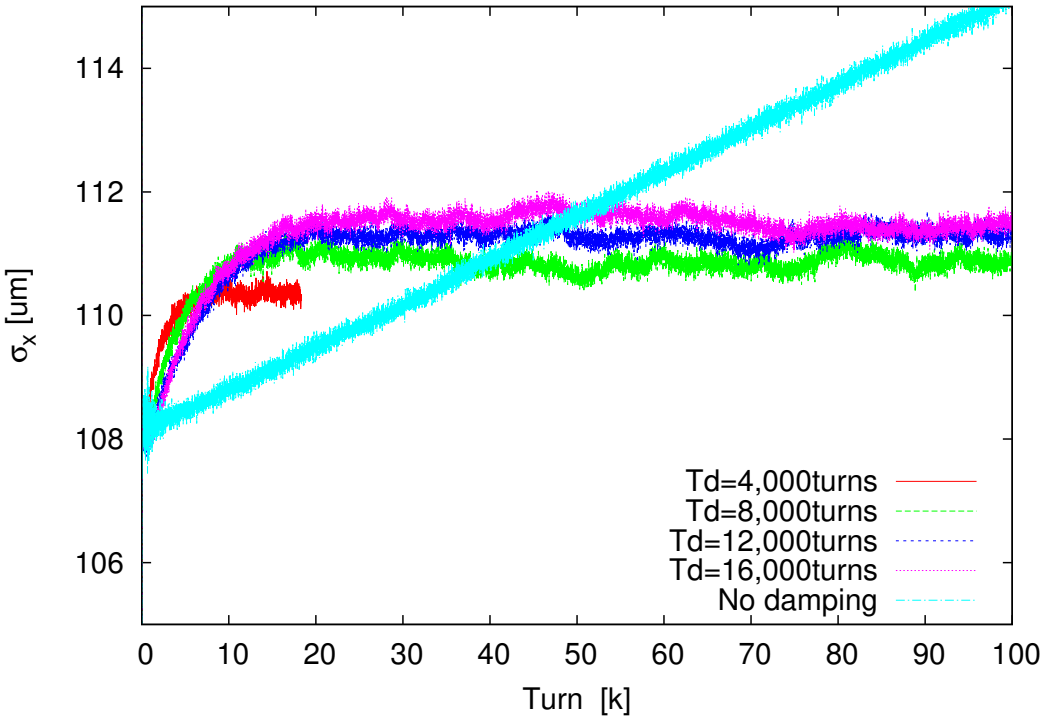

Figure 4.103: Evolution of electron horizontal beam size versus the radiation damping time.

Numerical Noises in Strong-strong Simulation

The strong-strong model is compared with the weak-strong model for the EIC beam parameters. The particle-in-cell (PIC) approach is widely used in strong-strong simulation. It uses a computational grid to obtain the charge density distribution. The beam-beam force can be calculated from an arbitrary beam distribution by solving the 2D Poisson equation. Both beam distribution are updated during collision. Therefore, this kind of method is self-consistent. However, the PIC based strong-strong simulation is subject to large numerical noise. The model parameters, such as the number of macro-particles, the number of longitudinal slices, and the transverse grid sizes, have a large impact on the simulation results [**?**].

Figure 4.104 compares the strong-strong and weak-strong simulation results. The proton beam size growth rate in strong-strong simulation is much larger than the weak-strong simulation. In strong-strong model, the vertical growth rate is twice larger than the horizontal one. It is important to understand the difference in case there is some coherent mechanism shadowed by the large numerical noise.

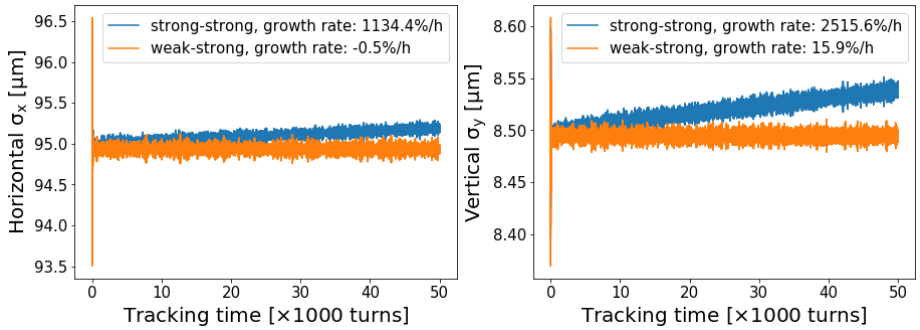

Figure 4.104: Proton beam size evolution in strong-strong and weak-strong simulation.

The numerical noise will cause the particle diffusion in phase space. More macro-particles can reduce the impact of numerical errors. If the beam size or emittance growth is purely determined by numerical noise, it should obey the scaling law [**?**]

$$\frac{1}{\sigma}\frac{\mathrm{d}\,\sigma}{\mathrm{d}\,t} \propto \frac{1}{M} \tag{4.68}$$

where M is the number of macro-particles, and σ is beam size. Figure 4.105 shows the growth rate for different number of electron macro-particles. Two different equations are used to fit the growth rate,

$$g_{x,y} = \frac{A_{x,y}}{M_{\mathrm{e}}^{B_{x,y}}}, \qquad g_{x,y} = \frac{A_{x,y}}{M_{\mathrm{e}}} + B_{x,y} \tag{4.69}$$

where $g_{x,y}$ are horizontal or vertical growth rate which is calculated from the tracking data, $A_{x,y}$ and $B_{x,y}$ are fitting parameters. From Fig. 4.105, the $1/M$ law is a better guess.

The number of longitudinal slices also impacts the numerical noise. Firstly, more slices make the beam-beam force more smooth along the longitudinal direction. In the strong-strong code, the integration is calculated by the drift-kick model. More slices will reduce the global numerical error. Secondly, the number of macro-particles per slice decreases as the number of slices increase. The Monte Carlo noise becomes more. Thirdly, the longitudinal beam-beam potential is linearly interpolated with the method by K. Ohmi [**?**]. The interpolation error also decreases with more slices.

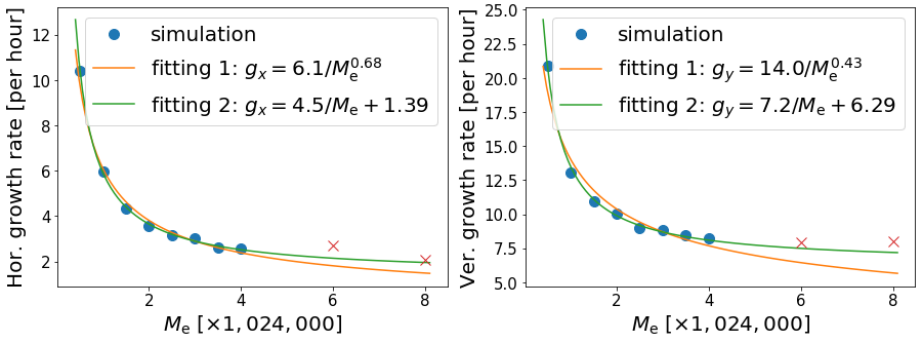

Figure 4.105: The proton beam size growth rate for different number of electron macro-particles. The fitting equations are shown in the legend. The blue circles are used to determine the fitting curves, and the red crosses are used for validation.

Figure 4.106 shows the fitting result for different electron slices. The coefficients $A_{x,y}$ and $B_{x,y}$ are defined by the 2nd fitting model in Eq. (4.69). B_y converges when the electron slice number is greater than 21. There is no clear pattern for $A_{x,y}$ and B_x.

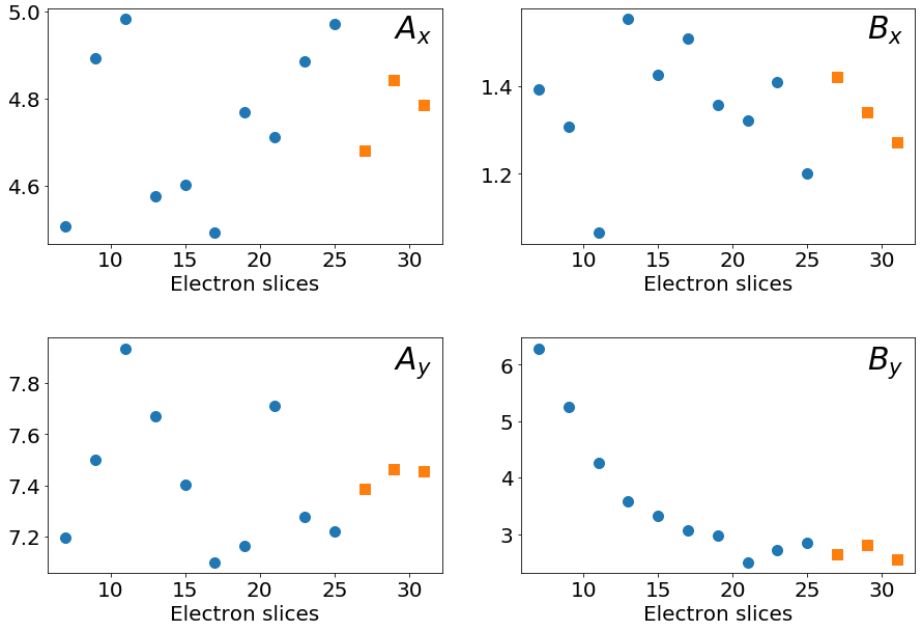

Figure 4.106: The fitting results for different number of electron slices. $A_{x,y}$ and $B_{x,y}$ are fitting coefficients in Eq. (4.69) . The blue circles are tracked by 50, 000 turns, and the orange squares are tracked by 40, 000 turns due to the limitation of computation time.

With more electron macro-particles and more longitudinal slices, the horizontal and vertical growth rates are largely reduced. The converged intercept in Fig. 4.106 is $B_x \approx 140\%/\text{h}, B_y \approx 300\%/\text{h}$. The vertical size still grows faster than the horizontal plane. The asymmetrical growth between the horizontal and vertical plane comes from the nature of PIC noise. Figures 4.107 presents the relative error of PIC solver. The electron energy is artificially set to a huge number so that the electron beam is too "rigid" to be affected by the beam-beam interaction. Then the exact beam-

beam force can be calculated by the analytic formula. From the histogram, the horizontal error is smaller and the distribution shape becomes much "Gaussian" when more electron macro-particles are used. However, the ratio of large relative error in vertical plane is not reduced. It explains why B_y is twice than B_x.

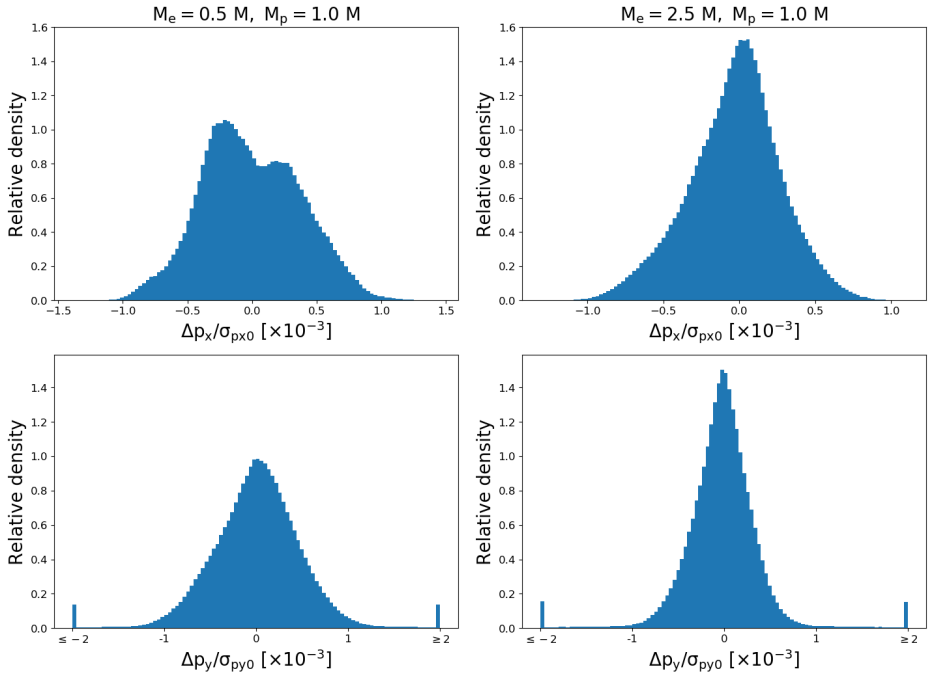

Figure 4.107: The histogram of relative error introduced by PIC solver, top: horizontal, bottom: vertical, left: less electron macro-particles $M_e = 2.5$ M, right: more electron macro-particles $M_e = 2.0$ M. The area under the histogram is normalized to 1. The grid size is 128×128.

Figure 4.108 shows the weak-strong simulation with the information exported from strong-strong simulation. The electron centroid ripple, the electron size ripple, and the PIC solver noise in Fig. 4.107 are compared. The PIC solver distribution is reproduced by Markov Chain Monte Carlo method. Compared with the PIC noise, the growth caused by the electron orbit or size ripple is negligible. The growth rate with the PIC noise is comparable with the number by the strong-strong simulation in Fig. 4.104. Therefore, the emittance growth in the strong-strong simulation is dominated by the PIC noise.

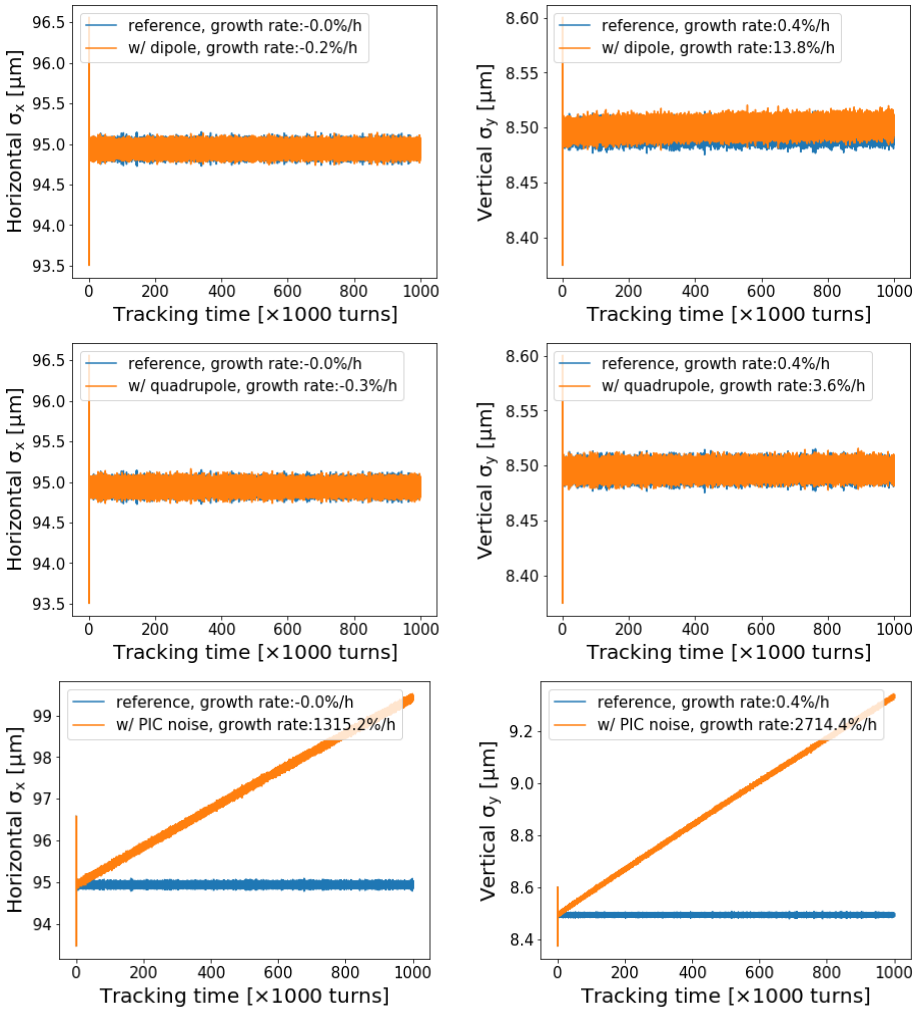

Figure 4.108: Weak-strong simulation with the information exported from strong-strong simulation, top: electron centroid ripple, middle: electron size ripple, bottom: PIC noise.

4.6 Luminosity Model

In order to understand the evolution of the luminosity in the EIC, we have developed a luminosity model. Due to their frequent replacement, we assume that the electron beam parameters are constant. We therefore focus our attention on simulating the evolution of the hadron beam with time. This includes emittance growth due to intrabeam scattering (IBS) and the beam-beam effect, particle losses from the Touschek effect, as well as improvements due to stochastic cooling.

4.6.1 Simple Lattice

We track the hadrons through the hadron storage ring (HSR) using simple transfer matrices, as in Fig. 4.109. These simply rotate the transverse coordinates through some phase advance, alter the beta function when tracking to the interaction point (IP) at IR 6, and adjust the particle's longitudinal position in accordance with its fractional momentum offset and the lattice's phase slip factor. At the RF cavities at IR 10, we provide a momentum kick based on the hadron's longitudinal position assuming a sinusoidal RF at both 591 and 197 MHz. This ensures that the hadrons fully sample the available phase space during their evolution. We also apply kicks for stochastic cooling, as will be detailed in that subsection.

To allow simulation of billions of turns in a realistic amount of time, we implement a time rescaling where each simulated turn represents R real turns. Incoherent effects are increased by a factor of $\sqrt{R}$ and coherent effects are increased by a factor R. We also use a number of hadron macroparticles much less than the real number of hadrons in order to run our simulations in a reasonable time. If we do not include stochastic cooling, the factors for time-rescaling and macroparticle-rescaling can be chosen independently. However, if stochastic cooling is on, these two rescaling factors must be equal; see further discussion in the subsection on stochastic cooling below.

4.6.2 Intrabeam Scattering

Intrabeam scattering is modeled using the methods described in [**?**]. The physics is equivalent to the well-known Bjorken-Mtingwa IBS model [**?**], but the integrals are transformed into elliptic integrals which can be quickly evaluated using the methods of [**?**]. These formulas require as inputs the bunch's horizontal and vertical emittances, bunch length, energy spread, and population. Since the bunch may become non-Gaussian, we extract the emittances from exponential fits to particle actions, and we extract the bunch length and energy spread from Gaussian fits to the particles' longitudinal positions and momentum offsets. In the case where we have multiple RF harmonics and hadrons sit in multiple side buckets, the longitudinal distribution can become incredibly non-Gaussian. In this case, we consider only the central RF bucket when extracting the bunch length, and set the bunch population equal to the population in that bucket. We also feed into the IBS formulas the lattice functions sampled at 1000 equidistant locations around the ring (using a full lattice model); little change is observed if we increase the resolution.

Once the IBS rates are calculated in all three planes, we ensure that the hadron beam is at a location in the lattice with zero dispersion, dispersion derivatives, and alpha function, then implement the heating by the transformations

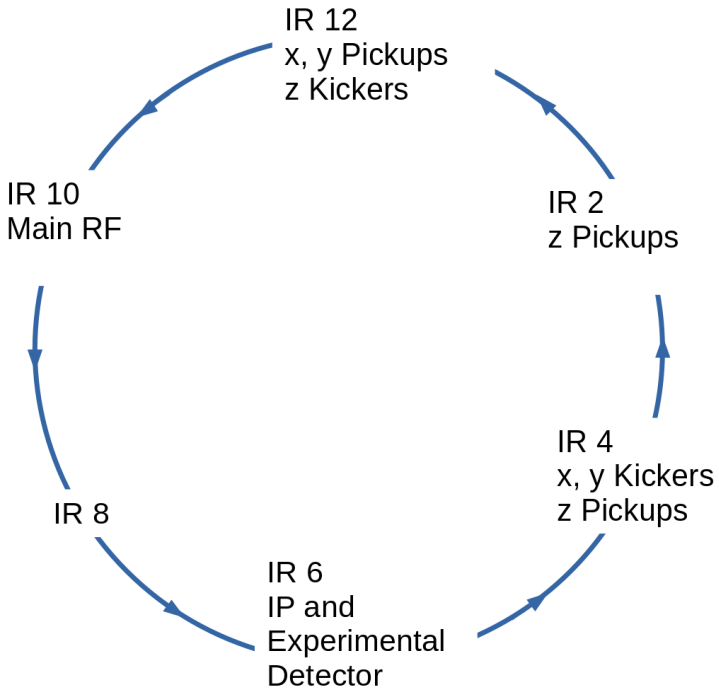

Figure 4.109: Layout of the HSR, including the locations of the stochastic cooling system components.

$$
\begin{aligned}
x' &\to x' + g_x \sqrt{\frac{2\lambda_x \epsilon_x \Delta T \rho}{\beta_x \langle \rho \rangle}} \\
y' &\to y' + g_y \sqrt{\frac{2\lambda_y \epsilon_y \Delta T \rho}{\beta_y \langle \rho \rangle}} \\
\delta &\to \delta + g_z \sigma_\delta \sqrt{\frac{2\lambda_z \Delta T \rho}{\langle \rho \rangle}}
\end{aligned}
\tag{4.70}
$$

where x' and y' are the hadron's horizontal and vertical momenta divided by its nominal longitudinal momentum, δ is the hadron's fractional longitudinal momentum error, g_x, g_y, and g_z are Gaussian random numbers with zero mean and unit RMS, λ_x, λ_y, and λ_z are the heating rates in the 3 planes, ΔT is the length of the time-step, ϵ_x and ϵ_y are the horizontal and vertical emittances, σ_δ is the RMS fractional momentum spread, β_x and β_y are the horizontal and vertical beta functions at the kick location, ρ is the local 3D hadron density at the location of the kicked hadron, and $\langle \rho \rangle$ is the local hadron density averaged over all hadrons in the central RF bucket. It can be verified that this procedure gives the correct emittance growth to the beam as a whole while giving proportionally stronger kicks to particles near the center of the bunch, due to their more frequent collisions.

4.6.3 Beam-Beam Growth

Calculations of the beam-beam effect are difficult, and implementing an exact solution within this code would be computationally prohibitive. We therefore assume that, for protons, the beam-beam growth time is a constant 4 hours in the vertical plane and 20 hours horizontally. We implement the actual heating of the beam in the same way as for IBS, but we do not include the density scaling factor, since figuring out the appropriate scaling is highly non-trivial.

4.6.4 Losses and the Touschek Effect

We declare that a particle is lost if

$$\frac{J_x}{J_{x,max}} + \frac{J_y}{J_{y,max}} + \frac{J_z}{J_{z,max}} \geq 1, \tag{4.71}$$

where $J_{x,y,z}$ are the particle's horizontal, vertical, and longitudinal actions, $J_{x,y,max}$ are the transverse actions corresponding to a particle with transverse position greater than 6 times the initial hadron beam size, and $J_{z,max}$ is the lesser of the longitudinal actions which result in the hadron either having a momentum offset greater than 6 times the initial RMS momentum spread of the bunch or a longitudinal position outside the appropriate RF bucket.[1] This all corresponds to an ellipse in the 6-dimensional phase space.

We include the Touschek effect by calculating the loss rate using Equations 41 and 42 of [**?**]. Note that this loss rate assumes zero initial action for the particle in question.

In order to handle the case where the particle has non-zero actions, we determine the maximum momentum kick that it can receive before it is lost. Under the generally reasonable assumption that the loss is due to growth in the longitudinal action, we find that the minimum change in longitudinal action which would result in particle loss is

$$\Delta J_z = J_{z,max}\left(1 - \frac{J_x}{J_{x,max}} - \frac{J_y}{J_{y,max}}\right) - J_z \tag{4.72}$$

Define the of longitudinal action

$$J_z(z,\delta) \equiv \frac{1}{2}\frac{\eta C}{T_0}\delta^2 + \sum_i \frac{ZeV_i}{k_i E_0 \beta^2 T_0}\big(1 - \cos(k_i z)\big) \tag{4.73}$$

where η is the phase slip factor, C is the ring circumference, β is the relativistic beta, T_0 is the revolution time, Ze is the particle charge, E_0 is its energy, and V_i and k_i are the voltages and wavenumbers of the various RF cavities. We then see that the fractional momentum kick which results in a particle loss is

[1] Due to the strong beam-beam force, we assume that any proton which lies outside of the central 591 MHz bucket is lost. For heavy ions, since the beam-beam force is reduced, we relax this constraint so that only those outside the full 197 MHz bucket are lost.

$$\Delta\delta_{\pm} = -\delta \pm \sqrt{\delta^2 + \frac{2\beta^2 T_0}{\eta C}\Delta J_z} \tag{4.74}$$

where the two solutions correspond to providing an energy kick toward the near or far loss-boundary. Since the loss rate from [**?**] assumes a zero-action particle, where positive and negative momentum kicks are equally effective, the loss rate for a general particle is the average of the loss rates obtained from those formulas in the case where we assume a maximum momentum kick of $|\Delta\delta_+|$ and the case where we assume a maximum momentum kick $|\Delta\delta_-|$.

Rather than recomputing the loss rate for each value of δ_{max}, we find empirically that the loss rate scales as $\frac{1}{\delta_{max}^3}$, where δ_{max} is the longitudinal kick which would result in a particle loss. This shows good agreement with data, as shown in Fig. 4.110.

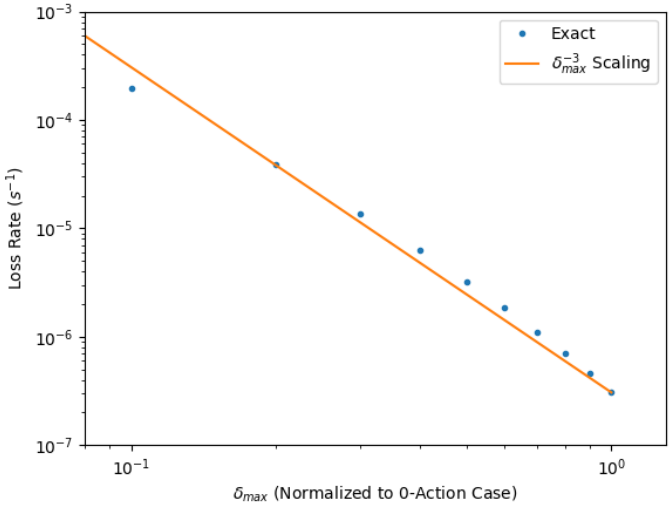

Figure 4.110: Loss rate for gold ions, for various values on δ_{max} (blue), normalized to the momentum kick which would cause a 0-action particle to be lost. This is compared to a simple scaling of δ_{max}^{-3} (orange). Decent agreement is observed. Note the log-log scale.

4.6.5 Stochastic Cooling

Stochastic cooling is being considered for the cooling of heavy ions, so it is also included in our simulation. The planned setup is to have horizontal and vertical pickups at IR 12 and longitudinal pickups at IR 4 and IR 2. Horizontal and vertical kickers are at IR4 and longitudinal kickers are at IR 12. See Fig. 4.109. In both transverse planes, the phase advance from IR 12 to IR 4 will be an odd multiple of $\pi/2$, so that an ion's transverse offset at the pickup will correspond to its transverse angle at the kicker. We use appropriate transfer matrices to translate the ions between all IRs.

At the transverse pickups, we take the Fast Fourier Transform (FFT) of the ion density, weighted by their transverse offsets. In each plane, we will have 16 pickups operating at frequencies from 25 to 40 times the fundamental RF frequency, and therefore in the simulation we zero out all frequencies

outside this bandwidth. We multiply this filtered frequency spectrum by an appropriate gain and invert the FFT to get the kicks to the ions in the transverse kickers.

For the longitudinal case, we use the two sets of pickups to construct a derivative of the longitudinal position, which will correspond to the ions' energy offsets. To do so, we take the FFT of the ion density at each longitudinal pickup, remove the frequencies outside the bandwidth, and take the difference of this spectrum between IR 4 and 2. We multiply the positive frequencies by the imaginary unit, multiply the negative frequencies by the negative imaginary unit, multiply by an appropriate gain, and invert the FFT to obtain the momentum kicks to the ions in the longitudinal kicker.

This procedure automatically includes the incoherent heating of the beam due to the fact that nearby ions influence the kicks their neighbors receive. In order to ensure that this scales correctly, we require that the number of hadrons represented by each macroparticle is equal to the number of real turns represented by each simulated turn. Consider a simple model: each turn, each ion receives a corrective kick which sends its transverse coordinate $x \to x - \lambda x$, but also receives kicks from N neighbors so that the total change is

$$x \to x - \lambda x - \lambda \sum_{i=1}^{N} x_i \tag{4.75}$$

Then the typical change to the particle's action, proportional to x^2, is

$$x^2 \to x^2 - 2\lambda x^2 + N\lambda^2 \langle x^2 \rangle \tag{4.76}$$

If we want a rescaling factor R, such that we simulate R real turns per simulated turn, we need to increase the gain of the system by R and reduce the number of particles by this same factor R (ie, $\lambda \to R\lambda$ and $N \to N/R$).

4.6.6 Microbunched Electron Cooling

This simulation code can also handle microbunched electron cooling; details are provided in **[?]**.

4.6.7 Initialization of Hadrons

Hadrons are initialized with transverse actions chosen from an exponential distribution $\rho(J_{x,y}) = \frac{1}{\epsilon_{x,y}} e^{-J_{x,y}/\epsilon_{x,y}}$, with cuts imposed at 6-sigma, so as to minimize immediate losses. Their phases are chosen uniformly on the interval $[0, 2\pi)$.

For the longitudinal distribution, they are given Gaussian random momentum offsets, then tracked for several thousand turns (with the number varying from hadron to hadron) to both spread them out in phase space and ensure they are within the RF bucket. Those lost are reseeded.

4.6.8 Beta-Star Scaling

As the beam evolves, we adjust the hadron and electron beta functions at the IP to maintain 3 conditions. First, if the hadron beam divergence at the IP would increase above its initial value, we raise the beta function to prevent large backgrounds in the forward detectors. Second, if the hadron beam size would decrease below its initial value, we also raise the beta function to prevent us from needing the shrink the electron beam size. Finally, we adjust the electron beta functions so that their beam size matches that of the hadrons.

4.6.9 Luminosity Evaluation

We evaluate the luminosity using a fairly general formula from [**?**], assuming that the crab cavities work perfectly, so that the particles' transverse velocities are negligible, and the longitudinal velocities are near the speed of light:

$$\mathcal{L} = 2cf_{rep} \int \rho_+(\vec{x},t)\rho_-(\vec{x},t)d^3\vec{x}dt \tag{4.77}$$

where c is the speed of light, f_{rep} is the frequency with which bunches collide at the IP, and $\rho_{+,-}(\vec{x},t)$ are the spatial and time dependent densities of the hadrons and electrons. This integral can be evaluated numerically by tracking the hadron macroparticles across the IP, integrating over the electron densities they see (assuming a Gaussian electron bunch and drift-like evolution of electron betas), and summing the results, multiplied by the number of real hadrons per macroparticle.

4.6.10 Luminosity Averaging

In order to have a fair comparison between different cases, we consider the average luminosity. We assume that it takes 2 hours to dump the hadrons, ramp down the machine, inject fresh bunches, perform pre-cooling, and ramp to top energy. Additionally, we assume that it takes half an hour to fill the electrons and turn on the detector, during which time the luminosity will be zero and the hadron beam will begin deteriorating. The average luminosity is found by integrating the luminosity over time and dividing by the store time plus turnaround time.

As an example, plots of the evolution of instantaneous, integrated, and average luminosity for 275 GeV protons colliding with 10 GeV electrons are shown in Fig. 4.111.

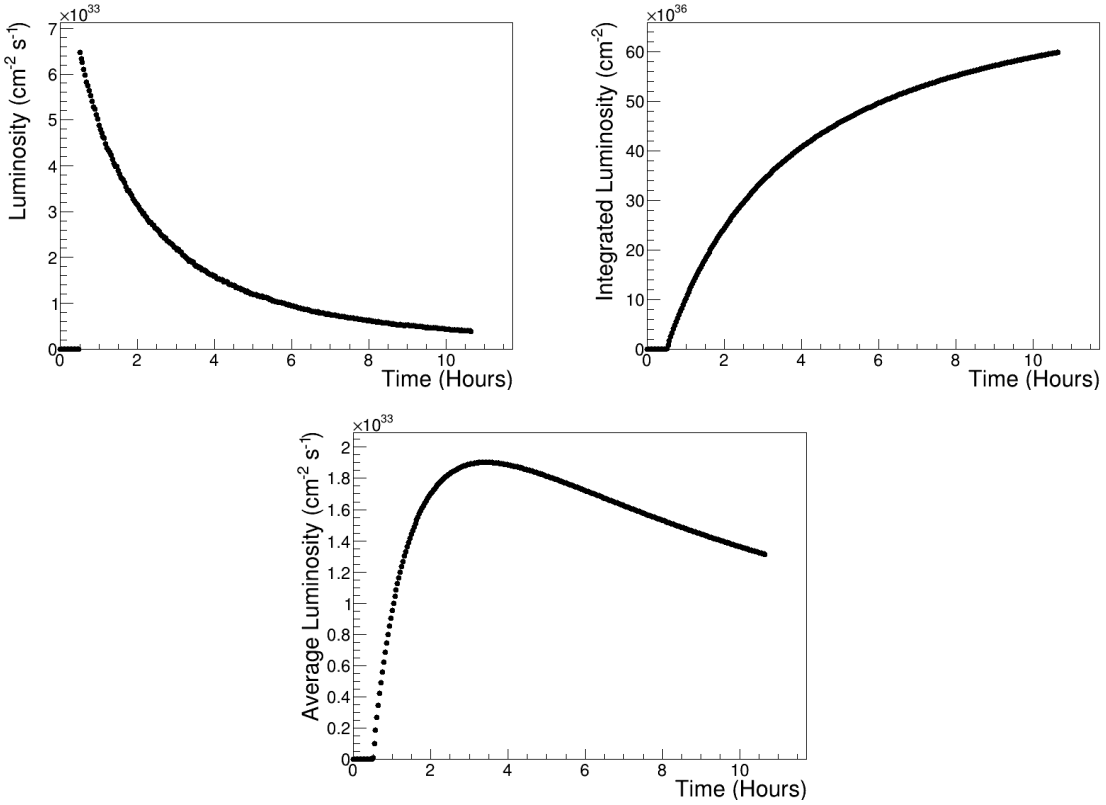

Figure 4.111: Instantaneous, integrated, and average luminosity for 275 GeV protons colliding with 10 GeV electrons.

Chapter 5

Polarization (editors: Ptitsyn & Ranjbar)

5.1 Hadron Injector

5.2 Hadron Storage Ring

5.2.1 Protons

RHIC has provided polarized proton beams over an energy range from 31 GeV to 255 GeV during the past decade. To preserve polarization through numerous depolarizing resonances over the whole accelerator chain, harmonic orbit correction, partial and full Siberian Snakes, and a horizontal tune jump system have been used. In addition, close attention has been paid to betatron tune control, orbit control and magnet alignment. A polarization of 60% at 255 GeV has been delivered to experiments with an intensity of 1.8×10^{11} protons per bunch. For the EIC, the beam brightness has to be maintained to reach the desired luminosity. Since the EIC will use only the present RHIC Yellow ring, spin rotators and snakes from the Blue ring can be converted into additional Siberian Snakes in the HSR. With a proper arrangement of six snakes in the hadron ring and additional reduction of emittance growth in the AGS, the polarization is expected to reach 70% at 275 GeV beam energy.

The AGS delivers polarized proton beams with 70% polarization at an intensity of 3×10^{11} protons per bunch. Strong hadron cooling will reduce the vertical emittance at store for the highest luminosities. During the acceleration ramp the emittances will be larger, initially as delivered by the AGS. This larger emittance has to be taken into account when calculating depolarizing resonance strengths.

The current proton acceleration chain is shown in Figure 5.1. High intensity, high polarization H^- is produced at the polarized proton source. The H^- beam polarization is measured at the end of the 200 MeV LINAC as 80–82%. The beam is then strip-injected into the AGS Booster. The Booster vertical tune is set high enough so that the intrinsic resonance in the Booster at $0 + \nu_y$ is avoided. Two imperfection resonances in Booster are corrected by harmonic orbit correction. In the AGS, two partial Siberian Snakes separated by 1/3 of the ring circumference are used to overcome the imperfection and vertical intrinsic resonances [**?**]. The vertical tune ν_y on the energy ramp is mostly above 8.98, so that it is in the spin tune gap, away from the high order snake resonances. To avoid the horizontal intrinsic resonances driven by the partial snakes, a pair of pulsed quadrupoles is employed to jump the tune across the many weak horizontal intrinsic resonances on the ramp [**?**]. Two full Siberian Snakes are used in each of the two present RHIC rings to maintain polarization [**?**]. Feedback during acceleration – on the betatron tune, coupling, and orbit – is crucial for polarization preservation.

The polarization measured at AGS extraction energy is shown in Figure 5.2 as a function of beam intensity. The apparent polarization dependence on intensity is really a dependence on emittance, since emittance and intensity were simultaneously reduced by scraping in the Booster. As higher intensity is always associated with larger emittance, greater depolarizing resonance strengths and lower polarization is expected at higher intensities. The polarization at 3×10^{11} is about 65%.

Emittances measured by the AGS Ionization Profile Monitor (IPM) are affected by space charge forces. To mitigate this effect, the RF is turned off during beam profile measurement at acceleration flattop. The emittance reported by the IPM with RF off is plotted in Figure 5.3. The projected emittance at zero intensity is non-zero because there is some emittance growth in the Booster and mismatch in the transfer line. The horizontal and vertical RMS normalized emittances are about 2.4 µm and 2.6 µm, respectively, at an AGS extraction intensity of 3×10^{11} protons per bunch,

The vertical emittance of ion beams will be cooled at the injection of HSR down to 0.75 µm. As the experience at RHIC shows, the polarization transmission efficiency up to 100 GeV is close to 100% but only about 92% for 250 GeV at 1.8×10^{11} bunch intensity due to stronger intrinsic resonances.

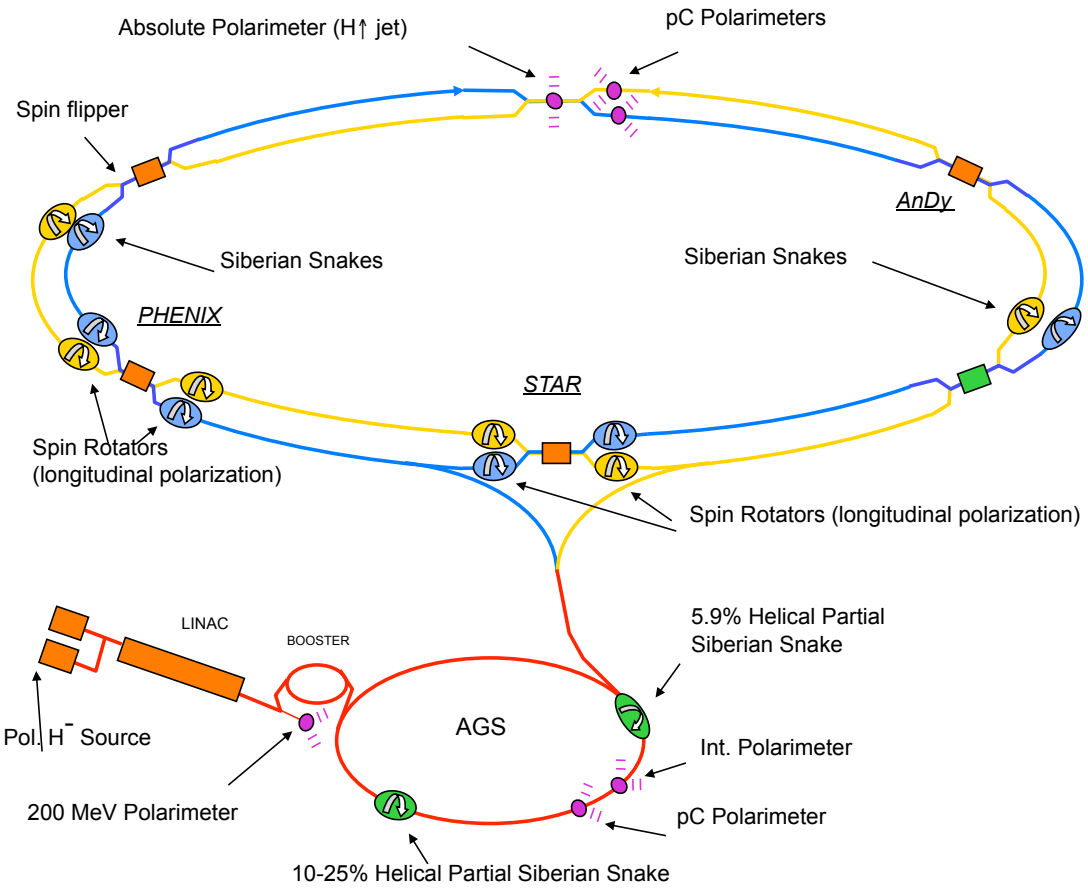

Figure 5.1: Layout of the current RHIC complex.

The vertical emittance is about 2.4 µm. Figure 5.4 shows that the highest resonance strength, calculated by DEPOL [?], for a particle with 10 µm normalized action invariant is about 0.18 below 100 GeV, and about 0.45 above 100 GeV. The intrinsic resonance strength is proportional to the square root of vertical emittance, so the resonance strength seen in RHIC is 0.09 below 100 GeV and 0.225 above 100 GeV. This implies that the two snakes can preserve polarization for an intrinsic resonance strength 0.09, but not for 0.225. The resonance strength threshold for 100% polarization transmission efficiency with two snakes is therefore in the range from 0.09 to 0.22.

As a rule of thumb, the resonance strength threshold increases in proportion to the number of snakes. The depolarizing resonances are stronger during ^{3}He operation (see below) so spin manipulating magnets will be moved from the RHIC Blue ring to the Yellow HSR, to build a configuration with a total of six Siberian Snakes from Yellow snakes, Blue snakes, and Blue rotators magnets. Since the real resonance threshold is unknown, simulations are needed to determine the level of polarization preservation.

All the existing RHIC snakes consist of four magnets with right-handed helicity. The inner and outer magnets are powered separately with currents I_{in} and I_{out}. One of the snakes made from the

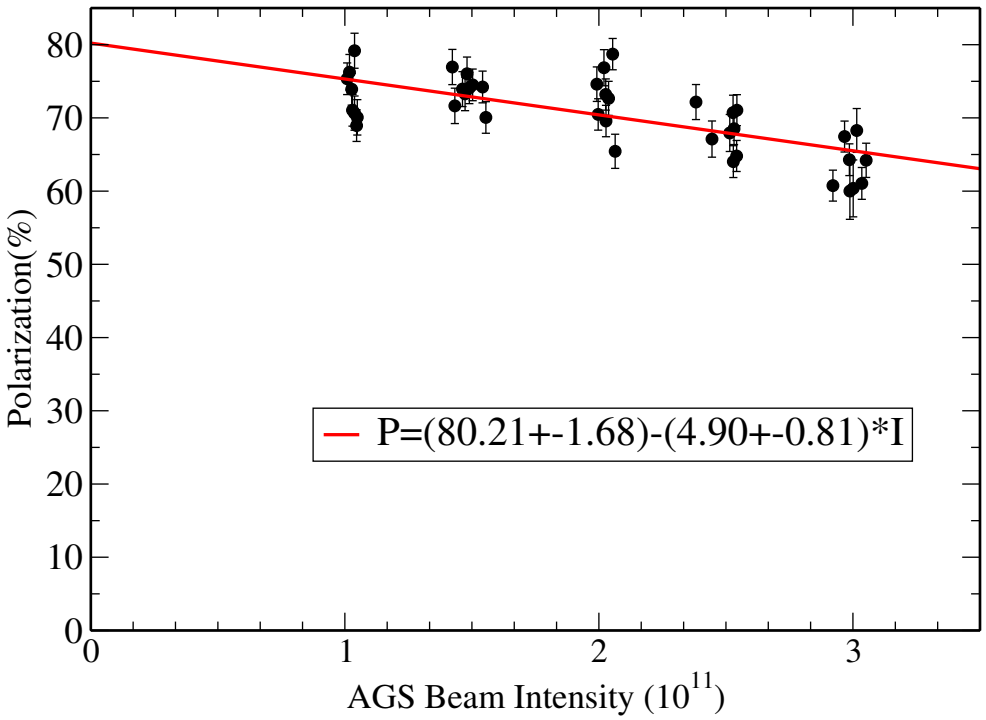

Figure 5.2: AGS polarization at extraction as function of bunch intensity. The polarized proton source can deliver an intensity of 9×10^{11} at the Booster input. Booster scraping (both horizontal and vertical) is used to reduce the beam emittance for AGS injection. The intensity in this figure is changed by varying the Booster scraping level.

RHIC rotator magnets will need to have left-handed helicity coils. The precession axis of protons for right handed and left handed helicities are shown in Figure 5.5. To match the orbit generated in the snake with the rest of the accelerator, it is preferential to have $I_{in} > I_{out}$. For protons, the achievable axes are from $\theta_{s,x}$=0 to 45° with a favorable orbit, or up to 60° with a less favorable orbit.

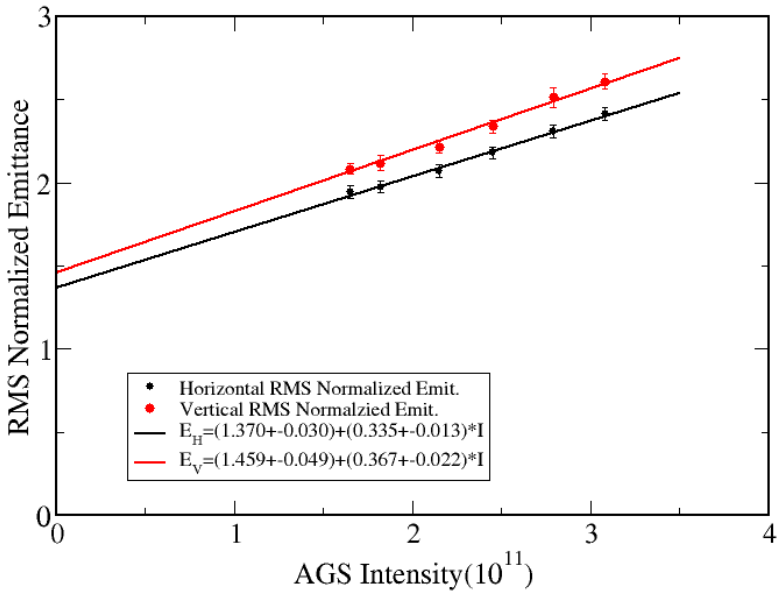

Figure 5.3: AGS emittance measured by the IPM versus intensity at AGS extraction.

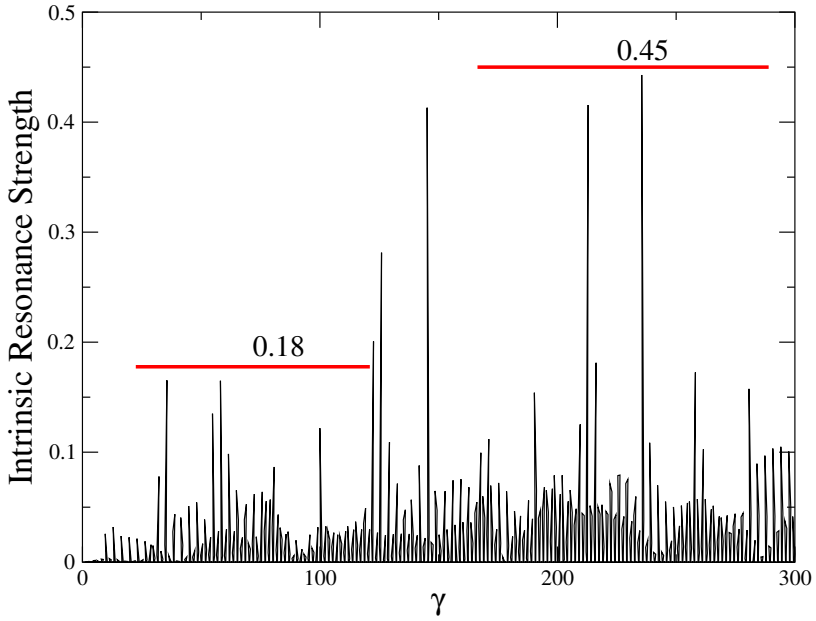

Figure 5.4: Intrinsic resonance strengths of the present RHIC lattice for a particle on a 10 µm action ellipse as function of the Lorentz factor γ. Below 100 GeV, the resonance strength is less than 0.18. A stronger resonance strength of 0.45 has to be overcome, in order to accelerate a proton beam to 275 GeV.

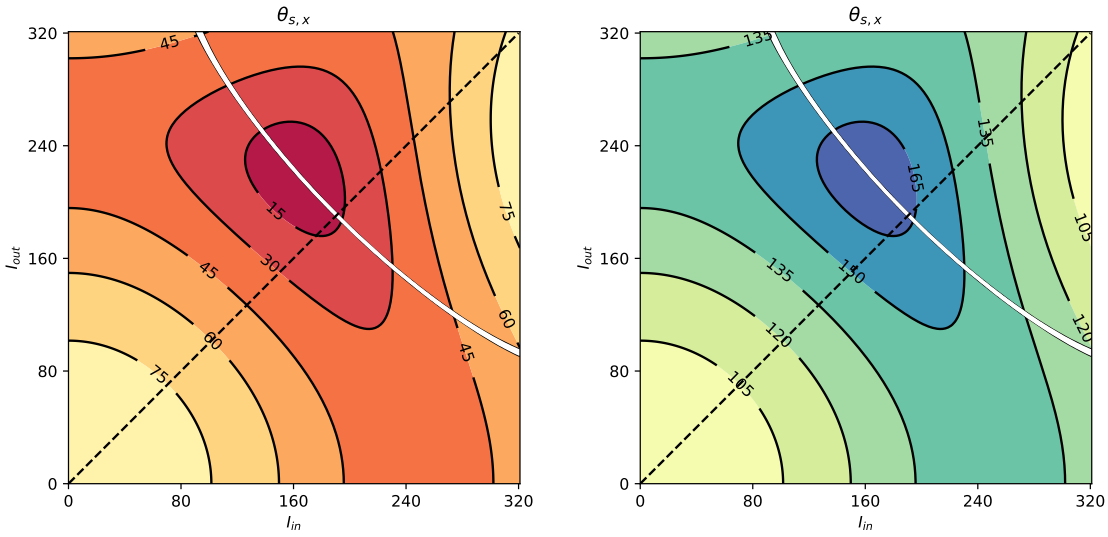

Figure 5.5: Achievable snake precession axes for right helicity (left) and left helicity (right) magnet coils as a function of inner and outer power supply current. The white line corresponds to a full spin-flip, and the dashed line represents currents that provide a symmetric orbit.

Acceleration simulations

Spin tracking was performed with Zgoubi for one of the three strongest depolarizing resonances, $411 - \nu_y$, to estimate polarization transmission efficiency during acceleration [**?**]. The tracking was done for 8 particles on the ϵ =2.5 µm vertical action ellipse, with an acceleration rate 7 times faster than the actual, to speed up tracking. In the presence of a Siberian Snake the polarization loss is not sensitive to resonance crossing speed. Only vertical betatron motion was taken into account in the simulation.

For a configuration with multiple snakes, the snake arrangement has to satisfy the conditions for an energy independent spin tune, namely

$$\sum_{k=1,3,5} \theta_{k,k+1} = \pi \tag{5.1}$$

$$\sum_{k=2,4,6} \theta_{k,k+1} = \pi. \tag{5.2}$$

where $\theta_{k,k+1}$ are azimuthal distances defined in terms of design momentum rotation angle between the snakes. The snake axis angles are $\phi = \pm\pi/4$ from the longitudinal axis in the local Serret-Frenet frame, ensuring a spin tune of $\nu_{\rm spin} = 3/2$ since

$$\nu_{\rm spin} = \frac{1}{\pi} \left| \sum_{k=1}^{N_s=6} (-1)^k \phi_k \right|. \tag{5.3}$$

where $N_s = 6$ is the number of snakes. A symmetric arrangement with the 6 snakes equally spaced by $2\pi/6$ preserves polarization, although not all snake arrangements satisfying the above conditions do so.

The snake in the injection region near IP6 is constrained from being placed in the ideal location, so the snake near IP12 is moved to meet Equations 5.1 and 5.2. The snakes are located at the 6 bending angles $(\phi,\ \pi/3-\phi,\ 2\pi/3-\phi,\ \pi+\phi,\ 4\pi/3-\phi,\ 5\pi/3-\phi)$, where $\phi = 0.0435$ rad. If snakes 1 and 4 were not in their ideal locations, $-\phi$ and $\pi-\phi$, then all snakes would be separated by $\pi/3$. The simulation results shown in Figures 5.6 and 5.7 for ideal snake locations and for a pair of snakes with an offset in a RHIC lattice show little visible difference over the action range considered. Polarization is preserved for both the small and the large emittance cases, and the transmission efficiency through acceleration is close to 100%. Simulations with many particles in a 6-D distribution and with the true acceleration rate will follow.

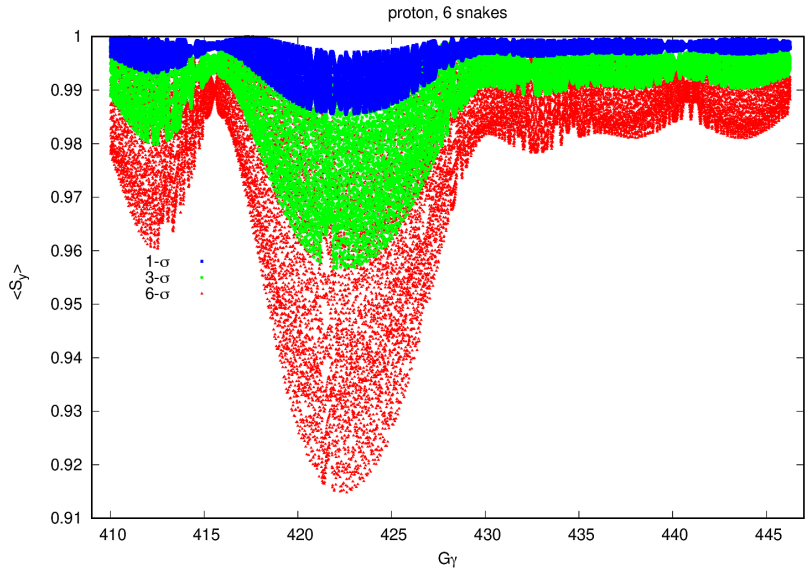

Figure 5.6: Simulation results for 6 snakes at ideal locations during acceleration through the strongest depolarizing resonance at $393 + \nu_y$. The vertical invariant is $\epsilon_y = 1,\ 3,\ 6\ \sigma$, with σ =0.75 µm the normalized action. Each trace shows the average vertical projection of the spin, computed by tracking 8 particles evenly distributed on the invariant ellipse. These results are used as a reference, for comparison with the case of one pair of snakes with an offset.

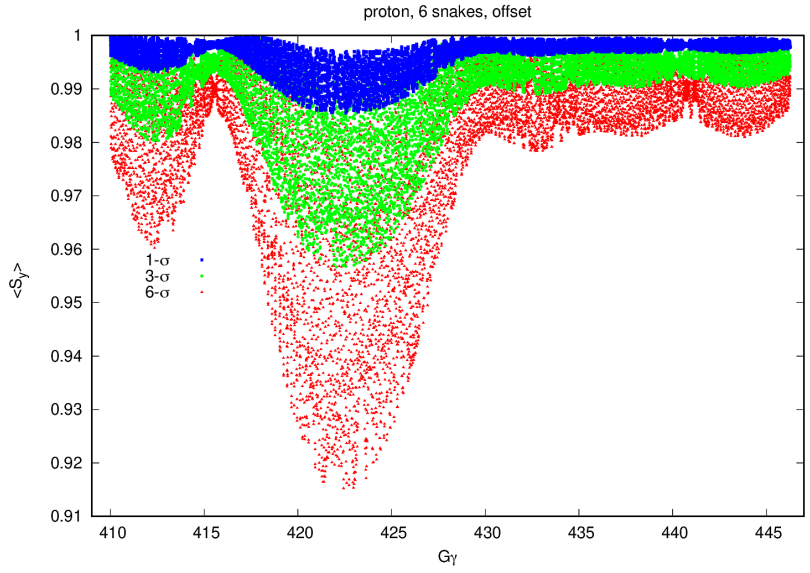

Figure 5.7: Simulation results for 6 snakes, with one pair of snakes with an offset of $\phi = 0.0435$ rad and snake axes at $\pm\pi/4$, for passage through the strongest depolarizing resonances at $393 + \nu_y$. The vertical invariant is $\epsilon_y = 1,\ 3,\ 6\ \sigma$, with σ =0.75 µm. Each trace shows the average vertical projection of the spin, computed by tracking 8 particles evenly distributed on the invariant ellipse. The effect of the horizontal invariant on spin is negligible. Polarization is preserved in all cases.

Space charge effects at low energies

The space charge tune shift at injection (25 GeV) is 0.1 and at the low collision energy (41 GeV) is 0.05, with a cooled ion beam. Although the depolarizing resonances are weaker at lower energies, the available betatron tune spread is larger. There are two configurations, depending on the proton collision energy:

1. In the range 100 GeV to 275 GeV, injection at 25 GeV is followed by acceleration in the HAR (if it is present) before storage in the HSR.
2. At 41 GeV, injection directly into the HSR at 25 GeV is followed by acceleration and storage. Beam passes through the inner arc from IP4 to IP2, instead of through the outer arc.

Operating the HSR at injection energy with only two snakes is most challenging. Space charge effect have been studied at both 25 GeV and 41 GeV. The polarization lifetime was simulated with lattice independent model [**?**]. The polarization loss rate is scanned as function of vertical betatron tune over a range of vertical emittances.

At 25 GeV the vertical emittance before cooling is 2.5 µm. The polarization decay rate with two snakes and a space charge tune shift of 0.1 is then flat at 0.0%/hr over a vertical tune range from 29.16 to 29.30, even for particles on the 10 µm action ellipse, due to the relative weak resonance strengths. Polarization lifetime is not a problem.

At 41 GeV, the vertical emittance after cooling is 0.75 µm. The polarization loss rate is also small over a wide range of vertical tune space from 29.16 to 29.30. The expected space charge tune shifts of 0.05 and 0.1 do not threaten the polarization lifetime.

Spin rotator settings

HSR will use existing RHIC spin rotators based on helical dipole magnets in order to transform the vertical beam polarization in the arcs into longitudinal polarization at IP6. The spin rotator includes 4 helical dipoles, each of them 2.4 m long with one period of helical twist. The rotator is characterized by two magnetic field values – B_1 and B_2 for outer and inner helices, respectively.

In the EIC interaction region, there is the bending angle +95 mrad between the upstream rotator and the IP and the bending angle +17 mrad between the IP and the downstream rotator. Thus, the rotators in EIC are placed much further away from the IP in terms of bending angles, and polarization vector may rotate more than one full turn between the rotator and the IP, depending on the beam energy.

The fields, B_1 and B_2, of the downstream spin rotator required for longitudinal polarization at the IP are shown in Figure 5.8, assuming maximum field of 3.6 T. The field plots show that at some energies the longitudinal polarization at the IP can not be achieved. Combining the data shown in Figure 5.8 with similar data from the upstream rotators, one can find that the IP longitudinal polarization can not be obtained in following energy ranges:
25.3–46.9 GeV, 120.9–127.4 GeV, 167.6–169.2 -GeV and 248.1–261.5 GeV.
Also it should be noted that unlike the RHIC spin rotator in the EIC the fields in helices will need to change their sign at different energies to cover as many energies as possible.

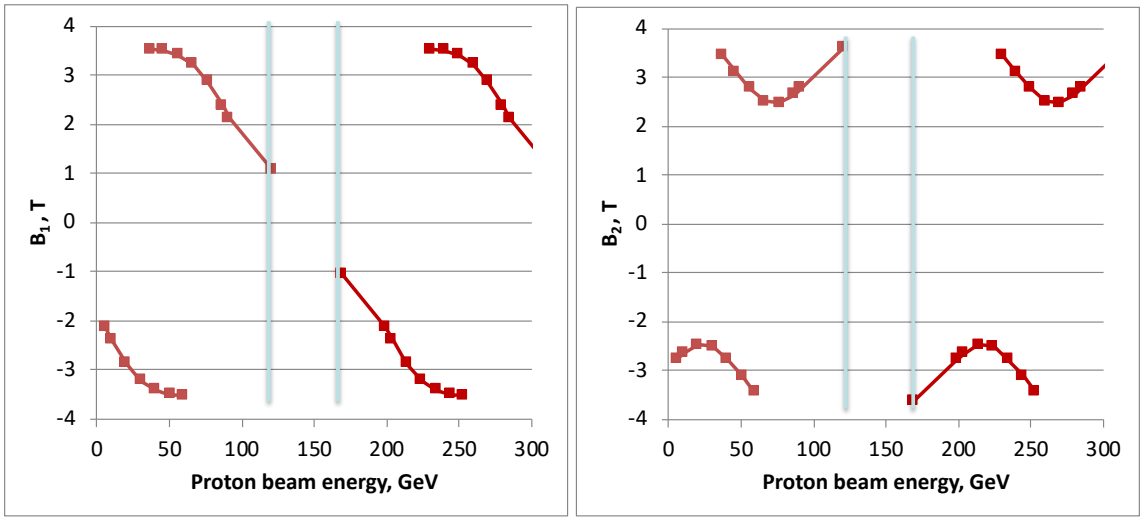

Figure 5.8: The magnetic fields of HSR spin rotators required for longitudinal polarization at IP6 versus the beam energy. Left: B_1 in the outer helices. Right: B_2 in the inner helices.

An alternative spin rotator configuration

As discussed in the previous section, the HSR includes two Siberian snakes and two spin rotators on the two sides of IP6. The spin rotators change the spin direction from vertical in the arcs to longitudinal at IP6. There is an asymmetry of the orbital bending angles between the IP and the spin rotators on the two sides of the IP. It may cause a dependence of the invariant spin field $\vec{n}$ on the phase space coordinates thus reducing the polarization lifetime as discussed below. Modification of the spin rotator configuration for the EIC may also result in a gap in energies of the hadron collider ring where the spin rotators can no longer provide the longitudinal polarization at IP6. These problems can be solved by running the hadron collider ring in the spin transparent mode. In this mode, the axes of the two Siberian snakes are adjusted to nearly the same direction while their strengths are set to nearly π spin rotation angles. The spin tune is then close to zero. The polarization direction at IP6 can, in this case, be controlled without the spin rotators.

The required polarization orientation $\vec{n} = (n_x, n_y, n_z)$ can be set at IP6 by adjusting a small angle $\delta\alpha$ between the snake axes and small offsets $\delta\mu_1$ and $\delta\mu_2$ of the snakes' spin rotation angles from π:

$$\nu_x = \frac{\delta\mu_1 - \delta\mu_2}{2\pi} \sin\left(\frac{\gamma G\pi}{2}\right) , \tag{5.4}$$

$$\nu_y = \frac{\delta\alpha}{\pi} , \tag{5.5}$$

$$\nu_z = -\frac{\delta\mu_1 + \delta\mu_2}{2\pi} \cos\left(\frac{\gamma G\pi}{2}\right) , \tag{5.6}$$

$$\nu = \sqrt{\nu_x^2 + \nu_y^2 + \nu_z^2} \tag{5.7}$$

where ν is the spin tune induced by the snakes serving as a 3D spin rotator. Equation (5.4) assumes that both snake axes are longitudinal.

The described rotator allows one to set any 3D polarization direction at the polarimeter by small variation of the snake currents. Exceptions are $\gamma G = k$ points where the snake rotators allows one

to set any 2D polarization orientation in the (yz) plane for even k and in the (yx) plane for odd k.

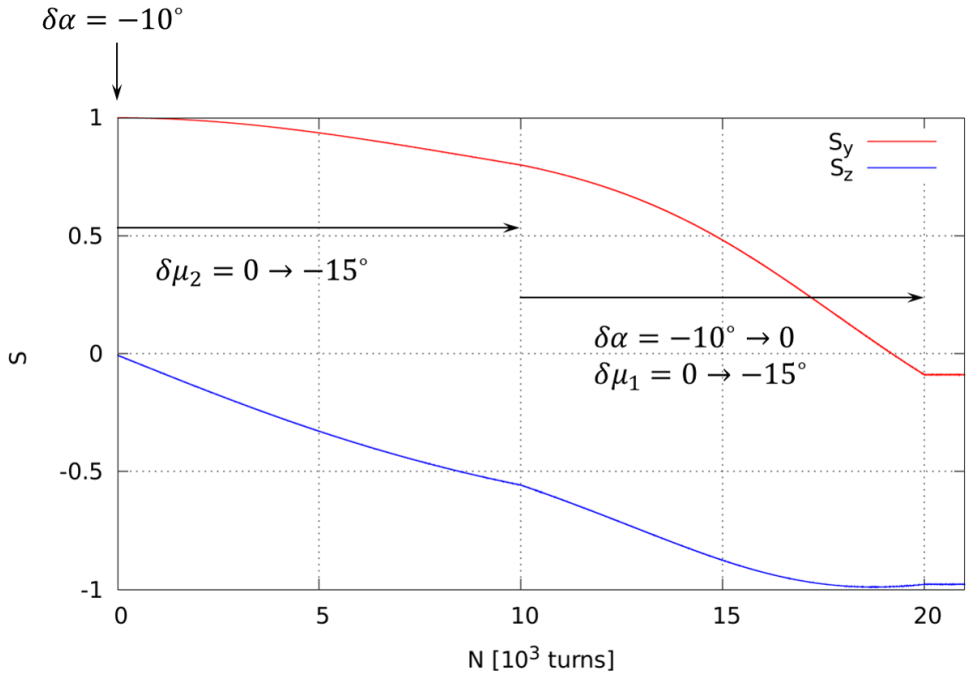

Figure 5.9: Illustration of adjustment of the polarization from vertical to longitudinal at the IP in the spin transparency mode without using the spin rotators.

Figure 5.9 illustrates the procedure for adjustment of the longitudinal polarization at the IP. The simulation is done using a spin tracking code Zgoubi. The calculation used the injection setup where $\gamma G = 45.5$ The beam is injected vertically polarized. An initially vertical stable polarization direction is set by running Snakes 1 and 2 with 180° spin rotation angles, making the Snake 2 axis longitudinal and tilting the Snake 1 axis by 10° from the beam direction in the horizontal plane. The Snake 2 angle is then ramped from 180° to 165° in 10 thousand turns while keeping its axis longitudinal. During the next 10 thousand turns, the Snake 1 angle is adjusted from 180° to 165° and its axis is at the same time changed to longitudinal. All ramps are linear. Figure 5.9 shows that final polarization direction is nearly longitudinal. The difference is due to a change of the orbital effects of the snakes during the ramps and magnet misalignments.

The simulation in Fig. 5.9 was done considering element misalignments for the closed orbit shown in Fig. 5.10. The large orbital spikes due to the snakes are not shown in Fig. 5.10 for a better view of the orbit distortion around the ring. The simulation accounted for the orbit excursion due to the snakes. A statistical approach was used to find a level of misalignments giving an rms closed orbit distortion of 0.2 mm consistent with RHIC experience. The horizontal and vertical rms closed orbit excursions in Fig. 5.10 are 0.22 and 0.18 mm, respectively, in agreement with our expectations.

The spin transparency mode is a novel technique that has not yet been used in operation. There is a plan to verify it experimentally in RHIC prior to construction of the EIC.

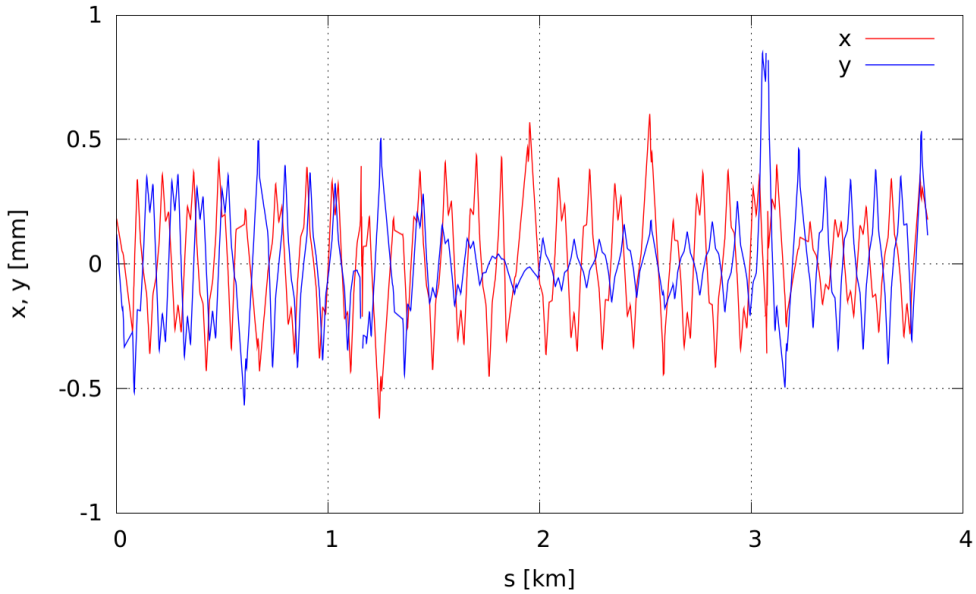

Figure 5.10: Closed orbit excursion used in the simulation shown in Fig. 5.9. The orbit distortion by the snakes is not shown for a better view of the orbit outside the snake sections but it is account for in the simulation.

The effects of IBS and cooling on polarization lifetime

Stochastic effects such as IBS, space charge, and cooling can potentially cause depolarization of the hadron beam. The mechanism is similar to that of the spin diffusion in electron rings. A stochastic scattering event instantaneously changes the particle phase space coordinates. The particle's spin orientation does not change but the stable spin field direction at the new coordinates may be different from that at the initial ones. Therefore, if the spin initially points along the spin field it is no longer aligned with the stable spin direction after the scattering event. Only the spin component along the new spin field direction is preserved. As this process continues on, the beam gradually gets depolarized.

The polarization lifetime is determined by the diffusion rate of the particle's phase space coordinates and the sensitivity of the stable spin direction $\vec{n}$ to changes in the coordinates. Using the analogy of electron polarization lifetime τ_{pol} due to the synchrotron radiation, the polarization lifetime can be written as

$$\frac{1}{\tau_{\mathrm{pol}}} \approx \frac{1}{2}\left\langle \left| \frac{\partial \vec{n}}{\partial \delta} \right| \frac{d(\delta^2)}{dt} \right\rangle_{\theta}, \tag{5.8}$$

where δ is the relative energy spread, $\partial\vec{n}/\partial\delta$ describes the change in the $\vec{n}$ direction with energy, and $d(\delta^2)/dt$ is the diffusion rate of the beam energy spread. Averaging inside the angular brackets is done over the accelerator azimuthal angle θ and, in general, over the beam phase space. In case of the hadron beam, the above equation describes the polarization lifetime due to the energy diffusion caused by the longitudinal IBS and electron cooling. One can write similar expressions for the polarization lifetime due to the transverse IBS and cooling rates and space charge.

The phase space diffusion rates are obtained using the appropriate analytic expressions with a specific linear optics design and design beam parameters. The sensitivity of $\vec{n}$ to changes in energy $\partial\vec{n}/\partial\delta$ and in other phase space coordinates can also be obtained to first order from the linear optics design. However, in complicated cases involving multiple Siberian snakes and spin rotators, it may be more efficient to obtain the derivatives of $\vec{n}$ with respect to the coordinates of interest by spin tracking.

The procedure for obtaining, e.g. $\partial\vec{n}/\partial\delta$, is the following. A set of particles with orthogonal spins is launched along the on-momentum closed orbit. The particles in the set have $\delta = \Delta p/p$ relative momentum offset. If a dispersion is present at the launch point the particles also have non-zero transverse coordinates, which can be described by the action J_δ and phase Φ_δ variables. J_δ and Φ_δ depend on δ and the dispersion value and slope. Therefore, they can in general be changing along the ring. The goal is to obtain

$$\frac{\partial\vec{n}}{\partial\delta} \approx \frac{\vec{n}(J_\delta, \Phi_\delta, \delta) - \vec{n}_0}{\delta} \tag{5.9}$$

at every element along the ring.

As the particles undergo transverse oscillations, their phase evolves and one can build up a multi-turn spin transfer matrix as

$$R(\vec{\Phi}_0, \vec{\Phi}_i) = \begin{pmatrix} s^i_{1x} & s^i_{2x} & s^i_{3x} \\ s^i_{1y} & s^i_{2y} & s^i_{3y} \\ s^i_{1z} & s^i_{2z} & s^i_{3z} \end{pmatrix}, \tag{5.10}$$

where i is the turn number and s^n_{jk} is the kth spin coordinate of the jth particle. The particles are tracked for a sufficiently large number of turns N. The spin direction at the initial phase-space coordinate $\vec{\Phi}_0$ can be obtained as

$$\vec{n}(\vec{\Phi}_0) \approx \frac{\vec{n}_{ave}}{|\vec{n}_{ave}|}, \qquad \vec{n}_{ave} = \frac{1}{N+1}\sum_{i=0}^{N} R^{-1}(\vec{\Phi}_0, \vec{\Phi}_i)\tilde{n}(\vec{\Phi}_i), \tag{5.11}$$

where $\tilde{n}(\vec{\Phi}_i)$ is the initial guess for the stable spin direction. It can be chosen as the periodic spin direction on the closed orbit, $\vec{n}_0$, which is straightforward to find using, e.g., a single-turn spin transfer matrix for the closed orbit. This procedure is called a stroboscopic averaging and has been extensively studied and validated in the past.

It is challenging to simulate the polarization lifetime directly. It requires accurate implementation of the depolarizing processes and is computationally demanding. Therefore, we validate our implementation of the above procedure by applying it to the EIC electron ring and comparing its results to the $\partial\vec{n}/\partial\delta$ and polarization lifetime calculations available from other verified codes such SLICK, SITROS, and more recently B-MAD. Figure 5.11 compares our Zgoubi simulation results for $\partial\vec{n}/\partial\delta$ to a SLICK calculation for the same lattice. The Zgoubi simulation used $N = 1000$ and $\delta = 10^{-5}$. Note the logarithmic vertical scale and the fact that the difference occurs at small values of $|\partial\vec{n}/\partial\delta|$.

The difference between the two calculations in Fig. 5.11 may originate from two reasons. The orbital motion in Zgoubi is non-linear while SLICK considers linearized motion. The ring lattice contains strong solenoids that are used to rotate the electron spin. The solenoid models are treated differently in Zgoubi and SLICK. Zgoubi uses a solenoid field model with extending fringe fields while SLICK uses a hard-edge solenoid model. It appears that Zgoubi calculations depend on a

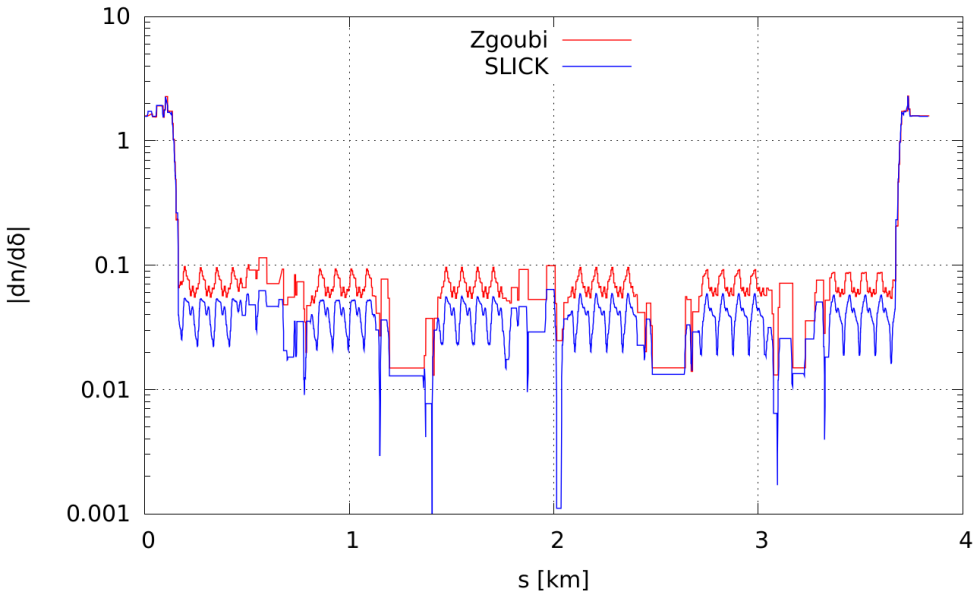

Figure 5.11: Comparison of the $|\partial\vec{n}/\partial\delta|$ calculations using Zgoubi and SLICK.

particular choice of the solenoid parameters. The polarization lifetimes calculated using Zgoubi and SLICK are 203 and 200 min, respectively. Even with the above differences, these numbers are still in a good agreement and the approach described above can be used for estimating the impact of stochastic effects on the electron and hadron polarization lifetimes.

The effects of crabbing on polarization spread

The transverse kick a particle receives when passing through a crabbing cavity depends on the particle's timing. Therefore, particles with different longitudinal positions along a bunch experience different fields, which results in different spin rotations correlated with the distance along the bunch. Assuming that the crabbing kick is closed and there are no bending dipoles in the crabbing section, the net vertical spin rotation per pass is given by

$$\Psi_{crab} = \frac{1+G}{\gamma\beta}\int_C \hat{E}_x dz, \tag{5.12}$$

where G is the anomalous part of the gyromagnetic ratio and $\hat{E}_x$ is the electric field normalized to the magnetic rigidity.

When the betatron phase advance between the rear and forward crab cavities is $\Delta\mu_{crab} = 2\pi k$,

$$\Psi_{crab} = 0. \tag{5.13}$$

The phase advance of $\Delta\mu_{crab} = \pi(2k+1)$ results in an rms spread of the vertical spin rotation of

$$\Psi_{crab} = \frac{1+G}{\gamma\beta}\frac{\sigma_z}{\sqrt{\beta_{crab}\beta_{IP}}}\tan\phi_{crab}, \tag{5.14}$$

where σ_z is the rms bunch length, β_{crab} and β_{IP} are the horizontal β function values at the crab cavity and IP, and ϕ_{crab} is a half of the beam crossing angle. For typical EIC parameters, this spread has a numerical value of the order of 10^{-6} rad and can be neglected.

Analysis of the case when the crabbing kick is not close requires calculation of the spin response functions at the crab cavity locations to account for contribution of the ring to the spread of the spin rotation.

In the presence of bending dipoles in the crabbing section, all spin rotations occur about the vertical axis. Therefore, dipoles do not change the combined spin effect of the crab cavities as long as one can ignore the longitudinal dynamics. However, dipoles may change the longitudinal positions of the different momentum particles in the bunch. This may result in an incomplete cancellation of the crabbing kick and transverse to longitudinal coupling that requires specific analysis of both beam and spin dynamics.

Another potential polarization effect of the crab cavities is a spin spread at the IP. The combined spin effect of the crabbing electric and magnetic fields is given by

$$\Psi_{crab} = \gamma G \Delta x', \tag{5.15}$$

where $\Delta x'$ is the net change of a particle's horizontal angle to the observation point. When a bunch initially exists the first set of the crab cavities, it has a correlated spread of the horizontal angles given by

$$\Delta x' = \frac{\sigma_z}{\sqrt{\beta_{crab}\beta_{IP}}} \tan\phi_{crab}, \tag{5.16}$$

Thus, there is a spin spread just after the cavities. However, considering only this correlated component of the betatron motion, the rms spin spread at the IP is

$$\Psi_{crab} = \gamma G R_{22} \Delta x' = \gamma G \frac{\sigma_z}{\beta_{IP}} \cos\Delta\mu \tan\phi_{crab} \approx \gamma G \frac{\sigma_z}{\beta_{IP}} \left(\frac{\pi}{2} - \Delta\mu\right) \tan\phi_{crab}, \tag{5.17}$$

Assuming typical EIC parameters and a betatron phase offset of 1°, this effect is of the order of 10^{-2} rad.

Summary

The AGS currently delivers 65% polarization with 3×10^{11} protons per bunch, while RHIC delivers 60% polarization in collisions at 250 GeV with 1.8×10^{11} protons per bunch [**?**].

The additional gains necessary to increase the EIC polarization will come in three ways. First, a skew quadrupole compensation scheme in the AGS will reduce polarization losses there. Second, hadron cooling at injection will reduce the depolarizing resonance strengths. Third, six snakes will preserve polarization through acceleration.

Simulation results show that the space charge effect does not pose a major threat to the polarization lifetime at lower energies – injection at 25 GeV injection and collisions at 41 GeV.

HSR spin rotators near IP6 are moved from their RHIC Yellow ring locations, providing longitudinal polarization at the experimental detector.

Simulation tools for polarization lifetime due to IBS and cooling section have been developed, and detailed simulations are underway.

5.2.2 Helium-3

The EIC is able to use polarized beams of ^{3}He and deuterium ions. The gyromagnetic factor of ^{3}He is $G = -4.18$, about twice as large as for the proton, so only a fraction of the available Siberian Snake magnetic field strength is needed. However, the depolarizing resonances crossed during acceleration are stronger and denser, also due to the larger $|G|$ value. In addition, the overlap of imperfection resonances due to closed orbit distortions and intrinsic resonances excites even order snake resonances, which otherwise do not occur in a dual-snake configuration. Other sources for even-order snake resonances include errors in the snake settings. The overlap of an intrinsic resonance with an imperfection resonance also splits the existing odd-order resonances.

Booster and Alternating Gradient Synchrotron

Polarized ^{3}He is injected into the Booster from EBIS at $|G\gamma| = 4.193$. There are two partial snakes in the AGS, separated by 1/3 of the ring, so the stable spin direction is closest to vertical in every three units of $|G\gamma|$. Values of 4.5, 7.5 and 10.5 are therefore natural for extraction from the Booster. Optical distortions at AGS injection with the partial snakes on are stronger for smaller $G\gamma$ or $B\rho$ values, so extraction at $|G\gamma| = 10.5$ is preferred. with $B\rho = 10.78$ Tm.

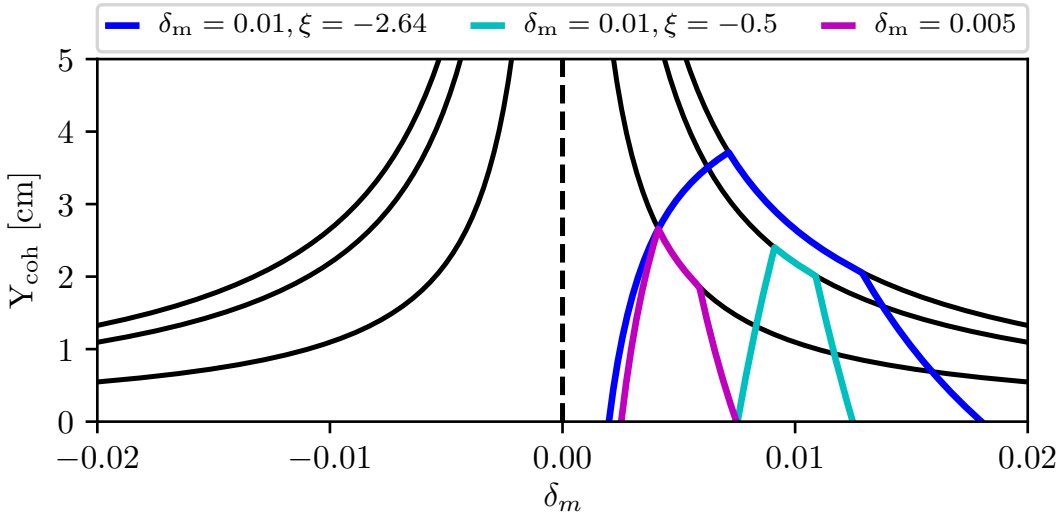

Figure 5.12: The coherent amplitude of the driven AC dipole oscillations at different δ_m and chromaticity values. The tune separation δ_m is preferred to be large and chromaticity is preferred to be near zero, in order to maintain the same coherent amplitude across the energy spread of the whole beam.

Polarized ^{3}He crosses two intrinsic resonances in the Booster, $|G\gamma| = 12 - \nu_y$ and $|G\gamma| = 6 + \nu_y$, as well as 6 imperfection resonances, $|G\gamma|$= 5, 6, 7, 8, 9, and 10. To overcome the intrinsic resonances, Simulations show that there is sufficient corrector strength to correct or enhance the imperfection resonances up to $|G\gamma| = 10$.

An AC dipole in the Booster mitigates the intrinsic resonance crossings by inducing 100% spin-flips [**?**, **?**, **?**]. It is 0.5 m long with a maximum strength of $B_m l = 0.0025$ Tm and a frequency of

$f_m = 250$ kHz [**?**,**?**]. With a nominal resonance proximity parameter of $\delta_m = 0.01$, the corresponding AC dipole driving tunes for the $|G\gamma| = 12 - \nu_y$ and $|G\gamma| = 6 + \nu_y$ resonances are $\nu_m = 0.199$ and $\nu_m = 0.177$, respectively. Because of the low injection energy and the large frequency sweep, ν_m for helions crossing $|G\gamma| = 12 - \nu_y$ can change by as much as 0.003. Due to this large variability and the natural vertical chromaticity, these parameters must be precisely controlled, as shown in Figure 5.12 [**?**].

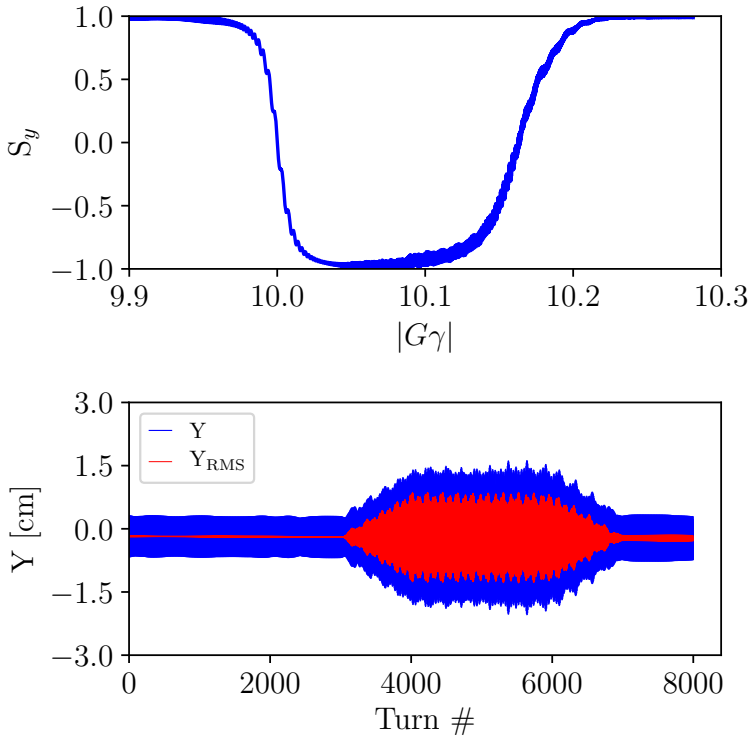

Figure 5.13: Booster acceleration simulation with 1,000 polarized ^{3}He particles crossing the $|G\gamma| = 10$ and $|G\gamma| = 6 + \nu_y$ resonances, with 100% transmission efficiency. The $|G\gamma|$=10 imperfection resonance is enhanced by dipole correctors to induce a full spin flip, and the intrinsic resonance at $|G\gamma| = 6 + \nu_y$ is enhanced by an AC dipole strength of $B_m l = 0.00141$ Tm to induce a full spin flip.

Simulations show that all 6 Booster imperfection resonances can be crossed while staying under the 25 A limit of the dipole corrector power supplies [**?**]. If necessary, stronger dipole corrector power supplies and magnets will be installed. Figure 5.13 shows that polarization is preserved through one imperfection resonance by orbit correctors and one intrinsic resonance by AC dipole.

The Booster to AGS transport line supports a maximum rigidity of $B\rho = 9.5$ Tm, limited mainly by the pulsed kicker power supplies, although Booster fast extraction bumps can be configured to provide some relief. Similarly, only two of the six Booster main magnet power supply stations are capable of exceeding a current corresponding to $B\rho = 9.5$ Tm, meaning the ramp rate will be slowed to a third of normal. The slower ramp rate does not compromise polarization preservation, because all the imperfection resonances are compensated and the AC dipole overcomes the two intrinsic resonances.

The vertical tunes in the AGS at injection are kept below the half integer, with $\nu_y < 4.1$, to avoid the $|G\gamma| = 0 + \nu_y$ resonance. AGS partial snakes can generate a total of ~40% relative strength, making it possible to push both betatron tunes into the spin tune gap so both vertical and horizontal intrinsic resonances and imperfection resonances are avoided. Polarization preservation through the AGS acceleration ramp is shown in Figure 5.14.

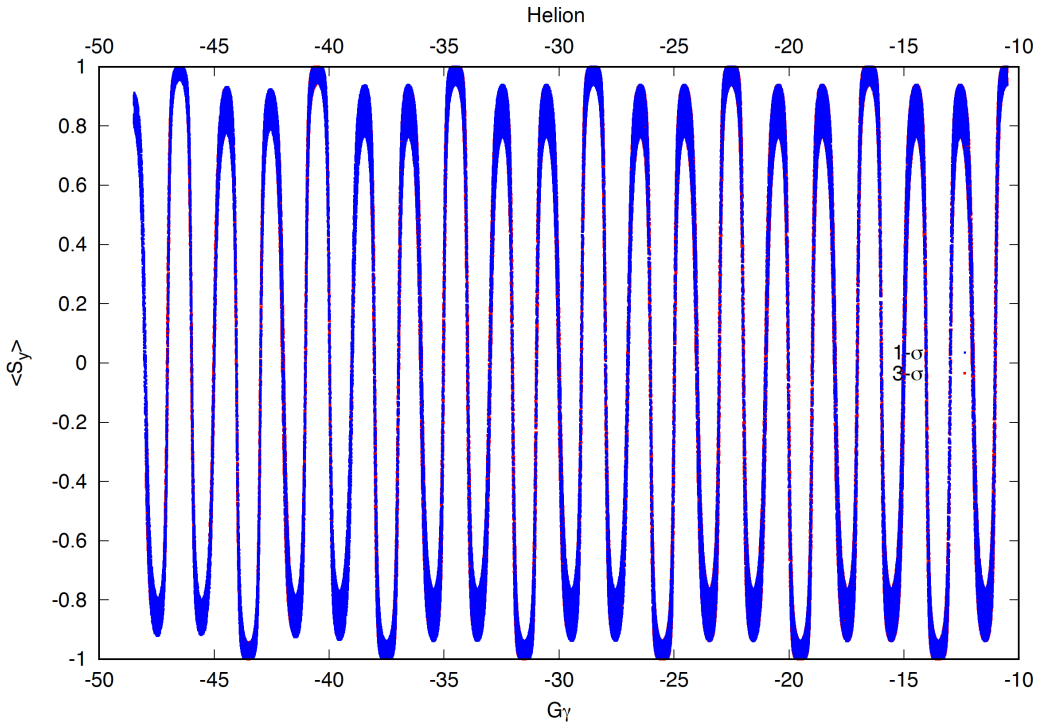

Figure 5.14: Tracking results of 8 polarized ^{3}He particles on each of the two emittance ellipses (σ=2.5 µm and 3σ=7.5 µm) through the $|G\gamma|$ range of 10.5 and 48.5. The two partial snakes were set as 25% and 14%, while ν_x and ν_y were set at 8.95 and 8.98, respectively. Both betatron tunes are inside the spin tune gap. Note that due to negative G value, the acceleration goes from right to left when energy increases.

Polarized ^{3}He in HAR and HSR

RHIC polarized proton transmission efficiency with two snakes is about 92% with a vertical emittance of 2.5 µm, equivalent to a depolarizing resonance strength of 0.225. Figure 5.15 shows the ^{3}He intrinsic resonance spectrum in RHIC, calculated using DEPOL [**?**]. In contrast a cooled ^{3}He vertical emittance of 0.75 µm leads to an intrinsic resonance strength is 0.3, larger than the strongest strength in RHIC. More snakes are therefore necessary to preserve ^{3}He polarization. The number of snake pairs should be an odd number, so the EIC accelerator has 6 snakes.

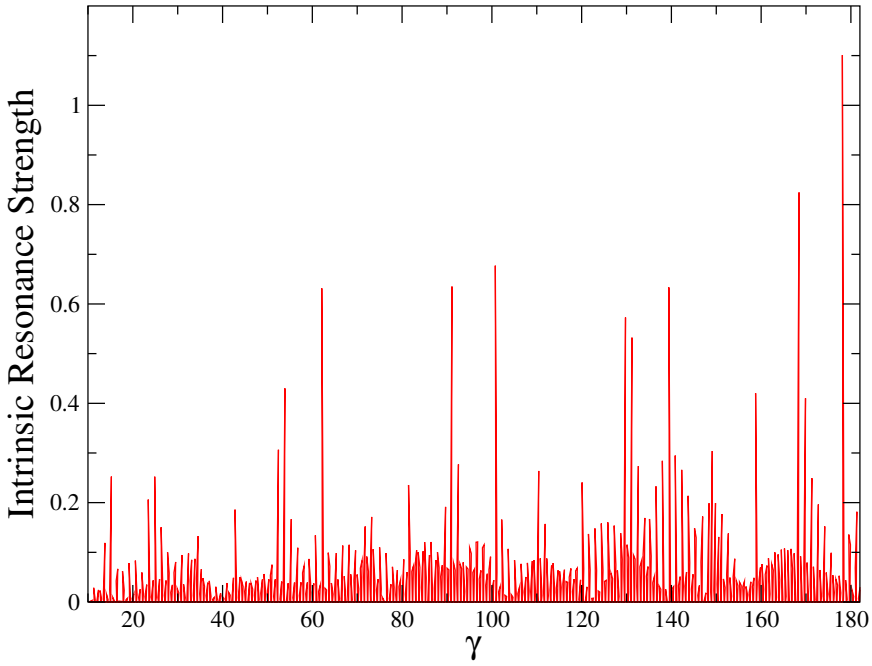

Figure 5.15: The intrinsic depolarizing resonance strengths in hadron ring of EIC for ^{3}He as a function of the Lorentz factor γ for a particle on a 10 µm action ellipse.

Figure 5.16 shows 2-snake spin tracking results from Zgoubi [**?**], accelerating ^{3}He ions from $G\gamma = -690$ to -790 and crossing the strongest intrinsic resonance at $|G\gamma| = 717 + \nu_y$. Eight particles with the same betatron amplitude were tracked with a perfect closed orbit and zero momentum offset. The results show that the 2-snake configuration maintains polarization for a 0.75 µm emittance, but not for 3×0.75 µm and 6×0.75 µm emittances. In contrast, Figure 5.17 shows that the 6-snake configuration maintains polarization through the strongest resonances between $\gamma = 168$ and 178.

These preliminary simulations show that the 6-snake configuration preserves ^{3}He polarization on the ramp up to a top energy of 183 GeV. More detailed spin tracking will be performed to determine the tolerance to orbit errors and momentum spread.

Due to the larger G of helions, essentially all snake axis angles can be realized as seen in Figure 5.18. This figure shows the full spin-flip rojection in white with the achievable axis angle for right-handed helcity (left) and left-handed helicity (right).

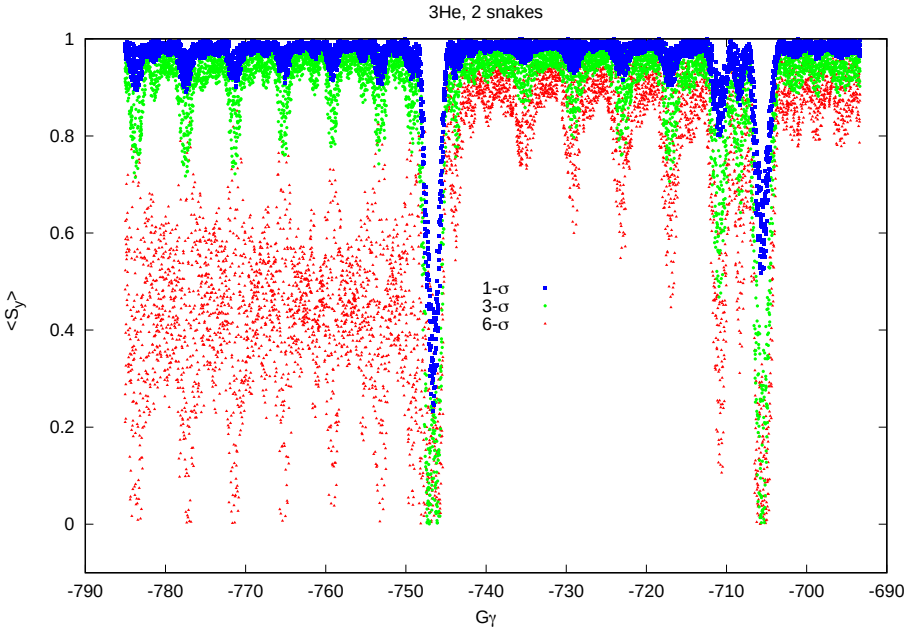

Figure 5.16: Zgoubi acceleration simulation results with a 2-snake configuration and with various beam emittances ($\epsilon_y = 1,\ 3,\ 6\sigma$, with σ =0.75 µm), crossing intrinsic resonance at $|G\gamma| = 717 + \nu_y$ ($\gamma \approx 178$) and $|G\gamma| = 735 - \nu_y$ ($\gamma \approx 168$). Acceleration goes from right to left, because G is negative.

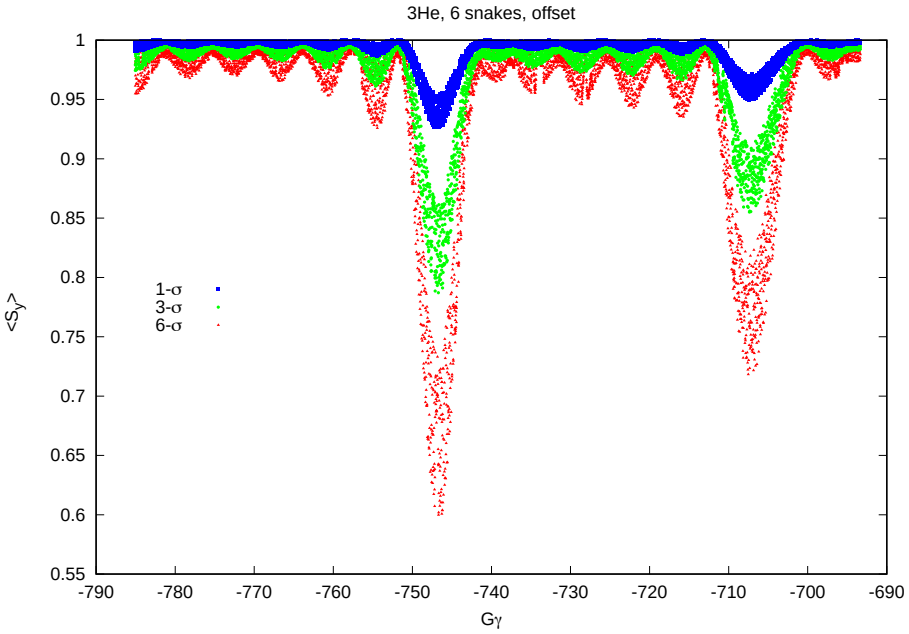

Figure 5.17: Zgoubi simulation results with a 6-snake configuration with one pair offset, and with various beam emittances ($\epsilon_y = 1,\ 3,\ 6\sigma$, with σ =0.75 µm), for intrinsic resonances at $|G\gamma| = 717 + \nu_y$ and $|G\gamma| = 735 - \nu_y$. Acceleration goes from right to left.

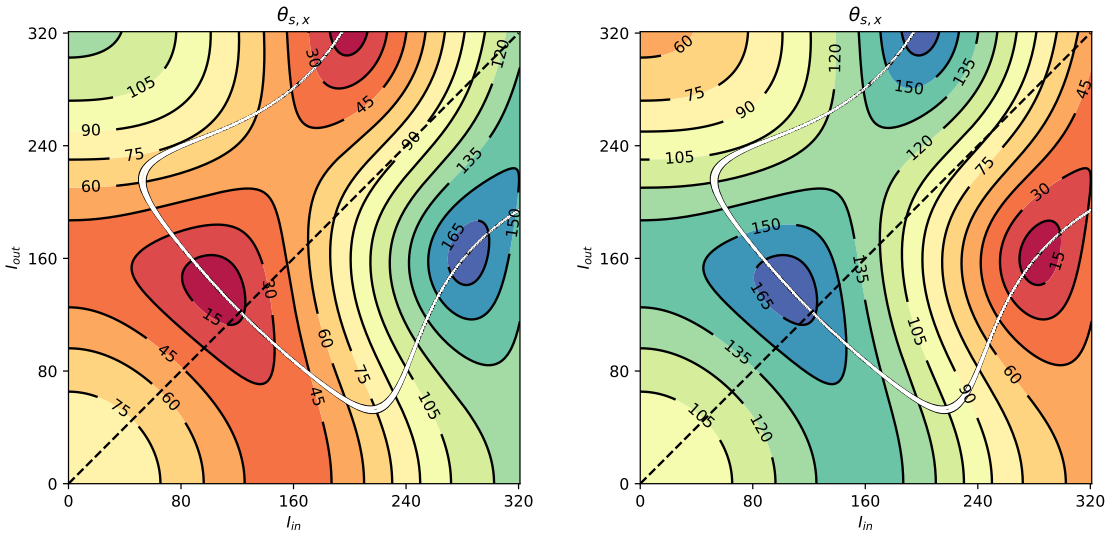

Figure 5.18: Achievable helion snake precession axes for helions in snakes with right helicity (left) and left helicity (right) magnet coils as a function of inner and outer power supply current. The white line corresponds to a full spin-flip, and the dashed line represents currents that provide a symmetric orbit.

^{3}He Polarization Lifetime

The 2-snake HSR configuration works for polarization preservation during proton stores, but it needs development for ^{3}He with stronger resonances. Store energies are usually far from strong intrinsic resonances, but there are nearby weak intrinsic and imperfect resonances. These overlapping resonances are one source of polarization loss [**?**]. A recently developed lattice independent spin tracking method delivers simulation results that are in reasonably good agreement with RHIC proton operation when the beam-beam effect is not strong, without introducing strong imperfection resonances [**?**].

Two simulation efforts on ^{3}He polarization preservation in a 2-snake configuration are continuing in parallel. One effort, which includes beam-beam force interactions over a shorter time frame of less than a minute, is still under development. The other, without beam-beam, tracks for a longer time frame on the order of one hour. Figure 5.19 shows preliminary simulation results from the second method for an imperfection resonance strength of 0.07 near top energy corresponding to $|G\gamma| = 820$. The most promising tune ranges are below 29.25. The polarization decay rate is around 5%/hr with the vertical emittance as 0.75 µm. The imperfection resonance strengths near top energy vary between 0.02 and 0.08 for an rms closed orbit error of 0.5 mm. Choosing a region with a strength around 0.025, the polarization decay rate is a fraction of 5%/hr. However, the beam-beam interaction generates a large betatron tune footprint, shortening the polarization lifetime.

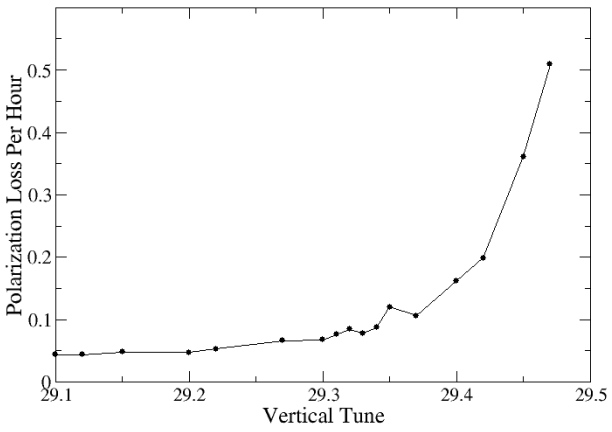

Figure 5.19: Polarization decay rate versus vertical tunes with emittance as 0.75 µm for ^{3}He with imperfection of 0.07 strength, with beam-beam turned on and a 2-snake configuration. A value of 0.1 on the vertical axis indicates a loss rate of 10%/hr.

Polarization loss rates observed in 2015 RHIC operations in three different scenarios showed significant beam-beam effects. The loss rate with pp collisions was much worse than for p-Al and p-Au collisions, with the same proton bunch intensity but with weaker beam-beam tune shift parameters. Beam-beam parameters in HSR are stronger, so more snakes probably are necessary for good polarized ^{3}He lifetime. More studies of a polarization lifetime model with beam-beam are planned.

5.2.3 Deuterons

The gyromagnetic factor of the deuteron is quite small, $G = -0.14$, so the present Siberian Snakes are too weak even to be used as efficient partial snakes. On the other hand the number of spin

resonances encountered by the deuteron beam during acceleration is significantly smaller, and the strength of those resonances is smaller than for protons or for ^{3}He ions. The feasibility of accelerating polarized deuteron beam was previously studied [**?**, **?**]. Further recent studies explored the acceleration of a polarized deuteron beam, using realistic ramp rate and beam emittance parameters that were used for unpolarized deuteron beam in RHIC [**?**].

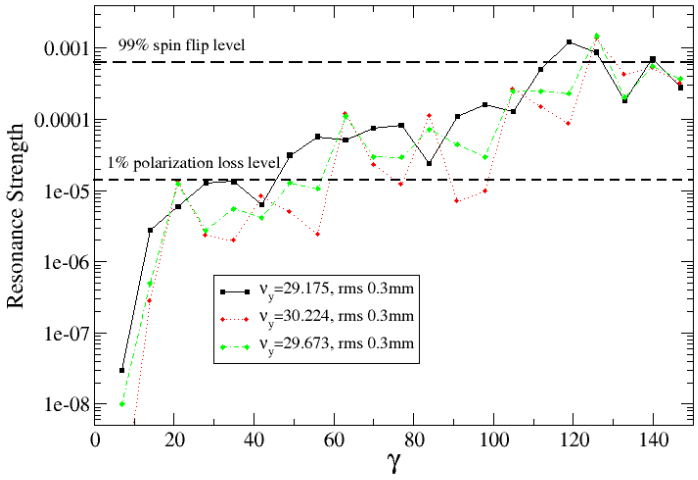

Figure 5.20: Imperfection resonance strengths for three ion ring lattices, including strength levels corresponding to 99% spin flip and 1% polarization loss.

Resonance strengths for various lattices are calculated with closed orbit RMS values of 0.3 mm, and transverse emittances of 2 µm, as shown in Figures 5.20 and 5.21. A partial snake with a 15 Tm solenoid – the same strength as the experimental detector solenoid at IP6 – takes care of all imperfection resonances. A 5.6 Tm solenoid is part of the second detector design that is under consideration for IP8. The more complicated two detector scenario has also been analyzed. Although the total partial snake strengths are modulated as a function of energy, they are sufficient to overcome the imperfection resonances.

With detector solenoids as partial snakes, the spin is in the longitudinal direction at deuteron energies corresponding to an integer spin tune. In the case of one detector this happens at every integer spin tune, but with two detectors the spin tune must be a multiple of 3. The induced resonance strength must be larger than the spin tune spread due to momentum spread, in order for all particles to maintain a longitudinal spin. The solenoidal field alone cannot do this, but the induced resonance strength is made strong enough by introducing orbit harmonics of a few mm at energies corresponding to an integer spin tune.

A 50-turn tune jump system with an amplitude of 0.03, similar to the AGS system, maintains polarization over the whole energy range. This amplitude takes into account the large spin tune spread at higher $|G\gamma|$ values. Figure 5.22 shows the polarization remaining after crossing each intrinsic resonance with a nominal ramp rate, a vertical emittance of 2 µm, and with a modest tune jump amplitude that is sufficient except for the $|G\gamma| = \nu_y - 12$ resonance, which is overcome without firing the tune jump quads. The resonance strength is reduced by about 40% when the deuteron beam emittance is cooled to 0.75 µm, providing additional margin to the tune jump system.

In summary, polarized deuteron beams are feasible in the EIC. Longitudinal polarization is achieved at discrete energies when the spin tune is an integer. A modest tune jump system is in-

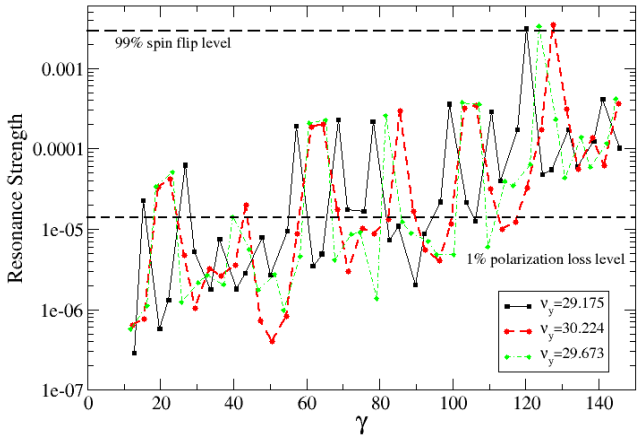

Figure 5.21: Intrinsic resonance strength for three ion ring lattices, including strength levels corresponding to 99% spin flip and 1% polarization loss.

cluded. Simulation studies to explore details of the deuteron polarization preservation and control are planned.

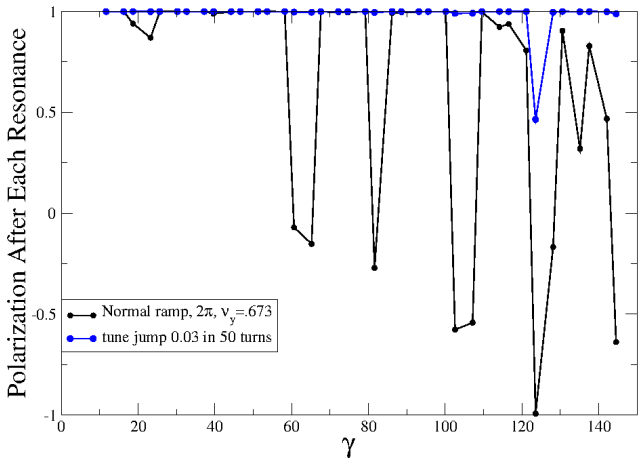

Figure 5.22: Deuteron polarization after crossing each intrinsic resonance during acceleration at a nominal ramp rate and with a modest tune jump.

5.3 Rapid Cycling Synchrotron and Electron Injectors

5.3.1 Intrinsic resonance free design

Several types of depolarizing spin resonances are encountered when polarized electrons are accelerated. The most important are the intrinsic spin resonances and the imperfection spin resonances. Both are due to coherent transverse spin kicks that occur primarily in the quadrupole fields of the lattice. Intrinsic spin resonances arise from vertical betatron oscillations, while imperfection spin resonances are due to vertical closed orbit distortions.

In a typical circular lattice where the field is dominated by the guide dipole field, the rate of spin precession per turn, or spin tune ν_s, is determined by the energy and conveniently expressed as $a\gamma$, where

$$a = \frac{g-2}{2} = 0.001159 \tag{5.18}$$

is the anomalous magnetic moment coefficient for an electron, and γ is the relativistic factor. Depolarizing intrinsic spin resonances occur whenever the spin tune

$$a\gamma = nP \pm Q_y \tag{5.19}$$

where n is an arbitrary integer, P is the periodicity of the lattice, and Q_y is the vertical betatron tune.

Thus the first two important intrinsic spin resonances that an accelerating electron will encounter occur at

$$\begin{aligned} a\gamma &= Q_y \\ a\gamma &= P - Q_y \qquad \text{for } P > Q_y \end{aligned} \tag{5.20}$$

If both Q_y and $P - Q_y$ are greater than the maximum $a\gamma$ value, (or Q_y is greater and $P - Q_y$ is less than the lowest $a\gamma$ value), then all the important intrinsic spin depolarizing resonances are avoided.

The spin tune $a\gamma$ increases from 1.702 to 41 in the RCS energy range from 750 MeV to 18 GeV. This sets a lower limit on the vertical tune

$$Q_y > 41 \tag{5.21}$$

Minimizing the periodicity P while also keeping the phase advance per cell not much greater that 120 degrees (to maintain good dynamic aperture performance) keeps the lattice compact, with a limit

$$Q_y/P < 1/3 \tag{5.22}$$

Taken together, these limits require a minimum periodicity of

$$P > 41 \times 3 = 123 \tag{5.23}$$

A side benefit of such a lattice is that imperfection resonances are also minimized, as well as intrinsic resonances, because the strongest imperfection resonances occur at

$$a\gamma = nP \pm Q_y \tag{5.24}$$

Weak imperfection resonances constrain the RMS vertical orbit displacement to be less than 0.4 mm.

5.3.2 Weak imperfection resonances

Although such a design ensures that there are no strong intrinsic or imperfection spin resonances in the RCS energy range, nonetheless weak imperfection spin resonances remain. The cumulative effect of these resonances has the potential to depolarize the beam during an 18 GeV acceleration cycle.

Studies show that the response to weak imperfections scales with the vertical tune and the periodicity, for a fixed level of quadrupole misalignment – the higher the tune and the number of arc FODO cells, the better the polarization response. This is illustrated by considering a simple FODO lattice. Using a thin lens approximation [**?**], the imperfection resonance strengths are given by

$$\begin{aligned} \epsilon_K &= \frac{1+a\gamma}{2\pi} \sum_{k=-\infty}^{\infty} \frac{Q_y^2 f_k}{Q_y^2 - k^2} e^{i\frac{S_p-1}{S_p}(k+K)\pi} \quad En_{S_p}\left(\frac{k+K}{S_p}\right) \times \\ &\left(En_M \left(\frac{K + k\frac{Q_{yarc}}{Q_y}}{MS_p} \right) \left[g_D \beta_y^{1/2}(D) - g_F \beta_y^{1/2}(F) e^{-i\left(K + k\frac{Q_{yarc}}{Q_y}\right)\pi/MS_p} \right] + X_I \right) \end{aligned} \tag{5.25}$$

where the enhancement function is

$$En_N(x) = \frac{\sin(N\pi x)}{\sin(\pi x)} \tag{5.26}$$

Here $g_{D,F}$ is the integrated quad gradient $k_1 L$, M is the number of FODO cells, S_p is the super-periodicity, Q_{yarc} is the total arc tune, and X_I the contribution from the insertion straights.

A further approximation is enabled by considering that the largest contribution of the k sum occurs when

$$k = [Q_y] \tag{5.27}$$

where [] represents rounding to nearest integer, and also that the vertical phase advance in each of the two straight sections is limited to a total of 4π. In this case

$$Q_{yarc} = Q_y - 4 \tag{5.28}$$

and the super-periodicity becomes 1, so that the contribution from X_I vanishes.

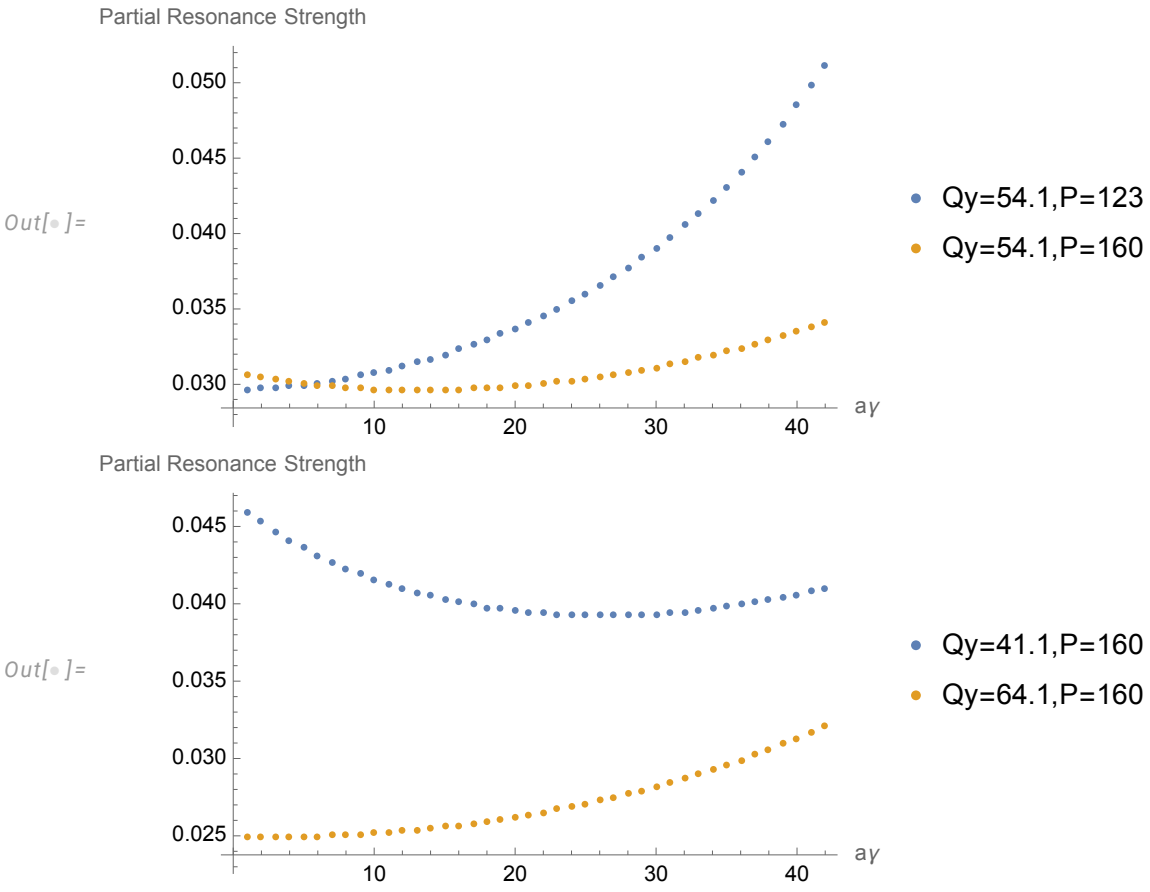

Figure 5.23: The dependence of imperfection spin resonance strengths in the RCS on periodicity P and vertical arc tune Q_{yarc}.

Further, ignoring the constant factors of $a\gamma$ and f_k in front of the expression yields the estimate

$$\begin{aligned}\epsilon_K &= \frac{Q_y^2}{Q_y^2-[Q_y]^2}\; e^{i\frac{S_p-1}{S_p}([Q_y]+K)\pi}\quad En_{S_p}\left(\frac{[Q_y]+K}{S_p}\right)\times \\ & En_M\left(\frac{K+[Q_y]\frac{Q_y-4}{Q_y}}{MS_p}\right)\left[g_D\beta_y^{1/2}(D)-g_F\beta_y^{1/2}(F)e^{-i\left(K+[Q_y]\frac{Q_y-4}{Q_y}\right)\pi/MS_p}\right]\end{aligned} \tag{5.29}$$

Using values such as

$$\begin{aligned} g_D\beta_y^{1/2}(D) &= 1.25\ \left[\mathrm{m}^{-1/2}\right] \\ g_F\beta_y^{1/2}(F) &= 0.43\ \left[\mathrm{m}^{-1/2}\right]\end{aligned} \tag{5.30}$$

that are appropriate for each RCS lattice enables the effect of changes to periodicity and tune on the strength of the imperfection spin resonance to be studied, as shown in Figure 5.23.

A periodicity of $P = 160$ is chosen for the RCS lattice, based on these considerations and dynamic aperture performance, constraining the integer part of the vertical arc betatron tune to be 52. In consequence the two first intrinsic resonances occur near $a\gamma$ values of 52 and 160-52=108.

5.3.3 Straight section design

Two long straight sections in the racetrack layout of the RCS accommodate cryomodules for the SRF system, and perform injection and extraction. Unfortunately these straight sections nominally reduce the high periodicity of the lattice to $P = 2$, and re-introduce a slew of intrinsic and strong imperfection spin resonances across the spin tune range. However, the straight section quadrupoles don't contribute to any of the offending spin resonances if the vertical phase advance in each straight is

$$\Delta\mu_y = N\ 2\pi \tag{5.31}$$

where N is an integer [**?**]. A straight phase advance of 4π works well with the chosen arc optics and required straight section lengths. Fairly large deviations from this condition can be tolerated in practice, due to the high acceleration rate and vertical emittance damping at high energies. Deviations as large as 3 degrees can be tolerated while maintaining over 99% polarization transmission with RMS normalized vertical emittances as large as 500 µm – much larger than the nominal value.

RMS bend & quad roll	**RMS quad misalignment**	**Average RMS orbit**	**Average max. orbit**	**Polarization efficiency at 10 GeV**	**Polarization at 10 GeV**
mrad	mm	mm	mm	%	%
0.4	0.10	3.56	10.27	97	85
0.4	0.15	4.40	13.27	94	83
0.4	0.20	4.80	15.50	90	79

Table 5.1: Simulated orbit and polarization data at 10 GeV extraction using 100 random seeds.

5.3.4 Correction of imperfection spin resonances

Although there are no significant intrinsic spin resonances across the RCS energy range, nonetheless imperfection spin resonances have the potential to depolarize the beam. Modest orbit smoothing is sufficient to achieve the goal of 97% polarization transmission up to an energy of 10 GeV, as illustrated in Table 5.1. For example, without any orbit smoothing we can already tolerate 0.1 mm RMS quadrupole misalignments and 0.4 mm-rad rolls and still achieve 97% polarization transmission to 10 GeV. This can easily be raised to 99% transmission using Singular Value Decomposition (SVD) with RMS misalignments well above 0.2 mm RMS.

However, acceleration to 18 GeV makes it much more difficult to achieve 97% polarization transmission by relying just on conventional orbit smoothing. Table 5.2 shows that a polarization efficiency of only 95% can be achieved using plain orbit smoothing accelerating to 18 GeV with underlying quadrupole misalignments of 0.1 mm RMS and 0.1 mm-rad dipole rolls. This is much lower than the expected abilities to align magnets in the ring.

RMS bend & quad roll	**RMS quad misalignment**	**Average RMS orbit**	**Average max. orbit**	**Polarization efficiency at 18 GeV**	**Polarization at 18 GeV**
mrad	mm	mm	mm	%	%
Uncorrected					
0.01	0.01	0.44	1.25	96	84.48
0.015	0.015	0.708	1.95	91.5	80.52
0.02	0.02	0.848	2.50	85	75
Corrected					
0.2	0.2	0.55	1.5	81	71
0.1	0.1	0.24	0.64	95	83.6
0.1	0.05	0.056	0.15	98.6	86.7

Table 5.2: Simulated orbit and polarization data at 18 GeV extraction using 100 random seeds.

We should add that these estimates don't include other sources of errors (i.e. due to bpm misalignment, horizontal misalignments, quadrupole rolls and other field errors) so they are overly optimistic.

An orbit correction approach that accounts for the imperfection spin resonances is used, in which RCS tuning relies only on Beam Position Monitor (BPM) measurements. This is accomplished using the response matrix $\mathbf{M}_{rQm}$ that relates orbit measurements to magnet misalignments,

$$\mathbf{Y}_{orbit} = \mathbf{M}_{rQm}\,\mathbf{Q}_{\mathrm{mis}} \tag{5.32}$$

where $\mathbf{Y}_{orbit}$ is the measured vertical orbit, and $\mathbf{Q}_{\mathrm{mis}}$ is a vector of quadrupole vertical misalignments.

Once the misalignment errors are understood a good estimate of the imperfection spin resonances is calculated using the DEPOL algorithm [**?**]. Then another response matrix $\mathbf{M}_{rCW}$, which associates imperfection resonance strengths with dipole corrector settings, is used.

$$\mathbf{W}_{imp} = \mathbf{M}_{rCW}\,\mathbf{C} \tag{5.33}$$

Here $\mathbf{W}_{imp}$ is the vector of complex imperfection spin resonance strengths calculated by DEPOL [**?**], and **C** is a vector of vertical dipole corrector kicks. Such correction, together with ordinary orbit smoothing, controls both the orbit and reduces spin resonance strengths, as shown in Figure 5.24. This approach works well, with one BPM associated with every quadrupole, after using beam-based alignment to calibrate the BPMs.

Table 5.2 shows that an average transmission of almost 99% transmission is obtained with an RMS quad vertical misalignment of 50 µm, and RMS dipole rolls of 100 µrad. This drops to 95% transmission when the RMS vertical misalignment increases to 100 µm.

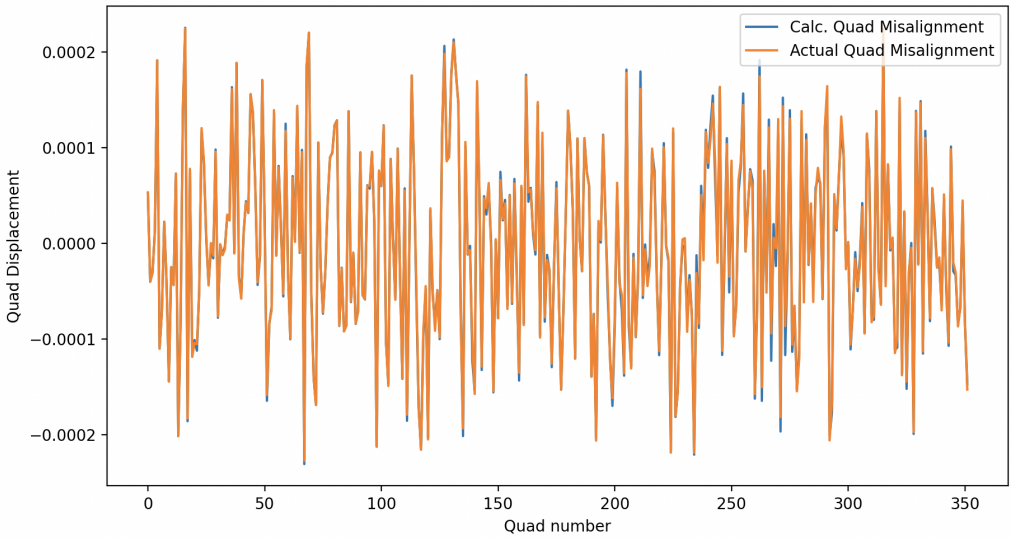

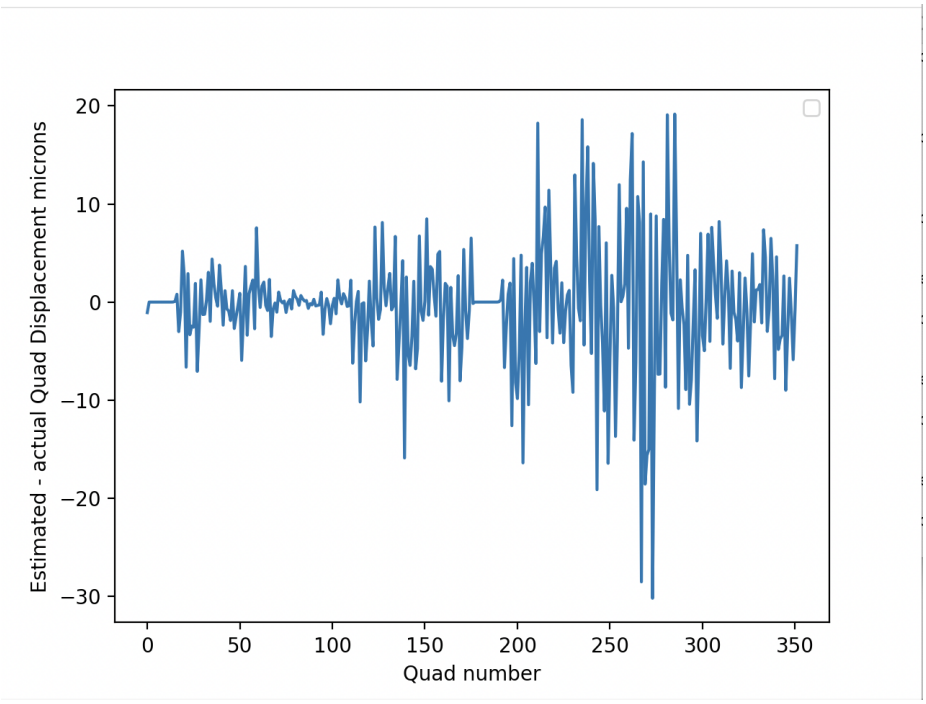

Figure 5.24: Fitting the vertical quadrupole misalignment using an orbit response matrix, in a misaligned and rolled RCS lattice that is corrected to achieve 99% polarization transmission. Top: For 100 µm RMS misalignment. Bottom: Difference between actual and fit imsalignments.

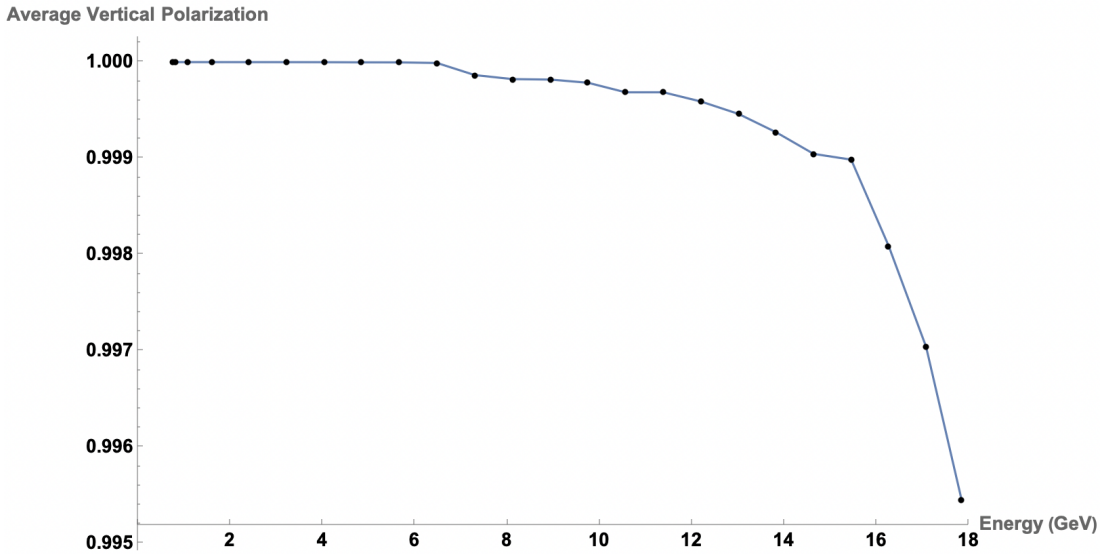

Figure 5.25: Polarization versus energy up to 18 GeV, with RMS vertical misalignment errors of 100 µm, and RMS rolls of 100 µrad. Uncorrected RMS vertical orbit distortions of 4.6 mm are reduced to 0.5 mm by orbital SVD correction and resonance correction

=======

Using this approach over 100 random seeds with 100 µm RMS quad vertical misalignment and 100 µrad dipole rolls we obtained an average of 99% transmission with 0.26 mm rms residual orbit distortion. Using 200 µm RMS quad vertical misalignment and 200 µrad dipole rolls, this dropped to an average of 96% transmission with 0.62 mm rms residual orbit distortion over 100 random seeds. The application of this correction approach was verified using direct spin-orbit tracking in BMAD [**?**] as shown in Figure 5.25. Here a misaligned and rolled RCS lattice was corrected using this method to achieve 99% polarization transmission for 30K particles.

The inclusion of random dipole rolls causes this approach to suffer, allowing the lattice to only tolerate up to 100 µrad of roll and vertical misalignment errors of 100 µm RMS. Going up to 200 µrad of roll and vertical misalignment errors of 200 µm drops our polarization transmission to below 96%. Realistically rolls are on the order of 400 µrad to 1 mrad. Thus this approach will require more development to disentangle the effects of quadrupole misalignment from dipole rolls. It will require building off of the so-called LOCO methods [**?**] or developing new promising machine learning approaches [**?**], [**?**].

Imperfection bumps

If the BPM-based orbit correction approach is insufficient to achieve 97% transmission, then an additional empirical polarimetry-based approach can be applied, using the internal Compton polarimeter that measures polarization continuously up the acceleration ramp. Measurements are non-destructive, and take approximately 5 minutes with one acceleration cycle per second. RMS ground motion is estimated to be between 0.1 and 1.0 µm, over a 5 minute interval [**?**]. This is significantly less than the RMS levels of 10 µm that are important to polarization loss up to 18 GeV.

The same corrector-to-imperfection matrix $\mathbf{M}_{rCW}$ is employed to build selective imperfection bumps that empirically suppress individual offending imperfection resonances. Figure 5.26 records a peak absolute imperfection resonance strength of 0.02, over all imperfection resonances, with an RMS quadrupole misalignment of 0.2 mm, and RMS dipole roll of 0.2 mrad.

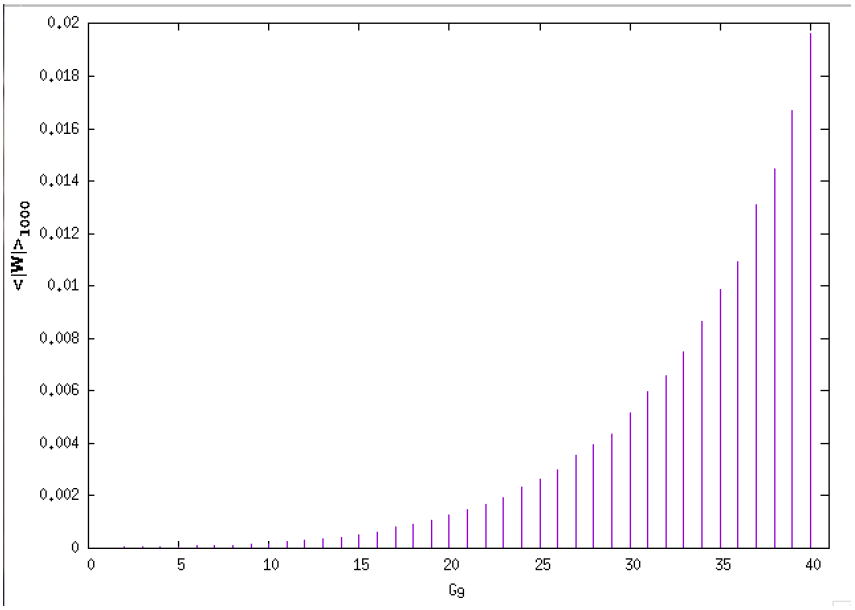

Figure 5.26: Average imperfection resonance strengths for an RMS quadrupole misalignment of 0.2 mm, and an RMS dipole roll of 0.2 mrad, over 1,000 random seeds

Figure 5.27 illustrates the use of imperfection bumps to cancel an imperfection resonance with a strength of 0.02, using dipole correctors with a maximum strength of 0.015 mrad, resulting in an RMS vertical orbit of 0.13 mm. This corrector strength is much smaller than the peak strength possible.

There are 38 imperfection resonances in the $a\gamma$ range from 2 to 40, becoming increasingly important above 22, so that 18 real and 18 imaginary imperfection bumps are required. An acceleration ramp time of 100 ms means that resonances are crossed every 2.63 ms, setting the required polarimetry measurement resolution time. There is no need to slew corrector settings during the ramp (as is common when using normal harmonic bumps), because the imperfection bumps occur naturally at the desired energy and phase.

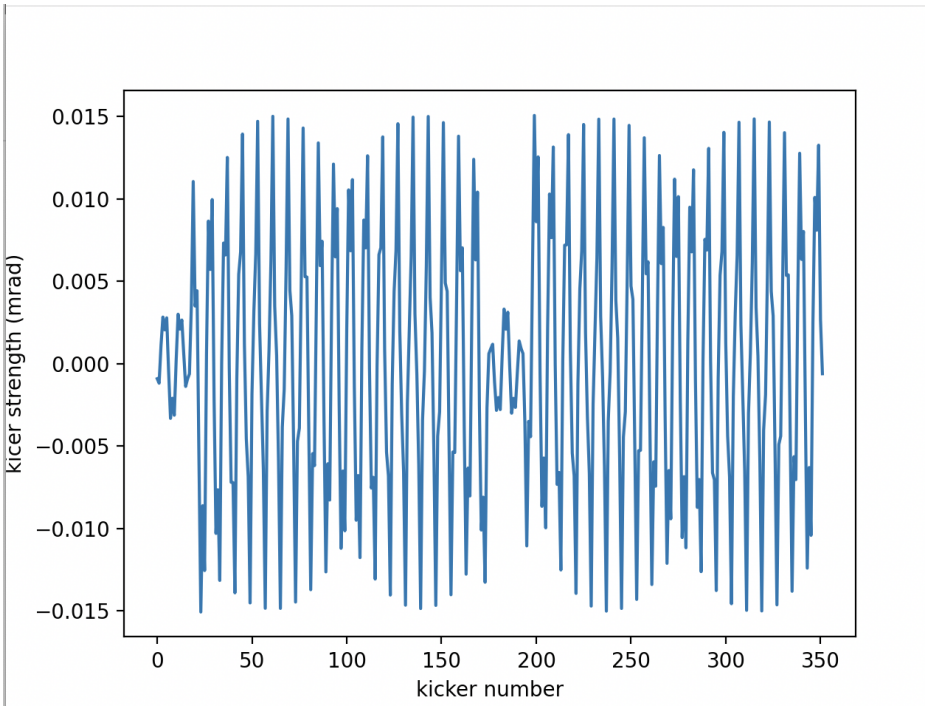

Figure 5.27: Dipole corrector strengths in an imperfection bump that corrects a single imperfection resonance of strength 0.02 at $a\gamma = 39$.

5.3.5 Alignment tolerances and beam-based alignment

Studies show that adiabatically slow changes to the orbit of order 2 mm, over a longitudinal distance of 100 m, are tolerated with little impact on polarization. Both spin-orbit BMAD [**?**] tracking and DEPOL [**?**] calculations show 99 % transmission up through 18 GeV. The required vertical alignment tolerance of 100 µm with a 2 sigma cut-off over 100 m is achievable, based on recent experience during the Advanced Photon Source upgrade. However, the 100 µrad dipole roll tolerance pushes the state of the art. Analysis tools are being developed to manage the estimation of rolls based on orbit response algorithms, and possibly leveraging the use of optical data as experienced at other machines, using the LOCO algorithm approach [**?**]. The Swiss Light Source and the Australian Light Source have both demonstrated the ability to determine and control rolls of less than 100 µrad.

The RCS will maintain a beam-based alignment system, in addition to maintaining tight alignment tolerances, using quadrupole magnets that are able to vary individual strengths slightly, enabling the measurement of their magnetic centers relative to the electrical centers of the neighboring BPMs to within 10 µm.

5.4 Electron Storage Ring

The Electron-Ion Collider (EIC) will collide spin-polarized electrons with light ions for a wide range of center-of-mass energies. The Electron Storage Ring (ESR) of the EIC will provide polarized electron beams at 5, 10, and 18 GeV with both positive and negative helicities at the interaction point(s) (IPs), for both a 1- and 2-IP configuration.

Electron polarization evolution in storage rings is defined by two major effects: (1) the *Sokolov-Ternov (ST) effect*, which is an asymmetry in the spin flip rate during photon emission leading to a buildup of polarization antiparallel to the bending field at a rate τ_{ST}^{-1}, and (2) *radiative depolarization*, which causes a rapid decoherence of a bunch's spins due to the stochasticity of photon emission at a rate τ_{dep}^{-1} [**?**, **?**, **?**, **?**]. These effects balance each other out, leading to an asymptotic polarization P_∞. The time evolution of a bunch's polarization is

$$P(P_0; t) = P_\infty(1 - e^{-t/\tau_{eq}}) + P_0 e^{-t/\tau_{eq}} \,, \tag{5.34}$$

where $\tau_{eq}^{-1} = \tau_{ST}^{-1} + \tau_{dep}^{-1}$, and P_0 is the initial bunch polarization. Polarized bunches will be injected into the ESR, and replaced once they become sufficiently depolarized. In order to simultaneously have both positive- and negative-helicity collisions, bunches with polarizations parallel to the arc fields (which the ST effect works against) and bunches with polarizations antiparallel to the arc fields (which the ST effect works for) will be stored at the same time. Therefore, the positively-polarized bunch replacement time T_+ will be less than the negatively-polarized bunch replacement time T_-. To measure polarization performance, we use the time-averaged polarization the ESR could maintain. The long-term average replacement time for any bunch is

$$T = \frac{2T_+T_-}{T_+ + T_-} = Nf_r \,, \tag{5.35}$$

where N is the total number of bunches in the ring and f_r is the bunch replacement rate. Using Eq. (5.34), the time averaged polarizations for positively- and negatively-polarized bunches are respectively

$$\frac{1}{T_+}\int_0^{T_+} P(+P_0; t)\, dt \,, \quad \frac{1}{T_-}\int_0^{T_-} P(-P_0; t)\, dt \,. \tag{5.36}$$

We require that the time-averaged polarizations for both positively- and negatively-polarized bunches are equal. Using (5.35) to relate T_+ and T_-, we numerically solve for either T_+ or T_-, and then obtain $\langle P \rangle_t$. For the ESR, $\langle P \rangle_t \geq 70\%$.

While τ_{ST}^{-1} is well-approximated analytically, nonlinear tracking is necessary to accurately estimate τ_{dep}^{-1}. In this work, *map tracking* refers to tracking through damped maps of the specified order generated by PTC between each bend center, with stochastic radiation kicks at the bend centers [**?**]. The sextupoles were set with the optimal solution [**?**].

5.4.1 Spin Rotator

The spin rotator of the ESR, shown in Fig. 5.28, consists of a symmetric arrangement of four solenoid modules and four bend modules around the IP [**?**]. $\hat{n}_0$ is the 1-turn periodic spin direction on the closed orbit. $\hat{l}_0$ and $\hat{m}_0$ are orthogonal unit vectors that obey the T-BMT equation

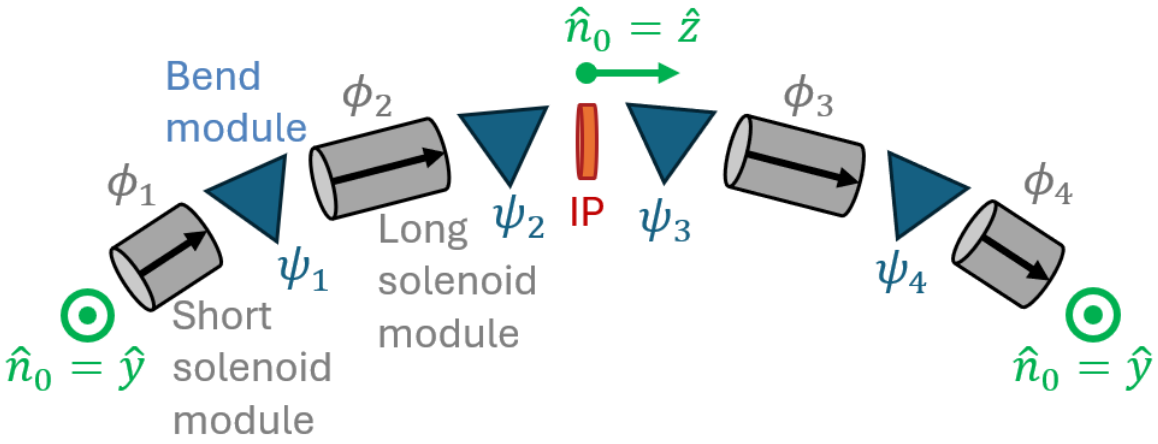

Figure 5.28: Top-down view of the spin rotator of the ESR, with the spin precession angles in each module labelled.

	Solenoids		Bends	
	$\phi_{1,4}$	$\phi_{2,3}$	$\psi_{1,4}$	$\psi_{2,3}$
17.846 GeV 1-IP/2-IP	0°	−90°	N/A	−90°
9.781 GeV 1-IP	−52.2°	−126.0°	−124.4°	−49.3°
9.650 GeV 2-IP	−51.7°	−124.4°	−122.7°	−48.7°
5.068 GeV 1-IP/2-IP	−90°	0°	−64.4°	−25.6°

Table 5.3: Solenoid ($\hat{z}$) and Bend ($\hat{y}$) Module Spin Precession Angles at Different Energies using the Right-handed Basis $(\hat{x}, \hat{y}, \hat{z})$ with $\hat{z}$ Pointing along the Longitudinal in Fig. 5.28

and $(\hat{l}_0, \hat{n}_0, \hat{m}_0)$ forms a right-handed basis. Each "solenoid module" consists of two half solenoids, separated by either 5 (short) or 7 (long) quadrupoles with strengths chosen for decoupling and spin matching. The spin rotator configuration was chosen so that at roughly 5 GeV, only the short solenoid modules are turned on, and at roughly 18 GeV, only the long solenoid modules are turned on (Table 1). In these two cases, the "on" solenoid module rotates $\hat{n}_0$ from the vertical to the horizontal, and the bend module(s) (where spin precession is proportional to γ_0) rotates $\hat{n}_0$ from the horizontal to the longitudinal. For the 10 GeV case, all solenoid modules must be used.

To avoid depolarizing integer spin resonances, the exact operating energies are those closest to 5, 10, and 18 GeV that give a half-integer fractional closed-orbit spin tune ν_0. At 5 and 18 GeV, because of the special rotator configuration chosen, the "net" spin precession of $\hat{l}_0$ and $\hat{m}_0$ across the rotator is exactly equal to 180°; in these special cases, the contribution to ν_0 of the rotator is equivalent to that had the rotator been turned off. Therefore, for 5 and 18 GeV, $\nu_0 = a\gamma_0$, and there is no difference in the energies of the 1-IP and 2-IP lattices. The 10 GeV lattice does not have this special configuration, and so there is a small difference in the energy (and solenoid settings) between the 1-IP and 2-IP lattices to maintain a half-integer ν_0; numerical solution was required to calculate the exact γ_0's closest to 10 GeV.

5.4.2 Spin Matching

To minimize the effects of radiative depolarization, spin matching, as was used in HERA, is employed [**?**, **?**, **?**, **?**]. Spin matching removes the first-order spin-orbit coupling across a region of the ring. For all energy cases of the ESR, only a horizontal spin match is satisfied across the entire spin rotator, from before the first solenoid to after the last solenoid. To satisfy a horizontal strong synchro-beta spin match across the entire rotator, the transfer matrix components M_{jk} across each solenoid module must satisfy the conditions,

$$\begin{pmatrix} -l_{0x}\cos\phi + l_{0y}\sin\phi \\ -m_{0x}\cos\phi + m_{0y}\sin\phi \end{pmatrix} = \begin{pmatrix} l_{0x} & \frac{1}{2}K_s l_{0y} \\ m_{0x} & \frac{1}{2}K_s m_{0y} \end{pmatrix} \begin{pmatrix} M_{11} \\ M_{12} \end{pmatrix}, \tag{5.37}$$

$$-\frac{1}{2}K_s \begin{pmatrix} l_{0x}\sin\phi + l_{0y}\cos\phi \\ m_{0x}\sin\phi + m_{0y}\cos\phi \end{pmatrix} = \begin{pmatrix} l_{0x} & \frac{1}{2}K_s l_{0y} \\ m_{0x} & \frac{1}{2}K_s m_{0y} \end{pmatrix} \begin{pmatrix} M_{21} \\ M_{22} \end{pmatrix}, \tag{5.38}$$

as well as be decoupled (zero off-diagonal block matrices of the 4×4 matrix), where K_s is the normalized solenoid strength and $\hat{l}_0$ and $\hat{m}_0$ are evaluated at the module entrance [**?**, **?**]. Only three quadrupoles are necessary for decoupling the solenoid module [**?**], and because the symplectic condition connects Eqs. (5.37) and (5.38), only three more quadrupoles are necessary for spin matching. However, when the entering/exiting $\hat{n}_0$ lies in the XY-plane (e.g. is vertical), the matrix in Eqs. (5.37) and (5.38) is degenerate. This leaves one variable free, and therefore only 5 quadrupoles are necessary for the outer-most (short) solenoid modules.

The horizontal spin match is sufficient for the 5 and 10 GeV cases, however only marginally sufficient for the 18 GeV 1-IP lattice, and insufficient for the 18 GeV 2-IP lattice. Significant efforts were made to achieve a longitudinal spin match, even partially, however the solenoid strengths necessary for such are not feasible [**?**]. A novel approach - the so-called BAGELS method - has been developed to restore very high levels of polarization for the 18 GeV case, in fact higher than that with a traditional longitudinal spin match [**?**].

5.4.3 Best Adjustment Groups for Electron Spin (BAGELS)

A new method called "Best Adjustment Groups for Electron Spin" (BAGELS) has been devised to achieve simultaneous control of the polarization, orbit, and optics by use of a minimal number of special groups of vertical orbit bumps [**?**]. In the 18 GeV EIC-ESR, BAGELS nearly doubles the asymptotic polarization in the 1-IP lattice, and more than triples it in the 2-IP lattice. We also use BAGELS to construct knobs for global coupling correction, and knobs that generate vertical emittance for beam size matching with the hadron beam at the IP, all while having minimal impacts on the polarization and orbit/optics.

BAGELS works by applying dimensionality reduction over the ring's vertical corrector coils to construct such special groups of vertical corrector coils. Each individual vertical corrector coil, with strength specified by θ_i, will have some impact on the polarization, orbit, and optics. A group of k vertical corrector coils is specified by $\vec{\theta} = (\theta_1, ...\theta_k)^T$, and this group is a knob which can be scaled up and down like $w\vec{\theta}$ where $w \in \mathbb{R}$. Letting R_A specify the Jacobian of the quantities we wish to maximally affect wrt $\vec{\theta}$, and R_B specify the Jacobian of those quantities we wish to minimally affect

wrt $\vec{\theta}$, we seek

$$\underset{\vec{\theta}}{\text{argmax}} \frac{||\mathsf{R}_A\vec{\theta}||^2}{||\mathsf{R}_B\vec{\theta}||^2} = \underset{\vec{\theta}}{\text{argmax}} \frac{\vec{\theta}^T\mathsf{A}\vec{\theta}}{\vec{\theta}^T\mathsf{B}\vec{\theta}}\,, \tag{5.39}$$

where $\mathsf{A} = \mathsf{R}_A^T\mathsf{R}_A$ and $\mathsf{B} = \mathsf{R}_B^T\mathsf{R}_B$. It can be shown that the k orthogonal groups which maximally scale the quotient of Eq. (5.39) are the k generalized eigenvectors of A and B with largest eigenvalues.

The method can be streamlined by using suitable "basis bumps" for each θ_i instead of individual corrector coils; this will ensure that the vertical orbit bump produced by each group is closed. Furthermore, by using basis bumps which by construction have no delocalized vertical dispersion and/or coupling, then the group will also have no delocalized vertical dispersion and/or coupling.

Spin Match the Ideal Lattice

For increasing polarization in the ideal EIC-ESR, we use BAGELS to construct four groups which maximally impact the radiative depolarization, but minimally impact the orbit and optics. We can then choose group strengths that minimize the radiative depolarization.

In order to ensure the spin matching groups do not create any delocalized coupling nor delocalized vertical dispersion, we use each "opposite π-pair" basis bump, shown in Fig. 5.29, in the four arcs surrounding the IP.

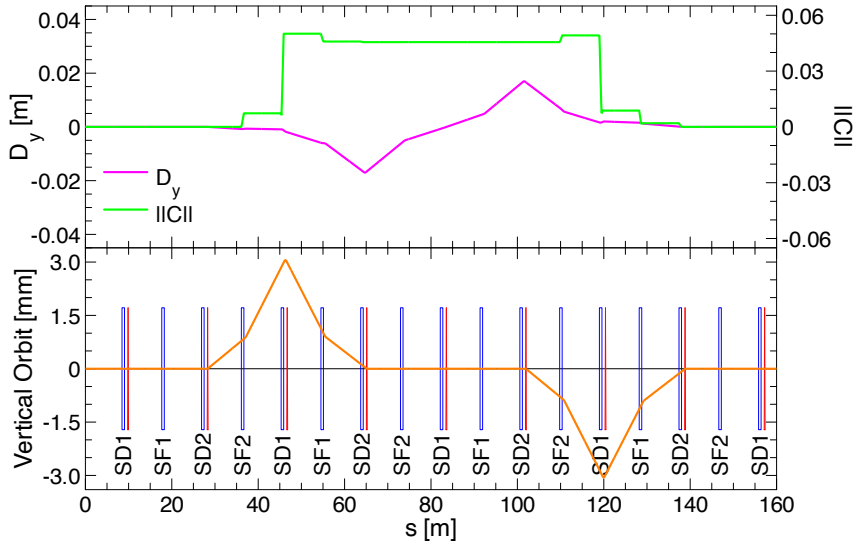

Figure 5.29: Opposite π pair placed in a periodic FODO beamline with 90° phase advance per cell and two sextupole families per plane (SF for the horizontal, SD for the vertical). Sextupoles are specified as blue rectangles, vertical corrector coils as red triangles, and the quadrupoles and bends are not shown. The bump's corresponding vertical dispersion D_y and normalized coupling matrix norm $||\bar{\mathsf{C}}||$ are plotted above. The opposite π pair creates only localized coupling and localized vertical dispersion, but a delocalized tilt to $\hat{n}_0$ due to the bending magnets between the corrector coils, making it ideal for spin matching.

We let R_A be the Jacobian of the contributions to radiative depolarization at each bend in the ring wrt the basis bump strengths $\vec{\theta}$, and R_B be the Jacobian of the vertical orbit at all lattice elements in the ring wrt $\vec{\theta}$. After choosing the four best adjustment groups, we can directly compute in the ideal lattice the group strengths to minimize the radiative depolarization. Figures 5.30 and 5.31 show scans of the asymptotic polarizations in the ideal 1- and 2-IP 18 GeV EIC-ESR lattices respectively, both before and after applying BAGELS. The maximum orbit excursion for both lattices is ≈ 1 mm. The "Requirement" line is the necessary asymptotic polarization to achieve $\langle P \rangle_t = 70\%$ for both positive- and negative-helicity bunches, given the maximum possible bunch replacement rate. BAGELS nearly doubles P_{dk} in the 1-IP, and more than triples it in the 2-IP.

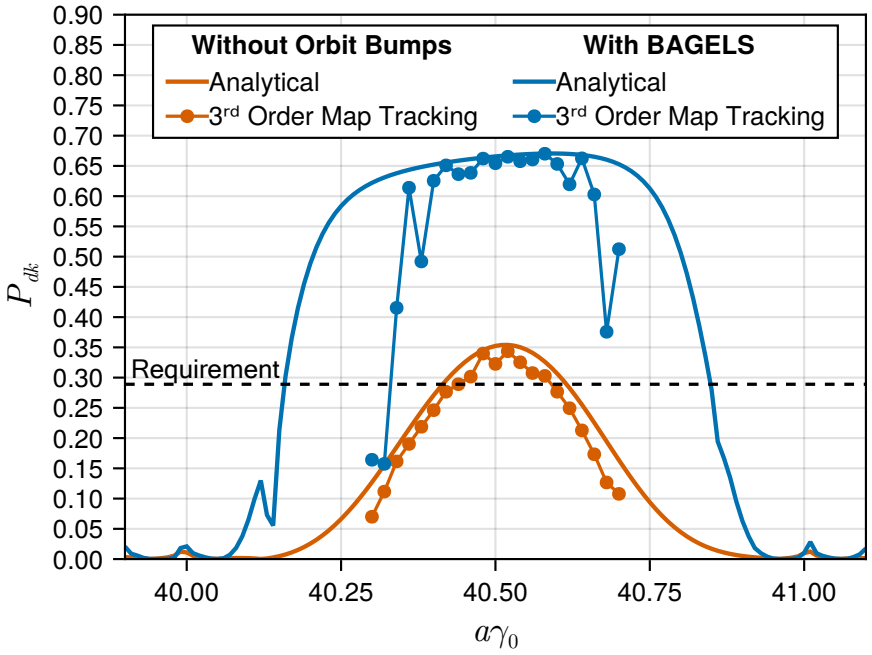

Figure 5.30: An energy scan of the asymptotic polarization in the ideal 1-IP 18 GeV EIC-ESR, both before and after applying BAGELS. Using only four BAGELS vertical orbit bumps, the asymptotic polarization is nearly doubled in nonlinear tracking.

Random Errors and Global Coupling Correction

The real ring will contain random errors and closed orbit distortions that will degrade the spin match. To correct this, the four BAGELS spin matching knobs, which have been computed *ab initio*, can be turned in the control room until the polarization is re-maximized.

Another side effect of these random errors is delocalized coupling around the entire ring, which must also be corrected. One way to do so is by use of vertical orbit bumps through sextupoles, which will create a skew-quadrupole term in the map that can be used to correct the coupling. Such bumps, however, will also degrade the spin match if not carefully constructed. Therefore, BAGELS is used to create groups that have a maximal impact on the coupling around the ring, and a minimal impact on the orbit, dispersion, and radiative depolarization.

In order to ensure the coupling correction groups do not create any delocalized vertical dispersion, we use each "equal π-pair" basis bump, shown in Fig. 5.32, in the arcs of the ring.

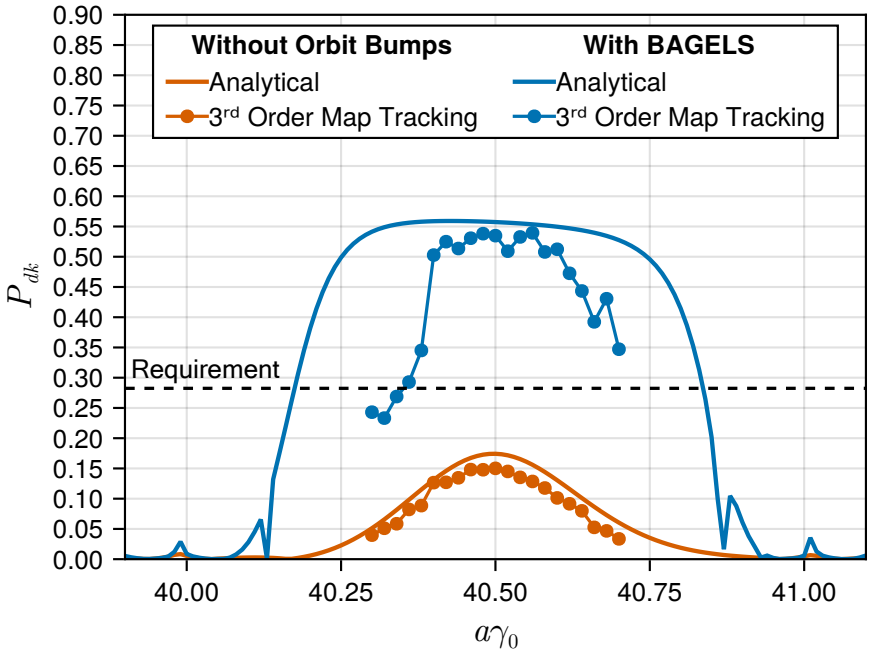

Figure 5.31: An energy scan of the asymptotic polarization in the ideal 2-IP 18 GeV EIC-ESR, both before and after applying BAGELS. Using only four BAGELS vertical orbit bumps, the asymptotic polarization is more than tripled in nonlinear tracking.

We let R_A be the Jacobian of the coupling matrix components at each lattice element in the ring wrt the basis bump strengths $\vec{\theta}$, and R_B be the Jacobian of both the contributions to radiative depolarization at each bend in the ring and the vertical orbit at each element in the ring, wrt $\vec{\theta}$. The four best groups are chosen as coupling correction knobs which have minimal impacts to the orbit, optics, and radiative depolarization.

We then tested the four BAGELS spin matching knobs and four BAGELS global coupling correction knobs for 10 1-IP 18 GeV ESR lattices with the random RMS error seeds shown in Table 5.4.

RMS Error	x [mm]	y [mm]	Roll [mrad]	$\Delta B/B$ [%]
Dipoles	0.2	0.2	0.5	0.1
Quadrupoles	0.2	0.2	0.5	0.1
Sextupoles	0.2	0.2	0.5	0.2
High-β Dipoles	0.2	0.2	0.5	0.05
Final Focus Quads	0.1	0.1	0.5	0.05

Table 5.4: RMS Errors used to study BAGELS spin-matching

For each lattice, we first corrected the RMS orbit at each BPM by varying all corrector coils in the ring; this consisted of dual plane BPMs and vertical corrector coils at each vertically-focusing quadrupole outside of the interaction region, and horizontal corrector coils at each horizontally-focusing quadrupole outside of the interaction region. In the interaction region, dual plane BPMs and dual plane correctors are used at each quadrupole. Then, the four BAGELS global coupling correction knobs were turned until the RMS coupling matrix components at each BPM were minimized. Finally, the four BAGELS spin matching knobs were turned until the polarization was

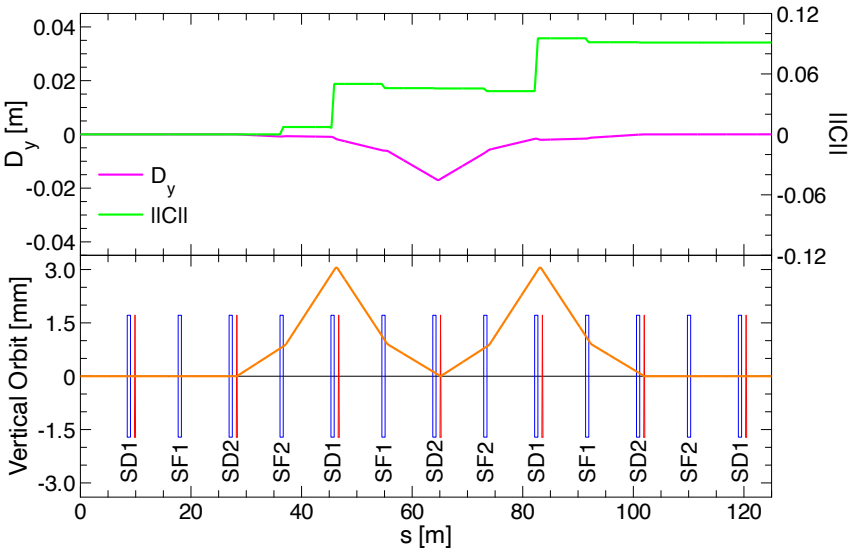

Figure 5.32: Equal π pair placed in a periodic FODO beamline with 90° phase advance per cell and two sextupole families per plane (SF for the horizontal, SD for the vertical). Sextupoles are specified as blue rectangles, vertical corrector coils as red triangles, and the quadrupoles and bends are not shown. The bump's corresponding vertical dispersion D_y and normalized coupling matrix norm $||\bar{C}||$ are plotted above. The equal π pair creates delocalized transverse coupling but localized vertical dispersion.

maximized. Figure 5.33 shows the upper and lower bounds of the vertical closed orbit across each error seed. In all cases, the analytical (first-order) ϵ_b was reduced to < 0.61 nm, indicating excellent first order coupling correction. The analytical (first-order) P_{dk} for all errors seeds was $\geq 55\%$, with the average analytical P_{dk} amongst all 10 seeds equal to 62.7%.

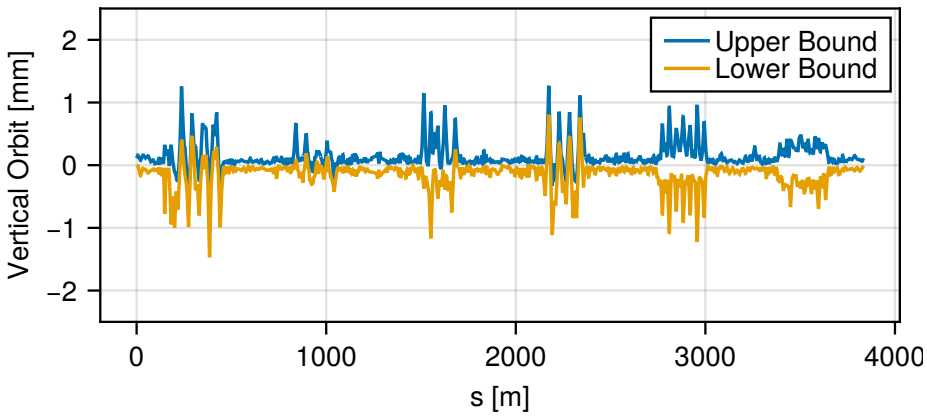

Figure 5.33: Upper and lower bounds of the vertical closed orbit across 10 error seeds of the 1-IP 18 GeV EIC-ESR after orbit correction, coupling correction using four BAGELS global coupling correction bumps, and spin match restoration using four BAGELS spin matching bumps. The IP is located at $s = 1277.948$ m.

Figure 5.34 shows nonlinear tracking energy scans of the asymptotic polarization for each error seed. The color of the line corresponds to the vertical-like eigenemittance. For all 10 error seeds, the polarization requirements for the 1-IP ESR are well exceeded. For two of the error seeds, linear coupling correction does not result in a sufficient reduction of the nonlinear vertical emittance. It is remarkable that even in the cases where nonlinearities are significant, BAGELS still gives sufficient P_{dk} to achieve the polarization goals of the ESR. For 7 of the 10 seeds, asymptotic polarizations of $\approx$ 60% or more are achieved while having vertical equilibrium emittances in nonlinear tracking that agree very well with their linear calculations, suggesting excellent coupling control in these cases. For the two seeds with lower asymptotic polarization and a nonlinear $\epsilon_{b,RMS}$ increase, it is likely that a further optimization of the chromatic solution and/or harmonic sextupoles may gain control of the nonlinear $\epsilon_{b,RMS}$ and obtain a corresponding increase in P_{dk}. In this case, because the BAGELS transverse coupling correction knobs rely on the sextupole strengths, some iteration will be required for an optimal solution.

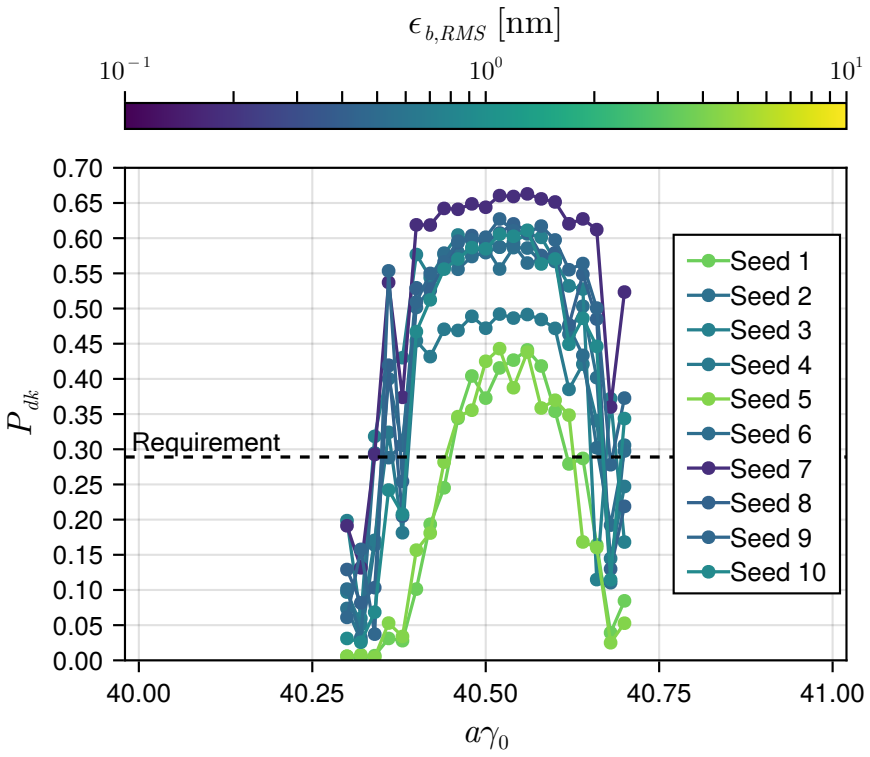

Figure 5.34: A 3rd order map tracking energy scan of the asymptotic polarizations in 10 different 1-IP 18 GeV EIC-ESR lattices including the RMS errors listed in Table 5.4. Four BAGELS global coupling correction knobs were used to correct the coupling, followed by four BAGELS spin matching knobs to restore the spin match. The line colors correspond to the vertical-like mean equilibrium eigenemittance obtained in tracking for each seed.

Vertical Beam Size Match

The electron beam size must be matched to the hadron beam size at the interaction point(s) for maximum luminosity. The electron beam however will naturally have a very small vertical beam size, much less than that of the hadron beam, due to radiation damping. Vertical beam size must

therefore be intentionally created, but this will have detrimental effects on the polarization if care is not taken. There are many ways of achieving the beam size match at the IP. One way is to create only vertical emittance via a special delocalized vertical dispersion wave which maximally excites a vertical amplitude when photons are emitted (primarily in the bends). At the IP this wave should cancel itself so that we just have $\langle y^2 \rangle = \beta_y \langle J_y \rangle$.

We apply BAGELS in the 1-IP 18 GeV ESR lattice to construct a group which creates the optimal vertical dispersion wave for vertical emittance creation, while also minimally impacting the orbit, the radiative depolarization, and the vertical dispersion at the IP (so it remains zero). In order to ensure the vertical emittance creation group does not create any delocalized coupling, we use each "2π bump", shown in Fig. 5.35, in all arcs as the basis bump.

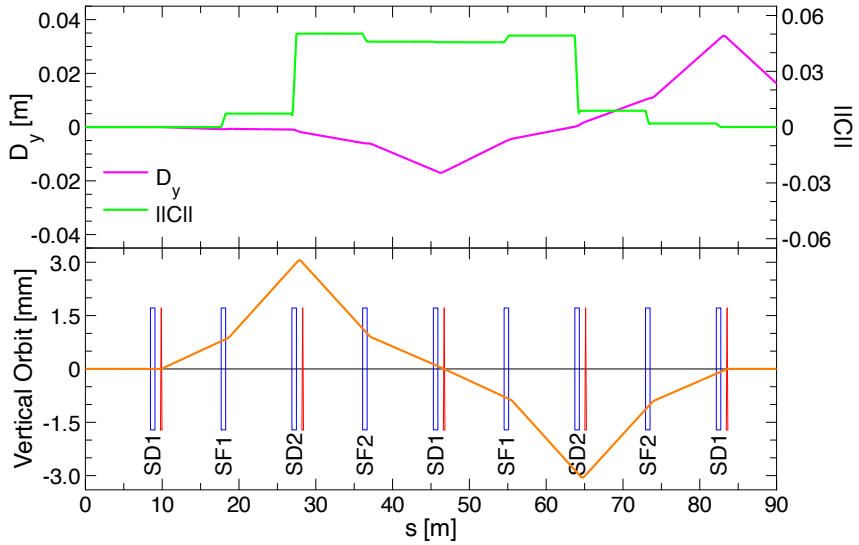

Figure 5.35: 2π bump placed in a periodic FODO beamline with 90° phase advance per cell and two sextupole families per plane (SF for the horizontal, SD for the vertical). Sextupoles are specified as blue rectangles, vertical corrector coils as red triangles, and the quadrupoles and bends are not shown. The bump's corresponding vertical dispersion D_y and normalized coupling matrix norm $||\bar{C}||$ are plotted above. The 2π bump creates delocalized vertical dispersion but localized coupling.

We let R_A be the Jacobian of the radiative contribution to vertical emittance at each bend in the ring wrt the basis bump strengths $\vec{\theta}$, and R_B be the Jacobian of both the contributions to radiative depolarization at each bend in the ring, the vertical orbit at each element in the ring, and the vertical dispersion and vertical dispersion slope at the IP, all wrt $\vec{\theta}$. The single best group was chosen as the vertical beam size matching knob. This knob was then turned until the analytical (first-order) equilibrium vertical emittance was set to $\langle J_y \rangle \approx 2$ nm. The four BAGELS spin matching knobs were then adjusted slightly to re-maximize the polarization. Figure 5.36 shows the resulting dispersion and closed orbit, and Fig. 5.37 shows an energy scan of the asymptotic polarization of this lattice. The polarization obtained in nonlinear tracking well exceeds the requirements, and only a small nonlinear increase in the vertical-like eigenemittance was observed.

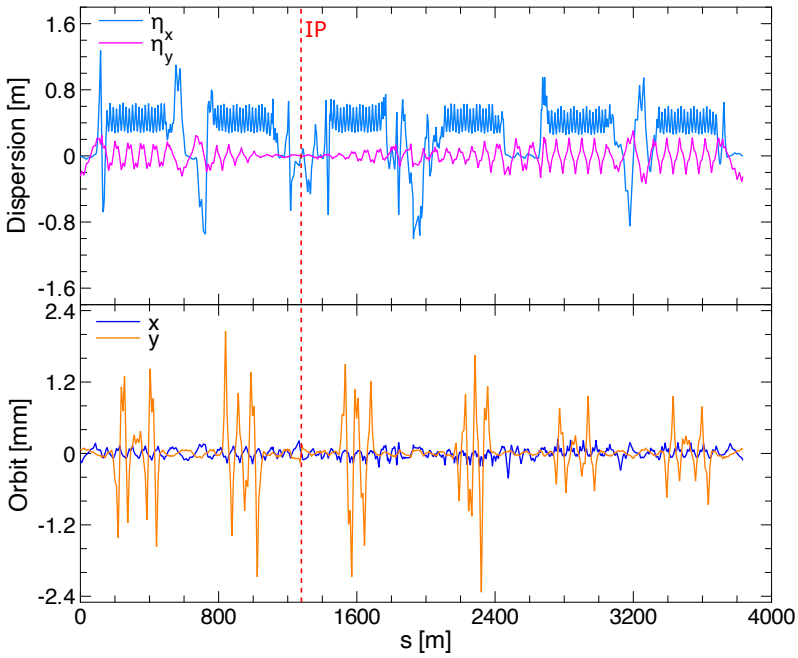

Figure 5.36: Dispersion and closed orbit in a 1-IP 18 GeV EIC-ESR after using a single BAGELS simultaneous vertical dispersion-creation and IP dispersion matching bump to generate sufficient vertical emittance for beam size matching. The small horizontal orbit is due to radiation damping. The IP is located at $s = 1277.948$ m and is denoted by the red dashed line.

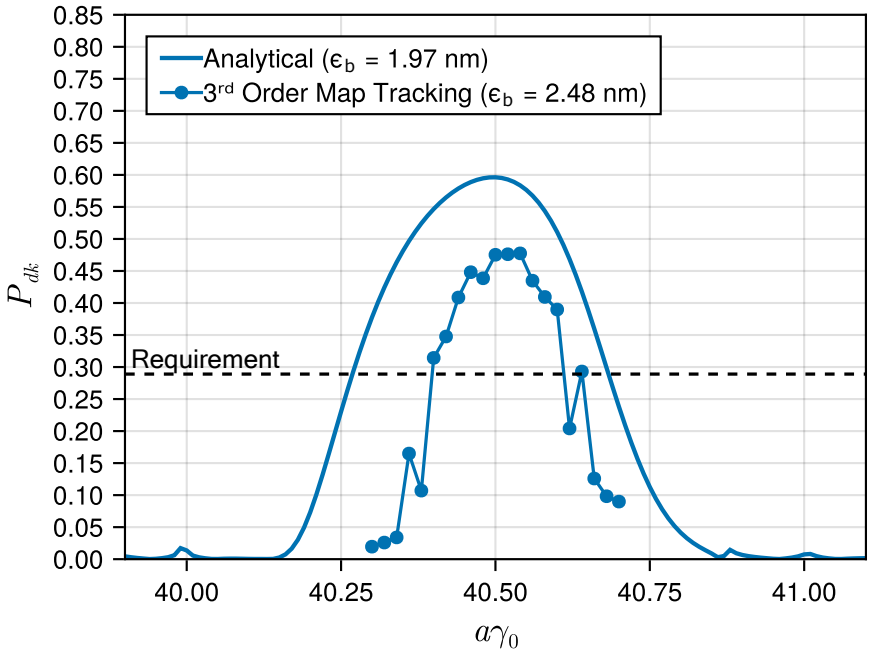

Figure 5.37: An energy scan of the asymptotic polarization in the ideal 1-IP 18 GeV EIC-ESR after using a single BAGELS simultaneous vertical dispersion-creation and IP dispersion matching bump to set the analytical vertical emittance to 1.97 nm. The disagreement of the analytical calculation with nonlinear tracking is expected because the phase space dependence of the spin-orbit coupling function, which can vary significantly in the vertical, is neglected in the analytical calculation.

5.4.4 Conclusions

The ESR will collide positively- and negatively- polarized bunches simultaneously, in a 1- and 2-colliding IP configuration for each of 5, 10, and 18 GeV, with $\langle P \rangle_t \geq 70\%$. A horizontal spin match is satisfied for all energy cases, which provides sufficient polarization at 5 and 10 GeV, however at 18 GeV is marginal for the 1-IP lattice and insufficient for the 2-IP. To solve this, the BAGELS method has been developed which maximizes the polarization with vertical orbit bumps. Using only four of the BAGELS spin matching bumps, polarization requirements are exceeded in the 18 GeV 1-IP and 2-IP lattices. To correct global coupling created by random errors, 8 special vertical orbit bumps through sextupoles that have minimum impacts on polarization, also calculated using BAGELS, are used. Nonlinear tracking showed excellent coupling control and sufficient polarization for 10 random error seeds in the 1-IP 18 GeV ESR. Finally, "polarization-safe" vertical orbit bumps generating either de-localized coupling, or de-localized η_y, to create sufficient ϵ_y were calculated using BAGELS, and showed sufficient polarization and emittances in nonlinear tracking.

Chapter 6

Accelerator Technical Systems (editor: Smith)

6.7 Superconducting RF

RF System	Function	Location	Freq. MHz	Cavity type	Cavities per mod.	Voltage per cav. MV	Power kW
Electron accelerators							
Preinjector	Buncher		197	NCRF	1	0.4	
	Capture 1		1300	NC SW	1	5	
	Capture 2		1300	NC SW	1	10	
	Linac		2856	NC TW	14	60	
BAR	Store		52.88	NCRF	1	0.1	
RCS commissioning	Accelerate, store		197	NCRF, 1-cell		0.8	
RCS	Accelerate, store	IR4	591	SRF, 5-cell	8/8	17	
ESR	Store	IR10	591	SRF, 1-cell	18/9	3.5	800
LEC	Main	IR2	197	NCRF	17	0.85	
	Energy corrn.	IR2	591	NCRF	4	0.375	
	Deflecting	IR2	197	NCRF	1	0.15	
		IR2	24.6	NCRF	1	0.01	
Hadron Storage Ring							
	Capture/Accel	IR4	24.6	NCRF, QWR	4	0.6	120
	Bunch Split 1	IR4	49.2	NCRF, QWR	3	0.6	120
	Bunch Split 2	IR4	98.5	NCRF, QWR	4	0.6	120
	Store 1	IR4	197	NCRF, 1-cell	7	0.85	65
	Store 2	IR10	591	SRF, 1-cell	6/3	3.5	70
Crab cavities							
HSR		IR6	197	SRF, RFD	8/4		35
HSR		IR6	394	SRF, RFD	4/4		35
ESR		IR6	394	SRF, RFD	2/2		35

Table 6.1: Radio Frequency systems summary. All superconducting RF cavities are designed to operate at 2 K. The RCS cavities will initially operate at 4.5 K, which is sufficient to accelerate electrons to 10 GeV.

Parameter	Unit	Injection	Low energy collisions	Medium energy collisions	High energy, low h	High energy collisions
Total energy	GeV	23.812	41.0	100.0	275.0	275.0
Rigidity	Tm	79.367	136.725	333.549	917.296	917.296
Harmonic number h		315	1260	1260	315	1260
Number of bunches M		290	1160	1160	290	1160
Bunch length σ_τ	ps	1670	250	234	200	200
Relativistic γ		25.379	43.697	106.579	293.092	293.092
Relativistic β		0.999223	0.999738	0.999956	0.999994	0.999994
Momentum	GeV/c	23.794	40.989	99.996	274.998	274.998
Particles per bunch N	10^{10}	27.6	2.6	6.9	19.1	6.9
Particles per bunch N	10^{10}	28.0	2.6	4.8	19.0	6.9
Bunch charge Ne	nC	44.2	4.2	11.0	30.6	11.0
Bunch charge Ne	nC	44.8	4.2	7.6	30.4	11.0
Average current I_{ave}	A	1.0	0.38	1.0	0.69	1.0
Single bunch current I_0	mA	3.5	0.3	0.6	2.4	0.9
Peak bunch current I_p	A	11.0	7.0	13.0	61	22.0
Transition γ_T		Protons do not cross transition				
RMS bunch length	mm	10.0	4.0	10.0	7.0	10.0
Slip factor		0.000353	0.001382	0.001817	0.001894	0.001894

Table 6.2: Proton-related RF parameters in the Hadron Storage Ring, required by accelerator physics. 231218: Values in red were marked by Alexei. Values in blue were marked by Steve.

Parameter	Unit	Injection	Low energy collisions	High energy, low h	High energy collisions
Total energy	GeV/u	9.796	40.7	110.0	110.0
Rigidity	Tm	81.114	338.454	914.946	914.946
Harmonic number h		315	1260	315	1260
Number of bunches M		290	1160	290	1160
Bunch length σ_τ	ps				234
Relativistic γ		10.520	43.710	118.136	118.136
Relativistic β		0.995472	0.999738	0.999964	0.999964
Momentum	GeV/(cu)	9.752	40.689	109.996	109.996
Particles per bunch N	10^{10}	10.52	43.710	118.14	118.14
Particles per bunch N	10^{10}				6.9
Bunch charge ZNe	nC				11.0
Average current I_{ave}	A	0.004	0.070	0.048	0.191
Average current I_{ave}	A				1.0
Single bunch current I_0	mA				0.9
Peak bunch current I_p	A				19
Transition γ_T		22.91	22.910	22.910	22.910
RMS bunch length	cm	315.0	1260.0	315.0	1260.0
Slip factor		-0.007130	0.001382	0.001834	0.001834

Table 6.3: Gold ion related RF parameters in the Hadron Storage Ring, required by accelerator physics. 231218: Values in red marked by Steve.

6.8 Pulsed systems

6.9 Polarization measurement

6.10 Controls

6.11 Beam instrumentation

6.12 Cryogenics

6.13 Personnel safety

6.14 Machine-detector protection

Chapter 7

Detector (editors: Aschenauer & Ent)

The EIC Detector, ePIC, consists of the central detector and several auxiliary detectors that are embedded in the hadron and electron accelerator lattice.

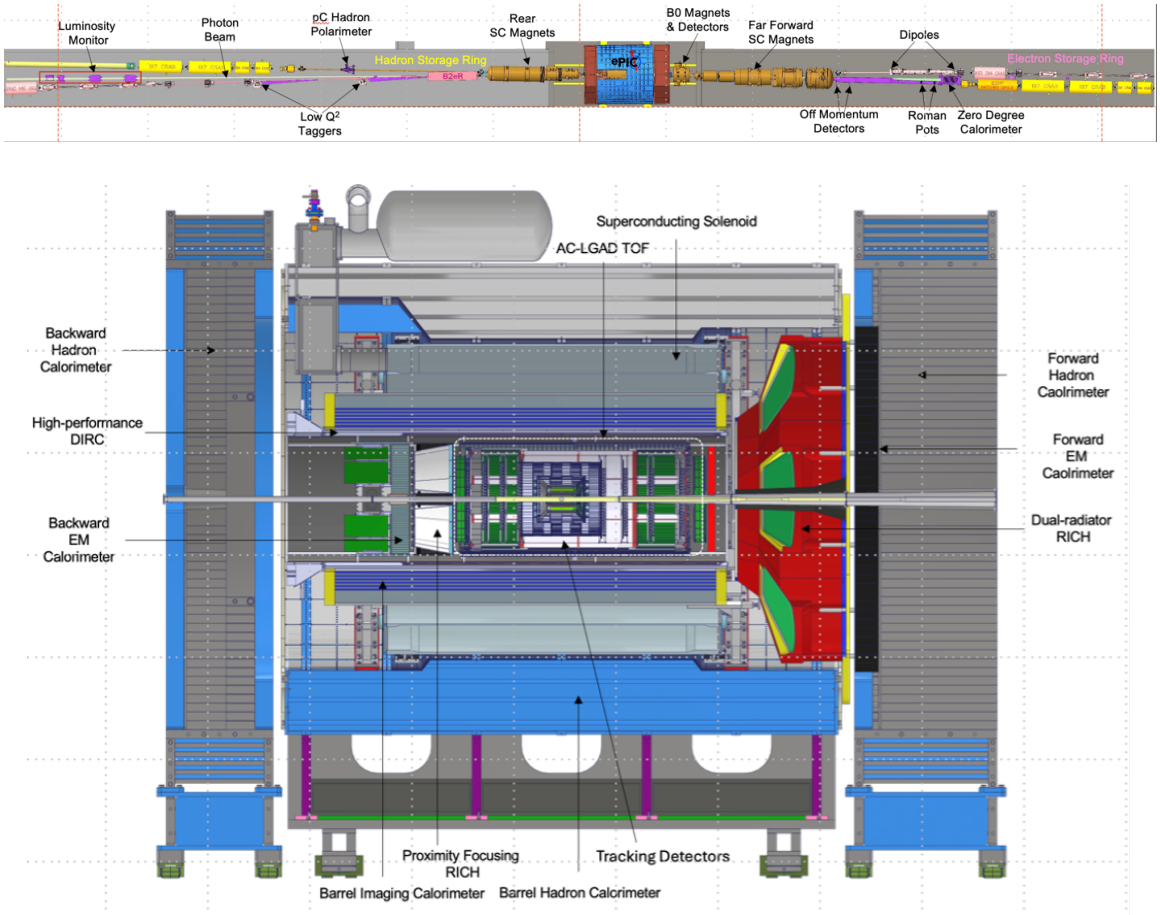

Figure 7.1: Top: The central ePIC detector and its auxiliary detectors embedded in the EIC lattice. Bottom: A CAD model rendering of the ePIC detector.

Due to the asymmetric electron ion collisions the ePIC detector consists of the central barrel detector and an electron and hadron endcap. Each region has an hadron, electromagnetic calorimeter, tracking and particle identification detectors. The ePIC detector has a 1.7 T solenoid with a 2 T stretch goal for the magnetic field. The auxiliary detectors are a zero-degree calorimeter, tracking detectors, and electromagnetic calorimetry embedded in the B0 magnet, as well as tracking detectors in the vacuum of the hadron beam to detect particles that scatter under small angles (Roman Pots) and charged particles from heavy ion decays (off-momentum detectors).

A luminosity detector is embedded in the electron lattice, with a tagger that detects electrons scattered under very small angles to reach Q^2 values below 0.1 GeV^2.

7.1 Detector parameters

η	Nomenclature			Tracking				Electrons and Photons			π/K/p		HCAL		Muons
				Resolution	Allowed	minimum-pT	Si-Vertex	Resolution σE/E	PID	min E	p-Range	Separati	Resolution σE/E	Energy	
-6.9 to -5.8		low-Q2 tagger	σθ/θ < 1.5%; 10-6 < Q2 < 10-2 GeV2												
-5.0 to -4.5					300 MeV pions										
-4.5 to -4.0		Instrumentation to separate charged particles from photons			300 MeV pions		2%/√E(+1-3%)		50 MeV						
-4.0 to -3.5	↓ p/A	Auxiliary De								50 MeV			~50%/√E + 6%		
-3.5 to -3.0										50 MeV					
-3.0 to -2.5		Backward Detector	σpT/pT ~ 0.1%⊕0.5%			σ_xy ~ 30/pT μm +40 μm			50 MeV	≤ 7 GeV/c		~45%/√E+6%		muons useful for bkg, improve resolution
-2.5 to -2.0			σpT/pT			σ_xy ~ 30/pT μm +20 μm	2%/√E(+1-3%)	π suppression up to 1:1E-4	50 MeV					
-2.0 to -1.5			σpT/pT 0.05%⊕0.5%				7%/√E(+1-3%)		50 MeV					
-1.5 to -1.0							7%/√E(+1-3%)		50 MeV					
-1.0 to -0.5		Barrel	σpT/pT ~0.05%×pT+0.5%	~5% or less X	<100MeV pions, 135MeV kaons	σxyz ~ 20 μm, d0(z) ~d0(rΦ) ~ 20/pTGeV μm + 5 μm	(10-12)%/√E(+1-3%)		50 MeV	≤ 10 GeV/c	≥ 3 σ	~85%/√E+7%	~500 MeV	
-0.5 to 0.0									50 MeV			~85%/√E+7%		
0.0 to 0.5									50 MeV			~85%/√E+7%		
0.5 to 1.0									50 MeV	≤ 15 GeV/c		~85%/√E+7%		
1.0 to 1.5		Forward Detectors	σpT/pT ~0.05%×pT+1.0%			σ_xy ~ 30/pT μm +20 μm		3σ e/π	50 MeV	≤ 30 GeV/c		35%/√E		
1.5 to 2.0									50 MeV	≤ 50 GeV/c				
2.0 to 2.5									50 MeV					
2.5 to 3.0			σpT/pT ~ 0.1%×pT+2.0%			σ_xy ~ 30/pT μm +40 μm			50 MeV	≤ 30 GeV/c				
3.0 to 3.5						σ_xy ~ 30/pT μm +60 μm			50 MeV	≤ 45 GeV/c				
3.5 to 4.0		Instrumentation to separate charged particles from photons	Tracking capabilities are desirable for forward tagging						50 MeV					
4.0 to 4.5	↑ e	Auxiliary Detectors							50 MeV			35%/√E (goal), <50%/√E (acceptable)*, 3mrad/√E (goal)		
4.5 to 5.0		Neutron Detection			300 MeV pions		4.5%/√E for photon energy > 20 GeV	<= 3 cm granularity	50 MeV					
>6.2		Proton Spectrometer	σintrinsic(|t|)/|t| < 1%; Acceptance: 0.2 < pt < 1.2 GeV/c											

Figure 7.2: Table presenting the Experimental Equipment Requirements Summary. Momentum and energy resolution as well as acceptance are shown for the different subsystems as function of rapidity for hadron, photons and electrons. This table will be updated as part of the detector-pre-TDR process.

Parameter	Unit	Values		Comment
		Hadron	Lepton	
Machine element free region				
ePIC longitudinal	m	-4.5 to $+5.0$		
ePIC angular	deg.	1.5		
Hadron calorimeter back-face to first magnet front-face	m	0.5		
Central barrel radius	m	8.23		
Interaction point location				
Vertical, above floor	m	4.32		
H, inside current RHIC IP6	m	0.97		
BO detector angular range				As rotationally symmentric as possible
minimum	mrad	5.5		
maximum	mrad	20.0		
Zero Degree Calorimeter				
Horizontal size	m	0.60		
Vertical size	m	0.60		
Longitudinal size	m	2.0		
Scattering angle acceptance				
ep collisions				All energies
Protons	GeV	$0.18 < p_t < 1.3$		Cone ≤ 5 mrad
Protons		$0.5 < x_L < 1.0$		$x_L = E'_p/E_{beam}$
Neutrons	GeV	$p_t < 1.3$		
eA collisions				Protons and neutrons
$\sqrt{s} =$ 50 GeV	mrad	$\Theta < 6.0$		
$\sqrt{s} =$ 100 GeV	mrad	$\Theta < 4.0$		
Bethe-Heitler photon acceptance	mrad		± 1.0	
Luminosity variation $\delta L/L$			≤ 0.01	

Table 7.1: Detector geometry and interaction region parameters

Parameter	Unit	Value	Comment
Central field at interaction point	T	2.0	
Operating field range	T	$0.5 - 2.0$	
Field polarity		Bipolar	
Coil length	m	3.492	
Warm bore diameter	m	2.84	
Cryostat length	m	< 3.85	
Cryostat outer diameter	m	< 3.54	
Flat field area			
Longitudinal	m	± 1.0	
Radial	m	0.80	
Field uniformity	%	12.5	
RICH detector area			
Longitudinal	m	1.80 to 2.80	
Projectivity	mrad	0.1	At 30 GeV/c
Projectivity	T/(Amm^2)	10.0	
Stray field requirement	G	10.0	$z = -5.3$ m, $+7.4$ m
Charging voltage	V	10	
Fast discharge voltage max.	V	500	
Quench hot spot temperature	K	< 150	
Temperature margin	K	> 1.5	
Current margin	%	< 30	
Charging time	h	$2 - 3$	
Cooldown time	weeks	$3 - 4$	
Cooling scheme		Thermosiphon	
Operating temperature	k	4.5	

Table 7.2: ePIC detector solenoid parameters

Chapter 8

Infrastructure (editor: Folz)

8.1 Overview and requirements

8.2 Civil construction and buldings

8.3 Mechanical cooling systems

8.4 Electrical power distribution

Chapter 9

Environmental Safety and Health (editor: C. Schaefer)

9.1 Introduction

Brookhaven Science Associates' (BSA's) contract with the Department of Energy (DOE) to operate Brookhaven National Laboratory includes the requirement to manage the Laboratory in compliance with Title 10 of the Code of Federal Regulations (CFR), Part 851, referred to as 10 CFR 851, Worker Safety and Health Program, and Part 835, Occupational Radiation Protection. The purpose of these programs is the prevention of injuries and illnesses to workers at the covered sites and to protect the health and safety of individuals from ionizing radiation resulting from the conduct of U.S. Department of Energy (DOE) activities. 10 CFR Part 851 in turn refers to a number of other DOE orders, policies, and guidelines that provide the framework for BSA's Worker Safety and Health Program (WSHP) and its Integrated Safety Management System (ISMS), which have been reviewed and accepted by the DOE.

BSA's implementation of these requirements is defined within the Brookhaven National Laboratory Standards Based Management System (SBMS) which is a set of Management System expectations, Program Description requirements, and Subject Area implementation. It is understood that the Electron-Ion Collider Project will comply with these requirements. BSA also has developed an Environmental Management System (EMS). An environment, safety, security and health policy, issued by the Laboratory Director, sets forth seven principles for working in an environmentally responsible and safe manner. Until recently, BNL's EMS was certified in conformance with the requirements of International Organization for Standardization (ISO) 14001:2004, Environmental Management Systems.

The Brookhaven accelerator facilities are further subject to the requirements of the Department of Energy (DOE) Accelerator Safety Order (ASO), DOE O 420.2D, Safety of Accelerator Facilities. These requirements are promulgated through BNL's Accelerator Safety Subject Area and the Radiological Control Manual.

All BNL staff are required to comply with the applicable procedures, instructions, and directives in order to perform safe, environmentally compliant work that protects the health and safety of the worker and the public while meeting quality requirements and preserving the integrity of DOE assets. Existing and mature programs at BNL will be followed to ensure that the design, installation,

testing, and commissioning phases of the EIC Project are consistent with these requirements.

9.2 Preliminary hazard analysis report overview

One of the key elements of an effective ESH program is the hazard identification process. Hazard identification produces a list of hazards present within a facility allowing these hazards to be screened, and those of concern, managed through a suitable set of controls.

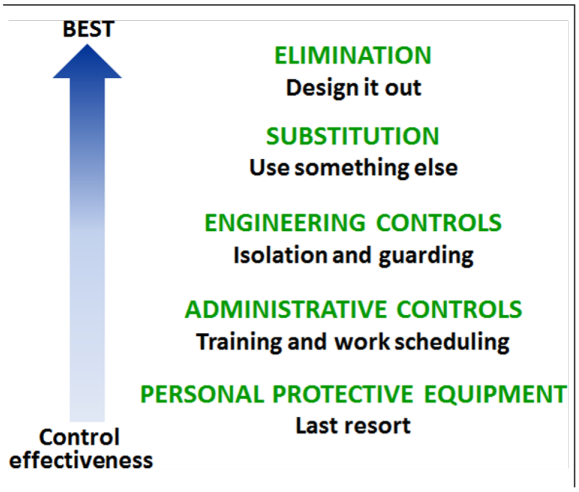

Figure 9.1: Hazard control effectiveness.

The EIC Project has completed a Preliminary Hazard Analysis Report (PHAR) to assure that identified hazards are mitigated early in the evolution of the design. The focus of the report is on process hazards rather than activity hazards that are typically covered in a job hazard analysis (JHA). The PHAR has been completed to identify the hazards anticipated to be encountered during the project's construction and operational phases.

The PHAR then looks at the consequences of the hazard to establish a pre-mitigation risk category. The hierarchy of controls is implemented as much as possible, in order of preference: Elimination, Substitution, Engineering Controls, Administrative Controls, and Personal Protective Equipment (PPE).

Proposed mitigations are applied to hazards of concern to mitigate risks and then establishes a post-mitigation risk category. As the EIC design matures, the PHAR is updated to ensure that all hazards have been properly identified and controlled through design and safety management system programs. The following sections describe the hazards in more detail and the design and operational controls used to mitigate them. The results of these evaluations confirm that the potential risks from construction, operations and maintenance are acceptable.

9.2.1 Electrical power supplies

The EIC will require many electrical and power supply systems to drive the various magnet and RF systems required to steer and collide the beams. A significant laboratory electrical power upgrade is needed to meet EIC's enhanced power supply requirements. Many additional substations will

be needed at each of the power supply houses and cryogenic buildings. Several of the systems requiring the additional electrical power include high-power solid state RF amplifiers for the ESR, HSR, and Crab cavities, larger capacity cryogenic system, and the new power supply buildings that will be located around the ring.

Electrical hazards from EIC include the potential for serious injury, death, and equipment damage. Electrical shock and arc flash can be caused by exposed live conductors, defective and substandard equipment, lack of adequate training, or improper procedures. Fire and smoke from defective equipment/components have been experienced at other accelerator complexes.

Particular attention will also be needed to address NFPA 70E requirements to protect workers against electrical arc flash and shock hazards. Arc flash analyses will be required prior to operation to ensure the proper labeling of all electrical panels and switch boxes. High voltage switches, breakers, etc. will be evaluated during design to provide remote operations where possible to eliminate the need for workers to have direct contact with the devices while operating them. Attention will also be applied during the design of electrical equipment to provide lock-out tag-out capability and to prevent the need to service energized components.

EIC will procure, install and use a large amount of high power and high voltage electrical equipment. Power distribution systems for EIC facilities will be designed in strict compliance with National Electric Code NFPA 70. Electrical transmission will be designed in accordance with the National Electrical Safety Code, ANSI C2 and OSHA 1910.269. All exposed surfaces for systems will be bonded to ground. Cable distribution will require particular care to ensure code compliance with cable tray loading and voltage rated content requirements. All electrical equipment and cables and cable trays will be protected against mechanical hazards.

9.2.2 Ionizing radiation

The primary hazard, prompt ionizing radiation, is limited to regions where the beam is maintained, and exists only when a beam is present. When the beam is turned off, minor amounts of residual activation in some accelerator components is expected, but based upon experience operating the RHIC, on-contact residual dose rates are expected to be a few micro-rem per hour above background and a few millirem per hour at beam dumps. This residual activity is mostly short-lived and decays quickly.

The hazard from exposure to the primary beam is present only when the machines are operating. Primary beam losses occur during machine instabilities, interaction with stripping foils, intrusive beam instrumentation, collimation, mistuned beam, and finally, when the beam strikes a beam dump. Typically, the hazards of neutrons dominate the design of the shielding for the hadron machines; above 10 GeV, muons can dominate the shielding requirement in the forward direction. For electron machines, Bremsstrahlung radiation is the most important consideration in the shielding design in the forward direction. All these potential sources of radiation cease as soon as EIC removes the electrical energy from the source; thereafter, only residual activity inside the accelerator enclosure will pose an exposure risk.

The EIC hadron beam radiation effects are currently being analyzed. Secondary radiation from hadrons will be much more significant than the secondary radiation from electrons and will drive the shielding analysis. Preliminary calculations indicate that the current soil berm shielding will be adequate. The locations of collimators and beam dumps will need evaluation and local shielding may be added or moved. In addition, an interlocked radiation monitoring system is planned that will limit the radiation levels outside the berm, and high levels beyond preset interlock setpoints will cause the beam to be dumped.

EIC employs semi-empirical methods and the CERN version of the FLUKA Monte Carlo radiation transport code for evaluating radiological hazards associated with beam operations. Shielding designs consider normal operations and unavoidable beam losses as well as worst-case beam losses which are the basis of maximum credible events (MCIs). EIC has developed a shielding policy that defines shielding performance criteria in terms of dose to people and maximum dose rate through the shielding. When the proposed shielding cannot meet the shielding policy criteria, additional controls are necessitated such as interlocking area radiation monitors.

9.2.3 Cryogenics and oxygen deficiency hazards

Much of the existing RHIC cryogenic plant will be re-used and upgraded for EIC. The RF system cryomodules require large amounts of cryogens (liquid nitrogen or helium) for cooling. In addition, superconducting magnets and detector components will be developed and tested using cryogens.

The release of a cryogenic liquid results in a quickly expanding vapor cloud which could displace the oxygen in the area. For this reason, oxygen deficiency hazards will be evaluated in each area and mitigations put into place to alleviate the hazard or prevent access. EIC will reuse a refurbished Vacuum ODH (VODH) system to provide early warning of a potential leak inside of a cryostat, and tunnel oxygen monitoring and interlocked fans will keep the oxygen deficiency to levels at ODH-0, as classified per BNL SBMS, and the proposed EIC design will not add significant quantities of cryogens or different types of components.

All piping systems and storage systems will be designed and installed to comply with applicable ASME and ANSI standards. Some specialized accelerator components that do not fall within code parameters will require engineering analysis to assure reliability. The BNL Pressure and Cryogenic Safety Sub-committee (PCSS) reviews and recommends approval of all cryogenic systems designs and installations.

With any cryogenic system there is a potential for thermal burns. The facility's distribution systems will be adequately marked and protected from inadvertent contact.

9.2.4 Chemicals and hazardous materials

Small quantities of chemicals and hazardous materials may be used during construction and accelerator operations. These chemicals will be included in BNL's Chemical Management System and used in accordance with the Chemical Hygiene Plan of the respective organizations, BNL or TJNAF or other collaborators. The Crab cavity prototypes will include chemical etching.

Demolition and construction activities may entail work with concrete and possible exposure to silica. Silica dust will be controlled using wet cutting or other approved work controls, as detailed in the Health and Safety Plans or work plans.

A potentially significant chemical hazard exists in the research/development and fabrication of cryomodule cavities at JLab. Various mixtures of acids are used, most notably containing hydrofluoric acid (HF). Worker hazards include burns, respiratory damage, and cardiac system impacts. Consequently, hazard mitigation is designed throughout the life-cycle of HF usage at JLab.

9.2.5 Material handling

Material handling will be applicable in almost every Work Breakdown Structure (WBS) element. The consequences of hazards encountered in material handling include serious injury or death to equipment operators and bystanders, damage to equipment, and interruption of the program. These hazards could be initiated by a dropped or shifted load, equipment failure, improper procedures, or insufficient training/qualification of operators. Operational experience across the DOE complex and with BNL accelerators with material handling related occurrences and injuries suggests that the post mitigation consequences are low because the probability of occurrence will be reduced through work planning and hazard analysis.

The nature of accelerator operations demands a significant amount of manual and mechanical material handling during construction as well as operation. The material/equipment being moved is typically one of a kind, potentially of high dollar or programmatic value, and generally may not have dedicated lifting points or an obvious center of gravity. Rigging/lifting plans will be developed for critical lifts. Qualified rigging personnel will be used for material handling with cranes and forklifts. In addition, manual lifting operations are evaluated for ergonomic issues using NIOSH guidelines.

9.2.6 Fire safety

Current project plans do not introduce new fire hazards. Combined with the DOE Accelerator Safety Order, the following codes and standards were used to assess fire safety risks:

- The Building Code of New York State 2020 Edition (BCNYS)
- The Fire Code of New York State (FC) 2020 Edition
- National Fire Protection Association (NFPA) Codes, Standards, and Recommended Practices (including the Life Safety Code)
- DOE-STD-1066 "Fire Protection"

Protection of lives, property, the environment, and programmatic continuity from the hazards of fire is the goal of the fire safety program. New facilities and renovations to existing facilities are being evaluated by BNL's Fire Protection Engineering staff through the life cycle of the project to ensure the fire safety goal is met.

All new construction with high valued electronic equipment will be provided with smoke detection in addition to any other fire protection system. Electronic equipment exceeding $250k loss potential or the ability to stop EIC operations for an extended period will be provided with smoke detection. The EIC tunnel will be provided with air aspirating smoke detection to provide early warning of developing fires and automatic sprinkler protection. Additionally, the fire standpipe system around the tunnel is at end of life and will be replaced.

9.2.7 Confined spaces

Entry into confined spaces may be necessary for equipment upgrades or access. Large vessels, tanks, and pits may be accessed during construction, installation, and operation. Atmospheres may be deficient in oxygen or may have other atmospheric contaminants. Ensuring adequate breathable

air is essential. Access will follow SBMS requirements for air monitoring or confined space permits as needed.

9.2.8 Mechanical hazards

Mechanical hazards may be present through various activities and kinds of equipment. The EIC project will include pressure and vacuum vessels and compressed gas systems. Some of these systems exist in the RHIC complex, and some will be new systems and equipment. Careful evaluation will be required for all pressure and vacuum systems during design, construction, and installation.

Machine shops will be used throughout the EIC complex. All machines are evaluated for compliance with current SBMS safety requirements. Machine shop stewards oversee operations and ensure all personnel using machines are trained.

9.2.9 Construction hazards

Conventional construction hazards will be present during the construction period of the project. Construction will begin with the clearing and grubbing of about 50 acres around the tunnel following the conclusion of RHIC operations to facilitate the addition of about 18 new buildings including the electron injector complex on the outside of the ring at the 4 o'clock sector.

9.3 Radiological design goals

The EIC Project will follow the facility design requirements in 10 CFR 835 and as codified in the BNL Radiological Control Manual, specifically, facilities designed for continuous occupancy will limit average dose rates to no more than 0.5 mem/hr. such that staff will not exceed 1,000 mrem/year. Specific requirements are contained in the EIC Shielding Policy which also includes optimization goals to further lower facility doses, for example, designing to less than 0.05 mrem/hr. in some facilities such that monitoring workers with dosimeters is not required.

The design and operation of all radiation producing facilities is governed by the As Low As Reasonably Achievable (ALARA) policy. BNL has historically maintained radiation dose limits well below regulatory limits.

Shielding designs will be supplemented with active area monitoring devices that will interlock the beam if elevated dose rates are detected outside the shielding. Active area monitor locations will be selected based upon areas where routine beam losses or maximum credible beam losses are likely.

9.4 Safety by design

Safety by design or Prevention through Design (PtD) is a process to integrate hazard identification and risk assessment early in the design process to eliminate or minimize risks throughout the life cycle of the system being designed. The process encourages engineers and designers to control risks to workers and the environment to an acceptable level "at the source" or as early as possible in the life cycle of the equipment.

PtD involves evaluating potential risks associated with processes, equipment and structures. It takes into consideration the product life cycle phases from design through disposal and increases the cost-effectiveness of enhancements to occupational safety and health.

Moving safety implementation upstream in the design process helps to controls risks early in the design process. Several benefits include:

- Prevent or reduce occupationally related injuries, illnesses, and fatalities
- Fewer delays due to accidents or unwanted outcomes
- Increase productivity
- Reduce operating costs
- Improved communications between engineers with interfaces between systems
- Improved specifications and interface documents
- Reduce retrofitting to correct design shortcomings

The PtD process has been integrated into the EIC project. The process involves ESH staff working with system designers to help identify and document the hazards at each life cycle stage of their deliverable. Mitigations are identified to reduce risks and in some instances includes special tooling to reduce ergonomic risks to workers. Project documentation is updated to include the identified mitigations into the design.

9.5 Safety authorization and the Accelerator Readiness Review process

EIC accelerators commissioning and operations are subject to the DOE Order 420.2D requirement to perform an Accelerator Readiness Review (ARR) prior to commissioning and routine operations. All 420.2D requirements are implemented via BNL's Accelerator Safety Subject Area in SBMS.

ARR Teams will be formed and consist largely of accelerator operations staff from other national laboratories. Lines of inquiry will be developed by EIC and provided to the ARR Teams to guide their readiness review of the people, equipment, and procedures needed to safely operate each accelerator.

A Safety Analysis Document (SAD) and Accelerator Safety Envelope (ASE) will be prepared for each accelerator and will in large part be based on the content of the Preliminary Hazards Analysis Report. Special attention will be given to the prompt and residual radiological conditions produced in the accelerators including maximum credible incidents (MCIs), activation levels, and environmental emissions, if any. Credited engineered and administrative controls will be derived in the SAD and identified in the ASE. Credited controls are a subset of all controls that are essential to protect people and the environment. Each SAD will be internally reviewed and approved by the EIC Project Director and BNL ESH Associate Laboratory Director. Each ASE will be approved by the DOE Brookhaven Site Office (BHSO).

9.6 Beam losses and residual activation

For Maximum Credible Incidents (MCIs) it is assuming that the full stored beam impacts on possible beam intercepting devices (collimators and dump), and half the stored beam impacts at a 1 mrad grazing angle with the beam pipe. For long term losses that are relevant for activation, the three primary locations that are designed to intercept beam are the hadron beam dump (re-used from RHIC), the electron beam spent-beam absorber (or transfer absorber), and the hadron and electron beam collimators.

Residual activation levels in the hadron beam dump are estimated from dose rate measurements taken at the RHIC beam dumps during the nearly 25 years of operations, and then scaled to the expected number of fills per year and the expected beam intensities. Activation levels scale linearly with the EIC hadron beam current, which for protons is about 60% higher than for RHIC. Short-term dose rates measured a few hours after a RHIC run varied between a few tens of mrem/h to as high as 100 mrem/h at one foot. After the short-lived radioactivity has died away, the measured longer-term dose rates were 5 to 10 mrem/h at one foot.

Preliminary FLUKA simulations have been performed for the early design of the electron spent-beam absorber, receiving 10 GeV pulses of 1.7×10^{17} electrons once per second for about 3,000 hours per year. Dose rates on the soil berm directly above the absorber are expected to be close to background levels. Absorber residual dose rates are expected to be about 10 mrem/h at one foot from the absorber without shielding. Several inches of stainless steel will shield the dump. Electron collimator locations are not yer finalized. Estimates of the annual cumulative beam losses on the collimators have not yet been determined, and so preliminary estimates of collimator activation levels have not yet been assessed. Collimator radiation levels are expected to be no higher than the in the electron spent-beam absorber.

9.7 Shielding evaluation

Independent FLUKA simulations have been run for electron beams at 18, 10, 5, and 0.75 GeV; for proton beams at 275 GeV and 255 GeV; and for gold ions at 110 and 100 GeV/u. Simulations were performed for beam angles of 90°, 45° and 1°. One-degree grazing is of the range sometimes used to estimate routine (or chronic) beam losses. Shielding materials evaluated include Portland concrete and local soil, with densities of 2.3 g.cm^{-3} and 1.6 g.cm $^{-3}$, respectively. Actual tunnel geometries have not yet been considered in the simulations. Add references, if there are any: "Results will be incorporated into a BNL Technical Note"

Data are plotted and tabulated at shielding depths corresponding to the upper edge of the bin, i.e., dose shown at x cm would be the binned averaged dose after traversing x cm of concrete or soil. Data are reported in rem per primary (electron, proton or gold ion) started. The physicist of the facility would multiply this value with the beam intensity (number of primaries [electrons, protons or gold ions] per hour) to obtain the effective dose rate in rem/h. Data tabulated and plotted in this way are to serve as a lookup reference which would remain applicable even as preliminary design layouts evolve. Simulations of specific, local built facilities/environments will follow when three-dimensional descriptions become available.

9.8 Unreviewed Safety Issue process

BNL has instituted a laboratory-wide Unreviewed Safety Issue (USI) process for all accelerators operating at beam energies greater than 10 MeV as required by DOE Order 420.2D. The USI process is contained in the Accelerator Safety Subject Area. The EIC will institute this USI process.

The USI process is used to determine who must approve planned accelerator changes or discovered conditions that are outside the bounds of the facility safety analysis. Changes that represent risks not bounded by the ASE must be approved by DOE-BHSO. Changes that are bound by the ASE but that are not sufficiently analyzed by the SAD may in most cases be approved by facility management in concert with the BNL ESH Associate Laboratory Director with notification to the DOE-BHSO.

9.9 Tunnel fire protection

A preliminary fire hazard analysis (PFHA - July 2023) has been developed for EIC facilities, including the tunnel, fulfilling the requirement for documentation of a PFHA as outlined in DOE Order 420.1C, Facility Safety. The PFHA documents a list of anticipated fire safety changes for the existing facilities:

- To eliminate the need for the current exemption request from the code requirement on maximum travel distance between exits, automatic sprinkler protection will be provided.
- Replace the fire standpipe due to concerns over Microbial Induced Corrosion attacking the pipe.
- Replace the spot heat detection with air-aspirating detection to improve fire detection sensitivity, provide a redundant level of protection for the high-value magnet systems, minimize smoke detector damage due to radiation exposure, and to provide a system not blocked by cable trays for maintenance access.
- Replace the obsolete fire alarm control panels around the tunnel.
- Replace cooling tower 7 (wooden structure) with a tower of limited combustibles.
- Minimize the impact of a potential wildland fire on EIC operations by continuing to implement recommendations from the BNL Wildland Urban Interface Summary (2019).

9.10 Environmental protection and the National Environmental Policy Act

The addition of new power supply, pumphouse, satellite cryogenics and RF support buildings and related tunnel decommissioning and construction activities were the subject of an Environmental Assessment (EA) under the National Environmental Protection Act (NEPA), for which a Categorical Exclusion was granted in CY2021 by DOE.

In late CY2024, to resolve several technical issues, the EIC project decided to relocate the RCS ring from the tunnel, and the linear accelerator injector, to an outside area adjacent to the 4 o'clock sector

of the tunnel. The new electron injector system will reside on about 65 acres of undisturbed property. It was not clear that this area was included in the CY2021 Categorical Exclusion. The EIC and BNL's Environmental Protection Division worked with DOE-BHSO to provide a supplemental Environmental Evaluation Notification Form describing the impacts to the undisturbed site. In June 2025 DOE-BHSO found that the changes in potential environmental impacts from the proposed modifications were negligible and that no further NEPA review was required.

9.11 Code compliance

Codes and consensus standards are developed to protect the public health, safety, and welfare.

Codes and standards function as requirements for engineers and designers of buildings and equipment. The EIC Project has implemented a Code of Record which provides code requirements (e.g., NFPA, NEC, ASME, etc.) applicable to all construction and project design work performed by or for the EIC Project.

Additionally, the Systems Engineering Group manages the requirements for all engineering tasks. Systems engineering documentation identifies the requirements and how cost account managers (CAMs) develop functional requirements for their respective deliverables. The functional and performance requirements tie back to the Global Requirements Document, which refers to the Code of Record, and drives the downstream technical designs.

Chapter 10

System Engineering and Quality Management (editors: T. Russo, C. Porretto)

Chapter 11

Integration and Installation (editor: Tuozzolo)

11.1 Introduction

The Installation and Integration scope for the EIC plans, coordinates, schedules, and manages work for multiple beam line accelerator systems in the EIC tunnel and their associated systems in the service buildings. This includes Superconducting and Normal Conducting Magnets, Power Supplies, Cable Plant, Controls, Cryogenics, RF, Beam Instrumentation, and Vacuum Systems.

Accelerator systems project managers, engineers, and designers are responsible for designing their systems for installation. This includes design of stands, survey points for proper location, vacuum design and beam line vacuum flange locations, any special installation lifting/transport fixtures, and other system specific equipment (such as vacuum leak detectors, system oscilloscopes, portable cleanrooms, etc). Accelerator system technicians and engineers will be responsible for their system installation. Installation of infrastructure systems and components is covered in infrastructure.

As noted in the following sections, the staging and scheduling installation of beam line components is dependent on infrastructure modifications to existing RHIC facility to adapt them to the EIC and the approved building occupancy dates for new support buildings and associated infrastructure. The ePIC detector assembly and installation is also a separate effort; but, as noted in the following sections, requires some infrastructure modifications to mitigate baseline schedule and installation staging difficulties between the detector and accelerator systems.

11.2 Integration

11.2.1 Electron and Hadron Storage Rings

Integration of accelerator beam line components is performed during the design process in the EIC tunnel by the Technical Systems Division Mechanical Engineering group. Area managers have been assigned for each of the six EIC tunnel interaction straight section regions and an area manager for the six arcs.

HSR and ESR magnet locations and beam trajectory with aperture requirements from the EIC physics teams are laid into the tunnel 3D model. From this approved baseline, magnet models and other component models from the various accelerator systems are installed in the model. This includes accelerator support systems: cryogenic distribution, cable and cable tray, water distribution, waveguide/coax, and infrastructure.

Area review meetings are ongoing to deal with component-to-component interferences and interfaces as well as ease of installation and maintenance. These area models will be baselined and approved prior to the Installation and System Integration Preliminary Design Review.

New and existing RHIC service buildings have also been 3D modeled. These buildings contain magnet power supplies, RF power amplifier systems, beam instrumentation, vacuum, and cryogenic system support electronics. The full models will also include the cable tray, cable, and RF coax/waveguide locations.

The existing RHIC service building models have been reviewed to note the removal of obsolete RHIC components that will not be needed for the HSR so the space can be reused for EIC components including ESR electronics.

The area manager team actively participates in component design reviews to maintain close coordination. Preliminary Design Review activities will be completed before CD2/3 in June 2026, ensuring that all requirements, interfaces, scheduling, and resource forecasts align with technical group planning.

11.3 Installation

11.3.1 Electron and Hadron Storage Ring tunnel systems

Accelerator system installation for EIC will be staged to allow various systems to be installed in an organized fashion. For subproject one, the RHIC tunnel design and the obsolete removals schedule provides the need for staging and interface.

The RHIC tunnel has major access points at the 6 interaction regions. The interconnecting arcs have the smallest cross-section and have personnel space limitations in arcs 01 and 11 where the ESR and HSR are both on the inner or outer radius of the tunnel.

Arc installation is being carefully planned to ensure both major systems are installed in the interaction regions before moving equipment into the arcs becomes more difficult.

In the EIC main tunnel arcs, the work will be staged with the removals effort for the RHIC blue magnets and the infrastructure modifications needed before ESR installation. The installation effort in each arc will follow this order:

1. Removal of adjacent IR beam line equipment to provide space for arc equipment removal and installed equipment staging. (IR08 and IR12 have direct access tunnels that provide some flexibility).
2. Removal of DX.
3. Removals of obsolete blue cables and ancillary equipment from the blue cryostats. Removal of any obsolete infrastructure.
4. Removal of blue superconducting magnets.

5. Removal of yellow superconducting magnet bellows assembly (this will be delayed until the beam screens are available for installation).
6. Installation of the yellow beam screens.
7. Re-installation of Siberian Snake magnets, DU7 cryostats, and other arc magnet modifications.
8. Infrastructure installations (ESR water cooling lines, additional cable trays and cable tray modifications, fire lines, tunnel HVAC system modifications, power distribution modifications, tunnel penetrations, outdoor cable tray, etc.)
9. ESR and HSR cable installation (after service building and BPM building installation and BORE dates).
10. ESR magnet girder installation and beam line assembly.

For the EIC main tunnel interaction regions (IR), the work will depend on equipment ready-for-installation date and the location of the ESR relative to the HSR. Access to the IR regions differs across the six IRs:

- **IR12** has magnet insertion tunnels on both sides.
- **IR04** has an open central staging area offering installation flexibility.
- **IR02 and IR10** have single direct entrances with limited rigging room.
- **IR08** features a large detector hall with a high-capacity crane and adjacent staging areas.
- **IR06** poses the greatest challenge for beamline component access due to conflicts with the detector assembly. The current access is via the experimental hall, limiting logistics. Some mitigation is planned via former RHIC X line tunnel access and new equipment access tunnels, though these are not yet funded.

11.3.2 Support buildings

The installation of supporting power supplies, beam line component electronics, and accelerator support system electronics in the service buildings should have some flexibility, as most buildings have good access and most equipment fits standard rack sizes. Integration of the system electronics in detailed building 3D models will support the planning and execution of this phase.

Chapter 12

Commissioning (editor: Blednykh)

12.1 Objectives

The primary objective of the EIC commissioning phase is to systematically bring the accelerator complex into an operational state that satisfies all performance, safety, and reliability criteria required to initiate scientific operations. Beam commissioning of the electron injector (LINAC and RCS), the Electron Storage Ring (ESR), and the Hadron Storage Ring (HSR) will be conducted in progressive stages, with increasing complexity and beam capabilities. This process will be aligned with the achievement of the project's Key Performance Parameters (KPPs), a staged increase in beam intensity, and the overall readiness for the physics program.

Commissioning objectives include:

- Commissioning of the Main Control Room (MCR), including verification of the new control system functionality with the integrated EPICS system, connectivity to accelerator subsystems, integration with safety and machine protection systems, and demonstration of operational readiness through simulations and operator training.
- System commissioning and verification of integrated performance across all major accelerator subsystems (e.g., RF, cryogenics, magnet power supplies, vacuum, diagnostics, timing, controls, and machine protection). This includes completion of an Internal Readiness Review (IRR) to ensure all systems are installed, connected, tested, and integrated prior to beam commissioning.
- Execution of the Accelerator Readiness Review (ARR), a formal DOE-required process that confirms all safety systems, operational procedures, trained personnel, and documentation are in place before initiating beam injection.
- Commissioning of beam injection, acceleration, circulation, and extraction processes in both the ESR and HSR.
- Beam-based alignment, lattice verification, and optics tuning, using trajectory and response matrix measurements to confirm proper beam transport and magnet polarity.
- Establishment and measurement of electron beam polarization during early commissioning stages. Hadron beam polarization systems will be commissioned in subsequent phases once polarized light ion species (e.g., deuterons, protons, He-3) are introduced.

- Commissioning and system-level integration of the crab cavity systems, which are essential for achieving high luminosity during later operation. Activities during commissioning will focus on RF conditioning, phase stability, timing synchronization, and initial evaluation of beam dynamics impact.
- Completion of detector installation and integration, including mechanical alignment, infrastructure commissioning, and interface testing with accelerator timing and control systems.
- Beam collision commissioning, including the establishment of stable beam-beam overlap in the interaction region, confirmation of collision vertex location, and validation of detector response under live beam conditions.
- Execution of final safety reviews, control system readiness checks, and operational planning necessary to support the transition to early physics operations following the achievement of the Threshold KPPs.
- Development and execution of a detailed commissioning plan that defines subsystem readiness criteria, test procedures, beam commissioning sequences, safety checks, and integration milestones to support an efficient transition to operations.

12.1.1 Rapid Cycling Synchrotron

Commissioning with normal-conducting cavities is planned to accelerate electrons from 0.750 to 5 GeV during the early phase of beam commissioning, while the superconducting RF system and cryogenic infrastructure are being prepared. Following this phase, the initial installation of two 591 MHz, 5-cell superconducting RF (SRF) cavities will replace the NC RF cavities and provide sufficient accelerating voltage to extend the energy range from 750 MeV to 10 GeV. Figure 12.1 shows the RF power that can be delivered by two installed 591 MHz, 5-cell SRF cavities as a function of beam energy and bunch charge. In alignment with the first-year science goals, this configuration provides sufficient RF power to accelerate the beam to 10 GeV with a bunch charge of 28 nC. This value represents the maximum bunch charge required to be delivered to the RCS and subsequently to the ESR. To achieve this, the Beam Accumulator Ring (BAR) must accumulate charge from multiple 1.5 nC injections from the LINAC, reaching the full 28 nC per bunch prior to transfer into the RCS. Ensuring that this charge level can be achieved in the RCS from the first day of beam commissioning represents a significant integration and performance milestone.

12.1.2 Electron Storage Ring

- Main RF cavities and beam intensity ?
- The planned installation of crab cavities for collisions with a crossing angle?

12.2 Threshold Key Performance Parameters

Threshold KPPs represent the minimum required operational performance for the project to be considered successful by DOE standards. Injection, capture, and intensity of 50 mA (electrons) in the ESR and 40 mA (heavy ions) in the HSR.

The physics programm begins after 6 months of beam commissioning followed by achievement of threshold KPPs.

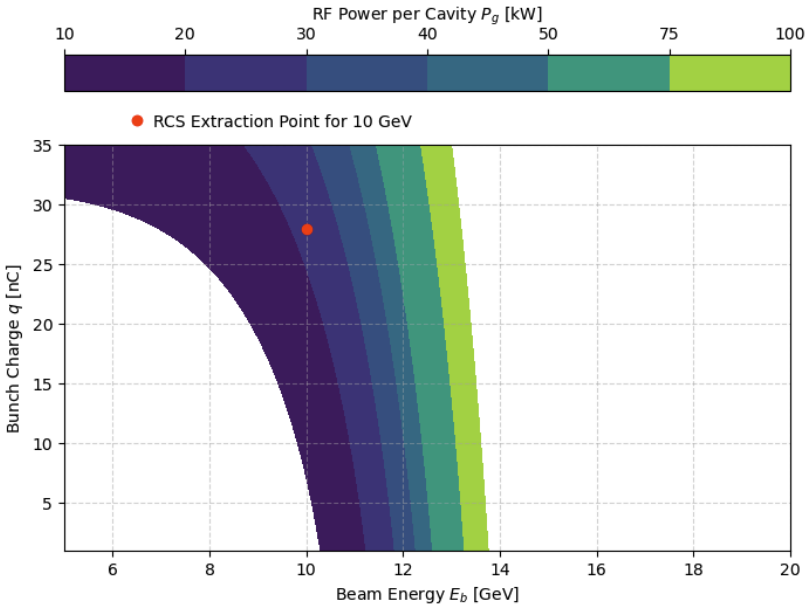

Figure 12.1: RF power per cavity P_g [kW] as a function of beam energy and bunch charge. The color map indicates the required power per cavity to accelerate the electron beam using two 591 MHz, 5-cell SRF cavities. The red dot marks the RCS extraction point at $E_b = 10\,\text{GeV}$ and $q = 28\,\text{nC}$, demonstrating that sufficient accelerating voltage can be delivered without exceeding the RF power limits of the installed cavities at this stage.

Objective KPPs are **... (This needs to be completed in accordance with the agreement with the DOE)**.

12.3 Integration with Early Science (Elke will help)

The transition from accelerator commissioning to the early science program at the EIC is designed as a phased and coordinated process, tightly integrated with the progressive readiness of both the collider complex and detector systems. The start of the science program depends on the successful installation of the central detector (ePIC) and its critical auxiliary systems, followed by beam commissioning through to the first collisions under stable and well-characterized beam conditions.

The physics program will begin after the threshold Key Performance Parameter (KPP) is achieved, initial beam commissioning is completed, and the detector is installed and integrated. Beam commissioning will continue in parallel with early physics operations to reach the objective KPPs.

Beam commissioning in the Hadron Storage Ring (HSR) will begin with heavy-ion beams at energies that do not require significant radial shifts, which would otherwise complicate commissioning, and that satisfy the early science program requirements. The heavy-ion beams will initially collide with unpolarized electrons at 10 GeV. This initial running phase is chosen to minimize complexity while enabling meaningful physics opportunities, particularly in nuclear structure. During this period, the electron injector (LINAC and RCS) and the Electron Storage Ring (ESR) will also be commissioned to deliver polarized electron beams. However, full operational polarization and luminosity performance will continue to evolve throughout the early years in accordance with the

detailed commissioning plan and the scheduled beam intensity increases.

First-year operational goals

During the first year of operations, beam parameters will continue to evolve as commissioning progresses in parallel with initial physics running. The delivery of physics data will be phased to align with machine protection readiness, including collimation system commissioning and the establishment of stable beam conditions to ensure detector safety.

The science program aims to deliver an integrated luminosity of $0.7\,\mathrm{fb}^{-1}$ over 30 weeks for heavy ions (REFERENCE TO SCIENCE PROGRAM DOCUMENT), which corresponds to an average luminosity of approximately $5.4 \times 10^{31}\,\mathrm{cm}^{-2}\,\mathrm{s}^{-1}$, accounting for an operational efficiency of 5/7 (weekly uptime).

Assuming there will be no low-energy cooler or stochastic cooling available in the HSR from the first day of commissioning, the initial beam parameters, especially beam sizes, will be based on the natural lattice and RF configuration, without cooling enhancements.

In Figure 12.2, Figure 12.3, and Figure 12.4, the average and instantaneous luminosity are presented for three different heavy-ion species colliding with 10 GeV electron beams: silver (Ag) at 118 GeV/u, niobium (Nb) at 121 GeV/u, and gold (Au) at 110 GeV/u. Four operational scenarios are compared: without cooling, with stochastic cooling (STC) only, with low-energy cooling only, and with both stochastic and low-energy cooling. The results demonstrate that cooling schemes significantly enhance both the instantaneous and average luminosities over a 10-hour store, with the combined STC and low-energy cooling providing the highest performance.

The beam parameters for gold-electron, niobium-electron, and silver-electron collisions are summarized in Table 12.1, Table 12.2 and Table 12.3. These tables present the key design inputs used in the luminosity estimates, including beam energy, number of bunches, bunch intensity, transverse emittance, β^* values at the interaction point, and bunch length. Together, these parameters establish the foundation for the projected integrated luminosity and define the operating envelope for the hadron storage ring optics as well as the beam-beam interaction considerations. Also in the table are the initial luminosities when the detector is switched on and the optimal average luminosity, calculated assuming one hour of deadtime between ion stores and zero luminosity during the first 15 minutes of the ion store, while we are filling electrons and turning on the detector.

To achieve the required peak luminosity without cooling, an average heavy-ion beam current of $I_{\mathrm{av}} \approx 90\,\mathrm{mA}$ with $M = 290$ bunches is considered in the HSR. Based on the expected capabilities of the electron injector system during the early days of commissioning, a bunch charge of 28 nC (corresponding to a single-bunch current $I_0 = 2.2\,\mathrm{mA}$) within $M = 290$ bunches is assumed in the ESR, resulting in an average electron beam current of $\sim 625\,\mathrm{mA}$.

This scenario assumes uncooled beams with horizontal beam size $\sigma_x \approx 110\,\mu\mathrm{m}$ and vertical beam size of $\sigma_y \approx 40\,\mu\mathrm{m}$ for niobium and silver. For gold, the uncooled beam sizes are somewhat larger, at $\sim 140\,\mu\mathrm{m}$ horizontal and $\sim 55\,\mu\mathrm{m}$ vertical. The actual current distribution may vary, with higher current in the ESR and lower in the HSR, depending on the commissioning status of each ring.

Based on the average luminosities ($1.0 \times 10^{32}\mathrm{cm}^{-2}\mathrm{s}^{-1}$ for silver and niobium and $0.6 \times 10^{32}\mathrm{cm}^{-2}\mathrm{s}^{-1}$ for gold), the science goal of delivering an average luminosity of $\langle L \rangle = 5.4 \times 10^{31}\,\mathrm{cm}^{-2}\mathrm{s}^{-1}$ ($0.7\,\mathrm{fb}^{-1}$ over 30 weeks) is satisfied in all three cases without cooling. In the reference scenario, this is achieved with an electron bunch charge of 28 nC, corresponding to an average ESR current of $\sim 625\,\mathrm{mA}$. This choice represents an ambitious but technically feasible target for early

	Without Low-Energy Cooling		With Low-Energy Cooling	
Species	Ag-109	Electrons	Ag-109	Electrons
Beam Energy (GeV/u)	118	10	118	10
Bunch Population (10^{10})	0.0515	17.2	0.0988	17.2
Number of Bunches	290	290	290	290
Beam Current (mA)	88	625	169	625
Emittance h/v (nm)	15.8 / 15.8	20 / 3	34.1 / 2.4	20 / 2.4
β^* h/v (cm)	80 / 10.9	63.2 / 57.7	151.4 / 9	257.8 / 8.9
Bunch Length (mm)	90	7	90	7
RMS $\Delta p/p$ (10^{-4})	7	5.8	7	5.8
Initial Luminosity ($10^{32}\,\mathrm{cm}^{-2}\mathrm{s}^{-1}$)	2.2		5.2	
Average Luminosity ($10^{32}\,\mathrm{cm}^{-2}\mathrm{s}^{-1}$)	1.0		1.7	

Table 12.1: Parameters for 118 GeV/u silver for early science. Average luminosities are calculated assuming 1 hour between ion stores and 0 luminosity during the first 15 minutes of the store while we fill the electrons and turn on the detector.

	Without Low-Energy Cooling		With Low-Energy Cooling	
Species	Nb-93	Electrons	Nb-93	Electrons
Beam Energy (GeV/u)	121	10	121	10
Bunch Population (10^{10})	0.0595	17.2	0.113	17.2
Number of Bunches	290	290	290	290
Beam Current (mA)	89	625	168	625
Emittance h/v (nm)	15.5 / 15.5	20 / 3	31.4 / 2.3	20 / 2.3
β^* h/v (cm)	80 / 10.7	62 / 55.5	139.5 / 9	219 / 9.2
Bunch Length (mm)	90	7	90	7
RMS $\Delta p/p$ (10^{-4})	7	5.8	7	5.8
Initial Luminosity ($10^{32}\,\mathrm{cm}^{-2}\mathrm{s}^{-1}$)	2.3		5.6	
Average Luminosity ($10^{32}\,\mathrm{cm}^{-2}\mathrm{s}^{-1}$)	1.0		1.9	

Table 12.2: Parameters for 121 GeV/u niobium for early science. Average luminosities are calculated assuming 1 hour between ion stores and 0 luminosity during the first 15 minutes of the store while we fill the electrons and turn on the detector.

operations, requiring efficient accumulation in the BAR. A more moderate scenario with 15 nC per bunch ($\sim$ 312 mA average current) for silver or niobium would still provide luminosities above the required $\langle L \rangle = 5.4 \times 10^{31}\,\mathrm{cm}^{-2}\,\mathrm{s}^{-1}$, indicating that the electron average current could be reduced while maintaining the program goals.

12.4 Transition to operations

The transition from construction to full operations for the Electron-Ion Collider (EIC) will follow a structured and phased approach as outlined in the Project Transition to Operations Plan (PTOP)

	Without Low-Energy Cooling		With Low-Energy Cooling	
Species	Au-197	Electrons	Au-197	Electrons
Beam Energy (GeV/u)	110	10	110	10
Bunch Population (10^{10})	0.029	17.2	0.059	17.2
Number of Bunches	290	290	290	290
Beam Current (mA)	83	625	170	625
Emittance h/v (nm)	21.2 / 21.2	20 / 3	35.7 / 6	20 / 2.2
β^* h/v (cm)	94.2 / 14.7	99.9 / 103.7	158.5 / 9	282.7 / 24.4
Bunch Length (mm)	90	7	90	7
RMS $\Delta p/p$ (10^{-4})	7	5.8	7	5.8
Initial Luminosity ($10^{32}\,\mathrm{cm}^{-2}\mathrm{s}^{-1}$)	1.5		3.6	
Average Luminosity ($10^{32}\,\mathrm{cm}^{-2}\mathrm{s}^{-1}$)	0.6		1.3	

Table 12.3: Parameters for 110 GeV/u gold for early science. Average luminosities are calculated assuming 1 hour between ion stores and 0 luminosity during the first 15 minutes of the store while we fill the electrons and turn on the detector.

[Ref: Project Transition to Operations Plan, August 30, 2024]. This plan ensures the safe and efficient handover of accelerator, infrastructure, and detector systems to the EIC Operating Organization (EOO). Key steps include completion of construction and installation, successful Beneficial Occupancy Readiness Evaluations (BOREs), Instrument and Accelerator Readiness Reviews (IRR/ARRs), and phased commissioning of technical systems, culminating in the DOE Critical Decision-4 (CD-4) milestone. Transition activities are closely coordinated through an Integrated Transition Management Team (ITMT) and cover infrastructure readiness, system safety documentation (SAD/ASE), staff training, operational documentation, and stakeholder alignment. Each accelerator and subsystem is brought online progressively, leading to full operational status and enabling the start of the science program.

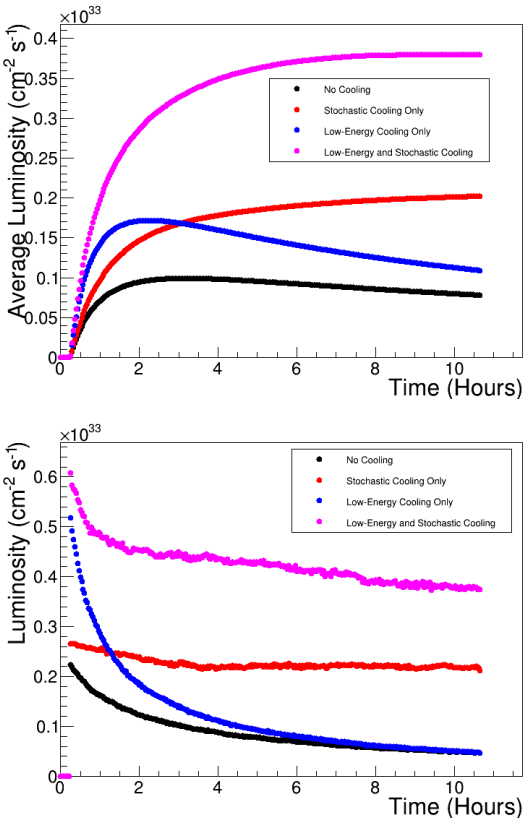

Figure 12.2: Average and instantaneous luminosity for 118 GeV/u silver colliding with 10 GeV electrons in four different scenarios. The black trace represents the case without stochastic or low-energy cooling, modeled with a non-zero crabbing angle and corrected only by the 197 MHz hadron crab cavity. The red trace shows the results with stochastic cooling (STC) only, the blue trace shows the results with low-energy cooling only, and the pink trace includes both STC and low-energy cooling. Average luminosities are calculated assuming 1 hour between ion stores and 0 luminosity during the first 15 minutes of the store while we fill the electrons and turn on the detector.

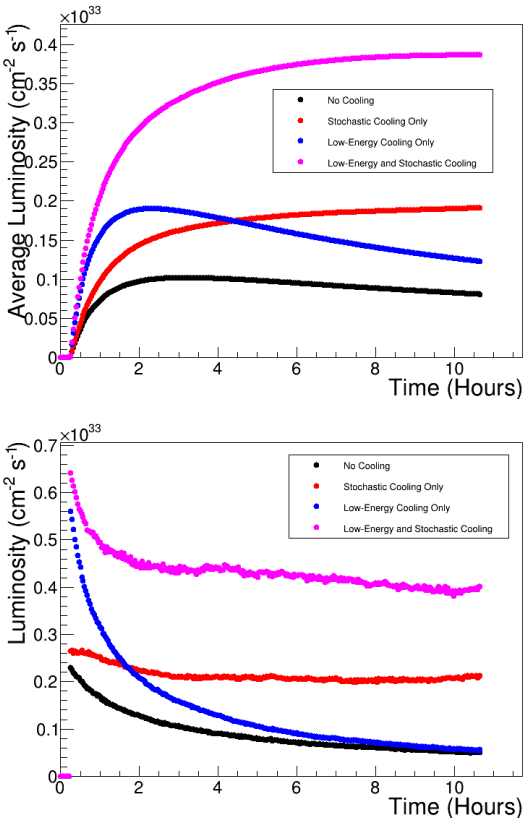

Figure 12.3: Average and instantaneous luminosity for 121 GeV/u niobium colliding with 10 GeV electrons in four different scenarios. The black trace represents the case without stochastic or low-energy cooling, modeled with a non-zero crabbing angle and corrected only by the 197 MHz hadron crab cavity. The red trace shows the results with stochastic cooling (STC) only, the blue trace shows the results with low-energy cooling only, and the pink trace includes both STC and low-energy cooling. Average luminosities are calculated assuming 1 hour between ion stores and 0 luminosity during the first 15 minutes of the store while we fill the electrons and turn on the detector.

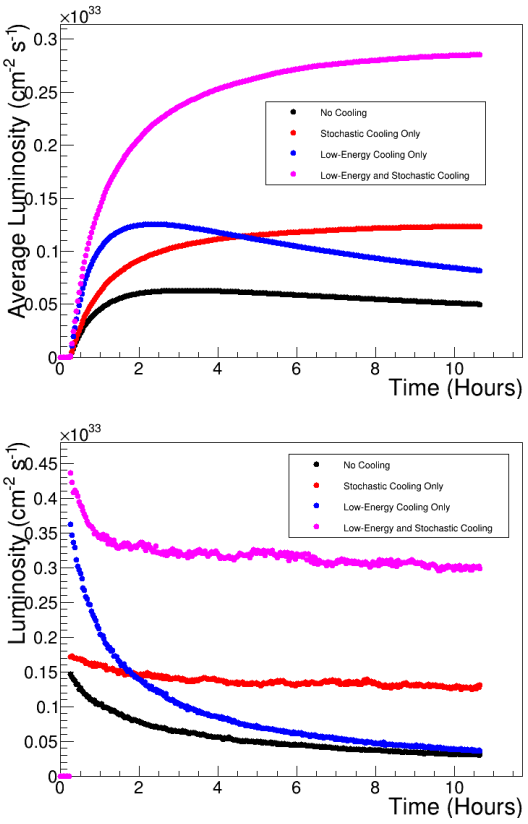

Figure 12.4: Average and instantaneous luminosity for 110 GeV/u gold colliding with 10 GeV electrons in four different scenarios. The black trace represents the case without stochastic or low-energy cooling, modeled with a non-zero crabbing angle and corrected only by the 197 MHz hadron crab cavity. The red trace shows the results with stochastic cooling (STC) only, the blue trace shows the results with low-energy cooling only, and the pink trace includes both STC and low-energy cooling. Average luminosities are calculated assuming 1 hour between ion stores and 0 luminosity during the first 15 minutes of the store while we fill the electrons and turn on the detector.

Appendix A

Global Parameter Tables (editors: Peggs, Satogata)

A.1 Electron Injector

The **Electron Injector** complex generates, accumulates, accelerates, and injects up to two 28 nC polarized electron bunches per second into the Electron Storage Ring. The complex minimizes intensity and polarization loss, and ensures reliable operation.

The **Preinjector** produces bunches with a charge as large as 1 nC at a rate of 30 Hz, and accelerates them to 750 MeV. Many bunches are accumulated into a single bunch with an intensity as large as 28 nC in the Beam Accumulator Ring, before being transferred to the Rapid Cycling Synchrotron, where they are further accelerated to a final energy in the range from 5 to 18 GeV. Beam is then extracted from the RCS and transported to the constant-energy Electron Storage Ring. The Preinjector consists of a High Voltage Direct Current (HVDC) polarized electron gun, a spin rotator, a ballistic bunching section employing a buncher and drift, a capture cavity, and a Traveling Wave (TW) linear accelerator. It includes a gun diagnostics beamline, a spin diagnostics beamline with Mott polarimetry, and energy spectrum diagnostics.

The **Beam Accumulator Ring** is a constant-energy storage ring dedicated to accumulating a single full intensity bunch from many electron linac bunches. Single bunches from BAR are injected into the RCS.

The **Rapid Cycling Synchrotron** accepts vertically polarized electron bunches from the Beam Accumulator Ring, or directly from the Preinjector, and accelerates them for delivery to the RCS-to-ESR transport line and the Electron Storage Ring.

Parameter	Unit	Value
General		
Beam extraction energy	MeV	750
Beam repetition rate	Hz	30
Energy spread at end of linac	%	0.25
Normalized RMS horizontal emittance	µm	60
Normalized RMS vertical emittance	µm	40
Bunch charge	nC	1
Polarization direction		Vertical
Polarization	%	$\geq$86
RMS bunch length	mm	0.75
Electron Gun		
Gun voltage	kV	310
Bunch length	ps	300
Laser parameters		
Laser pulse energy	µJ	≤ 6
Wave length tunable range	nm	760 -790
Repetition rate	Hz	30
Polarization	%	90
Polarization switch speed		1 Hz in 30 ms
Pulse duration	ps	200 - 350
Timing jitter (RMS)	ps	< 3
Low Energy RF		
Buncher frequency	MHz	197
Buncher voltage	kV	500
Capture cavities frequency	MHz	1300
Capture cavity 1 voltage	MV	5
Capture cavity 2 voltage	MV	10
Electron Linac		
Number of TW accelerating units		14
Linac frequency	MHz	2856
Linac voltage	MV	60

Table A.1: Preinjector lattice parameters. Electron polarization is longitudinal for 1.7 m from the gun to the spin rotator, where it is rotated to the vertical direction for the rest of the ESR injection process.

Parameter	Unit	Value
General		
Number of bunches		1
Bunch length	mm	43
Betatron tune, H		3.12
V		1.18
Injection		
Energy	MeV	750
Polarization	%	86
Bunch charge	nC	1
Repetition rate	Hz	30
Horizontal RMS emittance (norm)	µm	∼30
Vertical RMS emittance (norm)	µm	∼50
RMS energy spread		0.0045
Extraction		
Energy	MeV	750
Polarization	%	86
Bunch charge	nC	28
Repetition rate	Hz	1
Horizontal RMS emittance (geom)	nm	124
Horizontal RMS emittance (norm)	µm	182
Vertical RMS emittance (geom, 3% coupling)	nm	4
Vertical RMS emittance (norm, 3% coupling)	µm	5.9
RMS energy spread	10^{-3}	0.47
RF		
Frequency	MHz	52.88
Voltage	kV	100
Number of normal conducting cavities		1
Magnet		
Main dipole number		8
Main dipole effective length	m	1.5
Main dipole field	T	1.3099
Quad number		24
Quad effective length	m	0.3
Quad field gradient	T/m	4.6/-2.9/4.7

Table A.2: Beam Accumulator Ring lattice parameters.

Parameter	Unit	Value	Comment
General			
Repetition rate	Hz	1	
Acceleration time	ms, turns	100, 21000	
Number of bunches		1	
Bunch charge	nC	1–28	Varies with operating scenario
Circumference	m	1421.257	
Betatron tune, H		43.12	
V		56.16	
Max beta functions (x,y)	m	30.48, 35.73	
Max dispersion (x)	m	0.59	
Momentum compaction	10^{-4}	6.48	
Injection			
Energy	MeV	750	
RMS emittance (norm; x,y)	µm	$<$180	
RMS energy spread	10^{-3}	$<$0.5	
RMS bunch length	mm, ps	$<$12, $<$40	
Extraction			
Energy	GeV	5–18	
Polarization, 5 GeV	%	85	
10 GeV	%	85	
18 GeV	%	85	
RMS emittance (norm; x,y)	µm	196–845, 18–113	
RMS energy spread	10^{-3}	0.58–1.09	
RMS bunch length	mm, ps	7–9, 23–30	
Radiation per electron (18 GeV)	MeV/turn	101.3	
Horizontal damping time (18 GeV)	ms	2.75	
RF			
Frequency	MHz	591.039	
Voltage	MV	130	
Magnet/Vacuum			
Main dipole number		320	
Main dipole effective length	m	1.8	
Main dipole bend angle	mrad	19.635	
Main dipole field (max)	T	0.65	
Quad number		352	
Quad effective length	m	0.6	
Quad strength K_1 (max)	m^{-2}	0.785	
Sext number		640	
Sext effective length	m	0.2	
Sext strength K_2 (max)	m^{-3}	27.5	
Beam pipe ID, thickness	mm	36.32, 0.89	

Table A.3: Rapid Cycling Synchrotron lattice parameters.

A.2 Electron Storage Ring

The ESR is installed in the existing RHIC tunnel, where it intersects with the HSR in IR6 and IR8. IR6 is equipped with spin rotators, crab cavities, and dedicated low-β magnets, while IR8 contains only a simple cross-over section with the future potential to host a second detector. The circumference ensures that that the electron revolution frequency matches that of 133 GeV on-axis proton beams.

The ESR plane is tilted by 200 µrad with respect to the HSR, about an axis through IP6 and IP8. This results in elevation differences of 104 mm and 208 mm at IP4 and IP12, facilitating the accelerator cross-overs there.

Arc magnets are arranged in a FODO cell pattern. Each half-cell contains two 2.73 m long D13 dipoles and a single 0.89 m D2 dipole, in a "super-bend" structure. All three dipoles are powered uniformly at energies of 10 GeV and above, minimizing synchrotron radiation losses. The D2 dipoles are powered with reverse polarity below 10 GeV, increasing the equilibrium emittance to about 20 nm and increasing radiation damping in order to support a large beam-beam tune shift parameter even at low energy. Arc sextupoles are powered to maximize the dynamic aperture, in family structures that depend on the betatron phase advance in the arc FODO cells, which in turn is chosen depending on the beam energy.

Parameter	**Unit**	**Values**		
Beam energy	GeV	5	10	18
Average polarization	%	70	70	70
Asymptotic polarization	%	16.0	47.4	33.9
Sokolov-Ternov time constant	min	1124	679	33.4
Bunch replacement time, spin up	min	149	451	10.1
spin down	min	231	98.6	3.75
Maximum circulating current	mA	2500	2500	230
Bunch count		1160	1160	290
Maximum bunch charge	nC	28	28	11
Harmonic number		7560	7560	7560
Natural unnormalized RMS emittance	nm	20	20	30
RMS fractional momentum spread	10^{-3}	0.48	0.54	0.97
RMS bunch length	mm	7	7	9
Filling rate	bunches/s	1	1	1
Filling time	min	20	20	5
Beam stored energy	kJ	162	325	57.4

Table A.4: Top level Electron Storage Ring parameters. The Sokolov-Ternov **asymptotic polarization** values apply in the absence of swap-out injection. An average electron polarization of 70% is maintained by frequent bunch replacement. The polarization direction is vertical in the arcs, and longitudinal at the collision point. Spin rotators manipulate the turn-by-turn changes between vertical and longitudinal.

Parameter	Unit	Values		
Beam energy	GeV	5	10	18
Circumference	m	3834.0	3834.0	3834.0
Revolution frequency	kHz	78.193	78.193	78.193
Radio frequency	MHz	591	591	591
Harmonic number		7560	7560	7560
Energy loss per turn	MeV	1.15	3.71	40
Momentum compaction factor	10^{-3}	0.60	1.19	0.60
Betatron tune, H		43.08	43.08	51.08
V		35.14	35.14	43.14
RF Voltage	MV	5.0	22.5	56.0
Number of FODO cells per arc		16	16	16
Phase advance per arc FODO cell	deg.	60	60	90
Average arc bending radius	m	380	380	380
Arc dipole bending radius, D13	m	-52.44	262.26	262.26
D2	m	132.37	262.26	262.26
Arc dipole field, D13	T	-0.32	0.12	0.23
D2	T	0.13	0.12	0.23
Arc quadrupole gradient	T/m	3.74	7.22	18.56
Number of sextupole families per arc		6	6	4
Maximum integrated sextupole gradient	T/m	24.5	65.0	111.2

Table A.5: Electron Storage Ring lattice and orbit parameters

A.3 Hadron Storage Ring

The HSR, based on the Yellow ring, inherits RHIC's versatility to collide a large range of ion species over a wide energy range. It operates with three times more hadron beam current, a larger number of bunches, and a 10% larger maximum beam energy. Copper and amorphous carbon coated beam screens are installed in the vacuum chamber to mitigate resistive wall heating and electron cloud effects. The proton beam circumference is varied by changing the radial orbit, in order to synchronize collisions with the electron beam over an energy range from 100 to 275 GeV. Proton collisions at 41 GeV energy are realized by using an inner arc bypass in the sextant from IP12 to IP2. The warm AtR injection line is considerably extended, bringing hadron beams to IR4 before injection into cold HSR magnets.

Parameter	**Unit**	**Values**	
		Protons	**Gold**
Injection energy	GeV or GeV/u	23.8	10.0
Top energy	GeV or GeV/u	275	110
Injection polarization	%	72	–
Longitudinal/Transverse average polarization	%	70	–
Betatron tune, H		27.23	28.23
V		26.21	29.21
Bunch count, injection		290	290
top		1160	1160
Ions per bunch at store		69×10^9	0.5×10^9
Beam current	A	1.0	0.57
Beam stored energy	MJ	3.53	1.97

Table A.6: Top level Hadron Storage Ring parameters. The average proton polarization of 70% during collisions is an assumption.

Parameter		Unit	Value
Layout and lattice			
Magnetic rigidity, injection		Tm	79.3
	top	Tm	917.3
Arc dipole, bend radius		m	242.78
	top field	T	3.804
	current	kA	5.602
Arc quadrupole gradient		T/m	75.4
Arc beam screen aperture, H		mm	62.4
	V	mm	47.4
RF voltages			
$h = 315$	injection & ramp	MV	0.6
$h = 630$	bunch splitting	MV	0.6
$h = 1260$	bunch splitting	MV	0.6
$h = 2520$	bunch compression	MV	6.0
$h = 7560$	bunch compression	MV	20.0

Table A.7: Hadron Storage Ring lattice, layout, and RF parameters

Parameter	Unit	Values					
		protons				gold	
Total energy	GeV or GeV/u	41	100	133	275	40.7	110 .0
Relativistic γ		43.7	106.6	141.8	293.1	43.7	118.1
Circumference shift	mm	-908.7	-73.4	0.0	73.1	-908.7	-42.1
Average radial shift	mm	–	-11.7	0.0	11.6	–	-6.7

Table A.8: Radial shift parameters in the Hadron Storage Ring

Magnet style	Count	Length m	Bend angle mrad	Quad strength m^{-2}	Inventory
Combined function	25	3.657	48.15	0.03808	RHIC X-arc recycle
Quadrupole	42	0.6		variable	Build to APS Q5 design
Vertical dipole	2	0.5	1.7		New design
Horizontal dipole	2	2.0	30.2		New design
Current septum	1	3.976	50.11		New design
Induction septum	1	1.5	18.41		New design
Dipole corrector	TBD	TBD	TBD		Existing

Table A.9: Hadron Storage Ring injection line magnets

Parameter	Unit	Value
Transition energy	GeV	22.94
Phase Advance per Arc Cell	$^\circ$	87°,85°
Transition γ		24.64
RF voltage	kV	200
RF harmonic number		315
Stable phase	rad	0.074
Acceleration rate	γ/s	0.5
Momentum spread max.		0.0055
Nonlinear factor α_1		-0.53$\times 10^{-3}$

Table A.10: Transition crossing parameters in the Hadron Storage Ring

A.4 Superconducting magnets – Hadron Storage Ring

Electron and hadron beams collide with a crossing angle of 25 mrad at Interaction Point (IP6). There is a total of 27 new superconducting magnets in Interaction Region 6 (IR6), with a mixture of dipoles, quadruples, correctors, and solenoids. Multiple construction technologies are leveraged, including Direct Wind (DW) and cable. Cable magnets use a Rutherford style cable (Ruth.), while the Direct Wind magnets use a six-around-one conductor (6-R-1). Except for dipoles B2pF and B0pF, the new superconducting dipoles and quadrupoles share interconnected cryostats – four on the hadron-forward side, and three in the hadron-rear. The combined function B0pF magnet resides in a dedicated cryostat that includes Q0eF. Some magnets are tapered, with minimum and maximum coil and beampipe radii.

Spin rotator solenoids. Electron spin rotation is performed by solenoids, with help from neighboring dipoles. There are two sets of solenoids on each side of IP6 – a pair of long solenoids used at 18 GeV, and a pair of short solenoids used at 5 GeV. Both pairs are powered at intermediate energies.

		B0pF	**B0ApF**	**B1pF**	**B1ApF**	**B2pF**
Construction		DW	DW	Cable	Cable	Cable
Coil radius	mm	328	TBD	150	TBD	60
Beampipe radius	mm	TBD	43	135	168	50
Lattice length	m	< 1.2	< 0.6	< 3	< 1.5	2.47
Coil length	m	1.2	0.6	3	1.5	2.85
Reference radius	mm	50	26	45	45	30
Field	T	-1.3	3.3	3.4	2.7	6.28
Layers		2	12	1	1	2
Operating current	kA	1.2	2	11.9	13.4	8.2
Quench margin	%	> 20	> 20	> 20	> 20	> 20
Ramp rate	T/s	-0.0065	0.0165	0.017	0.0135	0.031
Temperature	K	1.9	1.9	1.9	1.9	1.9
Strand diameter	mm	0.473	0.473	1.065	1.065	1.065
Conductor style		6-R-1	6-R-1	Ruth.	Ruth.	Ruth.

Table A.11: Superconducting dipoles in the Hadron Storage Ring. The quench margins listed here are the minimum requirements – larger and more realistic values will be included as the magnet designs develop.

		Q1ApF	**Q1BpF**	**Q2pF**	**Q1ApR**	**Q1BpR**	**Q2pR**
Construction		Cable	Cable	Cable	DW	DW	DW
Focus/Defocus		D	D	F	D	D	F
Gradient max.	T/m	89	56	41	78	78	26
Coil rad. min.	mm	71	93		28.35		
max.	mm				34.65		
Pipe rad. min.	mm	56	78	131	20.0	28	54
max.	mm				25.5		
Lattice length	m	<1.46	<1.61	<3.8	<1.8	<1.4	<4.5
Coil length	m	1.46	1.61	3.8	1.8	1.4	4.5
Ref. radius	mm	45	45	83	17	19	36
Layers		2	1	2	8	8	4
Operating current	kA	11	16	8.5	0.9	0.89	1.3
Quench margin	%	> 20	> 20	> 20	> 20	> 20	> 20
Ramp rate	T/ms	-0.44	-0.28	0.21	-0.39	-0.39	0.17
Temperature	K	1.9	1.9	1.9	4.5	4.5	4.5
Strand diam.	mm				0.33	0.33	0.473
Conductor		Ruth.	Ruth.	Ruth.	6-R-1	6-R-1	6-R-1

Table A.12: Superconducting quadrupoles in the Hadron Storage Ring. The quench margins listed here are the minimum requirements – larger and more realistic values will be included as the magnet designs develop.

		B0ApF -SkQ	**B0ApF -Vcorr**	**Q1ApR -SkQ**	**Q2pR -Hcorr**	**Q2pR -Vcorr**
Construction		DW	DW	DW	DW	DW
Corrector type		Skew quad	V dipole	Skew quad	H dipole	V dipole
Coil rad. min.	mm	TBD	TBD	28.35		
max	mm			34.65		
Beampipe rad. min.	mm	43.0	43.0	20.0	54	54
max.	mm			25.5		
Lattice length	m	< 0.6	< 0.6	<1.8	<4.5	<4.5
Coil length	m	0.6	0.6	1.8	4.5	4.5
Field	T		0.6		0.6	0.6
Integrated gradient	T	3.0		3.0		
Layers		2	2	2	2	2
Operating current	kA	TBD	TBD	TBD	TBD	TBD
Quench margin	%	TBD	TBD	TBD	TBD	TBD
Temperature	K	1.9	1.9	4.5	4.5	4.5
Strand diam.	mm	0.33	0.33	0.33	0.33	0.33
Conductor		strand	strand	strand	strand	strand

Table A.13: Superconducting correctors in the Hadron Storage Ring

A.5 Superconducting magnets – Electron Storage Ring

		Q0eF	**Q1eF**	**Q1eR**	**Q2eR**
Construction		DW	DW	DW	DW
Corrector Focus/Defocus		D	F	D	F
Gradient max.	T/m	14	6.3	14	14.1
Coil radius	mm				
Beampipe rad min.	mm	26	64.8	47.6	64.5
max.	mm			55.5	
Lattice length	m	$<$1.2	$<$1.61	$<$1.8	$<$1.4
Coil length	m	1.2	1.61	1.8	1.4
Reference radius	mm	17	43	TBD	20
Layers		4	2	4	2
Operating current	kA	0.08	1	1.8	1.8
Quench margin	%	$>$ 20	$>$ 20	$>$ 20	$>$ 20
Temperature	K	4.5	1.9	4.5	4.5
Strand diameter	mm	0.33	1.0	0.33	1.0
Conductor style			6-R-1		6-R-1

Table A.14: Superconducting quadrupoles in the Electron Storage Ring. The quench margins listed here are the minimum requirements – larger and more realistic values will be included as the magnet designs develop. The abbreviation "DW" stands for Direct Wind.

		B2eRDrift -Vcorr	Q0eF -Hcorr	Q0eF -shield	Q1eF -Vcorr	Q1eF -SkQ	Q2eR -SkQ
Construction		DW	DW	DW	DW	DW	DW
Corrector type		V dipole	H dipole		V dipole	Skew Q	Skew Q
Coil radius	mm						
Pipe rad min.	mm	50.0	26.0	26.0	64.8	64.8	50.0
Lattice length	m	<5.5	<1.2	<1.2	<1.61	<1.61	<1.54
Coil length	m	TBD	1.2	1.2	1.61	1.61	1.54
Field	T	0.6	0.6	TBD	0.6		
Integ. gradient	T					3.0	3.0
Layers		2	2	2	2	2	2
Operating current	A	TBD	80	80	1	TBD	TBD
Quench margin	%					TBD	TBD
Temperature	K	4.5	4.5	4.5	1.9	1.9	4.5
Strand diameter	mm	0.33	0.33	0.33	0.33	0.33	0.33
Conductor style		strand	strand	strand	strand	strand	strand

Table A.15: Superconducting correctors in the Electron Storage Ring

Parameter	Unit	Values	
		Short	Long
Coil radius	mm	86.0	86.0
Beampipe radius	mm	50.0	50.0
Lattice length	m	2.5	6.2
Coil length	m	1.874	5.68
Reference radius	mm	33.0	33.0
Integrated field	Tm	15.30	46.75
Layers		33	33
Operating current	kA	0.866	0.874
Quench margin	%	> 20	> 20
Inductance	mH	6.04	18.71
Stored energy	MJ	2.26	7.14
Temperature	K	1.9	1.9
Strand diameter	mm	1.6	1.6
Conductor style		WIC	WIC

Table A.16: Superconducting spin rotator solenoids. The quench margins listed here are the minimum requirements – larger and more realistic values will be included as the magnet designs develop.

A.6 Cryogenic Systems

The Cryogenics Systems consist of the existing Central Plant located near sector 5, and Satellite Plants located near their associated loads. The Central Plant provides 4.5 K cooling to HSR components, interfaces with the Satellite Plants, and processes return gas from the Satellite Plants. Satellite Plants provide 1.92 K and 2 K cooling to components located in IR4, IR6, and IR10 by processing the 4.5 K helium down to 1.92 K for spin rotators, or 2.0 K for other SRF components. They also return helium gas back to the Central Plant.

Parameter	**Unit**	**Value**
Refrigeration capacity at 4.5 K	kW	55
Temperature	K	4.5
Pressure	bar	16
Compressor flow at full capacity	g/s	4500
Existing distribution length (RHIC)	km	~ 4
Liquefaction load (4.5 to 300 K)	g/s	45
Re-liquefaction load (4.5 to 4.5 K)	g/s	288
Non-isothermal load (4.5 to 10 K	g/s	282
Non-isothermal load (45 to 80 K)	g/s	102
Valve box count		8
Cryogenic controls I/O channel count		7500

Table A.17: Cryogenics central plant capacity and loads, after configuration for EIC operations.

Parameter	**Unit**	**Value**
Temperature	K	4.6
Cryogenic load at 4.6 K	W	100
Flow rate at 4.6 K load	g/s	6
Load on thermal shield (45 to 80 K)	W	600
Flow rate on thermal shield	g/s	3
Current lead intercepts load (4.5 to 300 K)	W	850
Flow rate on current lead intercepts (4.5 to 80 K)	g/s	0.5
Electrical cryogenic heater count		4
Cryogenic distribution length	m	40
Valve box count		2
Cryogenic valve count		14

Table A.18: ePIC Detector Solenoid cryogenics

Parameter	Unit	Values		
		IR4	**IR6**	**IR10**
Cryogenic load at 2 K	W	500	650	1250
Temperature – main load	K	2	1.92	2
Temperature – SRF cryomodules	K	2	2	2
Flow rate at 2 K load	g/s	24	45	63
Current lead intercepts load (4.5 to 80 K)	W	TBD	6050	2220
Flow rate on current lead intercepts (4.5 to 80 K)	g/s	TBD	17.14	24
Cryogenic distribution length	m	TBD	168	163
Valve box count		8	19	12
Cryogenic valve count		56	95	60
I/O channel count		1272	1744	1220
Electrical cryogenic heater count		32	76	50

Table A.19: Cryogenics satellite plants

A.7 Infrastructure

The Electron-Ion Collider Conventional Facilities provide the buildings, utility systems and site infrastructure systems necessary to enable installation and operation of the EIC electron injector, electron and hadron storage rings, the interaction region, the ePIC detector, and support components.

The EIC project leverages the existing accelerator tunnel and related existing buildings that were constructed in the late 1970's for the Relativistic Heavy Ion Collider. The primary EIC facilities, typically reinforced concrete structures, are located adjacent to the existing Insertion Regions IR2, IR4, IR6, IR8, IR10, and IR12. Smaller buildings, located outside the berm and tunnel profile at the 1 o'clock, 3 o'clock, 5 o'clock, 7 o'clock, 9 o'clock, and 11 o'clock arc positions, house power supplies that serve magnet systems within the tunnel. These buildings also contain the mechanical cooling water pump and heat exchanger systems that serve magnet, power supply and vacuum beam pipe cooling.

The largest new EIC building will be located at IR10. This building (1010C) houses the RF equipment that powers the RF cavities located within the existing Insertion Region. This complex also includes water cooling and electrical power distribution systems for the loads in this area.

Building 638 is also expanded, adding two additional 69 kV/13.8 kV transformers and associated switchgear to distribute additional power to the EIC site via new overhead lines.

Appendix B

Glossary (editors: Peggs, Satogata)

Name	Description
aC	amorphous Carbon
ACS	Access Control Systems
ADC	Analog to Digital Converter
ADO	Accelerator Device Object, device software manager in C++ programming
AGS	Alternating Gradient Synchrotron: an accelerator at Brookhaven National Laboratory that serves as injector to RHIC
ANL	Argonne National Laboratory
API	Application (Program) Interface
APS	Argonne Photon Source: a light source facility at Argonne National Laboratory
ARR	Accelerator Readiness Review
ATLAS	A colliding beams detector at the CERN Large Hadron Collider
AtR	AGS to RHIC beam transfer line: a part of RHIC accelerator complex
AWG	American Wire Gauge
B-factory	A particle collider designed to produce large numbers of B mesons
B-field	Magnetic field
BLA	Beam Line Absorbers
BLM	Beam Loss Monitor
BNL	Brookhaven National Laboratory
BPM	Beam Position Monitor
CAD	Computer Aided Design
C-AD	Collider-Accelerator Department, Brookhaven National Laboratory
CBI	Coupled bunch instability
CBM	Coupled bunch modes
CC	Crab Cavity
CCD	Charged Coupled Device: a silicon chip for capturing and manipulating digital data
CCG	Cold cathode ion gauge
CDEV	Common Device interface
CDR	Conceptual Design Report
CDS	Computers, Devices, and Software
CEBAF	Continuous Electron Beam Accelerator Facility at TJNAF, Virginia
CEC	Coherent Electron Cooling
CEM	Channeled Electron Multiplier

CERN	European Organization for Nuclear Research: accelerator laboratory in Switzerland
CESR	Cornell Electron Storage Ring facility
CM or c.m.	Center of mass
CME	Center of mass energy
CMOS	Complementary Metal-Oxide-Semiconductor: a silicon chip for manipulating digital data
CNS	Controls Name Server
COMPASS	An experiment at CERN utilizing muon and proton beams
COTS	Commercial off-the-shelf
CSR	Coherent synchrotron radiation
CVD	Chemical Vapor Deposition
DAC	Digital to Analog Converter
DAFNE	An accelerator facility in Frascati, Italy
DCCT	Direct Current Current Transformer: a precision DC current transducer
DESY	Deutsche Electronen Synchrotron Laboratory: an accelerator facility in Hamburg, Germany
DOE	U.S. Department of Energy
DoS	Density of State
DQW	Double Quarter Wave
DQWCC	Double Quarter Wave Crab Cavity
DVCS	Deeply Virtual Compton Scattering
DVVM	Deeply Virtual Vector Meson
EBIS	Electron Beam Ion Source
EBW	Electron Beam Welding
EH&S	Environment Health and Safety
EHS&Q	Environment Health Safety and Quality
EIC	Electron Ion Collider
EIS	Environmental Impact Statement
EMC	European Muon Collaboration experiment at CERN
EOM	Electro-Optic Modulator
EPS	Equipment control and Protection System at RHIC
ERL	Energy Recovery LINAC
ESR	Electron Storage Ring: a part of EIC accelerator complex
eSTAR	A proposed EIC detector based on the existing STAR detector at RHIC
FCT	Fast Current Transformer
FEC	Front End Controller/Computer
FEL	Free Electron Laser
FHA	Fire Hazard Analysis
FMD	Fundamental Mode Damper
FODO	A particular grouping of focusing and defocusing magnets used in accelerator beams
FONSI	Finding of No Significant Impact
FPC	Fundamental Power Coupler
FPGA	Field-Programmable Gate Array
FRIB	Facility for Rare Isotope Beams under construction at Michigan State University
FSAD	Final Safety Analysis Document
FY	Fiscal Year
GEMA	planar multi-electrode array used to measure particle trajectories in gas-filled detectors
GPIB	General Purpose Interface Bus, IEEE-488

GPM	General Purpose Monitor
HAR	Hadron Accelerator Ring: a part of EIC accelerator complex
HEBT	High Energy Beam Transport
HERA	Hadron-Electron Ring Accelerator at DESY in Hamburg, Germany
HERMES	A fixed-target experiment at HERA facility
HHOM	Horizontal Higher Order Modes
HOM	Higher Order Modes
HSR	Hadron Storage Ring: a part of EIC accelerator complex
HTTP	Hypertext Transfer Protocol
IBS	Intrabeam Scattering
ICR	Independent Cost Review
ICT	Integrating Current Transformer
IEEE	Institute of Electrical and Electronics Engineers
ILC	International Linear Collider
INT	Institute for Nuclear Theory at the University of Washington, Seattle
IOT	Inductive Output Tube: a vacuum tube used as a high power RF amplifier
IP	Interaction Point
IAD	Ion Assisted Deposition
IPM	Ionization Profile Monitor
IR	Interaction Region
ISO	Optical isolator, or International Standards Organization
IVA	Inductive Voltage Adder
JFT	A Japanese tokamak fusion research facility
TJNAF	Thomas Jefferson National Accelerator Facility, Newport News, Virginia
KEK	High Energy Accelerator Research Laboratory, Tsukuba, Japan
KEKB	A particle accelerator operating as a B-factory at KEK
KPP	Key Performance Parameter
LARP	Large Hadron Collider (LHC) Accelerator Research Program
LBNL	Lawrence Berkeley National Laboratory in California
LDRD	Laboratory Directed Research and Development
LEP	Large Electron Positron collider, predecessor to the LHC at CERN
LEReC	Low Energy RHIC electron Cooling
LHC	Large Hadron Collider at CERN in Geneva, Switzerland
LINAC	Linear Accelerator
LLRF	Low Level Radio Frequency
LPOL	Longitudinal polarization measurement of the electron beam at HERA
LtR	LINAC to RCS transfer line: a part of EIC accelerator complex
MAPS	A planar multi-electrode array on a microchip, used to measure charged particle trajectories in compact gas-filled detectors
MBEC	Micro-bunched electron beams
MCP	Micro Channel Plate detector
MPS	Machine Protection System
NAS	National Academy of Science and Network Attached Storage system
NCRF	Normal Conducting Radio Frequency
NEA	Negative Electron Affinity
NEG	Non-Evaporation Getter
NEPA	National Environmental Policy Act
NPCT	New Parametric Current Transformer
NSAC	Nuclear Science Advisory Committee for U.S. Department of Energy
NSLS-II	National Synchrotron Light Source-II at Brookhaven National Laboratory
NSRL	NASA Space Radiation Laboratory at Brookhaven National Laboratory

ODH	Oxygen Deficiency Hazard
OFHC	Oxygen-Free High Conductivity copper
OPPIS	A polarized ion source used for injection of polarized protons into RHIC
OTR	Optical Transition Radiation
PASS	Personnel Access Safety System
PDF	Particle Distribution Function
PED	Project Engineering and Design
PEP-II	Positron-Electron Project, a colliding beams facility at SLAC
PETRA	A high energy electron-positron accelerator facility at DESY, now operating as a light source
PFL	Pulse Forming Line
PHENIX	A large colliding-beams detector at RHIC
PID	Particle Identification
PLC	Programmable Logic Controller
PLL	Phase-Locked Loop
PoP	Proof of Principle
PPM	Office of Project Management
PPS	Personnel Protection System
PSAD	Preliminary Safety Assessment Document
PSD	Photon Stimulated Desorption, or Power Spectrum Density
PSEG	A local utility company providing electrical power to Brookhaven National Laboratory
PSI	Power Supply Interface
PVD	Physical Vapor Deposition
PWO	Lead Tungstate crystal
QCD	Quantum Chromodynamics
QE	Quantum Efficiency
QWR	Quarter-Wave Resonator
RACF	RHIC and ATLAS Computing Facility at Brookhaven National Laboratory
R&D	Research and Development
RCS	Rapid Cycling Synchrotron: a part of EIC accelerator complex
RCStSR	The beam transfer line from RCS to the EIC Storage Ring
REST	Representational State Transfer protocol
RF	Radio Frequency
RFD	RF-Dipole
RGA	Residual Gas Analyzer
RHIC	Relativistic Heavy Ion Collider at Brookhaven National Laboratory
RICH	Ring Imaging Cherenkov detector
RMS	Root Mean Square
RRR	Residual Resistivity Ratio
RTD	Resistance Temperature Detector
RTDL	Real Time Data Link
RtS	RCS to electron Storage Ring transfer line, a part of EIC accelerator complex
SAD	Safety Assessment Document
SBEND	Sector Bend in RCS ring lattice
SBMS	Standards-Based Management System
SCCR	Short Circuit Current Rating
SEY	Secondary Emission Yield
SIDIS	Semi-Inclusive Deep Inelastic Scattering (of high energy electrons)
SIL	Safety Integrated Level
Sindi	Synoptic Display tool

SIP	Sputtering Ion Pump
SLAC	Stanford Linear Accelerator Center in California SLC SLAC Linear Collider
SLM	Synchrotron Light Monitor
SM	Standard Model of particle physics
sPHENIX	A proposed new RHIC detector to replace PHENIX
SPS	Super Proton Synchrotron, and accelerator at CERN
SR	Synchrotron Radiation
SRF	Superconducting Radio-Frequency
SRP/CS	Safety Related Parts of Control Systems
SRS	Spin Rotator Solenoid
SW	Standing Wave
SOC	System on a Chip
Tape	Tool for Automated Procedure Execution
T-BMT	Thomas-BMT equation, named after Thomas, Bargmann-Michel-Telegdi
TAL	Triplet Achromat Lattice
TBA	Triple Bend Achromat
TEC	Total Estimated Cost
TIG	Tungsten Inert Gas (a specialized form of welding)
TMCI	Transverse Mode Coupling Instability
TMD	Transverse Momentum Distribution
TMP	Turbomolecular Pump
TPC	Time Projection Chamber
TPOL	Transverse Polarization measured for the electron beam at HERA
TSP	Titanium Sublimation Pumps
TWP	Traveling Wave Plates
UHV	Ultra-High Vacuum
UPC	Ultra-Peripheral Collisions
UPS	Uninterruptable Power Supply
VCO	Voltage Controlled Oscillator
VCXO	Voltage Controlled Crystal Oscillator
VHOM	Vertical Higher Order Modes
VME	VERSAModule Europa, IEEE-1014-1987, chassis for electronic control modules
WCM	Wall Current Monitor
WOW	Wide Open Waveguide
XDB	Xray Diagnostic Beamline
XHV	Extremely High Vacuum
YAG	A type of laser using a Yttrium-Aluminum-Garnet crystal
ZDC	Zero Degree Calorimeter
ZEUS	A large detector at the HERA collider
ZFCT	Zero Flux Current Transformer, a type of DCCT